HYDROGEN- AND HALOGEN-BOND DRIVEN CO-CRYSTALLIZATIONS: FROM FUNDAMENTAL SUPRAMOLECULAR CHEMISTRY TO PRACTICAL MATERIALS SCIENCE

by

THARANGA KUMUDINI WIJETHUNGA WIDANALAGE DONA

B.S., University of Colombo, 2010

AN ABSTRACT OF A DISSERTATION

submitted in partial fulfillment of the requirements for the degree

DOCTOR OF PHILOSOPHY

Department of Chemistry
College of Arts and Sciences

KANSAS STATE UNIVERSITY
Manhattan, Kansas

2015

Abstract

A series of co-crystallizations between four biimidazole based compounds with nine symmetric aliphatic di-acids and fifteen perfluorinated halogen-bond donors were carried out to determine if a MEPS based ranking can be used to effectively assign selectivity in hydrogen- and halogen-bond interactions. The results suggested that a simple electrostatic view provides a reliable tool for successfully implementing the practical co-crystal synthesis with desired connectivity.

MEPS based selectivity guidelines for halogen-bond interactions were explored in co-crystallizations between twelve asymmetric ditopic acceptors and nine halogen-bond donors. If the difference between the two acceptor sites is below 35 kJ/mol, no selectivity was observed; above 65 kJ/mol halogen bond selectivity dominates and mid ΔE range was recognized as the grey area where predictions cannot be made.

To examine competition between hydrogen and halogen bonds, five heteroaryl-2-imidazoles were co-crystallized with fifteen halogen-bond donors. It was found that halogen bonds prefer best the acceptor site, demonstrating that a suitably activated halogen-bond donor can compete with a strong hydrogen-bond donor.

The benefits of 'double activation' for promoting halogen bond effectiveness was explored with nine haloethynylnitrobenzenes. The positive potential on halogen atoms was enhanced through a combination of an *sp*-hybridized carbon and electron-withdrawing nitro group(s). Iodoethynylnitrobenzenes were identified as the most effective halogen-bond donors reported to date and the compounds were exploited for the interaction preferences of nitro group and nitro···X-C_{sp} interactions were identified as synthetic tools for energetic co-crystal assembly.

A synthetic strategy for the deliberate assembly of molecular polygons was developed utilizing bifurcated halogen bonds constructed from N-oxides and complementary halogen-bond donors via co-crystallization.

A convenient, effective, and scalable protocol for stabilizing volatile liquid chemicals with co-crystallization was achieved. Through the use of halogen-bonding, liquid iodoperfluoroalkanes were transformed into crystalline materials with low-vapor pressure, considerable thermal stability and moisture resistance.

To stabilize the energetic compound ethylenedinitramine, a co-crystallization approach targeting the acidic protons was employed. Eight co-crystals were obtained and the acceptors were identified as supramolecular protecting groups leading to diminished reactivity and enhanced stability while retaining the desirable energetic properties.

HYDROGEN- AND HALOGEN-BOND DRIVEN CO-CRYSTALLIZATIONS: FROM FUNDAMENTAL SUPRAMOLECULAR CHEMISTRY TO PRACTICAL MATERIALS SCIENCE

by

THARANGA KUMUDINI WIJETHUNGA WIDANALAGE DONA

B.S., University of Colombo, 2010

A DISSERTATION

submitted in partial fulfillment of the requirements for the degree

DOCTOR OF PHILOSOPHY

Department of Chemistry
College of Arts and Sciences

KANSAS STATE UNIVERSITY
Manhattan, Kansas

2015

Approved by:

Major Professor
Christer B. Aakeröy

Copyright

Abstract

A series of co-crystallizations between four biimidazole based compounds with nine symmetric aliphatic di-acids and fifteen perfluorinated halogen-bond donors were carried out to determine if a MEPS based ranking can be used to effectively assign selectivity in hydrogen- and halogen-bond interactions. The results suggested that a simple electrostatic view provides a reliable tool for successfully implementing the practical co-crystal synthesis with desired connectivity.

MEPS based selectivity guidelines for halogen-bond interactions were explored in co-crystallizations between twelve asymmetric ditopic acceptors and nine halogen-bond donors. If the difference between the two acceptor sites is below 35 kJ/mol, no selectivity was observed; above 65 kJ/mol halogen bond selectivity dominates and mid ΔE range was recognized as the grey area where predictions cannot be made.

To examine competition between hydrogen and halogen bonds, five heteroaryl-2-imidazoles were co-crystallized with fifteen halogen-bond donors. It was found that halogen bonds prefer best the acceptor site, demonstrating that a suitably activated halogen-bond donor can compete with a strong hydrogen-bond donor.

The benefits of 'double activation' for promoting halogen bond effectiveness was explored with nine haloethynylnitrobenzenes. The positive potential on halogen atoms was enhanced through a combination of an *sp*-hybridized carbon and electron-withdrawing nitro group(s). Iodoethynylnitrobenzenes were identified as the most effective halogen-bond donors reported to date and the compounds were exploited for the interaction preferences of nitro group and nitro···X-C_{sp} interactions were identified as synthetic tools for energetic co-crystal assembly.

A synthetic strategy for the deliberate assembly of molecular polygons was developed utilizing bifurcated halogen bonds constructed from N-oxides and complementary halogen-bond donors via co-crystallization.

A convenient, effective, and scalable protocol for stabilizing volatile liquid chemicals with co-crystallization was achieved. Through the use of halogen-bonding, liquid iodoperfluoroalkanes were transformed into crystalline materials with low-vapor pressure, considerable thermal stability and moisture resistance.

To stabilize the energetic compound ethylenedinitramine, a co-crystallization approach targeting the acidic protons was employed. Eight co-crystals were obtained and the acceptors were identified as supramolecular protecting groups leading to diminished reactivity and enhanced stability while retaining the desirable energetic properties.

Table of Contents

List of Figures

List of Tables

Acknowledgements

First of all, I would like to express my utmost gratitude to my advisor Professor Christer Aakeröy whose care, immense support, encouragement and patience, guided me to achieve my Ph.D. goal and beyond. He made me a better writer, a better presenter, a better scientist and a confident individual. I consider myself so fortunate to join his group and he is the best supervisor I could have ever asked for. Thank you very much for being my guiding star and I hope to follow your footsteps to the very end in an academic career…!

I would also like to thank my Ph.D. advisory committee, Professor Christine Aikens, Professor Emily McLaurin, Professor Jennifer Anthony and Professor Mohammad Hosni for their valuable time and input…!

A special thank is extended to Professor Eric Maatta, Professor Kenneth Klabunde and Professor Christopher Levy for helping me to widen my knowledge in Chemistry.

I also wish to extend my deepest gratitude to Dr. John Desper for all the crystal structures he has solved. Those structures made my dissertation a meaningful, complete, alive and an attractive one. I am also grateful to Dr. Curtis Moore, Dr. Marijana Đaković and Dr. Tomce Runcevski for solving structures for this dissertation.

I want to acknowledge Department of Chemistry, Kansas State University, National Science Foundation, US Army Research Office and US Army Research Laboratory for funding throughout my Ph.D. life. I also want to extend a special gratitude to Professor Adam Matzger and the Multidisciplinary University Research Initiative (MURI) team for all the knowledge and opportunities given.

A special gratitude is extended to Dr. Yasmin Patel, Dr. Leila Maurmann, Ms. Earline Dikeman, Mr. Jim Hodgson, Mr. Ron Jackson, Mr. Tobe Eggers, Ms. Mary Dooley, Ms. Kimberly Ross and, Ms. Lisa Percival for making my life at K-State a memorable one.

I was fortunate to share my Ph.D. life with all the past and present members of Aakeröy group. You all have a special place in my heart. Thank you very much for all the fun times…! A special thank is extended to Janaka, Chamara and Stefan for all the help in conducting drop impact tests.

My special regards to all my teachers because of whose teachings at different stages of my education have made it possible to pursue my dreams. I also want to thank all my friends in Sri Lanka and here in Manhattan, for making my life a joyful one.

My heartfelt gratitude goes to my brother for always being there for me and for taking care of my mom and dad while I am thousands and thousands miles away from home. Thank you so much for all the love and affection you have extended…!

I am also immensely thankful to my parents for their unconditional love, blessings and the support that they have given me in each and every step of my life. They have sacrificed a lot to make me the person who I am today and gave me the strength to reach for the stars. Thank you very much for letting me pursue my dreams even it meant that I have to be far away from you…!

Finally, I want to thank my husband Amendra, for being my best friend and love of my life. You have always been there by my side in each and every step of my life. Your infallible love, care, support, encouragement and understanding, walked me through these years. Thank you very much for being the best partner ever…!

Dedication

To my mom and dad

For their endless love, support and encouragement

To my brother

For being the best brother in the world

&

To my husband

For being the greatest supporter and the best partner in life

Thank you all…!

Preface

Research carried out at Kansas State University for this dissertation led to the following publications in scientific journals:

1. Aakeröy, C.B.; Wijethunga, T.K.; Desper, J. "Constructing molecular polygons using halogen bonding and bifurcated N-oxides", *CrystEngComm* **2014**, *16*, 28-31.
2. Aakeröy, C.B.; Wijethunga, T.K.; Haj, M.A.; Desper, J.; Moore, C. "The structural landscape of heteroaryl-2-imidazoles: competing halogen- and hydrogen-bond interactions", *CrystEngComm* **2014**, *16*, 7218-7225.
3. Aakeröy, C.B.; Wijethunga, T.K.; Desper, J. "Practical crystal engineering using halogen bonding: A hierarchy based on calculated molecular electrostatic potential surfaces", *J. Mol. Struct.* **2014**, *1072*, 20-27.
4. Aakeröy, C.B.; Wijethunga, T.K.; Benton, J.; Desper, J. "Stabilizing volatile liquid chemicals using co-crystallization", *Chem. Commun*. **2015**, *51*, 2425-2428.
5. Aakeröy, C.B.; Wijethunga, T.K.; Desper, J. "Molecular electrostatic potential dependent selectivity of hydrogen bonding", *New J. Chem.* **2015**, *39*, 822-828 (Featured on the cover).
6. Aakeröy, C.B.; Wijethunga, T.K.; Desper, J.; Moore, C. "Halogen-bond preferences in co-crystal synthesis", *J. Chem. Crystallogr*. **2015**, *45*, 267-276.
7. Aakeröy, C.B.; Wijethunga, T.K.; Desper, J. "Crystal engineering of energetic materials: Co-crystals of ethylenedinitramine (EDNA) with modified performance and improved chemical stability", *Chem. Eur. J.* **2015**, *21*, 11029-11037 (Featured on the cover).
8. Aakeröy, C.B.; Wijethunga, T.K.; Desper, J.; Đakovic, M. "Crystal engineering with iodoethynylnitrobenzenes: A group of highly effective halogen-bond donors", *Cryst. Growth Des.* **2015**, *15*, 3853-3861.

Chapter 1 - Introduction

1.1 Structure-property relationship in chemistry

The axiom that "function follows form" is of fundamental importance in chemistry and the design and preparation of materials with desired properties are principal goals of chemists.[1] The very essence of chemistry, the periodic table, provides a systematic classification of all known elements into different periods and groups to help chemists in rationalizing the properties of these elements based on their structure at an atomic level. Moving from the atomic to the molecular level, a pioneering investigation conducted in 1947 on saturated hydrocarbons recognized that the properties of these compounds varied with molecular bulk and branching.[2]

One of the many examples of structure-property relationship in molecules comes from the enantiomers of thalidomide, Figure 1.1.[3] It turns out that one enantiomer has effective antidepressant properties while the other is teratogenic.[4] The property difference is directly connected to the chirality of the molecular structure.

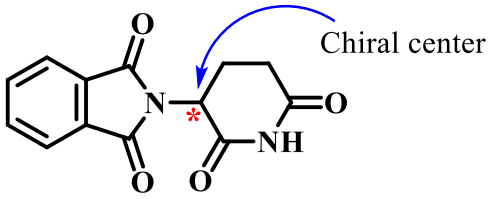

Figure 1.1 Chemical structure of thalidomide

1.1.1 Structure-property relationship in bulk materials

For bulk materials, structure-property relations fall into two broad categories,[5] Figure 1.2. In the first, the property alterations are due to variations in molecular structure and molecular conformation. In the second category property alterations arise from differences in the spatial relationships between molecules in the crystal, such as intermolecular arrangement, interactions and packing of individual building blocks with respect to each other in a crystal lattice. Thus, in

order to manipulate the properties of bulk materials, either alterations of molecular structure and conformations or refinements in packing arrangements are required.

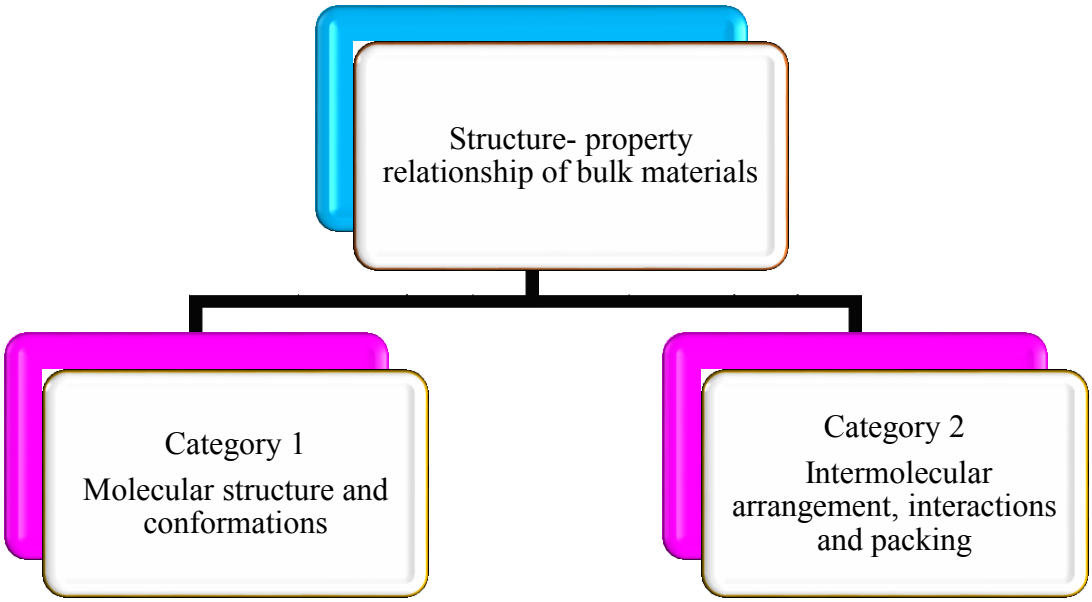

Figure 1.2 Categorization of structure-property relationships in bulk materials

The best examples which show property alterations under both above categories are polymorphs. A polymorph is defined as "*Different crystalline forms of the same substance*".[6] Polymorphs of a substance can be attained in two ways (Figure 1.3), if the molecule can have different conformations and if the molecule is flexible, polymorphs can be attained by conformational changes (conformational polymorphism) and if the molecule is rigid, polymorphs can be attained by changing the packing arrangements (packing polymorphism).[7] Conformational polymorphs give rise to property alterations under category 1 and packing polymorphs under category 2, Figure 1.2.

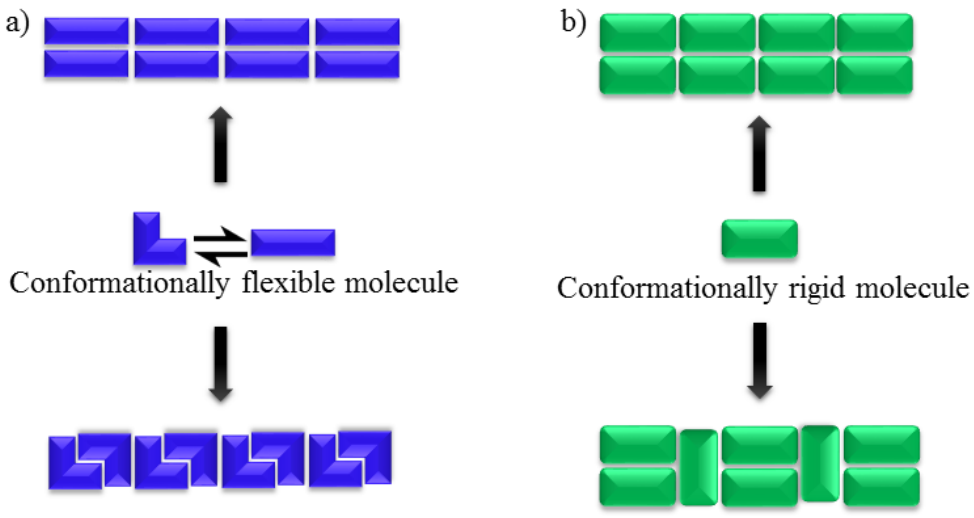

Figure 1.3 Schematic representation of a) conformational polymorphism and b) packing polymorphism

Ritonavir provides an example of conformational polymorphism where form 1 is comprised of beta like stacks of ritonavir molecules held together via hydrogen bonding while in form II, OH groups are participating in hydrogen bonding due to the change in conformation of ritonavir molecule. As a result, solubility of the two forms are distinct from each other. Form 1 has 90 mg/mL of solubility in a 99:1 ethanol water mixture at 5 °C and form II has only 19 mg/mL of solubility under same conditions,[8] Figure 1.4.

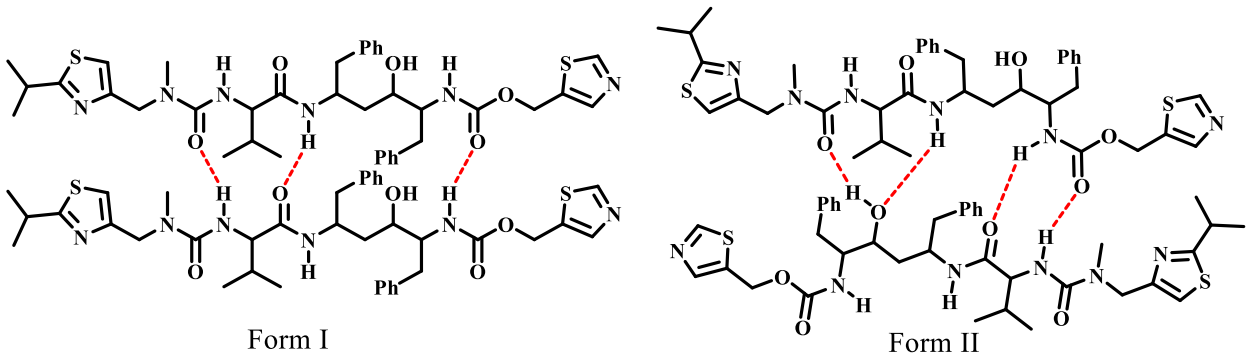

Figure 1.4 Conformational polymorphs of ritonavir and their solubilities[8]

Polymorphic forms of aspirin provide an example of packing polymorphism. Both form I and II consist of layers of aspirin molecules with same conformation and similar interactions, and the subtle difference between the two forms is the position of the molecules in one layer relative to the molecules of the adjacent layer, Figure 1.5. When considering the properties, form II is unstable under mechanical stress such as milling and tableting, and readily converted to stable form I.[9]

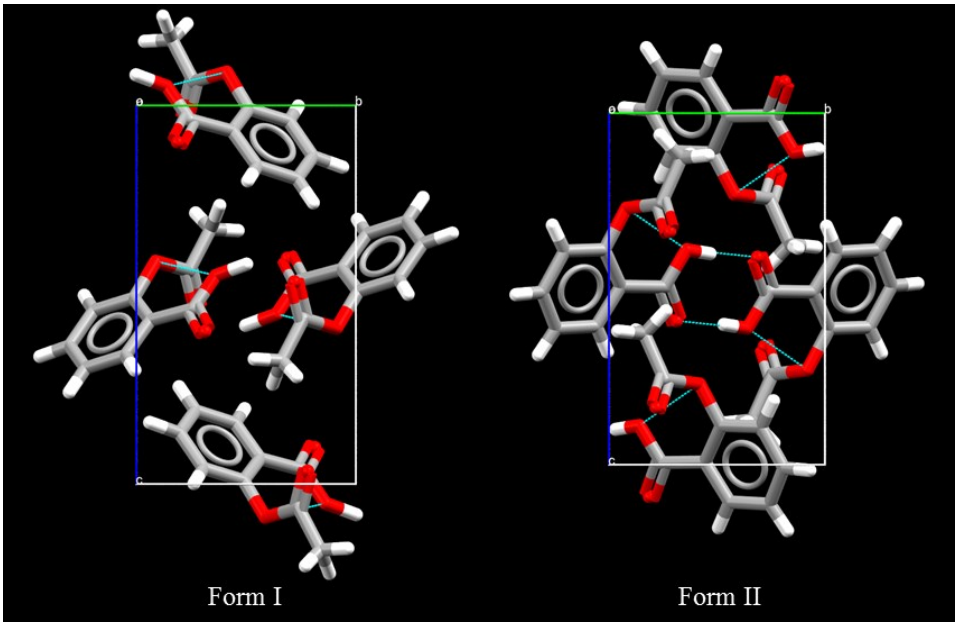

Figure 1.5 Packing of aspirin polymorphs shown along the a axis[9]

One of the well-known example for how the changes in molecular structure correlate with the materials properties comes from even numbered aliphatic dicarboxylic acids. It has been observed that melting points of dicarboxylic acids decrease monotonically with increasing number of methylene groups in the chain, Figure 1.6.[10] Thus alteration of molecular structure by adding methylene groups, leads to a predictable alteration of melting properties in the bulk.

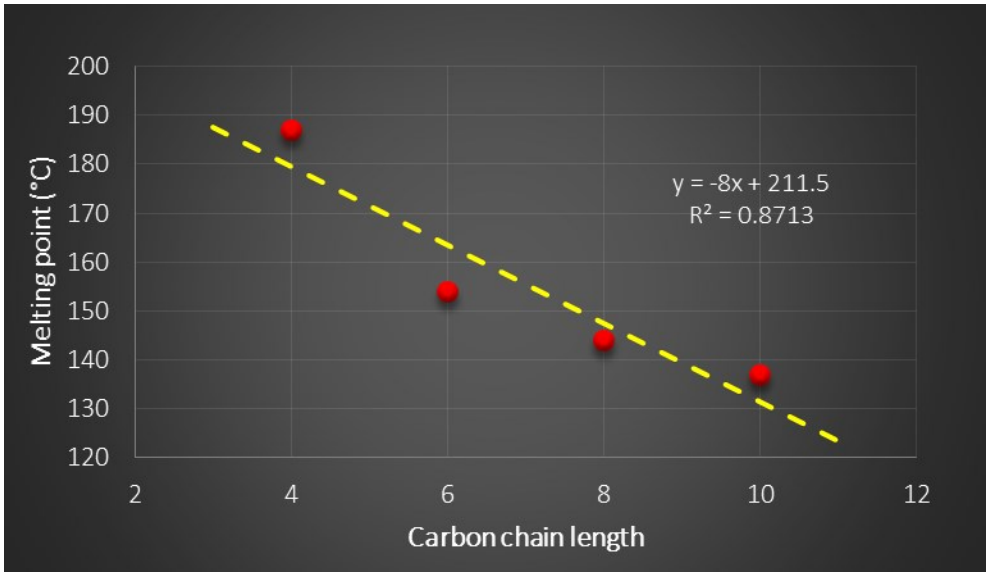

Figure 1.6 Correlation between the carbon chain length and the melting temperature of aliphatic dicarboxylic acids[10]

1.2 Supramolecular chemistry: A way to modify spatial relationships of a molecule

Supramolecular chemistry has been defined as *"…the chemistry of the intermolecular bond, covering the structures and functions of the entities formed by association of two or more chemical species…"* by Jean-Marie Lehn.[11] In simple terms, supramolecular chemistry refers to chemistry beyond molecules and focuses on chemical systems composed of molecular subunits brought together via intermolecular interactions.[12] One of the underlying goals of supramolecular chemistry is to control assembly and arrangement of individual components in a predictable way and thus to control macroscopic properties of materials.

Because supramolecular chemistry can lead to modifications in the spatial relationships of a molecule of interest, it directly affects macroscopic properties. As an example, *trans*-stilbene molecule is known to give only weak fluorescence in solution and inside loosely-fitting synthetic capsules. But it has been shown that by encapsulating *trans*-stilbene in an elongated

supramolecular capsule made up of cavitand molecules, where the molecule is allowed to adapt a fully coplanar arrangement, fluorescence of the molecule is enhanced, Figure 1.7.[13]

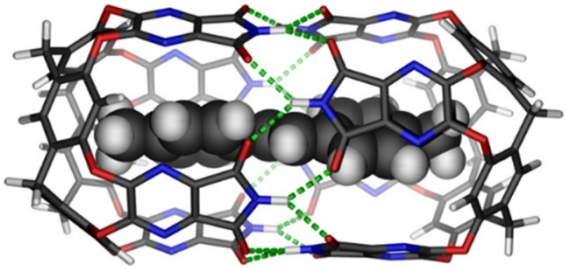

Figure 1.7 Encapsulated *trans*-stilbene inside a cavitand derived capsule[13]

1.3 Crystal engineering: Design of ultimate supramolecules

Organic crystals can be recognized as the best examples of supramolecules. Indeed Jack Dunitz has referred to organic crystals as "supermolecule(s) *par excellence"*[14] where millions of molecules are held together in a periodic arrangement by non-covalent interactions. The subsection of supramolecular chemistry which focuses on crystals, their packing and property alterations has been identified as crystal engineering. Thus, crystal engineering has defined as "*The understanding of intermolecular interactions in the context of crystal packing and the utilization of such understanding in the design of new solids with desired physical and chemical properties*".[15]

1.3.1 Supramolecular synthons

If crystals can be recognized as supramolecular equivalents of molecules, then crystal engineering can be recognized as the supramolecular equivalent of organic synthesis.[16] Organic synthesis mainly depends on traditional synthons, likewise definite spatial arrangements of intermolecular interactions are required to establish reliable connections between individual building blocks in crystal engineering. Supramolecular synthons are such recognition units and have been defined as "*structural units within a supermolecule which can be formed andlor assembled by known or conceivable synthetic operations involving intermolecular interactions".*[17]

Supramolecular synthons can be categorized as homosynthons (occur between same complementary functional groups) and heterosynthons (occur between different functional groups),[18] Figure 1.8.

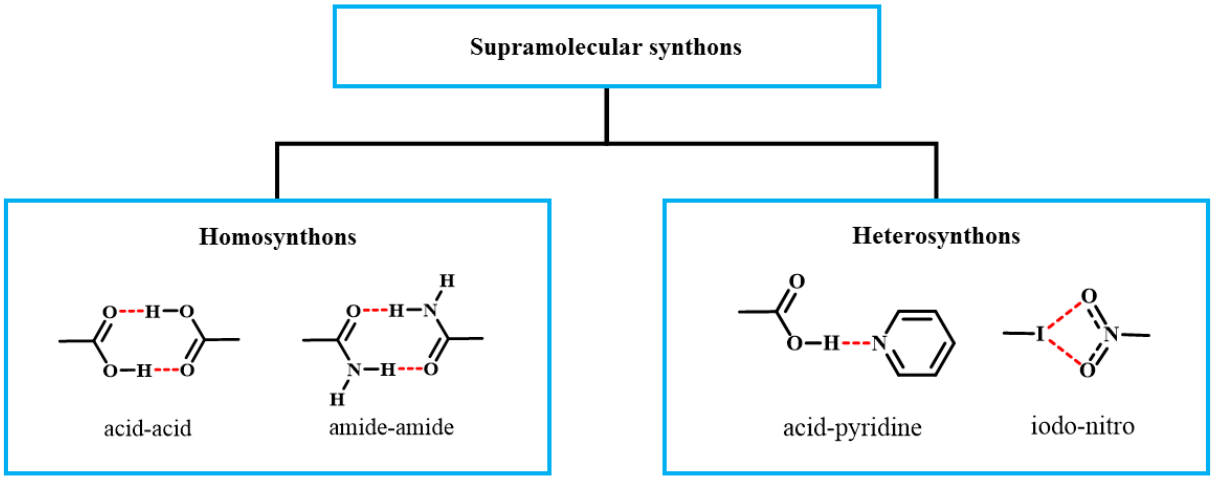

Figure 1.8 Supramolecular synthons

1.4 Co-crystal: A supramolecular entity

The definition of what a co-crystal is, remains under debate.[19] Thus, for the scope of this dissertation, a co-crystal will be defined as, *solids that are crystalline single phase materials composed of two or more different molecular compounds generally in a stoichiometric ratio*. In simple terms, a co-crystal is comprised of two or more distinctly different molecular entities known as co-formers that are brought together via non-covalent interactions within the same crystal lattice. This is done without making or breaking any covalent bonds, thus the chemical integrity of each individual molecule is preserved. The end result is the formation of a heteromeric species via co-crystallization over the natural tendency to form homomeric species via re-crystallization, Figure 1.9. Thus, a co-crystal can be recognized as a supramolecular entity which enables the

modification of physical properties of a material by changing the spatial relationships between molecules in the crystal.

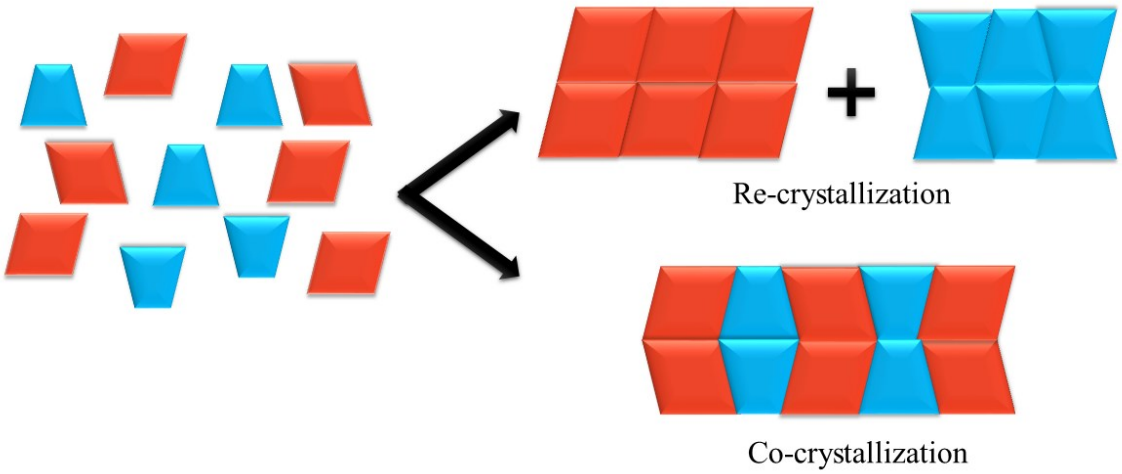

Figure 1.9 Schematic representation of re-crystallization and co-crystallization

1.5 Intermolecular interactions: Glue to design co-crystals

Co-crystals contain periodic assemblies of molecules connected via intermolecular interactions such as π-π stacking interactions,[20] dipole-dipole interactions,[21] halogen bonds,[22] and hydrogen bonds,[23] Figure 1.10. Knowledge of the intermolecular interactions and their effects on crystal packing allows for the engineering of co-crystals with desired properties.

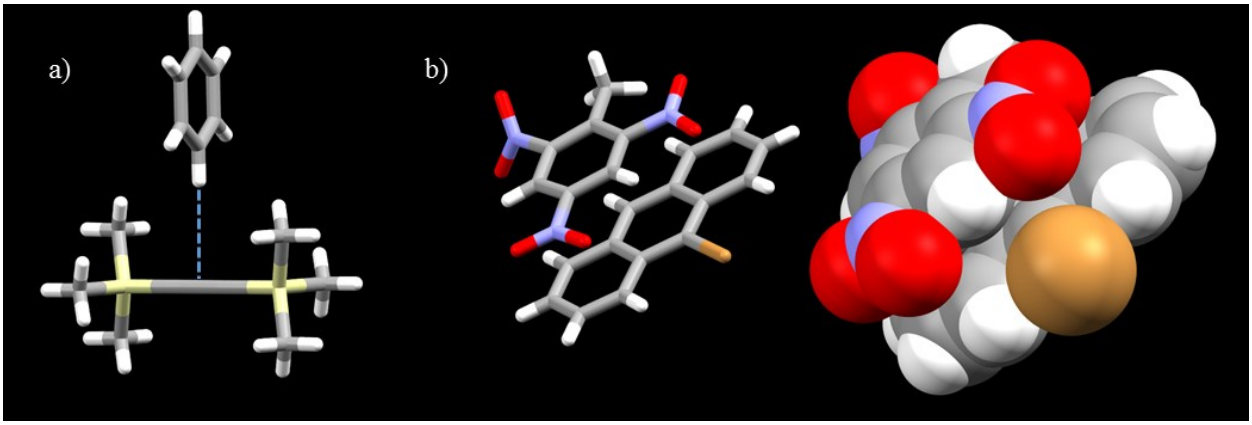

Figure 1.10 a) CH···π interactions in the co-crystal of bis(trimethylsilyl)acetylene with benzene[24] and b) π-π interactions in the co-crystal between trinitrotoluene (TNT) and 9-bromoanthracene[25]

1.5.1 Hydrogen bond based co-crystals

A hydrogen bond (HB) is defined as "*an attractive interaction between a hydrogen atom from a molecule or a molecular fragment, X−H···A in which X is more electronegative than H, and an atom or a group of atoms in the same or different molecule, in which there is evidence of bond formation*",[26] Figure 1.11.

Figure 1.11 Schematic diagram showing the formation of a hydrogen bond (X-more electronegative atom than hydrogen; H-hydrogen; A-acceptor)

Hydrogen bonds are useful tools for assembling supramolecular structures because they are both strong and directional and arguably the most widely used interaction for constructing co-crystals,[27] Figure 1.12. In order to recognize the preferred connectivity patterns, the hydrogen-bond rules proposed by Margaret C. Etter are very useful.[28]

The general rules are,

1. All acidic hydrogens available in a molecule will be used in hydrogen bonding in the crystal structure of that compound.[29]
2. All good acceptors will be used in hydrogen bonding when there are available hydrogen-bond donors.[30]
3. The best hydrogen-bond donor and the best hydrogen-bond acceptor will preferentially form hydrogen bonds to one another.[31]

These guidelines have provided the stage for important advances in co-crystallizations.

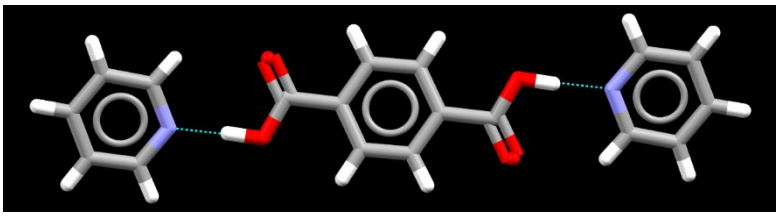

Figure 1.12 A binary co-crystal between pyridine and terephthalic acid formed via acid···pyridine heterosynthon[32]

1.5.2 Halogen bond based co-crystals

The definition of halogen bond (XB) states that, "*A halogen bond R–X···Y–Z occurs when there is evidence of a net attractive interaction between an electrophilic region on a halogen atom X belonging to a molecule or a molecular fragment R–X (where R can be another atom, including X, or a group of atoms) and a nucleophilic region of a molecule, or molecular fragment, Y–Z*",[33] Figure 1.13

Figure 1.13 Schematic diagram showing the formation of a halogen bond (R and Z-molecular fragments or atoms; X-halogen atom; Y-nucleophilic atom)

As a new addition to the toolbox of supramolecular chemistry, the halogen bond has gained widespread attraction due to its strong, specific and directional nature.[34] Key to this interaction is the electron-poor nature of the tip of the halogen atom known as the σ hole,[35] whose electron-density is depleted by virtue of the presence of an electron withdrawing group, Figure 1.14. The R–X···Y angle is typically close to 180°.[36] The strength of the interaction increases in going from chlorine to bromine to iodine depending on the polarizability of the halogen atom.[37] Electrostatic attractive nature of halogen bonds result in a shorter distance between the donor and acceptor to the sum of their van der Waals radii.[38] Figure 1.15 shows a conventional halogen bond formed between iodine and nitrogen.

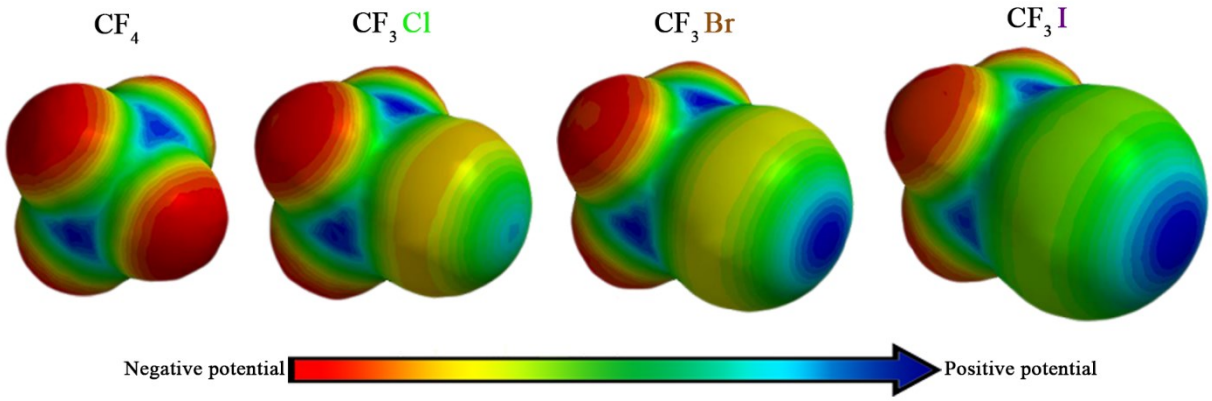

Figure 1.14 Formation of the σ hole in halogen atoms

Figure 1.15 A halogen bond formed between the iodine of 1,4-diiodotetrafluorobenzene and pyridine nitrogen of 4-dimethylaminopyridine[39]

1.5.2.1 Techniques to detect halogen bonds

The best method to detect halogen bond formation in solid state is single crystal X-ray diffraction (SCXRD). This is the most common experimental method of obtaining a detailed 3D structure of a molecule that allows resolution of individual atoms, and provides detailed information about the internal lattice of crystalline substances, including unit cell dimensions, bond-lengths, bond-angles, and intermolecular interactions.[40] SCXRD is performed by analyzing the pattern of X-rays diffracted by an ordered array of many identical molecules (single crystal) and requires diffractable crystals in good quality and reasonable size, which is not easily accessible always. Thus, other characterization techniques like NMR, IR, Raman, UV-Vis, EPR and calorimetry based techniques are utilized for the purpose of detecting halogen bond formation in solid, solution and gas phases.

NMR spectroscopy is the method of choice in detecting halogen bonds in solution. For example, ^{19}F NMR spectroscopy has been utilized to detect chemical shift alterations of polyfluorinated XB donors upon interaction with solvents of varying electron donating properties. It has observed that a stronger Lewis basic solvent causes a larger ^{19}F shift alteration reflecting the strength of the formed XB interactions, Figure 1.16.[41]

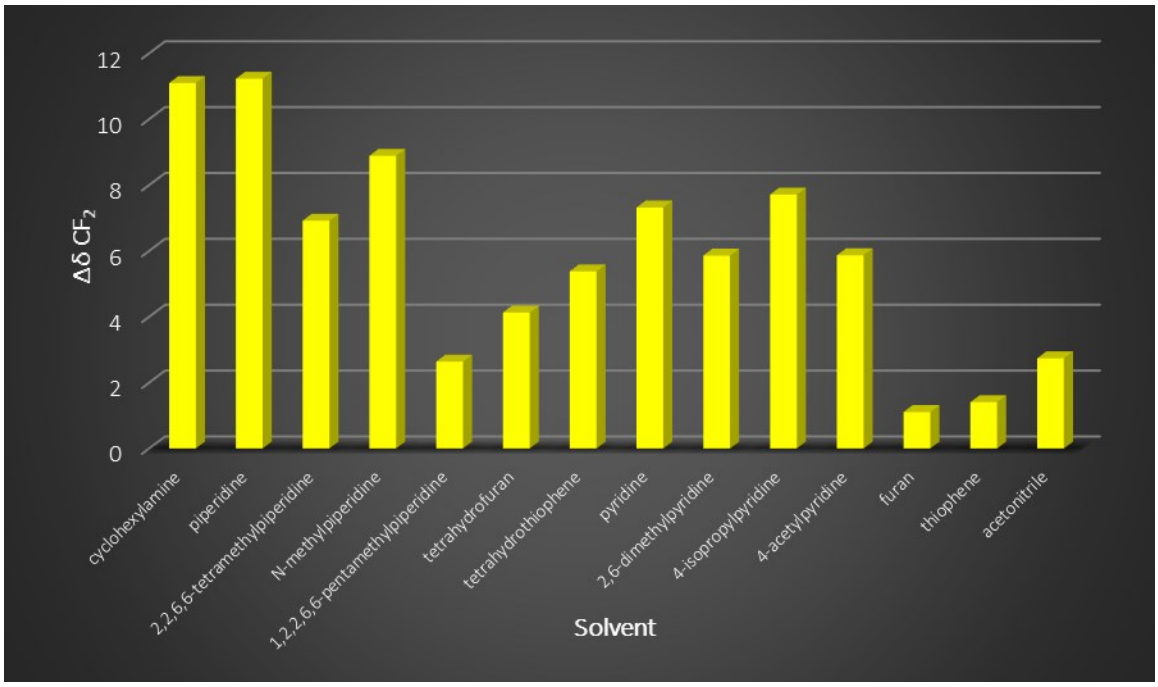

Figure 1.16 ^{19}F NMR chemical shift differences ($\Delta\delta$) of 1,2-diiodoperfluoroethane in cyclohexane and the given solvent[41]

IR spectroscopy is a simple and effective method in detecting halogen bond formation both in solid and solution phases. For example, when a halogen bond is formed with an ethynyl iodine atom, the weakening of triple bond occurs, which is accompanied by a red shift of the triple bond stretch in IR spectra,[42] Figure 1.17.

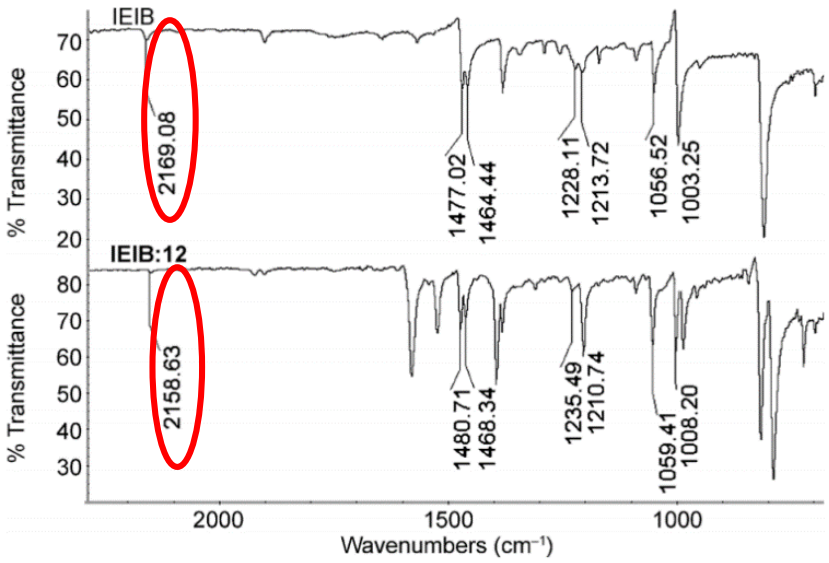

Figure 1.17 Comparison of IR spectra between 1-iodoethynyl-4-iodobenzene (IEIB) and the co-crystal of IEIB formed with 4,4'-bipyridine (IEIB:12); red circles highlights the shifts in triple bond stretch[42]

1.6 Application of co-crystals

Co-crystal technology has been used for altering the physical properties of pharmaceuticals,[43] energetic materials,[44] agrochemicals,[45] nutraceuticals,[46] organic semiconductors,[47] optoelectronic materials,[48] ferroelectric materials,[49] charge transfer complexes,[50] non-linear optics[51] and liquid crystals.[52] Furthermore, co-crystallization approaches have been applied in solid state solvent free synthesis,[53] separation and purification processes,[54] chiral resolution,[55] and crystallization of non-solid compounds to facilitate manufacturing processes.[56]

1.6.1 Pharmaceutical co-crystals

The most widely applied field of co-crystallization is development of pharmaceutical co-crystals. In this area co-crystallization has shown prominent results in the formation, design and implementation of active pharmaceutical ingredients (API).[57] Changing the solid form of an API can greatly influence its bioavailability, thermal stability and solubility.[58] Pharmaceutical co-

crystals focus on developing superior physico-chemical properties of the API while holding the properties of the drug molecule itself constant.[59]

For instance, one study showed how to systematically modulate the aqueous solubility and melting behavior of an anticancer drug hexamethylene-4-pyridineacetamide with the assistance of hydrogen-bond based co-crystallization, Figure 1.18.[60]

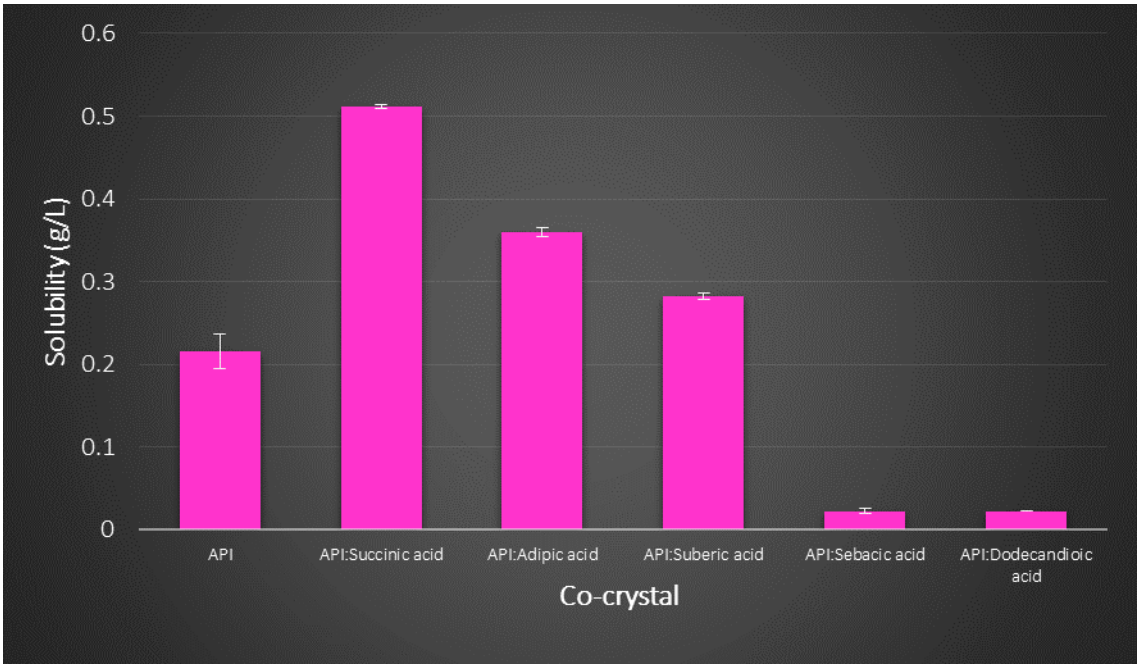

Figure 1.18 Aqueous equilibrium solubilities of the API of interest and the five co-crystals obtained with even chain dicarboxylic acids[60]

Another example provides evidence for the halogen-bond based co-crystals of the antimicrobial drug 3-iodo-2-propynyl-N-butylcarbamate (IPBC). Angle of repose tests were conducted to study the powder flow properties of the drug and the co-crystals obtained. Free IPBC has poor flow properties (no angle of repose is detectable), while the co-crystal involving the excipient $CaCl_2$ has shown superior powder flow characteristics (20° angle of repose form funnel/flat surface distance of 25 mm), representing a promising solution to the handling issues related to the manufacturing of products containing IPBC.[61]

1.6.2 Energetic co-crystals

Energetic materials are a class of compounds that rapidly release energy through a chemical reaction or change of state, often accompanied by the expansion of gas.[62] The term energetic materials encompasses three basic materials classes: explosives, propellants, and pyrotechnics.[63] Explosives contain destructive power, while propellants supply thrust for rockets and engines. Pyrotechnics include both explosives and propellants and are used to produce various effects, including light, color, smoke and sound.

When designing safe and effective energetic compounds, a large number of critical properties need to be addressed. The main property to consider is the explosive power, and this property is affected by the other factors such as density, detonation enthalpy, oxygen balance and gas formation upon detonation.[64] Another factor to consider is safety, which is based on the sensitivity of the material to shock, impact and spark[65] and also the toxicity of the compound and detonation products.[66] Furthermore, cost, processability, water solubility and chemical stability are critical factors to consider when designing novel energetics.[67]

Traditional methods for improving these properties focus on modifying the chemical structure.[68] Co-crystallization is an alternative route to modify the properties of available energetic materials to design superior materials.[69]

One of the most famous examples in the field of energetic co-crystals is the 1:2 hybrid co-crystal of HMX and CL-20. The co-crystal is a combination of the low sensitivity of HMX and high power of CL-20, thus provided a solution to overcome the drawbacks associated with both starting energetic compounds, Figure 1.19.[64]

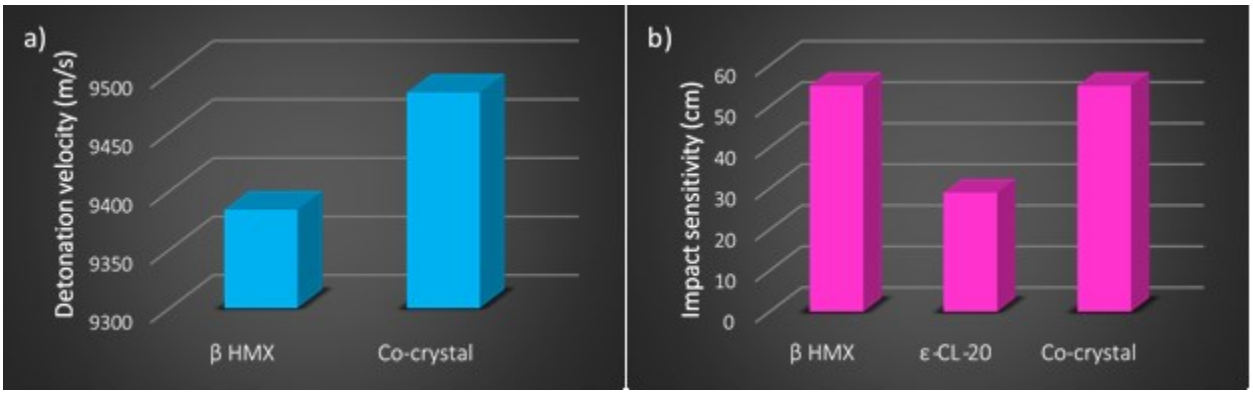

Figure 1.19 a) Detonation velocity comparison and b) impact sensitivity comparison for HMX and CL-20 co-crystal and starting compounds[64]

1.6.3 Agrochemical co-crystals

Agrochemicals refers to chemicals used for agricultural purposes such as pesticides, insecticides, herbicides and fungicides and are used to protect crops from pests and thus help to improve the quality and quantity of crop production.[70] Co-crystallizations provides means for altering the physical properties such as solubility, hygroscopicity, thermal stability, filterability and flowability of agrochemicals and thereby affecting the overall usability and efficacy of a given agrochemical. For example, flupyradifurone is an active ingredient (AI) with insecticidal properties. Co-crystal of the AI with salicylic acid (1:1) has been synthesized which displays a higher melting point, 85 °C when compared to that of the active by itself (72-74 °C).[71]

Another study highlights the ability of fine-tuning the solubility of an agrochemical active, cyprodinil, via co-crystallization. Co-crystals of cyprodinil have been obtained with even chain aliphatic dicarboxylic acids (C4-C12) and for the co-crystal with succinic acid (C4), more than threefold increase in the solubility has observed, Figure 1.20.[72]

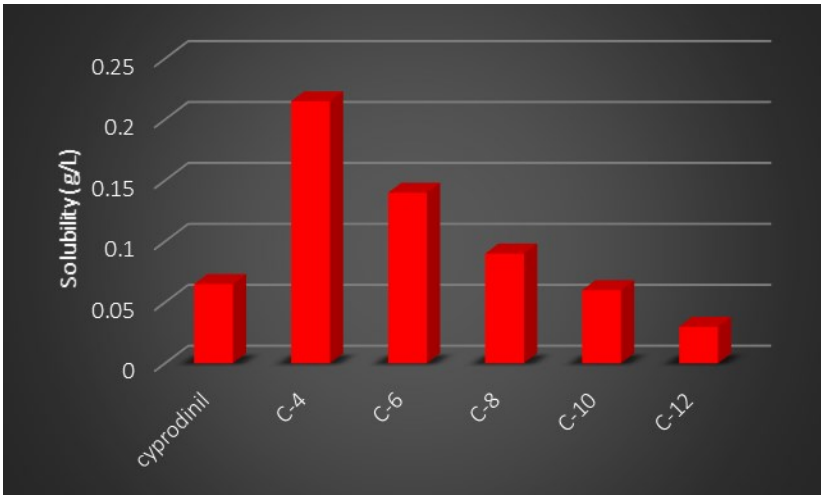

Figure 1.20 Solubility profile of cyprodinil co-crystals[72]

1.6.4 Nutraceutical co-crystals

Nutraceuticals are defined as "*a food (or part of a food) that provides medical or health benefits, including the prevention and/or treatment of a disease and possesses a physiological benefit or reduces the risk of chronic disease*".[73] Nutraceuticals have become attractive targets for co-crystallizations as many of them have major problems with solubility and bioavailability. For an instance co-crystals of curcumin with resorcinol and pyrogallol have obtained and the melting point analysis has shown the co-crystals (with resorcinol - 166 °C; with pyrogallol - 158 °C) to have lower melting points than curcumin (177 °C).[74]

In another study, co-crystals of pterostilbene have obtained with carbamazepine, piperazine and caffeine. The solubility studies have shown that co-crystal obtained with piperazine to show six fold higher aqueous solubility and co-crystal with caffeine to have 27 fold solubility compared to single-component pterostilbene. On the other hand, co-crystal with carbamazepine has decreased the overall solubility of pterostilbene nearly by threefold, Figure 1.21.[75]

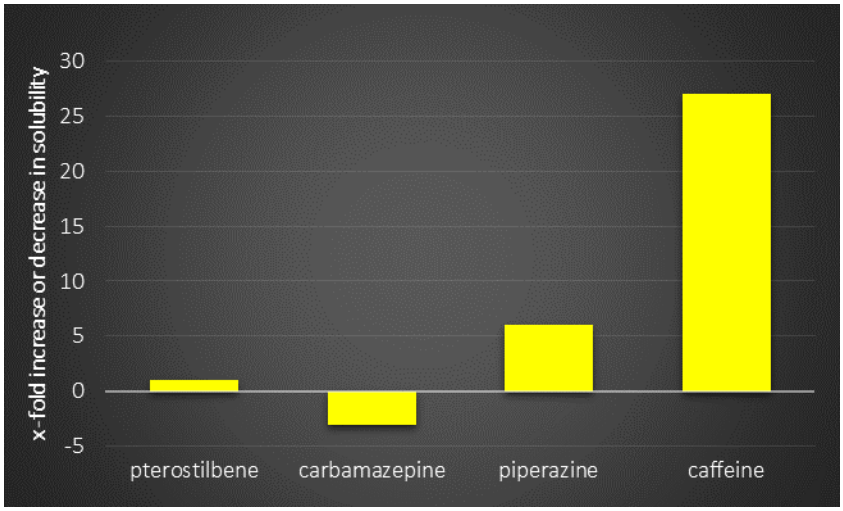

Figure 1.21 Aqueous solubility of pterostilbene and co-crystals[75]

1.6.5 Organic semiconductor co-crystals

Organic semiconductors are extended conjugated π-systems that have the ability to transport charge when an electrical bias is applied. Enforced face-to-face stacking of aromatics in the solid state is important to achieve efficient charge transport properties of these materials. Co-crystallization provides effective means in stacking the semiconductor building blocks. One such study has shown how the co-former, resorcinol could enforce face-to-face π-stacking of the semiconductor building block 9,10-bis(4-pyridylethynyl)anthracene, Figure 1.22.[76]

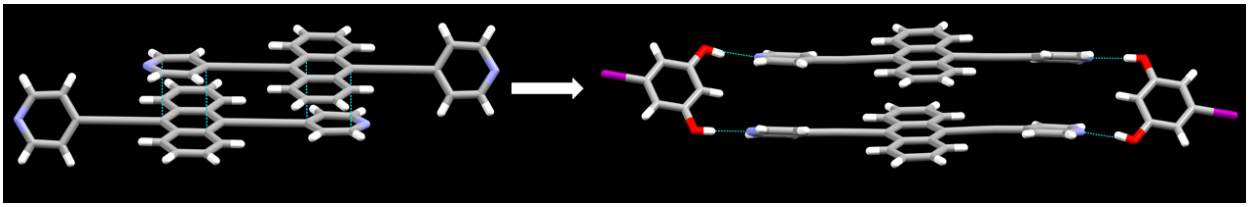

Figure 1.22 Effective face to-face π-stacking achieved via co-crystallization[76]

1.7 Goals of the dissertation

Designing co-crystals with practical applications in materials science requires a thorough understanding of solid state behavior of non-covalent interactions and a good rationale to control

the supramolecular architectures in a predictable manner. Such controlled supramolecular assemblies can lead to a better understanding of structure-property relationships. The basic concepts can then be focused on spatial modifications of functional materials leading to fine-tuning of macroscopic properties.

Thus, this dissertation will focus on the following goals,

1. Chapter 2 focuses on understanding the molecular electrostatic potential dependent selectivity behaviors of hydrogen bond interactions in the solid state and on implementing a simple electrostatic view for co-crystal synthesis.[77]
2. Chapter 3 focuses on the solid state behavior of halogen bonding, specifically how a simple molecular electrostatic potential surface (MEPS) based view can be used in predicting selectivity in halogen bonding.[78]
3. Chapter 4 explores if MEPS based selectivity of halogen bonding can lead to guidelines that can be used for predicting preferable halogen bonds.
4. Chapter 5 focuses on the competitive nature of hydrogen bonding and halogen bonding when probed with multiple acceptor sites.[79]
5. Chapter 6 focuses on design and synthesis of more effective halogen-bond donors, haloethynylnitrobenzenes, using double activation phenomena.[80]
6. Chapter 7 combines complementary geometric factors of selected halogen-bond donors in designing well-defined and discrete supramolecular architectures.[81]
7. The capability of halogen-bond based co-crystallization to stabilize volatile liquid chemicals and the effectiveness, scalability, isolation capabilities and property alterations of this technology is explored in Chapter 8.[82]

8. Chapter 9 focuses on establishing the effectiveness of co-crystal technology to modify the properties of an energetic compound, ethylenedinitarmine (**EDNA**). The main goal is to eliminate the high chemical reactivity of **EDNA** by introducing a supramolecular protecting group.[83]

1.8 References

1. Seybold, P.G.; May, M.; Bagal, U.A. *J. Chem. Educ.* **1987**, *64*, 575-581.

2. Wiener, H. *J. Am. Chem. Soc.* **1947**, *69*, 17-20; Wiener, H. *J. Am. Chem. Soc.* **1947**, *69*, 2636-2638.

3. Eriksson, T.; Björkman, S.; Roth, B.; Fyge, Å; Höglund, P. *Chirality* **1998**, *10*, 223-228.

4. D'Amato, R.J.; Loughnan, M.S.; Flynn, E.; Folkman, J. *Proc. Nati. Acad. Sci. USA* **1994**, *91*, 4082-4085.

5. Bernstein, J. *J. Phys. D: Appl. Phys.* **1993**, *26*, B66.

6. Desiraju, G.R. *Cryst. Growth Des.* **2008**, *8*, 3-5.

7. Redinha, J.S.; Lopes Jesus, A.J.; Pais, A.A.C.C.; Almeida, J. A. S. *Crystallization: From the Conformer to the Crystal, Advanced Topics on Crystal Growth*, InTech, **2013**.

8. Bauer, J.; Spanton, S.; Henry, R.; Quick, J.; Dziki, D.; Porter, W.; Morris, J. *Pharmaceut. Res.* **2001**, *18*, 859-866.

9. Bond, A.D.; Boese, R.; Desiraju, G.R. *Angew. Chem. Int. Ed. Engl.* **2007**, *46*, 618-622.

10. Thalladi, V. R.; Nusse, M.; Boese, R. *J. Am. Chem. Soc.* **2000**, *122*, 9227-9236; Vishweshwar, P.; Nangia, A.; Lynch, V. M. *Cryst. Growth Des.* **2003**, *3*, 783-790.

11. Lehn, J.M. Nobel Lecture, December 8, **1987**.

12. Desiraju, G. R. *Nature* **2001**, *412*, 397-400; Lehn, J.M. *Supramolecular Chemistry: Concepts and Perspectives*, VCH, Weinheim, **1995**; Lehn, J.M. *Pure & Appl. Chem.* **1980**, *52*, 2441-2459.

13. Ams, M.R.; Ajami, D.; Craig, S.L.; Yang, J.; Rebek, J. *Beilstein J. Org. Chem*. **2009**, *5*, 79.

14. Desiraju, G. R.; Sharma, C. V. K. *Crystal Engineering and Molecular Recognition-Twin Facets of Supramolecular Chemistry. In Perspectives in Supramolecular Chemistry*. John Wiley & Sons, **2007**.

15. Desiraju, G. R. *Crystal Engineering: The design of Organic Solids*, Elsevier, **1989**.

16. Thalladi, V.R.; Goud, B.S.; Hoy, V.J.; Allen, F.H.; Howard, J.A.K.; Desiraju, G.R. *Chem. Commun.* **1996**, 401-402.

17. Desiraju, G. R. *Angew. Chem., Int. Ed. Engl.* **1995**, *34*, 2311-2327.

18. Almarsson, Ö.; Zaworotko, M.J. *Chem. Commun.* **2004**, 1889-1896.

19. Dunitz, J.D. *CrystEngComm* **2003**, *5*, 506-506; Desiraju, G.R. *CrystEngComm* **2003**, *5*, 466-467; Bond, A.D. *CrystEngComm* **2007**, *9*, 833-834**;** Aakeröy, C. B.; Salmon, D. J. *CrystEngComm* **2005**, *7*, 439-448.

20. Chang, Y.C.; Chen, Y.D.; Chen, C.H.; Wen, Y.S.; Lin, J.T.; Chen, H.Y.; Kuo, M.Y.; Chao, I. *J. Org. Chem.* **2008**, *73*, 4608-4614.

21. Madura, I. D.; Czerwińska, K.; Jakubczyk, M.; Pawełko, A.; Adamczyk-Woźniak, A.; Sporzyński, A. *Cryst. Growth Des.* **2013**, *13*, 5344-5352.

22. Meazza, L.; Foster, J. A.; Fucke, K.; Metrangolo, P.; Resnati, G.; Steed, J. W. *Nature Chem.* **2013**, *5*, 42-47; Präsang, C.; Whitwood, A.C.; Bruce, D.W. *Cryst. Growth Des.* **2009**, *9*, 5319-5326.

23. Skovsgaard, S.; Bond, A. D. *CrystEngComm* **2009**, *11*, 444-453; Glidewell, C.; Ferguson, G.; Gregson, R. M.; Lough, A. J. *Acta Crystallogr., Sect. C.: Cryst. Struct. Commun.* **1999**, *55*, 2133-2136.

24. Wegner, F.M.; Lerner, H.W.; Bolte, M. *Acta Cryst.* **2010**, *C66*, o182-o184.

25. Landenberger, K.B.; Matzger, A.J. *Cryst. Growth Des.* **2010**, *10*, 5341-5347.

26. Arunan, E.; Desiraju, G.R.; Klein, R.A.; Sadlej, J.; Scheiner, S.; Alkorta, I.; Clary, D.C.; Crabtree, R.H.; Dannenberg, J.J.; Hobza, P.; Kjaergaard, H.G.; Legon, A.C.; Mennucci, B.; Nesbitt, D.J. *Pure Appl. Chem*. **2011**, *83*, 1619-1636.

27. Seto, C. T.; Whitesides, G. M. *J. Am. Chem. Soc.* **1991**, *113*, 712-713; Aakeröy, C. B.; Seddon, K. R. *Chem. Soc. Rev.* **1993**, *22*, 397-407; Tiekink, E. R. T.; Vittal, J.; Zaworotko, M. *Organic Crystal Engineering: Frontiers in Crystal Engineering*, Wiley, John & Sons Inc., **2010**.

28. Etter, M. C. *Acc. Chem. Res.* **1990**, *23*, 120-126; Etter, M. C. *J. Phys. Chem.* **1991**, *95,* 4601-4610.

29. Donohue, J. *J. Phys. Chem*. **1952**, *56*, 502-510.

30. Etter, M.C. *J. Am. Chem. Soc*. **1982**, *104,* 1095-1096.

31. Taylor, R.; Kennard, O. *Acc. Chem. Res*. **1984**, *17*, 320-326.

32. Dale, S.H.; Elsegood, M.R.J.; Hemmings, M.; Wilkinson, A.L. *CrystEngComm* **2004**, *6*, 207-214.

33. Desiraju, G.R.; Ho, S.; Kloo, L.; Legon, A.C.; Marquardt, R.; Metrangolo, P.; Politzer, P.A.; Resnati, G.; Rissanen, K. *Pure Appl. Chem.* **2013**, *85*, 1711-1713.

34. Gavezzotti, A. *Mol. Phys.* **2008** *106*, 1473-1485; Crihfield, A.; Hartwell, J.; Phelps, D.; Walsh, R.B.; Harris, J.L.; Payne, J.F.; Pennington, W.T.; Hanks, T.W. *Cryst.Growth Des* **2003**, *3*, 313-320; Karpfen, A.; *Theor. Chem. Acc.* **2003**, *110*, 1-9; Shen, Q.J.; Jin, W.J. *Phys. Chem. Chem. Phys.* **2011**, *13*, 13721-13729.

35. Clark, T.; Hennemann, M.; Murray, J.; Politzer, P. *J. Mol. Model.* **2007**, *13*, 291-296.

36. Zheng, Y.Z.; Deng, G.; Zhou, Y.; Sun, H.Y.; Yu Z.W. *Chemphyschem*. **2015**, *16*, 2594-601.

37. Metrangolo, P.; Murray, J.S.; Pilati, T.; Politzer, P.; Resnati, G.; Terraneo, G. *CrystEngComm* **2011**, *13*, 6593-6596; Lommerse, J.; Stone, A.; Taylor, R. *J. Am. Chem. Soc.* **1996**, *118*, 3108-3116.

38. Metrangolo, P.; Neukirch, H.; Pilati, T.; Resnati, G. *Acc. Chem. Res*. **2005**, *38*, 386-395.

39. Roper, L.C.; Prasang, C.; Kozhevnikov, V.N.; Whitwood, A.C.; Karadakov, P.B.; Bruce, D.W. *Cryst. Growth Des.* **2010**, *10*, 3710-3720.

40. Hasegawa, K. *The Rigaku Journal*, **2012**, *28*, 14-18.

41. Metrangolo, P.; Resnati, G. *Chem. Eur. J.* **2001**, *7*, 2511-2519.

42. Aakeröy, C.B.; Baldrighi, M.; Desper, J.; Metrangolo, P.; Resnati, G. *Chem. Eur. J.* **2013**, *19*, 16240-16247.

43. Vishweshwar, P.; McMahon, J.A.; Bis, J. A.; Zaworotko, M.J. *J. Pharm. Sci*. **2006**, *95*, 499-516; Aakeröy, C.B.; Forbes, S.; Desper, J. *CrystEngComm* **2014**, *16*, 5870-5877; Blagden, N.; Coles, S. J.; Berry, D. J. *CrystEngComm* **2014**, *16*, 5753-5761.

44. Millar, D.I.A.; Casely, H. E. M.; Allan, D.R.; Cumming, A.S.; Lennie, A.R.; Mackay, A.J.; Oswald, I.D.H.; Tang, C.C.; Pulham; C.R. *CrystEngComm* **2012**, *14*, 3742-3749; Wang, Y.; Yang, Z.; Li, H.; Zhou, X.; Zhang, Q.; Wang, J.; Liu, Y. *Propellants Explos. Pyrotech*. **2014**, *39*, 590-596; Landenberger, K.B.; Matzger, A.J. *Cryst. Growth Des*. **2012**, *12,* 3603-3609; Bolton, O.; Simke, L.R.; Pagoria, P.F.; Matzger, A.J. *Cryst. Growth. Des.* **2012**, *12,* 4311-4314.

45. Nauha, E.; Kolehmainen, E.; Nissinen, M., *CrystEngComm* **2011**, *13*, 6531-6537; Mereiter, K. *Acta Crystallogr Sect E*. **2011**, *67*, 2321-2322; George, N.; Forrest, J.O.; Burton, R.C.; Aakeröy, C.B., *US Pat.* US2013/0203792A1, **2013**.

46. Sinha, A.S.; Maguire, A.R.; Lawrence, S.E. *Cryst. Growth Des.* **2015**, *15*, 984-1009.

47. Sokolov, A.N.; Friščić, T.; Blais, S.; Ripmeester, J.A.; MacGillivray, L.R. *Cryst Growth Des.* **2006**, *6*, 2427-2428.

48. Weigang, Z.; Yonggang, Z.; Huanli, D.; Hongbing, F.; Wenping, H. *Prog. Chem.* **2014**, *26*, 1292-1306.

49. Horiuchi, S.; Tokura, Y. *Nat. Mater.* **2008**, *7*, 357-366; Tayi, A. S.; Shveyd, A. K.; Sue, A. C. H.; Szarko, J. M.; Rolczynski, B. S.; Cao, D.; Kennedy, T. J.; Sarjeant, A. A.; Stern, C. L.; Paxton, W. F.; Wu, W.; Dey, S. K.; Fahrenbach, A. C.; Guest, J. R.; Mohseni, H.; Chen, L. X.; Wang, K. L.; Stoddart, J. F.; Stupp, S. I. *Nature* **2012**, *488*, 485-489.

50. Zhu, W.; Zheng, R.; Zhen, Y.; Yu, Y.; Dong, H.; Fu, H.; Shi, Q.; Hu, W. *J. Am. Chem. Soc.* **2015**, *137*, 11038-11046.

51. Marder, S. R.; Perry, J. W.; Schaefer, W. P. *Science* **1989**, *245*, 626-628; Pan, F.; Wong, M. S.; Gramlich, V.; Bosshard, C.; Gunter, P. *J. Am. Chem. Soc.* **1996**, *118*, 6315-6316.

52. Nguyen, H.L.; Horton, P.N.; Hursthouse, M.B.; Legon, A.C.; Bruce, D.W. *J. Am. Chem. Soc.* **2004**, *126*, 16-17.

53. Hutchins, K.M.; Sumrak, J.C.; MacGillivray, L.R. *Org. Lett.*, **2014**, *16*, 1052-1055.

54. Urbanus, J.; Roelands, C.P.M.; Verdoes, D.; Jansens, P.J.; ter Horst, J.H. *Cryst. Growth Des*. **2010**, *10*,1171-1179; Metrangolo, P.; Carcenac, Y.; Lahtinen, M.; Pilati, T.; Rissanen, K.; Vij, A.; Resnati, G. *Science* **2009**, *323*, 1461-1464.

55. Springuel, G.; Leyssens, T. *Cryst. Growth Des*. **2012**, *12*, 3374-3378.

56. Golovanov, D.G.; Lyssenko, K.A.; Antipin, M.Y.; Vygodskii, Y.S.; Lozinskaya, E.I.; Shaplov, A.S. *Cryst. Growth Des*. **2005**, *5*, 337-340.

57. Qiao, N.; Li, M.; Schlindwein, W.; Malek, N.; Davies, A.; Trappitt, G. *Int. J. Pharm.* **2011**, *419*, 1-11; Schultheiss, N.; Newman, A. *Cryst. Growth Des.* **2009**, *9*, 2950-2967.

58. Good, D.J.; Rodríguez-Hornedo, N. *Cryst. Growth Des.* **2009**, *9*, 2252-2264; Stanton, M.K.; Bak, A. *Cryst. Growth Des.* **2008**, *8*, 3856-3862.

59. Vishweshwar, P.; McMahon, J. A.; Bis, J. A.; Zaworotko, M. J. *J Pharm Sci,* **2006**, *95*, 499-516; Sarma, B.; Reddy, L. S.; Nangia, A. *Cryst Growth Des*. **2008**, *8*, 4546-4552.

60. Aakeröy, C. B.; Forbes, S.; Desper, J. *J. Am. Chem. Soc.* **2009**, *131*, 17048-17049.

61. Baldrighi, M.; Cavallo, G.; Chierotti, M. R.; Gobetto, R.; Metrangolo, P.; Pilati, T.; Resnati, G.; Terraneo, G. *Mol. Pharm.* **2013**, *10*, 1760-1772.

62. Millar, D.I.A.; Maynard-Casely, H.E.; Allan, D.R.; Cumming, A.S.; Lennie, A.R.; Mackay, A.J.; Oswald, I.D.H.; Tang, C.C.; Pulham, C.R. *CrystEngComm* **2012**, *14*, 3742-3749.

63. Thottempudi, V.; Shreeve, J. M. *J. Am. Chem. Soc.* **2011**, *133*, 19982-19992; Bolton, O.; Matzger, A. J. *Angew. Chem., Int. Ed.* **2011**, *50*, 8960-8963.

64. Bolton, O.; Simke, L. R.; Pagoria, P. F.; Matzger, A. J. *Cryst. Growth Des.* **2012**, *12*, 4311-4314.

65. Sikder, A. K.; Sikder, N. *J. Hazard. Mater.* **2004**, *A112*, 1-15.

66. Pagoria, P.F.; Lee, G.S.; Mitchell, A.R.; Schmidt, R.D. *Thermochim. Acta* **2002**, *384*, 187-204.

67. Fischer, N.; Karaghiosoff, K.; Klapçtke, T. M.; Stierstorfer, J. *Z. Anorg. Allg. Chem.* **2010**, *636*, 735-749.

68. Roy, S.; Matzger, A. J. *Angew. Chem., Int. Ed.* **2009**, *48*, 8505-8508; Chan, H. C. S.; Kendrick, J.; Leusen, F. J. J. *Angew. Chem., Int. Ed.* **2011**, *50*, 2979-2981.

69. Yang, Z.; Li, H.; Zhou, X.; Zhang, C.; Huang, H.; Li, J.; Nie, F. *Cryst. Growth Des.* **2012**, *12*, 5155-5158; Zhang, H.; Guo, C.; Wang, X.; Xu, J.; He, X.; Liu, Y.; Liu, X.; Huang, H.; Sun, J. *Cryst. Growth Des.* **2013**, *13*, 679-687.

70. Sekhon, B.S. *Int J Agr Sci.* **2015**, *5*, 472-475.

71. Weiss, M.; Storch, D.; Wirth, W.; Olenik, B.; Weiss, M.; Schwiedop, U. *US Pat.* 20120252766Al, **2012**.

72. Neil, G.; Forrest, J.; Rebecca, B.; Aakeröy, C.B. *US Pat*. WO2011128618, **2011**.

73. Lockwood, B. *Nutraceuticals*, Pharmaceutical Press: London, UK, **2007**.

74. Sanphui, P.; Goud, N.R.; Khandavilli, U.B.R.; Nangia, A. *Cryst Growth Des.* **2011**, *11*, 4135-4145.

75. Bethune, S.J.; Schultheiss, N.; Henck, J.O. *Cryst Growth Des*. **2011**, *11*, 2817-2823.

76. Sokolov, A.N.; Friščić, T.; MacGillivray, L.R. *J. Am. Chem. Soc.* **2006**, *128*, 2806-2807.

77. Aakeröy, C.B.; Wijethunga, T.K.; Desper, J. *J. Mol. Struct.* **2014**, *1072*, 20-27.

78. Aakeröy, C.B.; Wijethunga, T.K.; Desper, J. *New J. Chem.* **2015**, *39*, 822-828; Aakeröy, C.B.; Wijethunga, T.K.; Desper, J.; Moore, C. *J. Chem. Crystallogr*. **2015**, *45*, 267-276.

79. Aakeröy, C.B.; Wijethunga, T.K.; Haj, M.A.; Desper, J.; Moore, C. *CrystEngComm* **2014**, *16*, 7218-7225.

80. Aakeröy, C.B.; Wijethunga, T.K.; Desper, J.; Đakovic, M. *Cryst. Growth Des.* **2015**, *15*, 3853-3861.

81. Aakeröy, C.B.; Wijethunga, T.K.; Desper, J. *CrystEngComm* **2014**, *16*, 28-31.

82. Aakeröy, C.B.; Wijethunga, T.K.; Benton, J.; Desper, J. *Chem. Commun*. **2015**, *51*, 2425-2428.

83. Aakeröy, C.B.; Wijethunga, T.K.; Desper, J. *Chem. Eur. J.* **2015**, *21*, 11029-11037.

Chapter 2 - Molecular electrostatic potential dependent selectivity in hydrogen bonding[1]

2.1 Introduction

The hydrogen bond[2] is undoubtedly the most extensively studied intermolecular interaction[3] and even after a century of investigations it is still of utmost interest, which is reflected by the IUPAC proposed change in 2011 of its very definition.[4] The new definition, "The hydrogen bond is an attractive interaction between a hydrogen atom from a molecule or a molecular fragment X–H in which X is more electronegative than H, and an atom or a group of atoms in the same or a different molecule, in which there is evidence of bond formation",[5] clearly recognizes electrostatics at being at the core of this interaction. Long lasting interest in hydrogen bonding is related to its importance in the fields of chemistry, physics, biochemistry, biology, materials science, organic synthesis, medicine, pharmacy, mineralogy, crystal engineering, supramolecular chemistry, surface science and many more.[6] It is indeed the basis of life due to its structural role in DNA,[7] enzymes,[8] and proteins.[9]

From a fundamental supramolecular[10] and crystal engineering[11] viewpoint, the hydrogen bond is a key synthetic tool in assembly of molecules into well-defined architectures.[12] An established set of guidelines in directing hydrogen bonds in a supramolecular context is required to design supramolecular architectures in a rational and predictable manner,[13] to recognize robust synthons,[14] to obtain reproducibility in experimental designing and to avoid "synthon crossover"[15] and "synthon polymorphism".[16]

In this context, Etter proposed that, in a system with multiple potential structural outcomes, the best hydrogen-bond donor and the best hydrogen-bond acceptor will preferentially interact

with each other,[17] Figure 2.1. This simple set of guidelines offers powerful and practical protocols for the directed assembly of solid-state architectures.

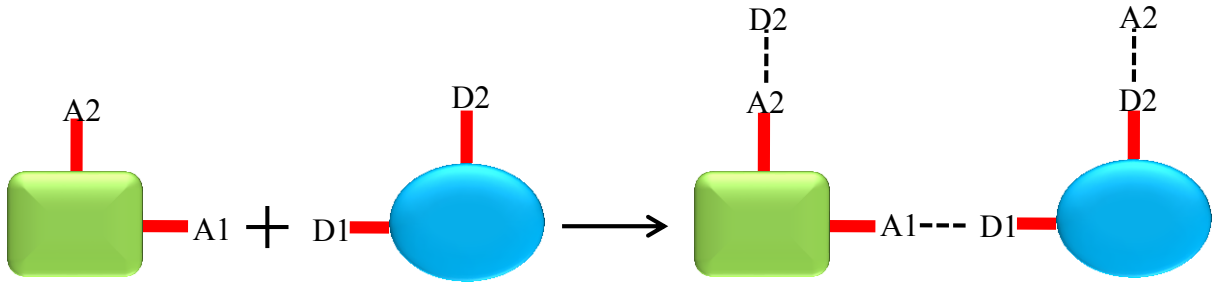

Figure 2.1 Schematic representation of Etter's rules in hydrogen bonding (A1-best acceptor, A2-2nd best acceptor, D1-best donor, D2-2nd best donor)

In order to take advantage of this approach, it is necessary to find a convenient method for recognizing and ranking the best donors and best acceptors in a given system. Several solutions to the challenge have been reported.[18] One such method utilizes pK_a/pK_b values of the participating molecules to rank the relative strength.[19] There are many examples in literature where the supramolecular outcome has been successfully predicted based on pK_a values.[20] This approach has been utilized in designing ternary co-crystal system where the strong acid binds to the best acceptor site while the weak acid binds to the second best acceptor site, Figure 2.2.[21]

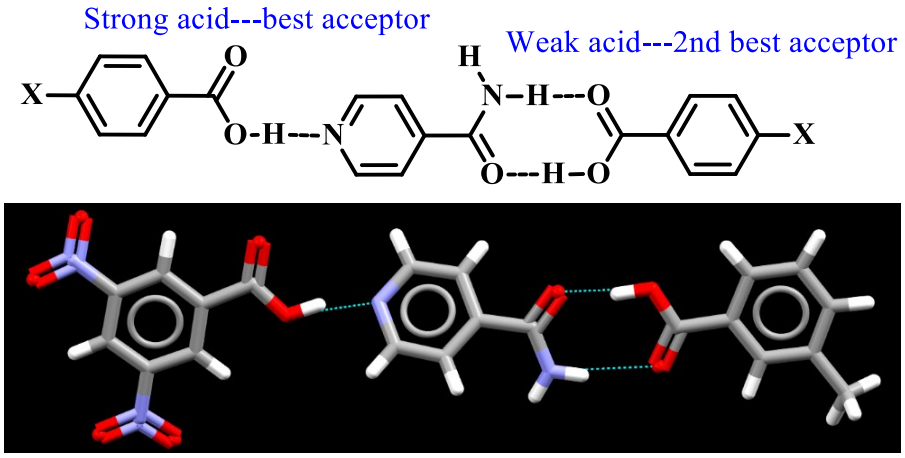

Figure 2.2 Designing ternary co-crystals utilizing the pK_a ranking method[21]

This method is effective as long as the molecules carry the same chemical functionality. For example, thiophenol has a pK_a of 6.61, which is considerably lower than that of phenol (pK_a=9.86), which indicates that thiophenol should be a better hydrogen bond donor. But phenols have significant hydrogen bond donor ability and are commonly used as hydrogen bond donors[22] whereas thiophenols hardly exhibit any hydrogen bond donor ability.[23]

A more general approach proposed by Hunter and co-workers utilizes calculated molecular electrostatic potential surface (MEPS) values,[24] where the best acceptor represents the highest negative value on the surface and the best donor carries the highest positive value. This approach has been used extensively in designing hydrogen bonded co-crystals. One such study focuses on the calculated molecular electrostatic potential values to rank the relative hydrogen bond strengths of hydroxybenzoic acids.[25] The structural results agree with the predicted outcome by MEPS and follow best-donor best-acceptor hierarchy, Figure 2.3.

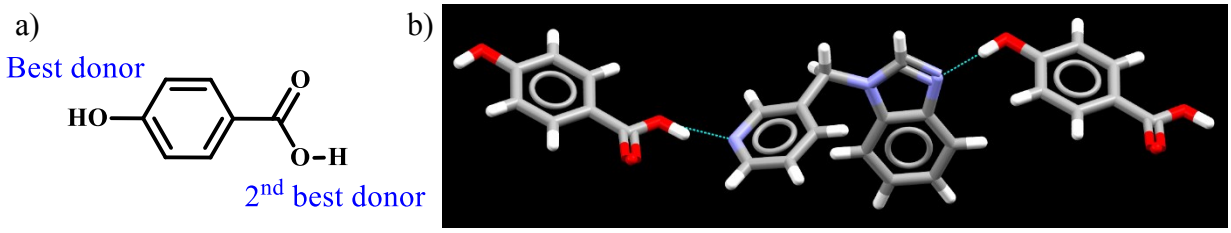

Figure 2.3 a) Ranking of hydrogen bonding sites of 4-hydroxybenzoic acid based on calculated MEPS and b) structural outcome: best donor binds to the best acceptor and 2nd best donor binds to the 2nd best acceptor[25]

In order to gather information on such studies where a ranking of acceptor sites have been done, a comprehensive Cambridge Structural Database (CSD)[26] search was conducted targeting interaction between any nitrogen and acid functionality. Results yielded 1141 hits and among them 180 structures contained an acceptor with multitopic of acceptor sites. Further analysis of these 180 hits revealed that, even though the underlying concepts of MEPS based ranking is applied in

few of the studies,[27] none of these studies directly utilize a ranking of acceptor sites based on calculated MEPS in hydrogen bonding.

Thus, designing of a system that can be used to study MEPS dependent ranking of hydrogen bond acceptor sites is of utmost interest. Because of this reason, a series of co-crystallizations between four biimidazole based compounds, (1,1'-bis(pyridin-4-ylmethyl)-2,2'-biimidazole **A1**, 1,1'-bis(pyridin-3-ylmethyl)-2,2'-biimidazole **A2**, 1,1'-bis(pyridin-2-ylmethyl)-2,2'-biimidazole **A3** and 1,1'-dibenzyl-2,2'-biimidazole **A4**) Figure 2.4 and nine symmetric aliphatic di-acids (Figure 2.5) were carried out in order to determine if a ranking based on calculated MEPS can be used to effectively assign selectivity in hydrogen-bond based intermolecular interactions. **A1**-**A3** have two identical pyridine nitrogen atoms (blue), and two identical imidazole nitrogen atoms (red) to give four acceptors per molecule. Acceptor **A4** (Figure 2.4) was synthesized as a control molecule, in order to study the impact of sterics when forming hydrogen bonds with imidazole nitrogen sites. Thus **A4** contain only imidazole nitrogen sites while retaining the structure similarities to other molecules of this family.

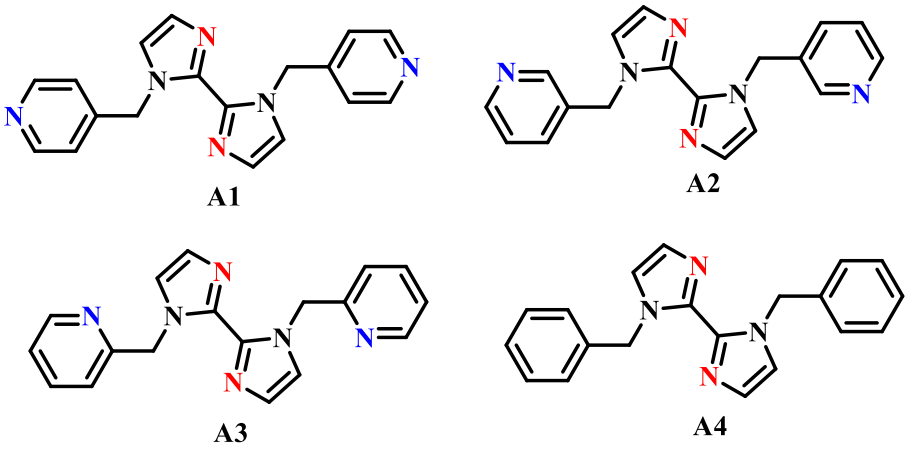

Figure 2.4 Acceptors employed in the study

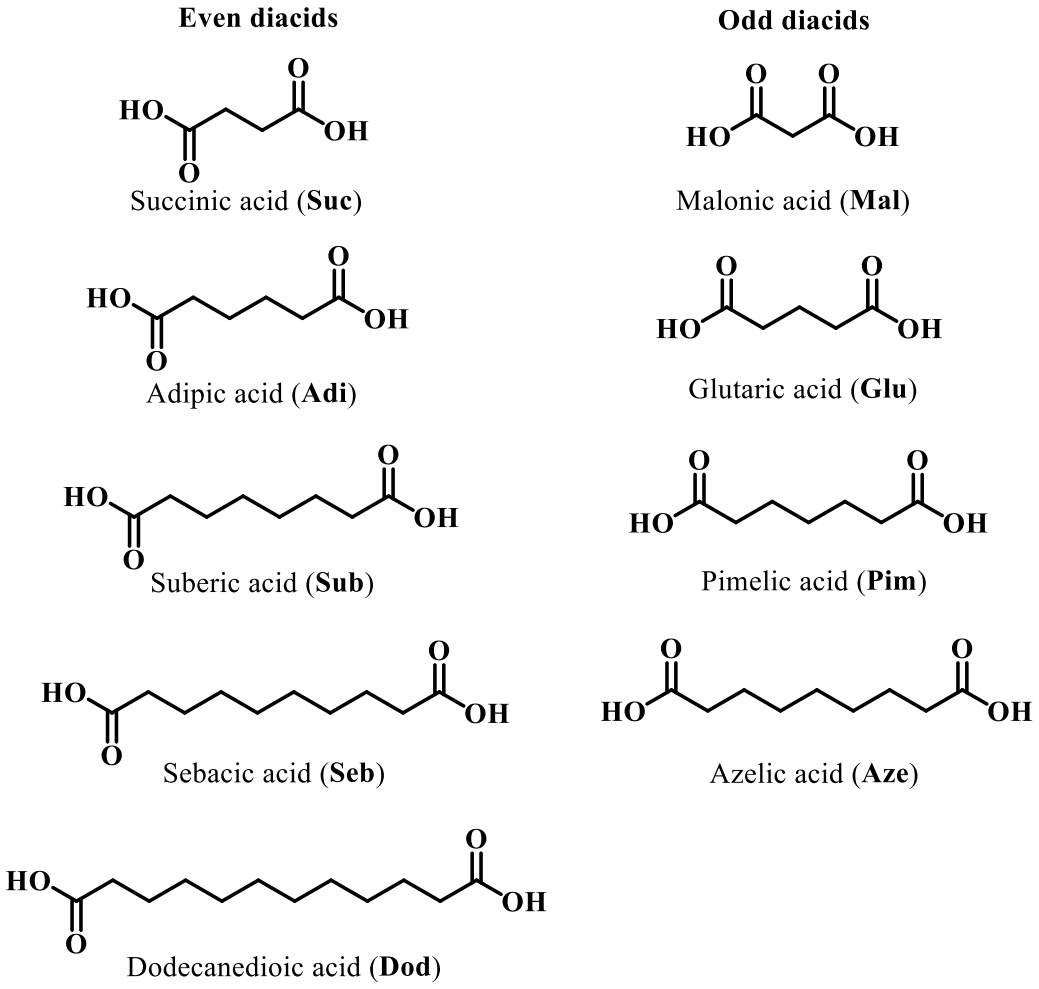

Figure 2.5 Donors (aliphatic di-acids) employed in the study

The different acceptor sites were ranked (best and second-best) with the utilization of calculated MEPS for **A1-A3**. Systematic co-crystallizations with nine aliphatic diacids[28] (Figure 2.5) in 1:2 stoichiometry were performed with these three molecules. With **A4**, 1:1 stoichiometric studies were performed. In addition, experiments using 1:1 and 1:4 stoichiometries (of acceptor to donor) were performed with **A1** and **A3**.

The study is undertaken in response to two hypotheses,

1. If a hydrogen-bond donor has a choice of two different acceptor sites, it will preferentially select the best-acceptor as determined by molecular electrostatic potentials surfaces (MEPS).
2. The selectivity in hydrogen bonding will not be affected by the relative amount of reactants present in the system.

2.2 Experimental

2.2.1 General

All precursors, solvents and dicarboxylic acids were purchased from commercial sources and used without further purification. 2,2'-Biimidazole was synthesized following a reported procedure.[29] ^{1}H NMR spectra were recorded on a Varian Unity plus 400 MHz spectrometer in $CDCl_3$ or DMSO-d_6. Infrared spectra were recorded with a Nicolet 380 FT-IR with a digital resolution of 0.9 cm^{-1} and data processed using Omnic[30] software. Melting points were determined using Fischer-Johns Mel-Temp melting point apparatus and are uncorrected.

2.2.2 Electrostatic potential calculations

Molecular electrostatic potential surfaces of **A1-A4** were generated with density functional B3LYP level of theory using 6-311++G** basis set in vacuum. All calculations were carried out using Spartan'08 software.[31] All molecules were geometry optimized and the maxima and minima on the electrostatic potential surface (0.002 e/au isosurface) determined using a positive point charge in the vacuum as a probe. The numbers indicate the interaction energy (kJ/mol) between the positive point probe and surface of the molecule at that particular point. These numbers are related to the electrostatic potentials on the atoms with the negative number corresponding to a negative potential and positive number corresponding to a positive potential.

2.2.3 Synthesis of acceptors

2.2.3.1 Synthesis of 1,1'-bis(pyridin-4-ylmethyl)-2,2'-biimidazole, A1

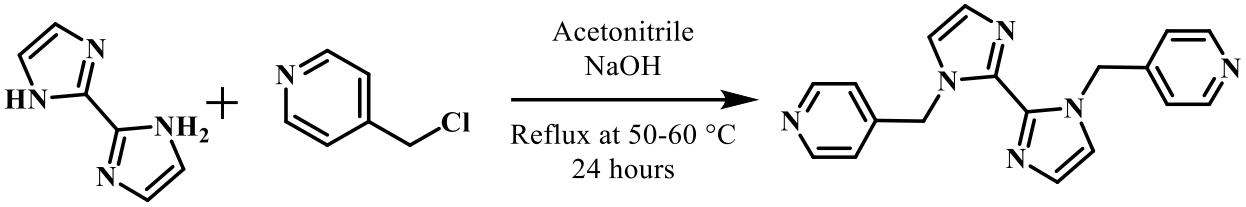

2,2'-Biimidazole (0.27 g, 2.0 mmol) and NaOH (0.32 g, 8.0 mmol) were placed in a 100 mL round bottomed flask with 20 mL of acetonitrile. The mixture was stirred at room temperature for two hours. 4-Picolyl chloride hydrochloride (0.65 g, 4.0 mmol) in acetonitrile (20 mL) was added to the mixture and refluxed for 24 hours at 50 °C - 60 °C. The reaction was monitored with TLC and after completion, the solvent was removed by rotary evaporation. The residue was dissolved in water (50 mL) and extracted with methylene chloride (30 mL x 3). Organic layers were combined, dried over anhydrous $MgSO_4$ and rotary evaporated to obtain the dark brown powder as the product. Yield: 0.35 g (56%); m.p. 157-160 °C; ^{1}H NMR (400 MHz, $CDCl_3$):8.49 (d, 4H), 7.11 (d, 2H), 6.94 (d, 2H), 6.91 (d, 4H), 5.84 (s, 4H).

2.2.3.2 Synthesis of 1,1'-bis(pyridin-3-ylmethyl)-2,2'-biimidazole, A2

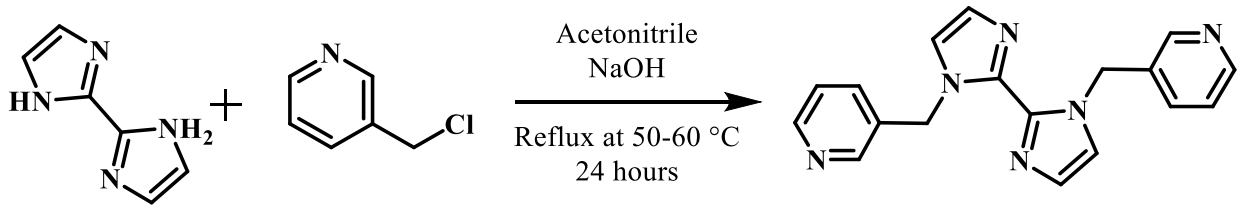

2,2'-Biimidazole (0.27 g, 2.0 mmol) and NaOH (0.32 g, 8.0 mmol) were placed in a 100 mL round bottomed flask with 20 mL of acetonitrile. The mixture was stirred at room temperature for two hours. 3-Picolyl chloride hydrochloride (0.65 g, 4.0 mmol) in acetonitrile (20 mL) was

added to the mixture and refluxed for 24 hours at 50 °C - 60 °C. The reaction was monitored with TLC and upon completion the solvent was removed by rotary evaporation. The residue was dissolved in water (50 mL) and extracted with methylene chloride (30 mL x 3). Organic layers were combined, dried over anhydrous $MgSO_4$ and rotary evaporated to obtain the brown powder as the product. Yield: 0.45 g (71%); m.p. 112-115 °C; ^{1}H NMR (400 MHz, $CDCl_3$):8.46 (d, 2H), 8.45 (s, 2H), 7.39 (d, 2H), 7.17 (m, 2H), 7.11 (d, 2H), 6.95 (d, 2H), 5.78 (s, 4H).

2.2.3.3 Synthesis of 1,1'-bis(pyridin-2-ylmethyl)-2,2'-biimidazole, *A3*

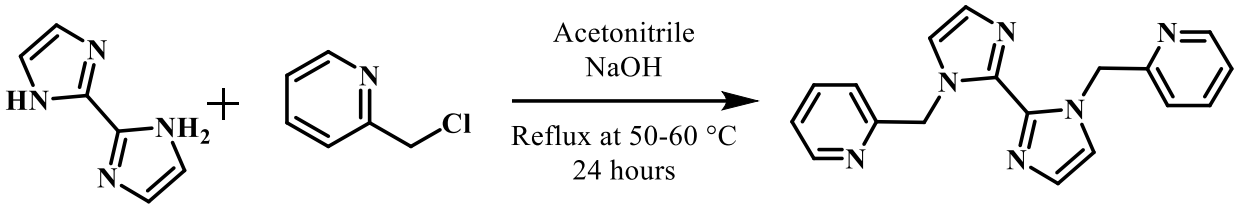

2,2'-Biimidazole (0.27 g, 2.0 mmol) and NaOH (0.32 g, 8.0 mmol) were placed in a 100 mL round bottomed flask with 20 mL of acetonitrile. The mixture was stirred at room temperature for two hours. 2-Picolyl chloride hydrochloride (0.65 g, 4.0 mmol) in acetonitrile (20 mL) was added to the mixture and refluxed for 24 hours at 50 °C - 60 °C. The reaction was monitored with TLC and upon completion the solvent was removed by rotary evaporation. The residue was dissolved in water (50 mL) and extracted with methylene chloride (30 mL x 3). Organic layers were combined, dried over anhydrous $MgSO_4$ and rotary evaporated to obtain the pale brown powder as the product. Yield: 0.25 g (40%); m.p. 180-183 °C; ^{1}H NMR (400 MHz, $CDCl_3$): 8.53 (d, 2H), 7.53 (t, 2H), 7.15 (t, 2H), 7.12 (s, 2H), 7.07 (s, 2H), 7.05 (d, 2H), 5.87 (s, 4H).

2.2.3.4 Synthesis of 1,1'-dibenzyl-2,2'-biimidazole, A4

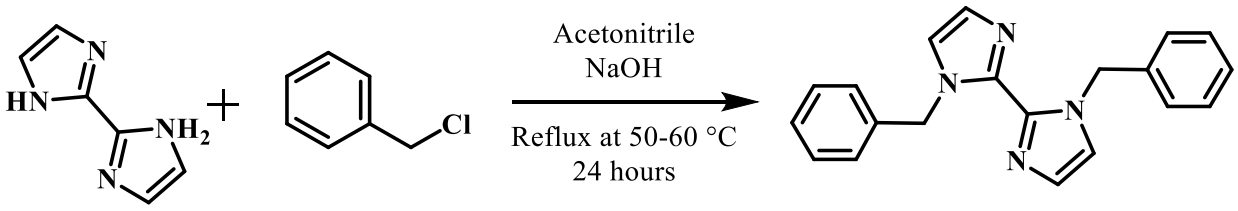

2,2'-Biimidazole (0.33 g, 2.5 mmol) and NaOH (0.39 g, 9.9 mmol) were placed in a 100 mL round bottomed flask with 20 mL of acetonitrile. The mixture was stirred at room temperature for two hours. Benzyl bromide (0.63 g, 5.0 mmol) in acetonitrile (20 mL) was added to the mixture and refluxed for 24 hours at 50 °C - 60 °C. The reaction was monitored with TLC and after completion the solvent was removed by rotary evaporation. The residue was dissolved in water (50 mL) and extracted with methylene chloride (30 mL x 3). Organic layers were combined, dried over anhydrous $MgSO_4$ and rotary evaporated to obtain the yellow powder as the product. Yield: 0.69 g (89%); m.p. 144-146 °C; ^{1}H NMR (400 MHz, $CDCl_3$):5.71 (s, 4H), 6.94 (d, 2H), 7.03 (m, 4H), 7.14 (d, 2H), 7.25 (m, 6H).

2.2.4 Grinding experiments and IR spectroscopy

A1-**A4** were initially put through a co-crystal screen using solvent-assisted grinding (a few drops of methanol) with nine aliphatic dicarboxylic acids. In all 36 reactions the acceptors and donors were mixed in 1:2 stoichiometric ratio (**A1**-**A3**) or 1:1 stoichiometric ratio (**A4**) and the solid resulting from each reaction was characterized using IR spectroscopy to determine if a co-crystal had formed. In each reaction, 10 mg of the acceptor was used with the respective stoichiometric amount of the acid. In 28 out of 36 experiments the vibrational spectra displayed broad stretches near 1,850 and 2,450 cm^{-1} (Figure 2.6) indicative of intermolecular O−H···N hydrogen bond formation.[32]

2.2.5 Synthesis of co-crystals

The mixtures obtained in the grinding experiments were dissolved in a minimum amount of methanol (2 ml) and placed in a 2 dram borosilicate vial for slow evaporation in order to obtain crystals suitable for single crystal X-ray diffraction. In the instances where the single crystals were not produced with the above approach, a range of methods such as slow evaporation with ethyl acetate, vapor diffusion with methanol and hexane as the solvent and anti-solvent, and crystallization under freezing conditions were used. All in all, thirteen crystals were obtained and analyzed with single crystal X-ray diffraction. Table 2.1 summarizes the experimental details. Appendix B.1 contains the relevant X-ray experimental data.

Table 2.1 Experimental details of the thirteen co-crystals obtained

Code	Mixed Mole ratio	Amounts used	Solvent and method	Crystal stoichiometry	Melting point (°C)	Crystal color & habit
A1:Suc	1:2	**A1** -10 mg, 0.032 mmol **Suc** - 7.5 mg, 0.063 mmol	Methanol Slow evaporation	1:1	161-165	Colorless prism
A1:Adi	1:2	**A1** - 10 mg, 0.032 mmol **Adi** - 9.2 mg, 0.063 mmol	Methanol Slow evaporation	1:1	167-170	Bronze plate
A1:Sub	1:2	**A1** - 10 mg, 0.032 mmol **Sub** - 11 mg, 0.063 mmol	Methanol Slow evaporation	1:1	148-151	Orange plate
A1:Seb	1:2	**A1** - 10 mg, 0.032 mmol **Seb** - 13 mg, 0.063 mmol	Methanol Slow evaporation	1:1	140-144	Orange plate
A1:Dod	1:2	**A1** - 10 mg, 0.032 mmol **Dod** - 15 mg, 0.063 mmol	Methanol Slow evaporation	1:1	138-143	Bronze prism
A1:Mal	1:2	**A1** - 10 mg, 0.032 mmol **Mal** - 6.6 mg, 0.063 mmol	Methanol Slow evaporation Freezing conditions	1:1	95-98	Colorless needle
A1:Glu	1:2	**A1** - 10 mg, 0.032 mmol **Glu** - 9.2 mg, 0.063 mmol	Methanol Slow evaporation	1:2	153-155	Bronze prism
A3:Adi	1:2	**A3** - 10 mg, 0.032 mmol **Adi** - 9.2 mg, 0.063 mmol	Methanol Slow evaporation	1:1	159-162	Colorless plate
A3:Sub	1:2	**A3** - 10 mg, 0.032 mmol **Sub** - 11 mg, 0.063 mmol	Methanol Slow evaporation	1:1	131-135	Colorless prism
A3:Seb	1:2	**A3** - 10 mg, 0.032 mmol **Seb** - 13 mg, 0.063 mmol	Methanol Slow evaporation	1:1	130-133	Colorless prism
A3:Dod	1:2	**A3** - 10 mg, 0.032 mmol **Dod** - 15 mg, 0.063 mmol	Methanol Slow evaporation	1:1	120-123	Colorless prism
A3:Pim	1:2	**A3** - 10 mg, 0.032 mmol **Pim** - 10 mg, 0.063 mmol	Methanol Slow evaporation Freezing conditions	1:2	90-93	Colorless plate
A4:Mal	1:1	**A4** - 10 mg, 0.033 mmol **Mal** - 3.3 mg, 0.032 mmol	Methanol Slow evaporation	1:1	90-94	Yellow prism

Freezing conditions were achieved by keeping the vials inside a freezer at 0 °C

2.2.6 Variable stoichiometric studies

To explore the possible influence of reaction stoichiometry in hydrogen bond selectivity, **A1** and **A3** were combined with adipic acid, suberic acid, sebacic acid and dodecandioic acid, respectively in 1:1 and 1:4 stoichiometries. The reactants were dissolved in a minimum amount of methanol and slow evaporated in pursuance of crystals and were analysed using IR spectroscopy in order to determine the co-crystal formation and ^{1}H NMR spectroscopy in order to determine the stoichiometry.

2.3 Results

2.3.1 Electrostatic potentials

The ditopic acceptorss used in this study (**A1**-**A3**) contain two different acceptor sites, pyridine nitrogen (N(py)) and imidazole nitrogen (N(im)). The control molecule **A4** contain only N(im) sites. The ranking of the acceptor sites is established using molecular electrostatic potential surfaces and the results from the density functional theory (DFT) calculations are shown in Table 2.2. Higher negative potential on the acceptor suggests better hydrogen-bond accepting ability.

Table 2.2 Calculated electrostatic potential values of the acceptors

Molecule	Atom	Electrostatic potential (kJ/mol^{-1})
1,1'-bis(pyridin-4-ylmethyl)-2,2'-biimidazole A1	Pyridine N	-188
	Imidazole N	-124
1,1'-bis(pyridin-3-ylmethyl)-2,2'-biimidazole A2	Pyridine N	-180
	Imidazole N	-125
1,1'-bis(pyridin-2-ylmethyl)-2,2'-biimidazole A3	Pyridine N	-150
	Imidazole N	-120
1,1'-dibenzyl-2,2'-biimidazole A4	Imidazole N	-149

2.3.2 Grinding experiments and characterization by IR spectroscopy

The solvent-assisted grinding experiments were analyzed through IR spectroscopy and 28 of the 36 experiments resulted a successful co-crystal formation, equivalent to a supramolecular yield of 78%. All co-crystals displayed broad bands near the 1,850 and 2,500 cm^{-1} region (as a

result of O-H···N hydrogen bonds)[33] and significant changes in the C=O stretch of the carboxylic acid indicating co-crystal formation Table 2.3. Figure 2.6 compare the IR spectrum of the co-crystal **A3:Dod** with the starting compounds (**A3**: blue; **A3:Dod** co-crystal: red; **Dod**: purple); green circles highlights the formation of broad stretches near 2495 and 1865 cm^{-1} and black circles highlights the shift of carbonyl stretch (1686 to 1698 cm^{-1}). The supramolecular yields from IR analysis are summarized in Table 2.4.

Table 2.3 IR data for the grinding experiments

Mixture	Carbonyl stretch (cm^{-1})		O-H···N stretches (cm^{-1})	Co-crystal?
	Di-acid	Ground mixture		
A1:Suc	1685	1692	2532,1870	Y
A1:Adi	1685	1687	2600,1900	Y
A1:Sub	1685	1688	2500,1906	Y
A1:Seb	1686	1689	2497,1896	Y
A1:Dod	1686	1689	2541,1914	Y
A1:Mal	1696	1692	2586,1900	Y
A1:Glu	1683	1694	2590,1900	Y
A1:Pim	1685	1688	2450,1900	Y
A1:Aze	1689	1688	2500,1940	Y
A2:Suc	1685	1686	2532,1900	Y
A2:Adi	1685	1688	2488,1915	Y
A2:Sub	1685	1689	2495,1900	Y
A2:Seb	1686	1686	2499,1924	Y
A2:Dod	1686	1686	2495,1922	Y
A2:Mal	1696	1716	2561,1964	Y
A2:Glu	1683	1701	2588,1941	Y
A2:Pim	1685	1690	2530,1941	Y
A2:Aze	1689	1690	2528,1924	Y
A3:Suc	1685	1695	2503,1943	Y
A3:Adi	1685	1691	2528,1895	Y
A3:Sub	1685	1690	2495,1850	Y
A3:Seb	1686	1701	2520,1888	Y
A3:Dod	1686	1698	2495,1865	Y
A3:Mal	1696	1708	2582,1980	Y
A3:Glu	1683	1689	2550,1957	Y
A3:Pim	1685	1689	2511,1942	Y
A3:Aze	1689	n/a	n/a	N
A4:Suc	1685	1681	n/a	N
A4:Adi	1685	1686	n/a	N
A4:Sub	1685	1686	n/a	N
A4:Seb	1686	1689	n/a	N
A4:Dod	1686	1686	n/a	N
A4:Mal	1696	1701	2586,1970	Y
A4:Glu	1683	1685	2600,1900	Y
A4:Pim	1685	1687	n/a	N
A4:Aze	1689	1686	n/a	N

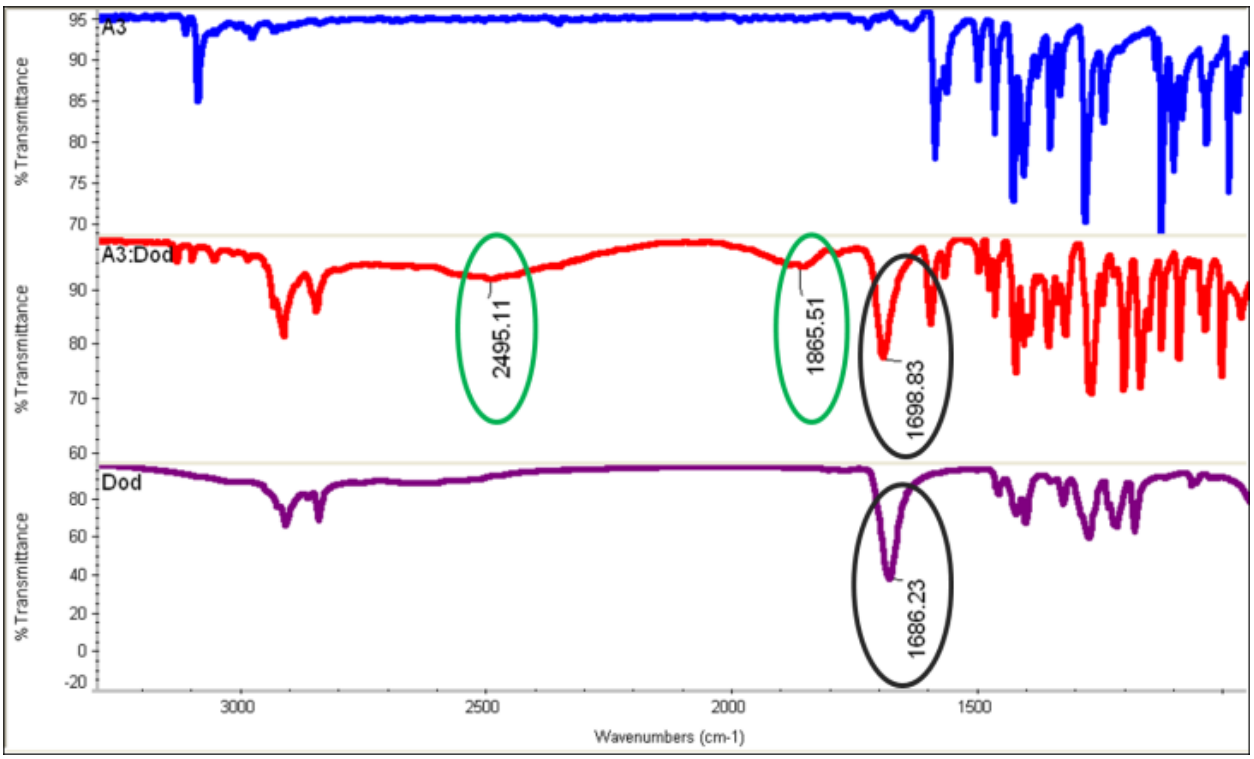

Figure 2.6 Comparison of hydrogen bond formation in **A3:Dod** (green circles highlight the formation of broad stretches and black circles highlight the shifts in the carbonyl stretch)

Table 2.4 Summary of supramolecular yields

Acceptor	Grinding experiments	
	Success rate	Supramolecular yield
1,1'-bis(pyridin-4-ylmethyl)-2,2'-biimidazole A1	9/9	100%
1,1'-bis(pyridin-3-ylmethyl)-2,2'-biimidazole A2	9/9	100%
1,1'-bis(pyridin-2-ylmethyl)-2,2'-biimidazole A3	8/9	89%
1,1'-dibenzyl-2,2'-biimidazole A4	2/9	22%

2.3.3 Crystal growth and structure analysis

Although vibrational spectroscopy provides unambiguous information about whether a co-crystal has formed or not, it does not reveal the actual interactions between the donor and acceptor sites. Thus, in order to examine any hydrogen-bond preferences, single crystal data are required. The initial approach for crystal growth was slow evaporation with methanol, but many of these experiments produced gels or powders, thus a variety of other methods were employed. Ultimately thirteen crystals suitable for single crystal analysis was obtained and structurally characterized.

Seven structures were obtained for **A1**-based co-crystals, five for **A3**-based co-crystals, and one co-crystal of **A4** was structurally characterized. Despite the fact that IR spectroscopy indicates that **A2** is also capable of forming co-crystals, suitable crystals of **A2** were not available even after repeated attempts.

Thirteen crystal structures were solved (**A1:Suc**, **A1:Adi**, **A1:Sub**, **A1:Seb**, **A1:Dod**, **A1:Mal**, **A1:Glu**, **A3:Adi**, **A3:Sub**, **A3:Seb**, **A3:Dod**, **A3:Pim** and **A4:Mal**) and the relevant crystallographic data and hydrogen bond geometries are provided in Appendix B.1.

2.3.4 Crystal structures

2.3.4.1 Structures of A1:Suc A1:Adi, A1:Sub, A1:Seb and A1:Dod

In **A1:Suc**, both acid groups form hydrogen bonds with the pyridine nitrogen atoms of the acceptor resulting in a 1:1 stoichiometric co-crystal. These interactions produce infinite 1-D chains, and imidazole nitrogen atoms are not participating in any noticeable short contacts, Figure 2.7.

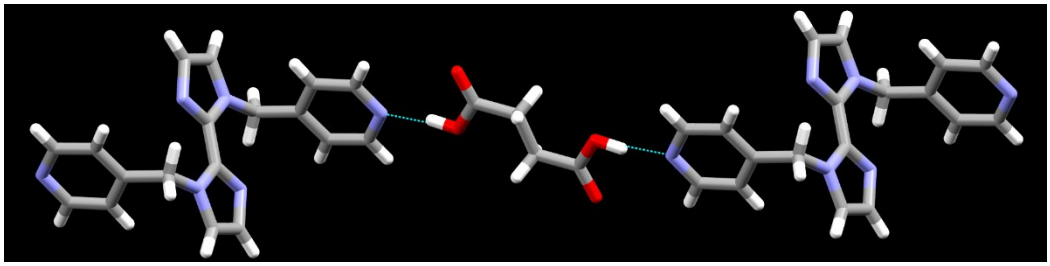

Figure 2.7 Primary hydrogen bond interactions in **A1:Suc**

The remaining four structures of **A1** with even-chain acids, **A1:Adi**, **A1:Sub**, **A1:Seb** and **A1:Dod**, all display the same primary hydrogen-bond interactions between the carboxylic acid functionality and the pyridine nitrogen atoms of the acceptor resulting in 1:1 stoichiometric co-crystals in each instance, Figure 2.8. The 1-D chains persist and no notable short contacts to the N(im) sites can be seen.

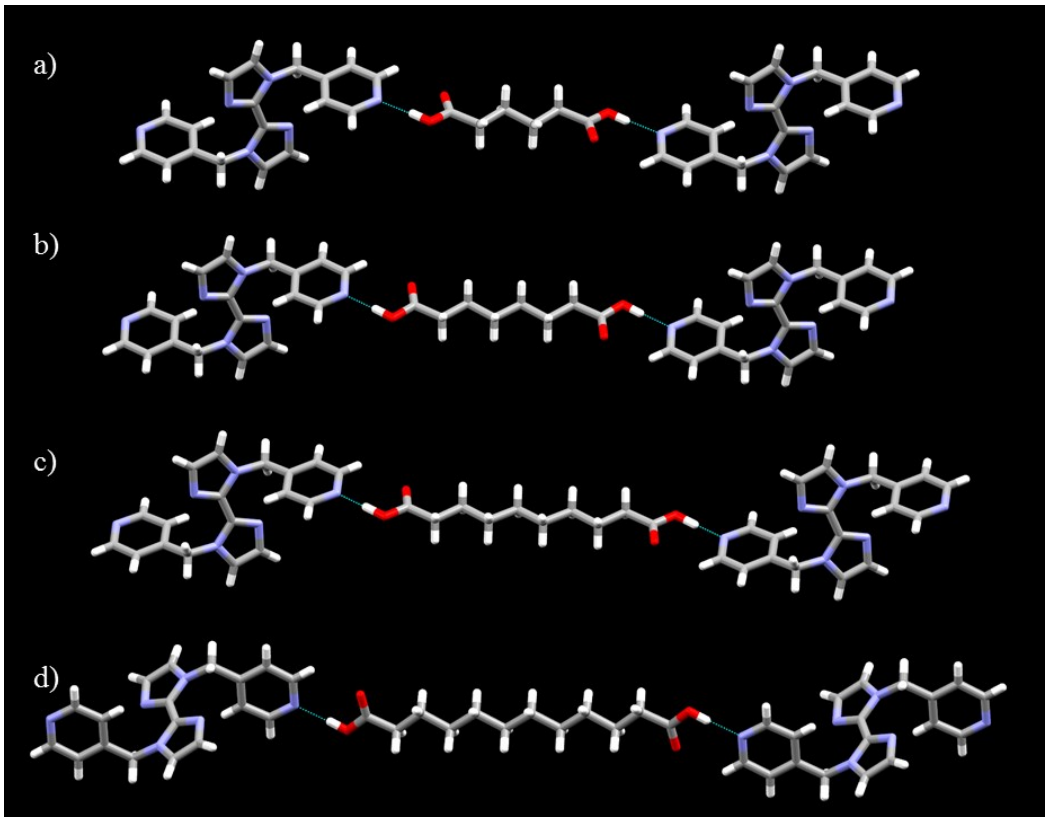

Figure 2.8 Primary hydrogen bond interactions in a) **A1: Adi**, b) **A1: Sub**, c) **A1: Seb** and d) **A1: Dod**

2.3.4.2 Structure of A1:Mal

The existence of an odd-chain diacid as the hydrogen-bond donor in **A1:Mal** does not affect the principle interaction trend. Each acid binds to two pyridine nitrogen atoms generating 1-D chains with a 1:1 stoichiometric co-crystal, Figure 2.9.

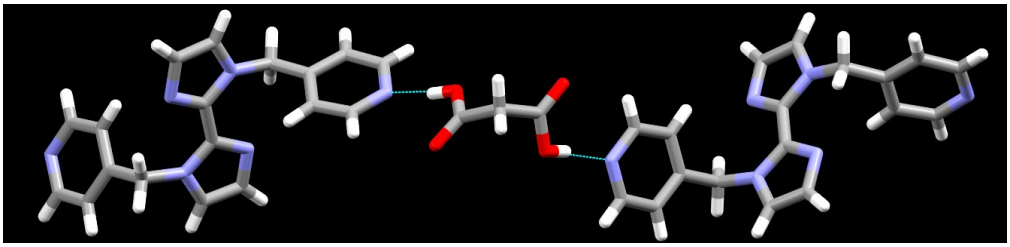

Figure 2.9 Primary hydrogen bond interactions in **A1:Mal**

2.3.4.3 Structure of A1:Glu

However, in the last crystal structure of **A1**, with glutaric acid as the donor, the expected O-H···N(py) hydrogen bonds are present, but at the same time a head-to-head acid···acid dimer formation can also be seen. Thus, the stoichiometry is changed to 1:2 (acceptor:donor) although the 1-D chains prevail, Figure 2.10.

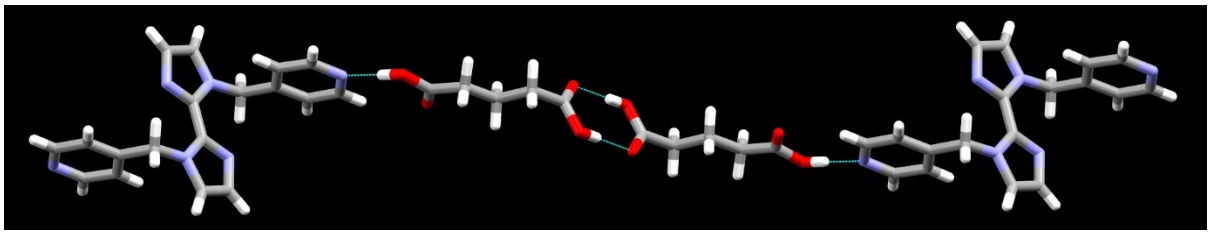

Figure 2.10 Primary hydrogen-bond interactions in **A1:Glu**

2.3.4.4 Structures of A3:Adi A3:Sub, A3:Seb and A3:Dod

In the crystal structure of **A3:Adi**, the primary hydrogen bonds occur between the acid functionality and the best acceptor site, the N(py) leading to a 1-D chain architecture, Figure 2.11.

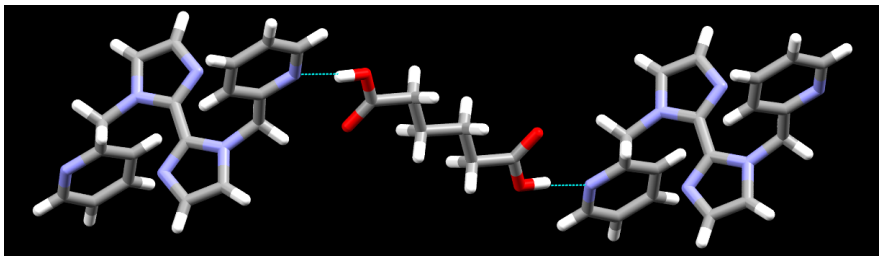

Figure 2.11 Primary hydrogen bond interactions in **A3:Adi**

All four even-acid co-crystals of **A3** essentially display the same structural features leading to 1:1 stoichiometric co-crystal formation via O-H···N(py) bonds resulting infinite 1-D chains, Figure 2.12.

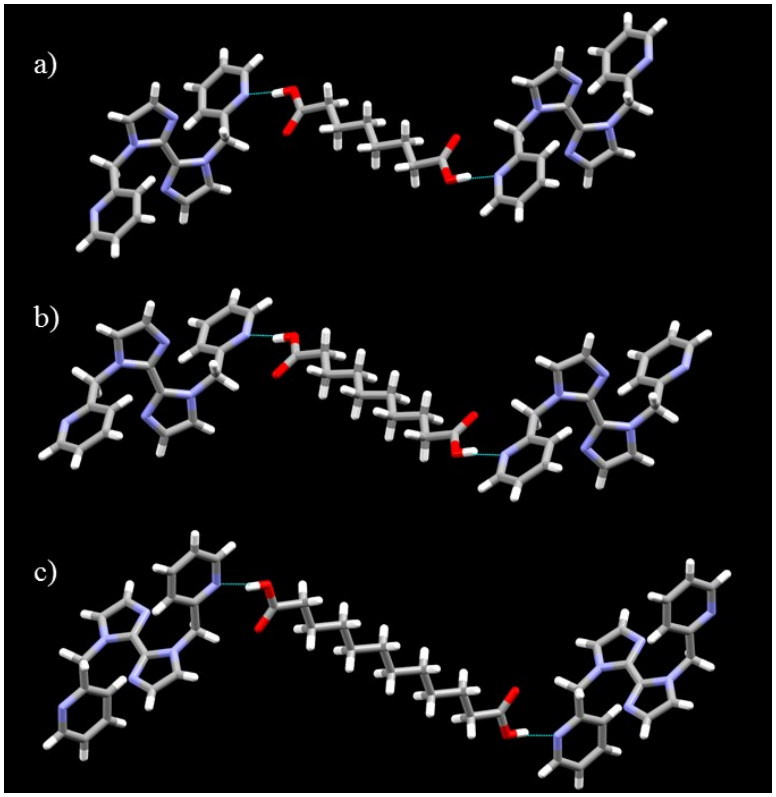

Figure 2.12 Primary hydrogen bond interactions in a) **A3:Sub** b) **A3:Seb** and c) **A3:Dod**

2.3.4.5 Structure of A3:Pim

A3:Pim is the only co-crystal of **A3** obtained with an odd-chain diacid and this structure is similar to that of **A1:Glu** with primary O-H···N(py) hydrogen bonds and an acid···acid dimer leading to 1:2 stochiometric 1-D chains, Figure 2.13.

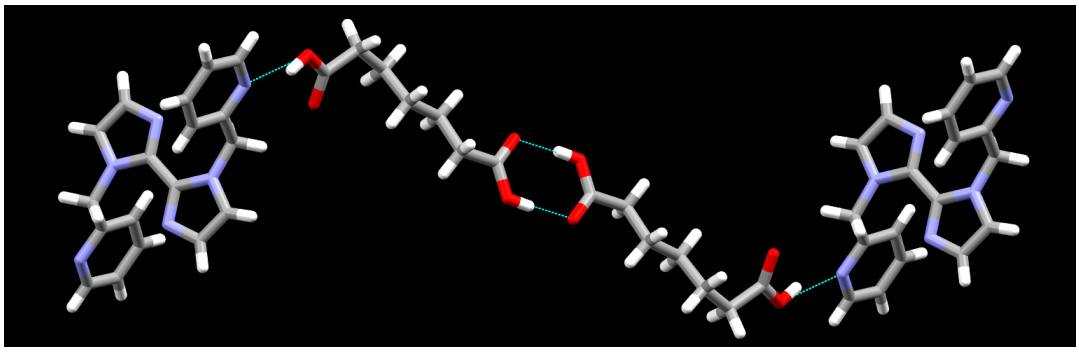

Figure 2.13 Primary hydrogen bond interactions in **A3:Pim**

2.3.4.6 Structure of A4:Mal

The only crystal structure obtained with **A4** shows primary O-H···N(im) hydrogen bond formation, Figure 2.14.

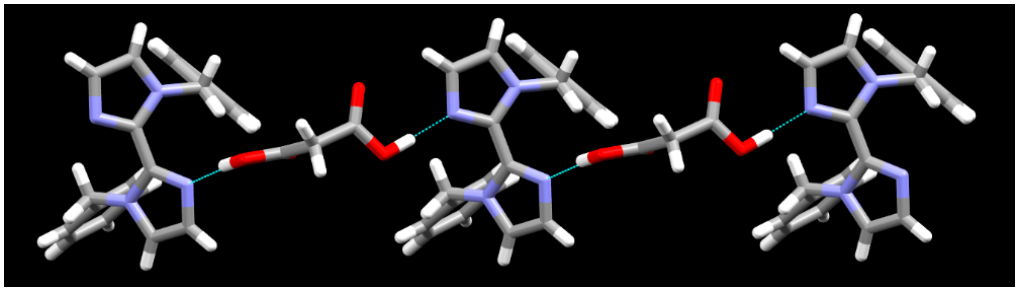

Figure 2.14 Primary hydrogen bond interactions in **A4:Mal**

2.4 Discussion

2.4.1 Characterization by IR spectroscopy

All co-crystallization experiments were first screened using IR spectroscopy. Co-crystal formation was confirmed by two broad stretches in the 1800-2500 cm^{-1} region as a result of O-H···N hydrogen bond formation. The other indication was the shifts of C=O stretch. According to these observations a 78% of supramolecular yield was obtained. In all cases, the C=O stretch appeared above 1670 cm^{-1} (Table 2.3) confirming the neutral co-crystal formation. If a salt formation occurs, the proton is transferred to the acceptor site and an asymmetric carboxylate (COO^-) band appears around 1650-1590 cm^{-1}, combined with a weaker symmetric carboxylate stretch in the 1400 cm^{-1} region.[34]

On the other hand, when a co-crystal is formed, the acid···acid dimer in the free carboxylic acid is breaking and the acid···acceptor interaction is forming, Figure 2.15. These changes can be picked up from the IR spectra. The carboxylic acid dimer has a center of symmetry, thus only asymmetric C=O stretching vibrations absorb in the infrared. When the co-crystal is formed, the dimer is converted to monomer and the C=O stretching frequency shifts to a higher wave number.

The lower absorption frequency of the carboxylic acid dimer is due to hydrogen bonding and resonance which lengthens the C=O bond, but when a co-crystal is formed the C=O is free of interactions and strengthens the bond leading to the higher wave number shifts of infrared.[35] Furthermore the O-H out-of-plane bending of an acid···acid dimer produces a broad, medium-weak band around 930 cm^{-1} and the co-crystal formation via acid···acceptor interactions leads to the disappearance of this band.

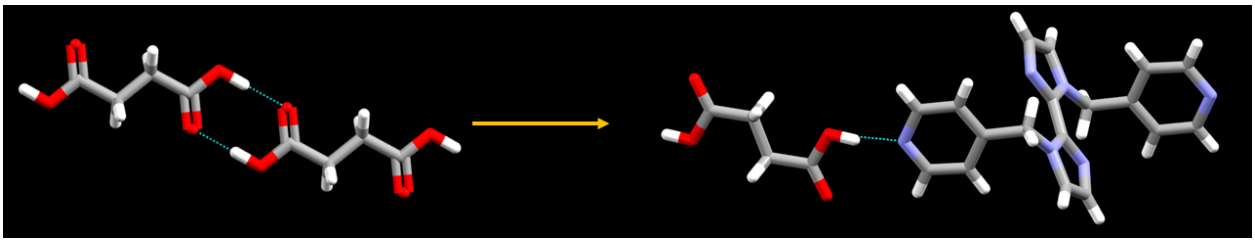

Figure 2.15 Conversion from acid···acid dimer to acid···pyridine heterosynthon

2.4.2 Relationship between molecular electrostatic potentials and interaction selectivity

The MEPS calculations indicate that the pyridine nitrogen atoms in **A1**-**A3** represent the best acceptor sites leaving the imidazole nitrogen atoms as the second-best acceptors. Thus if the molecular electrostatic potentials can be used to rank the acceptor sites, then the hydrogen bond formation should prefer the best acceptor site.

In fact, in all twelve crystal structures of **A1** and **A3**, the primary hydrogen bond involves the pyridine nitrogen atoms which were considered the best acceptors based on the calculated MEPS. In none of these cases, imidazole nitrogen site compete successfully for an acid-based O-H donor. These results underscores that a relatively simplified, electrostatic-based, view of hydrogen bonding can provide a powerful tool for predicting selectivity in competitive molecular recognition events. Furthermore, analysis of the relationship between the molecular electrostatic potential value on the pyridine nitrogen in **A1**-**A3** and their success rate in forming co-crystals determined by grinding results shows a good correlation, Figure 2.16.

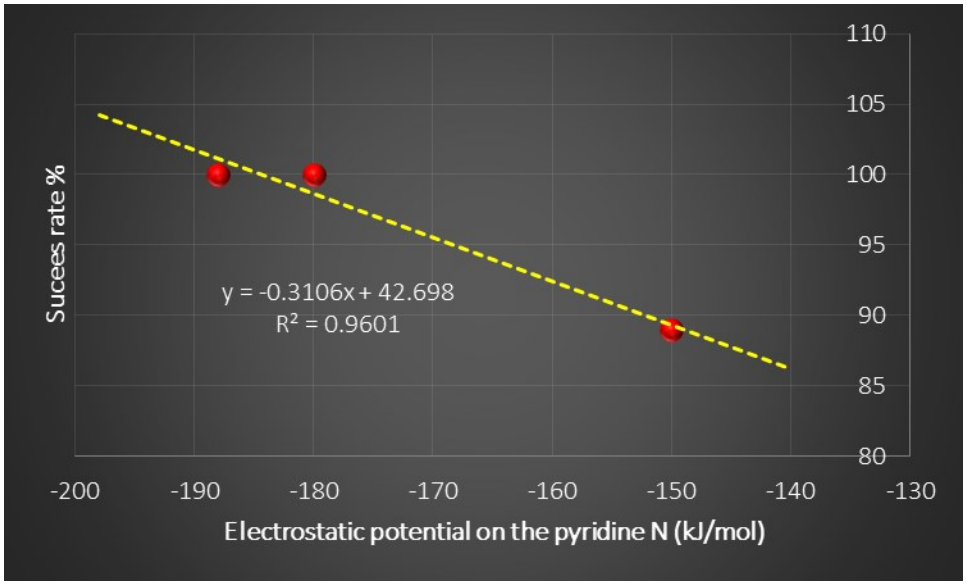

Figure 2.16 Relationship between the molecular electrostatic potential value on the pyridine nitrogen in **A1-A3** and their success rates in forming co-crystals

2.4.3 Selectivity or steric effects?

An alternative argument why the N(py) site was selected in all these structures, could point to unfavorable steric hindrance at the N(im) site. To discard such an idea, **A4** was utilized as a control molecule as it only contains N(im) acceptor sites, but otherwise displays the same shape and size as **A1-A3**. Two of nine attempted co-crystallization reactions yielded co-crystals and the crystal structure obtained for **A4:Mal** confirmed that the imidazole nitrogen sites of these molecules are in fact accessible for interactions. Thus, there is no inherent steric reason for why all co-crystals of **A1-A3** are constructed via O-H···N(py) instead of O-H···N(im) bonds.

2.4.4 Melting point analysis and structure relations

Melting points of all the co-crystals were plotted against the melting points of respective co-formers. For co-crystals of **A1**, the melting points does not show much of a trend, Figure 2.17. Other than the co-crystals of **A1:Mal** and **A1:Adi**, all co-crystals have a melting point between the two co-formers.

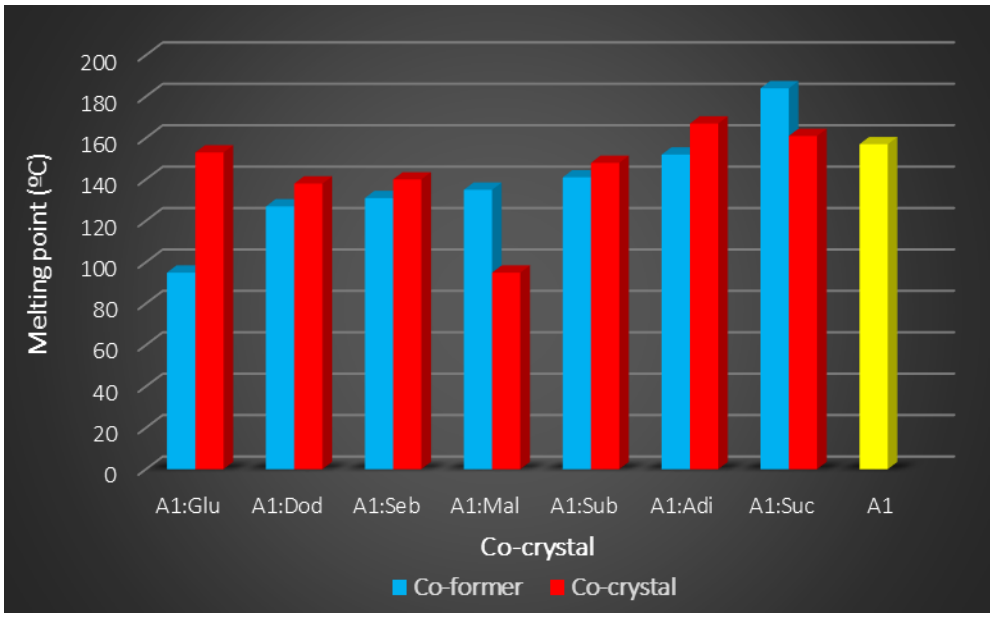

Figure 2.17 Melting points of **A1**-based co-crystals

Furthermore, the melting point of **A1:Glu** is considerably higher than the melting point of glutaric acid, almost close to the value of **A1**. This irregularity can be correlated to the structure of **A1:Glu**, where the 1:2 stoichiometry is observed compared to the other co-crystals of **A1** with 1:1 stoichiometry.

Melting points of **A3** co-crystals show a linear relationship with the melting points of the respective acid, Figure 2.18. Other than the **A3:Adi**, all melting points are lower than both the co-formers in each instance. As in the **A1:Adi** co-crystal the melting point of **A3:Adi** is also different, but a simple structural explanation for this anomaly is not apparent.

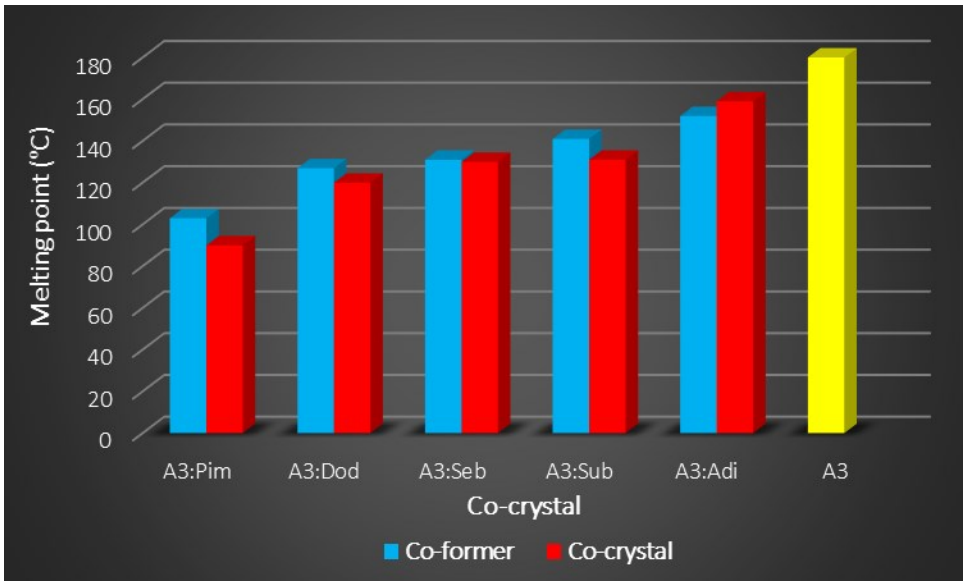

Figure 2.18 Melting points of **A3**-based co-crystals

2.4.5 Variable stoichiometries

In addition to investigating the viability of molecular electrostatic potential dependent selectivity of hydrogen bonding one of the other goals was to explore if the structural outcomes could be substantially affected by changes in reaction stoichiometries. Therefore, we focused our attention on a group of eight reactions that had produced 1:1 co-crystals with **A1** and **A3**, despite a starting reaction stoichiometry of two donors to one acceptor. **A1** and **A3** were then combined with four diacids (adipic acid, suberic acid, sebacic acid and dodecandioic acid) in two different stoichiometries, 1:1 and 1:4 respectively. The objective was to determine if different ratios would influence the nature or extent of O-H···N binding in this family of compounds. Crystalline solids were obtained in all sixteen instances and analyzed using IR spectroscopy and ^{1}H NMR on single-crystal samples. According to the ^{1}H NMR results, all eight crystals produced from 1:1 reaction mixtures yielded products with a 1:1 ratio of donor to acceptor. One of the ^{1}H NMR spectrum is shown in Figure 2.19 and the remaining spectra are provided in Appendix A.1. At this

stoichiometric ratio an excess of acid is not available, thus the hydrogen bond formation undoubtedly prefer the best acceptor pyridine site forming 1:1 co-crystals.

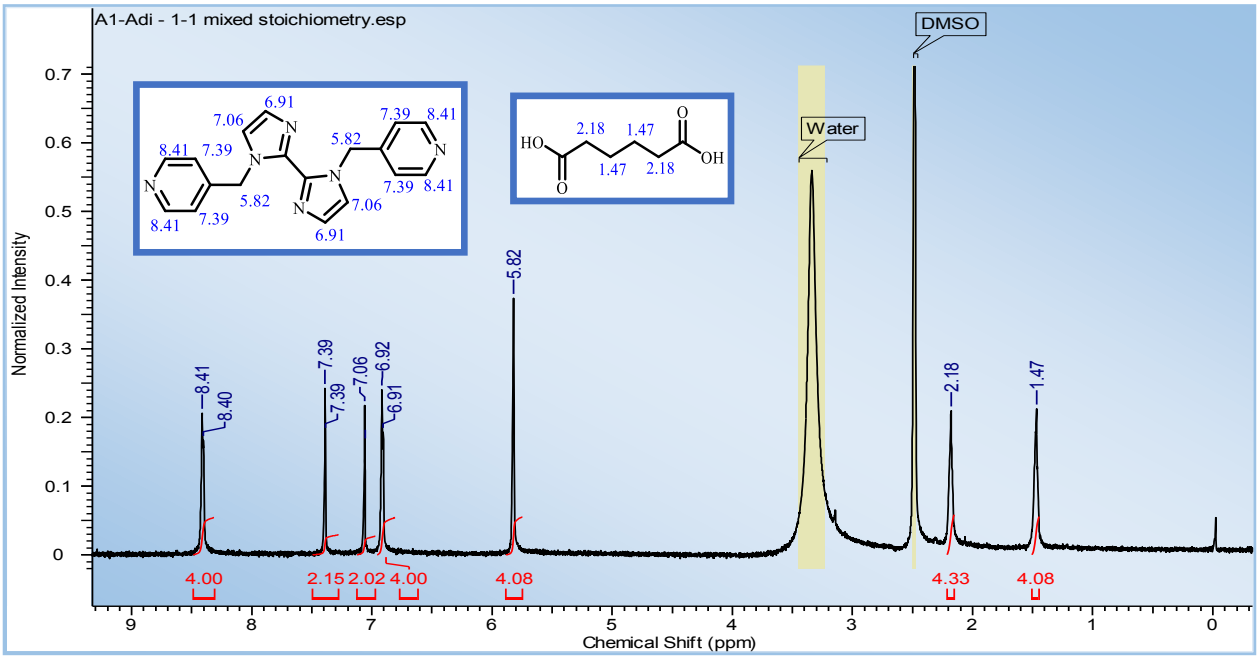

Figure 2.19 ^{1}H NMR of 1:1 stoichiometric co-crystal formation in **A1:Adi** with 1:1 reaction stoichiometry

In six out of eight reactions using 1:4 stoichiometry of reactants, the resulting co-crystals displayed a 1:1 ratio indicating the preference towards the best acceptor site. In two cases, **A1:Sub$_2$** and **A3:Sub$_2$**, the ^{1}H NMR spectra reveal the formation of 1:2 co-crystals, Figure 2.20 and Figure 2.21. Such 1:2 co-crystals can be envisioned as the result of either all four nitrogen atoms in the acceptor being engaged in an O-H···N hydrogen bond or, as observed in **A1:Glu** and **A3:Pim**, the involvement of two nitrogen atoms and a self-complementary acid···acid dimer formation. To distinguish between these two options, the fingerprint region in each infrared spectrum was examined to find evidence for the presence/absence of a symmetric acid···acid dimer, Figure 2.22.

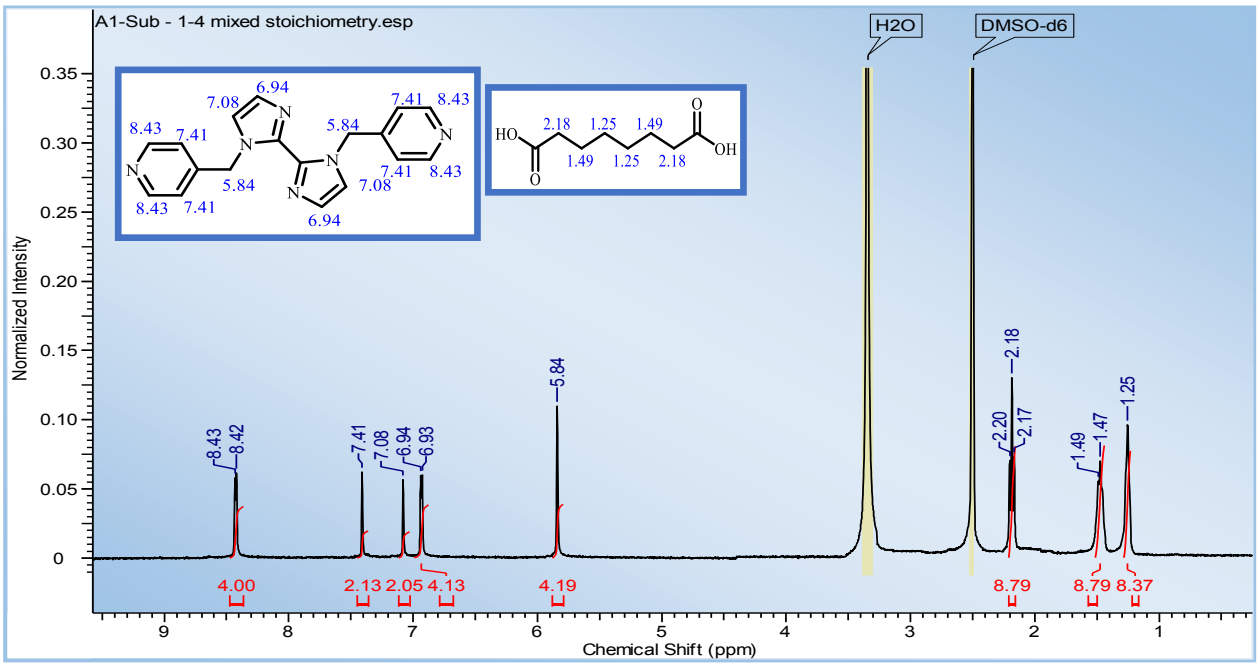

Figure 2.20 ^{1}H NMR of 1:2 stoichiometric co-crystal of **A1:Sub$_2$** with 1:4 reaction stoichiometry

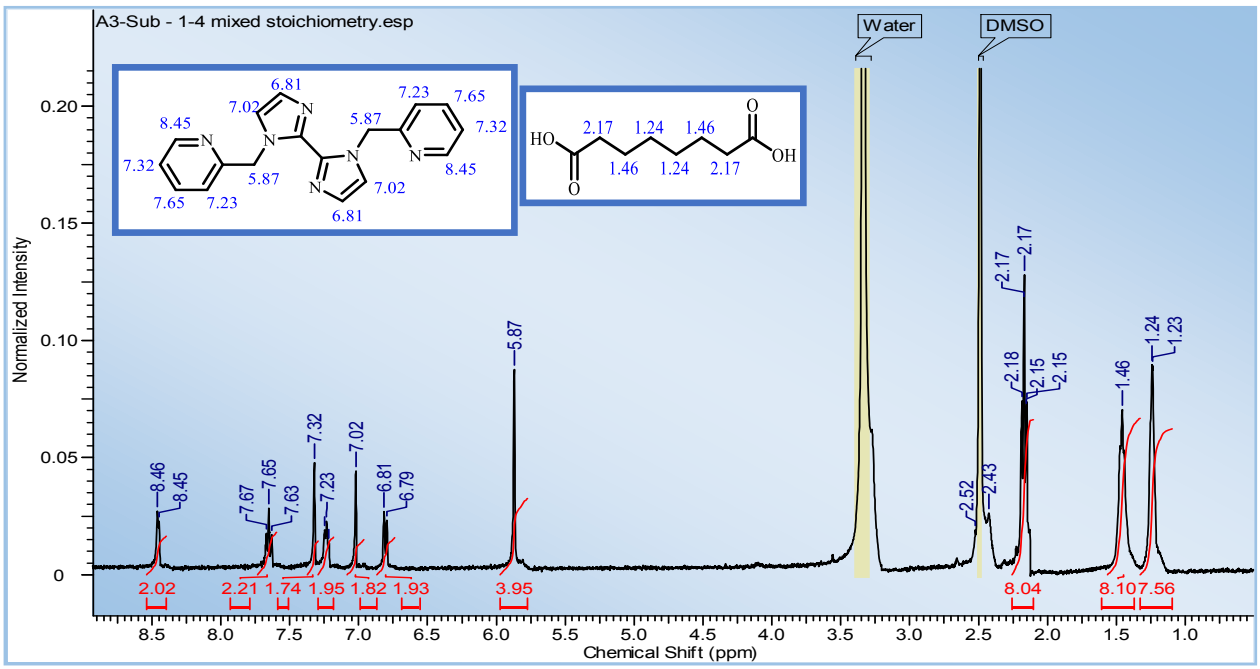

Figure 2.21 ^{1}H NMR of 1:2 stoichiometric co-crystal of **A3:Sub$_2$** with 1:4 reaction stoichiometry

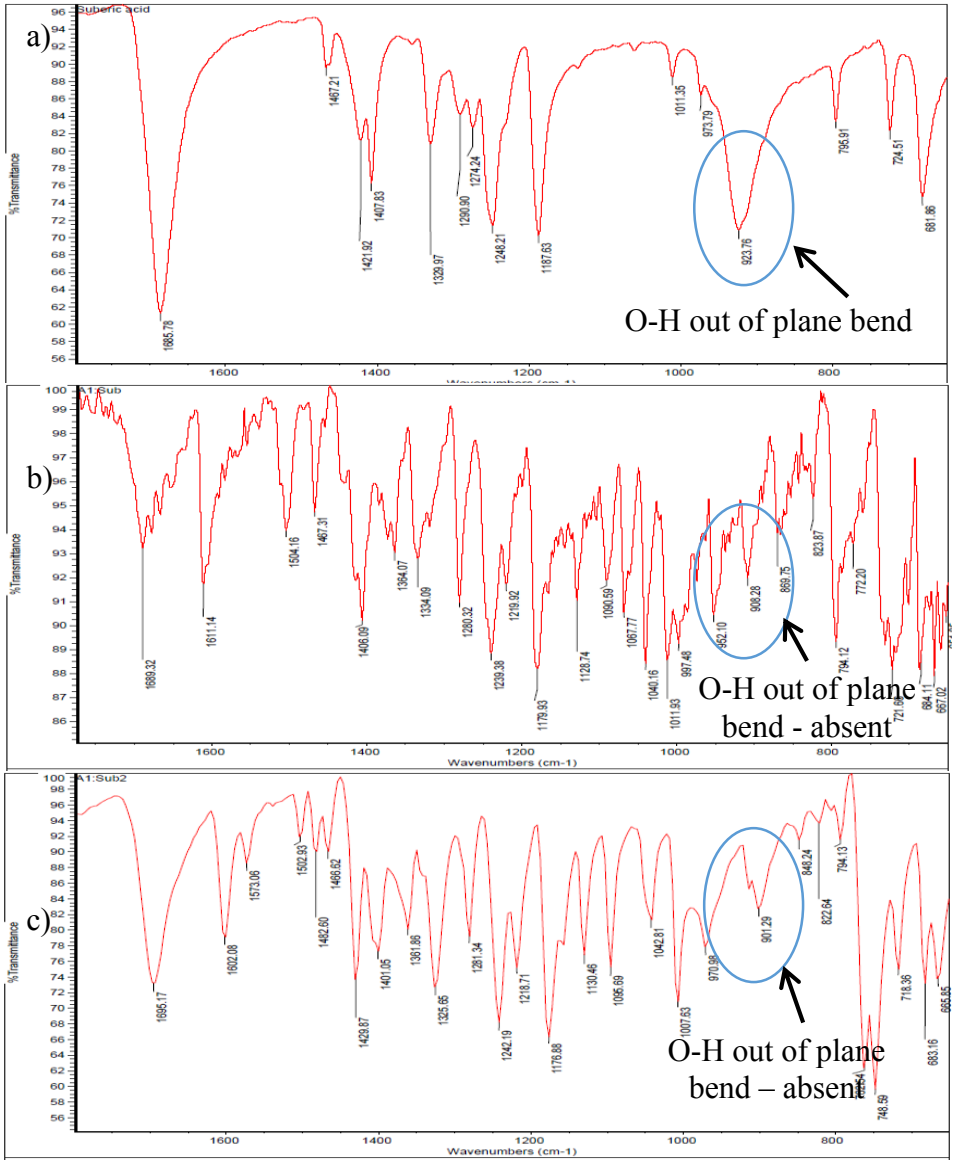

Figure 2.22 O-H out of plane bend for a) suberic acid b) **A1:Sub** and c) **A1:Sub$_2$**

The mode associated with an out-of-plane O-H bend in the acid···acid dimer in suberic acid itself shows up as broad stretch of medium intensity at 923 cm^{-1}. No such mode can be found in the IR spectra of either **A1:Sub$_2$** or **A3:Sub$_2$** which leads to the conclusion that the excess of acid has resulted in a 1:2 co-crystal where all available nitrogen atoms (both pyridine and imidazole) participate in O-H···N heterosynthons. Figure 2.22 compares the O-H out of plane bend stretch in the finger print region of Suberic acid, **A1:Sub** and **A1:Sub$_2$**. Similar results were observed for

A3:Sub and **A3:Sub$_2$** co-crystals providing evidence for the absence of acid···acid dimer, thus the presence of four O-H···N hydrogen bond interactions leading to 1:2 co-crystal formation in **A1:Sub$_2$** and **A3:Sub$_2$**. These results suggest that even in variable stoichiometry, electrostatic potential dependent selectivity still plays the major role in directing intermolecular hydrogen bonds.

2.5 Conclusions

A systematic structural study based on co-crystallizations of four biimidazole based-acceptors and nine aliphatic di-acids was carried out and the results indicate that the use of calculated molecular electrostatic potential surfaces provide a reliable and practical tool for predicting the resulting molecular recognition events. The carboxylic acid moieties in each of the twelve co-crystals always prefer to bind to the better acceptor predicted by MEPS calculations, which, in this case, is a pyridine nitrogen atom rather than an imidazole nitrogen atom, Figure 2.23. In other words, if a powerful hydrogen-bond donor has a choice of acceptor, the selection depends strongly on the molecular electrostatic potential on the acceptor.

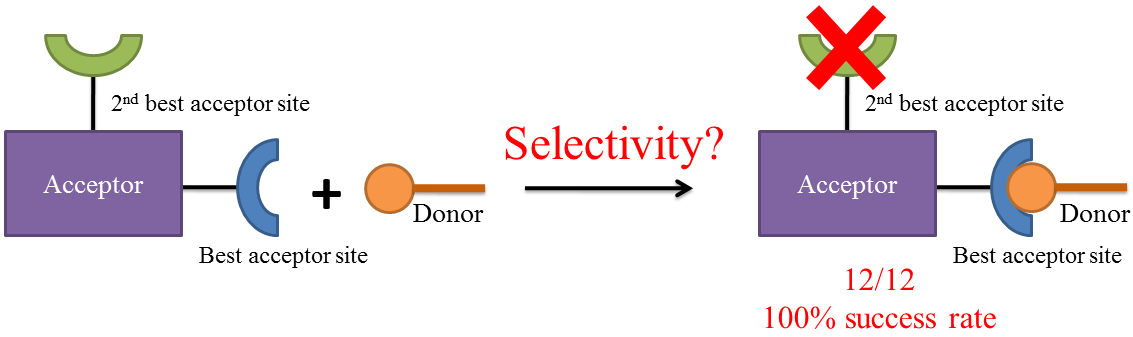

Figure 2.23 Results of the postulated structural outcome

Additionally, variable stoichiometric studies suggested that even the presence of an excessive amount of hydrogen-bond donor does not affect the molecular recognition event. This molecular electrostatic potential dependent selectivity of hydrogen bonding is likely to be a general

feature of strong hydrogen bonds and, as such, will facilitate the use of more complex synthetic strategies for desired supramolecular targets.

2.6 References

1. Aakeröy, C.B.; Wijethunga, T.K.; Desper, J. *J. Mol. Struct.* **2014**, *1072*, 20-27.

2. Buckingham, A.D.; Del Bene, J.E.; McDowell, S.A.C. *Chem. Phys. Lett.* **2008**, *463*, 1-10; Lehn, J.M. *Science* **2002**, *295*, 2400-2403; Moulton, B.; Zaworotko, M.J. *Chem. Rev*. **2001**, *101*, 1629-1658; Desiraju, G.R. *Angew. Chem., Int. Ed*. **1995**, *34*, 2311-2327; Bosch, E. *CrystEngComm* **2007**, *9*, 191-198; Aakeröy, C.B.; Desper, J.; Salmon, D.J.; Smith, M.M. *Cryst. Growth Des.* **2006**, *6*, 1033-1042; Aakeröy, C.B.; Desper, J.; Urbina, J.F. *CrystEngComm* **2005**, *7*, 193-201.

3. Aakeröy, C. B.; Wijethunga, T.K.; Abul Haj, M.; Desper J.; Moore, C. *CrystEngComm* **2014**, *16*, 7218-7225.

4. Gilli, P.; Gilli, G. *The Nature of the Hydrogen Bond*, Oxford University Press, **2009**.

5. Arunan, E.; Desiraju, G.R.; Klein, R.A.; Sadlej, J.; Scheiner, S.; Alkorta, I.; Clary, D.C.; Crabtree, R.H.; Dannenberg, J.J.; Hobza, P.; Kjaergaard, H.G.; Legon, A.C.; Mennucci, B.; Nesbitt, D.J. *Pure Appl. Chem*. **2011**, *83*, 1619-1636.

6. Steiner,T. *Angew. Chem. Int. Ed*. **2002**, *41*, 48-76; Głowacki, E.D.; Irimia-Vlad, M.; Bauer, S.; Sariciftci, N.S. *J. Mater. Chem*. **2013**, *B1*, 3742-3753; Sweetman, A.M.; Jarvis, S.P.; Sang, H.; Lekkas, I.; Rahe, P.; Wang, Y.; Wang, J.; Champness, N.R.; Kantorovich, L.; Moriarty, P. *Nat. Commun.* **2014**, *5*, 3931.

7. Głowacki, E. D.; Vladu, M.I.; Bauer, S.; Sariciftci, N.S. *J. Mater. Chem. B* **2013**, *1*, 3742-3753; Parkinson, G.; Gunasekera, A.; Vojtechovsky, J.; Zhang, X.; Kunkel, T. A.; Berman, H.; Ebright, R. H. *Nat. Struct. Biol.* **1996**, *3*, 837-841; Kool, E. T. *Annu. Rev. Biophys. Bio.* **2001**, *30*, 1-22.

8. Cleland, W.W.; Kreevoy, M.M. *Science* **1994**, *264*, 1887-1890; Cleland, W. W.; Frey, P. A.; Gerlt, J. A. *J. Biol. Chem.* **1998** , *273*, 25529-25532; Gerlt, J. A; Kreevoy, M.M.; Cleland; W.W.; Frey, P. A. *Chem. Biol.* **1997**, *4*, 259-276.

9. Pauling, L.; Corey, R. B.; Branson, H. R. *PNAS* **1951**, *37*, 205-211; Cordier, F.; Grzesiek, S. *J. Am. Chem. Soc*. **1999**, *121*, 1601-1602; Hooft, R. W. W.; Sander, C.; Vriend, G. *Proteins: Struct., Funct., Genet.* **1996**, *26*, 363-376.

10. Fyfe, M.C.T.; Stoddart, J.F. *Acc. Chem. Res.* **1997**, *30*, 393-401; Aakeröy, C. B.; Schultheiss, N.; Desper, J. *Org. Lett.* **2006**, *8*, 2607-2610.

11. Aakeröy, C. B.; Seddon, K. R. *Chem. Soc. Rev*. **1993**, *22*, 397-407; Desiraju, G. R. *Acc. Chem. Res*. **2002**, *35*, 565-573; Aakeröy, C.B.; Beatty, A.M. *Aust. J. Chem.* **2001**, *54*, 409-421.

12. Beijer, F. H.; Kooijman, H.; Spek, A. L.; Sijbesma, R. P.; Meijer, E. W. *Angew. Chem. Int. Ed*. **1998**, *37*, 75-78; Desiraju, G. R. *Acc. Chem. Res.* **1996**, *29*, 441-449.

13. Appel, W. P. J.; Nieuwenhuizen, M. M. L.; Lutz, M.; de Waal, B. F. M.; Palmans, A. R. A.; Meijer, E. W. *Chem. Sci*. **2014**, *5*, 3735-3745.

14. Aakeröy, C.B.; Desper, J.; Urbina, J.F. *Cryst. Growth Des*. **2005,** *5*, 865-873.

15. Aakeröy, C. B.; Chopade, P. D.; Desper, J. *Cryst. Growth Des*. **2011**, *11*, 5333-5336.

16. Mukherjee, A.; Desiraju, G. R. *Chem. Commun*. **2011**, *47*, 4090-4092; Sharma, B.; Sanphui, P.; Nangia, A. *Cryst. Growth Des*. **2010**, *10*, 2388-2399.

17. Etter, M. C. *Acc. Chem. Res*. **1990**, *23*, 120-126.

18. Laurence, C.; Berthelot, M. *Perspect. Drug Discov*. **2000**, *18*, 39-60; Raevsky, O. A. *J. Phys. Org. Chem*. **1997**, *10*, 405-413; Abraham, M. H.; Platts, J. A. *J. Org. Chem*. **2001**, *66*, 3484-3491.

19. Aakeröy, C. B.; Desper, J.; Salmon, D. J.; Smith, M. M. *CrystEngComm* **2009**, *11*, 439-443.

20. Lynch, D.E.; Sandhu, P.; Parsons, S. *Aust. J. Chem.* **2000**, *53*, 383-387.

21. Aakeröy, C. B.; Beatty, A. M.; Helfrich, B. A. *Angew. Chem. Int. Ed*. **2001**, *40*, 3240-3242.

22. Huang, K.; Britton, D.; Etter, M. C.; Byrn, S. R. *J. Mater. Chem.* **1997**, *7*, 713-720.

23. Desiraju, G. R. *Crystal Engineering. The Design of Organic Solids*, Elsevier, **1989**.

24. Hunter, C. A. *Angew. Chem*. **2004**, *43*, 5310-5324; Hunter, C. A. *Angew. Chem*. **2004**, *116*, 5424-5439; Musumeci, D.; Hunter, C. A.; Prohens, R.; Scuderi, S.; McCabe, J. F. *Chem. Sci*. **2011**, *2*, 883-890.

25. Aakeröy, C. B.; Epa, K.; Forbes, S.; Schultheiss, N.; Desper, J. *Chem. Eur. J*. **2013**, *19*, 14998-15003.

26. CSD ConQuest 1.18, **2014**, Cambridge Crystallographic Data Centre, U.K.

27. Saraswatula, V.S.; Bhat, M.A.; Gurunathan, P.K.; Saha, B.K. *CrystEngComm* **2014**, *16*, 4715-4721.

28. Thalladi, V. R.; Nu1sse, M.; Boese, R. *J. Am. Chem. Soc*. **2000**, *122*, 9227-9236; Shevchenko, A.; Miroshnyk, I.; Pietilä, L. O.; Haarala, J.; Salmia, J.; Sinervo, K.; Mirza, S.; Veen, B.; Kolehmainen, E.; Nonappa, Yliruusi, J. *Cryst. Growth Des*. **2013**, *13*, 4877-4887.

29. Xiao, J.; Shreeve, J. M. *J. Org. Chem.* **2005***, 70,* 3072-3078.

30. Omnic 8.0 © **1992-2008**, Thermo Fisher Scientific Inc.

31. Spartan'08, Wavefunction, Inc.

32. Aakeröy, C. B.; Panikkattu, S. V.; DeHaven, B.; Desper, J. *Cryst. Growth Des.* **2012**, *12*, 2579-2587.

33. Aakeröy, C. B.; Salmon, D.J.; Smith, M. M.; Desper, J. *Cryst. Growth Des*. **2006**, *4*, 1033-1042.

34. Silverstein, R. M; Webster, F. X.; Kiemle, D. J. *Spectrometric Identification of Organic Compounds*, Wiley, **2005**.

35. Yadav, L.D.S. *Organic Spectroscopy*, Springer, **2013**.

Chapter 3 - Halogen bond preferences in co-crystal synthesis: A hierarchy based on molecular electrostatic potential surfaces[1]

3.1 Introduction

Intermolecular interactions are important for all molecular recognition events, and represent the primary tools in supramolecular chemistry and crystal engineering.[2] Thus, it is crucial to have a better understanding of the fundamental nature of these interactions in order to successfully design complex supramolecules in a predetermined and effective manner.[3] Halogen bonding is a relatively recent addition to the tool box of supramolecular chemistry.[4] According to IUPAC, "A halogen bond R−X···Y−Z occurs when there is evidence of a net attractive interaction between an electrophilic region on a halogen atom X belonging to a molecule or a molecular fragment R–X (where R can be another atom, including X, or a group of atoms) and a nucleophilic region of a molecule, or molecular fragment, Y−Z".[5] According to this definition, the halogen-bond donor is the halogen atom with an electropositive tip which accepts the electrons from the electronegative acceptor atom, Figure 3.1. The convention is adopted to align it with the generally accepted definition of the hydrogen bond.[6]

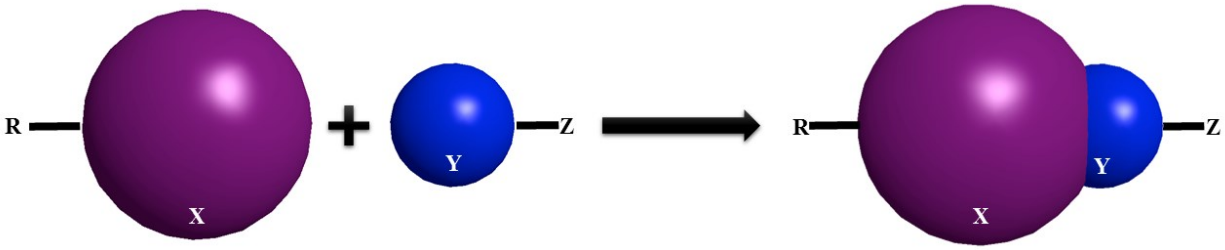

Figure 3.1 Formation of a halogen bond between the electropositive tip of a halogen atom (X) and an electronegative acceptor (Y); R and Z are molecular fragments

Halogen bonds have tunable strength[7] and directionality[8], thus possess the necessary requirements of a suitable supramolecular tool. Halogen-bond donor ability increases in the order of F<Cl<Br<I reflecting the ease of polarizability.[9] Presence of electron-withdrawing substituents

increase the halogen bond strength by serving to activate the halogen-bond donor atom by removing the electron density from the halogen atom.[10] Generally, the bond distance between acceptor and donor atoms in a halogen bond is significantly shorter than the sum of van der Waals radii.[11] In addition to conventional halogen bonds, two other halogen···halogen contacts, classified as type I and type II depending on the geometry of interactions, are frequently reported in crystal structures of halogen-substituted molecules, Figure 3.2.[12] Between these two halogen···halogen contacts, type II interactions are now considered true halogen bonds as they are analogous to conventional halogen bonds according to the IUPAC definition.[13]

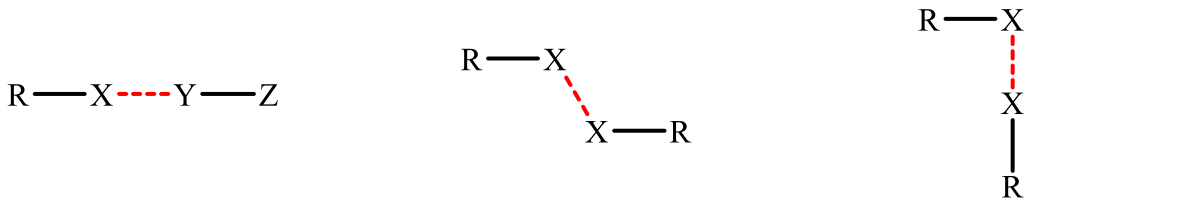

a) Conventional halogen bond b) Type I halogen contact c) Type II halogen contact

Figure 3.2 (a) Conventional halogen bond (b) type I halogen···halogen contact (c) type II halogen···halogen contact; (R & Z- connected molecular fragments, X-halogen atom, Y-acceptor atom)

The interest in halogen bonding started to expand in the last decade or so, rapidly making a transition from fundamental to applied chemistry. For example, halogen bonded mesomorphic and electronic components have been prepared,[14] and catalysis,[15] ion sensing,[16] macromolecular organizations,[17] solid state synthesis[18] and recycling or resolution processes[19] have all been performed with halogen bonding. In addition, halogen bonds have found uses in non-linear optical, photoresponsive and phosphorescent materials, liquid crystals, magnetic and conducting materials and in nanoparticle self-assembly.[20] Halogen bonds are also relevant to life sciences.[21]

As discussed in Chapter 2, in a system with multiple hydrogen-bond moieties, the best hydrogen-bond donor and the best hydrogen-bond acceptor (as determined by electrostatic

potential surfaces) preferentially bind to each other.[22] Considering the fundamental similarities between the hydrogen bond and halogen bond in strength, directionality and specificity,[23] it would be possible to rank and utilize the halogen bonds in a similar manner. Different approaches have been utilized in order to explore a possible hierarchy of halogen bonds.

One such approach[24] uses a basicity scale towards iodoorganic compounds and has found an interesting correlation between the pK_b and the I···Y normalized intermolecular distances. In another study[25] ^{19}F NMR titrations have been used to determine association constants for the interactions of a variety of Lewis bases with fluorinated iodoalkanes and iodoarenes. The results suggest linear free energy relationships for the halogen-bond donor ability of substituted iodoperfluoroarenes, demonstrating that both substituent constants (σ) and calculated molecular electrostatic potential surfaces are useful for constructing such relationships. Numerous theoretical studies[26] as well as experiments in solution phase[27] lead to further revelations about hierarchical halogen bonding. Furthermore, a supramolecular hierarchy among halogen-bond donors have been established using calculated molecular electrostatic potential values.[28] Another study has shown that the relative strength and capability of iodo- and bromo-based molecules to act as halogen-bond donors in a competitive scenario can be related to molecular electrostatic potentials, Figure 3.3.[29]

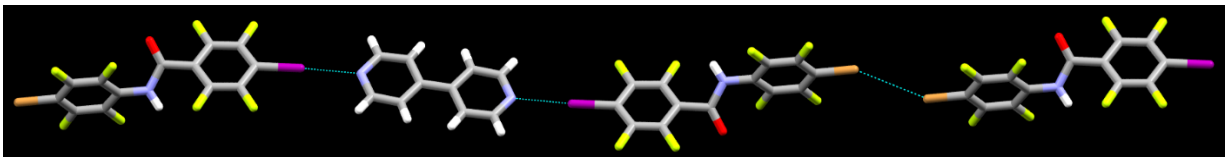

Figure 3.3 Hierarchical halogen bond formation of iodine and bromine (best donor (I) binds to the acceptor while second best donor (Br) forms a type I halogen contact)[27]

All these studies have focused on the ranking of halogen-bond donors, but there is a lack of systematic studies based on the molecular electrostatic potential surfaces for halogen bond

formations. At this point, it is not clear if an electrostatic potential-based ranking of acceptors will work in halogen bonding, due to the scarcity of relevant studies. Thus, we decided to carry out a systematic co-crystallizations on a series of N-heterocyclic halogen-bond acceptors, in order to establish if halogen bonds are also likely to follow best-donor/best-acceptor guidelines. Selected acceptors (**A1**-**A3**) are shown in Figure 3.4. Each of these molecules contain of two types of binding sites, pyridine nitrogen and imidazole nitrogen leading to a total of four acceptor sites per molecule. In addition, to ensure that the imidazole nitrogen atom was not inaccessible due to some steric hindrance, we also included ligand **A4**, with essentially the same shape, but with only one type of acceptor site.

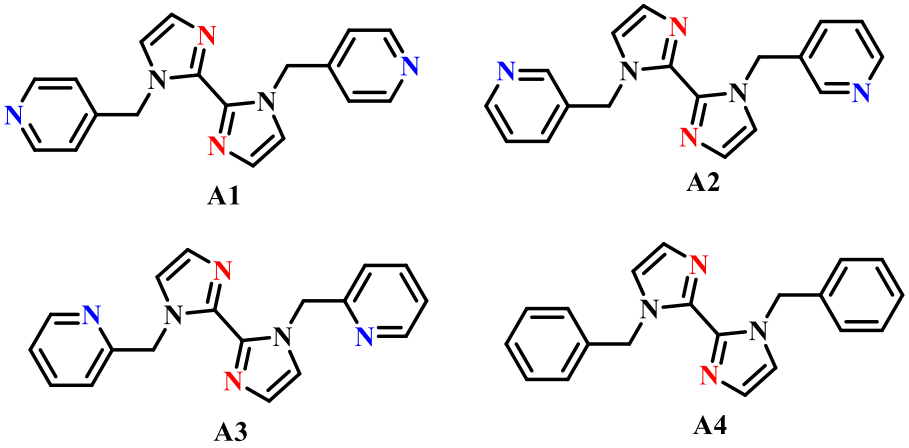

Figure 3.4 Acceptors employed in the study

Ranking of the acceptor sites were performed through calculated molecular electrostatic potential surfaces. These four compounds were then co-crystallized with 13 halogen-bond donors, including ten iodine-based donors (**D1**-**D10**) and three bromine donors (**D11**-**D13**), Figure 3.5. **D5** was included as a control molecule where the iodine is not activated.

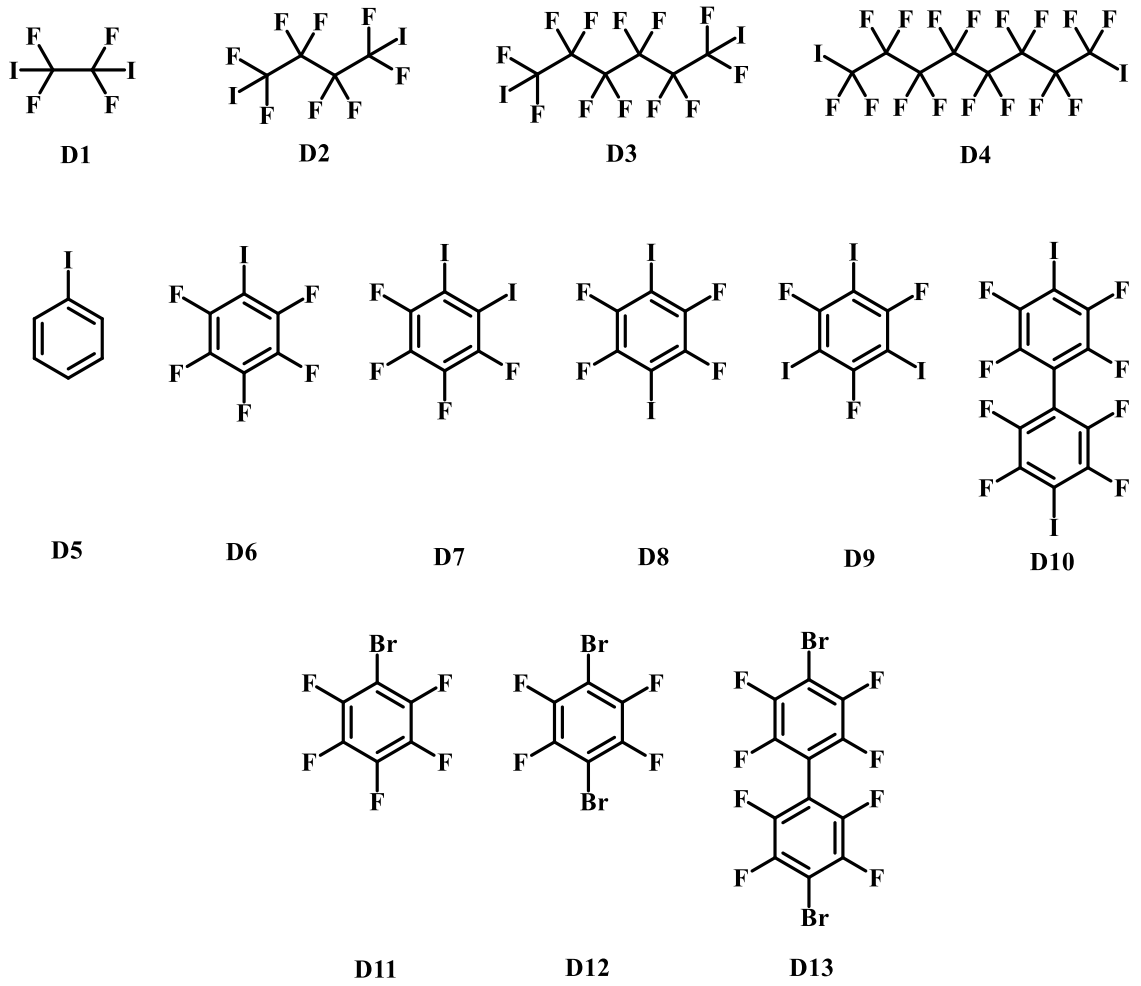

Figure 3.5 Halogen-bond donors employed in this study

The study is undertaken in response to three hypotheses,

1. If a halogen-bond donor has a choice of two different halogen-bond acceptors, it will preferentially select the best-acceptor as determined by molecular electrostatic potentials surfaces (MEPS).
2. A brominated halogen-bond donor will be less successful at forming co-crystals than the corresponding iodoinated analogues.
3. Activation of the halogen bond donor is crucial to form halogen bond interactions.

3.2 Experimental

3.2.1 General

All reagents, solvents, and donors **D1**-**D9** and **D11**-**D13** were purchased from commercial sources and used as received. 2,2'-Biimidazole[30] and **A1**-**A4** were synthesized according to previously reported methods[31] and discussed in Chapter 2. Donor **D10** was prepared according to the synthetic methods reported.[32] ^{1}H NMR spectra were recorded on a Varian Unity plus 400 MHz spectrometer in $CDCl_3$ or DMSO-d_6. Infrared spectra were recorded with a Nicolet 380 FT-IR with a digital resolution of 0.9 cm^{-1} and data processed using Omnic[33] software. Melting points were determined using Fischer-Johns Mel-Temp melting point apparatus and are uncorrected.

3.2.2 Electrostatic potential calculations

Electrostatic potentials on the acceptors and donors were calculated with density functional B3LYP level of theory with 6-311++G** basis set in vacuum. All calculations were carried out using Spartan 8 software.[34] All molecules were geometry optimized and the maxima and minima on the electrostatic potential surface (0.002 e/au isosurface) determined using a positive point charge in the vacuum as a probe. The numbers indicate the interaction energy (kJ/mol) between the positive point probe and the surface of the molecule at that particular point. These numbers are related to the electrostatic potentials on the atoms with the negative number corresponding to a negative potential and positive number corresponding to a positive potential.

3.2.3 Grinding experiments and IR spectroscopy

The initial screening was carried out with solvent-assisted grinding using methanol as the solvent. Acceptors and donors were mixed in respective stoichiometric quantities and the solid resulting from each reaction was characterized by IR spectroscopy. Successful interactions between the acceptor and donor were identified using specific shifts of the peaks of the mixture

compared to starting compounds, Figure 3.6. In each reaction, 10 mg of the acceptor was used with stoichiometric amount of the respective halogen-bond donor. In 25 of 52 experiments the vibrational spectra displayed shifts of peaks in the fingerprint region compared to their initial positions (Figure 3.6) indicative of halogen bond formation.

3.2.4 Synthesis of co-crystals

The resulting mixtures from grinding experiments were dissolved in a minimum amount of methanol and placed in a 2 dram borosilicate vial for slow evaporation in order to obtain crystals suitable for single crystal X-ray diffraction. Once the crystals were formed they were again analyzed using IR spectroscopy, melting point analysis and subjected to single crystal X-ray diffraction. 16 crystals were obtained and their structures subsequently solved with single crystal X-ray diffraction. Table 3.1 summarizes the experimental details. Appendix B.2 contains the relevant X-ray experimental data.

Table 3.1 Experimental details of the sixteen co-crystals obtained

Code	Mixed Mole ratio	Amounts used	Solvent and method	Crystal stoichiometry	Melting point (°C)	Crystal color & habit
A1:D1	1:2	**A1** -10 mg, 0.032 mmol **D1** - 22 mg, 0.063 mmol	Methanol Slow evaporation	1:1	57-60	Colorless prism
A1:D2	1:2	**A1** - 10 mg, 0.032 mmol **D2** - 29 mg, 0.063 mmol	Methanol Slow evaporation	1:1	118-120	Colorless plate
A1:D3	1:2	**A1** - 10 mg, 0.032 mmol **D3** - 35 mg, 0.063 mmol	Methanol Slow evaporation	1:2	94-97	Bronze prism
A1:D4	1:2	**A1** - 10 mg, 0.032 mmol **D4** - 41 mg, 0.063 mmol	Methanol Slow evaporation	1:2	99-103	Colorless plate
A1:D7	1:2	**A1** - 10 mg, 0.032 mmol **D7** - 25 mg, 0.063 mmol	Methanol Slow evaporation	1:2	152-154	Colorless prism
A1:D8	1:2	**A1** - 10 mg, 0.032 mmol **D8** - 25 mg, 0.063 mmol	Methanol Slow evaporation	1:1	139-143	Colorless plate
A1:D10	1:2	**A1** - 10 mg, 0.032 mmol **D10** - 35 mg, 0.063 mmol	Methanol Slow evaporation	1:2	140-142	Colorless prism
A2:D2	1:2	**A2** - 10 mg, 0.032 mmol **D2** - 29 mg, 0.063 mmol	Methanol Slow evaporation	1:1	75-78	Colorless plate
A2:D3	1:2	**A2** - 10 mg, 0.032 mmol **D3** - 35 mg, 0.063 mmol	Methanol Slow evaporation	1:1	95-97	Colorless block
A2:D7	1:2	**A2** - 10 mg, 0.032 mmol **D7** - 25 mg, 0.063 mmol	Methanol Slow evaporation	1:2	92-95	Colorless plate

A2:D8	1:2	**A2** - 10 mg, 0.032 mmol **D8** - 25 mg, 0.063 mmol	Methanol Slow evaporation	1:1	160-163	Colorless prism
A2:D9	1:2	**A2** - 10 mg, 0.032 mmol **D9** - 32 mg, 0.063 mmol	Methanol Slow evaporation	1:2	150-152	Colorless prism
A2:D10	1:2	**A2** - 10 mg, 0.032 mmol **D10** - 35 mg, 0.063 mmol	Methanol Slow evaporation	1:2	143-146	Colorless prism
A3:D9	1:2	**A3** - 10 mg, 0.032 mmol **D9** - 32 mg, 0.063 mmol	Methanol Slow evaporation	1:1	149-153	Colorless prism
A3:D10	1:2	**A3** - 10 mg, 0.032 mmol **D10** - 35 mg, 0.063 mmol	Methanol Slow evaporation	1:2	142-145	Colorless plate
A4:D9	1:1	**A4** - 10 mg, 0.032 mmol **D9** - 16 mg, 0.032 mmol	Methanol Slow evaporation	1:1	148-150	Colorless plate

3.3 Results

3.3.1 Electrostatic potentials

The ditopic acceptor molecules used in this study (**A1**-**A3**) contain two different types of acceptor sites, pyridine nitrogen (N(py)) and imidazole nitrogen (N(im)). The control molecule **A4** contains only N(im) sites. The ranking of the acceptor sites is established using molecular electrostatic potential surfaces and the results from the DFT calculations are provided in Table 3.2. Higher negative potential on the acceptor depicts better halogen-bond accepting ability. Table 3.2 also summaries the electrostatic potentials on halogen-bond donors. The higher the positive value on the donor site, the higher the expected halogen-bond donor ability.

Table 3.2 Calculated surface potential values of the acceptors and donors

	Molecule	Atom	Electrostatic potential (kJ/mol^{-1})
Acceptors	1,1'-bis(pyridin-4-ylmethyl)-2,2'-biimidazole **A1**	Pyridine N	-188
		Imidazole N	-124
	1,1'-bis(pyridin-3-ylmethyl)-2,2'-biimidazole **A2**	Pyridine N	-180
		Imidazole N	-125
	1,1'-bis(pyridin-2-ylmethyl)-2,2'-biimidazole **A3**	Pyridine N	-150
		Imidazole N	-120
	1,1'-dibenzyl-2,2'-biimidazole **A4**	Imidazole N	-149
Donors	1,2-diiodotetrafluoroethane **D1**	Iodine	+163
	1,4-diiodooctafluorobutane **D2**	Iodine	+168
	1,6-diiodoperfluorohexane **D3**	Iodine	+169
	1,8-diiodoperfluorooctane **D4**	Iodine	+169
	Iodobenzene **D5**	Iodine	+103
	Iodopentafluorobenzene **D6**	Iodine	+166

	1,2-diiodotetrafluorobenzene **D7**	Iodine	+162
	1,4-diiotetrafluorobenzene **D8**	Iodine	+169
	1,3,5-triiodotrifluorobenzene **D9**	Iodine	+158
	4,4'-diiodoperfluorobiphenyl **D10**	Iodine	+164
	Bromopentafluorobenzene **D11**	Bromine	+143
	1,4-diiodotetrafluorobenzene **D12**	Bromine	+139
	4,4'-dibromopurfluorobiphenyl **D13**	Bromine	+132

3.3.2 Grinding experiments and characterization by IR spectroscopy

Based on IR spectroscopy 25 of the 52 experiments resulted in successful co-crystal formation, equivalent to a supramolecular yield of 48%. All co-crystals showed the presence of peaks from both starting compounds as well as shifts of C-F vibrations compared to the respective halogen-bond donor. Table 3.3 summarizes the selected peak shifts of co-crystals identified by IR analysis along with the comparison of IR spectra for co-crystal **A2:D3**, Figure 3.6.

Table 3.3 IR analysis of C-F stretches for the ground mixtures

Co-crystal	Halogen-bond donor (cm^{-1})	Ground mixture (cm^{-1})
A1:D1	1153, 1099	1118, 1083
A1:D2	1192, 1133	1187, 1115
A1:D3	1199, 1141	1211, 1134
A1:D4	1204, 1146	1211, 1139
A1:D6	1488, 974	1483, 962
A1:D7	1489, 1438	1500, 1433
A1:D8	1459, 941	1455, 938
A1:D9	1403, 1049	1396, 1037
A1:D10	1459, 954	1456, 948
A2:D1	1153, 1099	1131, 1083
A2:D2	1192, 1133	1162, 1137
A2:D3	1199, 1141	1213, 1138
A2:D4	1204, 1146	1216, 1142
A2:D6	1488, 974	1479, 967
A2:D7	1489, 1438	1487, 1435
A2:D8	1459, 941	1461, 937
A2:D9	1563, 1049	1560, 1041
A2:D10	1459, 954	1453, 945
A3:D7	1489, 1438	1488, 1434
A3:D8	1459, 941	1462, 942
A3:D9	1403, 1049	1397, 1039
A3:D10	1459, 954	1455, 951
A4:D7	1489, 1438	1486, 1434
A4:D8	1459, 941	1461, 938
A4:D9	1563, 1403	1561, 1400

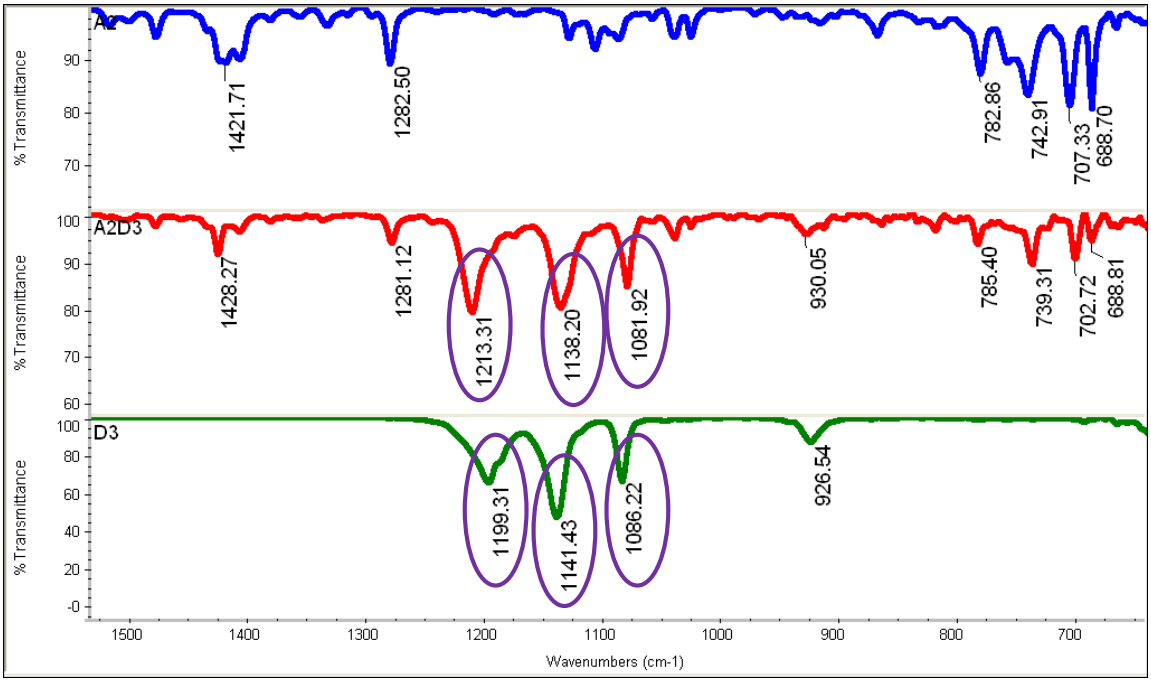

Figure 3.6 Comparison of IR spectra for **A2:D3** (red) with the IR spectra of **A2** (blue) and **D3** (green); purple circles highlight the shifts in C-F stretches

3.3.3 Crystal growth and structure analysis

All the reaction combinations were used in solvent based crystallization attempts even if the IR results did not show successful reaction. The method of crystallization for all attempts was slow evaporation from methanolic solutions. 16 crystals were obtained and analyzed using single crystal X-ray diffraction in order to examine any halogen-bond preferences.

Seven structures were obtained for **A1**-based co-crystals, six for **A3**-based co-crystals, and two co-crystals with **A2** and one with **A4** was structurally characterized. The supramolecular yields from the study are summarized in Table 3.4. Relevant crystallographic data and key halogen bond geometries for the 16 crystal structures are provided in Appendix B.2.

Table 3.4 Summary of supramolecular yields

	A1	A2	A3	A4
Potentials kJ/mol	$N_{pyridine}$ – (-188) $N_{imidazole}$ – (-124)	$N_{pyridine}$ – (-180) $N_{imidazole}$ – (-125)	$N_{pyridine}$ – (-150) $N_{imidazole}$ – (-120)	$N_{imidazole}$ – (-149)
Success rate - grinding	9/13	9/13	4/13	3/13
Success rate – slow evaporation	7/13	6/13	2/13	1/13
Total supramolecular yield	69%	69%	31%	23%
Success rate with iodine donors – grinding	9/10	9/10	4/10	3/10
Supramolecular yield with iodine donors	90%	90%	40%	30%
Total supramolecular yield – 48% Total supramolecular yield with iodine donors – 63% Total supramolecular yield with bromine donors – 0%				

3.3.4 Crystal structures

3.3.4.1 Structures of A1-based co-crystals

Seven co-crystals based on **A1** were obtained, **A1:D1**, **A1:D2**, **A1:D3**, **A1:D4, A1:D7**, **A1:D8** and **A1:D10.**

The crystal structure of **A1:D1** shows a 1:1 stoichiometry and primary halogen bonds take place with the N(py) atoms of the acceptor, Figure 3.7, leading to infinite 1-D chains. There are no obvious structure directing short contacts involving the imidazole nitrogen atoms.

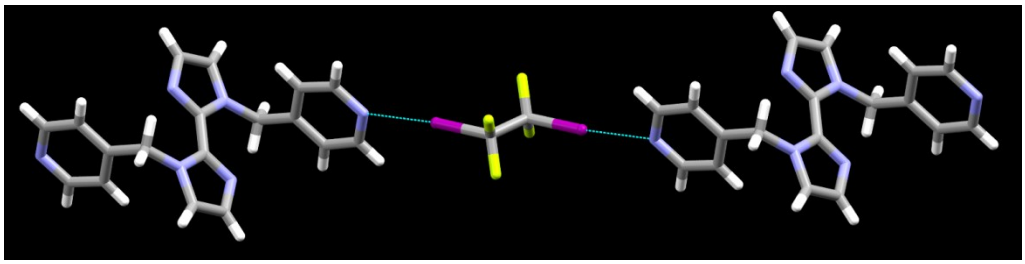

Figure 3.7 Primary halogen bond interactions in **A1:D1**

The crystal structure of **A1:D2** shows a 1:1 stoichiometry with primary halogen bond interactions between iodine and pyridine nitrogen atoms, Figure 3.8. The imidazole nitrogen atoms are not involved in any notable short contacts.

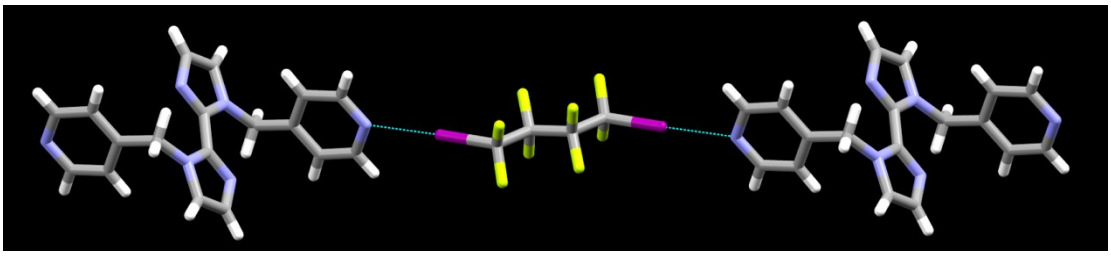

Figure 3.8 Primary halogen bonds in the crystal structure of **A1:D2**

Unlike in previous cases, the crystal structure of **A1:D3** shows 1:2 stoichiometry. Thus all four nitrogen atoms of **A1**, Figure 3.9, participate in halogen bonds. The extended architecture is composed of 1-D chains of molecular rectangles.

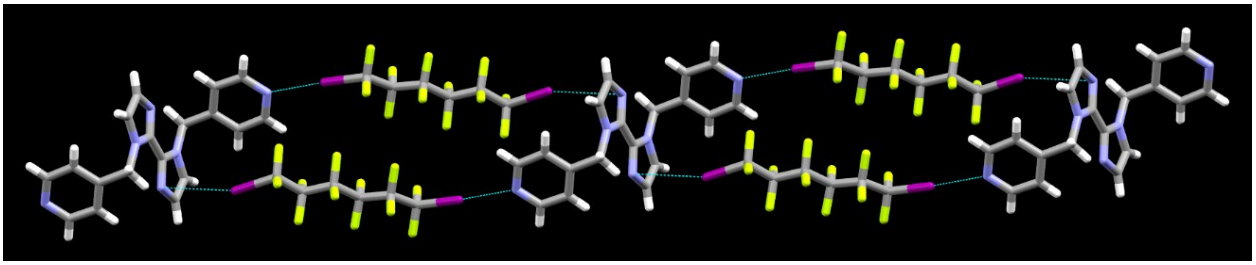

Figure 3.9 Primary halogen bond interactions in **A1:D3**

The crystal structure **A1:D4** has a 1:2 stoichiometry. Unlike in previous structures, iodine atoms in **D4** behave asymmetrically leading to a trimer formation in **A1:D4**, with only one iodine atom participating in a halogen bond with pyridine N, Figure 3.10. The second iodine atom and the imidazole nitrogen atoms are not involved in any notable short contacts.

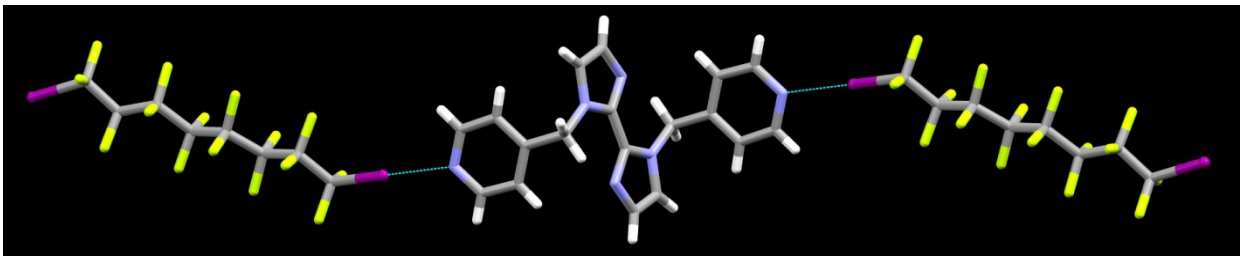

Figure 3.10 Primary halogen bond interactions in **A1:D4** leading to a trimer

The crystal structure of **A1:D7** displays 1:2 stoichiometry where one acceptor molecule interacts with two donor molecules forming a discrete trimer, Figure 3.11. The primary halogen bonds take place between one of the two iodine atoms and the N-pyridine moiety (the best acceptor) whereas the second iodine atom is involved in an I···I type II contact (Figure 3.2) with an iodine atom from a neighboring donor molecule, Figure 3.11.

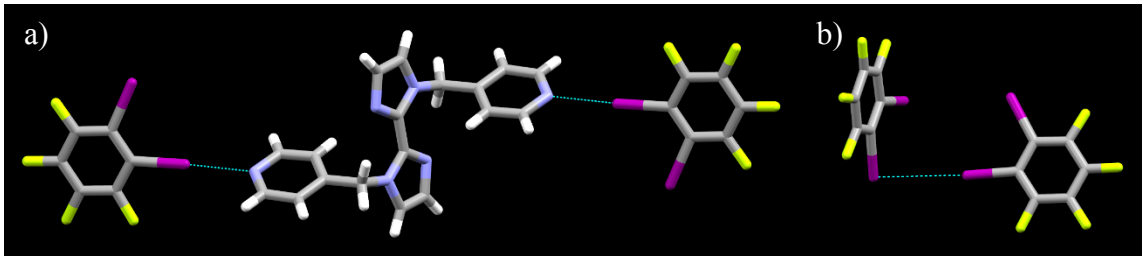

Figure 3.11 a) Primary halogen bond interactions in the co-crystal **A1:D7** and b) secondary interactions in co-crystal **A1:D7**

The crystal structure of **A1:D8** has a 1:1 stoichiometry and contains infinite 1-D chains constructed from I···N(py) halogen bonds, Figure 3.12. The imidazole nitrogen atoms do not participate in halogen bonding and instead form short contacts with C-H moieties of a neighboring acceptor molecule, resulting in a stacking of adjacent chains, Figure 3.12.

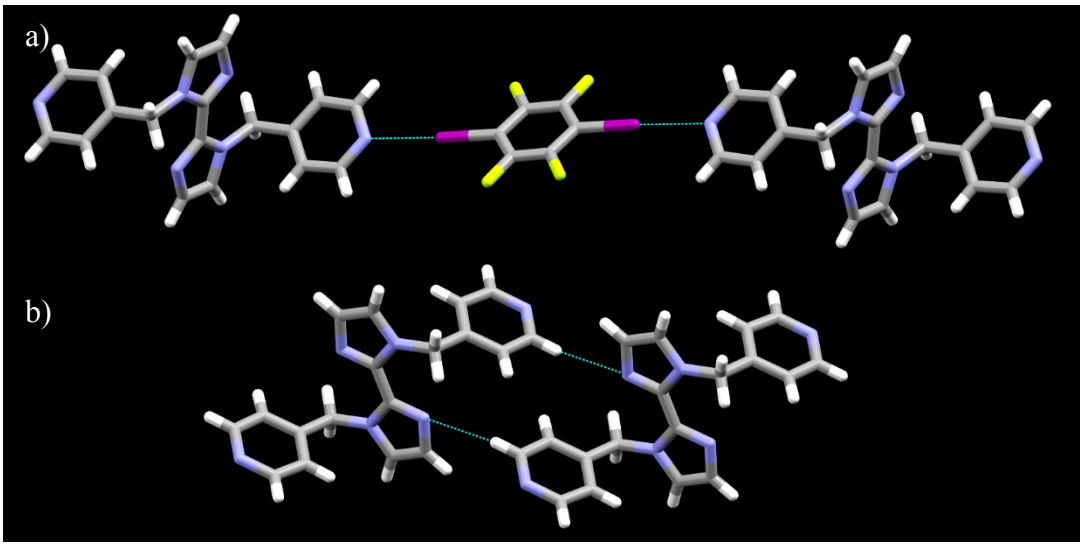

Figure 3.12 a) Formation of infinite chains via halogen bonds in **A1:D8** and b) secondary interactions of imidazole nitrogen atoms

The last co-crystal structure obtained with **A1**, **A1:D10** has 1:2 stoichiometry and contains discrete trimers as the second iodine atom does not participate in a halogen bond. Again, the best acceptor, N(py) is the preferred binding site, Figure 3.13. Neither imidazole nitrogen atom nor the second iodine atom of the donor participate in any notable intermolecular interactions.

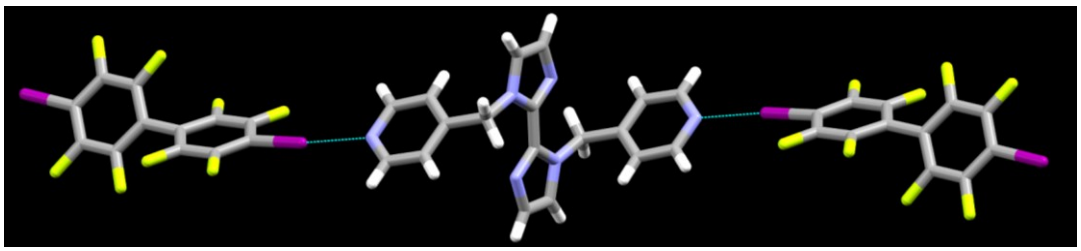

Figure 3.13 Trimer formation in co-crystal **A1:D10**

3.3.4.2 Structures of A2-based co-crystals

Six co-crystal structures were obtained with **A2**, **A2:D2**, **A2:D3 A2:D7**, **A2:D8**, **A2:D9** and **A2:D10**. Co-crystal **A2:D2** has a stoichiometry of 1:1. **A2:D2** is constructed via the primary halogen bonds between iodine and pyridine nitrogen atoms (the best acceptor) which lead to 1-D infinite chains, Figure 3.14. The imidazole nitrogen atoms are not engaged in any short contacts.

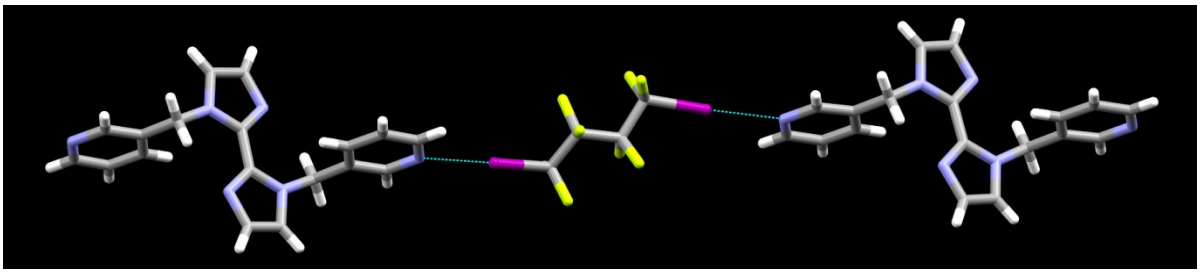

Figure 3.14 Halogen bonds in the crystal structure of **A2:D2**

The crystal structure of **A2:D3** also shows that the co-crystal has a 1:1 stoichiometry with I···N(py) halogen bonds, Figure 3.15. The structure contains 1-D chains in a zigzag pattern formed via I···N(py) and imidazole nitrogen atoms are participating in self-complementary hydrogen bonds, Figure 3.15.

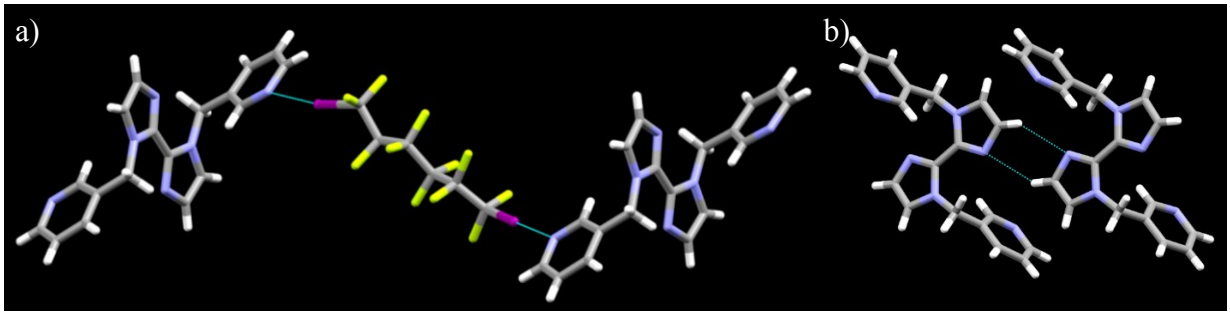

Figure 3.15 a) Primary halogen bond interactions in **A2:D3** and b) self-complementary hydrogen bonds of imidazole moiety

In the crystal structure of **A2:D7** the best-acceptor, N(py) forms a bifurcated halogen bond, Figure 3.16, which leads to the formation of chains of tetrameric rhombic shape architectures. No notable secondary interactions are found with the imidazole nitrogen atoms.

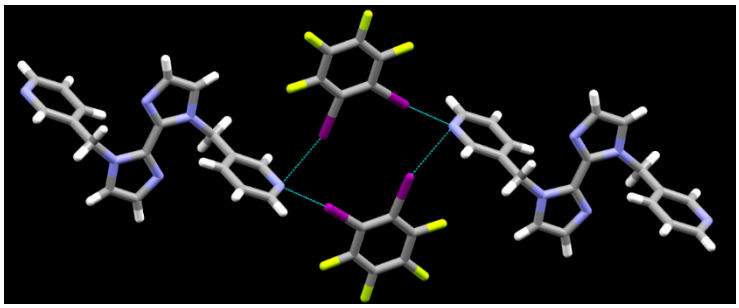

Figure 3.16 Primary halogen bond interaction in **A2:D7**

The crystal structure of **A2:D8** has a 1:1 stoichiometry and contains 1-D chains. Imidazole nitrogen atoms participate in secondary short contacts as observed in **A1:D8**, Figure 3.17.

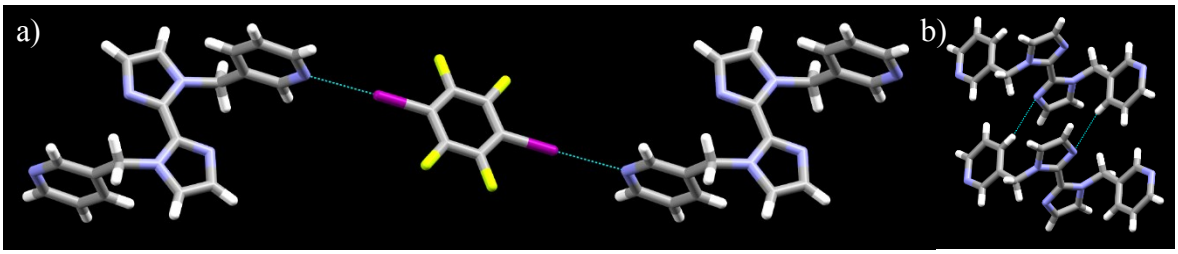

Figure 3.17 a) Primary and b) secondary interactions in **A2:D8**

The crystal structure of **A2:D9** also displays a 1:1 stoichiometry. Unlike in previous cases, this structure contains two distinct halogen-bond motifs. First, a trimer assembled via a I···N(py) halogen bonds, Figure 3.18. The latter leads to 'chains of hexamers' where all four nitrogen atoms form halogen bonds, Figure 3.18. The third iodine atom of the donor molecule is inactive, which is a documented phenomenon associated with this particular halogen-bond donor.[35]

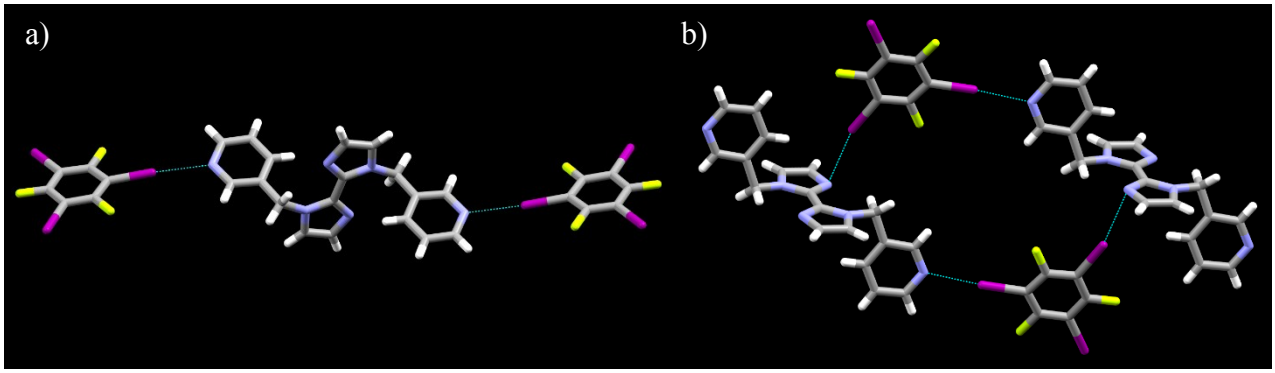

Figure 3.18 a) Trimer formation in **A2:D9** and b) a hexagon in the crystal structure of **A2:D9**

In crystal structure of **A2:D10** all four nitrogen atoms are participating in halogen bonds leading to infinite ribbons, Figure 3.19.

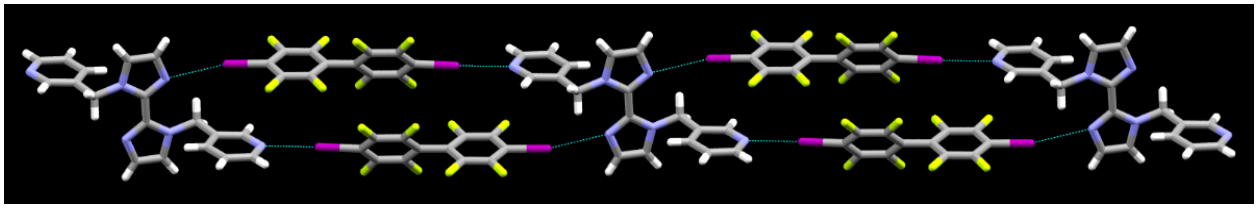

Figure 3.19 An infinite ribbon in **A2:D10**

3.3.4.3 Structures of A3-based co-crystals

Only two crystal structures were obtained with **A3**. **A3:D9** has a stoichiometry of 1:1 and contains 1-D chains assembled using I···N(py), Figure 3.20. The imidazole nitrogen atoms and the third iodine atom do not have any significant short contacts.

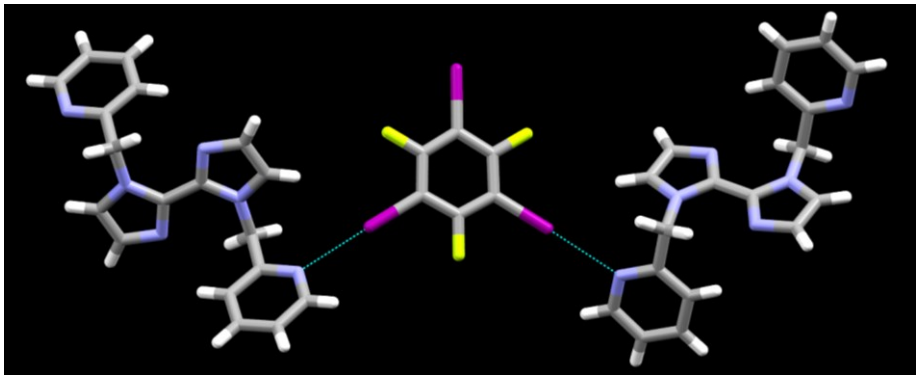

Figure 3.20 Primary halogen bond interactions in co-crystal **A3:D9**

The structure of **A3:D10** shows that the acceptor and donor are present in a 1:2 stoichiometry and, similarly to the structure **A2:D10**, contains chains of rectangles using all four nitrogen atoms on the acceptor, Figure 3.21.

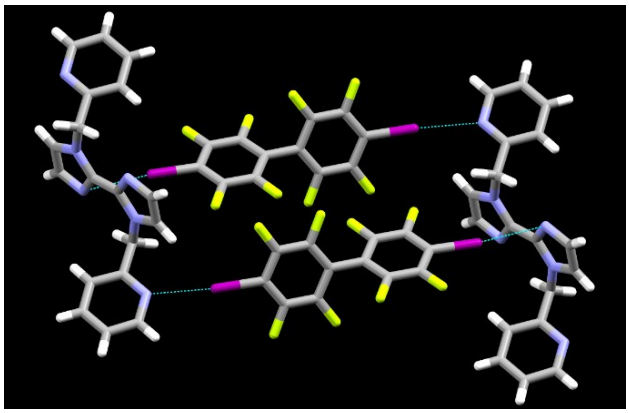

Figure 3.21 Rectangle in the structure of **A3:D10**

3.3.4.4 Structures of A4-based co-crystals

Only one crystal structure was obtained with **A4**, **A4:D9**. In the 1:1 co-crystal of **A4:D9**, the 'arms' of the acceptor are directed to same side of the molecule. One of the imidazole nitrogen atoms form a conventional, near-linear halogen bond, whereas the other imidazole nitrogen atom forms a bifurcated halogen bond with two adjacent donor molecules, Figure 3.22. Interestingly, all

three iodine atoms of the donor participate in halogen bonds which is unique in this series of crystal structures, Figure 3.22.

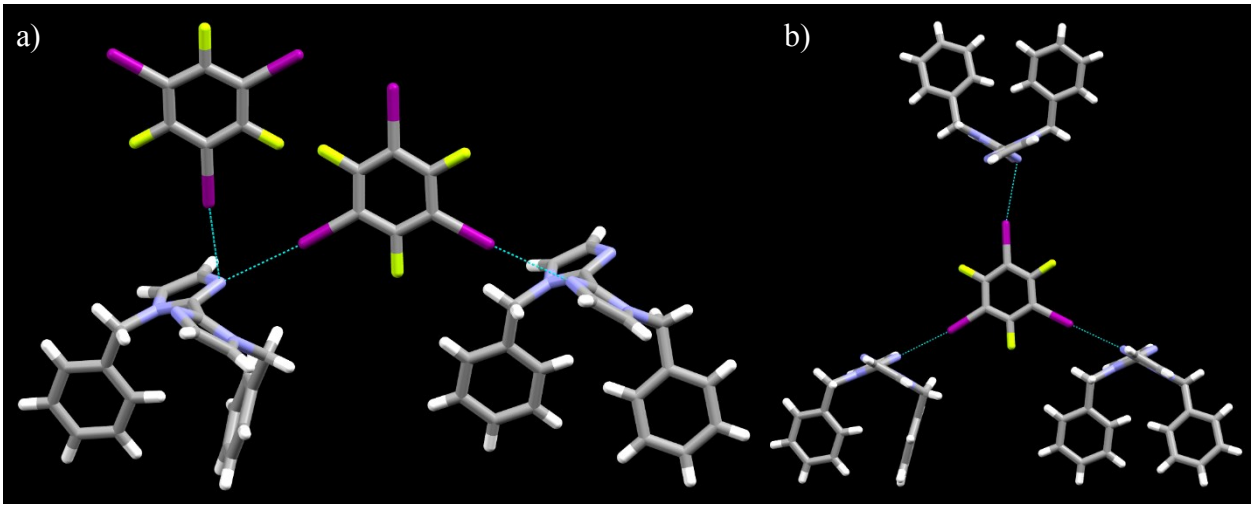

Figure 3.22 a) Halogen bond interactions in the structure of **A4:D9** and b) all three iodine atoms in **D9** participating in halogen bonding

3.4 Discussion

The sequence of experiments performed in this study represents an attempt at identifying patterns of behavior that can have a general applicability when it comes to understanding halogen-bond driven molecular recognition events and co-crystal synthesis, as well as to determine if halogen-bond interactions follow the same best-donor/best-acceptor rules (where the ranking is based on electrostatics) as are hydrogen bonds. 52 co-crystallizations were performed using three molecules with two different acceptor sites on each of them and one control molecule with only one type of nitrogen atoms. Co-crystallization attempts were conducted between the four acceptors and 13 halogen-bond donors.

3.4.1 Characterization by IR spectroscopy

IR spectroscopy is known to be a versatile, convenient and accurate screening method for determining if a particular combination of donors and acceptor resulted in the formation of a co-

crystal.[36] When the halogen bonds are formed between acceptors and donors, some of the original stretching bands are affected although it is sometimes difficult to find obvious patterns to the way in which some of modes are red or blue shifts compared to their original positions. This is consistent with previously reported observations of halogen bonds in the solid state.[37]

3.4.2 Relationship between molecular electrostatic potentials and halogen bond formation

The three ditopic acceptors **A1-A3** have two acceptor sites that differ primarily by their electrostatic potentials. According to the DFT calculated MEPS values, N(py) has more negative potential than N(im) making it the best acceptor. The grinding experiments showed a good correlation between the potential on the acceptor sites and the supramolecular yield (success of reaction) indicating that electrostatic potentials play a major role in ranking the relative strength and efficiency of competing halogen-bond sites, Table 3.4. Partial potential on the N(py) atoms of **A1** and **A2** are close, and their success rates are also similar. Upon moving from **A1** to **A4** the electrostatic potential on the nitrogen atoms are decreasing and their success rates are also decreasing indicating the strong dependency of electrostatic potential governing halogen bond formation in co-crystal synthesis. An examination of all 15 crystal structures with ditopic acceptors clearly demonstrate that, given a choice, a strong halogen-bond donor preferentially interacts with an acceptor atom with a higher negative electrostatic potential, which proves the initial hypothesis that halogen-bond selectivity follows a best-donor/best acceptor guideline. Four of these 15 structures showed the participation of an imidazole nitrogen atom in a halogen bond, **A1:D3**, **A2:D9**, **A2:D10** and **A3:D10**. In all four structures I···N(im) distances were substantially longer than the I···N(py) distances. An analysis of van der Waals radii reduction percentages for two types

of halogen bonds for these four structures provide an indication that I···N(py) interactions are more favorable and stronger than I···N(im) interactions,[38] Figure 3.23.

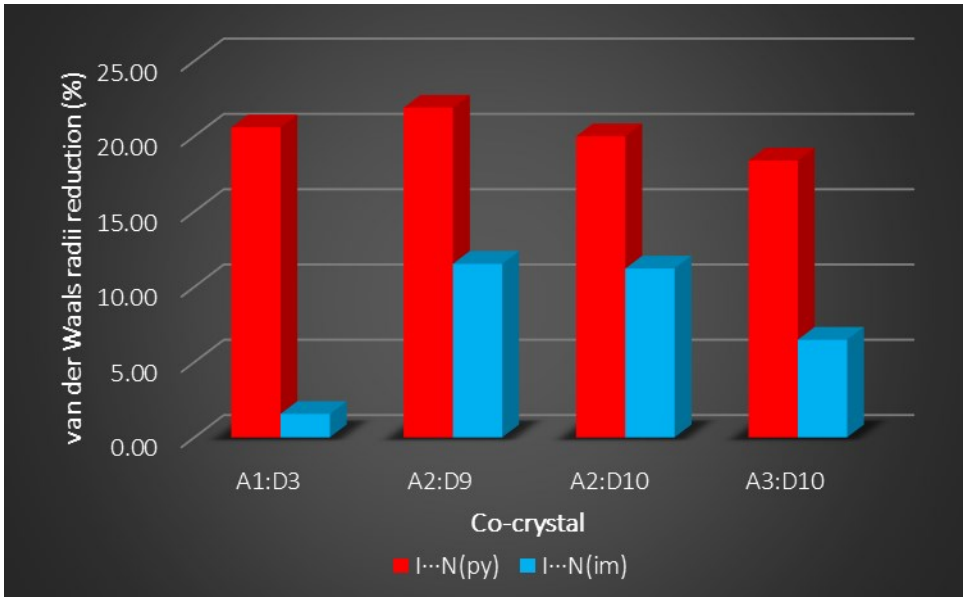

Figure 3.23 Van der Waals radii reduction percentages for **A1:D3**, **A2:D9**, **A2:D10** and **A3:D10**

3.4.3 Importance of activation and polarizability towards halogen bond formation

All activated iodine based halogen-bond donors showed comparable electrostatic potential values and the experimental data show the increased success in forming halogen bonds with these donors. Furthermore, there is a dramatic difference in halogen-bond ability between iodo- and bromo-substituted compounds, which reflect the polarizability, MEPS and size/depth of the respective σ-hole; the success rate of iodine based donors is 63%, whereas none of the bromo-substituted donors produced co-crystals. On the other hand, the control experiments with iodobenzene showed that the 'activation' offered by electron-withdrawing fluorine substituents increase the ability of halogen bond formation by boosting the size and strength of σ-hole and by influencing the MEPS on the halogen atom.

3.4.4 Electrostatic based selectivity or steric effects?

In order to ensure that observed binding preferences were not simply the result of steric hindrance, **A4** was included as a control molecule which only contains imidazole sites in the same steric environment as in **A1-A3**. Co-crystal structure **A4:D9** supports that fact that there is no steric effect that impacts the interactions with imidazole nitrogen. Furthermore, the structures **A1:D3**, **A2:D9**, **A2:D10** and **A3:D10** also supports this fact which show successful halogen bond formations with imidazole nitrogen atoms, apart from the major interactions with pyridine nitrogen atoms in each co-crystal. The conformational flexibility of the acceptor molecules means that they can adjust their shape according to the demand, thus the observed best-donor/best-acceptor interactions in each co-crystal is purely based on their molecular electrostatic potential values.

3.4.5 Variations in intermolecular interactions

Apart from the conventional halogen bonds and secondary interactions with pyridine and imidazole nitrogen atoms, in **A2:D7** and **A4:D9** the nitrogen atoms are participating in dissymmetric bifurcated halogen bonds, where one of the contacts is shorter than the other. Such halogen bonds are rare, as nitrogen atoms, with only one lone pair, tend to be satisfied with a single electron-pair acceptor, forming one non-covalent interaction.

When considering the donor molecules in these 16 co-crystal structures various patterns can be recognized. In **A1:D7**, one of the iodine atoms of halogen-bond donor is participating in forming an I···I halogen bond where the electropositive tip of the iodine atom is interacting with the electronegative region of another iodine atom, Figure 3.11. In **A1:D4** and **A1:D10**, even though the two iodine atoms in donors "should" have the same initial strength as they are symmetric molecules, the second iodine atom is not participating in any interactions leading to a trimer. It is possible that once the first halogen bond is formed, some electron density is donated into the donor

molecule and this new charge has to be dispersed through the remaining molecule which may lead to a slight reduction of the positively charge σ-hole on the remaining iodine atom thereby rendering it less effective. In **A4:D9**, all three donor atoms of **D9** are participating in halogen bonds, which is uncommon with this molecule, Figure 3.22b. On the other hand, this illustrates that all three iodine atoms of **D9** are capable of simultaneously forming halogen bonds in a single solid state structure.

3.5 Conclusions

This study highlights the importance of using molecular electrostatic potentials as a way of ranking halogen bond acceptor ability in a system with multiple acceptor sites. In fact, halogen bonds reflect the previously established guidelines of hydrogen bonding and follows a best-donor best-acceptor interaction hierarchy in the solid state. In all 15 crystal structures obtained with ditopic acceptors **A1-A3**, halogen bonds involving the better acceptor are favored, Figure 3.24. The supramolecular yield for each acceptor was a reflection of the maximum value of its electrostatic potential. Furthermore, halogen-bond ability of activated iodine donors is dramatically greater compared to that of activated bromo-analogues and unactivated iodo-compounds. These facts realize the importance of polarizability and activation in successful halogen bond formations.

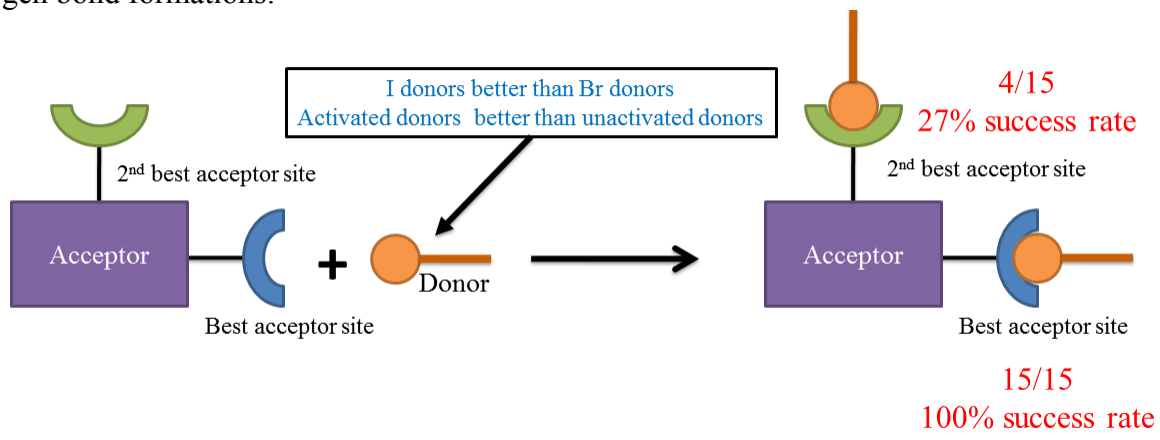

Figure 3.24 Results of the postulated structural outcome

3.6 Reference

1. Aakeröy, C.B.; Wijethunga, T.K.; Desper, J. *New J. Chem.* **2015**, *39*, 822-828; Aakeröy, C.B.; Wijethunga, T.K.; Desper, J.; Moore, C. *J. Chem. Crystallogr*. **2015**, *45*, 267-276.

2. Lehn, J.M. *Chem. Soc. Rev*. **2007**, *36*, 151-160.

3. Benedict, J.B. *Recent advances in crystallography*, **2012**, InTech; Meyer, F.; Dubois, P. *CrystEngComm* **2013**, *15*, 3058-3071; Cinčić, D.; Friščič, T.; Jones, W. *Chem. Eur. J*. **2008**, *14*, 747-753.

4. Metrangolo, P.; Meyer, F.; Pilati, T.; Resnati, G.; Terraneo, G. *Angew. Chem. Int. Ed.* **2008**, *47*, 6114-6127.

5. Desiraju, G.R.; Ho, S.; Kloo, L.; Legon, A.C.; Marquardt, R.; Metrangolo, P.; Politzer, P.A.; Resnati, G.; Rissanen, K. *Pure Appl. Chem.* **2013**, *85*, 1711-1713.

6. Priimagi, A.; Cavallo, G.; Metrangolo, P.; Resnati, G. *Acc.Chem.Res.* **2013**, *46*, 2686-2695; Tottadi, S.; Desiraju, G. R. *Chem. Commun.* **2013**, *49*, 7791-7793.

7. Gavezzotti, A. *Mol. Phys.* **2008** *106*, 1473-1485; Walsh, R.B.; Padgett, C.W.; Metrangolo, P.; Resnati, G.; Hanks, T.W.; Pennington, W.T.; *Cryst.Growth Des* **2001**, *1*, 165-175; Crihfield, A.; Hartwell, J.; Phelps, D.; Walsh, R.B.; Harris, J.L.; Payne, J.F.; Pennington, W.T.; Hanks, T.W. *Cryst.Growth Des* **2003**, *3*, 313-320.

8. Valerio, G.; Raos, G.; Meille, S.V.; Metrangolo, P.; Resnati, G. *J. Phys. Chem. A* **2000**, *104*, 1617-1620; Bailey, R.D.; Drake, G.W.; Grabarczyk, M.; Hanks, T.W.; Hook, L.L.; Pennington, W.T. *J. Chem. Soc., Perkin Trans. 2* **1997**, *12*, 2773-2779; Karpfen, A. *Theor. Chem. Acc.* **2003**, *110*, 1-9; Shen, Q.J.; Jin, W.J. *Phys. Chem. Chem. Phys.* **2011**, *13*, 13721-13729.

9. Politzer, P.; Lane, P.; Concha, M.C.; Ma, Y.; Murray, J.S. *J. Mol. Model.* **2007**, *13*, 305-311.

10. Metrangolo, P.; Resnati, G. *Chem. Eur. J.* **2001**, *7*, 2511-2519; Bauzá, A.; Quiñonero, D.; Frontera, A.; Deyà, P. M. *Phys. Chem. Chem. Phys*. **2011**, *13*, 20371-20379.

11. Metrangolo, P.; Neukirch, H.; Pilati, T.; Resnati, G. *Acc. Chem. Res*. **2005**, *38*, 386-395.

12. Aakeröy, C. B.; Sinha, A.S.; Chopade, P. D.; Desper, J. *Dalton Trans*. **2011**, *40*, 12160-12168.

13. Metrangolo, P.; Resnati, G. *IUCrJ* **2014**, *1*, 5-7.

14. Beale, T.M.; Chudzinski, M.G.; Sarwar, M.G.; Taylor, M.S. *Chem. Soc. Rev.* **2013**, *4*, 1667-1680.

15. Bruckmann, A.; Pena, M.A.; Bolm, C. *Synlett* **2008**, *6*, 900-902.

16. Chudzinski, M.G.; McClary, C.A.; Taylor, M.S. *J. Am. Chem. Soc.* **2011**, *133*, 10559-10657.

17. Shirman, T.; Freeman, D.; Posner, Y.D.; Feldman, I.; Facchetti, A.; Van der Boom, M.E. *J. Am. Chem. Soc.* **2008**, *130*, 8162-8163.

18. Marras, G.; Metrangolo, P.; Meyer, F.; Pilati, T.; Resnati, G.; Vij, A. *New J. Chem.* **2006**, *30*, 1397-1402.

19. Dordonne, S.; Crousse, B.; Delpon, D.B.; Legros, J. *Chem. Commun.* **2011**, *47*, 5855-5857.

20. Meyer, F.; Dubois, P. *CrystEngComm* **2012**, *15*, 3058-2071.

21. Politzer, P.; Murray, J.S.; Clark, T. *Phys. Chem. Chem. Phys.* **2010**, *12*, 7748-7757; Vallejos, M.J.; Auffinger, P.; Ho, P.S.; *International Tables of Crystallography F*, **2012**, 821-826; Scholfield, M.R.; Zanden, C.M.V.; Carter, M.; Ho, P.S. *Protein Sci.* **2013**, *22*, 139-152.

22. Etter, M.C. *Acc. Chem. Res.* **1990**, *23*, 120-126; Aakeröy, C.B.; Beatty, A.M.; Helfrich, B.A. *J. Am. Chem. Soc.* **2002**, *48*, 14425-12232; Aakeröy, C.B.; Salmon, D.J. *CrystEngComm* **2005**, *72*, 439-448; Bowers, J.R.; Hopkins, G.W.; Yap, G.P.A.; Wheeler, K.A. *Cryst.Growth Des.* **2005**, *5*, 727-736.

23. Aakeröy, C.B.; Wijethunga, T.K.; Desper, J. *CrystEngComm* **2014**, *16*, 28-31.

24. Questel, J.Y.L.; Laurence, C.; Graton, J. *CrystEngComm* **2013**, *15*, 3212-3221.

25. Sarwar, M.G.; Dragisic, B.; Salsberg, L.J.; Gouliaras, C.; Taylor, M.S. *J. Am. Chem. Soc.* **2010**, *132*, 1646-1653.

26. Riley, K.E.; Hobza, P. *Phys. Chem. Chem. Phys* **2013**, *15*, 17742-17752.

27. Lu, Y.; Li, H.; Zhu, X.; Zhu, W.; Liu, H. *J. Phys. Chem. A* **2011**, *115*, 4467-4475.

28. Aakeröy, C.B.; Baldrighi, M.; Desper, J.; Metrangolo, P.; Resnati, G. *Chem. Eur. J.* **2013**, *19*, 16240-16247.

29. Aakeröy, C.B.; Chopade, P.D.; Desper, J. *Cryst. Growth Des.* **2013**, *13*, 4145-4150.

30. Xiao, J.; Shreeve, J. M. *J. Org. Chem.* **2005***, 70,* 3072-3078.

31. Aakeröy, C.B.; Wijethunga, T.K.; Desper, J. *New J. Chem.* **2014**, *39*, 822-828.

32. Espallargas, G.M.; Recuenco, A.; Romero, F.M.; Brammer, L.; Libri, S. *CrystEngComm* **2012**, *14*, 6381-6383.

33. Omnic 8.0 © **1992-2008**, Thermo Fisher Scientific Inc.

34. Spartan'08, Wavefunction, Inc.

35. Lucassen, A. C. B.; Karton, A.; Leitus, G.; Shimon, L. J. W.; Martin, J. M. L.; van der Boom, M. E. *Cryst. Growth Des.* **2007**, *7*, 386-392.

36. Nagels, N.; Hauchecorne, D.; Herrebout, W.A. *Molecules* **2013**, *18*, 6829-6851; Erdélyi, M. *Chem. Soc. Rev.* **2012**, *41*, 3547-3557.

37. Dey, A.; Metrangolo, P.; Pilati, T.; Resnati, G.; Terraneo, G.; Wlassics, I. *J. Fluorine Chem.* **2009**, *130*, 816-823; Priimagi, A.; Cavallo, G.; Forni, A.; Gorynsztejn-Leben, M.; Kaivola, M.; Metrangolo, P.; Milani, R.; Shishido, A.; Pilati, T.; Resnati, G.; Terraneo, G. *Adv. Funct. Mater*. **2012**, *22*, 2572-2579.

38. Valerio, G.; Raos, G.; Meille, S.V.; Metrangolo, P.; Resnati, G. *J. Phys. Chem. A* **2000**, *104*, 1617-1620; Caronna, T.; Liantonio, R.; Logothetis, R.A.; Metrangolo, P.; Pilati, T.; Resnati, G. *J. Am. Chem. Soc.* **2004**, *126*, 4500-4501; Awwadi, F.F.; Willett, R.D.; Peterson, K.A.; Twamley, B. *Chem. Eur. J.* **2006**, *12*, 8952-8960.

Chapter 4 - Dependency of electrostatic potential differences in governing halogen bond selectivity

4.1 Introduction

Designing predictable supramolecular architectures requires a clear understanding of intermolecular interactions.[1] In this context, there is an abundance of studies on hydrogen bonding, the most well-known among non-covalent interactions.[2] Halogen bonding,[3] a recent addition to the tool box of supramolecular chemistry, has not yet received the same amount of attraction. Halogen bonding can be viewed as a primarily electrostatic interaction between an electron deficient halogen atom and an electronegative region of another atom or molecule.[4] The anisotropic distribution of the electrostatic potential leaves an amphiphilic character to the halogen atom, where there is a region of positive potential known as the "σ hole"[5] and a region of negative potential, Figure 4.1. Therefore, a covalently bound halogen can interact with both electronegative and electropositive entities depending on the approaching direction.

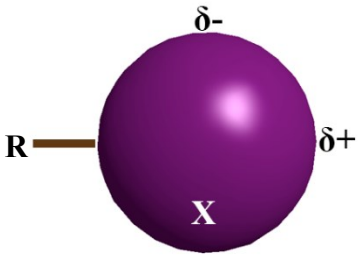

Figure 4.1 Anisotropic distribution of positive and negative electrostatic potential on a halogen atom (X); R- attached molecular fragment

Even though the concept of halogen bonding dates back more than a century,[6] the ability of halogen atoms to function as effective and reliable sites for structure directing molecular recognition processes remained underexplored until the 1990s.[7] Thus, halogen bonding (XB) and its potentials in the field of supramolecular chemistry are still in the infancy stage of realization.[8]

Fundamental studies on halogen bonding span a wide range including examination of the electrostatic nature,[9] geometric features of halogen bonding,[10] activation process for halogen atoms,[11] design of halogen-bond donors and acceptors,[12] hierarchy of halogen bonding[13] and the nature of halogen bonding in gas phase,[14] solution phase[15] and in the solid state.[16] Furthermore, studies on controlling halogen bonding in supramolecular architectures have been at the center of some studies.[17] Apart from these fundamental studies, halogen bonding has received attraction from material chemists due to applications in supramolecular gels,[18] nanoparticle self-assembly,[19] liquid crystals,[20] optical materials,[21] separation processes,[22] stabilization processes[23] and electric and magnetic materials.[24] In addition, halogen bonding in biological systems[25] is attracting much attention, and medicinal chemistry promises a bright future in applying halogen bonding in drug discoveries[26] and in transmembrane anion transport.[27]

Etter's rules on hydrogen bond selectivity[28] provide a clear understanding on the molecular recognition behavior of hydrogen bonding,[29] but a similar set of guidelines are still to be realized in halogen bonding. Chapter 3 describes the study on electrostatic potential dependent selectivity of halogen bonding and the results suggested that halogen bonding favors a better acceptor site as ranked by MEPS calculations while a second best acceptor site on the molecule did not form any noticeable interactions.[30] Even though the results were conclusive, in some structures, a best-donor/best-acceptor preference is missing. Further analysis lead to the realization that when the MEPS difference between the two acceptor sites is low, there is no binding preference. This was further confirmed by a CSD[31] survey conducted on halogen bonded systems of acceptors with two different acceptor moieties where even though a MEPS based ranking is possible in predicting the best acceptor site, halogen bond interactions did not follow any preference for binding.[32]

Thus in a system with two different types of acceptor sites and a halogen-bond donor probe, there are essentially three possible outcomes, Figure 4.2.

1. If the electrostatic potential difference on the two acceptor sites is sufficiently large; halogen bonding will follow best-donor/best-acceptor interaction hierarchy and will interact preferentially with best acceptor site.
2. If the electrostatic potential difference of the two acceptor sites are very small, halogen bonding will occur with both acceptor sites.
3. There might be a region of MEPS difference where binding preference cannot be predicted.

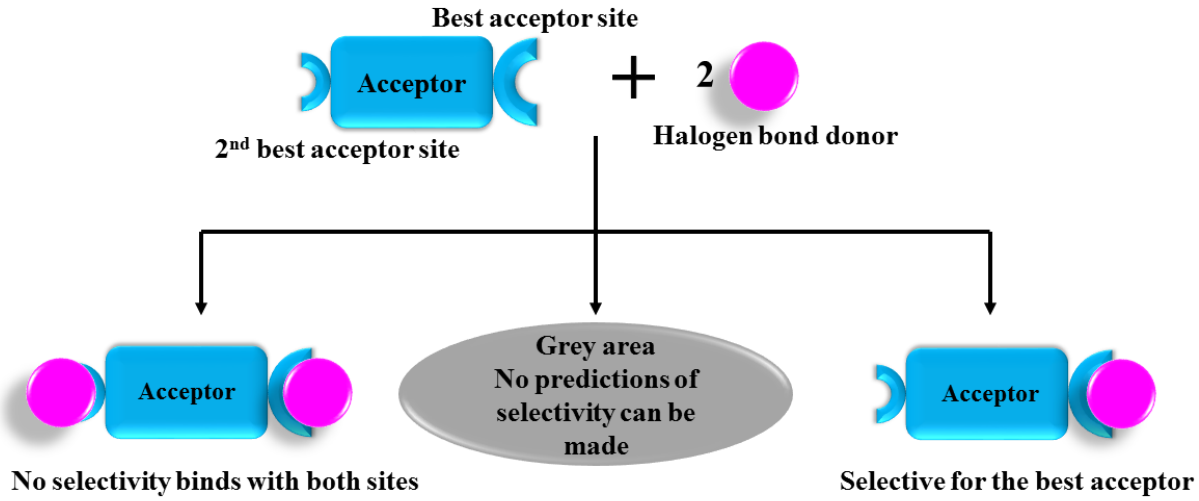

Figure 4.2 Three possible outcome of co-crystallizations between an asymmetric ditopic acceptor and halogen-bond donors

In order to address these possibilities, a library of acceptors with multitude of acceptor sites with different values of MEPS values on each acceptor were required. Furthermore, the selected library was required to include a wide range of MEPS difference between the two acceptor sites. The evaluated library of acceptors are shown in Figure 4.3, along with the MEPS value of each acceptor site and the MEPS difference for each molecule (ΔE value) is also provided.

Probing of halogen bond selectivity was done through a systematic co-crystallization approach. Nine iodine-based perfluorinated halogen-bond donors were selected (including aromatic and aliphatic donors), Figure 4.4. Co-crystallization experiments between the twelve acceptors and nine donors were conducted (108 reactions) and solid state structures were obtained for 36 combinations.

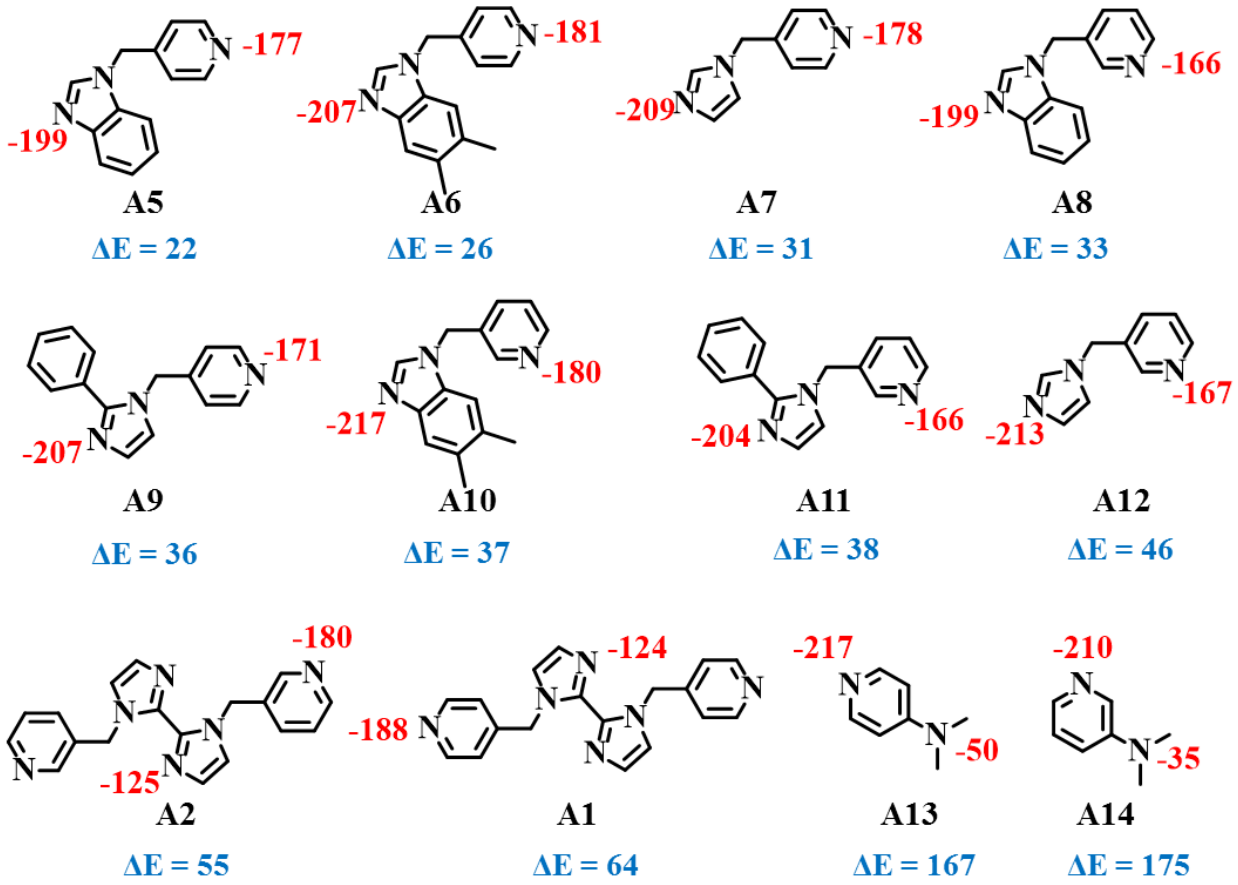

Figure 4.3 Acceptors under study; MEPS values on each acceptor site and ΔE value for each acceptor are shown in kJ/mol

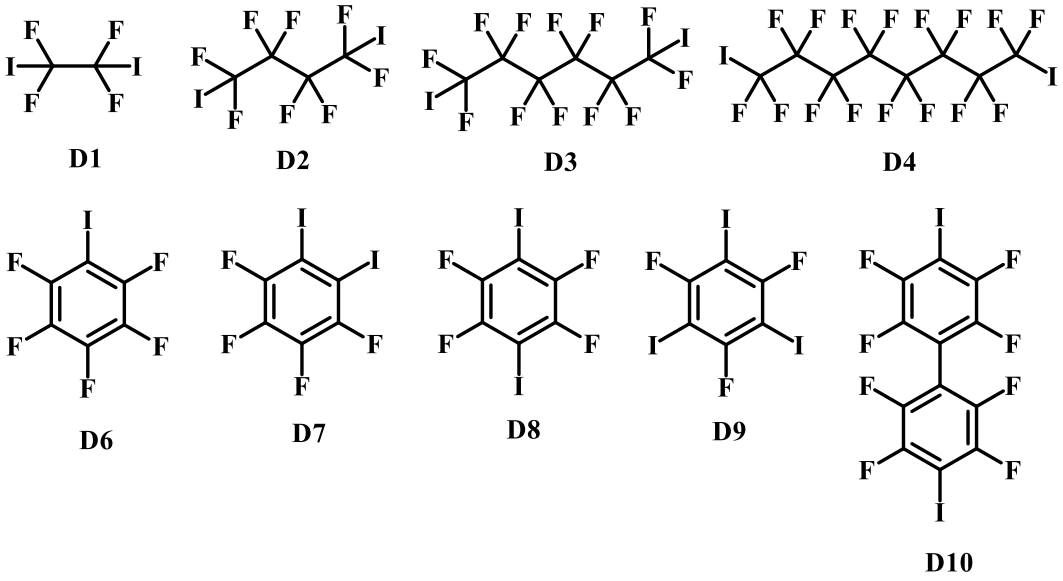

Figure 4.4 Halogen-bond donors under study

The study is undertaken in response to three hypotheses,

1. There is a cut off value for MEPS difference where halogen bonds lack selectivity.
2. There is a MEPS range that the halogen bond selectivity cannot be predicted (grey area of MEPS difference).
3. A systematic co-crystallization study would minimize the range of this grey area.

4.2 Experimental

4.2.1 General

All precursors, solvents, donors and acceptor **A13** were purchased from commercial sources and used without further purification. **A1** and **A2** were synthesized as reported in Chapter 2.[33] **A5-A12** were synthesized following a modified procedure of a literature report.[34] **A14**[35] and **D10**[36] were also synthesized following literature procedures. ^{1}H NMR spectra were recorded on a Varian Unity plus 400 MHz spectrometer in DMSO-d_6. Infrared spectra were recorded with a Nicolet 380 FT-IR with a digital resolution of 0.9 cm^{-1} and data processed using Omnic[37] software.

Melting points were determined using Fischer-Johns Mel-Temp melting point apparatus and are uncorrected.

4.2.2 Electrostatic potential calculations

Molecular electrostatic potentials surfaces on the acceptor molecules and donor molecules were calculated with density functional B3LYP level of theory using 6-311++G** basis set in vacuum. All calculations were carried out using Spartan 8 software.[38] All molecules were geometry optimized and the maxima and minima on the electrostatic potential surface (0.002 e/au isosurface) determined using a positive point charge in the vacuum as a probe. The numbers indicate the interaction energy (kJ/mol) between the positive point probe and surface of the molecule at that particular point. A positive value for the interaction energy indicates a positive surface potential while a negative value indicates a negative surface potential.

4.2.3 Synthesis of acceptors

4.2.3.1 Synthesis of 1-(pyridin-4-ylmethyl)-benzimidazole, A5

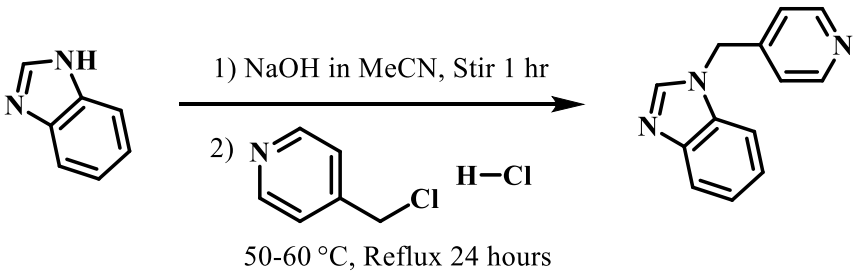

Benzimidazole (0.23 g, 2.0 mmol) and NaOH (0.16 g, 4.0 mmol) were placed in a 100 mL round bottomed flask with 20 mL of acetonitrile. The mixture was stirred at room temperature for one hour. 4-Picolyl chloride hydrochloride (0.33 g, 2.0 mmol) in acetonitrile (20 mL) was added to the mixture and refluxed for 24 hours at 50 °C - 60 °C. The reaction was monitored with TLC and after completion, the solvent was removed by rotary evaporation. The residue was dissolved

in water (50 mL) and extracted with methylene chloride (30 mL x 3). The organic layers were combined, dried over anhydrous $MgSO_4$ and rotary evaporated to obtain an orange colored solid. Yield: 0.35 g (85%); m.p. 105-107 °C (reported 105-110 °C);[34] ^{1}H NMR (400 MHz, DMSO-d_6):8.52 (d, 1H), 8.45 (s, 1H), 7.70 (d, 1H), 7.47 (d, 1H), 7.22 (m, 4H), 5.59 (s, 2H).

4.2.3.2 Synthesis of 5,6-dimethyl-1-(pyridin-4-ylmethyl)-benzimidazole, A6

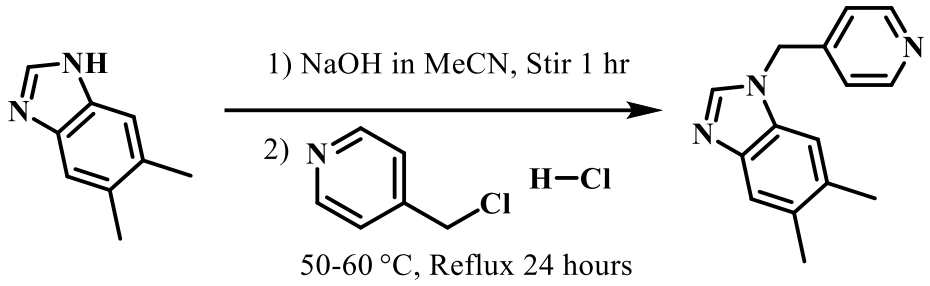

5,6-Dimethylbenzimidazole (0.29 g, 2.0 mmol) and NaOH (0.16 g, 4.0 mmol) were placed in a 100 mL round bottomed flask with 20 mL of acetonitrile. The mixture was stirred at room temperature for one hour. 4-Picolyl chloride hydrochloride (0.33 g, 2.0 mmol) in acetonitrile (20 mL) was added to the mixture and refluxed for 24 hours at 50 °C - 60 °C. The reaction was monitored with TLC and after completion the solvent was removed by rotary evaporation. The residue was dissolved in water (50 mL) and extracted with methylene chloride (30 mL x 3). The organic layers were combined, dried over anhydrous $MgSO_4$ and rotary evaporated to obtain the pale orange powder as the product. Yield: 0.34 g (72%); m.p. 180-185 °C (reported 185-190 °C);[34] ^{1}H NMR (400 MHz, DMSO-d_6): 8.51 (d, 2H), 8.26 (s, 1H), 7.45 (s, 1H), 7.22 (s, 1H), 7.14 (d, 2H), 5.51 (s, 2H), 2.27 (s, 6H).

4.2.3.3 Synthesis of 4-((imidazol-1-yl)methyl)pyridine, A7

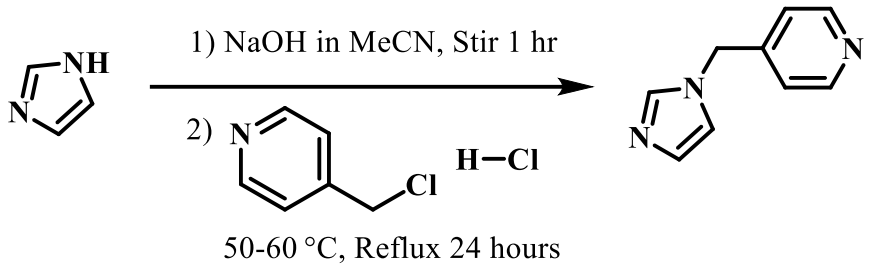

Imidazole (0.14 g, 2.0 mmol) and NaOH (0.16 g, 4.0 mmol) were placed in a 100 mL round bottomed flask with 20 mL of acetonitrile. The mixture was stirred at room temperature for one hour. 4-Picolyl chloride hydrochloride (0.33 g, 2.0 mmol) in acetonitrile (20 mL) was added to the mixture and refluxed for 24 hours at 50 °C - 60 °C. The reaction was monitored with TLC and after completion the solvent was removed by rotary evaporation. The residue was dissolved in water (50 mL) and extracted with methylene chloride (30 mL x 3). The organic layers were combined, dried over anhydrous $MgSO_4$ and rotary evaporated to obtain the dark green powder as the product and recrystallized with ethyl acetate to obtain dark green crystals. Yield: 0.32 g (62%); m.p. 65-68 °C; ^{1}H NMR (400 MHz, DMSO-d_6): 8.54 (d, 2H), 7.81 (s, 1H), 7.23 (s, 1H), 7.14 (d, 2H), 6.98 (s, 1H), 5.29 (s, 2H).

4.2.3.4 Synthesis of 1-(pyridin-3-ylmethyl)-benzimidazole, A8

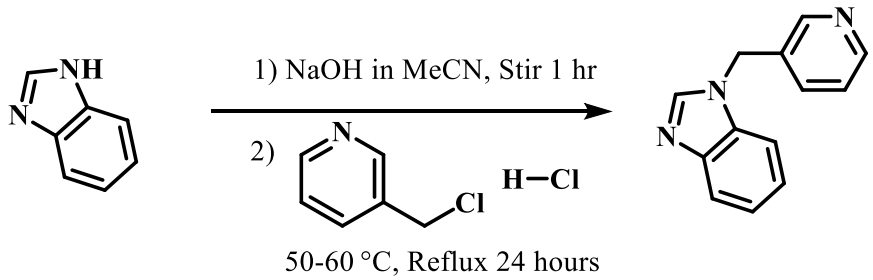

Benzimidazole (0.23 g, 2.0 mmol) and NaOH (0.16 g, 4.0 mmol) were placed in a 100 mL round bottomed flask with 20 mL of acetonitrile. The mixture was stirred at room temperature for one hour. 3-Picolyl chloride hydrochloride (0.33 g, 2.0 mmol) in acetonitrile (20 mL) was added

to the mixture and refluxed for 24 hours at 50 °C - 60 °C. The reaction was monitored with TLC and after completion the solvent was removed by rotary evaporation. The residue was dissolved in water (50 mL) and extracted with methylene chloride (30 mL x 3). The organic layers were combined, dried over anhydrous $MgSO_4$ and rotary evaporated to obtain a brown solid and recrystallized with ethyl acetate to obtain brown crystals as the product. Yield: 0.33 g (79%); m.p. 50-52 °C (reported 50-55 °C);[34] ^{1}H NMR (400 MHz, DMSO-d_6): 8.67 (s, 1H), 8.48 (d, 2H), 7.68 (m, 2H), 7.59 (m, 1H), 7.35 (m, 1H), 7.21 (m, 2H), 5.57 (s, 2H).

4.2.3.5 Synthesis of 4-((2-phenyl-imidazol-1-yl)methyl)pyridine, *A9*

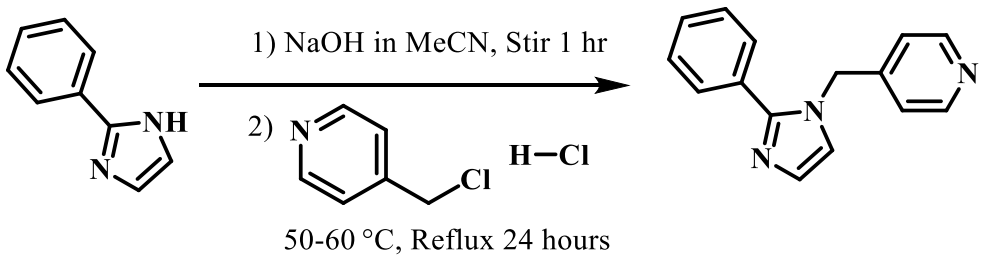

2-Phenylimidazole (0.29 g, 2.0 mmol) and NaOH (0.16 g, 4.0 mmol) were placed in a 100 mL round bottomed flask with 20 mL of acetonitrile. The mixture was stirred at room temperature for one hour. 4-Picolyl chloride hydrochloride (0.33 g, 2.0 mmol) in acetonitrile (20 mL) was added to the mixture and refluxed for 24 hours at 50 °C - 60 °C. The reaction was monitored with TLC and after completion the solvent was removed by rotary evaporation. The residue was dissolved in water (50 mL) and extracted with methylene chloride (30 mL x 3). The organic layers were combined, dried over anhydrous $MgSO_4$ and rotary evaporated to obtain the orange powder as the product and recrystallized in ethyl acetate to obtain the product as a dark orange crystals. Yield: 0.21 g (45%); m.p. 35-38 °C (reported 33-38 °C);[39] ^{1}H NMR (400 MHz, DMSO-d_6): 8.50 (d, 2H), 7.51 (m, 2H), 7.39 (m, 4H), 7.12 (s, 1H), 6.97 (s, 1H), 5.40 (s, 2H).

4.2.3.6 Synthesis of 5,6-dimethyl-1-(pyridin-3-ylmethyl)-benzoimidazole, A10

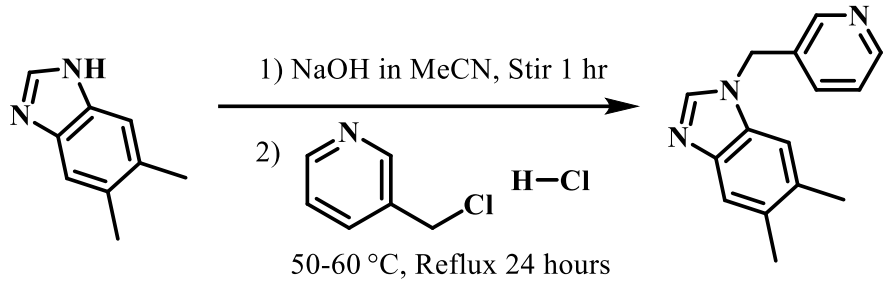

5,6-Dimethylbenzimidazole (0.29 g, 2.0 mmol) and NaOH (0.16 g, 4.0 mmol) were placed in a 100mL round bottomed flask with 20 mL of acetonitrile. The mixture was stirred at room temperature for one hour. 3-Picolyl chloride hydrochloride (0.33 g, 2.0 mmol) in acetonitrile (20 mL) was added to the mixture and refluxed for 24 hours at 50 °C - 60 °C. The reaction was monitored with TLC and after completion the solvent was removed by rotary evaporation. The residue was dissolved in water (50 mL) and extracted with methylene chloride (30 mL x 3). The organic layers were combined, dried over anhydrous $MgSO_4$ and rotary evaporated to obtain pale orange powder as the product. Yield: 0.29 g (63%); m.p. 87-90 °C (reported 91-93 °C);[40] ^{1}H NMR (400 MHz, DMSO-d_6): 8.62 (s, 1H), 8.48 (d, 1H), 8.30 (s, 1H), 7.65 (d, 1H), 7.43 (s, 1H), 7.33 (m, 2H), 5.49 (s, 2H), 2.27 (s, 6H).

4.2.3.7 Synthesis of 3-((2-phenylimidazol-1-yl)methyl)pyridine, A11

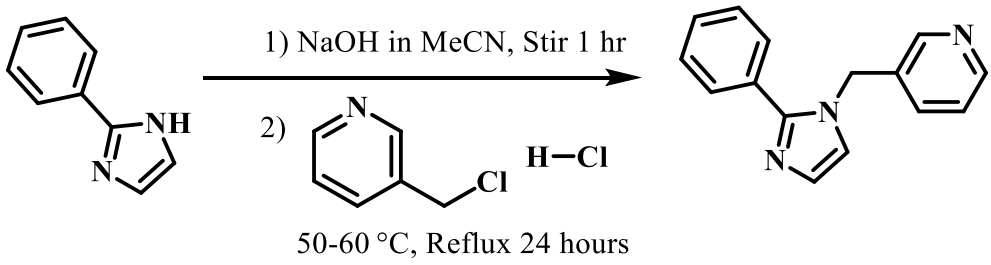

2-Phenylimidazole (0.29 g, 2.0 mmol) and NaOH (0.16 g, 4.0 mmol) were placed in a 100 mL round bottomed flask with 20 mL of acetonitrile. The mixture was stirred at room temperature

for one hour. 3-Picolyl chloride hydrochloride (0.33 g, 2.0 mmol) in acetonitrile (20 mL) was added to the mixture and refluxed for 24 hours at 50 °C - 60 °C. The reaction was monitored with TLC and after completion the solvent was removed by rotary evaporation. The residue was dissolved in water (50 mL) and extracted with methylene chloride (30 mL x 3). Organic layers were combined, dried over anhydrous $MgSO_4$ and rotary evaporated to obtain pale orange powder as the product. Yield: 0.35 g (69%); m.p. 39-42 °C (reported 33-38 °C);[34] ^{1}H NMR (400 MHz, DMSO-d_6): 8.46 (d, 1H), 8.26 (s, 1H), 7.56 (m, 2H), 7.38 (m, 6H), 6.08 (m, 1H), 5.39 (s, 2H).

4.2.3.8 Synthesis of 3-((imidazol-1-yl)methyl)pyridine, A12

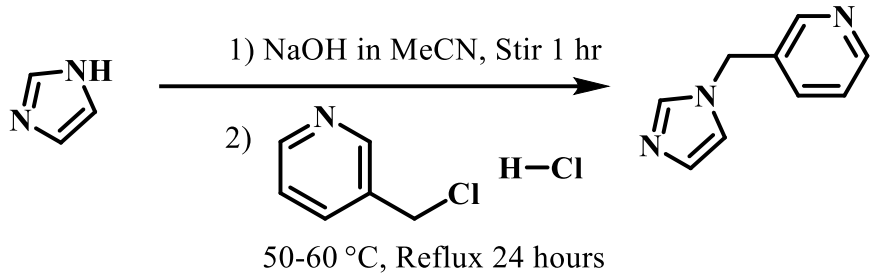

Imidazole (0.14 g, 2.0 mmol) and NaOH (0.16 g, 4.0 mmol) were placed in a 100 mL round bottomed flask with 20 mL of acetonitrile. The mixture was stirred at room temperature for one hour. 3-Picolyl chloride hydrochloride (0.33 g, 2.0 mmol) in acetonitrile (20 mL) was added to the mixture and refluxed for 24 hours at 50 °C - 60 °C. The reaction was monitored with TLC and after completion the solvent was removed by rotary evaporation. The residue was dissolved in water (50 mL) and extracted with methylene chloride (30 mL x 3). The organic layers were combined, dried over anhydrous $MgSO_4$ and rotary evaporated to obtain the dark brown color powder as the product. Yield: 0.32 g (82%); m.p. 41-45 °C; ^{1}H NMR (400 MHz, DMSO-d_6): 8.56 (s, 1H), 8.52 - 8.52 (d, 1H), 7.82 (s, 1H), 7.67 (d, 1H), 7.38, (d, 1H), 7.24 (d, 1H), 6.93 (d, 1H), 5.26 (s, 2H).

4.2.3.9 Synthesis of 1,1'-bis(pyridin-4-ylmethyl)-2,2'-biimidazole, A14

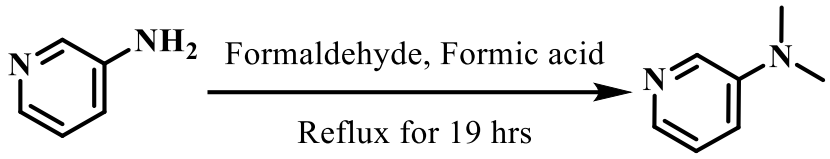

A round-bottom flask equipped with a magnetic stir bar was charged with 3-aminopyridine (1.0 g, 11 mmol), formaldehyde (2.5 mL, 37% in water), and formic acid (3.0 mL). The reaction mixture was stirred for 19 hours at reflux, allowed to cool to room temperature, acidified with 6M aqueous hydrochloric acid (pH < 2), and evaporated to dryness in vacuo. The dry material was mixed with 15 mL of saturated $NaHCO_3$ and extracted with chloroform (4 x 10 mL). The combined organic layers were dried (Na_2SO_4) and concentrated in vacuo to produce a brick red oil. The product was further purified via flash column chromatography on silica gel (eluent petroleum ether/ethyl acetate 15:1) to produce a light-tan oil as the product. Yield: 0.45 g (35%); ^1H NMR (400 MHz, DMSO-d_6) 8.10 (d, 1H), 7.89 (d, 1H), 7.15 (dd, 1H), 7.05 (m, 1H), 2.89 (s, 6H).

4.2.4 Co-crystal screening

The screening was carried out through solvent-assisted grinding with methanol. Each acceptor and donor was mixed together in stoichiometric ratio and ground with the assistance of a drop of methanol (a total of 108 experiments). In each experiment, 10 mg of the acceptor was used with the corresponding amount of donor. Once the solvent had evaporated, the solid was analyzed using IR spectroscopy to determine whether a co-crystal had formed or not. Successful interactions between the acceptor and donor were identified using the specific shifts of the peaks of the mixture compared to starting compounds.

4.2.5 Synthesis of co-crystals

Solids from grinding experiments were dissolved in a minimum amount (~2 ml) of methanol and left in a vial for slow evaporation in order to obtain crystals suitable for single crystal X-ray diffraction; 36 crystal growth experiments were successful. Details on thirteen of these were reported in Chapter 3.[30] Table 4.1 summarizes the experimental details for the remaining 23 structures.

Table 4.1 Experimental details of the 23 co-crystals obtained

Code	Mixed Mole ratio	Amounts used	Solvent and method	Crystal stoichiometry	Crystal color & habit
A5:D8	1:1	**A5** -10 mg, 0.048 mmol **D8** - 19 mg, 0.048 mmol	Methanol, Slow evaporation	2:3	Colorless needle
A5:D10	1:1	**A5** -10 mg, 0.048 mmol **D10** - 27 mg, 0.048 mmol	Methanol, Slow evaporation	1:1	Colorless plate
A6:D2	1:1	**A6** -10 mg, 0.042 mmol **D2** - 19 mg, 0.042 mmol	Methanol, Slow evaporation	1:1	Colorless plate
A6:D8	1:1	**A6** - 10 mg, 0.042 mmol **D8** - 17 mg, 0.042 mmol	Methanol, Slow evaporation	2:3	Colorless needle
A7:D3	1:1	**A7** - 10 mg, 0.063 mmol **D3** - 35 mg, 0.063 mmol	Methanol, Slow evaporation	1:1	Colorless plate
A7:D8	1:1	**A7** - 10 mg, 0.063 mmol **D8** - 25 mg, 0.063 mmol	Methanol, Slow evaporation	1:1	Colorless prism
A7:D10	1:1	**A7** - 10 mg, 0.063 mmol **D10** - 35 mg, 0.063 mmol	Methanol, Slow evaporation	1:1	Yellow plate
A8:D8	1:1	**A8** - 10 mg, 0.048 mmol **D8** - 19 mg, 0.048 mmol	Methanol, Slow evaporation	1:1	Colorless prism
A8:D9	1:1	**A8** - 10 mg, 0.048 mmol **D9** - 25 mg, 0.048 mmol	Methanol, Slow evaporation	1:2	Colorless rod
A9:D8	1:1	**A9** - 10 mg, 0.043 mmol **D8** - 17 mg, 0.043 mmol	Methanol, Slow evaporation	2:1	Colorless plate
A9:D9	1:1	**A9** - 10 mg, 0.043 mmol **D9** - 22 mg, 0.043 mmol	Methanol, Slow evaporation	1:1	Colorless block
A10:D4	1:1	**A10** - 10 mg, 0.042 mmol **D4** - 28 mg, 0.042 mmol	Methanol, Slow evaporation	2:3	Colorless rod
A10:D7	1:1	**A10** - 10 mg, 0.042 mmol **D7** - 17 mg, 0.042 mmol	Methanol, Slow evaporation	1:2	Bronze plate
A10:D8	1:1	**A10** - 10 mg, 0.042 mmol **D8** - 17 mg, 0.042 mmol	Methanol, Slow evaporation	1:1	Gold prism
A10:D9	1:1	**A10** - 10 mg, 0.042 mmol **D9** - 22 mg, 0.042 mmol	Methanol, Slow evaporation	1:2	Colorless prism
A11:D9	1:1	**A11** - 10 mg, 0.043 mmol **D9** - 22 mg, 0.043 mmol	Methanol, Slow evaporation	1:1	Colorless prism
A11:D10	1:1	**A11** - 10 mg, 0.043 mmol **D10** - 24 mg, 0.043 mmol	Methanol, Slow evaporation	1:2	Colorless prism
A12:D2	1:1	**A12** - 10 mg, 0.063 mmol **D2** - 29 mg, 0.063 mmol	Methanol, Slow evaporation	1:1	Colorless plate

A12:D8	1:1	**A12** - 10 mg, 0.063 mmol **D8** - 25 mg, 0.063 mmol	Methanol, Slow evaporation	1:1	Colorless prism
A13:D1	1:1	**A13** - 10 mg, 0.082 mmol **D1** - 29 mg, 0.082 mmol	Methanol, Slow evaporation	3:2	Colorless plate
A13:D2	1:1	**A13** - 10 mg, 0.082 mmol **D2** - 37 mg, 0.082 mmol	Methanol, Slow evaporation	2:1	Colorless plate
A13:D3	1:1	**A13** - 10 mg, 0.082 mmol **D3** - 46 mg, 0.082 mmol	Methanol, Slow evaporation	1:1	Colorless plate
A13:D7	1:1	**A13** - 10 mg, 0.082 mmol **D7** - 33 mg, 0.082 mmol	Methanol, Slow evaporation	1:1	Colorless prism

4.3 Results

4.3.1 Electrostatic potentials

MEPS values for the acceptor molecules are provided in Figure 4.3. For each acceptor molecule the difference of MEPS values were calculated using equation 4.1 and was defined as the ΔE value. Table 4.2 summarizes the calculated MEPS values for the donors under study.

$$\Delta E \text{ value} = |\text{MEP value on the best acceptor}| - |\text{MEP value on the } 2^{nd} \text{ best acceptor}| \quad (4.1)$$

Table 4.2 Calculated electrostatic potentials on halogen-bond donors under study

Molecule	Atom	Electrostatic potential (kJ/mol)
1,2-diiodotetrafluoroethane D1	Iodine	+163
1,4-diiodooctafluorobutane D2	Iodine	+168
1,6-diiodoperfluorohexane D3	Iodine	+169
1,8-diiodoperfluorooctane D4	Iodine	+169
Iodopentafluorobenzene D6	Iodine	+166
1,2-diiodotetrafluorobenzene D7	Iodine	+162
1,4-diiotetrafluorobenzene D8	Iodine	+169
1,3,5-triiodotrifluorobenzene D9	Iodine	+158
4,4'-diiodoperfluorobiphenyl D10	Iodine	+164

4.3.2 Grinding experiments and characterization by IR spectroscopy

Solvent-assisted grinding experiments were analyzed using IR spectroscopy to identify any notable interactions between the two potential co-formers. The analysis was done by comparing the IR spectra of the ground mixture with spectra of the respective co-formers. The key IR modes

targeted were the C-F stretches of the halogen-bond donor. A shift of three wave numbers or more was considered to be significant and indicative of a positive result. The summary of the IR analysis is provided in the Table 4.3 along with the success rate for each acceptor and donor; 89 of 108 reactions produced co-crystals resulting in an 82% supramolecular yield.

Table 4.3 IR analysis for grinding experiments

		Donors												
		Potential (kJ/mol)		D1	D2	D3	D4	D6	D7	D8	D9	D10	% Success	
				+163	+168	+169	+169	+166	+162	+169	+158	+164		
		Best acceptor	2nd best acceptor											
Acceptors	**A1**	-199	-177	✗	✗	✗	✓	✓	✓	✓	✓	✓	6/9	67
	A2	-207	-181	✗	✓	✓	✓	✗	✓	✓	✓	✗	6/9	67
	A3	-209	-178	✗	✓	✓	✓	✓	✓	✓	✓	✓	8/9	89
	A4	-199	-166	✗	✓	✓	✗	✓	✓	✓	✓	✓	7/9	78
	A5	-207	-171	✗	✓	✓	✓	✓	✓	✓	✓	✗	7/9	78
	A6	-217	-180	✗	✓	✓	✓	✗	✓	✓	✓	✓	7/9	78
	A7	-204	-166	✗	✓	✓	✗	✓	✓	✓	✓	✓	7/9	78
	A8	-213	-167	✗	✓	✓	✓	✓	✓	✓	✓	✓	8/9	89
	A9	-180	-125	✓	✓	✓	✓	✓	✓	✓	✓	✓	9/9	100
	A10	-188	-124	✓	✓	✓	✓	✓	✓	✓	✓	✓	9/9	100
	A11	-217	-50	✓	✓	✓	✓	✓	✓	✓	✓	✓	9/9	100
	A12	-210	-35	✗	✓	✓	✓	✓	✓	✓	✓	✗	7/9	78
% Success				3/12	11/12	11/12	10/12	10/12	12/12	12/12	12/12	9/12		
				25	92	92	83	83	100	100	100	75		

4.3.3 Crystal growth and structure analysis

Even though the IR analysis provides unambiguous results for the successful co-crystal formation, it does not provide details about specific interaction sites, which is crucial for determining the selectivity of interactions in halogen bonding, thus single crystal data were required. Suitable crystals were obtained in 36 experiments and details on thirteen crystal structures have reported in Chapter 3,[30] remaining 23 structures are presented in the order of increasing ΔE value on the ditopic acceptor. X-ray experimental data and crystallographic data and halogen bond geometries are provided in the Appendix B.3.

With **A5** (ΔE = 22 kJ/mol) two crystal structures were obtained (**A5:D8** and **A5:D10**) and in both cases both binding sites N(im) and N(py) form a halogen bond; no XB preference is noted, Figure 4.5.

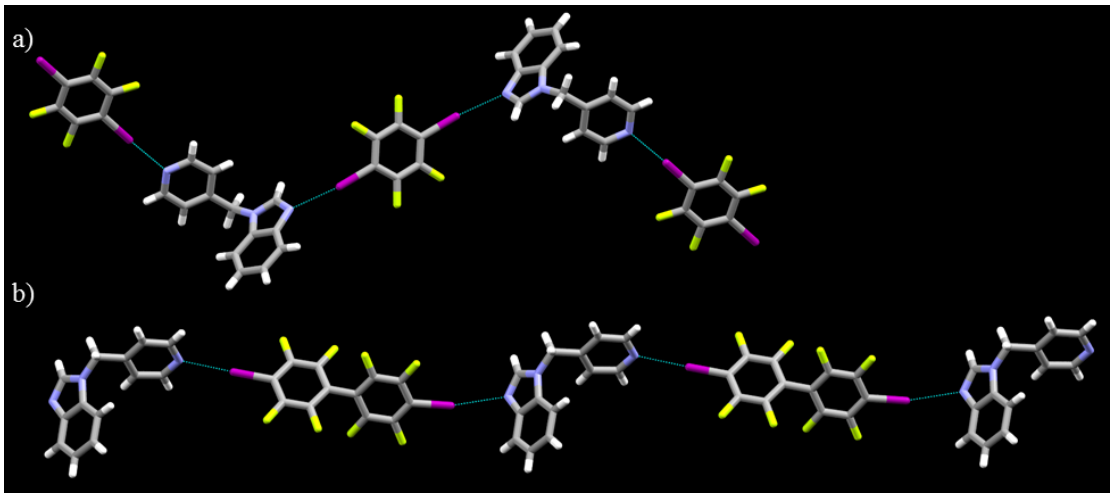

Figure 4.5 Primary halogen bond interactions in a) **A5:D8** and b) **A1:D10**; both acceptor sites engage in halogen bonding

Two structures (**A6:D2** and **A6:D8**) were obtained with **A6** (ΔE = 26 kJ/mol) and again both binding sites form halogen bonds, Figure 4.6.

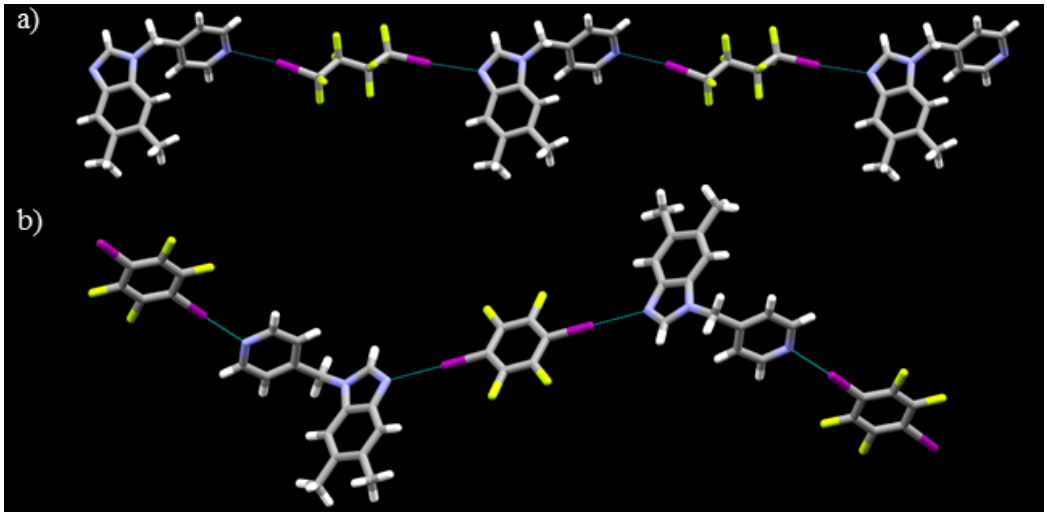

Figure 4.6 Primary halogen bond interactions in a) **A6:D2** and b) **A6:D8**

Similarly, **A7** (ΔE = 31 kJ/mol) produced three structures (**A7:D3**, **A7:D8** and **A7:D10)** with all acceptor moieties participating in halogen bonding, Figure 4.7.

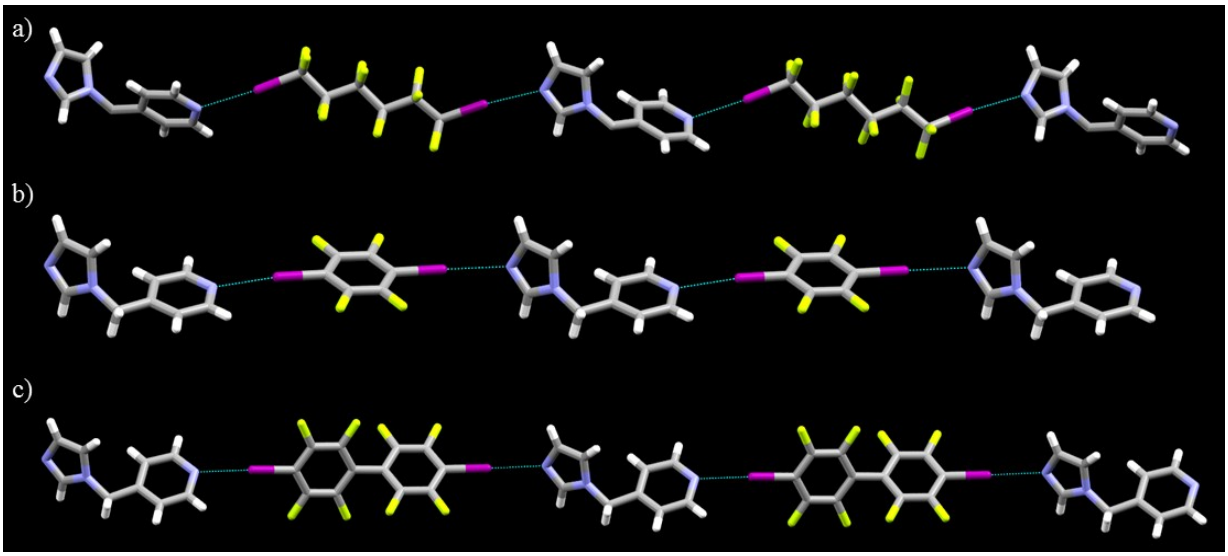

Figure 4.7 Primary halogen bond interactions in a) **A7:D3** b) **A7:D8** and c) **A7:D10**

In the two structures (**A8:D8** and **A8:D9**) of **A8** (ΔE = 33 kJ/mol), again all acceptors were involved in halogen bonding, Figure 4.8.

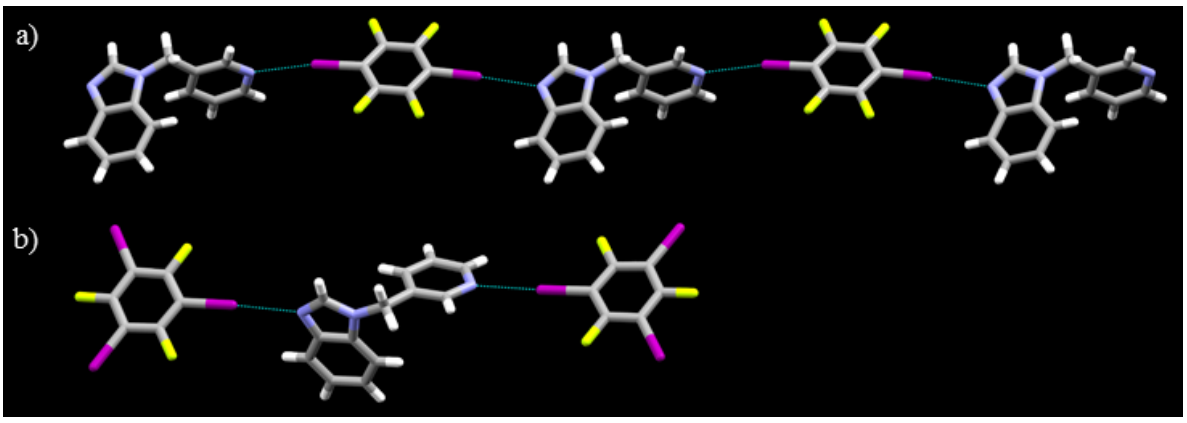

Figure 4.8 Primary halogen bond interactions in a) **A8:D8** and b) **A8:D9**

However, with **A9** (ΔE = 36 kJ/mol), two structures (**A9:D8** and **A9:D9**) were obtained and they behave differently. **A9:D8** shows a preferential halogen bond formation with the best

acceptor, imidazole, while the pyridine nitrogen site is forming a weak hydrogen bond dimer with a nearby pyridine ring. **A9:D9** shows no preference over binding, Figure 4.9.

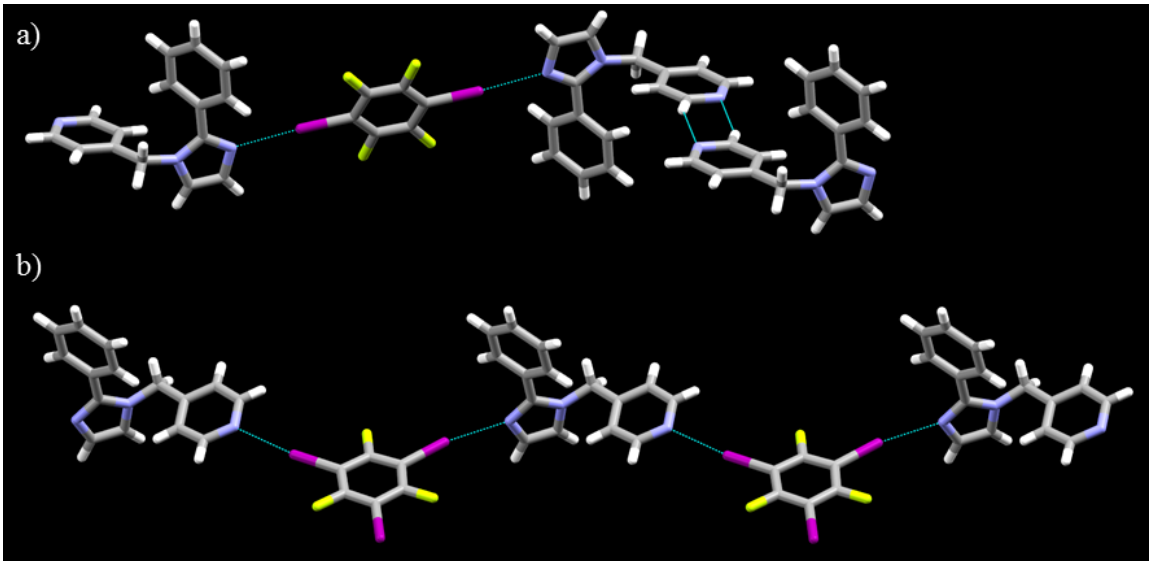

Figure 4.9 Primary halogen bond interactions in a) **A9:D8**: only the best acceptor, N(im) participate in halogen bonding and b) **A9:D9**: both acceptor sites form halogen bonds

Four structures (**A10:D4**, **A10:D8**, **A10:D9** and **A10:D9**) were obtained with **A10** (ΔE = 37 kJ/mol) again all acceptors were involved in halogen bonding, Figure 4.10.

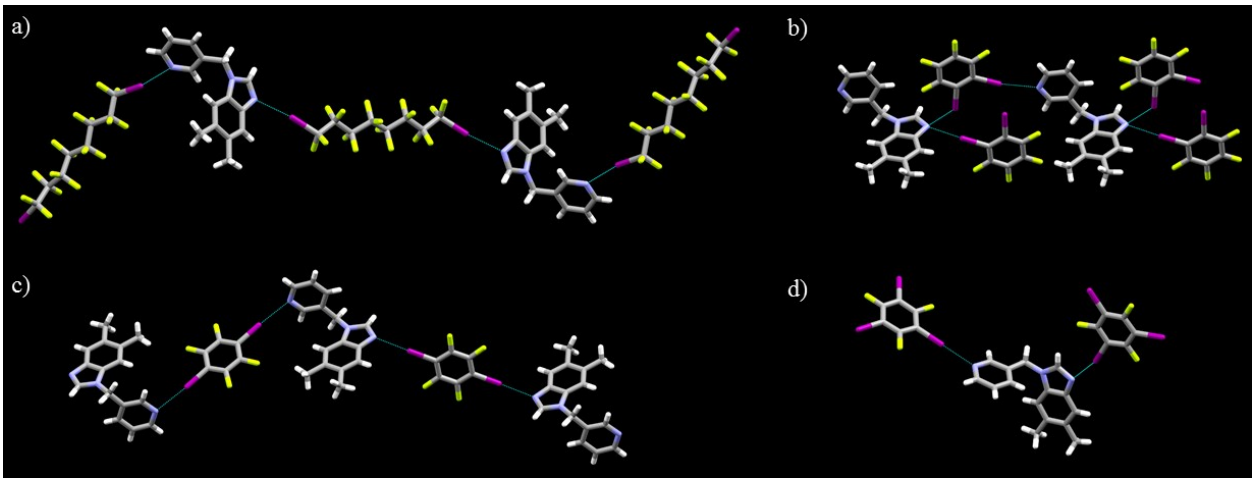

Figure 4.10 Primary halogen bond interactions in a) **A10:D4** b) **A10:D7** c) **A10:D8** and d) **A10:D9**

Similarly, **A11** (ΔE = 38 kJ/mol), produced two structures (**A11:D9** and **A11:D10**) where all acceptors are engaged in halogen bonding, Figure 4.11, which is true for the two structures (**A12:D2** and **A12:D8**) obtained with **A12** (ΔE = 46 kJ/mol) as well, Figure 4.12.

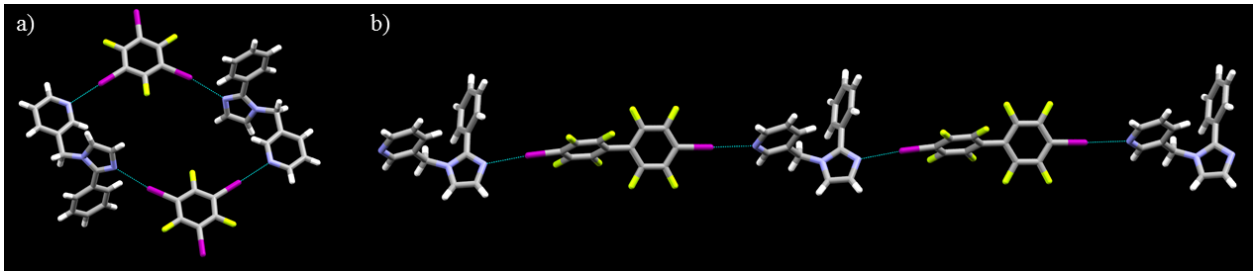

Figure 4.11 Primary halogen bond interactions in a) **A11:D9** and b) **A11:D10**

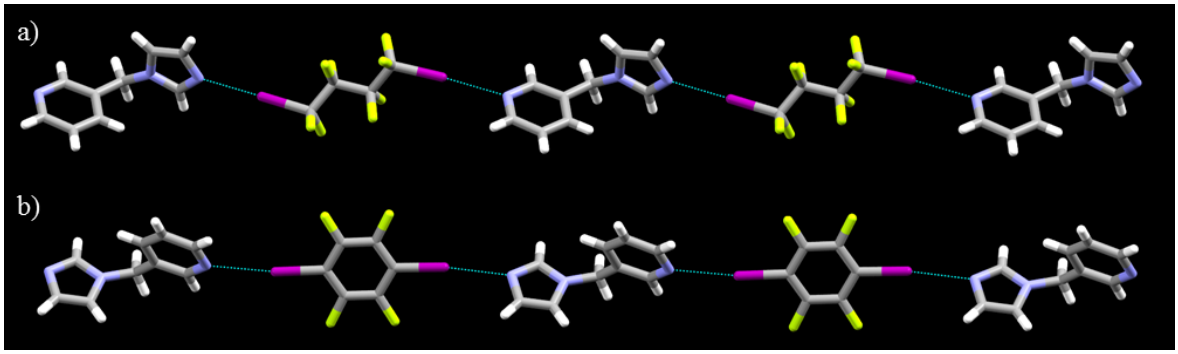

Figure 4.12 Primary halogen bond interactions in a) **A12:D2** and b) **A12:D8**

Six structures (**A2:D2, A2:D3, A2:D7, A2:D8, A2:D9** and **A2:D10**) with **A2** (ΔE = 55 kJ/mol) and seven structures (**A1:D1, A1:D2, A1:D3, A1:D4, A1:D7, A1:D8** and **A1:D10**) with **A1** (ΔE = 64 kJ/mol) were obtained. Structural data and crystallographic data for these thirteen structures have been reported in Chapter 3.[30] Out of these thirteen structures, ten structures preferred binding with the best acceptor site; while only three structures (**A2:D9**, **A2:D10** and **A1:D7**) showed halogen bond formation with all acceptor sites.

Four structures (**A13:D1**, **A13:D2**, **A13:D3** and **A13:D7**) were obtained with **A13** (ΔE = 167 kJ/mol) and all of them show binding with the best acceptor site, while in **A13:D3**, there is an additional short contact formed with the 2nd best acceptor site, Figure 4.13. Even though the

grinding results showed a 67% success in forming co-crystals with **A14** (ΔE = 175 kJ/mol), none of the solution based experiments yielded any co-crystals which could lead to the recognition of halogen bond interactions.

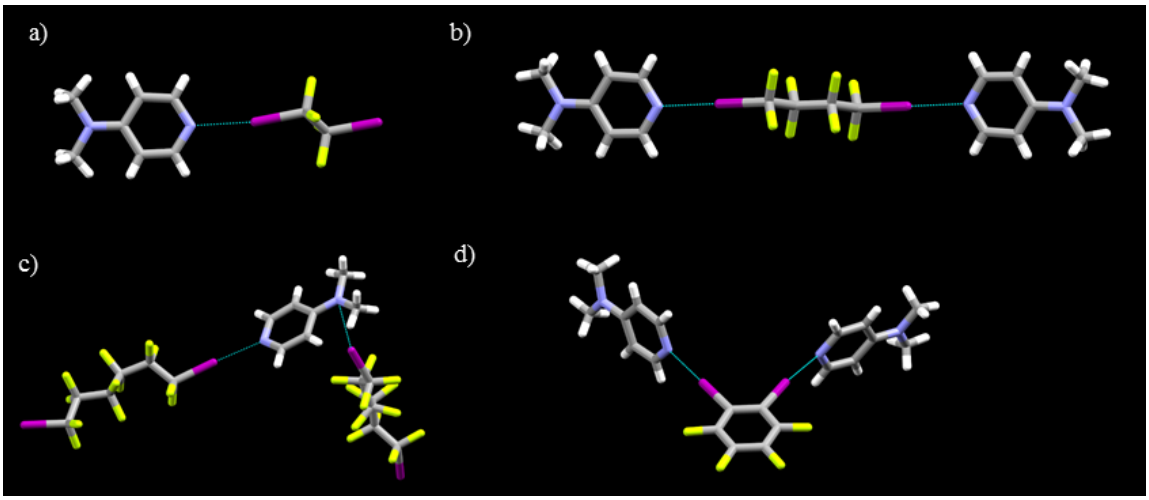

Figure 4.13 Primary halogen bond interactions in a) **A13:D1** b) **A13:D2** c) **A113:D3** and d) **A13:D7**

4.4 Discussion

4.4.1 Structure analysis depending on the ΔE parameter

A CSD search was carried for any previously reported structures between the acceptors and donors of interest in this study. This search yielded three crystal structures,[41] **A12:D5**, **A12:D7** and **A12:D8** where all of them show preferential halogen bond formation with best acceptor site. These three structures will also be included as a part of the discussion, Figure 4.14.

In a previous study on hydrogen and halogen bond competition in a supramolecular system, the MEPS difference between the two donor sites has defined with a Q parameter.[42] Likewise we wanted a parameter to define the MEPS difference between the two acceptor sites in each acceptor molecule and the parameter we defined is the ΔE value. Depending on the ΔE value and the halogen bond selectivity, the structural data from the 39 crystal structures can be divided into three categories, Figure 4.15. This discussion will follow focusing on these three categories.

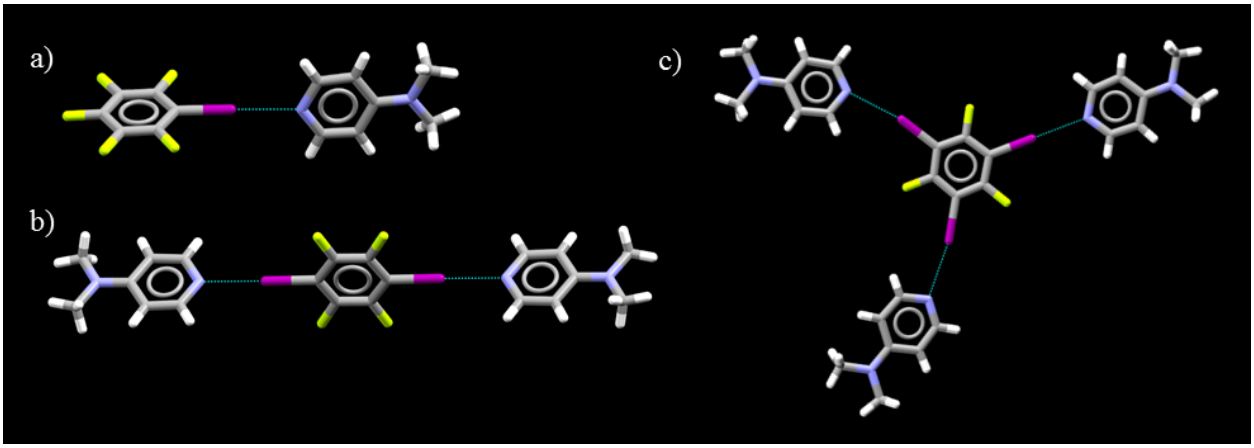

Figure 4.14 Structures reported in the CSD relevant to current study a) **A13:D6** b) **A13:D8** and c) **A13:D9**

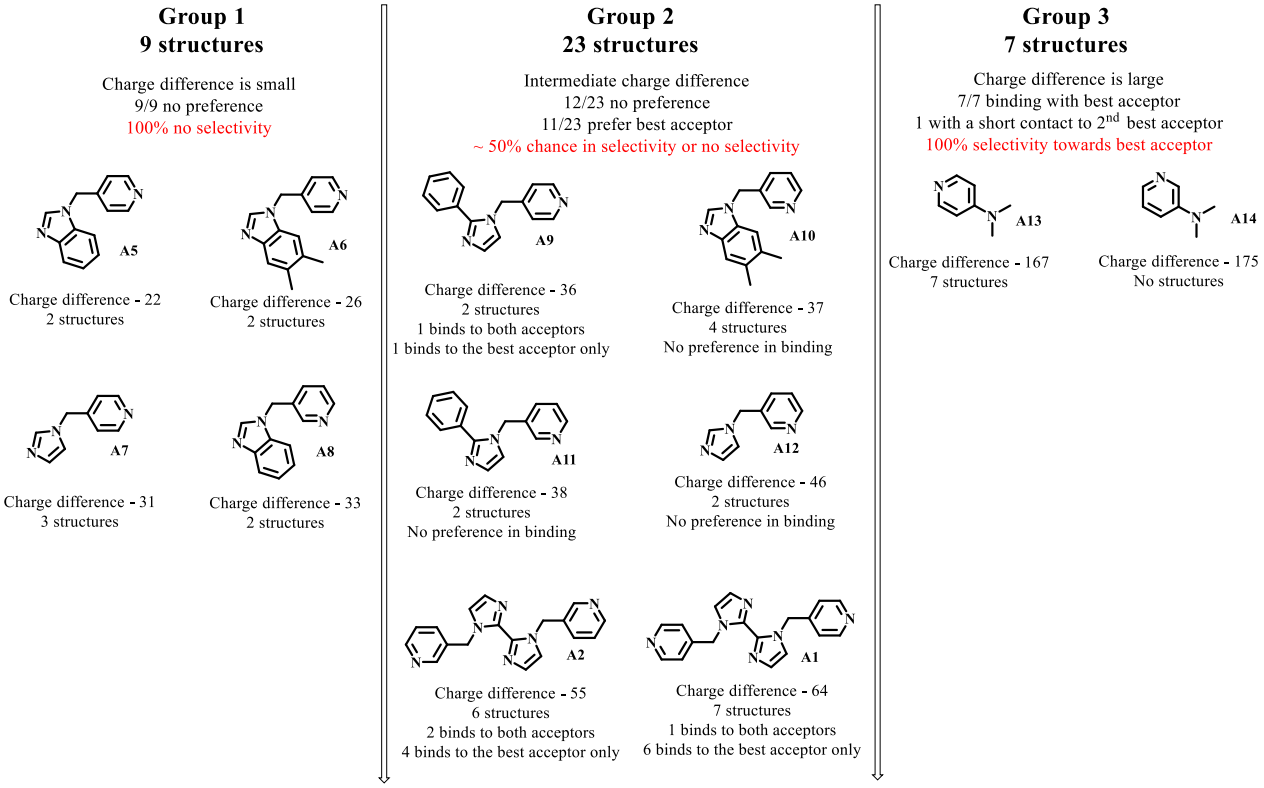

Figure 4.15 Categorization based on ΔE value and halogen bond selectivity

Group 1 contains nine structures with acceptors **A5-A8**. None of them show preference in binding as both acceptor sites are interacting. The MEPS difference between the two acceptor sites

in each molecule is below 35 kJ/mol. The results clearly indicate that this potential difference is not enough to induce selectivity and both acceptors are equally competitive.

Group 2 contains 23 structures with acceptors **A9-A12**, **A2** and **A1**. Out of these 23 structures twelve structures show no preference in binding and display conventional halogen bonds with both pyridine nitrogen and imidazole nitrogen in each case. The remaining eleven structures show preferential binding with the best acceptor site as ranked by the calculated MEPS. These results suggest that this is an intermediate potential difference region (35 kJ/mol to 65 kJ/mol), where a donor is unable to distinguish between two acceptors in a predictable way.

Group 3 contains seven structures all with **A13**. All of them preferentially form halogen bonds with the best acceptor site indicating the higher potential difference between the two acceptor sites leads to halogen bond selectivity. Based on the results from group 2, it can be assumed that best-donor/best-acceptor selectivity begins somewhere from the potential difference of 65 kJ/mol as for **A1** the supramolecular yield of selectivity is 86%. Unfortunately we could not find other asymmetric ditopic acceptor molecules that would cover the MEPS difference range from 65 kJ/mol to 167 kJ/mol to verify this hypothesis. Thus, the following conclusions can be made.

1. If the MEPS difference between the two acceptor sites are in the range of 35-65 kJ/mol, a prediction of binding preference cannot be made. Furthermore, if the MEPS difference is less than 35 kJ/mol, both sites will be involved in halogen bonding.
2. The MEPS difference range from 35 to 65 kJ/mol can be identified as the grey area where a prediction of halogen bond selectivity cannot be made.
3. If the MEPS difference is higher than 65 kJ/mol, halogen bond selectivity for the best acceptor can be observed.

4.4.2 Effect of the MEPS on the donor atoms

According to Table 4.2, MEPS values on the activated iodine in all the donors are almost the same other than for **D9**, which is about 8 kJ/mol units less than the average value for other donors. This means that all the donors should have similar effects on the final selectivity process. A close look at the success rates depending on the donors (Table 4.3) revealed that, apart from **D1** all of them show comparable success in forming co-crystals. The low yields with **D1** can be attributed to the high vapor pressure of the compound. Even though **D9** has a lower MEPS value on the donor site it also has a comparable supramolecular yields. Five structures were obtained with **D9** and all of them show only two of the three iodine atoms participating in halogen bond formations, thus it is possible that the potential on the third iodine atom is depleted towards the other two iodine atoms, which boost the MEPS value on those iodine atoms leading to comparable strength to other donors in the study.

4.4.3 Can we use the ΔE parameter to predict the outcome in other systems?

To find the validity of the results of this study we thought of using this MEPS outcome in predicting the structural outcome of the reported crystal structures. A comprehensive CSD search was carried out targeting the halogen-bond donors utilized in this study and the outcome was seventeen suitable structures where an asymmetric acceptor with two or more acceptor sites are present. Lack of structural data based on halogen bond studies with asymmetric acceptor sites further enhances the importance of this study. The group of acceptors contained ditopic as well as multitopic acceptors and also acceptors based on N, O and S giving exposure to a diverse group. MEPS calculations on these selected systems were carried out and results are summarized in the Table 4.4.

According to this analysis the predicted outcome from the ΔE value based system is in agreement with the actual structural outcome for fourteen of seventeen structures leading to the prediction success of 82%. This success rate underscores the importance of such a simple method based on easily accessible MEPS calculations in designing halogen-bond based molecular recognition studies.

Table 4.4 Results comparison for CSD reported structures

Donor	CSD code	Electrostatic potentials (kJ/mol)		ΔE value (kJ/mol)	Predicted outcome	Structural outcome
		Best acceptor	2nd best acceptor			
D1	ULOKOV	-160	-41	119	Preferred for best acceptor	Preferred for best acceptor
	ULOLAI	-164	-152	12	No preference	No preference
D2	BEWXOS	-175	-154	21	No preference	No preference
D3	BEWXIM	-175	-154	21	No preference	No preference
	COKNOG	-171	-58	113	Preferred for best acceptor	Preferred for best acceptor
D4	COKNUM	-171	-58	113	Preferred for best acceptor	Preferred for best acceptor
	ECASAE	-182	-150	32	No preference	Preferred for best acceptor
D6						
D7						
D8	COGKAM	-164	-30	134	Preferred for best acceptor	Preferred for best acceptor
	DIVCIV	-152	-108	44	Grey region	No preference
	KABLAC	-174	-30	144	Preferred for best acceptor	Preferred for best acceptor
	JAQMEU	-191	-145	46	Grey region	Preferred for best acceptor
	LUKMIN	-137	-102	53	Grey region	Preferred for best acceptor
	PEFPAT	-212	-57	155	Preferred for best acceptor	Preferred for best acceptor
	QOLJIK	-142	-106	36	Grey region	Preferred for best acceptor
	TOJBUQ	-178	-174	4	No preference	Preferred for best acceptor
	TOJCAX	-195	-155	40	Grey region	No preference
	VABNUJ	-175	-149	26	No preference	Binds to 2nd best acceptor
D9						
D10						

4.5 Conclusions

A systematic co-crystallization study was carried out between twelve asymmetric ditopic acceptors and nine halogen-bond donors (108 experiments) in order to identify halogen bond selectivity depending on the MEPS difference between the two acceptor sites. 36 crystal structures were obtained and together with three structures from the CSD lead to the identification of three categories based on halogen bond selectivity, Figure 4.16. If the ΔE value is less than 35 kJ/mol, there is no halogen bond selectivity. In the intermediate region (35 kJ/mol < ΔE < 65 kJ/mol), no prediction can be made. This is recognized as the grey area. If the ΔE value is more than 65 kJ/mol, then the halogen bond is selective for the best acceptor site as ranked by electrostatics. These results provide a set of guidelines which can be utilized in designing more complex supramolecular architectures with halogen bonding, but further studies based on different donor acceptor systems are required for the compilation of well-defined rules for halogen bond binding preferences.

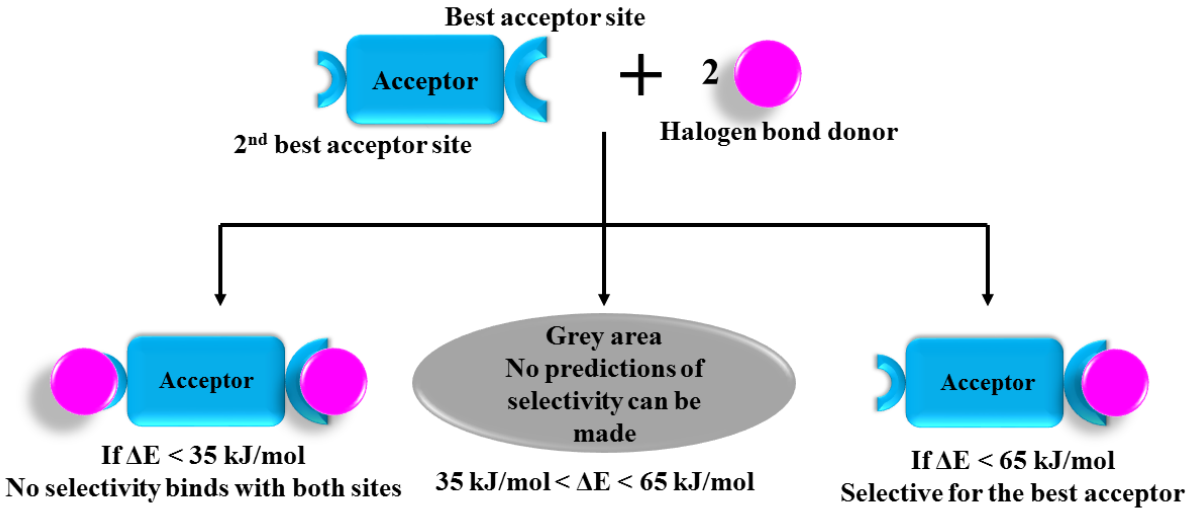

Figure 4.16 Outcome of the study

4.6 References

1. Lehn, J.M. *Chem. Soc. Rev*. **2007**, *36*, 151-160; Benedict, J.B. *Recent advances in crystallography*, InTech, **2012**; Meyer, F.; Dubois, P. *CrystEngComm* **2013**, *15*, 3058-3071; Cinčić, D.; Friščič, T.; Jones, W. *Chem. Eur. J*. **2008**, *14*, 747-753.

2. Steiner,T. *Angew. Chem. Int. Ed*. **2002**, *41*, 48-76; Głowacki, E.D.; Irimia-Vlad, M.; Bauer, S.; Sariciftci, N.S. *J. Mater. Chem*. **2013**, *B1*, 3742-3753; Sweetman, A.M.; Jarvis, S.P.; Sang, H.; Lekkas, I.; Rahe, P.; Wang, Y.; Wang, J.; Champness, N.R.; Kantorovich, L.; Moriarty, P. *Nat. Commun.* **2014**, *5*, 3931.

3. Metrangolo, P.; Meyer, F.; Pilati, T.; Resnati, G.; Terraneo, G. *Angew. Chem. Int. Ed.* **2008**, *47*, 6114-6127; Aakeröy, C.B.; Wijethunga, T.K.; Haj, M.A.; Desper, J.; Moore, C. *CrystEngComm* **2014**, *16*, 7218-7225.

4. Desiraju, G.R.; Ho, S.; Kloo, L.; Legon, A.C.; Marquardt, R.; Metrangolo, P.; Politzer, P.A.; Resnati, G.; Rissanen, K. *Pure Appl. Chem.* **2013**, *85*, 1711-1713.

5. Politzer, P.; Murray, J.S.; Clark, T. *Phys. Chem. Chem. Phys.* **2013**, *15*, 11178-11189. Clark, T.; Hennemann, M.; Murray, J.S.; Politzer, P. *J. Mol. Model*. **2007**, *13*, 291-296.

6. Colin, M. *Ann. Chim*. **1814**, *91*, 252−272; Guthrie, F. *J. Chem. Soc.* **1863**, *16*, 239-244.

7. Metrangolo, P.; Resnati, G. *Cryst. Growth Des*. **2012**, *12*, 5835-5838.

8. Gilday, L.C.; Robinson, S.W.; Barendt, T.A.; Langton, M.J.; Mullaney, B.R,; Beer, P.D. *Chem. Rev*. **2015**, *115*, 7118-7195.

9. Auffinger, P.; Hays, F. A.; Westhof, E.; Ho, P. S. *Proc. Natl. Acad. Sci. U. S. A.* **2004**, *101*, 16789-16794; Brinck, T.; Murray, J. S.; Politzer, P. *Int. J. Quantum Chem*. **1992**, *44*, 57-64; Politzer, P.; Lane, P.; Concha, M.; Ma, Y.; Murray, J. *J. Mol. Model.* **2007**, *13*, 305-311.

10. Aakeröy, C. B.; Sinha, A. S.; Chopade, P. D.; Desper, J. *Dalton Trans.* **2011**, *40*, 12160-12168. Mukherjee, A.; Tothadi, S.; Desiraju, G. R. *Acc. Chem. Res.* **2014**, *47*, 2514-2524; Pavan, M. S.; Durga Prasad, K.; Guru Row, T. N. *Chem. Commun.* **2013**, *49*, 7558-7560.

11. Fourmigué, M. *Curr. Opin. Solid State Mater. Sci*. **2009**, *13*, 36-45. Bauzá, A.; Quiñonero, D.; Frontera, A.; Deyà, P.M. *Phys. Chem. Chem. Phys*. **2011**, *13*, 20371-20379.

12. Alkorta, I.; Sanchez-Sanz, G.; Elguero, J. *CrystEngComm* **2013**, *15*, 3178-3186; Dumele, O.; Wu, D.; Trapp, N.; Goroff, N.; Diederich, F. *Org. Lett.* **2014**, *16*, 4722-4725; Aakeröy, C.B.; Wijethunga, T.K.; Desper, J.; Đakovic, M. *Cryst.Growth Des.* **2015**, *15*, 3853-3861.

13. Aakeröy, C. B.; Baldrighi, M.; Desper, J.; Metrangolo, P.; Resnati, G. *Chem. Eur. J.* **2013**, *19*, 16240-16247; Aakeröy, C. B.; Chopade, P. D.; Desper, J. *Cryst. Growth Des.* **2013**, *13*, 4145-4150.

14. Legon, A. C. *Phys. Chem. Chem. Phys.* **2010**, *12*, 7736-7747; Legon, A. C. *Phys. Chem. Chem. Phys.* **2014**, *16*, 12415-12421.

15. Caballero, A.; Zapata, F.; White, N. G.; Costa, P. J.; Felix, V.; Beer, P. D. *Angew. Chem., Int. Ed.* **2012**, *51*, 1876-1880.

16. Rissanen, K. *CrystEngComm* **2008**, *10*, 1107-1113; Chandran, S. K.; Thakuria, R.; Nangia, A. *CrystEngComm* **2008**, *10*, 1891-1898; Metrangolo, P.; Pilati, T.; Terraneo, G.; Biella, S.; Resnati, G. *CrystEngComm* **2009**, *11*, 1187-1196; Aakeröy, C.B., Spartz, C.L. *Topics in Current Chem*. **2015**, *358*, 155-182.

17. Gonnade, R. G.; Bhadbhade, M. M.; Shashidhar, M. S.; Sanki, A. K. *Chem. Commun.* **2005**, 5870-5872; Aakeröy, C.B.; Wijethunga, T.K.; Desper, J. *CrystEngComm*, **2014**, *16*, 28-31; Aakeröy, C.B.; Rajbanshi, A.; Metrangolo, P.; Resnati, G.; Parisi, M.F.; Desper, J.; Pilati, T. *CrystEngComm*, **2012**, *14*, 6366-6368.

18. Meazza, L.; Foster, J. A.; Fucke, K.; Metrangolo, P.; Resnati, G.; Steed, J. W. *Nat. Chem.* **2013**, *5*, 42-47.

19. Shirman, T.; Arad, T.; van der Boom, M. E. *Angew. Chem., Int. Ed*. **2010**, *49*, 926-929; Shirman, T.; Kaminker, R.; Freeman, D.; van der Boom, M. E. *ACS Nano* **2011**, *5*, 6553-6563.

20. Bertani, R.; Metrangolo, P.; Moiana, A.; Perez, E.; Pilati, T.; Resnati, G.; Rico-Lattes, I.; Sassi, A. *Adv. Mater.* **2002**, *14*, 1197-1201; Nguyen, H. L.; Horton, P. N.; Hursthouse, M. B.; Legon, A. C.; Bruce, D. W. *J. Am. Chem. Soc.* **2003**, *126*, 16-17.

21. Saha, B. K.; Nangia, A.; Nicoud, J.F. *Cryst. Growth Des.* **2006**, *6*, 1278-1281; Cariati, E.; Forni, A.; Biella, S.; Metrangolo, P.; Meyer, F.; Resnati, G.; Righetto, S.; Tordin, E.; Ugo, R. *Chem. Commun*. **2007**, 2590-2592.

22. Farina, A.; Meille, S. V.; Messina, M. T.; Metrangolo, P.; Resnati, G.; Vecchio, G. *Angew. Chem., Int. Ed*. **1999**, *38*, 2433-2436; Takeuchi, T.; Minato, Y.; Takase, M.; Shinmori, H. *Tetrahedron Lett.* **2005**, *46*, 9025-9027.

23. Aakeröy, C.B.; Wijethunga, T.K.; Benton, J.; Desper, J. *ChemCommun*. **2015**, *51*, 2425-2428.

24. Metrangolo, P.; Resnati, G. *Science* **2008**, *321*, 918-919.

25. Lu, Y.; Wang, Y.; Zhu, W. *Phys. Chem. Chem. Phys.* **2010**, *12*, 4543-4551; Voth, A. R.; Hays, F. A.; Ho, P. S. *Proc. Natl. Acad. Sci. U. S. A.* **2007**, *104*, 6188-6193.

26. Lu, Y.; Shi, T.; Wang, Y.; Yang, H.; Yan, X.; Luo, X.; Jiang, H.; Zhu, W. *J. Med. Chem.* **2009**, *52*, 2854-2862; Ibrahim, M.A.A. *J. Comput. Chem.* **2011**, *32*, 2564-2574.

27. Vargas Jentzsch, A.; Emery, D.; Mareda, J.; Metrangolo, P.; Resnati, G.; Matile, S. *Angew. Chem., Int. Ed.* **2011**, *50*, 11675-11678; Jentzsch, A. V.; Emery, D.; Mareda, J.; Nayak, S. K.; Metrangolo, P.; Resnati, G.; Sakai, N.; Matile, S. *Nat. Commun*. **2012**, *3*, 905-913; Vargas Jentzsch, A.; Matile, S. *J. Am. Chem. Soc.* **2013**, *135*, 5302-5303.

28. Etter, M.C. *Acc. Chem. Res.* **1990**, *23*, 120-126; Aakeröy, C.B.; Beatty, A.M.; Helfrich, B.A. *J. Am. Chem. Soc.* **2002**, *48*, 14425-12232; Aakeröy, C.B.; Salmon, D.J. *CrystEngComm* **2005**, *72*, 439-448; Bowers, J.R.; Hopkins, G.W.; Yap, G.P.A.; Wheeler, K.A. *Cryst.Growth Des.* **2005**, *5*, 727-736.

29. Aakeröy, C. B.; Desper, J.; Salmon, D. J.; Smith, M. M. *CrystEngComm* **2009**, *11*, 439-443; Lynch, D.E.; Sandhu, P.; Parsons, S. *Aust. J. Chem.* **2000**, *53*, 383-387; Hunter, C. A. *Angew. Chem*. **2004**, *43*, 5310-5324; Hunter, C. A. *Angew. Chem*. **2004**, *116*, 5424-5439; Musumeci, D.; Hunter, C. A.; Prohens, R.; Scuderi, S.; McCabe, J. F. *Chem. Sci*. **2011**, *2*, 883-890.

30. Aakeröy, C.B.; Wijethunga, T.K.; Desper, J. *J. Mol. Struct*. **2014**, *1072*, 20-27; Aakeröy, C.B.; Wijethunga, T.K. Desper, J. *J. Chem. Cryst.,* **2015**, *45*, 267-276.

31. CSD ConQuest 1.17, **2014**, Cambridge Crystallographic Data Centre, U.K.

32. Aakeröy, C.B.; Desper, J.; Fasulo, M.; Hussain, I.; Levin, B.; Schultheiss, N. *CrystEngComm* **2008**, *10*, 1816-1821.

33. Aakeröy, C.B.; Wijethunga, T.K.; Desper, J. *New J. Chem.* **2014**, *39*, 822-828.

34. Aakeröy, C.B.; Epa, K.; Forbes, S.; Schultheiss, N.; Desper, J. *Chem. A Eur. J.* **2013**, *19*, 14998-15003.

35. Felten, A.E.; Zhu, G.; Aron, C.D. *Org. Lett.*, **2010**, *12*, 1916-1919.

36. Espallargas, G.M.; Recuenco, A.; Romero, F.M.; Brammer, L.; Libri, S. *CrystEngComm* **2012**, *14*, 6381-6383.

37. Omnic 8.0 © **1992-2008**, Thermo Fisher Scientific Inc.

38. Spartan'08, Wavefunction, Inc.

39. Aakeröy, C.B.; Desper J.; Smith, M.M. *Chem. Commun*. **2007**, 3936-3938.

40. Aakeroy, C.B.; Desper J.; Urbina, J.F. *Chem. Commun*. **2005**, 2820-2822.

41. Roper, L.C.; Präsang, C.; Kozhevnikov, V.N.; Whitwood, A.C.; Karadakov, P.B.; Bruce, D.W. *Cryst. Growth Des.* **2010**, *10*, 3710-3720; Präsang, C.; Whitwood, A.C.; Bruce, D.W. *Cryst. Growth Des.* **2009**, *9*, 5319-5326.

42. Aakeröy, C.B.; Spartz, C.L.; Desper, J. *IUCrJ* **2015**, *2*, 498-510.

Chapter 5 - Structural landscape of heteroaryl-2-imidazoles: Competing halogen- and hydrogen-bond interactions[1]

5.1 Introduction

Non-covalent interactions reside at the center of fundamental and applied supramolecular chemistry and are responsible for any molecular recognition event that initiates the formation and stabilization of different supramolecules.[2] The practical utilizations of these interactions are readily found in crystal engineering,[3] biochemistry,[4] physics[5] and materials science.[6] Intermolecular interactions cover a broad range of binding energies, thus are particularly interesting as means for intermolecular communication.[7] Although hydrogen bonding is arguably the most well-understood non-covalent interaction,[8] the halogen bond has been recognized as displaying many similarities[9] and, consequently, it has gained considerable attention focusing on its directionality,[10] strength,[11] and potential applications.[12]

A hydrogen bond is often defined as a chemical bond formed between an electropositive hydrogen atom and a strongly electronegative atom,[13] and the halogen bond has been defined as an attractive interaction between an electrophilic region of a halogen atom and an electron-pair donor.[14] These definitions acknowledge that there are substantive similarities between the two types of interactions.[15] Energetically, halogen bonds cover a wide range from less than 5 kJ/mol in Cl···Cl interactions between chlorocarbons to 180 kJ/mol in $I^-\cdots I_2$ contacts in I^-_3.[16] Likewise, hydrogen bonds can vary from very weak (1–2 kJ/mol) in $CH_4\cdots FCH_3$[17] to extremely strong (161.5 kJ/mol) in HF^-_2.[18]

Recent experimental[19] and theoretical studies[20] underscore that it is not straightforward to predict what the outcome is likely to be when hydrogen-bond (HB) and halogen-bond (XB) donors compete[21] for a limited number of binding sites or for multiple binding sites of different strengths.[22]

One experimental study suggested that the hydrogen bond can outperform halogen bond interactions in a competitive scenario where the best acceptor benzimidazole moiety of the probe acceptor molecule interact with the oxime functionality while the fluoro-activated organoiodine is interacting with the second best acceptor pyridine site, Figure 5.1.[23]

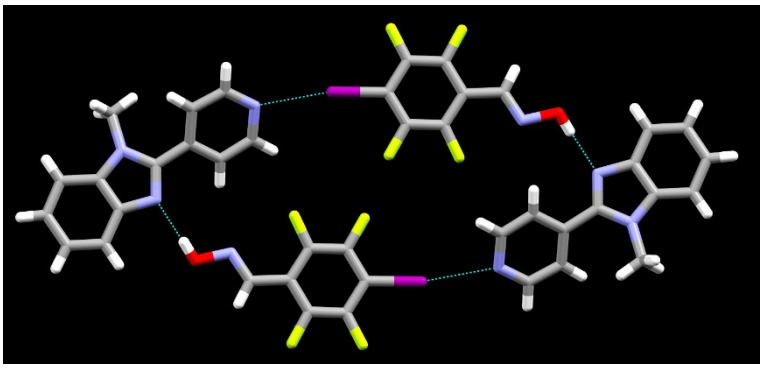

Figure 5.1 A competitive scenario between hydrogen and halogen bond (best acceptor benzimidazole nitrogen atom interacts with the oxime hydrogen atom; while the 2nd best acceptor the pyridine nitrogen atom interacts with iodine)[23]

Another study suggested that the halogen bond can outperform the hydrogen bond.[24] In equimolar mixtures of 1,2-bispyridylethane, 1,4-diiodoperfluorobenzene and 1,4-dihydroxybenzene co-crystal formation took place between the 1,2-bispyridylethane and 1,4-diiodoperfluorobenzene while in a non-competitive setting both the XB donor and the HB donor were successful in forming co-crystals with the acceptor, Figure 5.2

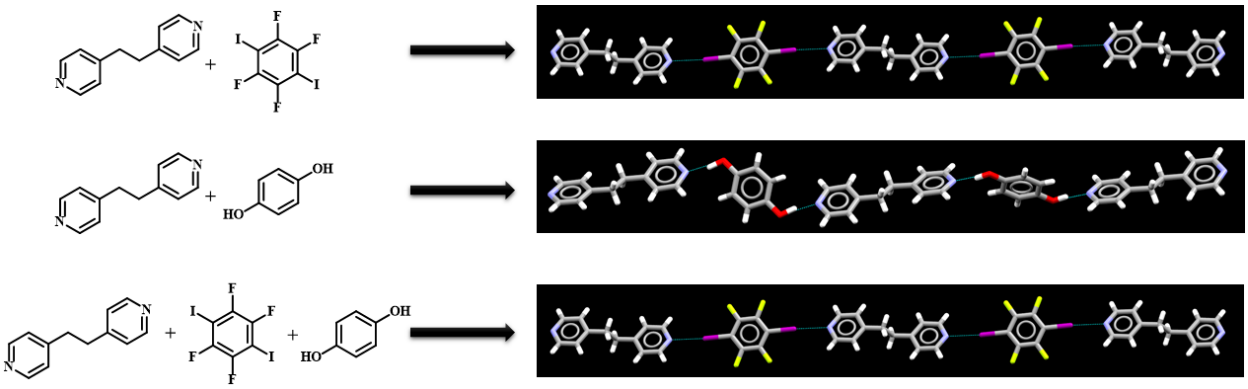

Figure 5.2 Outcome of a competitive study between hydrogen bond and halogen bond[24]

Thus, there is a need for further systematic studies to identify possible guidelines for combining HB/XB interactions into concise synthetic strategies in such a way that "synthon cross-over"[25] is minimized resulting in reliable synthetic protocols for the directed assembly of desired architectures in the solid state.

In order to examine the balance between XB and HB interactions in a practical crystal engineering context, five heteroaryl-2-imidazole molecules **A16-A20**, Figure 5.3 were utilized as probe molecules.

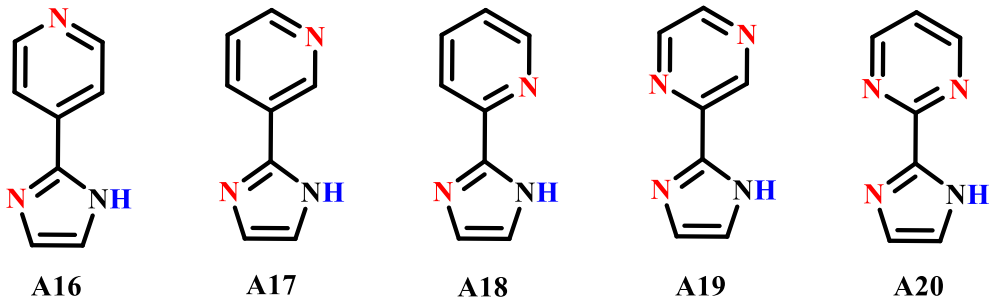

Figure 5.3 Heteroaryl-2-imidazoles employed in this study (hydrogen-bond donor sites are depicted in blue and acceptor sites are depicted in red)

The reason for selecting these molecules is due to the fact that they contain a single hydrogen-bond donor site and two or three acceptor sites on the same molecule. In addition, many heteroaryl-2-imidazoles are recognized as key intermediates in the synthesis of pharmacologically active compounds[26] and have gained much attention in the field of coordination chemistry[27] and palladium-catalyzed cross-coupling chemistry.[28]

The primary objective of this study is to use co-crystallizations as a way of determining binding preferences in the solid state when hydrogen-bond and halogen-bond donors compete for two or more different acceptor sites. The combination of a molecule decorated with one hydrogen-bond donor and two or three different acceptor sites and one halogen-bond donor can, in principle lead to three different outcomes, Figure 5.4. If the halogen-bond donor is unable to bring about

the formation of a co-crystal, nothing will happen. Alternatively, a co-crystal will form with the XB donor finding one of the acceptors (best acceptor or 2nd best acceptor), leaving the HB donor to interact with the remaining acceptor, Figure 5.4. The acceptor sites are differentiated from each other by their different electrostatic potentials which make them more or less competitive in the context of electrostatically driven intermolecular interactions.

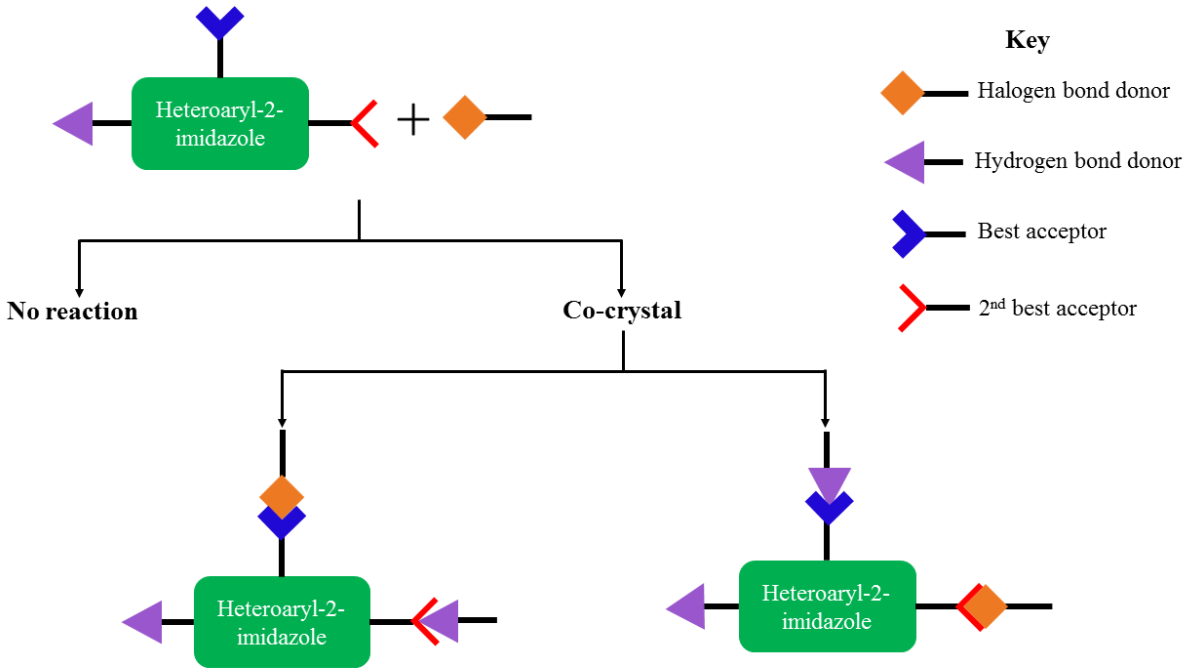

Figure 5.4 The three most likely outcomes in co-crystallizations between **A16-A20** with a halogen-bond donor

Fifteen potential halogen-bond donors were selected, **D1-D15**, Figure 5.5, that can be divided into three subcategories: iodine-based halogen-bond donors (**D1-D10**), bromine-based halogen-bond donors (**D11-D13**), and mixed donors (**D14-D15**). A systemic co-crystallization study comprising 75 experiments between five acceptors and 15 donors were conducted with the intention of providing more details regarding the structural landscape of competing hydrogen and halogen bonds in the solid state.

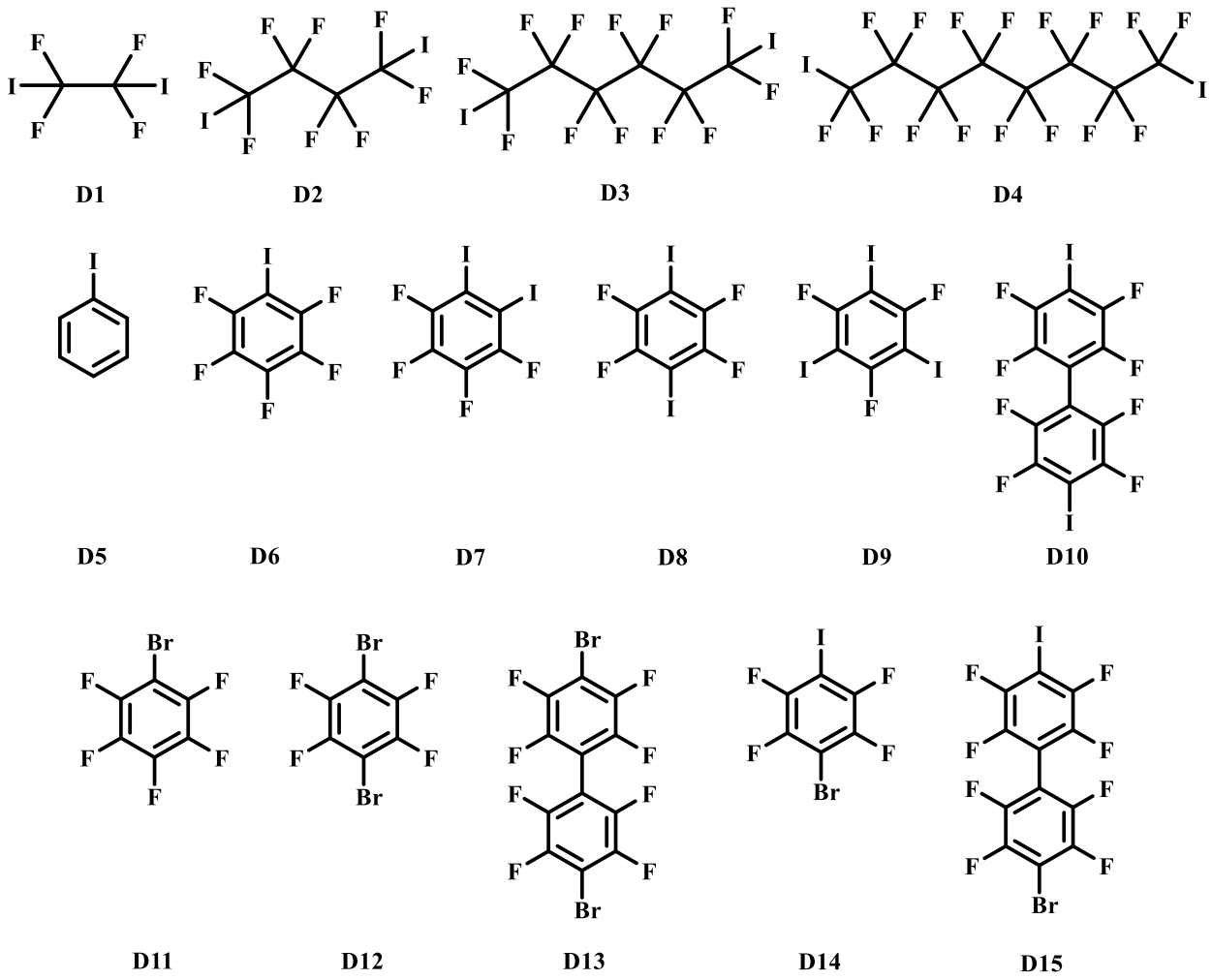

Figure 5.5 Halogen-bond donors employed in this study

This study is undertaken in response to the hypothesis,

1. As hydrogen bond and halogen bond have comparable bond strengths, if a hydrogen-bond donor and a halogen-bond donor have the choice of interacting with an acceptor with a multitude of acceptor sites, both donors will have an equal chance to compete for the best acceptor site ranked by molecular electrostatic potentials surfaces (MEPS).

5.2 Experimental

5.2.1 General

All the precursors, solvents and **D1-D9** and **D11-D13** were purchased from commercial sources and used without further purification. **A16-A20** were synthesized according to the reported procedures by Zhichkin and co-workers.[29] **D10**,[30] **D14**[31] and **D15**[31] were synthesized using literature procedures. ^{1}H NMR spectra were recorded on a Varian Unity plus 400 MHz spectrometer in $CDCl_3$ or DMSO-d_6. Infrared spectra were recorded with a Nicolet 380 FT-IR with a digital resolution of 0.9 cm^{-1} and data processed using Omnic[32] software. Melting points were determined using a Fischer-Johns Mel-Temp melting point apparatus and are uncorrected.

5.2.2 Electrostatic potential calculations

Molecular electrostatic potentials were obtained with density functional B3LYP level of theory using 6-311++G** basis set in vacuum. All calculations were carried out using Spartan 8 software.[33] All molecules were geometry optimized with the maxima and minima on the electrostatic potential surface (0.002 e/au isosurface) determined using a positive point charge in the vacuum as a probe. The numbers indicate the interaction energy (kJ/mol) between the positive probe and surface of the molecule at that particular point. These numbers are related to the electrostatic potentials on the atoms with the negative value corresponding to a negative potential and positive value corresponding to a positive potential.

5.2.3 Synthesis of acceptors

5.2.3.1 Synthesis of 4-(imidazol-2-yl)pyridine, A16

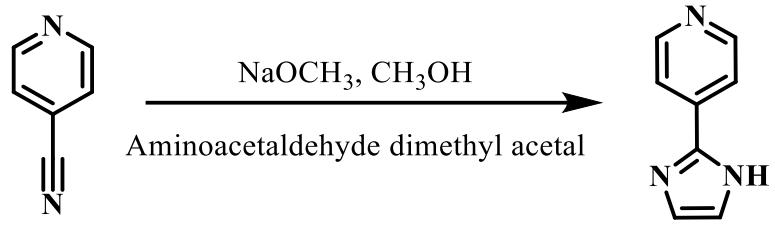

To a flask containing 4-cyanopyridine (2.0 g, 0.019 mol) and MeOH (20 mL) a 30% solution of NaOMe in MeOH (0.36 mL, 1.9 mmol) was added. The reaction mixture was stirred for one hour at room temperature. Aminoacetaldehyde dimethyl acetal (2.2 mL, 0.019 mol) followed by AcOH (2.1 mL, 37 mmol) were added dropwise. The reaction mixture was heated under reflux for 30 min. After cooling the reaction mixture to room temperature, MeOH (15 mL) and 6 M HCl in H_2O (10 mL) were added, and the mixture was heated under reflux for three hours. Once the cyclization was complete, the solution was evaporated to dryness on a rotary evaporator. A freshly prepared warm solution of K_2CO_3 (50% w/w in water) was added carefully, bringing the pH to 10. The resulting suspension was allowed to cool to room temperature and recrystallized from boiling water to obtain 4-(imidazol-2-yl)pyridine, **A16**, as an off-white solid. Yield: 1.9 g (72%); m.p. 207-210 °C (reported 210-211 °C)[29]; ^{1}H NMR (400 MHz, DMSO-d_6) 12.90 (br s, 1H), 8.62 (dd, 2H), 7.86 (dd, 2H), 7.39 (br s, 1H), 7.13 (br s, 1H).

5.2.3.2 Synthesis of 3-(imidazol-2-yl)pyridine, A17

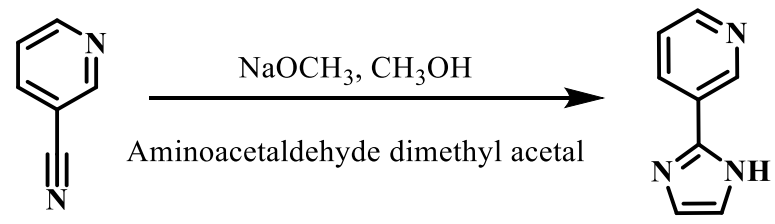

To a flask containing 3-cyanopyridine (2.0 g, 0.019 mol) and MeOH (20 mL) a 30% solution of NaOMe in MeOH (0.36 mL, 1.9 mmol) was added. The reaction mixture was stirred for one hour at room temperature. Aminoacetaldehyde dimethyl acetal (2.2 mL, 0.019 mol) followed by AcOH (2.1 mL, 37 mmol) were added dropwise. The reaction mixture was heated under reflux for 30 min. After cooling the reaction mixture to room temperature, MeOH (15 mL) and 6 M HCl in H_2O (10 mL) were added, and the mixture was heated under reflux for eight hours. Once the cyclization was complete, the solution was evaporated to dryness on a rotary evaporator. A freshly prepared warm solution of K_2CO_3 (50% w/w in water) was added carefully, bringing the pH to 10. The resulting suspension was allowed to cool to room temperature and recrystallized from boiling water to obtain 3-(imidazol-2-yl)pyridine, **A17**, as an off-white solid. Yield: 2.3 g (85%); m.p. 204-207 °C (reported 208-209 °C)[29]; ^{1}H NMR (400 MHz, DMSO-d_6) 12.71 (br s, 1H), 9.13 (d, 1H), 8.53 (dd, 1H), 8.26 (dt, 1H), 7.47 (dd, 1H), 7.20 (br s, 2H).

5.2.3.3 Synthesis of 2-(imidazol-2-yl)pyridine, A18

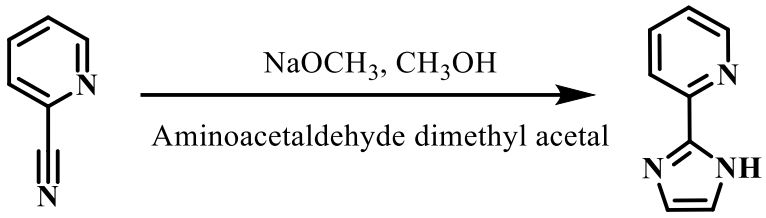

To a flask containing 2-cyanopyridine (2.0 g, 0.019 mol) and MeOH (20 mL) a 30% solution of NaOMe in MeOH (0.36 mL, 1.9 mmol) was added. The reaction mixture was stirred for one hour at room temperature. Aminoacetaldehyde dimethyl acetal (2.2 mL, 0.019 mol) followed by AcOH (2.1 mL, 37 mmol) were added dropwise. The reaction mixture was heated to reflux for 30 min. After cooling the reaction mixture to room temperature, MeOH (15 mL) and 6 M HCl in H_2O (10 mL) were added, and the mixture was heated under reflux for five hours. Once the cyclization was complete, the solution was evaporated to dryness on a rotary evaporator.

A freshly prepared warm solution of K_2CO_3 (50% w/w in water) was added carefully, bringing the pH to 10. The resulting suspension was allowed to cool to room temperature and recrystallized from boiling EtOAc to afford 2-(imidazol-2-yl)pyridine, **A18** as an off-white solid. Yield: 2.0 g (73%); m.p. 132-135 °C (reported 137-138 °C)[29]; ^{1}H NMR (400 MHz, DMSO-d_6) 12.69 (br s, 1H), 8.52 (d, 1H), 7.95 (d, 1H), 7.80 (td, 1H), 7.28 (m, 1H), 7.15 (br s, 1H), 7.00 (br s, 1H).

5.2.3.4 Synthesis of 2-(imidazol-2-yl)pyrazine, *A19*

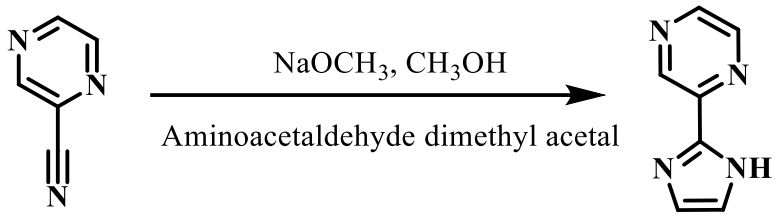

A 100 mL flask was charged with pyrazine-2-carbonitrile (1.1 g, 10 mmol), MeOH (10 mL), and a 30% solution of NaOMe in MeOH (0.38 mL, 1.0 mmol). The reaction mixture was stirred for 40 minutes at room temperature. Aminoacetaldehyde dimethyl acetal (1.1 mL, 10 mmol) was added to the reaction mixture followed by AcOH (1.2 mL, 20 mmol). The reaction mixture was heated to 50 °C for one hour and then cooled to room temperature. MeOH (20 mL) and 6 M HCl in H_2O (5.0 mL) were added, and the reaction mixture was heated under reflux for five hours. Once the cyclization was complete, the solution was removed on a rotary evaporator, and the residue was taken up in a 1:1 mixture of H_2O and Et_2O. The layers were separated and the pH of the aqueous layer was adjusted to pH 9 with 2 M aqueous NaOH. Then the aqueous mixture was stirred for 30 min to allow complete precipitation of the product. The solid was collected by filtration and dried under vacuum to obtain pure 2-(imidazol-2-yl)pyrazine, **A19**, as a white solid. Yield: 0.83 g (57%); m.p. 196-198 °C (reported 199-201 °C)[29]; ^{1}H NMR (400 MHz, $CDCl_3$) 10.34 (br s, 1H), 9.44 (d, 1H), 8.53 (d, 1H), 8.49 (m, 1H), 7.31 (br s, 1H), 7.23 (br s, 1H).

5.2.3.5 Synthesis of 2-(imidazol-2-yl)pyrimidine, A20

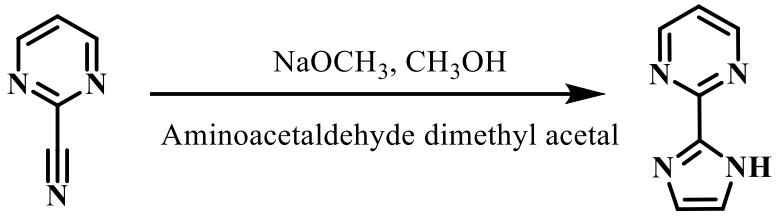

To a flask containing pyrimidine-2-carbonitrile (2.0 g, 0.019 mol) and MeOH (20 mL) a 30% solution of NaOMe in MeOH (0.36 mL, 1.9 mmol) was added. The reaction mixture was stirred for two hours at room temperature. Aminoacetaldehyde dimethyl acetal (2.1 mL, 0.019 mol) followed by AcOH (2.1 mL, 37 mmol) were added dropwise. The reaction mixture was heated under reflux for 30 min. After cooling the reaction mixture to room temperature, MeOH (15 mL) and 6 M HCl in H_2O (10 mL) were added, and the mixture was heated under reflux for five hours. Once the cyclization was complete, the solution was evaporated to dryness on a rotary evaporator. A freshly prepared warm solution of K_2CO_3 (50% w/w in water) was added carefully, bringing the pH to 10. The resulting suspension was allowed to cool to room temperature and washed with ice-cold water to obtain pure 2-(imidazol-2-yl)pyrimidine, **A20**, as a white solid. Yield: 2.61 g (36%); m.p. 193-195 °C (reported 196-197 °C)[29]; ^{1}H NMR (400 MHz, DMSO-d_6) 12.90 (br s, 1H), 8.83 (d, 2H), 8.28 (s, 1H), 7.39 (d, 1H), 7.18 (d, 2H).

5.2.4 Grinding experiments and IR spectroscopy

A16-**A20** were initially combined with all fifteen donors in a screening using solvent-assisted (a few drops of methanol) grinding. In all 75 combinations the acceptors and donors were mixed in respective stoichiometries and the solid resulting from each reaction was characterized using IR spectroscopy to determine if a co-crystal had formed. The IR analysis was done by comparing the spectra of the initial compounds with the ground mixture. More than three wave number shifts of C-F stretches of the halogen-bond donor was considered as a positive

interaction.[34] In 30 of the 75 experiments the vibrational spectra unambiguously showed that a co-crystal had been obtained.

5.2.5 Synthesis of co-crystals

Subsequently, the mixtures obtained in the grinding experiments were dissolved in a minimum amount of methanol and placed in a 2 dram borosilicate vial for slow evaporation in order to obtain crystals suitable for single crystal X-ray diffraction. If this approach did not yield appropriate single crystals, a range of solvents were used as well as vapor diffusion with methanol and hexane as the solvent and anti-solvent, respectively. Once crystals were formed they were again analyzed using IR spectroscopy and subjected to single crystal X-ray diffraction. In the end, crystallographic data for fifteen compounds were obtained. Table 5.1 summarizes the experimental details. Appendix B.4 contains the relevant X-ray experimental data.

Table 5.1 Experimental details of the fifteen co-crystals obtained

Code	Mixed Mole ratio	Amounts used	Solvent and method	Crystal stoichiometry	Crystal color & habit
A16:D8	1:1	**A16** -10 mg, 0.069 mmol **D8** - 28 mg, 0.069 mmol	Methanol and hexane, Vapor diffusion	2:1	Colorless needle
A17:D1	1:1	**A17** - 10 mg, 0.069 mmol **D1** - 24 mg, 0.069 mmol	Methanol, Slow evaporation	2:1	Colorless rod
A17:D2	1:1	**A17** - 10 mg, 0.069 mmol **D2** - 31 mg, 0.069 mmol	Methanol, Slow evaporation	2:1	Colorless prism
A17:D7	1:1	**A17** - 10 mg, 0.069 mmol **D7** - 28 mg, 0.069 mmol	Methanol, Slow evaporation	2:1	Colorless block
A17:D8	1:1	**A17** - 10 mg, 0.069 mmol **D8** - 28 mg, 0.069 mmol	Methanol, Slow evaporation	2:1	Colorless plate
A17:D9	3:2	**A17** - 10 mg, 0.069 mmol **D9** - 23 mg, 0.046 mmol	Methanol, Slow evaporation	2:1	Colorless plate
A17:D10	1:1	**A17** - 10 mg, 0.069 mmol **D10** - 38 mg, 0.069 mmol	Methanol, Slow evaporation	2:1	Colorless prism
A17:D14	1:1	**A17** - 10 mg, 0.069 mmol **D14** - 24 mg, 0.069 mmol	Methanol, Slow evaporation	2:1	Colorless rod
A18:D3	1:1	**A18** - 10 mg, 0.069 mmol **D3** - 38 mg, 0.069 mmol	Methanol, Slow evaporation	4:1	Colorless prism
A18:D8	1:1	**A18** - 10 mg, 0.069 mmol **D8** - 28 mg, 0.069 mmol	Methanol, Slow evaporation	1:1	Colorless prism

A18:D10	1:1	**A18** - 10 mg, 0.069 mmol **D10** - 38 mg, 0.069 mmol	Methanol, Slow evaporation	2:1	Colorless prism
A19:D2	2:3	**A19** - 10 mg, 0.068 mmol **D2** - 47 mg, 0.10 mmol	Methanol, Slow evaporation	2:1	Colorless prism
A19:D8	2:3	**A19** - 10 mg, 0.068 mmol **D8** - 41 mg, 0.10 mmol	Methanol, Slow evaporation	2:1	Colorless plate
A19:D9	1:1	**A19** - 10 mg, 0.068 mmol **D9** - 35 mg, 0.068 mmol	Methanol, Slow evaporation	2:1	Colorless rod
A19:D10	2:3	**A19** - 10 mg, 0.068 mmol **D10** - 56 mg, 0.10 mmol	Methanol, Slow evaporation	2:1	Yellow prism

5.3 Results

5.3.1 Electrostatic potentials

The acceptor molecules in this study have one hydrogen-bond donor and either two (**A16-A18**) or three (**A19** and **A20**) acceptor sites. The concept of preferential based best-donor/best-acceptor interactions in hydrogen-bonded[35] and halogen-bonded[36] co-crystals were used as a guideline for predicting the primary motifs in the solid state, and molecular electrostatic potentials (obtained via DFT calculations) were used to rank the relative strength of each donor and acceptor site, Figure 5.6 and Table 5.2.

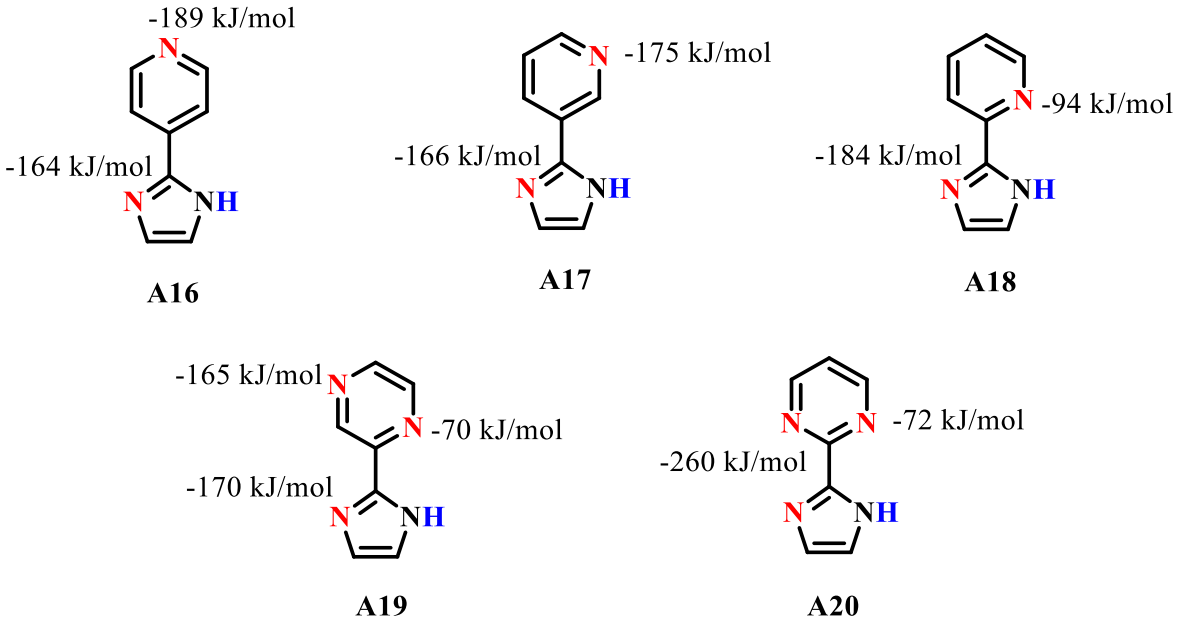

Figure 5.6 Electrostatic potential values of selected heteroaryl-2-imidazole molecules

Table 5.2 Calculated surface potential values of selected halogen-bond donors

Molecule	Donor atom(s)	Electrostatic potential(kJ/mol)
1,2-Diiodotetrafluoroethane D1	Iodine	+163
1,4-Diiodooctafluorobutane D2	Iodine	+168
1,6-Diiodoperfluorohexane D3	Iodine	+169
1,8-Diiodoperfluorooctane D4	Iodine	+169
Iodobenzene D5	Iodine	+103
Iodopentafluorobenzene D6	Iodine	+166
1,2-Diiodotetrafluorobenzene D7	Iodine	+162
1,4-Diiotetrafluorobenzene D8	Iodine	+169
1,3,5-Triiodotrifluorobenzene D9	Iodine	+158
4,4'-Diiodoperfluorobiphenyl D10	Iodine	+164
Bromopentafluorobenzene D11	Bromine	+143
1,4-Diiodotetrafluorobenzene D12	Bromine	+139
4,4'-Dibromopurfluorobiphenyl D13	Bromine	+132
1-Bromo-4-iodotetrafluorobenzene D14	Iodine/Bromine	+165/+132
4-Bromo-4'-iodperfluorobiphenyl D15	Iodine/Bromine	+168/+140

For the acceptor atoms on **A16-A20**, the pyridine nitrogen atoms of **A16** and **A17** represent the best acceptors, while the imidazole nitrogen atoms are second best acceptors. In **A18** and **A19**, the best acceptor sites are the imidazole nitrogen atoms while the remaining heterocyclic nitrogen atoms are second and third, respectively. In the electrostatic potential calculation of **A20**, the imidazole nitrogen and the adjacent pyrimidine nitrogen are too close in space such that it is not possible to identify a specific value of the potential associated with either individual nitrogen atom, thus the value is reported as a combination for both nitrogen acceptors (-260 kJ/mol).

5.3.2 Grinding experiments and characterization by IR spectroscopy

Initial grinding experiments were analyzed using the IR spectroscopy which gave insight into the success rate of co-crystal formation in each case. 30 experiments out of 75 experiments showed interactions between the acceptors and donors, Table 5.3. All co-crystals showed the presence of peaks from starting compounds and significant shifts of C-F vibrations of co-crystals compared to the pure halogen-bond donor. Summary of IR analysis is provided in Table 5.3 and detailed IR analysis is provided in Appendix C.1.

Table 5.3 Summary of grinding IR results

		Acceptors					% Success	
		A16	A17	A18	A19	A20		
Donors	D1	✗	✓	✗	✓	✗	2/5	40
	D2	✓	✓	✗	✓	✗	2/5	40
	D3	✗	✓	✓	✓	✗	3/5	60
	D4	✗	✗	✗	✓	✗	1/5	20
	D5	✗	✗	✗	✗	✗	0/5	0
	D6	✓	✓	✗	✓	✗	3/5	60
	D7	✓	✓	✓	✗	✓	4/5	80
	D8	✓	✓	✓	✓	✓	5/5	100
	D9	✗	✓	✗	✓	✗	2/5	40
	D10	✓	✓	✓	✓	✗	4/5	80
	D11	✗	✗	✗	✗	✗	0/5	0
	D12	✗	✗	✗	✗	✗	0/5	0
	D13	✗	✗	✗	✗	✗	0/5	0
	D14	✗	✓	✓	✗	✗	2/5	40
	D15	✗	✓	✗	✗	✗	1/5	20
% Success		5/15	10/15	5/15	8/15	2/15		
		33	67	33	53	13		

5.3.3 Crystal growth and structure analysis

Although vibrational spectroscopy provides unambiguous information about whether a co-crystal has formed or not, it does not show which acceptor site is engaged by the XB- and HB-donor respectively, thus there is a need for single crystal data. The initial approach for crystal growth was slow evaporation, but due to the differences in solubility between the donors and acceptors used in this study, the less soluble component (in this case the acceptor) often precipitated as a homogenous solid. Even though **A16** showed formation of co-crystals on 5/15 occasions, slow evaporation studies did not yield crystals with **A16**, due to its poor solubility. However, single crystals of **A16:D8** was obtained using vapor diffusion. Unfortunately, no single crystals were obtained with **A20** for the same reasons. Supramolecular yields for the co-crystallizations are provided in Table 5.4.

Table 5.4 Summary of grinding and solvent based experiments

	Acceptor					Overall
	A16	**A17**	**A18**	**A19**	**A20**	
Grinding	5/15	10/15	5/15	8/15	2/15	30/75
Slow evaporation	1/15	7/15	3/15	4/15	0/15	15/75
Supramolecular arrangement	1/1 Ribbons	7/7 Sheets	3/3 Chains	3/4 sheets 1/4 chains	-	1 ribbon 10 sheets 4 chains
Supramolecular yield	33%	67%	33%	53%	13%	40%

In total, fifteen compounds yielded suitable quality crystals to be analyzed with X-ray diffraction. Crystallographic data and halogen-bond and hydrogen-bond geometry data for all fifteen structures are provided in Appendix B.4.

5.3.4 Crystal structures

5.3.4.1 Structures of A16-based co-crystals

With acceptor **A16** only one crystal structure (**A16:D8**) could be obtained, where the imidazole molecules are held together by N-H···N hydrogen bonds formed between the two adjacent rings. The pyridine nitrogen atom of **A16** forms a halogen bond with **D8**. The halogen bond formation takes place at both ends of **D8**, resulting in a supramolecular ribbon architecture Figure 5.7.

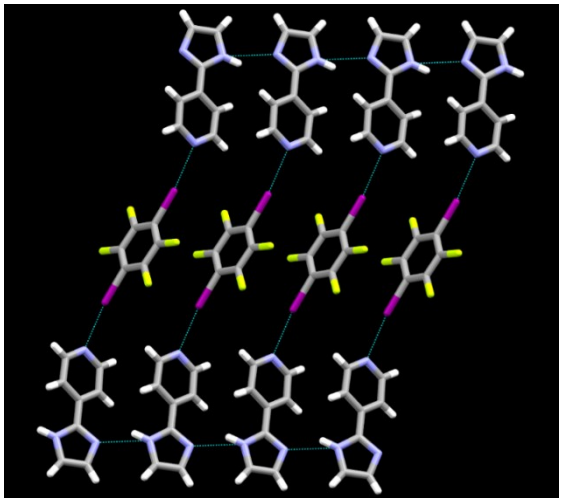

Figure 5.7 Primary intermolecular interactions in the crystal structure of **A16:D8**

5.3.4.2 Structures of A17-based co-crystals

With **A17**, seven crystal structures were obtained (**A17:D1**, **A17:D2**, **A17:D7**, **A17:D8**, **A17:D9**, **A17:D10** and **A17:D14**). In **A17:D1** a hydrogen-bonded chain is constructed by adjacent imidazole moieties via N-H···N interactions. The best acceptor site, N(py), again interacts with the halogen-bond donor, Figure 5.8. Adjacent acceptors are twisted about 70^0 with respect to each other leading to a corrugated 2-D assembly, Figure 5.8. The crystal structure of **A17:D2** displays similar features, Figure 5.8.

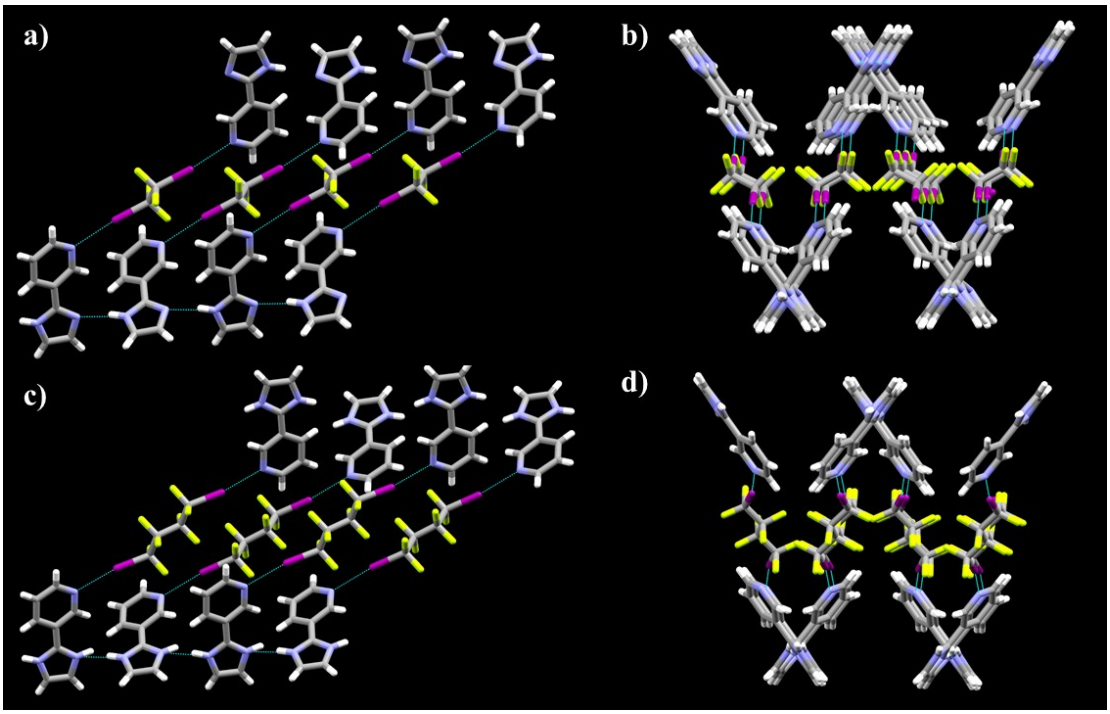

Figure 5.8 HB and XB interactions in structures **A17:D1** and **A17:D2**; a) primary interactions in **A17:D1** b) corrugated sheet in **A17:D1** c) primary interactions in **A17:D2** d) side view of the corrugated layer in the structure of **A17:D2**

In **A17:D7**, a hydrogen-bonded chain is again formed between adjacent imidazole moieties via N-H···N interactions. The **D7** ditopic donors provide a crosslink between chains through two symmetry related I···N halogen bonds with the N(py) atom, Figure 5.9. The same primary synthons and assemblies are present in the crystal structures of **A17:D8**, **A17:D9**, **A17:D10** and **A17:D14**, Figure 5.9.

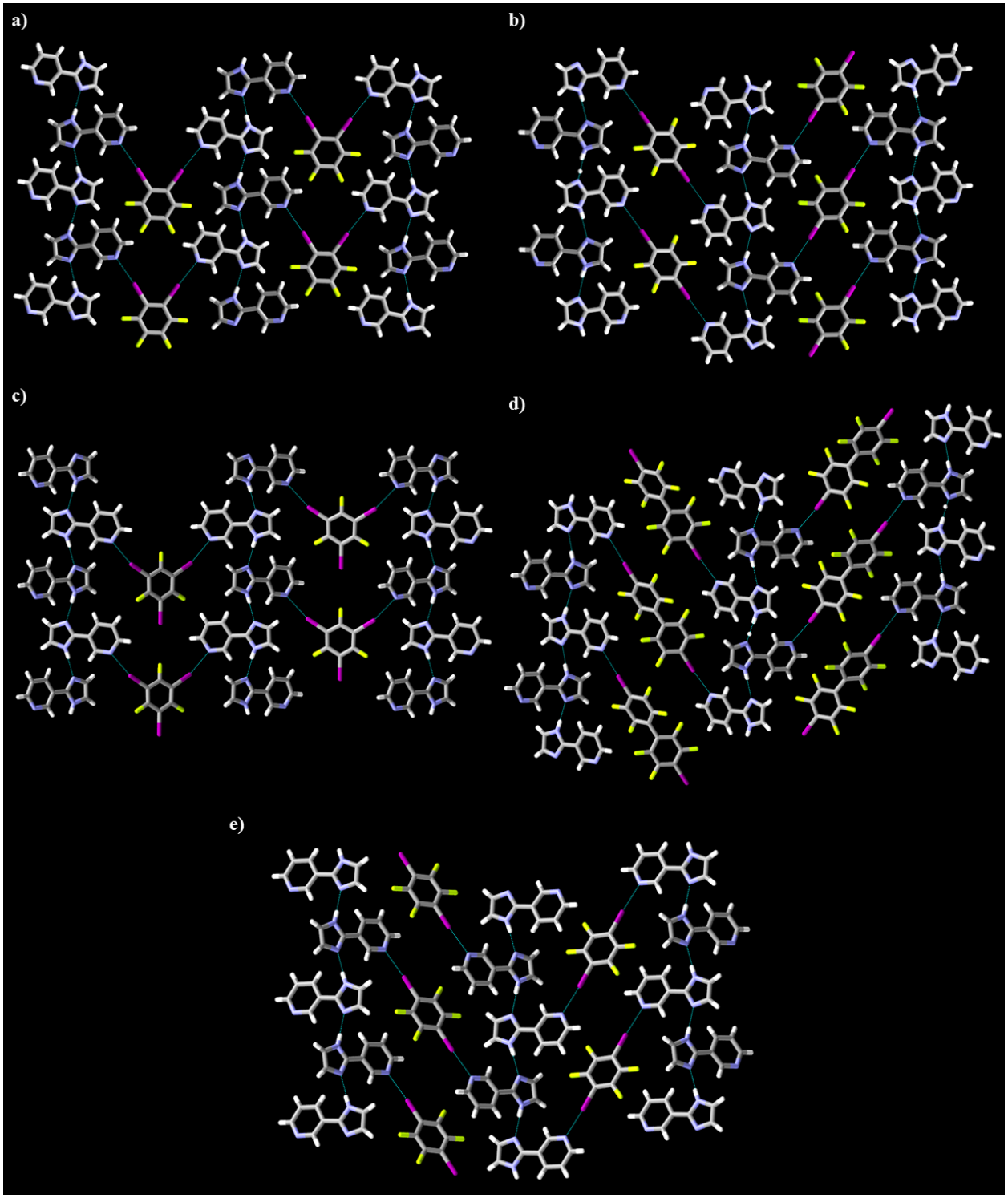

Figure 5.9 Primary synthons and layers in the crystal structures of a) **A17:D7** b) **A17:D8** c) **A17:D9** d) **A17:D10** and e) **A17:D14**

In all seven structures the hydrogen-bonded ladders create cores which are interlinked through halogen bonds, leading to infinite 2-D assemblies. The **A17:D1** and **A17:D2** contain layers that are more highly corrugated, and the only difference is that they contain aliphatic halogen-bond donors.

5.3.4.3 Structures of A18-based co-crystals

With acceptor **A18**, three structures were obtained, **A18:D3**, **A18:D8** and **A18:D10**, all of which contain a hydrogen-bonded dimer comprising two molecules connected via two symmetry-related N-H(im)···N(py) hydrogen bonds. The remaining acceptor, the imidazole nitrogen atom, participates in halogen bonding. These interactions lead to the formation of chain architectures. **A18:D3** also shows the same interaction as in **A18:D8** and **A18:D10**, but contains an additional disordered imidazole molecule in between that does not seem to participate in any significant structure directing short contacts. Figure 5.10 shows the interactions and the formation of chains in **A18:D8** and **A18:D10**. Structure of **A18:D3** is disordered and not shown.

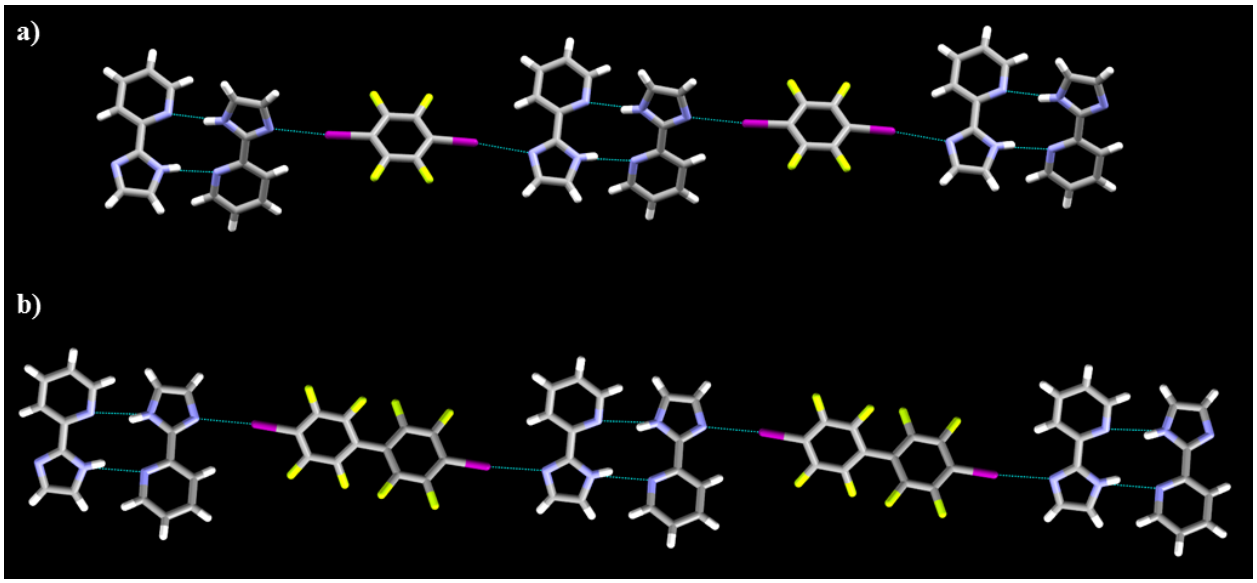

Figure 5.10 Primary interactions and the formation of chains in structures a) **A18:D8** and b) **A18:D10**

5.3.4.4 Structures of A19-based co-crystals

With **A19**, four crystal structures were obtained, **A19:D2**, **A19:D8**, **A19:D9** and **A19:D10**. In **A19:D2** and **A19:D9**, **A19** is essentially replicating the behavior of **A17** and only one of the nitrogen atoms on the pyrazine ring is participating in significant intermolecular interactions. The imidazole nitrogen atom acts as a HB acceptor, forming N-H···N interactions, while I···N halogen bond involves a pyrazine nitrogen atom resulting in a 2-D layer, Figure 5.11.

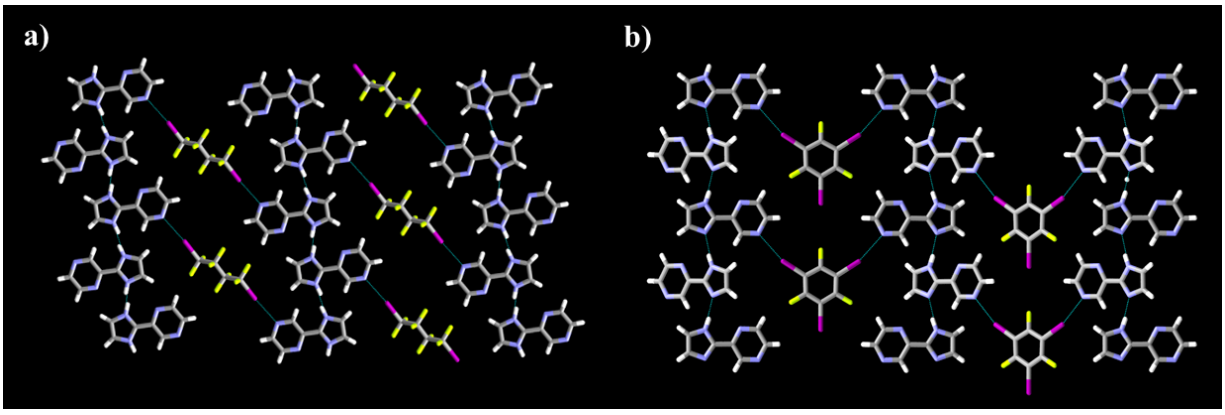

Figure 5.11 Primary synthons and the 2-D layers in the crystal structures of a) **A19:D2** and b) **A19:D9**

The interactions in **A19:D8** are similar to those in **A19:D2** and **A19:D9** but the sheets are more corrugated compared to what was found in the structures of **A17:D1** and **A17:D2**, Figure 5.12.

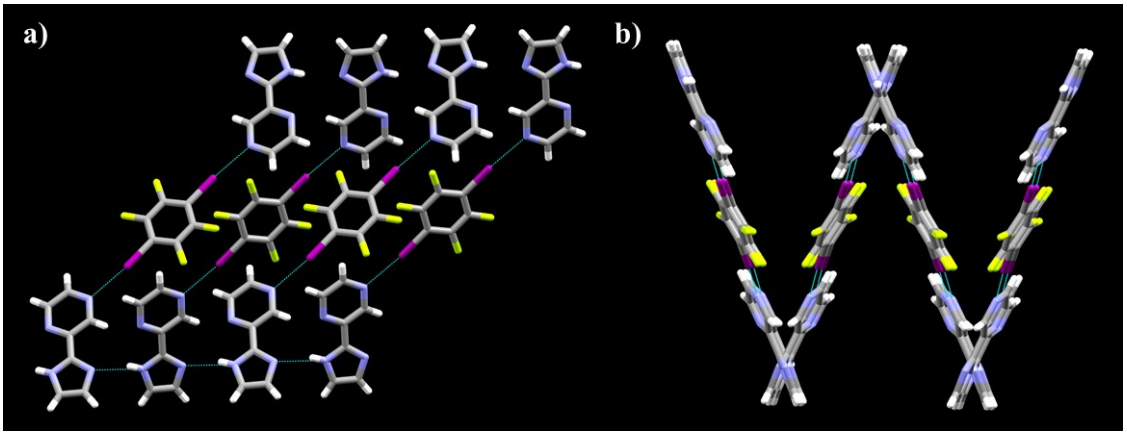

Figure 5.12 Primary synthons in the crystal structure of **A19:D8**; a) top view of the layer b) side view of the corrugated layer

The crystal structure of **A19:D10** contains a very different set of interactions compared to the other three structures with **A19**. In this case, the acceptor essentially behaves as **A18** where the pyrazine nitrogen at the third position is inactive. As in the structures with **A18**, a hydrogen-bond dimer is formed between two acceptor molecules via N-H(im)···N(py) interactions and the imidazole nitrogen is participating in the formation of halogen bonds leading to a chain architecture, Figure 5.13.

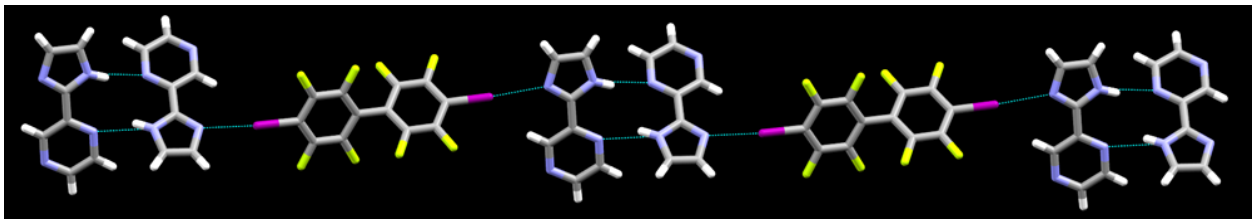

Figure 5.13 Primary synthons producing a 1-D chain in the structure of **A19:D10**

5.4 Discussion

5.4.1 Relationship between molecular electrostatic potentials and hydrogen- and halogen-bond competition

For **A16**, based on the DFT calculations, the pyridine nitrogen atom is recognized as the best acceptor site and in **A16:D8** it is engaged in a halogen bond whereas the second best acceptor, the imidazole nitrogen atom, forms N-H···N hydrogen bonds. In all seven structures with **A17**, the imidazole nitrogen atom, which is ranked as the second-best acceptor according to the MEPS calculations, engage in hydrogen bonds, whereas the best acceptor atom, N(py), participates in halogen bond formation. As was the case in the structures of **A16** and **A17**, with **A18** the halogen-bond involves the best acceptor (as ranked by the relative MEPS). In three of the four structures obtained with **A19**, the best acceptor imidazole nitrogen atom is participating in a hydrogen bond while the second-best acceptor is forming halogen bonds. In the fourth structure with **A19**, the best acceptor is participating in the formation of halogen bonds while the third best acceptor is

participating in the formation of hydrogen bonds. Surprisingly in this case the second best acceptor is not participating in any short contacts. As with **A16**, **A17** and **A18**, in this structure the halogen bond interaction "wins" over the hydrogen bond by engaging with the best acceptor site.

No crystal structures of co-crystals with acceptor **A20** were obtained, possibly due to its low solubility relative to that of each co-former. Another reason may be due to the fact that the acceptor site on this molecule displays relatively low values for the MEPS (-72 kJ/mol) on the heteroaryl ring compared to those values on the other acceptor molecules.

All in all, in twelve of the fifteen structures obtained, the XB donor interacted with the "best acceptor", which indicates that in a competitive co-crystallization event, it is possible for the XB donor to outperform an HB donor for the electrostatically most attractive acceptor site. Despite extensive theoretical studies of the HB and XB strength it is still difficult to predict the outcome of a supramolecular assembly process that contains multiple viable XB and HB bonds.

5.4.2 Effect of MEPS on halogen bond donors

Supramolecular yields based on halogen-bond donors are summarized in Table 5.5. Based on these results, it is clear that iodine-based donors are far superior to their bromine analogues when it comes to driving co-crystal formation. Despite the fact that Br···N/O/S interactions have been shown to display considerable thermodynamic strength, they seem unlikely to become prominent primary synthetic tools in supramolcular synthesis, even though they are capable of exercising some structure-directing influence in both solution and solid state.[37] Similarly, iodine atoms that have not been sufficiently polarized by the presence of electron-withdrawing substituents are also not effective at driving co-crystal formation by themselves. This is illustrated by the fact that the only non-activated XB donor, iodobenzene, **D5**, did not produce any co-crystals in this study.

Table 5.5 Supramolecular yields as a function of halogen-bond donor type

	Halogen-bond donor category		
	Iodine-based donors	**Bromine-based donors**	**Mixed donors**
No of donors	10	3	2
No of experiments	50	15	10
Success rate grinding experiments	27/50	0/15	3/10
Success rate solvent experiments	14/50	0/15	1/10
Supramolecular yield	54%	0%	30%

5.4.3 Different supramolecular outcomes

Depending on the intermolecular interactions and the relative orientations of the heteroaryl-2-imidazole molecules in each structure, the supramolecular architectures can be organized in three outcomes, chains, ribbons and sheets, Table 5.4. The only structure obtained with **A16**, contains a ribbon architecture where the ladder of **A16** molecules are oriented in the same direction. For **A17**, all the structures are comprised of a sheet architecture, due to the twisted nature and the alternate orientation of the **A17** molecules. With **A18** all structures form chains, starting with the **A18** dimer formation and extend via halogen bond formations. The possible reason behind this is that the pyridine nitrogen atom at the 2nd position of the heteroaryl ring leads to N-H···N dimer formation via chelate effect which is not possible in **A16** and **A17**. As mentioned earlier, **A19** behaves both as **A17** and **A18**, thus three of the four structures are forming sheet architectures, while the fourth one forming a chain architecture.

5.5 Conclusions

Based on the results of our systematic co-crystallizations intended to probe competition between XB and HB donors for acceptor sites with different electrostatic potentials, it is clear that halogen bonds can readily outperform hydrogen bonds, Figure 5.14.

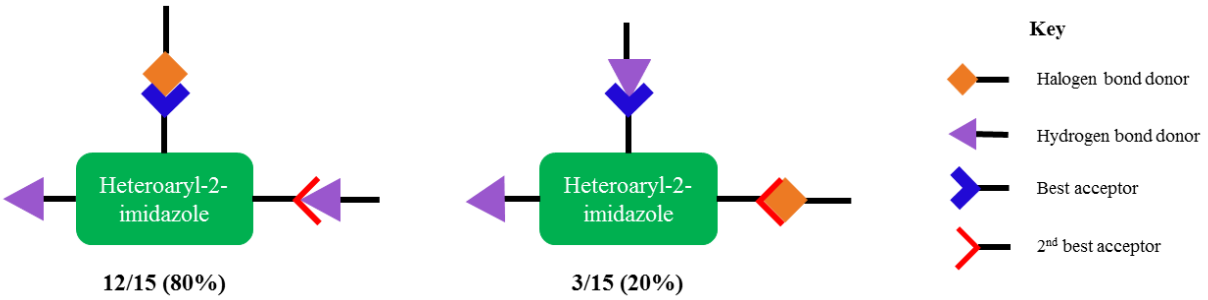

Figure 5.14 Total outcome of fifteen experiments

The better acceptor site ranked by calculated MEPS values provided the interaction site for a XB donor in twelve of fifteen cases where a crystal structure was obtained. Overall, 30 of 75 attempts produced co-crystals (40%) and the success rate, the supramolecular yield, rose to 60% (27/45) when only activated iodine-based donors were considered.

At this point it is unclear how the balance between different XB and HB donors will manifest itself when they are competing for acceptors sites of different electrostatic characteristics. Fundamentally, both interaction types have a large electrostatic component, but it is probably necessary to carefully examine additional factors such as geometry and symmetry, before reliable predictions can be made. However, it is clear that no one interaction is dominating and their thermodynamically comparable strengths mean that the simultaneous use of these interactions in supramolecular synthesis offers both tough challenges and interesting opportunities.

5.6 References

1. Aakeröy, C.B.; Wijethunga, T.K.; Haj, M.A.; Desper, J.; Moore, C. *CrystEngComm* **2014**, *16*, 7218-7225.

2. Lehn, J.M. *Chem. Soc. Rev*. **2007**, *36*, 151-160; Steed, J.W.; Atwood, J.L. *Supramolecular Chemistry*, John Wiley & Sons, **2009**.

3. Aakeröy, C.B.; Champness, N.R.; Jania, C. *CrystEngComm* **2010**, *12*, 22-43; Aakeröy, C.B.; Seddon, K.R. *Chem. Soc. Rev.* **1993**, *22*, 397-407.

4. Auffinger, P.; Hays, F.A.; Westhof, E.; Shing Ho, P. *Proc. Natl. Acad. Sci. U.S.A.* **2004**, *101*, 16789-16794; Scholfield, M.R.; Vander Zanden, C.M.; Carter, M.; Shing Ho, P. *Protein science* **2013**, *22*, 139-152; Abraham, M.H. *Chem. Soc. Rev*. **1993**, *22*, 73-83.

5. Hobza, P.; Zahradník, R.; Müller-Dethlefs, K. *Collect. Czech. Chem. Commun*. **2006**, *71*, 443-531.

6. Johnson, E.R.; Keinan, S.; Mori-Sánchez, P.; Contreras-García, J.; Cohen, A.J.; Yang, W. *J. Am. Chem. Soc*. **2010**, *132*, 6498-6506.

7. Frieden, E. *J. Chem. Educ.* **1975**, *52*, 754-756; Smith, B.M.; Bean, S.R.; Selling, G.; Sessa, G.; Aramouni, F.M. *Food Chem.* **2014**, *147*, 230-238; Raynal, M.; Ballester, P.; Vidal-Ferranab, A.; Van Leeuwena, P.W.N.M. *Chem. Soc. Rev*. **2014**, *43*, 1660-1773.

8. Czyżnikowska, Z. J. *J. Mol. Struct*. **2009**, *895*, 161-167.

9. Zou, J.W.; Jiang, Y.J.; Guo, M.; Hu, G.X.; Zhang, B.; Liu, H.C.; Yu, Q.S. *Chem. Eur. J*. **2005**, *11,* 740-751; Riley, K.E.; Merz, K.M. *J. Phys. Chem. A*. **2007**, *111*, 1688-1694.

10. Politzer, P.; Murray, J.S.; Clark, T. *Phys. Chem. Chem. Phys*. **2010**, *12*, 7748-7757.

11. Kolář, M.; Hostaša, J.; Hobza, P. *Phys. Chem. Chem. Phys*. **2014**, *16*, 9987-9996; Beyeh, N.K.; Cetina, M.; Rissanen, K. *Chem. Commun*. **2014**, *50*, 1959-1961.

12. Meyer, F.; Dubois, P. *CrystEngComm.* **2013**, *15*, 3058-3071; Wilcken, R.; Zimmermann, M.O.; Lange, A.; Joerger, A.C.; Boeckler, F. M. *J. Med. Chem*. **2013**, *56*, 1363-1388.

13. Desiraju, G.R.; Steiner, T. *The Weak Hydrogen Bond: In Structural Chemistry and Biology*, Oxford University Press, **2001**.

14. Priimagi, A.; Cavallo, G.; Metrangolo, P.; Resinati, G. *Acc. Chem. Res.* **2013**, *46*, 2686-2695.

15. Legon, A.C. *Angew. Chem., Int. Ed*. **1999**, *38*, 2686-2714; Aakeröy, C.B.; Wijethunga, T.K.; Desper, J. *CrystEngComm*. **2014**, *16*, 28-31.

16. Metrangolo, P.; Neukirch, H.; Pilati, T.; Resinati, G. *Acc. Chem. Res*. **2005**, *38*, 386-395.

17. Steiner, T. *Angew. Chem. Int. Ed*. **2002**, *41*, 48-76.

18. Larson, J. W.; McMahon, T. B. *Inorg. Chem.* **1984**, *23*, 2029-2033.

19. Aakeröy, C.B.; Fasulo, M.; Schultheiss, N.; Desper, J.; Moore, C. *J. Am. Chem. Soc.* **2007**, *129*, 13772-13773; Bouchmella, K.; Boury, B.; Dutremez, S.G.; Van der Lee, A. *Chem. Eur. J.* **2007**, *13*, 6130-6138; Aakeröy, C.B.; Panikkattu, S.; Chopade, P.D.; Desper, J. *CrystEngComm* **2013**, *15*, 3125-3136; Aakeröy, C.B.; Chopade, P.D.; Ganser, C.; Desper, J. *Chem. Commun*. **2011**, *47*, 4688-4690.

20. Li, Q.; Xu, X.; Liu, T.; Jing, B.; Li, W.; Cheng, J.; Gonga, B.; Suna, J. *Phys. Chem. Chem. Phys*. **2010**, *12*, 6837-6843; Zheng, Y. Z.; Wang, N.N.; Zhoua, Y.; Yu, Z.W. *Phys. Chem. Chem. Phys*. **2014**, *16*, 6946-6956; Li, Q.Z.; Li, R.; Guo, P.; Li, H.; Li, W.Z.; Cheng, J.B. *Comp. Theor. Chem.* **2012**, *980*, 56-61.

21. Fourmigué, M.; Batail, P. *Chem. Rev*. **2004**, *104*, 5379-5418.

22. Voth, A. R.; Hays, F. A.; Ho, P. S. *Proc. Natl. Acad. Sci. U.S.A*. **2007**, *104*, 6188-6193; Alkorta, I.; Blanco, F.; Solimannejad, M.; Elguero, J. *J. Phys. Chem. A*. **2008**, *112*, 10856-10863; Politzer, P.; Murray, J.; Lane, P. *Int. J. Quant. Chem.* **2007**, *107*, 3046-3052.

23. Aakeröy, C. B.; Fasulo, M.; Schultheiss, N.; Desper, J.; Moore, C. *J. Am. Chem. Soc*. **2007**, *129*, 13772-13773.

24. Corradi, E.; Meille, S. V.; Messina, M. T.; Metrangolo, P.; Resnati, G. *Angew. Chem., Int. Ed*. **2000**, *39*, 1782-1786.

25. Aakeröy, C.B.; Chopade, P.D.; Desper, J. *Cryst. Growth Des*. **2011**, *11*, 5333-5336.

26. Vaher, B.; Bonnaud, B.; Funes, F.; Jubault, N.; Kock, W.; Assie, M.B.; Cosi, C. *J. Med. Chem*. **1998**, *41*, 5070-5083; Mano, T.; Stevens, R.W.; Ando, K.; Okumura, Y.; Sakakibara, M.; Okumura, T.; Tamura, T.; Miyamoto, K. *Bioorg. Med. Chem*. **2003**, *11*, 3879-3887; Murray, M.; Wilkinson, C.F. *Chem. Biol. Interact.* **1984**, *50*, 267-275.

27. Abul Haj, M.; Aakeröy, C.B.; Desper, J. *New J.Chem*. **2013**, *37*, 204-211; Yang, L.; Zeng, L.; Gu, W.; Tian, J.; Liao, S.; Zhang, M.; Wei, X.; Xin, L.; Liu, X. *Inorg. Chem. Commun.* **2013**, *29*, 76-81; Cai, S.L.; Zheng, S.R.; Wen, Z.Z.; Fan, J.; Zhang, W.J. *Cryst. Growth Des.* **2012**, *12*, 2355-2361.

28. Akiharu, S.; Hiroyuki, K.; Tadashi, N. *Chem. Lett*. **1999**, *28*, 49-50; Wang, R.; Xiao, J.C.; Twamley, B.; Shreeve, J.M. *Org. Biomol. Chem*. **2007**, *5*, 671-678.

29. Voss, M. E.; Beer, C. M.; Mitchell, S. A.; Blomgren, P. A.; Zhichkin, P. E. *Tetrahedron* **2008**, *64*, 645-651.

30. Espallargas, G.M.; Recuenco, A.; Romero, F.M.; Brammer, L.; Libri, S. *CrystEngComm* **2012**, *14*, 6381-6383.

31. Aakeröy, C.B.; Chopade, P.D.; Desper, J. *Cryst. Growth Des*. **2013**, *13*, 4145-4150.

32. Omnic 8.0 © **1992-2008**, Thermo Fisher Scientific Inc.

33. Spartan'08, Wavefunction, Inc.

34. Nagels, N.; Hauchecorne, D.; Herrebout, W.A. *Molecules* **2013**, *18*, 6829-6851; Hawthorne, B.; Fan-Hagenstein, H.; Wood, E.; Smith, J.; Hanks, T. *Int. J. Spectrosc*. **2013**, 216518.

35. Etter, M. C. *Acc. Chem. Res*. **1990**, *23*, 120-126; Bowers, J. R.; Hopkins, G. W.; Yap, G. P. A.; Wheeler, K. A. *Cryst.Growth Des*. **2005**, *5*, 727-736; Aakeröy, C.B.; Beatty, A.M.; Helfrich, B. A. *Angew. Chem. Int. Ed.* **2001**, *40*, 3240-3242; Desiraju, G. R.; Vittal, J. J.; Ramanan, A. *Crystal Engineering: A Textbook*, World Scientific, **2011**.

36. Riley, K. E.; Hobza, P. *Phys. Chem. Chem. Phys*. **2013**, *15*, 17742-17752.

37. Cinčić, D.; Friščić, T.; Jones, W. *Chem. Mater*. **2008**, *20*, 6623-6626; Nayak, S.K.; Forni, G.; Terraneo, A.; Metrangolo, P.; Resnati, G. *CrystEngComm* **2012**, *14*, 4259-4261.

Chapter 6 - Synthesis, structure, intermolecular interactions and crystal engineering with iodoethynylnitrobenzenes: A group of highly effective halogen-bond donors[1]

6.1 Introduction

The halogen bond[2] is becoming increasingly important in many aspects of crystal engineering and materials design[3] because of the possibilities of fine-tuning the strength and effectiveness of this non-covalent interaction.[4] A halogen bond is, according to a recent IUPAC definition, the result of "a net attractive interaction between an electrophilic region associated with a halogen atom in a molecular entity and a nucleophilic region in another, or the same, molecular entity",[5] which emphasizes the electrostatic component of this interaction. The electrophilic region on a halogen atom is referred to as the "σ-hole", Figure 6.1.[6]

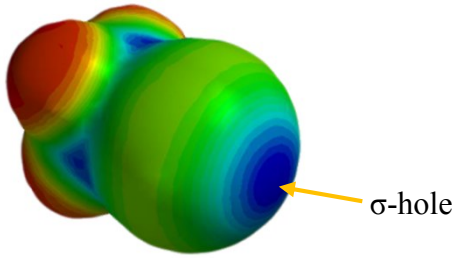

Figure 6.1 Formation of the σ-hole on iodine of CF_3I due to the electron withdrawing nature of fluorine atoms

If the σ-hole of a potential halogen-bond donor can be boosted in some manner, the resulting halogen bond (XB) is likely to display increased strength. This process is known as 'activation"[7] which includes adding one or more electron-withdrawing groups[8] to the molecular scaffold of the intended XB donor in order to promote depletion of negative charge from the σ-hole, Figure 6.2.[9] In this way, perfluorinated halogen-bond donors,[10] nitro activated halogen-bond donors,[11] and cationic aromatic systems[12] have been employed successfully in XB-driven crystal

engineering. It has also been shown that the number of fluorine substituents on the backbone of iodobenzene has an additive effect on the molecular electrostatic potential[13] that characterizes the σ-hole.[14] Alternatively, the intended XB donor can be connected to an *sp*-hybridized carbon atom which facilitates polarization and leads to an enhanced positive charge.[15] Furthermore, studies have confirmed that an sp^2-hybridized carbon atom is enough to polarize an iodine to make it a better halogen-bond donor.[16] Only in very rare cases has a combination of approaches been deliberately utilized in order to create an activated XB donor.[17]

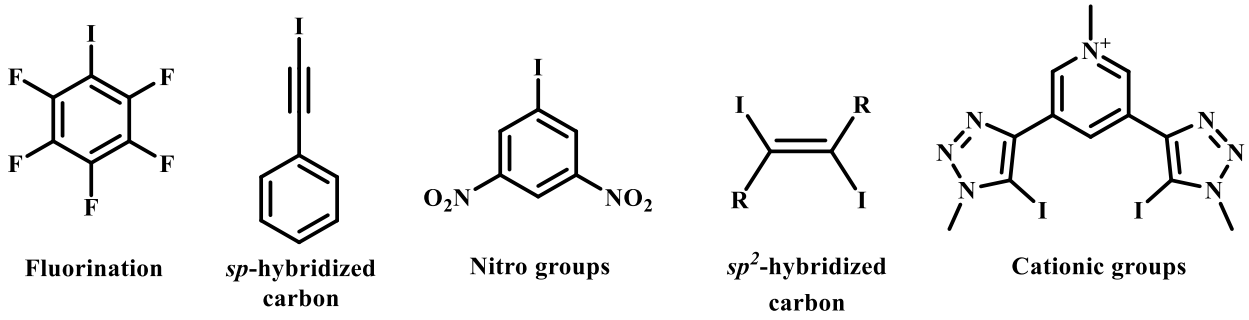

Figure 6.2 Methods currently used to activate halogen-bond donors

In order to develop a new series of potent XB donors for effective co-crystal synthesis, we decided to combine the electron-withdrawing capabilities of -NO_2 moieties with the polarizing effects of an *sp*-carbon atom thereby providing a path to highly electrophilic halogen atoms through a 'double-activation' process, Figure 6.3.

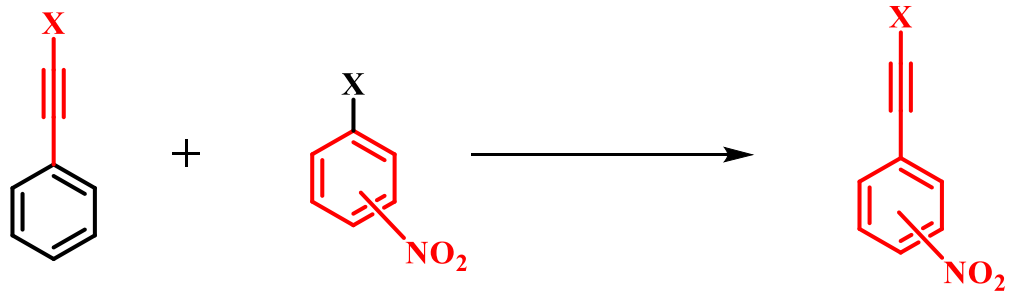

Figure 6.3 "Double activation" of a halogen-bond donor (X represents any halogen atom)

Since the polarizability of the halogen atom plays an important part in determining the magnitude of the σ-hole,[18] the study was primarily focused on iodoethynylnitrobenzene compounds as potential halogen-bond donors, since halogen atom polarizability decreases in the order I>Br>Cl.[19] Three molecules based on the design criteria described above were prepared; 1-(iodoethynyl)-4-nitrobenzene (**4N-I**), 1-(iodoethynyl)-3-nitrobenzene (**3N-I**) and 1-(iodoethynyl)-3,5-dinitrobenzene (**3,5DN-I**), Figure 6.4.[20]

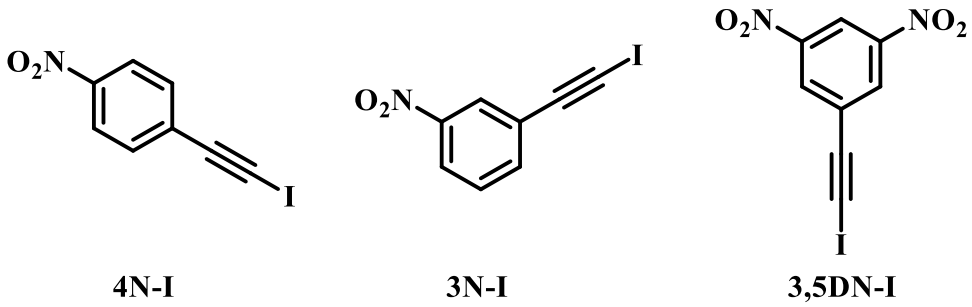

4N-I **3N-I** **3,5DN-I**

Figure 6.4 Iodoethynylnitrobenzene compounds under study

Even though the primary focus on this study was to evaluate the halogen bonding potential of iodoethynylnitrobenzenes, it seemed important to examine if the double activation would be sufficient to the make the corresponding bromo- and chloro- analogues capable XB donors as well. C-Br based halogen-bond donors are known,[21] but no crystallographic data exist to indicate that C-Cl based moieties are strong enough to drive co-crystal formation through halogen bonds. Thus, three bromo- and three chloroethynylnitrobenzenes, 1-(bromoethynyl)-4-nitrobenzene (**4N-Br**), 1-(bromoethynyl)-3-nitrobenzene (**3N-Br**), 1-(bromoethynyl)-3,5-dinitrobenzene (**3,5DN-Br**), 1-(chloroethynyl)-4-nitrobenzene (**4N-Cl**), 1-(chloroethynyl)-3-nitrobenzene (**3N-Cl**) and 1-(chloroethynyl)-3,5-dinitrobenzene (**3,5DN-Cl**), Figure 6.5, were also synthesized.

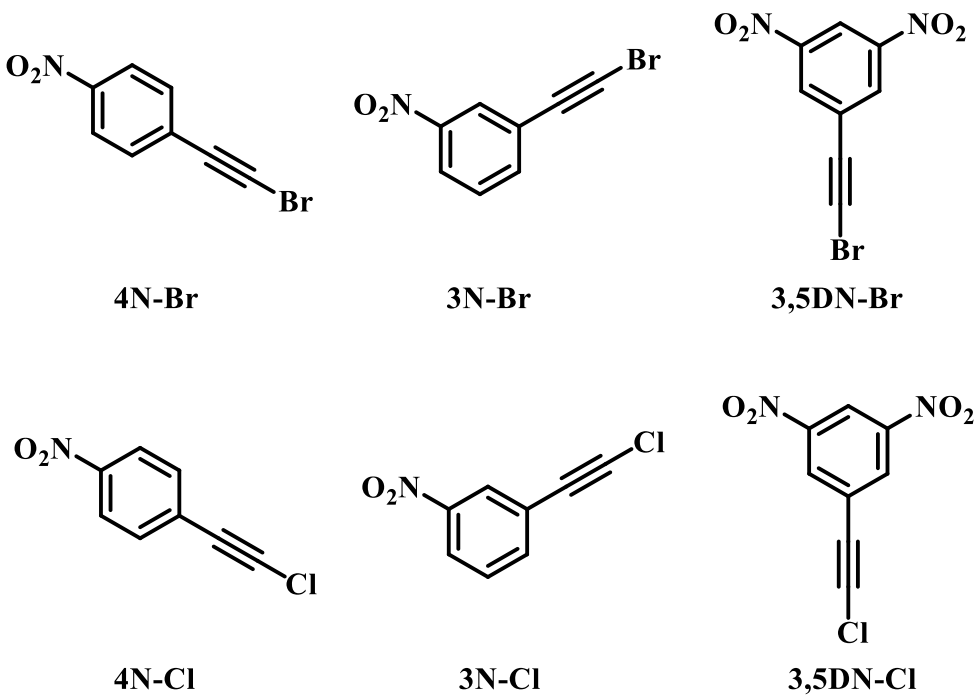

Figure 6.5 Bromo- and chloroethynylnitrobenzene compounds in this study

Having one or two nitro groups and an activated halogen domain, these nine molecules were also used to study the interaction preferences of nitro groups. The nitro group has not been employed extensively as a recognition group in supramolecular chemistry due to poor accepting nature of nitro group in a supramolecular context.[22] But in the recent literature, with the emergence of energetic co-crystallizations,[23] nitro group has become of central importance. When synthesizing energetic co-crystals, the design strategy needs to use functional groups available on the energetic compound of interest, and the most common functional group in energetic materials is the nitro group.[24] The reported literature on energetic co-crystals relies on different non-covalent interactions such as hydrogen bonding and π stacking between electron rich and electron poor moieties.[25] Apart from these, weak interactions between nitro-amino, nitro-nitro or nitro-aromatic functional groups have been used as secondary interactions.[26] It seems that most of these design

strategies try to avoid the use of nitro group in directing intermolecular interactions. Thus there is a quest for reliable synthons containing nitro group as one of the recognition groups.

With this in mind, an extensive search on the interactions containing nitro group as the central group was performed. For this, initial mapping of interactions between nitro groups and other functional groups were performed using IsoStar,[27] a web-based application using an extensive knowledge-based library of intermolecular interactions. According to the data presented in IsoStar maps, it was surprising that the number of crystal structures reported between the nitro group and halogen atoms were less compared to other reported interactions with nitro group, even though the nitro···halogen interaction is documented as a reliable synthon. The search for the interaction between nitro group and any C-I contact group was not reported in the IsoStar knowledge base. Thus, a CSD search was performed on reported nitro···iodo non covalent interactions. The number of hits came out to be 124 without applying any filters, which was quite small for a known synthon. One of the other thing that we noted is short contacts between nitro groups and an activated halogen atom are particularly rare.[28] Thus the library of haloethynylnitrobenzenes in this study were optimal candidates to learn more.

Six of the nine compounds (**4N-I**,[29] **4N-Br**,[30] **4N-Cl**,[31] **3N-I**,[32] **3N-Br**[33] and **3N-Cl**[34]) were previously reported as reaction intermediates, substrates for reaction mechanism studies or in the development of new organic synthetic methods, but none of them were studied in the context of recognition properties of nitro groups or as potential halogen-bond donors.

After successful synthesis and characterization of the library of compounds, interaction modes for iodinated compounds were predicted using IR spectroscopy. For all nine compounds we tried to obtain structures in order to map their interactions and to compare the actual experimental results with the IR postulated results.

In order to examine the propensity of these three XB donors to form co-crystals, each of them was allowed to react with fifteen potential acceptors through solvent-assisted grinding. This library includes N-based acceptors (**A21-A27**, **A31** and **A32**) O-based acceptors (**A28-A30**) and N-and O-based mixed acceptors (**A33-A35**), and the co-formers can be further categorized as symmetric ditopic (**A21-A30**), monotopic, (**A31** and **A32**) and dissymmetric ditopic (**A33-A35**), Figure 6.6. The bromo- and chloroethynylnitrobenzene compounds were also subjected to solvent-assisted grinding and solution based crystallizations with five acceptors **A23**, **A24**, **A27**, **A31** and **A33**. A total of 75 attempted co-crystallizations were carried out in order to determine relative success rates (as indicated by IR spectroscopy) for these compounds. The relative propensity for co-crystal formation was rationalized in the context of calculated molecular electrostatic potential surfaces, and complemented by single-crystal structure determinations of ten new co-crystals.

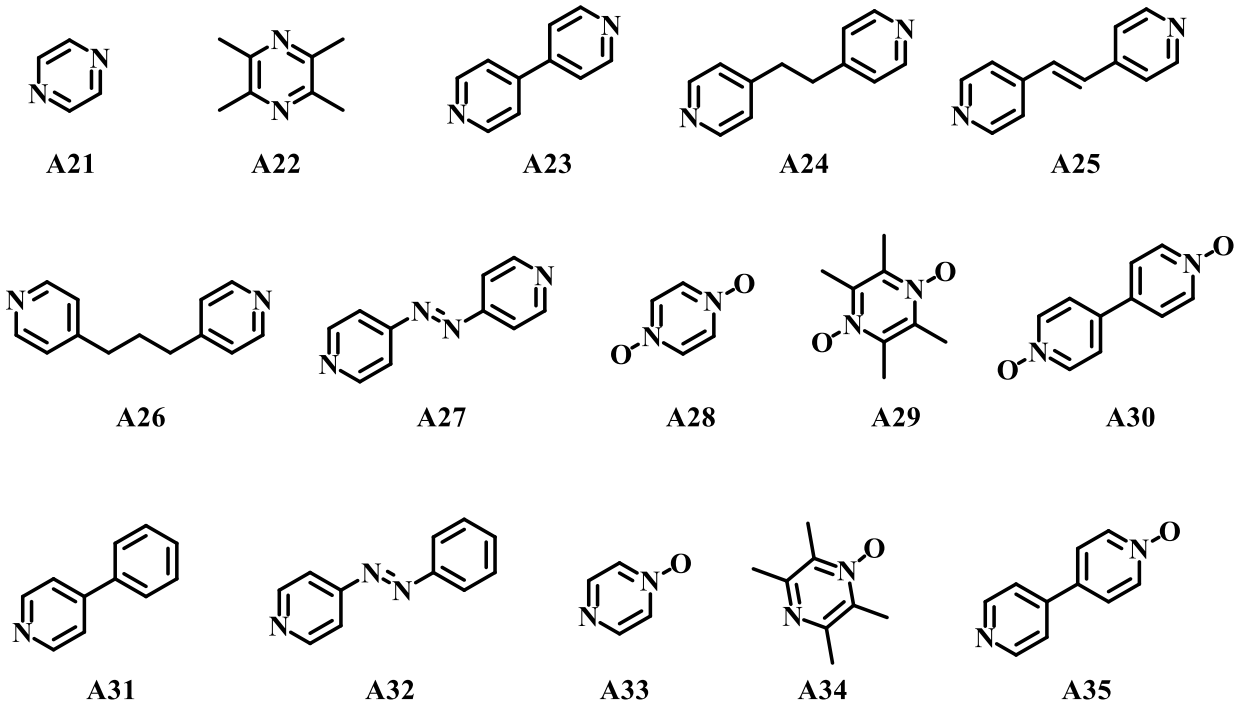

Figure 6.6 Acceptors utilized in this study

The study is undertaken in response to three hypotheses,

1. Double activation of an iodine atom increases the size and strength of the σ hole and leads to the formation of effective halogen-bond donors.
2. Double activation of a bromine atom or a chlorine atom leads to effective bromine- and chlorine-based halogen-bond donors.
3. Haloethynylnitrobenzene compounds show a diversity of intermolecular interactions between the nitro group and the activated halogen atom thus can be utilized as potential synthons in co-crystallizations with nitro containing energetics.

6.2 Experimental

6.2.1 General

All precursors, solvents and acceptors **A21**-**A26** and **A31** were purchased from commercial sources and used without further purification. **A28**-**A30** and **A33**-**A35** were synthesized following previously reported procedures,[35] as were **A27**[36] and **A32**.[37] ^{1}H NMR spectra and ^{13}C NMR spectra were recorded on Varian Unity plus 400 MHz spectrometer. Differential scanning calorimetry (DSC) measurements were carried out on haloethynylnitrobenzene compounds with a TA Instruments Q20, using Tzero aluminum pans under nitrogen (50.0 mL/min) purge at a heating rate of 10 °C/min over a range from 20 °C to 200 °C. For iodinated compounds DSC measurements were carried out until the melting occurs. Melting points of co-crystals were determined using a Fischer–Johns Mel-Temp melting point apparatus and uncorrected.

6.2.2 Synthesis of haloethynylnitrobenzene compounds

6.2.2.1 Synthesis of trimethyl((4-nitrophenyl)ethynyl)silane

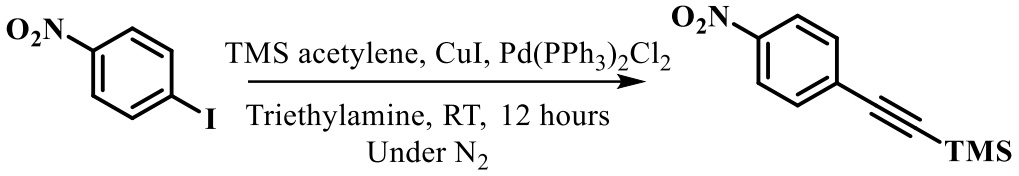

4-Iodonitrobenzene (1.7 g, 7.0 mmol), trimethylsilylacetylene (1.0 mL, 7.7 mmol), CuI (0.060 g, 0.35 mmol), and bis(triphenylphosphine)palladium(II) dichloride (0.15 g, 0.21 mmol) were dissolved in 50 mL of degassed trimethylamine. The mixture was stirred overnight at room temperature under a dinitrogen atmosphere. Completion of reaction was confirmed with TLC. The reaction mixture was concentrated in vacuo and the residue was dissolved in diethyl ether (50 mL). The ethereal solution was washed with 1 M HCl (10 mL), water (2 x 20 mL) and saturated NaCl solution (20 mL). The organic layer was dried with anhydrous $MgSO_4$ and concentrated in vacuo. The crude product was purified by flash chromatography in 50:1 hexane: ethyl acetate yielding the final product. Yield: 1.3 g (88%); ^{1}H NMR (400 MHz, $CDCl_3$): 0.28 (s, 9H), 7.59 (d, 2H), 8.17 (d, 2H).

6.2.2.2 Synthesis of 1-(iodoethynyl)-4-nitrobenzene, 4N-I

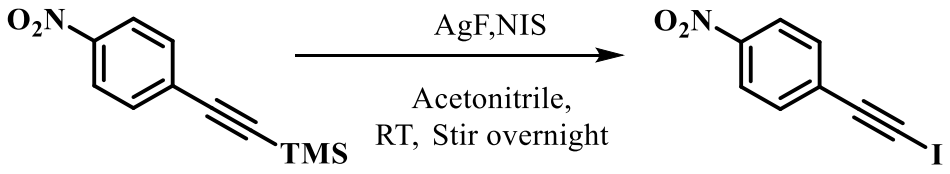

Acetonitrile (20 mL) was degassed with dinitrogen. Trimethyl((4-nitrophenyl)ethynyl)silane (1.0 g, 4.6 mmol), and AgF (0.58 g, 4.6 mmol) were added to acetonitrile and the mixture was covered with aluminum foil before the introduction of N-iodosuccinimide (1.0 g, 4.6 mmol). The mixture was connected to a nitrogen inlet and stirred

overnight. Completion of the reaction was monitored with TLC and the resulting suspension was passed through a 2 cm silica plug and the filtrate with acetonitrile as the solvent was concentrated in vacuo. The residue was dissolved in diethyl ether and washed with water (2 x 20 mL). The organic layer was dried with anhydrous $MgSO_4$ and concentrated in vacuo to obtain 1-(iodoethynyl)-4-nitrobenzene (**4N-I**) as a yellow powder. Yield: 1.1 g (85%); m.p. 195-198 °C; ^{1}H NMR (400 MHz, $CDCl_3$): 7.59 (d, 2H), 8.20 (d, 2H); ^{13}C NMR (400 MHz, $CDCl_3$): 15.52, 93.29, 124.46, 130.91, 134.08, 173.24.

6.2.2.3 Synthesis of 1-(bromoethynyl)-4-nitrobenzene, *4N-Br*

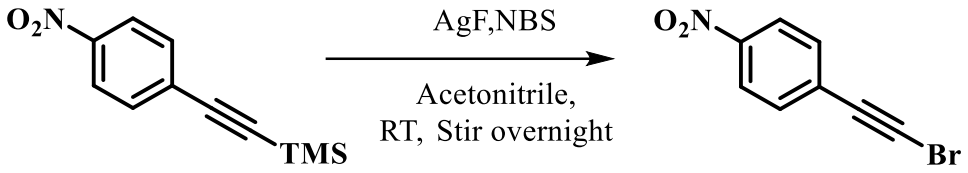

Acetonitrile (20 mL) was degassed with dinitrogen. Trimethyl((4-nitrophenyl)ethynyl)silane (1.0 g, 4.6 mmol), and AgF (0.58 g, 4.6 mmol) were added to acetonitrile and the mixture was covered with aluminum foil before the introduction of N-bromosuccinimide (0.81 g, 4.6 mmol). The mixture was connected to a nitrogen inlet and stirred overnight. Completion of the reaction was monitored with TLC and the resulting suspension was passed through a 2 cm silica plug and the filtrate with acetonitrile as the solvent and was concentrated in vacuo. The residue was dissolved in diethyl ether and washed with water (2 x 20 mL). The organic layer was dried with anhydrous $MgSO_4$ and concentrated in vacuo to obtain 1-(bromoethynyl)-4-nitrobenzene (**4N-Br**) as a pale yellow powder. Yield: 0.83 g (81%); m.p. 174.66 °C (decompose); ^{1}H NMR (400 MHz, $CDCl_3$): 7.61 (d, 2H), 8.18 (d, 2H); ^{13}C NMR (400 MHz, $CDCl_3$):56.37, 78.36, 123.59, 129.43, 132.79, 147.30.

6.2.2.4 Synthesis of 1-(chloroethynyl)-4-nitrobenzene, 4N-Cl

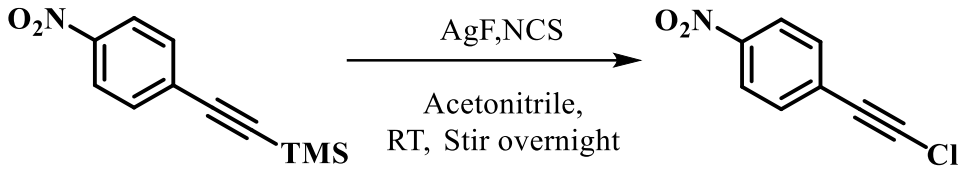

Acetonitrile (20 mL) was degassed with dinitrogen. Trimethyl((4-nitrophenyl)ethynyl)silane (1.0 g, 4.6 mmol), and AgF (0.58 g, 4.6 mmol) were added to acetonitrile and the mixture was covered with aluminum foil before the introduction of N-chlorosuccinimide (0.60 g, 4.6 mmol). The mixture was connected to a nitrogen inlet and stirred for two days. Completion of the reaction was monitored with TLC and the resulting suspension was passed through a 2 cm silica plug and the filtrate with acetonitrile as the solvent was concentrated in vacuo. The residue was dissolved in diethyl ether and washed with water (2 x 20 mL). The organic layer was dried with anhydrous $MgSO_4$ and concentrated in vacuo to obtain 1-(chloroethynyl)-4-nitrobenzene (**4N-Cl**) as a white powder. Yield: 0.29 g (35%); m.p. 148-150 °C; ^{1}H NMR (400 MHz, $CDCl_3$): 7.61 (d, 2H), 8.21 (d, 2H); ^{13}C NMR (400 MHz, $CDCl_3$): 67.70, 73.86, 123.56, 128.93, 132.74, 177.90.

6.2.2.5 Synthesis of trimethyl((3-nitrophenyl)ethynyl)silane

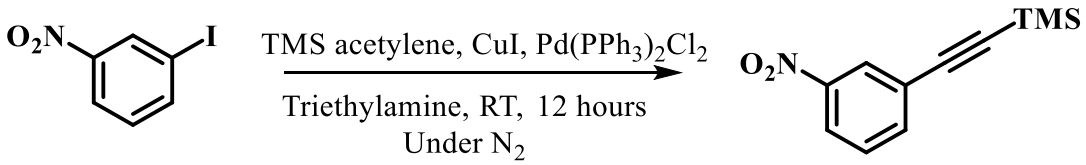

3-Iodonitrobenzene (1.7 g, 7.0 mmol), trimethylsilylacetylene (1.0 mL, 7.7 mmol), CuI (0.060 g, 0.35 mmol), and bis(triphenylphosphine)palladium(II) dichloride (0.15g, 0.21 mmol) were dissolved in 50 mL of degassed trimethylamine. The mixture was stirred overnight at room temperature under a dinitrogen atmosphere. Completion of reaction was confirmed with TLC. The reaction mixture was concentrated in vacuo and the residue was dissolved in diethyl ether (50 mL).

The ethereal solution was washed with 1 M HCl (10 mL), water (2 x 20 mL) and a saturated NaCl solution (20 mL). The organic layer was dried with anhydrous $MgSO_4$ and concentrated in vacuo. The crude product was purified by flash chromatography in 50:1 hexane: ethyl acetate yielding the final product. Yield: 1.4 g (91%); ^{1}H NMR (400 MHz, $CDCl_3$): 0.27 (s, 9H), 7.48 (t, 1H), 7.74 (d, 1H) 8.15 (d, 1H) 8.31 (s, 1H).

6.2.2.6 Synthesis of 1-(iodoethynyl)-3-nitrobenzene, *3N-I*

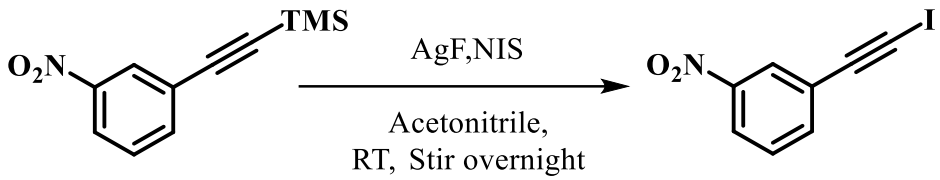

Acetonitrile (20 mL) was degassed with dinitrogen. Trimethyl((3-nitrophenyl)ethynyl)silane (1.0 g, 4.6 mmol), and AgF (0.58 g, 4.6 mmol) were added to acetonitrile and the mixture was covered with aluminum foil before the introduction of N-iodosuccinimide (1.0 g, 4.6 mmol). The mixture was connected to a nitrogen inlet and stirred overnight. Completion of the reaction was monitored with TLC and the resulting suspension was passed through a 2 cm silica plug and the filtrate with acetonitrile as the solvent and was concentrated in vacuo. The residue was dissolved in diethyl ether and washed with water (2 x 20 mL). The organic layer was dried with anhydrous $MgSO_4$ and concentrated vacuo to obtain 1-(iodoethynyl)-3-nitrobenzene (**3N-I**) as a brown solid. Yield: 1.1 g (90%); m.p. 41-47 °C; ^{1}H NMR (400 MHz, $CDCl_3$): 7.51 (t, 1H), 7.75 (d, 1H) 8.20 (d, 1H) 8.29 (s, 1H); ^{13}C NMR (400 MHz, $CDCl_3$):11.14, 91.61, 123.45, 124.98, 127.18, 129.29, 137.92, 155.26.

6.2.2.7 Synthesis of 1-(bromoethynyl)-3-nitrobenzene, 3N-Br

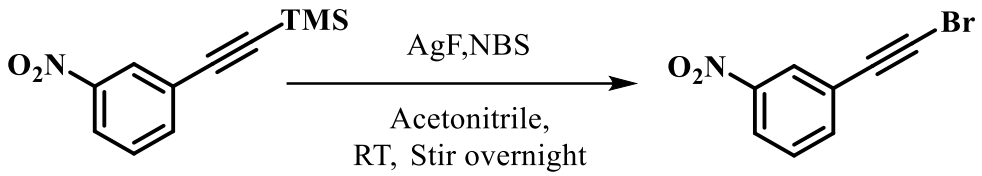

Acetonitrile (20 mL) was degassed with dinitrogen. Trimethyl((3-nitrophenyl)ethynyl)silane (1.0 g, 4.6 mmol), and AgF (0.58 g, 4.6 mmol) were added to acetonitrile and the mixture was covered with aluminum foil before the introduction of N-bromosuccinimide (0.81 g, 4.6 mmol). The mixture was connected to a nitrogen inlet and stirred overnight. Completion of the reaction was monitored with TLC and the resulting suspension was passed through a 2 cm silica plug and the filtrate with acetonitrile as the solvent and was concentrated in vacuo. The residue was dissolved in diethyl ether and washed with water (2 x 20 mL). The organic layer was dried with anhydrous $MgSO_4$ and concentrated in vacuo to obtain 1-(bromoethynyl)-3-nitrobenzene (**3N-Br**) as an off white powder. Yield: 0.90 g (87%); m.p. 55-60 °C; ^{1}H NMR (400 MHz, $CDCl_3$): 7.51 (t, 1H), 7.73 (d, 1H) 8.18 (d, 1H) 8.29 (s, 1H); ^{13}C NMR (400 MHz, $CDCl_3$):53.58, 77.72, 123.37, 124.38, 126.82, 129.38, 137.61, 147.96.

6.2.2.8 Synthesis of 1-(chloroethynyl)-3-nitrobenzene, 3N-Cl

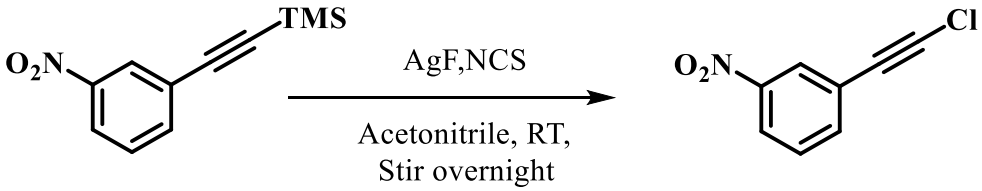

Acetonitrile (20 mL) was degassed with dinitrogen. Trimethyl((4-nitrophenyl)ethynyl)silane (1.0 g, 4.6 mmol), and AgF (0.58 g, 4.6 mmol) were added to acetonitrile and the mixture was covered with aluminum foil before the introduction of N-chlorosuccinimide (0.60 g, 4.6 mmol). The mixture was connected to a nitrogen inlet and stirred

for two days. Completion of the reaction was monitored with TLC and the resulting suspension was passed through a 2 cm silica plug and the filtrate with acetonitrile as the solvent was concentrated in vacuo. The residue was dissolved in diethyl ether and washed with water (2 x 20 mL). The organic layer was dried with anhydrous $MgSO_4$ and concentrated in vacuo to obtain 1-(chloroethynyl)-3-nitrobenzene (**3N-Cl**) as a brown solid. Yield: 0.34 g (42%); m.p. 50-54 °C; ^{1}H NMR (400 MHz, $CDCl_3$): 7.52 (t, 1H), 7.74 (d, 1H) 8.21 (d, 1H) 8.29 (s, 1H); ^{13}C NMR (400 MHz, $CDCl_3$): 67.11, 71.22, 123.31, 123.85, 126.79, 129.41, 137.61, 149.44.

6.2.2.9 Synthesis of ((3,5-dinitrophenyl)ethynyl)trimethylsilane

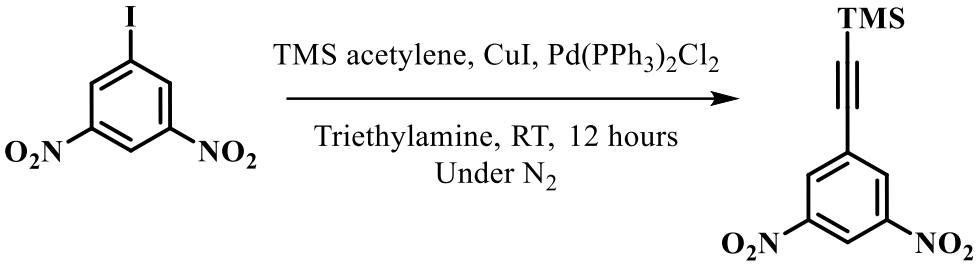

1-Iodo-3,5-dinitrobenzene (2.0 g, 6.8 mmol), trimethylsilylacetylene (1.1 mL, 7.5 mmol), CuI (0.065 g, 0.34 mmol), and bis(triphenylphosphine)palladium(II) dichloride (0.14 g, 0.20 mmol) were dissolved in 50 mL of degassed trimethylamine. The mixture was stirred overnight at room temperature under a dinitrogen atmosphere. Completion of the reaction was confirmed with TLC. The reaction mixture was concentrated in vacuo and the residue was dissolved in diethyl ether (50 mL). The ethereal solution was washed with 1 M HCl (10 mL), water (2 x 20 mL) and saturated NaCl solution (20 mL). The organic layer was dried with anhydrous $MgSO_4$ and concentrated in vacuo. The crude product was purified by flash chromatography in 50:1 hexane: ethyl acetate yielding the final product. Yield: 1.7 g (94%); ^{1}H NMR (400 MHz, $CDCl_3$): 0.31 (s, 9H), 8.59 (s, 2H), 8.97 (s, 1H).

6.2.2.10 Synthesis of 1-(iodoethynyl)-3,5-dinitrobenzene, *3,5DN-I*

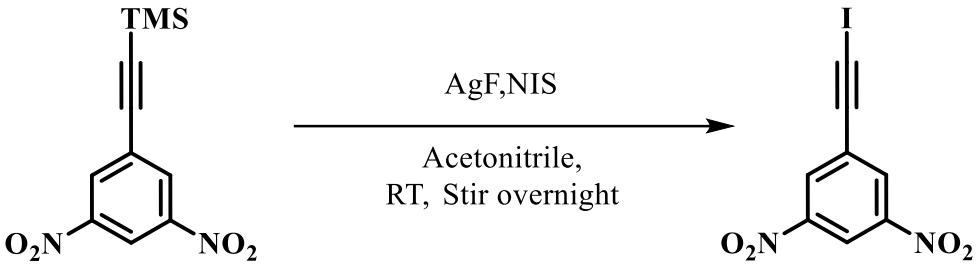

Acetonitrile (20 mL) was degassed with dinitrogen. ((3,5-dinitrophenyl)ethynyl)trimethylsilane (1.0 g, 3.9 mmol), and AgF (0.48 g, 3.9 mmol) were added to acetonitrile and the mixture was covered with aluminum foil before the introduction of N-iodosuccinimide (0.85 g, 3.9 mmol). The mixture was connected to a nitrogen inlet and stirred overnight. Completion of the reaction was monitored with TLC and the resulting suspension was passed through a 2 cm silica plug and the filtrate with acetonitrile as the solvent was concentrated in vacuo. The residue was dissolved in diethyl ether and washed with water (2 x 20 mL). The organic layer was dried with anhydrous $MgSO_4$ and concentrated in vacuo to obtain 1-(iodoethynyl)-3,5-dinitrobenzene (**3,5DN-I**) as a pale brown solid. Yield: 0.98 g (81%); m.p. 111-113 °C; ^{1}H NMR (400 MHz, $CDCl_3$): 8.57 (s, 2H), 8.98 (s, 1H); ^{13}C NMR (400 MHz, $CDCl_3$): 16.59, 89.78, 118.50, 126.85, 132.10, 148.30.

6.2.2.11 Synthesis of 1-(bromoethynyl)-3,5-dinitrobenzene, *3,5DN-Br*

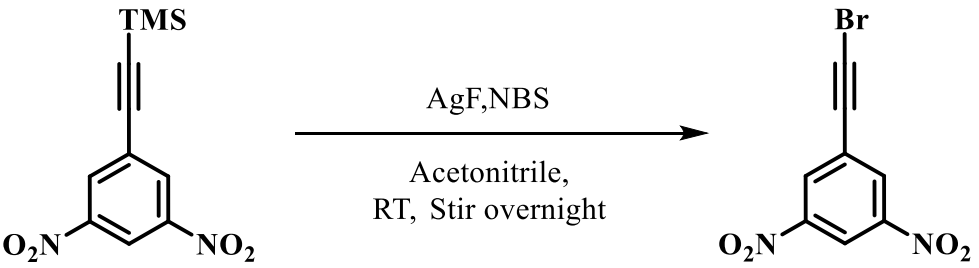

Acetonitrile (20 mL) was degassed with dinitrogen. ((3,5-dinitrophenyl)ethynyl)trimethylsilane (1.0 g, 3.8 mmol), and AgF (0.48 g, 3.8 mmol) were added to acetonitrile and the mixture was covered with aluminum foil before the introduction of N-

bromosuccinimide (0.67 g, 3.8 mmol). The mixture was connected to a nitrogen inlet and stirred overnight. Completion of the reaction was monitored with TLC and the resulting suspension was passed through a 2 cm silica plug and the filtrate with acetonitrile as the solvent was concentrated in vacuo. The residue was dissolved in diethyl ether and washed with water (2 x 20 mL). The organic layer was dried with anhydrous $MgSO_4$ and concentrated in vacuo to obtain 1-(bromoethynyl)-3,5-dinitrobenzene (**3,5DN-Br**) as a brown solid. Yield: 0.85 g (83%); m.p. 103-107 °C; ^{1}H NMR (400 MHz, $CDCl_3$): 8.58 (s, 2H), 9.00 (s, 1H); ^{13}C NMR (400 MHz, $CDCl_3$): 57.97, 76.01, 118.45, 126.27, 131.75, 148.34.

6.2.2.12 Synthesis of 1-(chloroethynyl)-3,5-dinitrobenzene, *3,5DN-Cl*

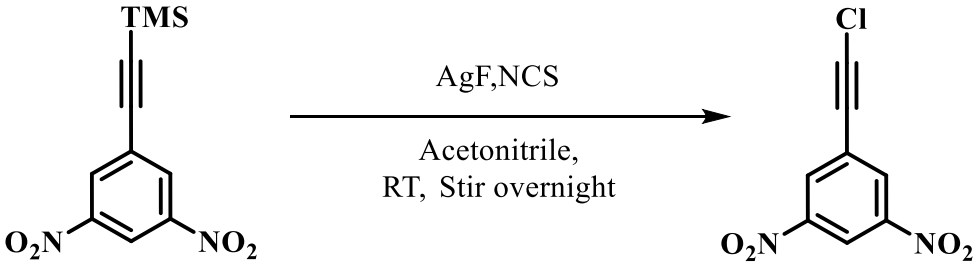

Acetonitrile (20 mL) was degassed with dinitrogen. ((3,5-dinitrophenyl)ethynyl)trimethylsilane (1.0 g, 3.8 mmol), and AgF (0.48 g, 3.8 mmol) were added to acetonitrile and the mixture was covered with aluminum foil before the introduction of N-chlorosuccinimide (0.50 g, 3.8 mmol). The mixture was connected to a nitrogen inlet and stirred for two days. Completion of the reaction was monitored with TLC and the resulting suspension was passed through a 2 cm silica plug and the filtrate with acetonitrile as the solvent was concentrated in vacuo. The residue was dissolved in diethyl ether and washed with water (2 x 20 mL). The organic layer was dried with anhydrous $MgSO_4$ and concentrated in vacuo to obtain 1-(chloroethynyl)-3,5-dinitrobenzene (**3,5DN-Cl**) as a brown solid. Yield: 0.51 g (60%); m.p. 93-

102 °C; ^{1}H NMR (400 MHz, $CDCl_3$): 8.59 (s, 2H), 9.00 (s, 1H); ^{13}C NMR (400 MHz, $CDCl_3$): 65.45, 75.07, 118.46, 125.84, 131.77, 148.10.

6.2.3 FTIR spectroscopy

IR spectra of the solid haloethynylnitrobenzene compounds were recorded on a Nicolet 380 FTIR spectrometer from 500 to 3500 cm^{-1}. Solution spectra for iodinated compounds were collected using solutions of 0.1 M in THF. Complete solid state IR spectra and solution IR spectra are provided in Appendix C.2. Collected spectra were analyzed for specific IR markers as in literature[38] in order to identify the interaction modes.

6.2.4 IsoStar and CSD searches

All the interaction maps reported in the IsoStar knowledge base were analyzed and three main trends were identified, Figure 6.7. 3D scatter plots and contour surfaces for the interactions between nitro group and the halogen moieties were generated using IsoStar. When generating the plots only the interactions less or equal to van der Waals radii sum was used. Figure 6.8 shows the respective contour surfaces and 3D scatter plots generated. CSD searches for nitro···I contact was done using Conquest[39] without applying any filters.

6.2.5 Growing crystals of haloethynylnitrobenzenes

Crystals suitable for single crystal X-ray analysis (**4N-Br**, **3,5DN-I**, **3,5DN-Br** and **3,5-DN-Cl**) were grown by slow evaporation of respective haloethynylnitrobenzene compound in a mixture of dichloromethane and methanol. Crystals of **4N-I** were obtained by slow evaporation from ethyl acetate. Crystals of **4N-Cl** and **3N-I** were too small to analyze using single crystal X-ray diffraction thus analyzed using powder structure determination along with **4N-I** where both single crystal strutures and structure from powder data were obtained. Even though **3N-Br** and **3N-Cl** were crystalline in nature, it was not possible to obtain large enough crystals to analyze

using single crystal X-ray diffraction. The attempts to solve these two structures using powder X-ray analysis were also not possible. Even though good quality crystals of **3,5DN-Cl** were obtained, due to the presence of unknown impurities in the crystal lattice, it was not possible to obtain the structure solution. All the X-ray experimental data and halogen bond geometries are provided in the Appendix B.5.

6.2.6 Electrostatic potential calculations

Molecular electrostatic potential surfaces for iodoethynylnitrobenzenes were calculated with density functional B3LYP level of theory with 6-311++G** basis set in vacuum. The same level of theory was used to calculate the electrostatic potentials for iodobenzene, pentafluoroiodobenzene, iodoethynylbenzene and 3,5-dinitroiodobenzene, Figure 6.15. Electrostatic potential surfaces for bromoethynylnitrobenzenes and chloroethynylnitrobenzenes were also calculated using the same level of theory and conditions, Figure 6.16. All calculations were carried out using the Spartan 8 software.[40] All molecules were geometry optimized with the maxima and minima in the electrostatic potential surface (0.002 e/au isosurface) determined using a positive point charge in the vacuum as a probe. The numbers indicate the interaction energy (kJ/mol) between the probe and the surface of the molecule. A positive value for the interaction energy indicates a positive surface potential while a negative value indicate a negative surface potential.

6.2.7 Co-crystal screening and crystallography

Initial screening was carried out through solvent-assisted grinding using methanol. Iodoethynylnitrobenzenes were combined with each acceptor in stoichiometric ratios (45 experiments). All bromoethynylnitrobenzenes and chloroethynylnitrobenzenes were combined with five acceptors (**A23**, **A24**, **A27**, **A31** and **A33**) in stoichiometric amounts and ground with the

assistance of a drop of methanol (a total of 30 experiments). In each experiment 10 mg of the haloethynylnitrobenzene was used with the respective stoichiometric amount of the acceptor.

Once the solvent had evaporated the ground mixtures were analyzed using IR spectroscopy to determine whether a co-crystal had formed or not. Successful interactions between the acceptor and donor were identified using the specific shifts of the peaks of the mixture compared to starting compounds.

For each successful reaction, the resulting solid was dissolved in a minimum amount (2 mL) of either ethyl acetate or methylene chloride and methanol (1:1) mixture and then left in a vial for slow evaporation in order to obtain crystals suitable for single crystal X-ray diffraction.

Good quality crystals were obtained from the majority of co-crystals of iodoethynylnitrobenzenes and nine of these were crystallographically characterized. For the remaining two groups of XB donors, only one reaction yielded suitable single crystals. Table 6.1 summarizes the experimental details. X-ray crystallographic data and all halogen-bond geometries are provided in the Appendix B.5.

Table 6.1 Experimental details for the ten co-crystals obtained

Code	Mixed Mole ratio	Amounts used	Solvent and method	Crystal stoichiometry	Melting point (°C)	Crystal color & habit
4N-I:A23	2:1	**4N-I** -10 , 0.037 mmol **A23** – 3.0 mg, 0.019 mmol	ethyl acetate, Slow evaporation	2:1	61-64	Yellow plate
4N-I:A24	2:1	**4N-I** - 10 mg, 0.037 mmol **A24** - 3.5 mg, 0.019 mmol	DCM & methanol (1:1) mixture, Slow evaporation	2:1	72-76	Bronze plate
4N-I:A32	1:1	**4N-I** - 10 mg, 0.037 mmol **A32** - 6.8 mg, 0.037 mmol	DCM & methanol (1:1) mixture, Slow evaporation	1:1	107-109	Orange plate
3N-I:A25	2:1	**3N-I** - 10 mg, 0.037 mmol **A25** - 3.5 mg, 0.019 mmol	DCM & methanol (1:1) mixture, Slow evaporation	2:1	102-105	Orange plate
3N-I:A31	1:1	**3N-I** - 10 mg, 0.037 mmol **A31** - 5.7 mg, 0.037 mmol	DCM & methanol (1:1) mixture, Slow evaporation	1:1	122-126	Bronze prism
3N-I:A33	2:1	**3N-I** - 10 mg, 0.037 mmol **A33** - 1.8 mg, 0.019 mmol	DCM & methanol (1:1) mixture, Slow evaporation	1:1	110-112	Bronze rod

3,5DN-I:A22	2:1	**3,5DN-I** - 10 mg, 0.031 mmol **A22** - 2.2 mg, 0.016 mmol	DCM & methanol (1:1) mixture, Slow evaporation	2:1	140-144	Bronze prism
3,5DN-I:A29	2:1	**3,5DN-I** - 10 mg, 0.031 mmol **A29** - 2.7 mg, 0.016 mmol	DCM & methanol (1:1) mixture, Slow evaporation	2:1	140-142	Bronze plate
3,5DN-I:A34	2:1	**3,5DN-I** - 10 mg, 0.031 mmol **A34** - 2.4 mg, 0.016 mmol	DCM & methanol (1:1) mixture, Slow evaporation	1:1	132-135	Red block
3N-Br:A27	2:1	**3N-Br** - 10 mg, 0.044 mmol **A27** - 4.1 mg, 0.022 mmol	DCM & methanol (1:1) mixture, Slow evaporation	2:1	98-101	Bronze prism

6.3 Results

6.3.1 IsoStar and CSD analysis

An extensive IsoStar search on nitro group interactions were done and three different interaction patterns were identified, Figure 6.7. It is clear that polar groups prefer interacting with the nitro group in three different modes, mode I: symmetric bifurcated type, mode II: asymmetric bifurcated type and mode III: single interaction with oxygen.

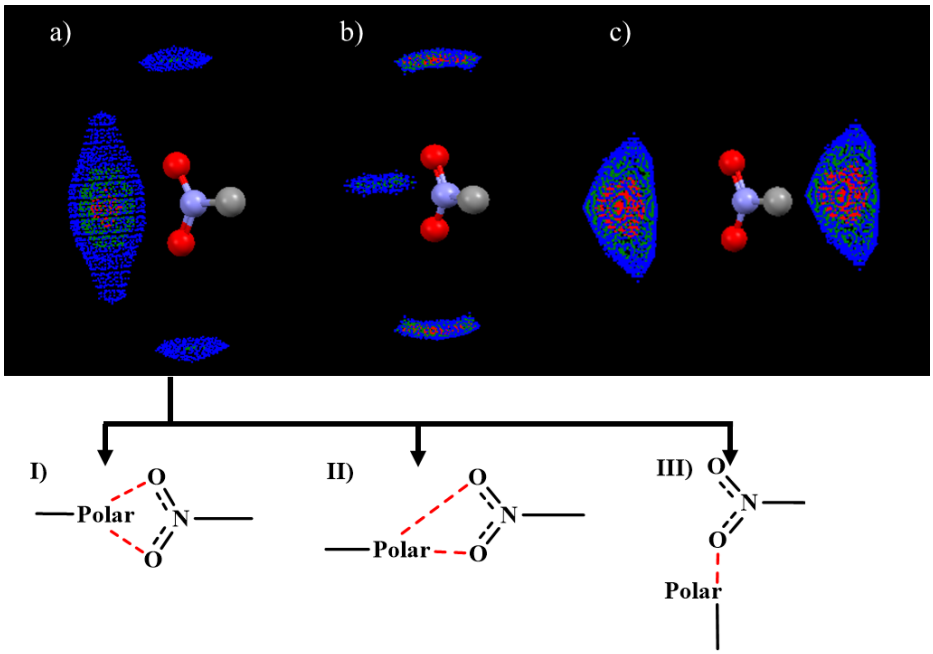

Figure 6.7 Most common interactions of nitro groups with a) polar groups (three modes can be identified as I: symmetric bifurcated type, II: asymmetric bifurcated type and III: single interaction with oxygen b) cationic groups and c) anionic groups; red zone are the most probable interaction zones

Furthermore, the interactions of nitro groups with cationic groups mainly prefer the interactions with the oxygen atoms. Anionic groups prefer interacting with positively charged nitrogen atom. Apart from these trends non polar neutral groups interact with nitro group without showing any special patterns, thus the contour maps of these interactions were equally distributed around the central nitro group.

When analyzing interactions of nitro groups with different halogen moieties in IsoStar, only three maps were reported, interactions with C-F contact group, C-Cl contact group and C-Br contact group. The contour surfaces and scatter plots of these interactions are shown in Figure 6.8. Even though the most common nitro···halogen interaction is reported with iodine, the interaction map was not reported in IsoStar, due to the small number of data points reported in the CSD for generating the IsoStar interaction map. Thus, we performed a CSD search on structures with nitro···iodo contacts equal or less than the sum of van der Waals radii and 124 hits were obtained.

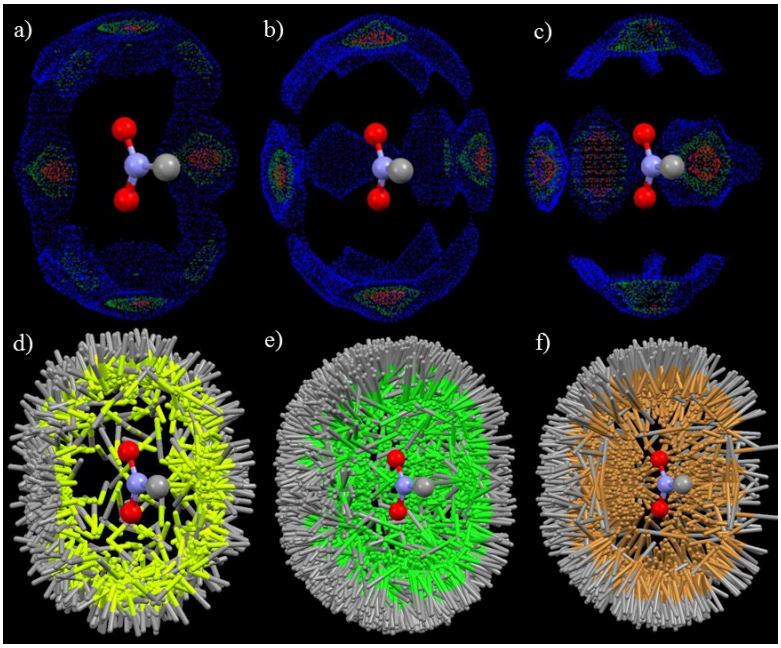

Figure 6.8 Contour surfaces and 3D scatter plots for the interactions between nitro group and C-X group (X-any halogen); a) contour surface for C-F group, b) contour surface for C-Cl group c) contour surface for C-Br group d) 3D scatter plot for C-F group e) 3D scatter plot for C-Cl group and f) 3D scatter plot for C-Br group

6.3.2 Interaction mode predictions using FTIR

For **4N-I**, **3N-I** and **3,5DN-I** the intermolecular interaction mode was analyzed using IR spectroscopy,[38] Table 6.2.

Table 6.2 Interaction modes predicted using FTIR for iodoethynylnitrobenzenes

	4N-I	3N-I	3,5DN-I
(ν_{as})solid [cm^{-1}]	1498	1514	1525
(ν_{as})solution [cm^{-1}]	1521	1531	1542
$\Delta\nu_{as}$ [cm^{-1}] – (ν_{as} solution - ν_{as} solid)	23	17	17
(ν_s)solid [cm^{-1}]	1335	1343	1336
[I_{as}/I_s]solid	$I_{as}>I_s$	$I_{as}\sim I_s$	$I_{as}<I_s$
Splitting in ν_s	No	No	Yes
$\delta(NO_2)$ [cm^{-1}]	848	841	838
7a ring vibration mode [cm^{-1}]	-	771	780
Synthon predicted	Mode I	Mode II	Mode III

6.3.3 Experimental structures of haloethynylnitrobenzenes

Once the compounds were successfully synthesized the next step was to analyze them with single crystal X-ray diffraction to determine the nature of their intermolecular interactions. Even though a few of these compounds were reported in the previous literature, none of their structures were known. Of the nine compounds that were synthesized suitable crystals were obtained for four (**4N-I**, **4N-Br, 3,5DN-I** and **3,5DN-Br**). For the purpose of comparison, the crystal structure from powder data was also obtained for **4N-I**.[41] For **4N-Cl** and **3N-I** structures were obtained from powder data.[41] Other compounds were not structurally characterized. Single crystal X-ray experimental data and the halogen bond geometries for the solved structures are provided in the Appendix B.5. Powder experimental data are provided elsewhere.[41]

The crystal structure of **4N-I** is shown in Figure 6.9. The iodine atom participates in a symmetric bifurcated type (mode I) interaction with the oxygen atoms of nitro group in the neighboring molecule. The structure results are similar for the structure obtained with powder data as well.[41]

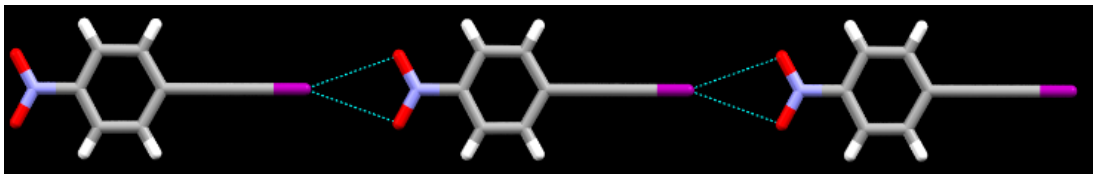

Figure 6.9 Main intermolecular interactions in the crystal structure **4N-I**

The crystal structure of **4N-Br** is consistent with the interactions in **4N-I** where symmetric bifurcated type (mode I) of halogen bonding between the nitro group and the adjacent bromine atom can be seen, Figure 6.10.

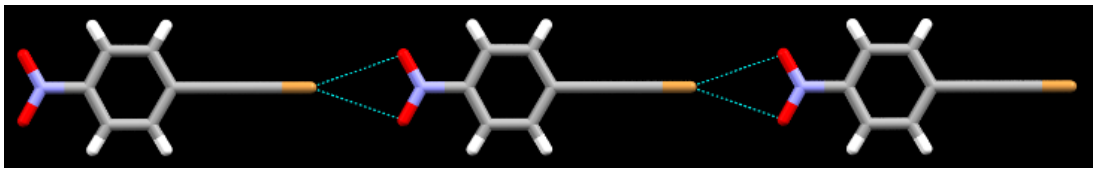

Figure 6.10 Primary intermolecular interactions in the crystal structure of **4N-Br**

The structural consistency is persistent in the structure of **4N-Cl** as well,[41] which shows symmetric bifurcated halogen bond formation, similar to **4N-I** and **4N-Br**, Figure 6.11.

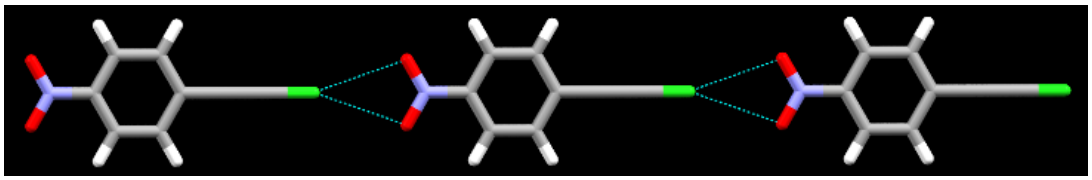

Figure 6.11 Primary intermolecular interactions in the structure of **4N-Cl**[41]

The structure of **3N-I** obtained with powder data[41] is shown in Figure 6.12. Not like in the 1,4-substituted isomers, this molecule has an asymmetric bifurcated type interaction (mode II) between the nitro oxygen atoms and iodine atoms. The shape of the molecule and the asymmetric nature of the intermolecular interaction leads to the zig-zag motifs.

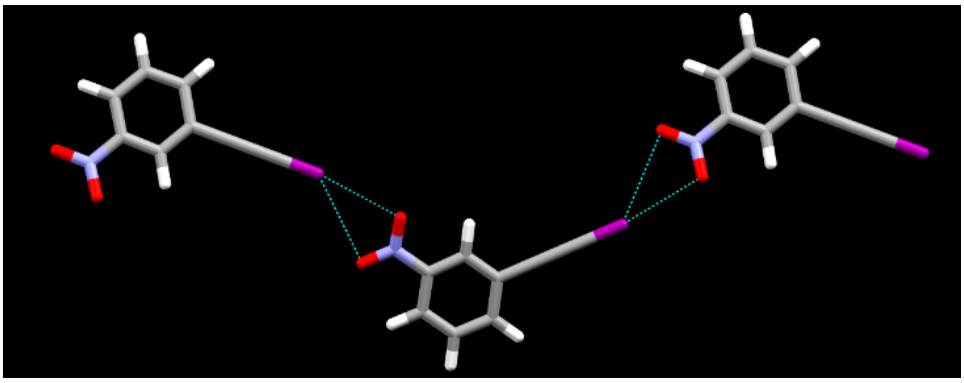

Figure 6.12 Primary intermolecular interactions in the structure of **3N-I**[41]

The crystal structure of **3,5DN-I** shows a single interaction between the iodine atom and one of the oxygen atoms of the nitro group, Figure 6.13. This interaction and the molecular orientation leads to the formation of zig-zag type tapes in this structure.

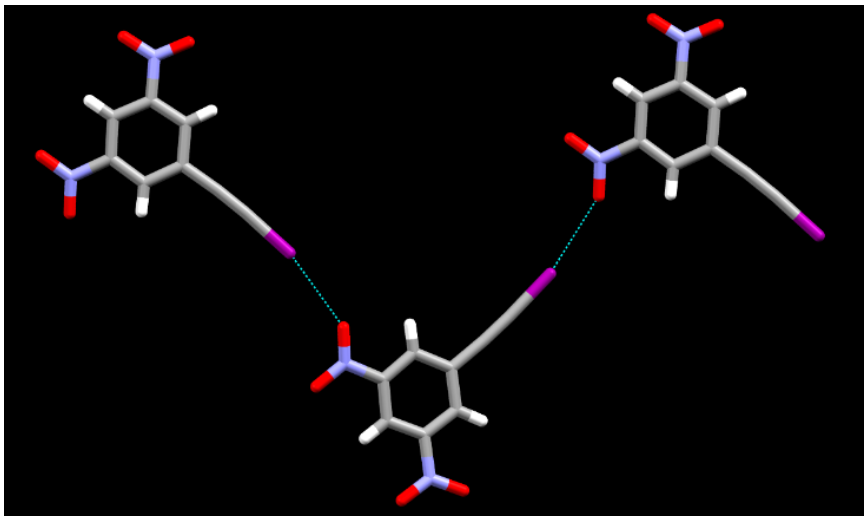

Figure 6.13 Primary intermolecular interactions in the crystal structure of **3,5DN-I**

The crystal structure of **3,5DN-Br** shows interactions similar to that of **3,5-DN-I**, Figure 6.14. This single point interaction leads to the formation of zig-zag motifs.

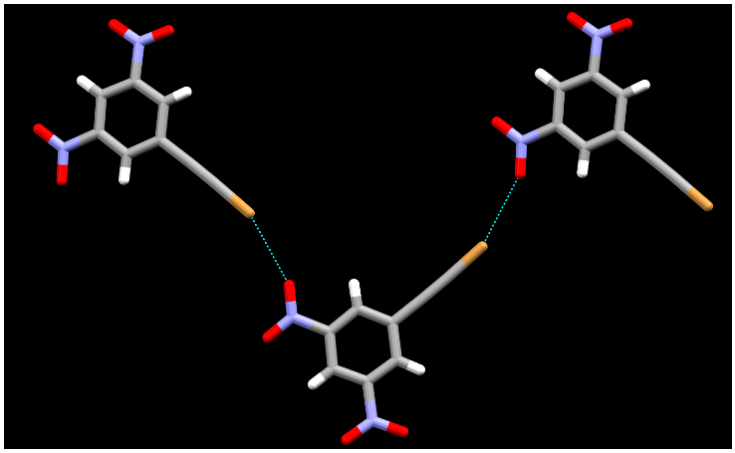

Figure 6.14 Primary intermolecular interactions in the crystal structure of **3,5DN-Br**

6.3.4 Electrostatic potentials

Electrostatic potential values for the activated iodine atoms of the three iodoethynylnitrobenzenes (**4N-I**, **3N-I** and **3,5DN-I**) are shown in Figure 6.15, along with the corresponding values for iodobenzene, pentafluoroiodobenzene, iodoethynylbenzene and 3,5-dinitriodobenzene.

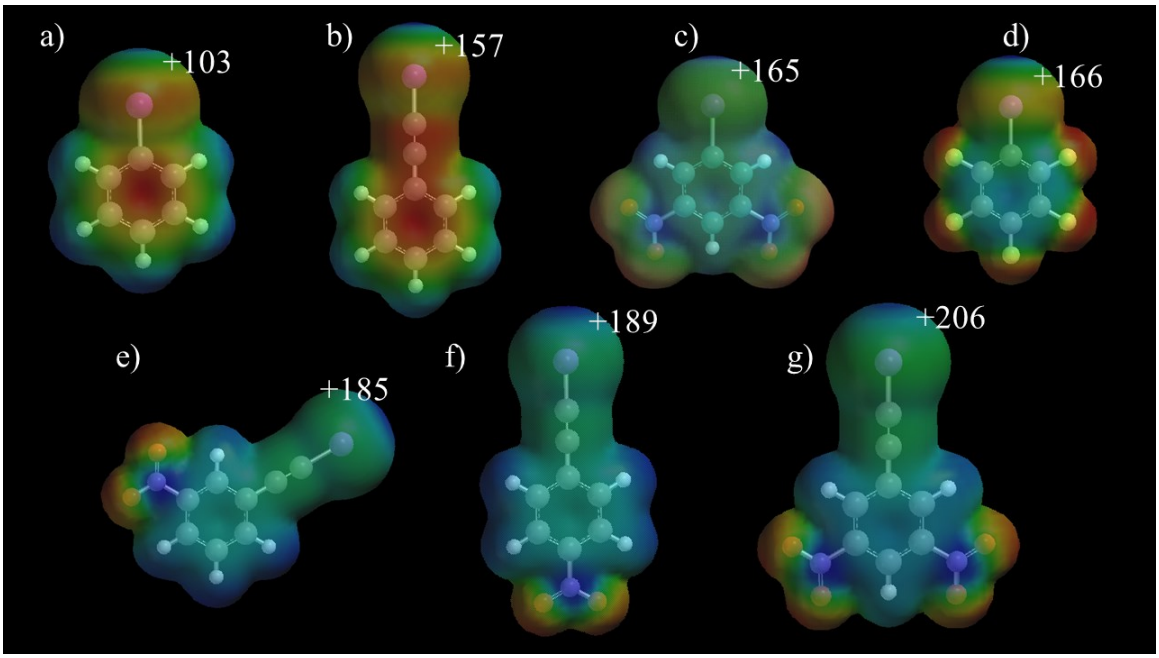

Figure 6.15 Electrostatic potentials values on the XB donor atom (in kJ/mol); a) iodobenzene b) iodoethynylbenzene c) 3,5-dinitroiodobenzene d) pentafluoroiodobenzene e) **3N-I** f) **4N-I** and g) **3,5DN-I**

Figure 6.16 shows the molecular electrostatic potential values on the bromo- (**4N-Br**, **3N-Br** and **3,5DN-Br**) and chloroethynylnitrobenzene (**4N-Cl**, **3N-Cl** and **3,5DN-Cl**) compounds.

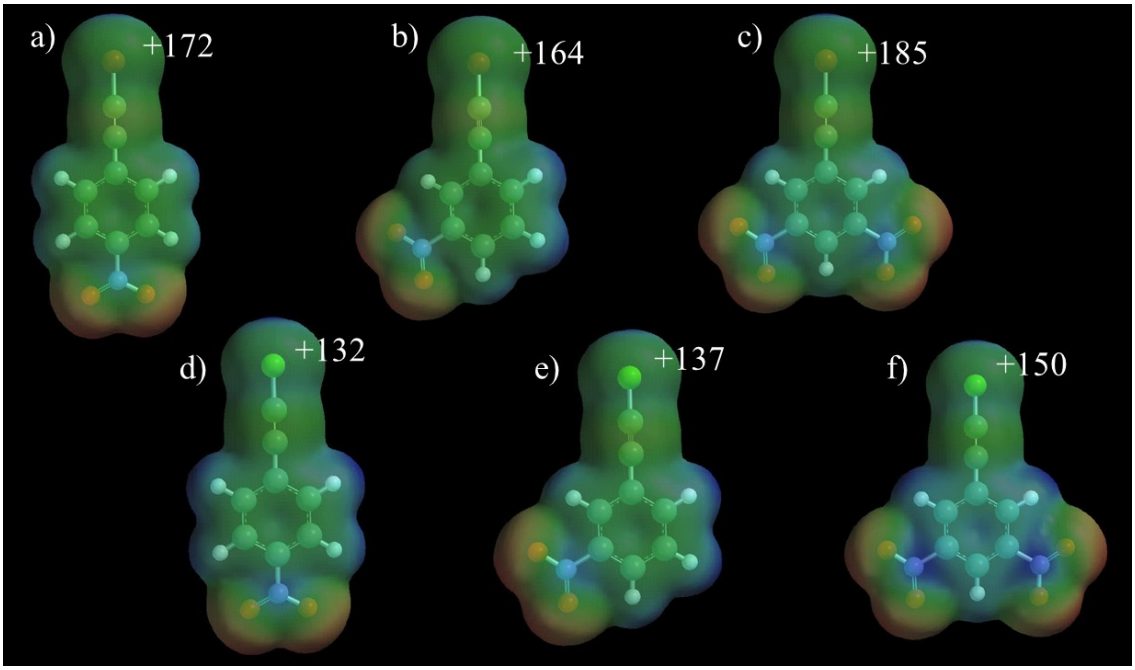

Figure 6.16 Electrostatic potential surfaces for bromo- and chloro- compounds (in kJ/mol); a) **4N-Br** b) **3N-Br** c) **3,5DN-Br** d) **4N-Cl** e) **3N-Cl** and f) **3,5-DN-Cl**

6.3.5 Grinding experiments and characterization by IR spectroscopy

Solvent-assisted grinding experiments between each of the three iodoethynylnitrobenzenes and 15 acceptors were analyzed using IR spectroscopy to identify notable interactions between the two potential co-formers. The key IR modes targeted were C≡C triple bond stretch of the halogen-bond donor and the symmetric and asymmetric stretches of the nitro group in each halogen-bond donor. The IR analysis was done by looking at the shifts of these three IR modes with respect to their initial positions of the haloethynylnitrobenzene compound. If any one of those three key IR modes were shifted by three or more wave numbers that combination was considered to be a successful co-crystal formation. Table 6.3 summarizes the outcomes from grinding experiments. Detailed IR analysis for grinding and solvent based experiments is provided in Appendix C.2.

For bromo- and chloro- compounds each potential donor was allowed to react with five acceptors (**A23**, **A24**, **A27**, **A31** and **A33**), and nine of fifteen bromoethynylnitrobenzenes resulted in a co-crystal whereas none of the fifteen attempts with a chloroethynylnitrobenzene produced a co-crystal, Table 6.3.

Table 6.3 Summary of grinding results

		Donors								
		iodoethynylnitrobenzenes			bromoethynylnitrobenzenes			chloroethynylnitrobenzenes		
		4N-I	3N-I	3,5DN-I	4N-Br	3N-Br	3,5DN-Br	4N-Cl	3N-Cl	3,5DN-Cl
Acceptors	A21	✓	✓	✓						
	A22	✓	✓	✓						
	A23	✓	✓	✓	✓	✓	✓	✗	✗	✗
	A24	✓	✓	✓	✓	✗	✗	✗	✗	✗
	A25	✓	✓	✓						
	A26	✓	✓	✓						
	A27	✓	✓	✓	✗	✓	✓	✗	✗	✗
	A28	✓	✓	✓						
	A29	✓	✓	✓						
	A30	✓	✓	✓						
	A31	✓	✓	✓	✓	✓	✗	✗	✗	✗
	A32	✓	✓	✓						
	A33	✓	✓	✓	✗	✓	✗	✗	✗	✗
	A34	✓	✓	✓						
	A35	✓	✓	✓						
% Success		15/15	15/15	15/15	3/5	4/5	2/5	0/5	0/5	0/5
		100	100	100	60	80	40	0	0	0

6.3.6 Crystal growth, IR analysis and crystallography

To gather more detail about the exact nature of the binding of XB donor and acceptor, crystallographic data were required. Crystals of **4N-I:A23** were grown in ethyl acetate, and all the other crystals were grown in a 1:1 mixture of methanol and methylene chloride. The selection of the solvent systems for crystal growth are based on the solubility. The first choice of solvents to grow crystals was pure methanol but iodoethynylnitrobenzenes were less soluble in pure methanol compared to the acceptors of choice. Then the second choice was to use pure ethyl acetate; even though the crystal growth was successful in ethyl acetate one of the crystal structure (**4N-I:A23**)

showed solvent incorporation into the lattice. Finally, a mixture of methylene chloride and methanol was selected as the donors are highly soluble in methylene chloride, while the acceptors are highly soluble in methanol. Thus, a mixture of the two solvents provided a suitable medium for both acceptors and donors. The majority of the combinations with iodoethynylnitrobenzenes produced suitable crystals, Appendix C.2. The structures for **4N-I:A23**, **4N-I:A24**, **4N-I:A32**, **3N-I:A25**, **3N-I:A31**, **3N-I:A33**, **3,5DN-I:A22**, **3,5DN-I:A29** and **3,5DN-I:A34** were solved. Only one of the nine co-crystals from a bromoethynylnitrobenzene, **3N-Br:A27**, produced crystals of sufficient quality and the remaining compounds yielded either flimsy crystals, gels or fine powders, Appendix C.2. For all ten combinations with the structures an extensive IR analysis was done to predict the interaction preferences of the nitro group in the co-crystals,[42] Table 6.4. Crystallographic data and halogen bond geometries are provided in the Appendix B.5.

Table 6.4 IR analysis for the nitro stretches of co-crystals

Co-crystal	IR prediction			Actual interaction present in the crystal structure
	Splitting in Symmetric stretch	Intensity of stretches	Type of interaction predicted	
4N-I:A23	No	I sym < I asym	Linear $NO_2\cdots$H-C interaction	Linear $NO_2\cdots$H-C interaction
4N-I:A24	No	I sym ~ I asym	Inconclusive	Linear $NO_2\cdots$H-C interaction
4N-I:A32	No	I sym < I asym	Linear $NO_2\cdots$H-C interaction	Linear $NO_2\cdots$H-C interaction
3N-I:A25	No	I sym > I asym	Inconclusive	No considerable interactions
3N-I:A31	No	I sym > I asym	Inconclusive	$NO_2\cdots$H-C dimer
3N-I:A33	Yes	I sym > I asym	$NO_2\cdots$H-C dimer	$NO_2\cdots$H-C dimer
3,5DN-I:A22	Peak broadened	I sym > I asym	Most probably $NO_2\cdots$H-C dimer	$NO_2\cdots$H-C dimer
3,5DN-I:A29	No	I sym ~ I asym	Inconclusive	Linear $NO_2\cdots$H-C interaction and $NO_2\cdots NO_2$ dimer
3,5DN-I:A34	No	I sym < I asym	Linear $NO_2\cdots$H-C interaction	Linear $NO_2\cdots$H-C interaction and $NO_2\cdots NO_2$ dimer
3N-Br:A27	Yes (Shoulder)	I sym > I asym	$NO_2\cdots$H-C dimer	$NO_2\cdots$H-C dimer

6.3.7 Crystal structures for the co-crystals

6.3.7.1 Structures with iodoethynylnitrobenzenes

The structure determination of **4N-I:A23** shows the expected trimer constructed from two symmetry related C-I···N(py) halogen bonds, resulting in a trimer with a 1:2 stoichiometry. Short contacts between nitro oxygen atoms and nearby acidic hydrogen atoms from a bipyridine molecule leads to the extension of the structure, Figure 6.17. There is also a disordered solvent molecule in the lattice (ethyl acetate) but it does not form any noteworthy intermolecular interactions.

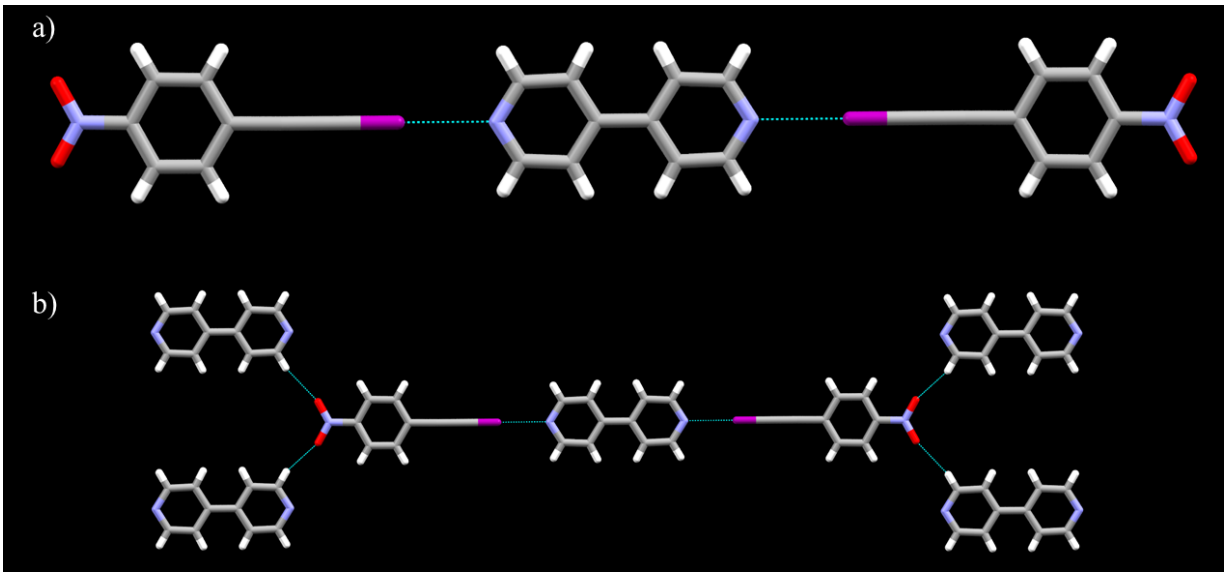

Figure 6.17 (a) C-I···N(py) halogen bonds and (b) C-H···O_2N hydrogen bonds in the crystal structure of **4N-I:A23**

The crystal structure of **4N-I:A24** is similar to that of **4N-I:A23** as it also contains a central trimer held together by symmetry related halogen bonds, Figure 6.18. This time, however, there is only one hydrogen bond between the nitro group and one of the acidic protons of the heterocycle.

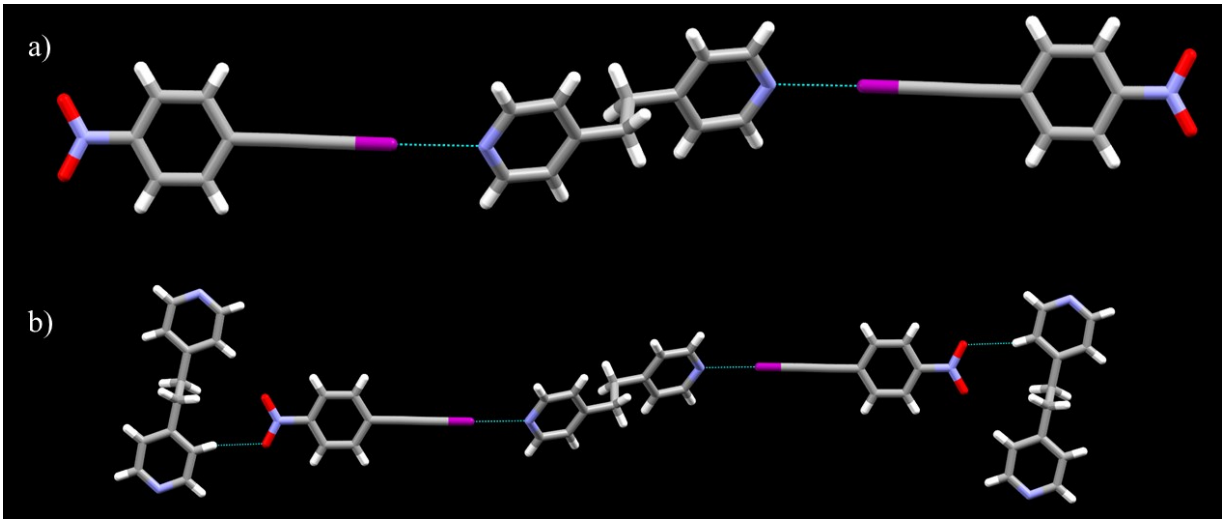

Figure 6.18 (a) Halogen bonds and (b) hydrogen bonds in the crystal structure of **4N-I:A24**

As expected with a monotopic acceptor the crystal structure of **4N-I:A32** contains 1:1 dimers connected via C-I···N halogen bonds, Figure 6.19. Both oxygen atoms of the nitro group act as hydrogen-bond acceptors for C-H donors.

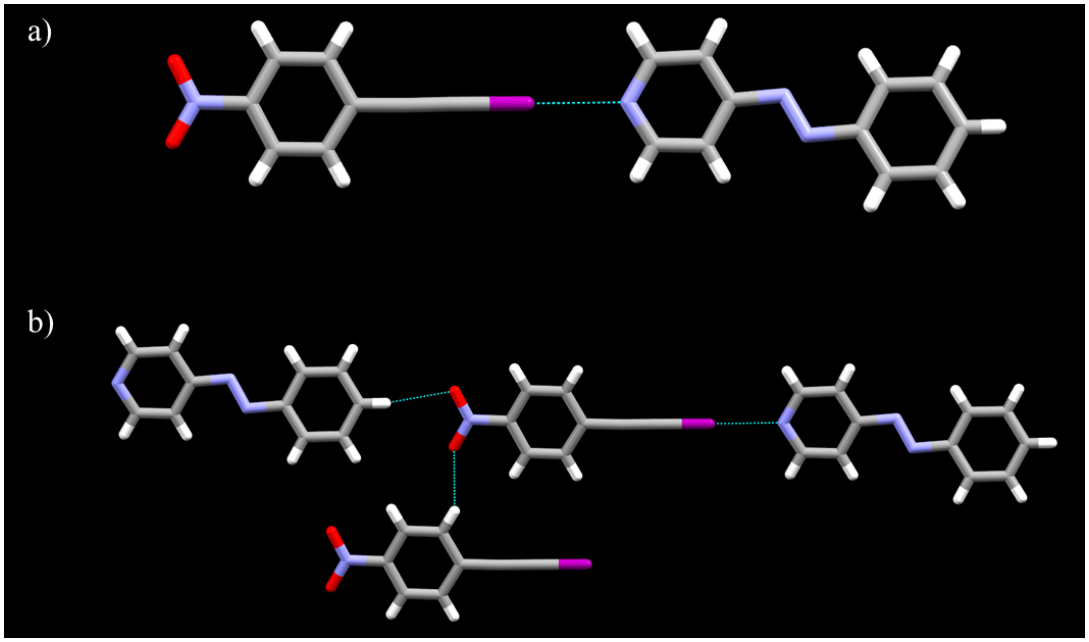

Figure 6.19 (a) Halogen bonds and (b) hydrogen bonds in the crystal structure of **4N-I:A32**

Switching the nitro group from the four to the three position does not affect the way that the XB donor interacts with a ditopic acceptor; the expected trimer is present in the crystal structure of **3N-I:A25**, Figure 6.20.

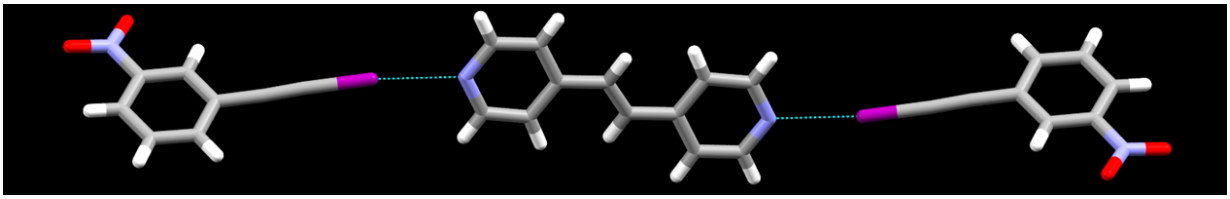

Figure 6.20 Trimer in the crystal structure of **3N-I:A25**

The monotopic acceptor **A31** ensures the formation of a halogen-bonded dimer in the crystal structure of **3N-I:A31**, Figure 6.21. Adjacent XB donors are connected through a C-H···O/O···H-C homosynthon.

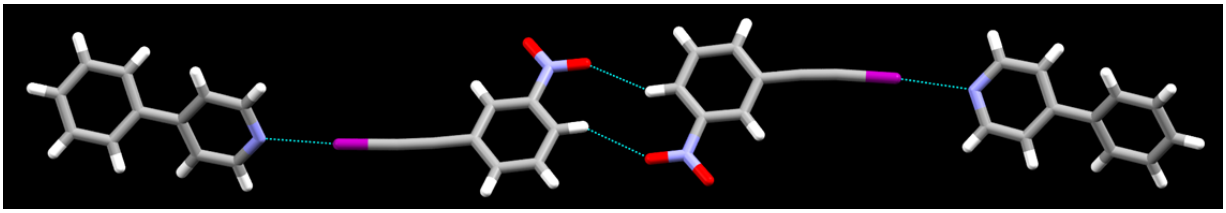

Figure 6.21 Halogen bonded dimer and supramolecular tetramer in the crystal structure of **3N-I:A31**

The crystal structure of **3N-I:A33** is somewhat different compared to the other members in the series; even though **A33** is an asymmetric ditopic acceptor the outcome is not a trimeric motif; instead, we observe a C-I···N halogen bond and a homosynthon between adjacent XB donors which gives rise to a linear tetramer, Figure 6.22.

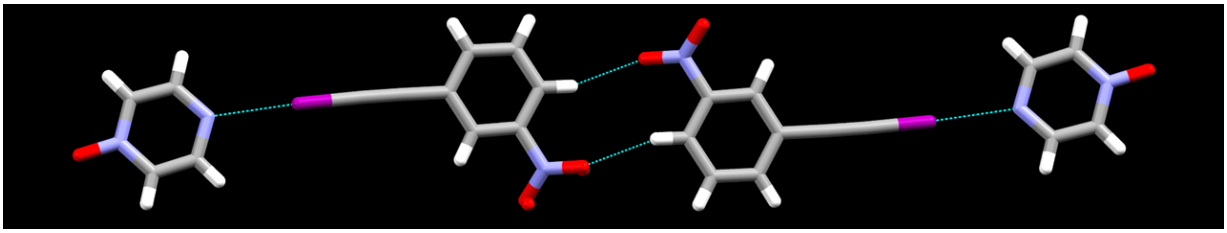

Figure 6.22 Tetrameric motif in the crystal structure of **3N-I:A33**

3,5DN-I:A22 shows the expected halogen bonded trimer with a 1:2 ratio of ditopic acceptor to XB donor, Figure 6.23. Again, there is a self-complementary C-H···O/O···H-C homosynthon between adjacent XB donors.

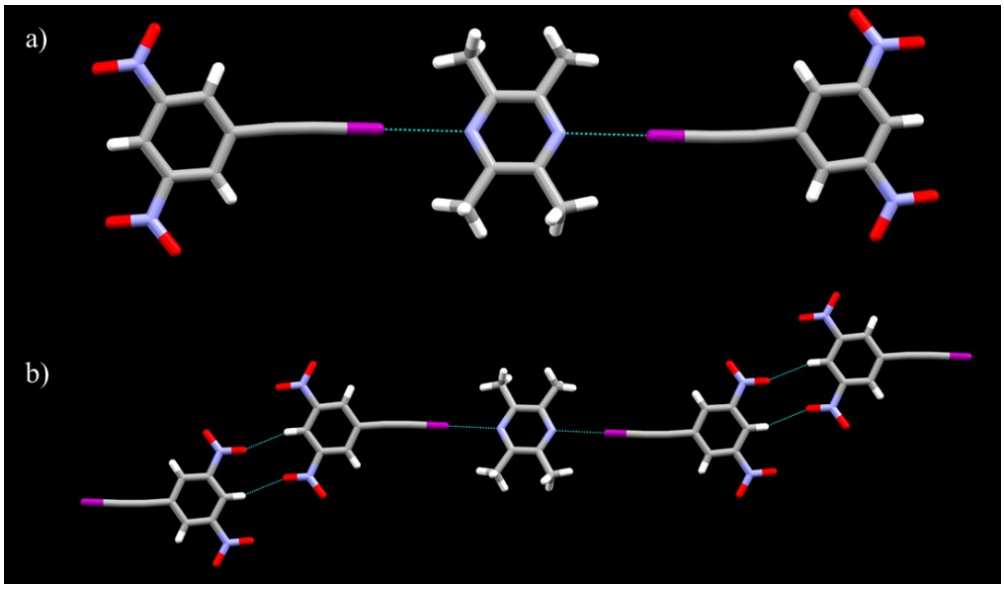

Figure 6.23 (a) Halogen-bonded trimer and (b) C-H···O/O···H-C homosynthons in the crystal structure of **3,5DN-I:A22**

The main motif in the structure of **3,5DN-I:A29**, a 1:2 halogen-bonded trimer, is consistent with what was found in all structures in this series involving symmetric ditopic acceptors, Figure 6.24. However, the two nitro groups behave differently when it comes to secondary interactions, where one nitro group shows a nitro···nitro interaction, while the other nitro group participates in a short contact with a hydrogen atom from an adjacent XB donor.

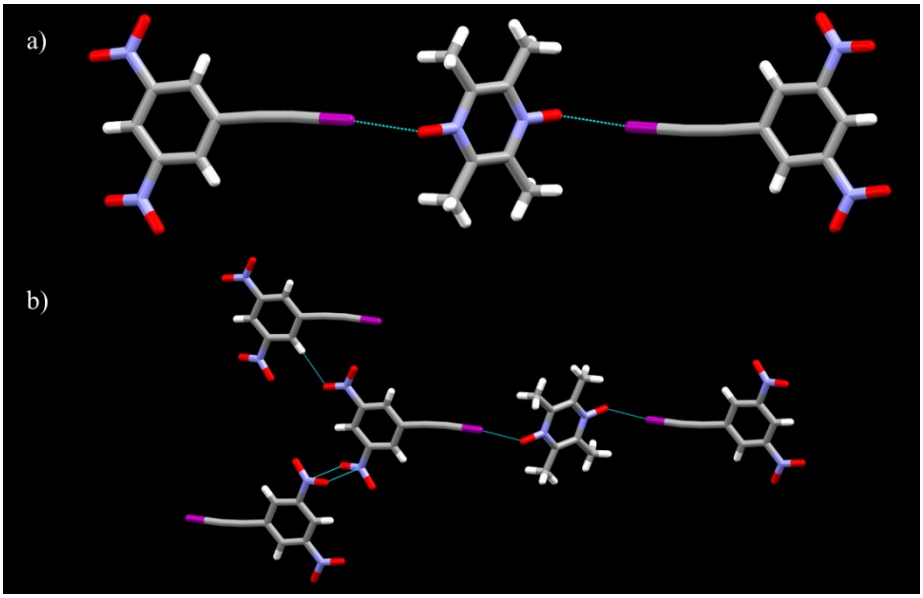

Figure 6.24 (a) Halogen-bonded trimer and (b) short contacts involving the nitro groups in the crystal structure of **3,5DN-I:A29**

In **3,5DN-I:A34** the acceptor **A34** is disordered, but the outcome is another halogen-bonded 1:2 trimer, Figure 6.25. The nitro groups are participating in two different types of short contacts: one group is forming a short contact with another nitro group while the other is forming a short contact with a hydrogen atom of the adjacent **3,5DN-I** molecule.

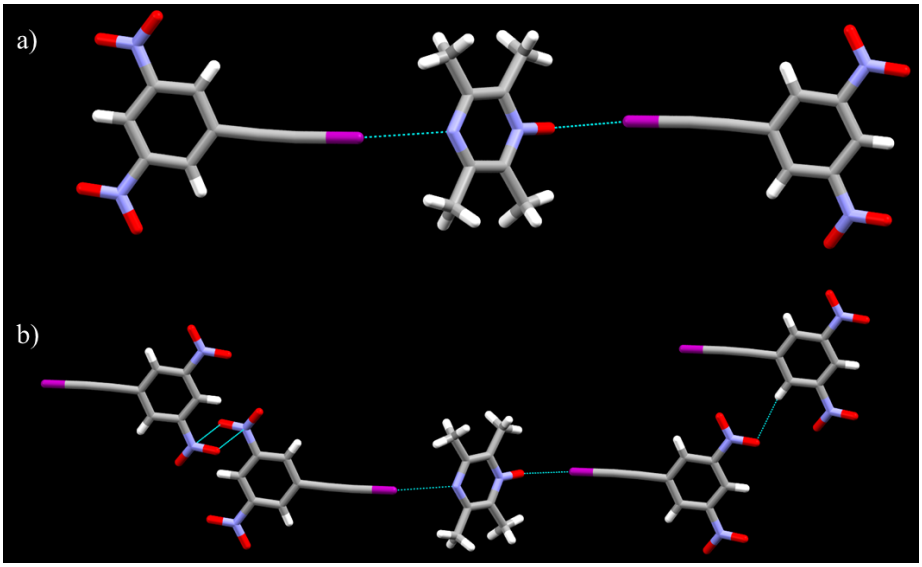

Figure 6.25 (a) A halogen-bonded trimer and (b) short contacts involving the nitro groups in the crystal structure of **3,5DN-I:A34**

6.3.7.2 Structures with bromoethynylnitrobenzenes

The only crystal structure that could be obtained with bromoethynylnitrobenzenes was **3N-Br:A27**. This structure contains a halogen-bonded trimer in a 1:2 ditopic acceptor:XB donor ratio, Figure 6.26. The nitro groups participate in a homosynthon, the same as was found on three occasions with co-crystals of iodoethynylnitrobenzenes.

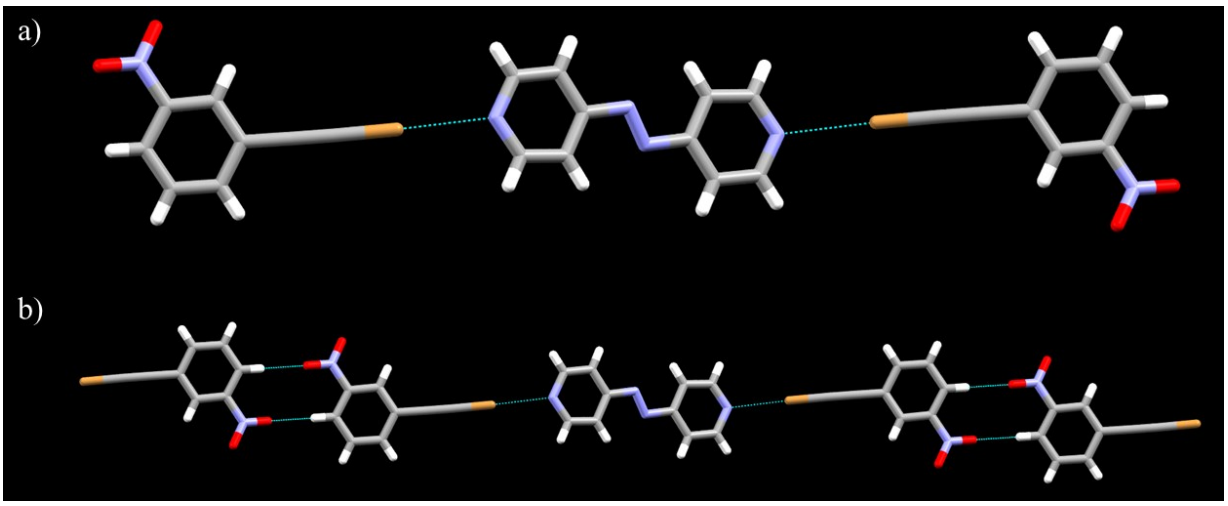

Figure 6.26 (a) Halogen-bonded trimer and (b) nitro-based homosynthons in the crystal structure of **3N-Br:A27**

6.4 Discussion

6.4.1 Synthesis of haloethynylnitrobenzene

The synthesis of these compounds start with the respective iodonitrobenzenes and as the first step the starting compound is coupled with trimethylsilylacetylene via a Sonogashira coupling.[43] In most of the Sonogashira couplings the reaction conditions require high temperatures for the reaction to be complete. But in these family of compounds the reactions happen at room temperature indicating the activated nature of the leaving iodine atom due to the presence of highly electron withdrawing nitro groups. On the other hand, halogenation of these reactions were straightforward directly from the TMS protected compounds. In most cases, the halogenation reaction needs to go through the TMS deprotected compound.[44] The straightforward nature of this

reaction again emphasize the effect of having nitro groups in the moiety. The yields of the reactions were in the range of 80% to 90% other than for the chlorinated compounds. In chlorination reactions more time was required for the reactions to complete and the yields were in the 35-60% range. This indicates the weak leaving group nature of chlorine, even though it is activated by the presence of nitro groups.

6.4.2 IsoStar and CSD analysis

When looking at the contour surface of nitro···F-C interactions (Figure 6.27a) it seems the interactions are mostly occurring "sideways" to the nitrogen atom. This is expected if we consider the C-F moiety as a negatively charged species due to the high electronegativity of fluorine. There are few structures that show interactions between C-F group and nitro oxygen atoms directly from top and bottom; these structures should have an induced positive charge on the fluorine atom in order to interact with the oxygen. Due to the electronegativity of chlorine, nitro···Cl-C interaction map (Figure 6.27b), is also similar to the behavior with C-F. But in this case there are some interactions occurring from the middle of the nitro group directly with oxygen atoms. These interactions should happen due to the activated chlorines with a positive charged tip. When moving on to the interactions between nitro···Br-C groups the "hot zone" of interactions are concentrated around the middle of the nitro group, Figure 6.27c. This can be directly related to the activated nature of bromine in these structures.

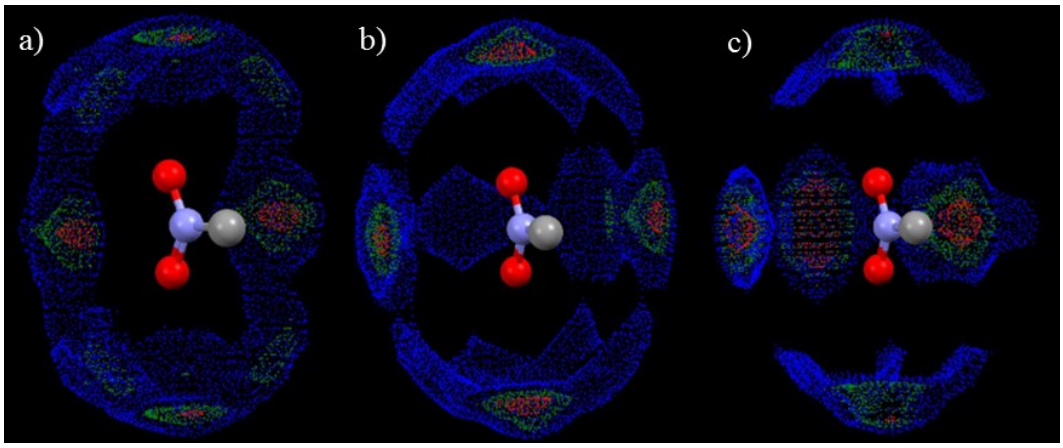

Figure 6.27 Contour surfaces for the interactions between nitro group C-X group (X-any halogen); a) C-F group, b) C-Cl group and c) C-Br group; red zones are most favorable interaction zones

6.4.3 Interaction mode predictions using FTIR and experimental structures

Interaction modes predicted by the IR analysis (Table 6.2) were manifested in the experimental structures obtained for the **4N-I**, **3N-I** and **3,5DN-I**. Thus, FTIR analysis for the compounds containing nitro···iodo synthon can be successfully utilized in predicting the interaction modes between the nitro group and the iodine atom,[38] even when no other structural analysis methods is available. Unfortunately, a successful set of steps is not yet accessible for other nitro···halogen interactions (nitro···Br or nitro···Cl).

When comparing the three isomers of the 1,4 family (Figure 6.9, Figure 6.10 and Figure 6.11) it is clear that they all interact via symmetric bifurcated interactions (mode I) leading to 1D-tape architectures, Figure 6.28. When comparing the three compounds with iodine, **4N-I**, **3N-I** and **3,5DN-I**, the structural complexity that a nitro group can show when interacting with a polar halogenated compound is clear. **4N-I** shows a polar bifurcated type interaction (mode I, Figure 6.28); **3N-I** shows an asymmetric bifurcated type interaction (mode II, Figure 6.28); and **3,5DN-I** shows an interaction rather in between the mode II and mode III, Figure 6.28. All in all the nitro···halogen interaction is present as the structure directing interaction in all six compounds;

thus activated halogen bonds can be introduced as convenient and predictable interacting groups for nitro functional group to be utilized in co-crystallizations with nitro containing energetic compounds.

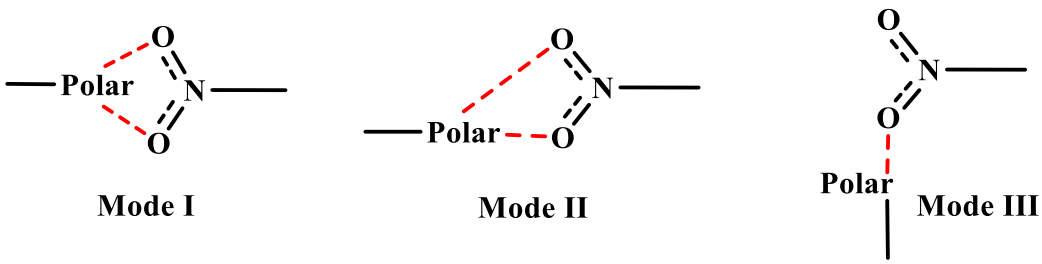

Figure 6.28 Interaction types of a nitro group with a polar group; mode I: symmetric bifurcated type, mode II: asymmetric bifurcated type and mode III: single interaction with oxygen

6.4.4 Electrostatic potentials and success rates in co-crystal formation

It is evident that the iodoethynylnitrobenzenes display more positive electrostatic potential values than other well-known XB donors; *cf.* pentafluoroiodobenzene is about 20 kJ/mol below the value displayed by **3N-I** (the least positive of the three new XB donors) and about 40 kJ/mol below that of **3,5DN-I** which has the highest positive electrostatic potential in this group. The combination of nitro groups and an *sp*-hybridized carbon atoms does afford the desired double activation with a commensurate increase in positive potential. Even this boost in positive electrostatic potential on bromo- or chloro- analogues is enough that all bromo- compounds have MEPS values higher than iodoethynylbenzene while **3,5DN-Cl** has a positive electrostatic potential value of 150 kJ/mol, which is only 6 kJ/mol less than that of iodoethynylbenzene.

The IR analysis showed that in all 45 experiments with an iodoethynylnitrobenzene, the outcome was a co-crystal, Table 6.3 and Figure 6.29, which emphasizes that double activated XB donors represent powerful new tools for robust supramolecular solid-state synthesis.

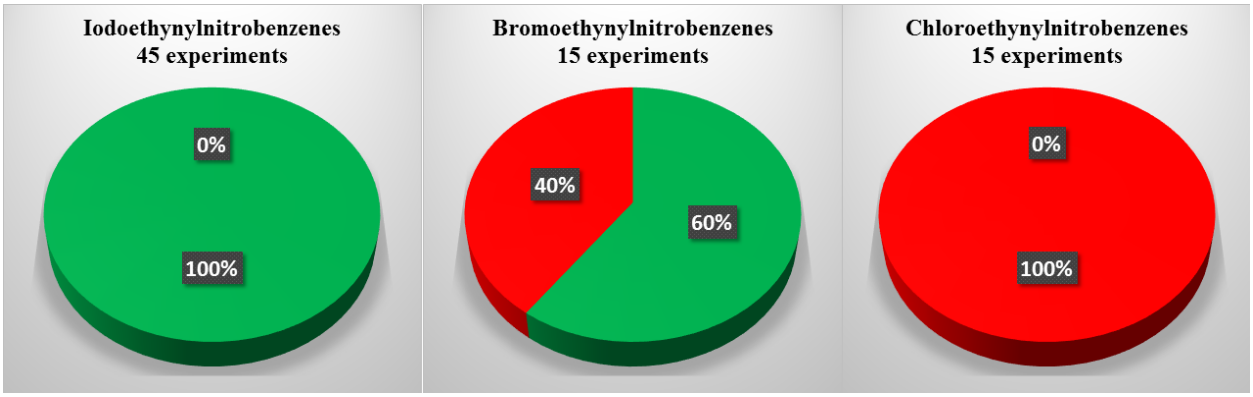

Figure 6.29 Success rates of co-crystallization experiments; green-positive results and red negative results

The inherently lower polarizability of bromine and chlorine, respectively, manifested itself in drastically lower success rates. Only nine of fifteen bromoethynylnitrobenzenes resulted in a co-crystal whereas none of the fifteen attempts with a chloroethynylnitrobenzene produced a co-crystal (Figure 6.29 and Table 6.3). These numbers emphasize the connection between practical co-crystal synthesis capability and calculated electrostatic potential values.

Even though perfluorinated bromine-based XB donors are known,[45] a CSD search for bromoethynylbenzene showed that there are no crystallographically characterized co-crystals reported in the literature where a bromoethynyl moiety drives the co-crystal synthesis. However, by adding an extra activating functionality it is clear that a bromoethynyl group can now drive the formation of co-crystals with suitable XB acceptors by the increment of positive electrostatic potential on the bromine atom.

However, the double activation was not sufficient to make a chlorine atom electrophilic enough to make it a synthetic vector for co-crystal synthesis. Even though theoretical[46] and spectroscopic[47] data show that chlorine atoms can, in principle, form halogen bonds, it does not necessarily mean that such XB donors are strong enough to drive the formation of heteromeric co-crystal in practice.

6.4.5 Grinding experiments and characterization by IR spectroscopy

A close look at the IR spectra for the ten compounds with crystallographic data showed there is a significant red shift of the band associated with the triple bond of the XB donor when compared to the spectrum of the compound itself. Usually, the formation of a C≡C-I···acceptor halogen bond weakens the triple bond which is accompanied by a redshift of the triple bond stretch.[48] However, in some of the grinding experiments a blue shift of the triple bond mode was observed, a possibility which has been noted in some theoretical studies.[49] Different explanations for this kind of blue shifting phenomena are proposed. One such suggestion is that the negative permanent dipole moment derivative of donor molecule is responsible for the blue shifting.[50] All in all there is no clear evidence to exactly explain the reason behind the blue shifting halogen bonds.

As for the nitro stretches, in all ten co-crystals the nitro asymmetric and symmetric stretches show a blue shift. In all these structures, the nitro group is participating in some kind of weak interaction leading to the blue shift of nitro stretching frequencies. Furthermore, for seven out of ten structures IR analysis predicted weak interaction present in the crystal structure, Table 6.4. Thus, the application of IR spectroscopy in determining what type of a weak interaction that a nitro group is involved in, is applicable when designing supramolecules and co-crystals with nitro containing compounds. This simple and effective method can provide much details about the weak interactions of a nitro group whenever structure details from single crystal X-ray diffraction are not available.

6.4.6 The effectiveness of the new halogen bond donors

The remarkable success rate in co-crystal synthesis displayed by these iodoethynylnitrobenzenes leads to questions about the halogen-bond strengths that these donors

can generate and we addressed this in an indirect manner by examining halogen-bond distances in co-crystals of other well-known XB donors with the same acceptor molecules that were employed herein. Obviously a non-covalent bond distance in the solid state does not give a direct measure of 'bond strength' but a systematic comparison of closely related data may offer an important indication of the relative strengths of different interactions. Thus, van der Waals radii reductions (Figure 6.30) can be used as an indirect method to obtain some evidence of bond strengths. The observed reduction in combined van der Waals radii for halogen bonds in reported structures[51] of co-crystals with acceptors that were used in this study are summarized in Figure 6.31.

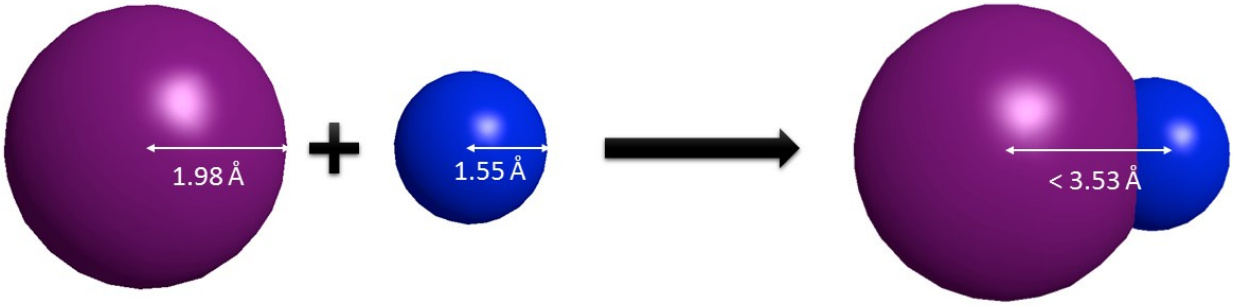

Figure 6.30 Schematic representation of the occurrence of van der Waals radii reduction when a halogen bond is formed between an iodine atom (purple) and a nitrogen atom (blue)

A total of 22 relevant crystal structures distributed over six different acceptors were identified and, remarkably, the I···acceptor distance involving an iodoethynylnitrobenzene XB donor was the shortest for each of the six donors. Apart from the results provided in Figure 6.31, the C-I···O bond in the co-crystal **3,5DN-I:A34** with a distance of 2.673(3) Å represents one of the shortest C-I···O bonds in the reported structures. It is shorter than the previously reported short C-I···O halogen bonds with **A30**,[52] **A35**[53] and electron rich carbonyl compounds.[54] A much shorter C-I···O halogen bond is reported with t-BuOK but the shortness of the interaction is presumably due to high ionic character of the oxygen atom.[55] The increased reductions in combined van der Waals radii and short C-I···acceptor bond lengths do suggest that this new group of XB donors

represents a very important addition to the reliable and robust synthetic tools[56] that are essential to practical supramolecular synthesis.

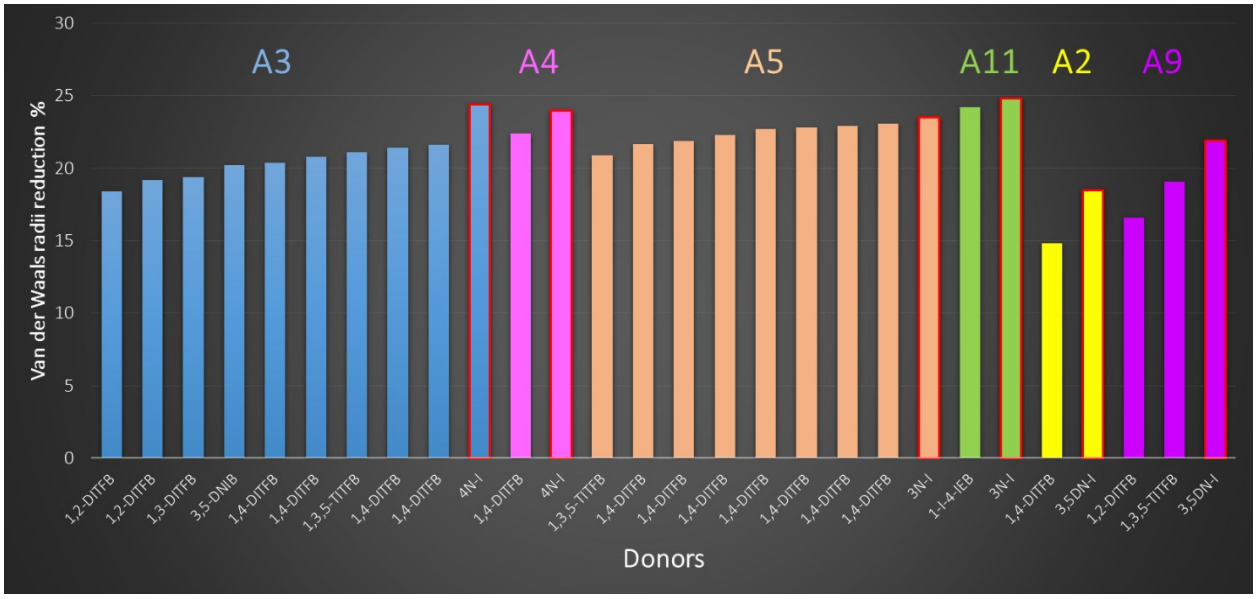

Figure 6.31 Van der Waals radii reduction comparison; for each acceptor category structures obtained in this study are highlighted in red

6.5 Conclusions

Nine novel halogen-bond donors based on the double activation phenomena were synthesized and the structure analysis of the novel compounds revealed the possibility of utilizing the nitro···ethynyl-activated halogen synthon in structure directing interactions in complex systems and the ability to act as effective halogen-bond donors, Figure 6.32. The initial IR screening results for the systematic co-crystallizations (75 experiments) showed the success rate to be 100% for iodoethynylnitrobenzene compounds and 60% for the bromethynylnitrobenzenes while none of the chloroethynyllnitrobenzenes formed co-crystals. The results can be readily rationalized against calculated molecular electrostatic surface potentials which serves to emphasize the importance of the electrostatic contributions to halogen bonds in practical supramolecular synthesis. These iodoethynylnitrobenzenes may be the most effective and powerful halogen-bond donors to be

explored to date which, coupled with their ease of synthesis, is likely to make them valuable additions to the crystal engineering tool box.

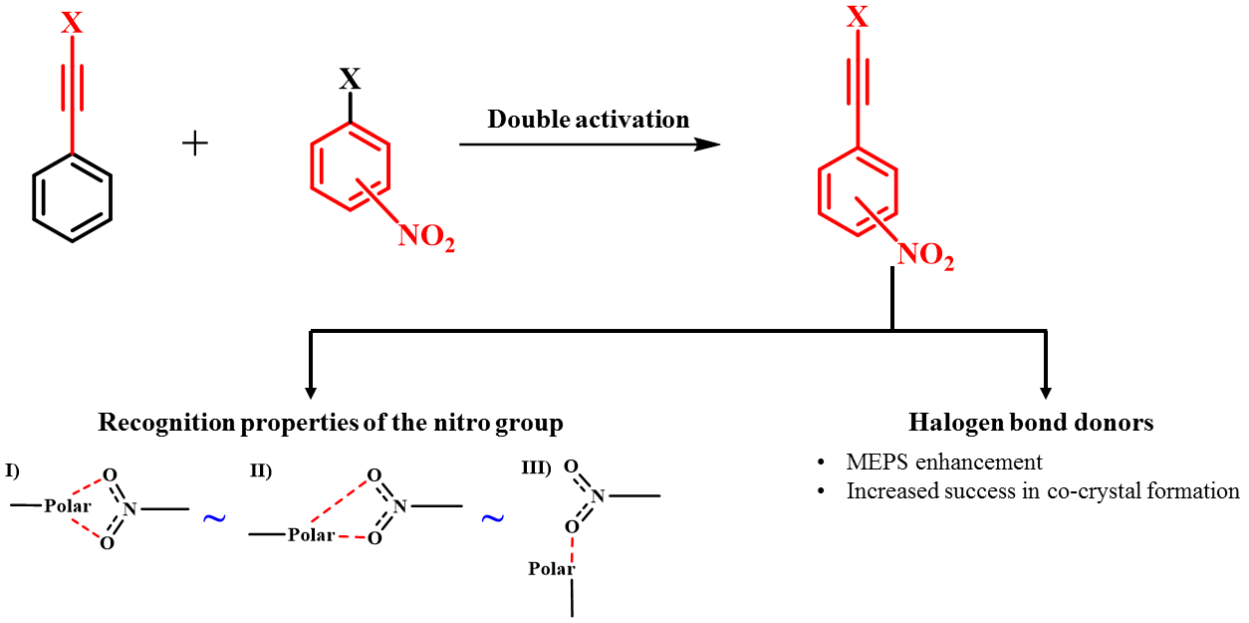

Figure 6.32 Outcome of the study

6.6 References

1. Aakeröy, C.B.; Wijethunga, T.K.; Desper, J.; Đakovic, M. *Cryst. Growth Des.* **2015**, *15*, 3853-3861.

2. Politzer, P; Lane, P; Concha, M.C.; Ma, Y.; Murray, J.S. *J. Mol.Model*. **2007**, *13*, 305-311; Legon, A.C. *Phys. Chem. Chem. Phys.* **2010**, *12*, 7736-7747; Metrangolo, P.; Resnati, G. *Chem. Eur.J.* **2001**, *7*, 2511-2519.

3. Meyer, F.; Dubois, P. *CrystEngComm* **2013**,*15*, 3058-3071; Wilcken, R.; Zimmermann, M.O.; Lange, A.; Joerger, A.C.; Boeckler, F. M. *J. Med. Chem*. **2013**, *56*, 1363-1388.

4. Riley, K.E.; Murray, J.S.; Fanfrlík, J.; Řezáč, J.; Solá, R.J.; Concha, M.C.; Ramos, F.M.; Politzer, P. *J. Mol.Model.* **2013**, *19*, 4651-4659; Metrangolo, P.; Neukirch, H.; Pilati, T.; Resinati, G. *Acc. Chem. Res*. **2005**, *38*, 386-395; Politzer, P.; Murray, J.S.; Clark, T. *Phys. Chem. Chem. Phys.* **2010**, *12*, 7748-7757

5. Desiraju, G.R.; Ho, P.S.; Kloo, L.; Legon, A.C.; Marquardt, R.; Metrangolo, P.; Politzer, P.; Resnati, G.; Rissanen. K. *Pure Appl. Chem*. **2013**, *85*, 1711-1713.

6. Politzer, P.; Murray, J.S.; Clark, T. *Phys. Chem. Chem. Phys.* **2013**, *15*, 11178-11189; Clark, T.; Hennemann, M.; Murray, J.S.; Politzer, P. *J. Mol. Model*. **2007**, *13*, 291-296.

7. Aakeröy, C.B.; Wijethunga, T.K.; Desper, J. *J. Mol. Struct*. **2014**, 1072, 20-27; Fourmigué, M. *Curr. Opin. Solid State Mater. Sci*. **2009**, *13*, 36-45.

8. McDowell, S.A.C. *Chem. Phys. Lett.* **2014**, *598*, 1-4; Politzer, P.; Riley, K.R.; Bulat, F.A.; Murray, J.S. *Comp. Theor. Chem*. **2012**, *998*, 2-8.

9. Bauzá, A.; Quiñonero, D.; Frontera, A.; Deyà, P.M. *Phys. Chem. Chem. Phys*. **2011**, *13*, 20371-20379.

10. Aakeröy, C.B.; Wijethunga, T.K.; Haj, M.A.; Desper, J.; Moore, C. *CrystEngComm* **2014**, *16*, 7218-7225.

11. Raatikainen, K.; Rissanen, K. *CrystEngComm* **2009**, *11*, 750-752.

12. Langton, M.J.; Robinson, S.W.; Marques, I.; Félix, V.; Beer, P.D. *Nat. Chem*. **2014,** *6*, 1039-1043; Taylor, M.S. *Nat. Chem*. **2014**, *6*, 1029-1031.

13. Politzer, P.; Laurence, P.R.; Jayasuriya, K. *Environ. Health Persp.* **1985**, *61*, 191-202; Hagelin, H.; Murray, J.S.; Brinck, T.; Berthelot, M.; Politzer, P. *Can. J. Chem*. **1995**, *73*, 483-488; Aakeröy, C.B.; Wijethunga, T.K.; Desper, J. *New J. Chem.* **2015**, *39*, 822-828.

14. Präsang, C.; Whitwood, A.C.; Bruce, D.W. *Cryst. Growth Des.* **2009**, *9*, 5319-5326.

15. Perkins, C.; Libri, S.; Adams, H.; Brammer, L. *CrystEngComm* **2012**, *14*, 3033-3038; González, L.; Gimeno, N.; Tejedor, R.M.; Polo, V.; Ros, M.B.; Uriel, S.; Serrano, J.L. *Chem. Mater.* **2013**, *25*, 4503-4510; Goroff, N.S.; Curtis, S.M.; Webb, J.A.; Fowler, F.W.; Lauher, J.W. *Org. Lett*. **2005**, *7*, 1891-1893.

16. Dahl, T. *Acta Cryst*. **1999**, *C55*, 1568-1570; Padgett, C.W.; Walsh, R.D.; Drake, G.W.; Hanks, T.W.; Pennington; W.T. *Cryst. Growth Des*. **2005**, *5*, 745-753; Webb, J.A.; Liu, P.; Malkina, O.L.; Goroff. N.L. *Angew. Chem. Int. Ed*. **2002**, *41*, 3011-3014.

17. Bosch, E. *Cryst. Growth Des*. **2014**, *14*, 126-130; Lieffrig, J.; Jeannin, O.; Fourmigu, F. *J. Am. Chem. Soc*. **2013**, *135*, 6200-6210.

18. Lieffrig, J.; Jeannin, O.; Frąckowiak, A.; Olejniczak, I.; Świetlik, R.; Dahaoui, S.; Aubert, E.; Espinosa, E.; Senzier, P.A.; Fourmigu, M. *Chem. Eur. J.* **2013**, *19*, 14804-14813; Clark, T.; Murray, J.S.; Politzer, P. *Aust. J. Chem*. **2013**, *67*, 451-456

19. Metrangolo, P.; Murray, J.S.; Pilati, T.; Politzer, P.; Resnati, G.; Terraneo, G. *CrystEngComm* **2011**, *13*, 6593-6596; Lommerse, J.; Stone, A.; Taylor, R. *J. Am. Chem. Soc.* **1996**, *118*, 3108-3116.

20. The ortho substituted iodoethynylnitrobenzene compound was successfully synthesized but it was quite unstable. Thus did not use in any co-crystallization experiments.

21. Forni, A. *J.Phys.Chem.A* **2009**, *113*, 3403-3412.

22. Allen, F. H.; Baalham, C. A.; Lommerse, J. P. M.; Raithby P. R.; Sparr, E. *Acta Crystallogr., Sect. B* **1997**, *53*, 1017- 1024; Steiner, T. *New J. Chem.* **1998**, *22*, 1099-1103.

23. Matzger, A.; Bolton, O. *US Pat* 20120305150 A1, **2012**; Yang, Z.; Wang, Y.; Zhou, J.; Li, H.; Huang, H.; Nie, F. *Propellants Explos. Pyrotech*. **2014**, *39*, 9-13; Zhang, C.; Cao, Y.; Li, H.; Zhou, Y.; Zhou, J.; Gao, T.; Zhang, H.; Yang, Z.; Jiang, G. *CrystEngComm* **2013**, *15*, 4003-4014; Bolton, O.; Matzger, A. *Angew. Chem. Int. Ed*. **2011**, *50*, 8960-8963.

24. Zhang, C.; Shu, Y.; Huang, Y.; Zhao, X.; Dong, H. *J. Phys. Chem. B* **2005**, *109*, 8978-8982; Galik, M.; OMahony, A.M.; Wang, J.; *Electroanalysis* **2011**, *23*, 1193-1204; Zhang, C. *J. Hazard. Mater.* **2009**, *161*, 21–28; Agrawal, J.P.; Hodgson, R. *Organic Chemistry of Explosives*, John Wiley & Sons, **2007**.

25. Landenberger, K.B.; Bolton, O.; Matzger, A.J. *Angew. Chem. Int. Ed.* **2013**, *52*, 6468-6471; Vishnoi, P.; Walawalkar, M.G.; Murugavel, R. *Cryst. Growth Des*. **2014**, *14*, 5668-5673; Wang, Y.; Yang, Z.; Li, H.; Zhou, X.; Zhang, Q.; Wang, J.; Liu, Y. *Propellants Explos. Pyro, tech*. **2014**, *39*, 590-596; Landenberger, K.B.; Matzger, A.J. *Cryst. Growth Des.* **2012**, *12*, 3603-3609; Zhang, H.; Guo, C.; Wang, X.; Xu, J.; He, X.; Liu, Y.; Liu, X.; Huang, H.; Sun, J. *Cryst. Growth Des.* **2013**, *13*, 679-687.

26. Bolton, O.; Matzger, A.J. *Angew. Chem. Int. Ed*. **2011**, *50*, 8960-8963; Landenberger, K.B.; Matzger, A.J. *Cryst. Growth Des.* **2010**, *10*, 5341-5347.

27. Bruno, I. J.; Cole, J. C.; Lommerse, J. P. M.; Rowland, R. S.; Taylor, R.; and Verdonk, M. L. *J. Comput. Aided Mol. Des.* **1997**, *11*, 525-537; Battle, G. M.; Allen, F. H. *J. Chem. Ed.* **2012**, *89*, 38-44.

28. Raatikainen, K.; Rissanen, K. *CrystEngComm* **2009**, *11*, 750-752; Stein, M.; Schwarzer, A.; Hulliger, J.; Weber, E. *Acta Cryst*. **2011**, *E67*, o1655.

29. Dumele, O.; Wu, D.; Trapp, N.; Goroff, N.; Diederich, F. *Org. Lett.* **2014**, *16*, 4722-4725; Banday, A. H.; Hruby, V.J. *Synlett* **2014**, *25*, 2463-2466; Yan, J.; Li, J.; Cheng, D. *Synlett* **2007**, *15*, 2442-2444; Ricci, A.; Taddei, M.; Dembech, P.; Guerrini, A.; Seconi, G. *Synthesis* **1989**, *6*, 461-463; Laurence, C.; Queignec-Cabanetos, M.;

Wojtkowiak, B. *Can. J. Chem.* **1983**, *61*, 135-138; Wilson, C. J.; Wenzke, H. H. *J. Am. Chem. Soc.* **1934**, *56*, 2025-2027.

30. Chen, X.Y.; Wang, L.; Frings, M.; Bolm, C. *Org. Lett.* **2014**, *16*, 3796-3799; Li, Y.B.; Liu, X.H.; Jiang, H.f.; Liu, B.F.; Chen, Z.W.; Zhou, P. *Angew. Chem. Int. Ed.* **2011**, 50, 6341-6345, Leyva-Perez, A.; Rubio-Marques, P.; Al-Deyab, S.S.; Al-Resayes, S.I.; Corma, A. *ACS Catal.* **2011**, *1*, 601-606.

31. Gulia, N.; Pigulski, B.; Charewicz, M.; Szafert, S. *Chem. Eur. J.* **2014**, *20*, 2746-2749; Tang, J.S.; Tian, M.; Sheng, W.B.; Guo, C.C. *Synthesis* **2012**, *44*, 541-546; Vilhelmsen, M.H.; Andersson, A.S.; Nielsen, M.B.; *Synthesis* **2012**, *44*, 158.

32. Meng, L.G.; Cai, P.J.; Guo, Q.X.; Xue, S. *Synth. Commun*. **2008**, *38*, 225-231.

33. Yanga, Y.; Huanga, H.; Liua W.; Lianga, Y. *Synth. Commun*. **2015**, *45*, 86-93; Chen, X.Y.; Wang, L.; Frings, M.; Bolm, C. *Org. Lett.* **2014**, *16*, 3796-3799; Chen, Z.W.; Ye, D.N.; Ye, M.; Zhou, Z.G.; Li, S.H.; Liu, L.X. *Tetrahedron Lett*. **2014**, *55*, 1373-1375; Alberti, A.; Pedulli, G.F.; Ciminale, F. *Tetrahedron* **1982**, *38*, 3605-3608.

34. An, D.; Liu, S.; Shi, L.; Feng, L.; Peng, Z. *Pat.* CN 103524281, **2014**.

35. Aakeröy, C.B.; Wijethunga, T.K.; Desper, J. *CrystEngComm* **2014**, *16*, 28-31.

36. Iranpoor, N.; Firouzabadi, H.; Khalili, D.; Motevalli, S. *J. Org. Chem*. **2008**, *73*, 4882-4887.

37. Ayyangar, N.R.; Naik, S.N.; Srinivasan, K.V. *Tetrahedron Lett*. **1989**, *30*, 7253-7256.

38. Saha, S.; Ganguly, S.; Desiraju, G.R. *Aust. J. Chem.* **2014**, *67*, 1840-1848.

39. CSD ConQuest 1.17, **2013** Cambridge Crystallographic Data Centre, U.K.

40. Spartan'08, Wavefunction, Inc.

41. The powder data were collected at Max Planck Institute for Solid State Research, Germany, by Dr. Tomce Runcevski, manuscript in´ preparation.

42. Saha, S.; Rajput, L.; Joseph, S.; Mishra, M.K.; Ganguly, S.; Desiraju, G.R. *CrystEngComm* **2015**, *17*, 1273-1290.

43. Sonogashira, K.; Tohda, Y.; Hagihara, N. *Tetrahedron Lett.* **1975**, *16*, 4467-4470; Chinchilla, R.: Najera, C. *Chem. Soc. Rev.* **2011**, *40*, 5084-5121.

44. Li, M.; Li, Y.; Zhao, B.; Liang, F.; Jin, L.Y. *RSC Adv.* **2014**, *4*, 30046-30049.

45. Santis, A.D.; Forni, A.; Liantonio, L.; Metrangolo, P.; Pilati, T.; Resnati, D. *Chem. Eur. J.* **2003**, *9*, 3974-3983.

46. Bene, J.E.D.; Alkorta, I.; Elguero, J. *J. Phys. Chem. A* **2010**, *114*, 12958-12962.

47. Feng, G.; Evangelisti, L.; Gasparini, N.; Caminati, W. *Chem. Eur. J.* **2012**, *18*, 1364-1368.

48. Aakeröy, C.B.; Baldrighi, M.; Desper, J.; Metrangolo, P.; Resnati, G. *Chem. Eur. J.* **2013**, *19*, 16240-16247.

49. Wang, W.; Wong, N.; Zheng, W.; Tian, A. *J. Phys. Chem. A* **2004**, *108*, 1799-1805; Wang, W.; Zhang, Y.; Ji, B. *J. Phys. Chem. A* **2010**, *114*, 7257-7260.

50. Hermansson, K. *J. Phys. Chem. A* **2002**, *106*, 4695-4707.

51. CSD ConQuest 1.17, **2013**, Cambridge Crystallographic Data Centre, U.K.

52. Messina, M.T.; Metrangolo, P.; Panzeri, W.; Pilati, T.; Resnati, G. *Tetrahedron* **2001**, 57, 8543-8550; Bianchi, R.; Forni, A.; Pilati, T. *Acta Cryst.* **2004**, *B60*, 559-568; Forni, A.; Metrangolo, P.; Pilati, T.; Resnati, G. *Cryst. Growth Des.* **2004**, *4*, 291-295.

53. Aakeröy, C.B.; Chopade, P.D.; Desper, J. *Cryst. Growth Des.* **2013**, *13*, 4145-4150.

54. Geer, M.F.; Mazzuca, J.; Smith, M.D.; Shimizu, L.S. *CrystEngComm* **2013**, *15*, 9923-9929.

55. Xu, L.; Cramer, R.E.; Vicic, D.A. *J. Fluorine Chem.* **2015**, DOI: 10.1016/j.jfluchem.2015.04.008.

56. Etter, M.C.; Frankenbach, G.M. *Chem. Mater.* **1989**, *1*, 10-12; Etter, M.C. *Acc. Chem. Res.* **1990**, *23*, 120-126.

Chapter 7 - Constructing molecular polygons using halogen bonding and bifurcated N-oxides[1]

7.1 Introduction

N-oxides represent an interesting group of molecules that are highly polar due to the charge separation of the N-O bond.[2] The oxygen atom in the N-oxide group of heteroaromatic N-oxide is in a state of sp^2-hybridization in conjugation with a heteroaromatic ring,[3] which lead to their high water solubility[4] and lipophobicity.[5] N-oxides have found applications as ligands in metal coordination complexes[6] and they have been used as synthetic intermediates,[7] biologically important compounds,[8] drugs,[9] protecting groups, auxiliary agents, photo-active compounds,[10] oxidants and in catalysis.[11]

One of the significant structural characteristic of N-oxides is their ability to form bifurcated non-covalent bonds.[12] Bifurcation can be defined as the participation of one atom in two or more different intermolecular interactions,[13] and this is well known in many hydrogen-bonded systems where the N-oxide oxygen atom is interacting with two different hydrogen-bond donors simultaneously, Figure 7.1.[14] An examination of known N-oxide crystal structures with bifurcated bonds shows that most of the time the bifurcated angle (donor···O···donor) is close to 120°.

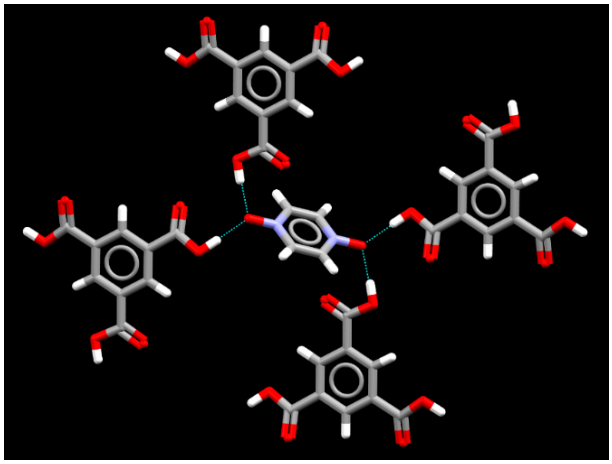

Figure 7.1 Bifurcated interactions with pyrazine-*bis*-N-oxide[15]

Heteroaromatic N-oxides have shown to interact effectively as electron donors towards perfluorocarbon iodides.[16] Despite the many similarities between hydrogen bonding and halogen bonding, there are no reports on the deliberate use of bifurcated halogen bonds in combination with N-oxides to assemble supramolecular architectures with predetermined topologies and stoichiometries. Hypothetically, such an assembly should be possible as the halogen bond is mainly electrostatic in nature, and involves an electropositive σ-hole on a halogen atom and an electron-pair donor.[17]

Many elegant approaches for the synthesis of discrete polygons in the solid state have been presented using coordinate-covalent bonds as the primary synthetic tool;[18] this is mainly due to the reason that the geometries around the metals are fixed, and thus selecting the proper metals with proper coordination geometry leads to the desired outcome. In comparison, relatively few efforts using purely organic building blocks are known to assemble such deliberate architectures.[19] There are reports where halogen bonds have been used with nitroxides[20] and ions as halogen bond linkers[21] for polygon designing to some extent, Figure 7.2, but halogen bonds have not been used in the deliberate construction of well-defined polygons in the solid state, where all interactions are rationalized in a synthetic strategy.

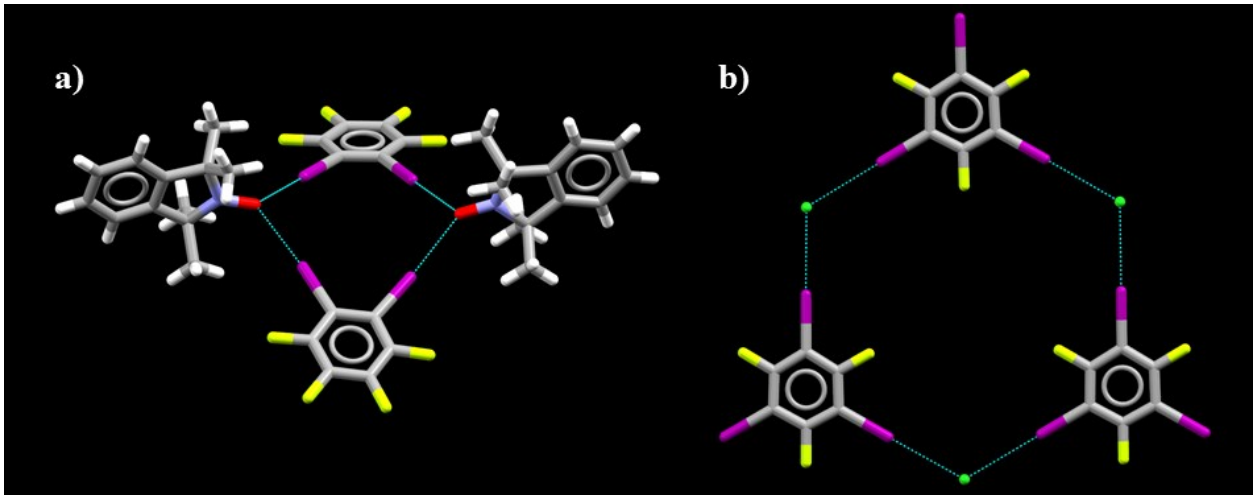

Figure 7.2 Halogen-bond based polygons a) with radicals[20] b) with ions[21]

Thus, this study was conducted in an attempt to make supramolecular polygons (rhombuses and hexagons) utilizing the bifurcated nature of N-oxides and the halogen bonding, Figure 7.3.

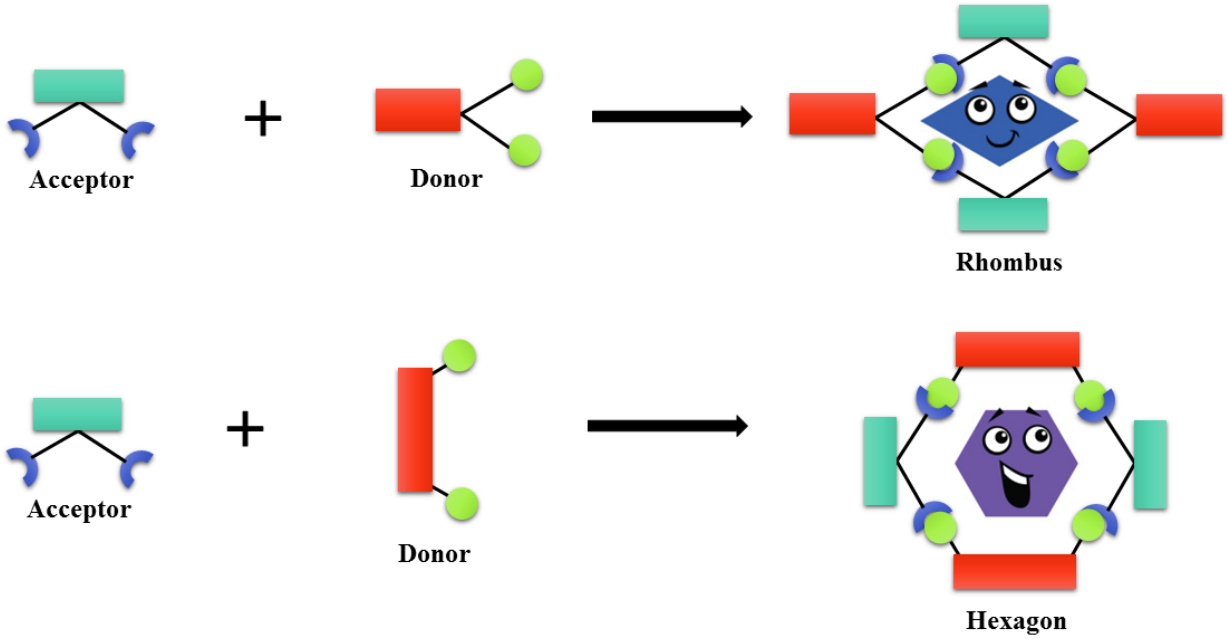

Figure 7.3 Design strategy for molecular rhombus and hexagon

Ten N-oxides were employed as potential halogen-bond acceptors (six *mono*-N-oxides and four *bis*-N-oxides), Figure 7.4.

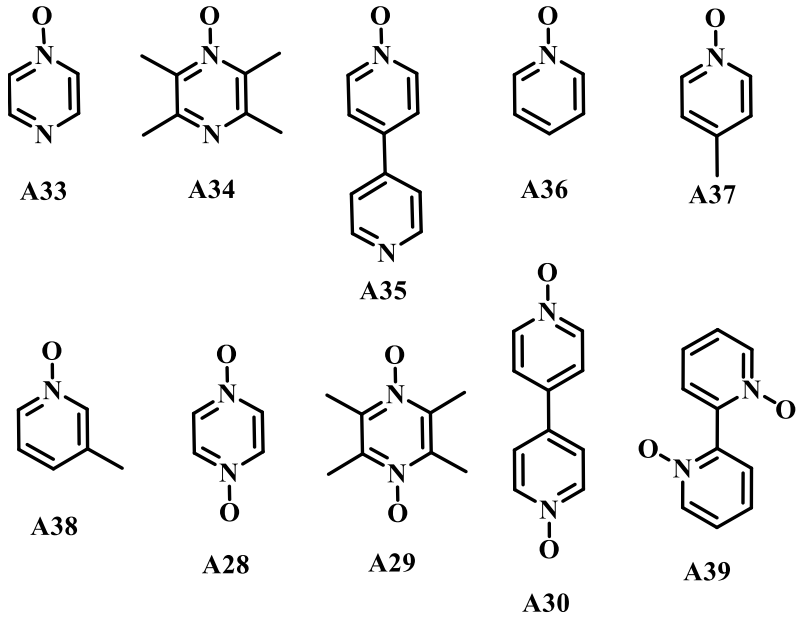

Figure 7.4 Library of N-oxides under study

The halogen-bond donors were selected such that the relative orientation of their donor sites would offer the appropriate geometric complementarity to the most commonly observed angle in bifurcated N-oxides in order to enable to assembly of the desired polygons.

In order to build a rhomb, a donor molecule with an approximate angle of 60° between the two donor sites to complement the inherent X···O···X bond angle of 120° in a bifurcated N-oxide acceptor site was needed as this would complete the overall 360° requirement, Figure 7.5. In order to make a hexagon, the donor moieties needed to be positioned at a 120° angle with respect to each other resulting in a total sum of 720° for the desired synthetic target, Figure 7.5.

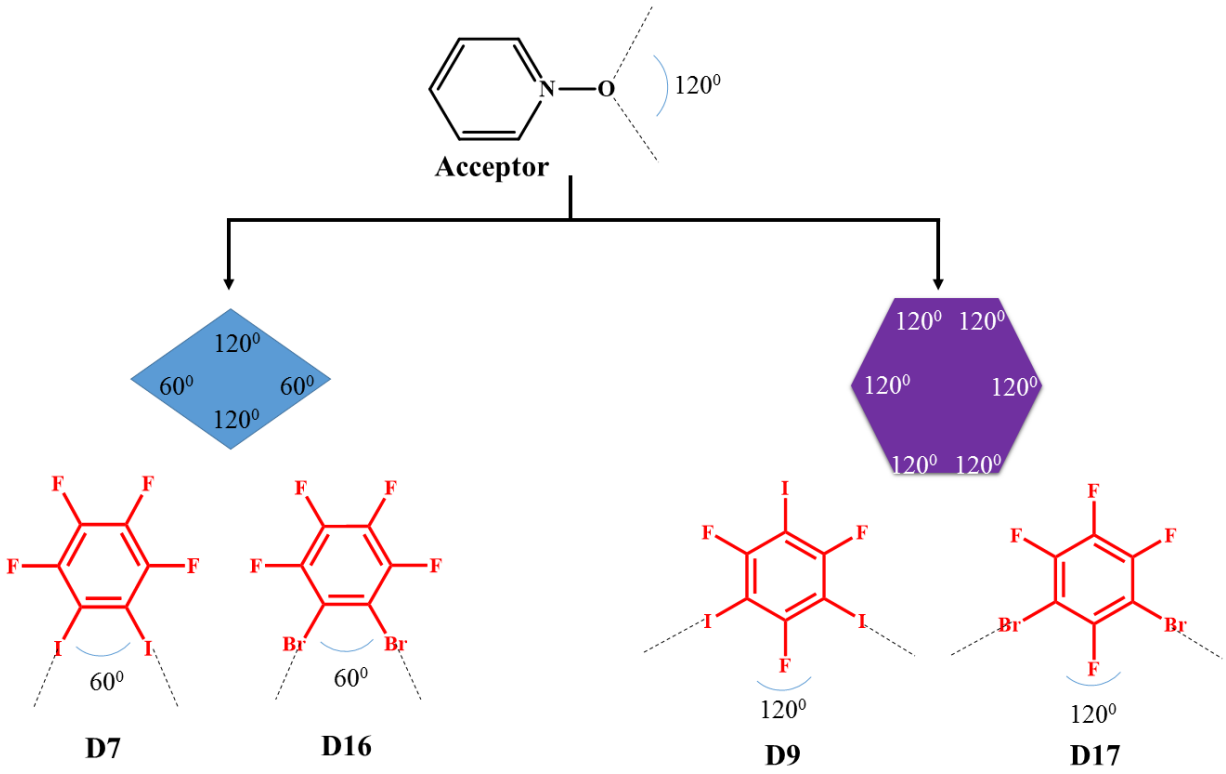

Figure 7.5 Halogen-bond donors and selection rationale

Furthermore, it was assumed that a switch from a monotopic acceptor molecule to a *bis*-N-oxide, should change the outcome from discrete architectures to chains of polygons, Figure 7.6.

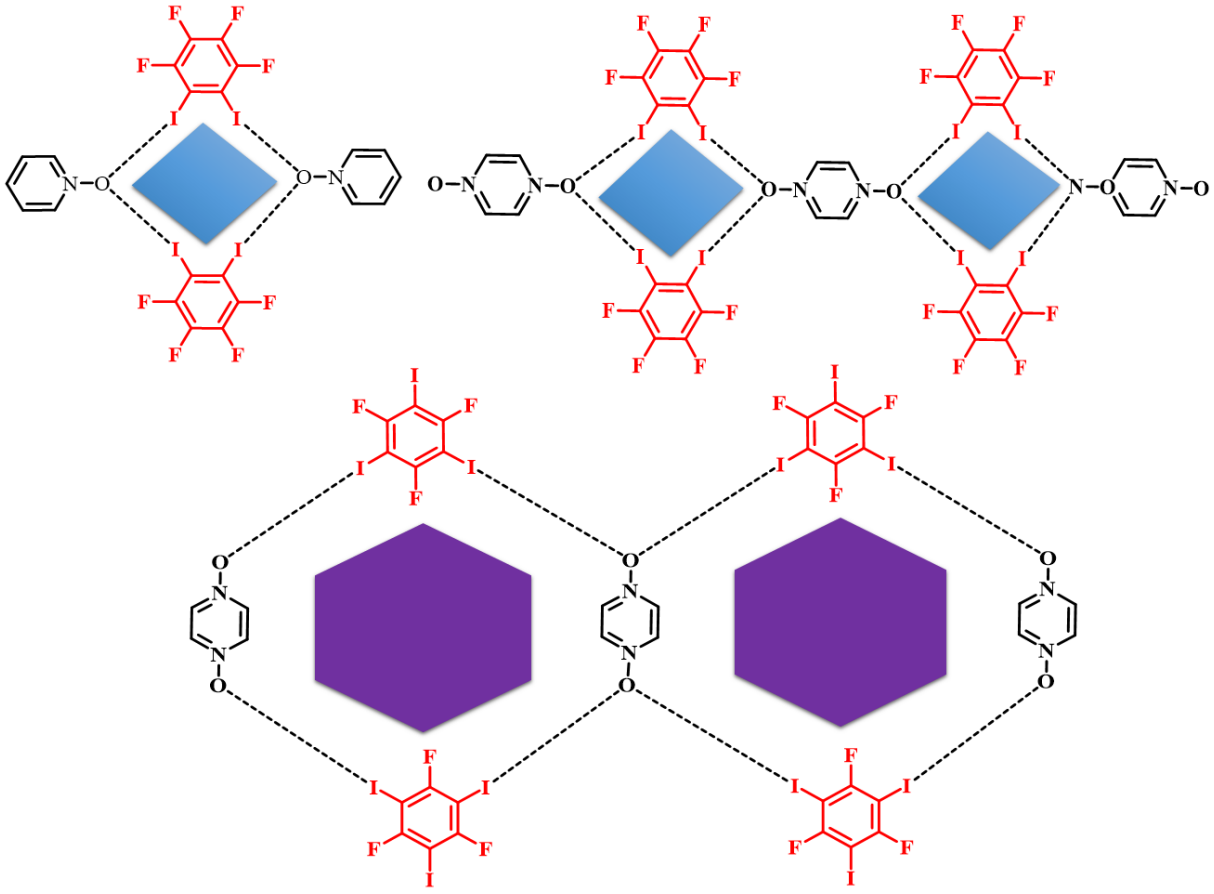

Figure 7.6 Design of discrete and chains of polygons

The study is undertaken in response to two hypotheses,

1. Complementarity of geometry and angles between the two compounds leads to the successful polygon formation
2. Iodo-compounds are better halogen-bond donors than their bromo-analogues

7.2 Experimental

7.2.1 General

A33-A35 were prepared using a previously reported method.[22] The method was modified in order to obtain both *mono*- (**A33-A35**) and *bis*- (**A28-A30**) products at once. **A36-A39** and halogen-bond donors were purchased from commercial sources and used without further

purification. ^{1}H NMR spectra were recorded on a Varian Unity plus 400 MHz spectrometer in $CDCl_3$ or DMSO-d_6. Infrared spectra were recorded with a Nicolet 380 FT-IR with a digital resolution of 0.9 cm^{-1} and data processed using Omnic[23] software. Melting points were determined using Fischer-Johns Mel-Temp melting point apparatus and are uncorrected.

7.2.2 Synthesis of N-oxides

7.2.2.1 Synthesis of pyrazine-N-oxide (A33) and pyrazine-bis-N-oxide (A28)

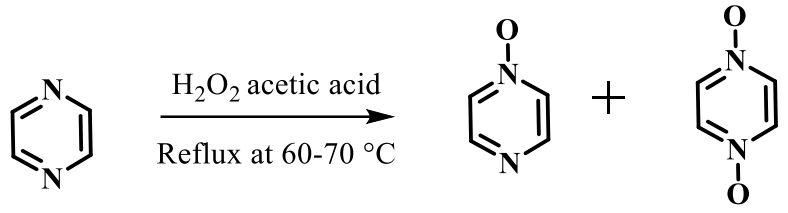

A33 **A28**

A solution of 30% hydrogen peroxide (2.8 g, 0.084 mol) in 20 mL of acetic acid was added dropwise using a drop funnel over a period of 2.5 hours to a solution of pyrazine (1.0 g, 0.013 mol) in 15 mL of acetic acid at 70-80 °C. Refluxing was continued for about 24 hours until the TLC confirmed the presence of two products. Acetic acid was removed on a rotary evaporator, and then 10 mL of water was added followed by evaporation. The residue was dissolved in 50 mL of hot chloroform and dried with a mixture of sodium sulfate and sodium carbonate and the solvent was removed on a rotary evaporator. The residue was chromatographed on silica with variant ratio mixtures of chloroform:methanol as the eluant. **A33** and **A28** were isolated as off white solids. **A33 -** Yield: 0.48 g (77%); m.p. 110-113 °C (reported 113-115 °C)[24]; ^{1}H NMR (400 MHz, $CDCl_3$): 8.47 (d, 2H), 8.09 (d, 2H); **A28** - Yield: 0.37 g (50%), m.p. > 300 °C (reported > 300 °C)[25]; ^{1}H NMR (400 MHz, DMSO-d_6): 8.27 (s, 4H).

7.2.2.2 Synthesis of tetramethylpyrazine-N-oxide (A34) and tetramethylpyrazine-bis-N-oxide (A29)

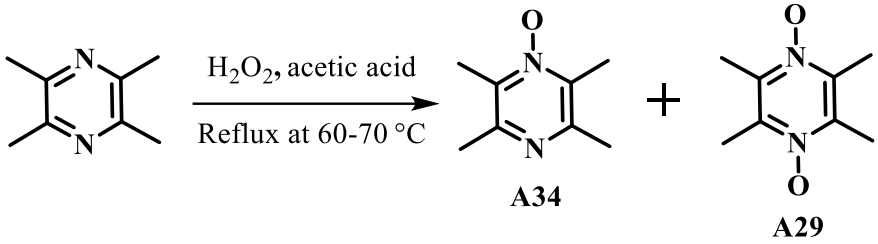

A solution of 30% hydrogen peroxide (2.8 g, 0.084 mol) in 20 mL of acetic acid was added dropwise using a drop funnel over a period of 2.5 hours to a solution of tetramethylpyrazine (1.8 g, 0.013 mol) in 15 mL of acetic acid at 70-80 °C. Refluxing was continued for about 24 hours until the TLC confirmed the presence of two products. Acetic acid was removed using a rotary evaporator, 10 mL of water was added followed by evaporation. The residue was dissolved in 50 mL of hot chloroform and dried with a mixture of sodium sulfate and sodium carbonate and the solvent removed on a rotary evaporator. The residue was chromatographed on silica with variant ratio mixtures of chloroform-methanol as the eluant. **A34** was isolated as an off white solid and **A29** was isolated as a pure white solid. **A34** - Yield: 0.65 g, 66%), m.p. 97-99 °C (reported 98-100 °C)[22]; ^{1}H NMR (400 MHz, $CDCl_3$): 2.51 (d, 6H), 2.46 (d, 6H); **A29** - Yield: 0.58 g (53%), m.p. 220-222 °C; ^{1}H NMR (400 MHz, $CDCl_3$): 2.56 (s, 12H).

7.2.2.3 Synthesis of 4,4'-bipyridine-N-oxide (A35) and 4,4'-bipyridine-bis-N-oxide (A30)

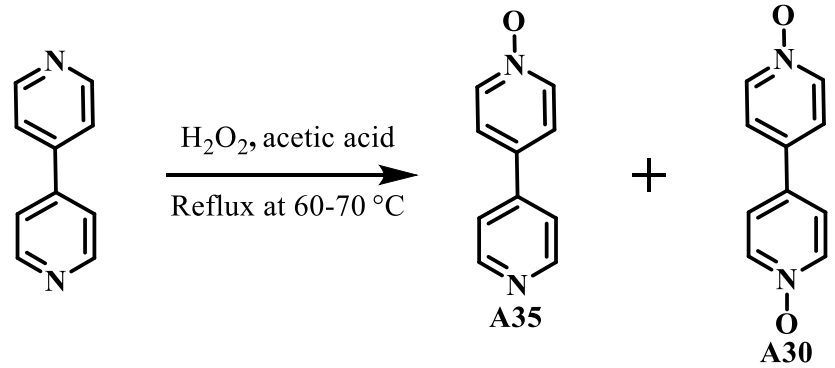

A mixture of 4,4′-bipyridine (2.0 g, 13 mmol), 30% hydrogen peroxide (2.7 g, 78 mmol) and glacial acetic acid (25 mL) was stirred in a round bottom flask for 24 hours at 70 °C. Reaction

was monitored with TLC and after completion, reaction mixture was cooled to room temperature and the solvent was removed via a rotary evaporator and diluted with 20 mL water. The solution was basified with excess sodium carbonate (2.0 g) and extracted with chloroform (3 x 50 mL). The organic layers were combined and then concentrated under reduced pressure using a rotary evaporator. Mixture was further purified via column chromatography with variant mixtures of ethyl acetate-methanol. **A35** and **A30** were isolated as off white solids. **A35** - Yield: 0.78g (70%); m.p. 170-172 °C (reported 170-171 °C)[22]; ^{1}H NMR (400 MHz, DMSO-d_6): 8.69 (d, 2H), 8.34 (d, 2H), 7.93 (d, 2H), 7.81 (d, 2H); **A30** - Yield: 0.43 g (34%); m.p. 297-299 °C; ^{1}H NMR (400 MHz, $CDCl_3$): 8.74 (d, 4H), 7.53 (d, 4H).

7.2.3 Grinding experiments and IR spectroscopy

The synthetic procedure follows well-established solvent-assisted grinding protocols for co-crystallization reactions.[26] All ten N-oxides were subjected to grinding experiments with four donors. For grinding, 1:1 stoichiometric amounts of acceptors and halogen-bond donors were mixed together and ground using a drop of methanol for several minutes. Each resulting solid was analysed using IR spectroscopy in order to establish if the reaction resulted in a co-crystallization or simply a physical mixture of the two reactants (a re-crystallization). A total of 40 grinding experiments were carried out and the desired outcomes were,

1. Discrete tetrameric rhombi in reactions between 1,2-disubstituted donors and *mono*-N-oxide acceptors
2. Chains of rhombi when 1,2-disubstituted donors and *bis*-N-oxides were employed
3. Chains of hexagons when the 1,3- halogenated donors were allowed to react with *bis*-N-oxides

All in all, fifteen of the 40 experiments provided unambiguous IR spectroscopic evidence for co-crystal formation.

7.2.4 Synthesis of co-crystals

Once a co-crystalline phase had been obtained, we attempted to grow crystals for single-crystal diffraction. The solid ground mixtures were dissolved in 2 mL of methanol and kept in a slightly open vial for the single crystal formation. Once the crystals are formed they were analyzed using IR spectroscopy. Structures were obtained for five co-crystals: **A36:D9**, **A37:D7**, **A29:D7**, **A38:D7** and **A29:D9**. Table 7.1 summarizes the experimental details. Appendix B.6 contains the relevant X-ray experimental data.

Table 7.1 Experimental details of the five co-crystals obtained

Code	Mixed Mole ratio	Amounts used	Solvent and method	Crystal stoichiometry	Melting point °C	Crystal color & habit
A36:D9	1:1	**A36** -10 mg, 0.10 mmol **D9** - 54 mg, 0.10 mmol	Methanol, Slow evaporation	1:1	210-212	Colorless plate
A37:D7	1:1	**A37** - 10 mg, 0.09 mmol **D7** - 37 mg, 0.09 mmol	Methanol, Slow evaporation	1:1	165-167	Colorless prism
A29:D7	1:1	**A29** - 10 mg, 0.059 mmol **D7** - 24 mg, 0.059 mmol	Methanol, Slow evaporation	1:1	118-120	Colorless prism
A38:D7	1:1	**A38** - 10 mg, 0.092 mmol **D7** - 37 mg, 0.092 mmol	Methanol, Slow evaporation	1:2	120-123	Colorless cube
A29:D9	1:1	**A29** - 10 mg, 0.059 mmol **D9** - 30 mg, 0.059 mmol	Methanol, Slow evaporation	1:1	153-155	Colorless prism

7.3 Results

7.3.1 Grinding experiments and characterization by IR spectroscopy

Fifteen of the 40 experiments provided unambiguous IR spectroscopic evidence for co-crystal formation, resulting in a supramolecular yield of 37.5% (15/40). None of the bromo-substituted donors produced a co-crystal, resulting in an effective success rate of 75% (15/20) for the iodo-based donors, Table 7.2. Detailed IR analysis is provided in Appendix C.3.

Table 7.2 Grinding IR analysis

		Donors				% Success	
		D7	D9	D16	D17		
Acceptors	A33	✓	✓	✗	✗	2/4	50
	A34	✓	✓	✗	✗	2/4	50
	A35	✓	✓	✗	✗	2/4	50
	A36	✗	✓	✗	✗	1/4	25
	A37	✗	✓	✗	✗	1/4	24
	A38	✓	✓	✗	✗	2/4	50
	A28	✗	✗	✗	✗	0/4	0
	A29	✓	✓	✗	✗	2/4	50
	A30	✓	✓	✗	✗	2/4	50
	A39	✗	✓	✗	✗	1/4	25
% Success		6/10	9/10	0/10	0/10		
		60	90	0	0		

7.3.2 Crystal structures

The structure determination of **A36:D9** established that the N-oxide was bifurcated (with an I···O···I angle of 117°) but instead of the desired discrete hexagon, an infinite polymer appeared, Figure 7.7. The formation of a polymer is always a possibility and on this occasion the synthetic target did not materialize.

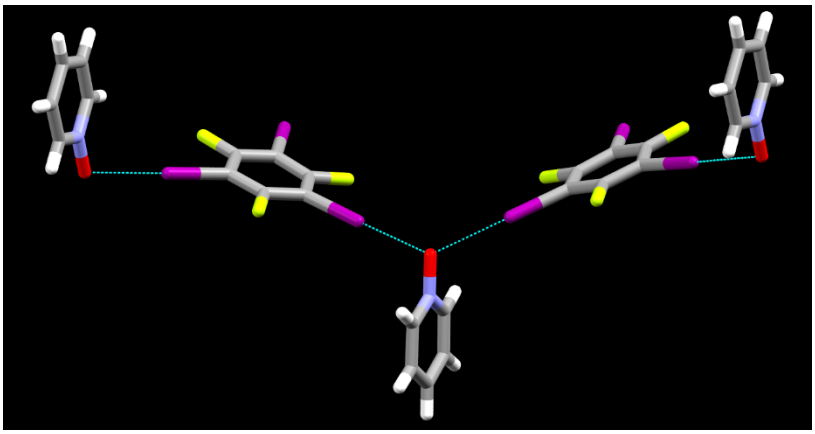

Figure 7.7 Bifurcated halogen bonds in **A36:D9**

The crystal structure of **A37:D7** also shows bifurcation at the N-oxide moiety, this time with a smaller I···O···I angle (93°). Whether this small angle is preventing the formation of a

rhomb, or is the result of other interactions is impossible to determine but, either way, a halogen-bonded chain is formed instead of the desired discrete polygon, Figure 7.8.

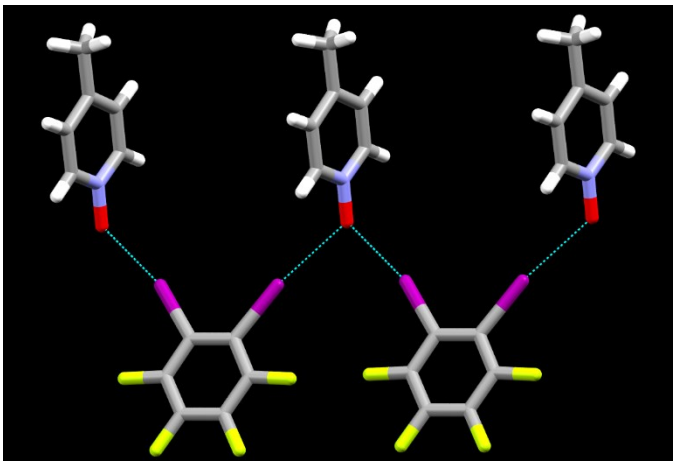

Figure 7.8 Bifurcated halogen-bonded chain in **A37:D7**

The crystal structure of **A29:D7** contains two crystallographically unique N-oxides, one with bifurcated halogen bonds with four **D7** molecules and the other with a single halogen bond formed with two **D7** molecules, Figure 7.9.

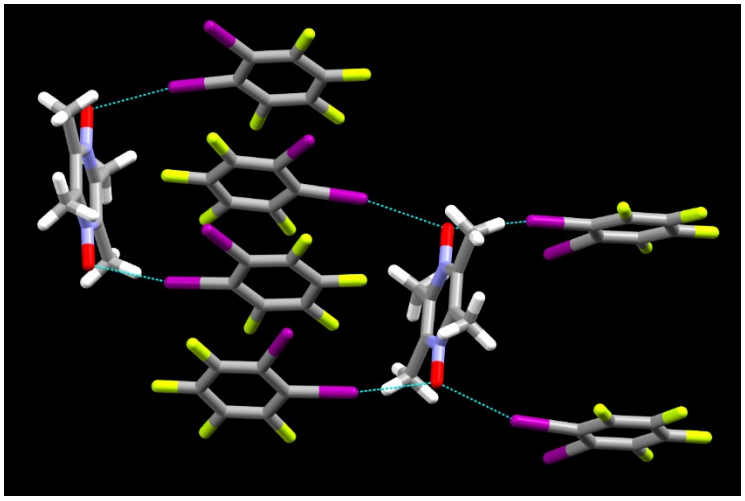

Figure 7.9 Columnar stacking in the crystal structure of **A29:D7**

In this structure, the N-oxide entities with single halogen bonds interact with a nearby hydrogen atom forming a bifurcated hydrogen- and halogen-bond combination with an angle of

88°. N-oxide entities with bifurcated halogen bonds have an I···O···I angle of 153° resulting in a chain of polygons, but not with the intended topology and relative orientation of building blocks, Figure 7.10. Neighboring halogen-bond donors are stacked into columns with a distance of 3.4 Å, and hence are stabilized by π-π interactions,[27] Figure 7.10.

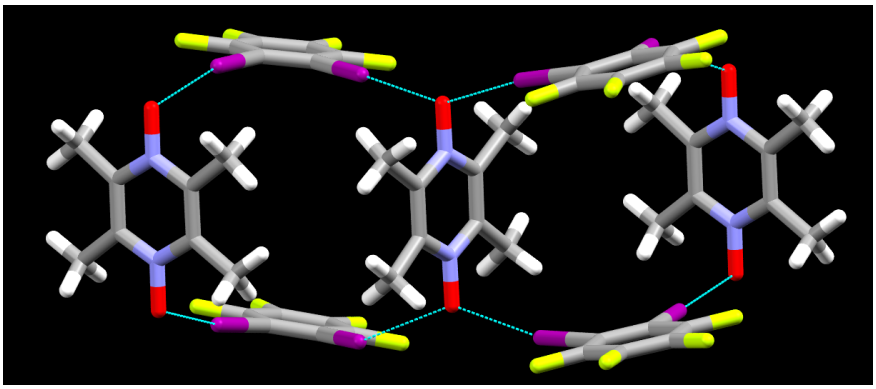

Figure 7.10 A chain of polygons in the crystal structure of **A29:D7**

The first successful supramolecular synthesis in this study was realized in the crystal structure of **A38:D7**. Bifurcation at the N-oxide (I···O···I, 105°) is present, and this time, the result is a discrete tetrameric rhombic architecture, Figure 7.11.

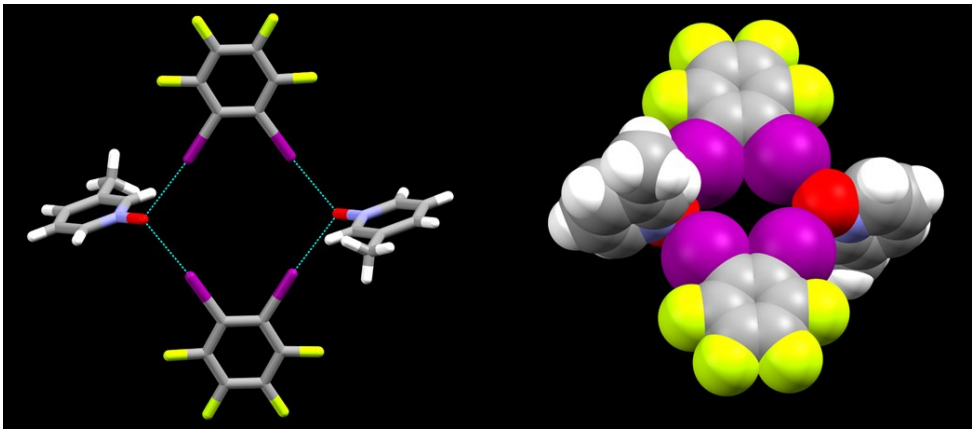

Figure 7.11 Geometric complementarity leading to a discrete tetrameric rhomb in the crystal structure of **A38:D7**

The second successful synthesis was achieved with the crystal structure **A29:D9**. This time, the bifurcated I···O···I angle is close to 120°, and the complementary geometry furnished by the 1,3-substituted donor molecule affords the intended chain of hexagonal polygons, Figure 7.12. Each hexagon offers a small interior 'window' approximately 0.72 x 0.92 nm.

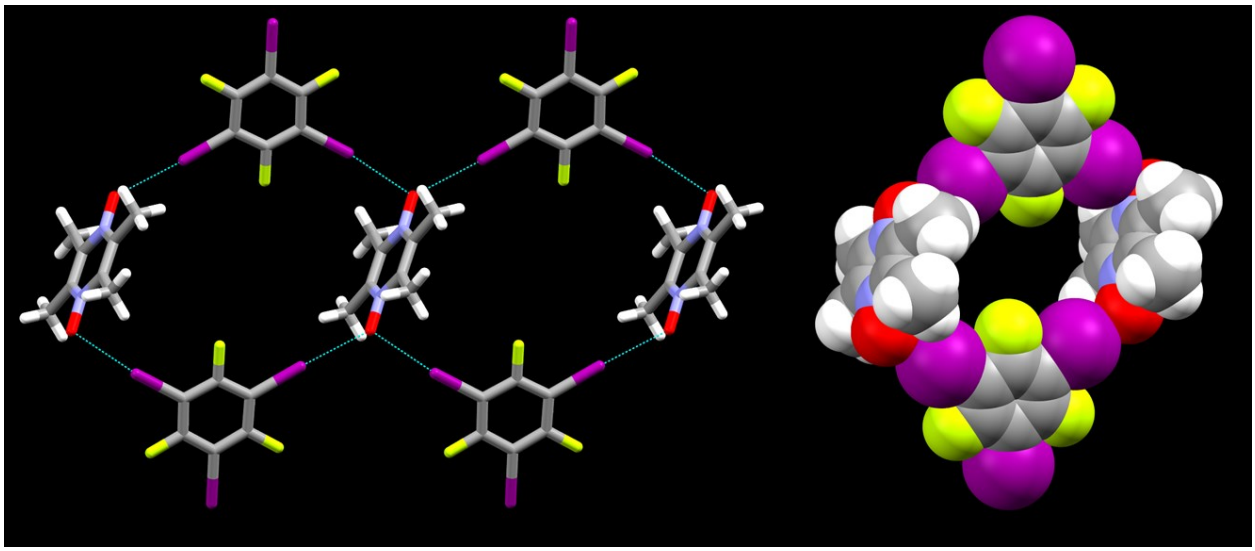

Figure 7.12 Complementarity of angle and geometry leading to fused hexagons and Space filling model of a hexagon in **A29:D9**

7.4 Discussion

7.4.1 Relative effectiveness of bromo- and iodo- substituted halogen-bond donors

Iodo-based donors showed a success rate of 75% (15/20) while none of the bromo-substituted donors produced a co-crystal. These results underscore that large difference in effective halogen-bond strength between iodo- and bromo-based halogen-bond donors for crystal engineering purposes. From an electrostatic point of view the positive potential on an iodine atom is much greater than on a bromine atom. Thus, iodine preferentially form halogen bonds with electronegative oxygen atoms.

7.4.2 Bifurcated halogen bonds

All five co-crystal structures contained the desired bifurcated halogen bond to the N-oxide oxygen atom, despite the fact that there have been only a small number of reports describing bifurcated halogen bonds,[28] most of which are theoretical studies.[29] A survey of structures in the CSD produces over 800 hits containing at least one I···O halogen bond, but less than 5% of those contain bifurcated bonds, and none of them include N-oxides as the acceptors even though there are about 30 structures in the CSD involving an N-oxide as a halogen-bond acceptor.

7.4.3 Polymers vs discrete architectures

It was clear that obtaining a polymer in this type of co-crystallization setting is more feasible than obtaining a discrete polygonal architecture. The weak, noncovalent interactions of the monomer units along a polymer chain tend to add up cooperatively, amplifying supramolecular effects. Thus, polymers are naturally predisposed to self-organize. In these structures, both polymers and discrete architectures contain very similar intermolecular interactions. Thus, the enthalpy contribution towards the formation of the final architecture is similar and thermodynamic contribution towards either a polymer or a discrete architecture is similar. But kinetically, formation of polymers are favored due to higher collision rates of monomers which can be more easily attached to the ends of polymers than making individual discrete architectures. Furthermore, at supersaturation stage different architectures are formed as nuclei. Compared to discrete architectures chains are favorable as they become dominant nuclei due to higher collision rates; thus all the other architectures are unable to compete for critical nuclei size and undergo Oswald ripening.[30] Oswald ripening is a phenomenon which describes the change of an inhomogeneous structure over time. In simple terms, in a system like this many small nuclei (discrete architectures) form initially, but slowly disappear except for a few that grow larger (polymer architectures), at

the expense of the small nuclei. The smaller nuclei act as "nutrients" for the bigger nuclei, Figure 7.13.

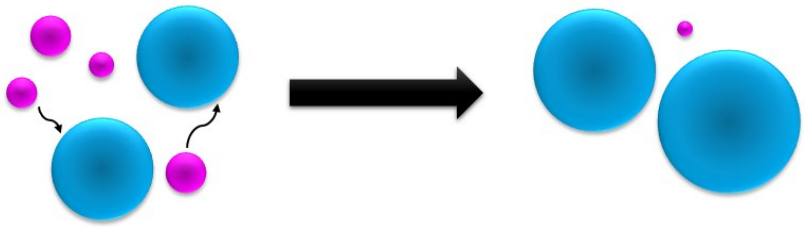

Figure 7.13 Oswald Ripening leading to domination of polymeric nuclei (blue: nuclei of polymer architectures, pink: nuclei of discrete architectures)

In the cases where a successful polygonal architectures were formed preorganization play the major role.[31] Because of the preorganization of the few molecules that initially interact with each other, next colliding molecules have to interact in such a way that it is easier to form a discrete architecture than a polymer, Figure 7.14. These nuclei with discrete architectures then act as seeds to grow crystals.[32]

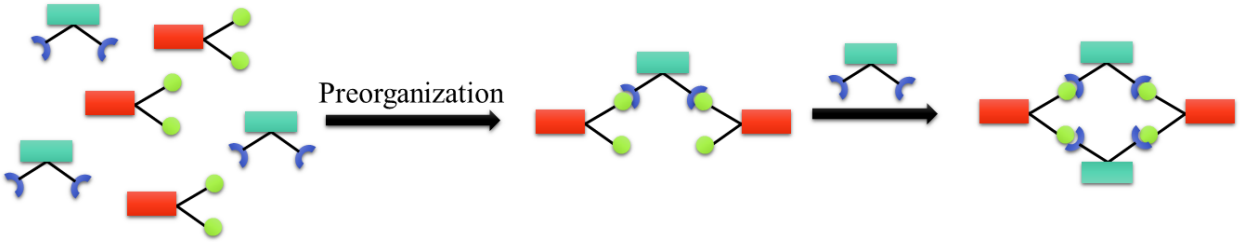

Figure 7.14 Preorganization leading to discrete architectures

7.5 Conclusions

By using the geometric complementarity of two appropriate molecular building blocks it is possible to build polygons of specific dimensions using the strength and directionality of I···O halogen bonds, Figure 7.15. A key component of the synthetic strategy utilizes the propensity of the N-oxide moiety to form bifurcated intermolecular interactions with donor···O···donor angles close to 120°. Furthermore, this study underscore the importance of electrostatics in halogen bond

formation where iodo-based halogen-bond donors contain much higher electrostatic potential compared to bromo- analogies and thus more effective in forming halogen bonds.

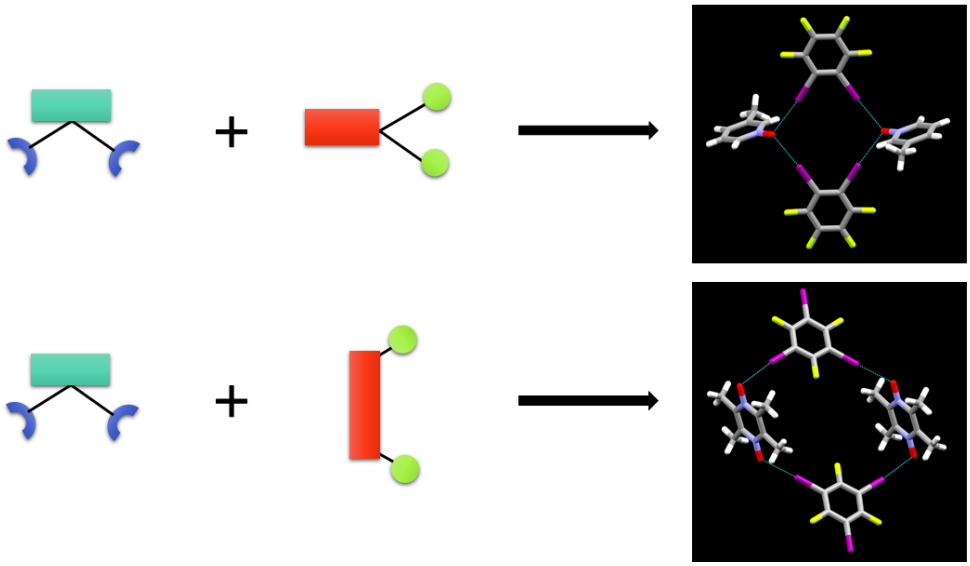

Figure 7.15 Supramolecular outcome of the study

7.6 Reference

1. Aakeröy, C.B.; Wijethunga, T.K.; Desper, J. *CrystEngComm* **2014**, *16*, 28-31.

2. Ulku, D.; Huddle, B.P.; Morrow, J.C. *Acta Cryst.* **1971**, *B27*, 432-436.

3. Andreev, V. P.; Vapirov, V. V.; Nizhnik, Y.P.; Aleshina, L. A.; Semenova, T. A. *Rus. J. Gen. Chem*. **2008**, *78*, 973-983.

4. Verdejo, B.; Gil-Ramirez, G.; Ballester, P. *J. Am. Chem. Soc.* **2009**, *131*, 3178-3179.

5. Abraham, M. H.; Honcharova, L.; Rocco, S. A.; Acree, W. E.; De Fina, K. M. *New J. Chem*. **2011**, *35*, 930-936.

6. Atria, A.M.; Cortes, P.; Garland, M.T.; Baggio, R. *Acta Cryst*. **2003**, *59*, m967-m969.

7. Freeman, J. P.; Grabiak, R. C. *J. Org. Chem*. **1976**, *41*, 3970-3974; Freeman, J. P.; Grabiak, R. C. *J. Org. Chem.* **1976**, *41*, 2531-2535.

8. Monge, A.; Palop, J. A.; De Cerain, A.L.; Senador, V.; Martinez-Crespo, F. J.; Sainz, Y.; Narro, S.; Garcia, E.; De Migue1, C.; Gonzalez, M.; Hamilton, E.; Barker, A. J.; Clarke, E.D.; Greenhowl, D.T. *J. Med. Chem.* **1995**, *38*, 1786-1792.

9. Chopra, S.; Koolpe, G. A.; Tambo-ong, A. A.; Matsuyama, K. N.; Ryan, K. J.; Tran, T.B.; Doppalapudi, R.S.; Riccio, E.S.; Iyer, L. V.; Green, C.E.; Wan, B.; Franzblau, S.G.; Madrid, P.B. *J. Med. Chem*. **2012**, *55*, 6047-6060.

10. Albini, A.; Alpegiani, M. *Chem. Rev*. **1904**, *84*, 43-71

11. Takenaka, N.; Sarangthem, R. S.; Captain, B. *Angew.Chem*. **2008**, *120*, 9854-9856.

12. CSD ConQuest 1.15, Cambridge Crystallographic Data Centre, U.K., **2012**.

13. Taylor, R.; Kennard, O.; Versichel, W. *J. Am. Chem. Soc.* **1984**, *106*, 244-248.

14. Goud, N.R.; Babu, N.J.; Nangia, A. *Cryst.Growth Des*. **2011**, *11*, 1930-1939; Babu, N.J.; Nangia, A.; Reddy, L.S. *Mol.Pharmaceutics* **2007**, *4*, 417-434; Koehn, S. K.; Tran, N. L.; Gronert, S.; Wu, W. *J. Am. Chem. Soc.* **2010**, *132*, 390-395.

15. Yadav, V.N.; Gorbitz; C.H. *Acta Cryst.* **2014**, *C70*, 43-45.

16. Messina, M.T.; Metrangolo, P.; Panzeri, W.; Pilati, T.; Resinati, G. *Tetrahedron* **2001**, *57*, 8543-8550.

17. Metrangolo, P.; Meyer, F.; Pilati, T.; Resnati, G.; Terraneo, G. *Angew. Chem. Int. Ed.* **2008**, *47*, 6114-6127.

18. Kawano, T.; Kuwana, J.; Xu Du, C.; Ueda, I. *Inorg.Chem.* **2002**, *41*, 4078-4080; Kim, K. *Chem. Soc. Rev.* **2002**, *31*, 96-107.

19. Sharma, C.V.K.; Clearfield, A. *J. Am. Chem. Soc.* **2000**, *122,* 4394-4402.

20. Davy, K.J.P.; McMurtrie, J.; Rintoul, L.; Bernhardt, P.V.; Micallef, A.S. *CrystEngComm* **2011**, *13*, 5062-5070.

21. Pfrunder, M.C.; Micallef, A.S.; Rintoul, L.; Arnold, D.P.; Davy, K.J. P.; McMurtrie, J. *Cryst. Growth Des.* **2012**, *12*, 714-724

22. Forbes, S. *Hydrogen bonded driven supramolecular chemistry for modulating physical properties of pharmaceutical compounds*, Ph.D. thesis, Kansas State University, **2010**.

23. Omnic 8.0 © **1992-2008**, Thermo Fisher Scientific Inc.

24. Aakeröy, C.B.; Epa, K.; Forbes, S.; Schultheiss, N.; Desper, J. *Chem. A Eur. J.* **2013**, *19*, 14998-15003.

25. Babu, N.J.; Nangia, A. *CrystEngComm* **2007**, *9*, 980-983.

26. James, S. L.; Adams, C. J.; Bolm, C.; Braga, D.; Collier, P.; Friscic´, T.; Grepioni, F.; Harris, K.D.M.; Hyett, G.; Jones, W.; Krebs, A.; Mack, J.; Maini, L.; Orpen, A.G.; Parkin, I. P.; Shearhouse, W.C.; Steed, J.W.; Waddell, D.C. *Chem. Soc. Rev*. **2012**, *41*, 413-447; Aakeröy, C. B.; Chopade, P.D.; Ganser, C.; Rajbanshi, A.; Desper, J. *CrystEngComm* **2012**, *14*, 5845-5853.

27. Roesky, H.W.; Andruh, M. *Coord. Chem. Rev.* **2003**, *236,* 91-119; Mei, X.; Liu, S.; Wolf, C. *Org. Lett*. **2007**, *9*, 2729-2732; Klosterman, J. K.; Yamauchi, Y.; Fujita, M. *Chem. Soc. Rev*. **2009**, *38*, 1714-1725; Hunter, C. A.; Lawsonb, K. R.; Perkinsa, J.; Urch, C.J. *J. Chem. Soc. Perkin Trans. 2* **2001**, 651-669.

28. Ji, B.; Wang, W.; Deng, D.; Zhang, Y. *Cryst. Growth Des*. **2011**, *11*, 3622-3628.

29. Bauzá, A.; Quiñonero, D.; Frontera, A.; Deyà, P. M. *Phys. Chem. Chem. Phys*. **2011**, *13*, 20371-20379.

30. Leubner, I.H. *J. Phys. Chem.* **1987**, *91,* 6069-6073; Madras, G.; McCoy, B.J. *Chem. Eng. Sci.* **2002**, *57*, 3809-3818.

31. Tabellion, F.M.; Seidel, S.R.; Arif, A.M.; Stang, P.J. *J. Am. Chem. Soc.* **2001**, *123*, 7740-7741; Reinhoudt, D.N. *Supramolecular Materials and Technologies*, John Wiley & Sons, **2008**; Prohens, R.; Portell, A.; Alcobé, X. *Cryst. Growth Des.* **2012**, *12*, 4548−4553.

32. Bergfors, T. *J. Struct. Biol*. **2003**, *142*, 66-76.

Chapter 8 - Stabilizing volatile liquid chemicals using halogen-bond based co-crystallization[1]

8.1 Introduction

Chemicals that exist as liquids at ambient conditions tend to be less stable and more difficult to handle than solid chemicals, and the relatively weak intermolecular interactions in liquids[2] are often associated with properties such as high vapor pressure, low boiling points and flammability.[3] As a result, liquids often present considerable environmental, health and cost-related challenges when it comes to the handling, transportation and storage of these materials.[4] Consequently, there is an ongoing need for simple and scalable methods for stabilizing a wide spectrum of liquid chemicals.

Iodoperfluoroalkanes represent an important class of compounds that are employed as refrigerants, foam blowing agents, propellants, heat transfer agents, and in electronic applications.[5] These compounds are also of considerable fundamental interest as halogen-bond donors,[6] reactive intermediates,[7] reactants[8] and as ligands[9] in chemical synthesis. Most of the compounds in this family are liquids at room temperature accompanied by high vapor pressures.[10] Furthermore, iodoperfluoroalkanes are recognized as persistent organic pollutants (POPs) and also bio-accumulate thereby carrying potential environmental and health-related hazards.[11] The general method for stabilizing this class of compounds is refrigeration, which is both expensive and complicated from the point of view of handling and transporting. Thus, a different protocol for stabilizing iodoperfluoroalkanes without damaging their chemical integrity is desirable.

Co-crystallization technologies are currently being applied in the fields of pharmaceuticals,[12] agrochemicals,[13] and energetic materials[14] for enhancing or altering the physico-chemical properties while keeping the molecular structure and composition of the

individual components constant. Co-crystallizations have also been applied to chiral resolution,[15] separation and purification,[16] and in crystallization of non-solid compounds to aid in robust and efficient manufacturing processes,[17] but have not been widely applied for providing long-term stability of liquid chemicals to simplify storage and handling. This study describes a simple protocol (Figure 8.1) using halogen-bond based synthons for converting liquid iodoperfluoroalkanes into more stable crystalline materials without loss of chemical integrity of the high-value compound.

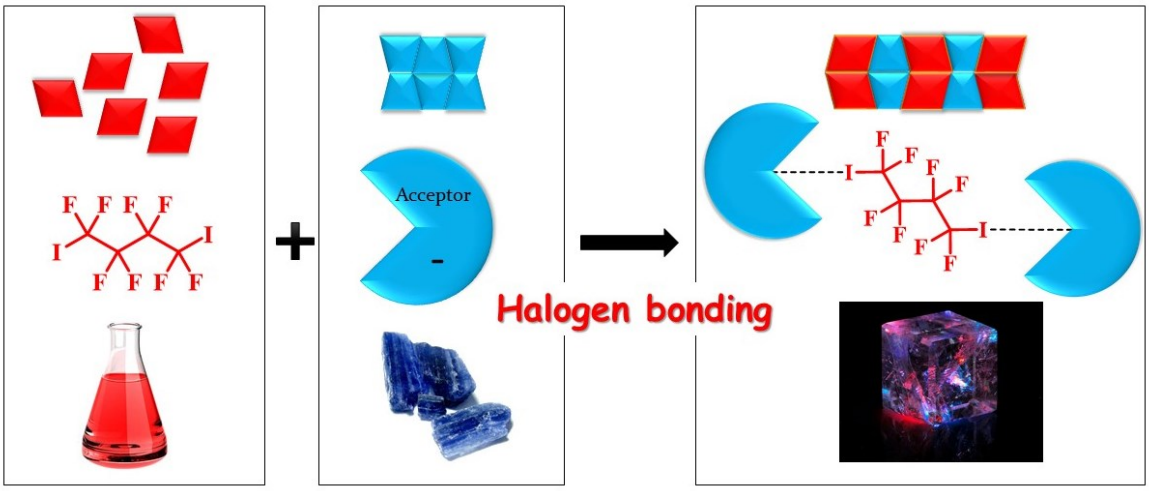

Figure 8.1 Approach for converting unstable liquids to stable solids

Three iodoperfluoroalkanes were selected, Figure 8.2. 1,2-Diiodoperfluoroethane (**D1**) and 1,4-diiodoperfluorobutane (**D2**) are highly volatile liquids at room temperature while 1,6-diiodoperfluorohexane (**D3**) has a melting temperature of 25 °C thus even a slight increment above room temperature leads to the liquification of this compound, which can make transport and storage particularly challenging.

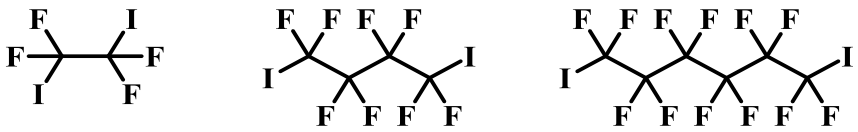

D1 **D2** **D3**

Figure 8.2 Iodoperfluoroalkanes employed in this study

Since iodoperfluoroalkanes are well-known halogen-bond donors, selected acceptors were limited to effective halogen bond acceptors with relatively high thermal stability, Figure 8.3. All these compounds contain an aromatic backbone decorated with either nitrogen- or oxygen atoms as suitable electron-pair donors, thus facilitating the formation of strong, structure directing halogen-bond interactions.[18]

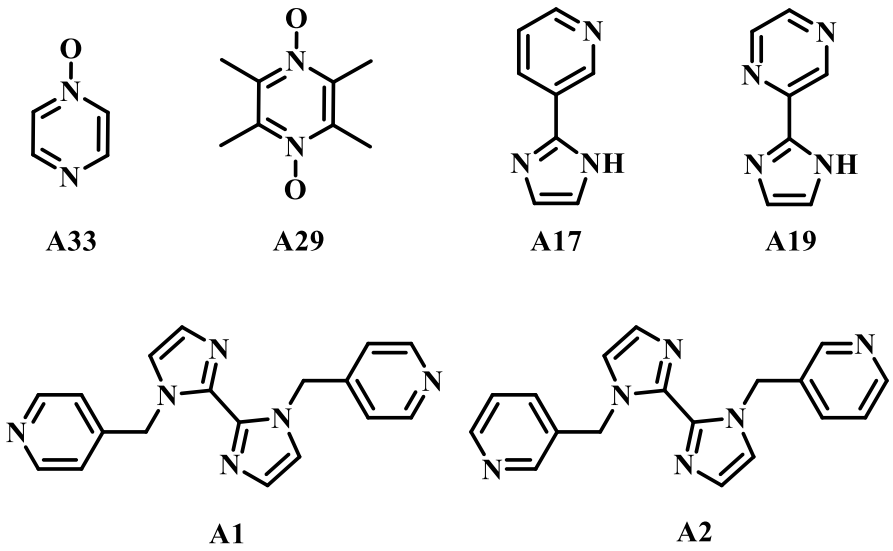

Figure 8.3 Co-formers used in the current study

The study is undertaken in response to three hypotheses,

1. Co-crystallization of an unstable liquid chemical with a stable solid chemical can successfully convert the liquid in to a stable crystalline material.
2. The conversion give rise to the gained stability and extended shelf life of the liquid chemical under different conditions.
3. Co-crystallization technology is a simple protocol, thus the method can be easily scaled up while utilizing the concepts of green chemistry.

8.2 Experimental

8.2.1 General

All the acceptors were prepared using previously reported methods and described in Chapters 2, 5 and 7.[19] Donors **D1**-**D3** were purchased from commercial sources and used without any purification. The determinations of melting points were carried out on Fisher-Johns melting point apparatus and are uncorrected. NMR spectra were recorded on a Varian Unity plus 400 MHz spectrometer in $CDCl_3$. Infrared spectroscopy was carried out on a Nicolet 380 FT-IR with a digital resolution of 0.9 cm^{-1} and data processed using Omnic[20] software. Powder diffraction patterns were recorded on a Bruker AXS D8 advance X-ray diffractometer.

8.2.2 Grinding experiments and IR spectroscopy

The three donors and six acceptors were combined using a standard solvent assisted grinding protocol. For grinding, 1:1 (iodoperfluoroalkane: **A33, A29, A19** and **A17**) or 2:1 (iodoperfluoroalkane: **A1** and **A2**) stoichiometric amounts were mixed together and was ground using a drop of methanol for several minutes. The outcomes of the eighteen attempted reactions were analyzed using IR spectroscopy in order to determine if a co-crystal had indeed formed, or if the two reactants simply reappeared as two separate homomeric liquid and a solid.

8.2.3 Synthesis of co-crystals

All the grinding experiments were subsequently converted to solvent based experiments to grow crystals suitable for single crystal X-ray diffraction by dissolving the ground mixtures in methanol followed by slow evaporation of the solvent. Once the crystals are formed they were analyzed using IR spectroscopy. Subsequently suitable crystals were analyzed using single crystal X-ray diffraction. Thirteen of the eighteen experiments yielded crystals suitable for single crystal X-ray diffraction. **A29:D1**, **A33:D2**, **A29:D2**, and **A29:D3** are presented here, whereas details of

the other nine crystal structures have been reported in Chapters 3 and 5 (**A17:D1**, **A1:D1**, **A17:D2**, **A19:D2**, **A1:D2**, **A2:D2**, **A19:D3**, **A1:D3** and **A2:D3**). Table 8.1 summarizes the experimental details for **A29:D1**, **A33:D2**, **A29:D2**, and **A29:D3**. Appendix B.7 contains the relevant X-ray experimental data.

Table 8.1 Experimental details of the four new co-crystals obtained

Code	Mixed Mole ratio	Amounts used	Solvent and method	Crystal stoichiometry	Melting point °C	Crystal color & habit
A29:D1	1:1	**A29** -10 mg, 0.059 mmol **D1** - 21 mg, 0.059 mmol	Methanol, Slow evaporation	1:1	120-122	Colorless plate
A33:D2	1:1	**A33** - 10 mg, 0.10 mmol **D2** - 49 mg, 0.10 mmol	Methanol, Slow evaporation	1:1	85-89	Yellow prism
A29:D2	1:1	**A29** - 10 mg, 0.059 mmol **D2** - 27 mg, 0.059 mmol	Methanol, Slow evaporation	1:1	165-157	Colorless plate
A29:D3	1:1	**A29** - 10 mg, 0.059 mmol **D3** - 33 mg, 0.059 mmol	Methanol, Slow evaporation	1:1	119-122	Colorless prism

8.2.4 Thermal stability experiments

The melting/decomposition temperatures for all thirteen co-crystals were determined in order to investigate the thermal stability of the co-crystals. Furthermore, melting points of all the co-formers were recorded in order to compare the melting points for obtained co-crystals with the starting reactants.

8.2.5 Stability studies of co-crystals for an extended time period

Once the initial IR analysis and melting point analysis for the obtained co-crystals were done, three co-crystals, representing one for each iodoperflouoroalkane **A17:D1**, **A1:D2** and **A29:D3** were selected to study their stability for extended period of time. For this, selected co-crystals were kept open to the environment and the IR spectra and melting points for these crystals were recorded at different time intervals for up to six months.

8.2.6 Synthesis of co-crystals in bulk quantities

To study the stability of these co-crystals further, a bulk quantity of co-crystals were required. Thus different crystallization attempts were made in order to obtain the selected co-crystals (**A17:D1**, **A1:D2** and **A29:D3**) in gram quantities. The first attempt was to use solvent assisted grinding, but the method failed as the solid co-former in each case was left in the final mixture. The second attempt was made using a crash cooling method. For this, stoichiometric amounts of co-formers were dissolved in a minimum amount of methanol and the solution was refluxed for one hour. After that, the solution was crash cooled in an ice bath. This method also failed as the solid co-former crashed from the solution instead of the co-crystal. Third choice was to use solvent evaporation, but it was not suitable for preparation of bulk quantities as this method is time consuming and needs to use large amounts of organic solvents. Finally a seed crystallization method was selected, where the seeds obtained from small scale slow evaporation experiments were used in a large scale saturated solution of co-formers in methanol to obtain the respective co-crystal in bulk quantities. In this case, seeds are acting as nucleates or templates for crystal growth leading to the formation of pure co-crystals and in high yields.

8.2.7 Stability studies of co-crystals under different conditions

Powder X-ray diffraction (PXRD) was selected as the method of choice to study the stability of co-crystals. First, the homogeneity of the solids obtained by seed crystallization was established using PXRD. After confirming the structural homogeneity, the three solids were divided into three portions (0.20 g each) and left them exposed to ambient conditions, 43% humidity and 83% humidity, respectively. The X-ray powder patterns for the nine samples were recorded in three weeks, six weeks and twelve weeks of time intervals and compared with the powder pattern obtained for solid co-formers.

8.2.8 Separation of individual components from co-crystals

For the separation studies, co-crystal **A29:D3** was selected. Initially the two co-formers were used in a solubility study in different solvents in order to find the suitable solvent system for the separation. Solubility studies showed that **D3** to be highly soluble in hexane, while not to be soluble in water. On the other hand, **A29** was highly soluble in water but not soluble in hexane. Thus, hexane water mixture was used for the solvent extraction experiments. 0.20 g of co-crystal **A29:D3** was taken into hexane (20 mL) and extracted with water (10 mL x 4). Water was removed under vacuum to obtain pure **A29** from the aqueous layer. The organic layer was kept inside the fridge for hexane to evaporate and pure **D3** was obtained. The purity and the successful separation of co-formers were clarified using NMR spectroscopy.

8.3 Results

8.3.1 Grinding experiments and characterization by IR spectroscopy

The IR analysis for initial grinding experiments showed that each single reaction (18/18) did produce a co-crystal, Table 8.2.

Table 8.2 IR analysis for grinding experiments

Mixture	IR bands (cm^{-1})		Shifts Δcm^{-1}	Result
	Halogen-bond donors	Grounded Mixture		
A33:D1	1153 1099	1168 1075	+15 -24	Co-crystal
A29:D1	1153 1099	1184 1117	+31 +18	Co-crystal
A17:D1	1153 1099	1181 1108	+28 +9	Co-crystal
A19:D1	1153 1099	1140 1082	-13 -17	Co-crystal
A1:D1	1153 1099	1118 1083	-35 -16	Co-crystal
A2:D1	1153 1099	1131 1083	-22 -16	Co-crystal
A33:D2	1192 1133	1184 1117	-8 -16	Co-crystal
A29:D2	1192 1133	1182 1103	-10 -30	Co-crystal

A17:D2	1192 1133	1189 1130	-3 -3	Co-crystal
A19:D2	1192 1133	1166 1117	-26 -16	Co-crystal
A1:D2	1192 1133	1157 1099	-35 -34	Co-crystal
A2:D2	1192 1133	1162 1137	-30 +4	Co-crystal
A33:D3	1199 1141	1211 1168	+12 +27	Co-crystal
A29:D3	1199 1141	1202 1137	+3 -4	Co-crystal
A17:D3	1199 1141	1196 1137	-3 -4	Co-crystal
A19:D3	1199 1141	1209 1137	+10 -4	Co-crystal
A1:D3	1199 1141	1211 1134	+12 -7	Co-crystal
A2:D3	1199 1141	1213 1138	+14 -3	Co-crystal

8.3.2 Crystal structures

In all thirteen cases, where a crystal structure was possible, the co-crystal formation is achieved via near-linear C-I···N/O halogen bonds. Structure details of **A17:D1**, **A1:D1**, **A17:D2**, **A19:D2**, **A1:D2**, **A2:D2**, **A19:D3**, **A1:D3** and **A2:D3** are provided in Chapter 3 and 5. The primary supramolecular assemblies in **A29:D1** and **A29:D2** are 1-D chains comprising alternating halogen-bond donor and acceptor molecules, Figure 8.4.

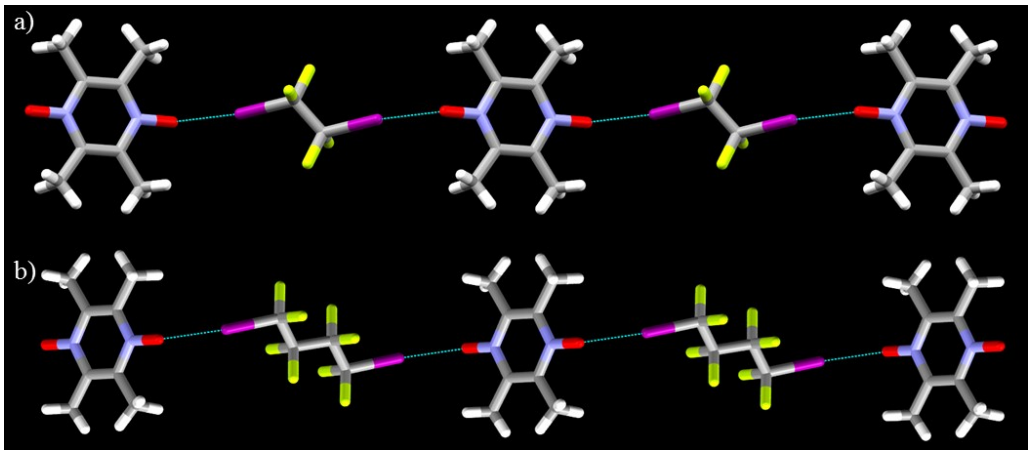

Figure 8.4 Primary halogen bonds in the crystal structures of a) **A29:D1** and b) **A29:D2**

This is also the case for **A33:D2** despite the fact that there are two different acceptor sites on pyrazine-*mono*-N-oxide, Figure 8.5.

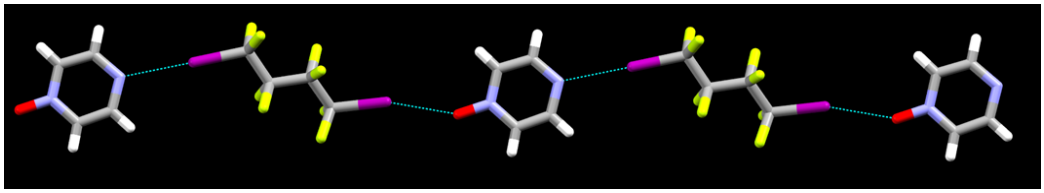

Figure 8.5 Primary halogen bonds in **A33:D2**

The crystal structure of **A29:D3** is more complicated as there are two crystallographically distinct acceptors, one of which engages in bifurcated halogen bonds whereas the other participates in conventional single-point halogen bonds, Figure 8.6.

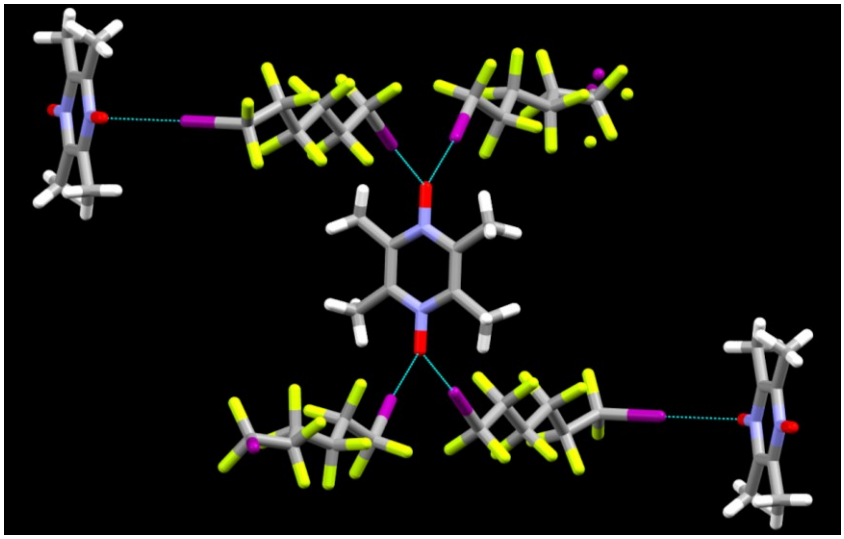

Figure 8.6 : Primary halogen bonds in **A29:D3**

8.3.3 Thermal stability of co-crystals

The melting/decomposition temperatures for all thirteen co-crystals are provided in Table 8.3. The melting point comparison results are shown in Figure 8.7, Figure 8.8 and Figure 8.9.

Table 8.3 Melting point analysis for the co-crystals obtained

Co-crystal	Melting point of the iodoperfluoroalkane (°C)	Melting point of the acceptor (°C)	Melting point/decomposition point of the co-crystal (°C)
A29:D1	-21	220-222	120-122
A17:D1	-21	197-201	95-98
A1:D1	-21	157-160	57-60
A33:D2	-9	110-113	85-89
A29:D2	-9	220-222	165-167
A17:D2	-9	197-201	132-135
A19:D2	-9	196-198	150-154
A1:D2	-9	157-160	118-120
A2:D2	-9	112-115	75-78
A29:D3	25	220-222	119-122
A19:D3	25	196-198	125-127
A1:D3	25	157-160	94-97
A2:D3	25	112-115	95-97

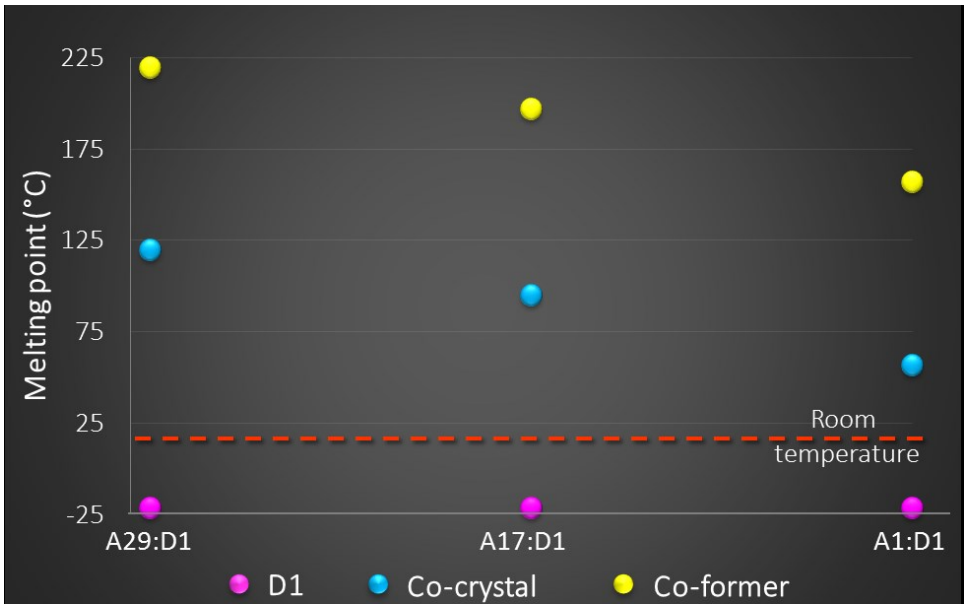

Figure 8.7 Melting point analysis for the co-crystals of **D1**

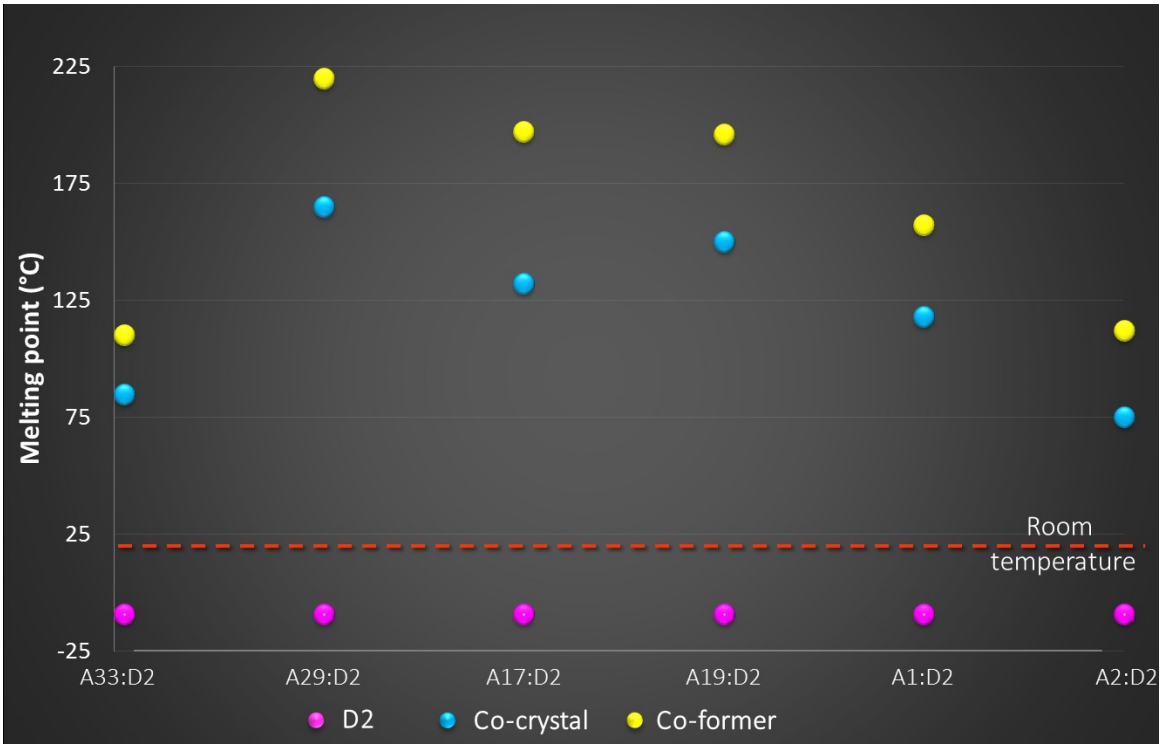

Figure 8.8 Melting point analysis for the co-crystals of **D2**

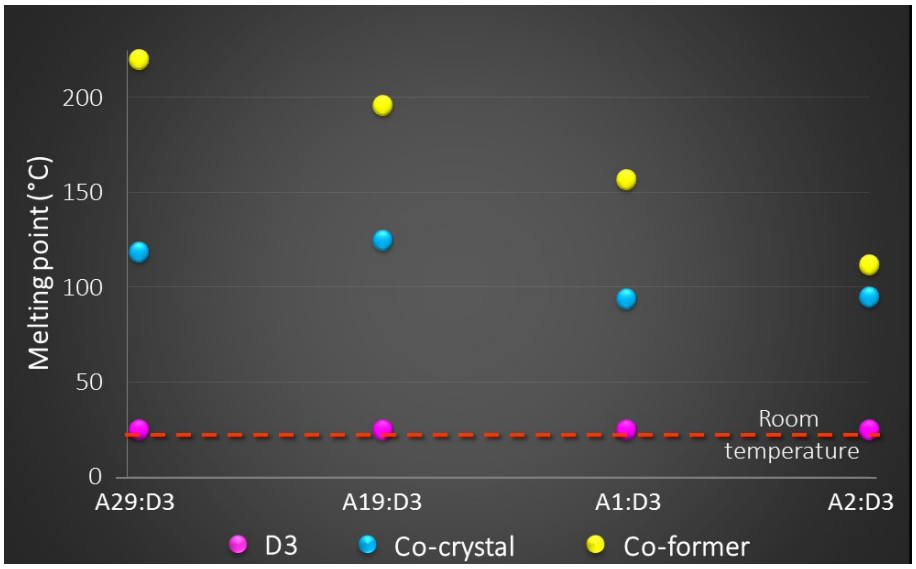

Figure 8.9 Melting point analysis for the co-crystals of **D3**

8.3.4 Stability studies of co-crystals for an extended time period

Crystalline samples of **A17:D1**, **A1:D2** and **A29:D3** were kept open to the environment for up to six months and regularly examined using IR spectroscopy and thermal analysis. No change in the vibrational spectroscopic features or thermal stability were observed for the duration of the trial. In contrast, the pure iodoperfluoroalkanes completely evaporated in a matter of minutes to hours when left exposed to ambient conditions. Table 8.4 summarizes the melting point data, while Figure 8.10 and Figure 8.11 show the IR results obtained for co-crystal **A17:D1**. IR results for **A1:D2** and **A29:D3** are provided in Appendix C.4.

Table 8.4 Melting point analysis of the selected co-crystals up to six months

	Melting point of A17:D1 (°C)	Melting point of A1:D2 (°C)	Melting point of A29:D3 (°C)
Initial	95-98	118-121	119-122
2 weeks	90-93	115-118	119-122
4 weeks	95-99	114-116	115-118
2 months	96-101	117-120	117-121
6 months	97-100	115-119	120-122

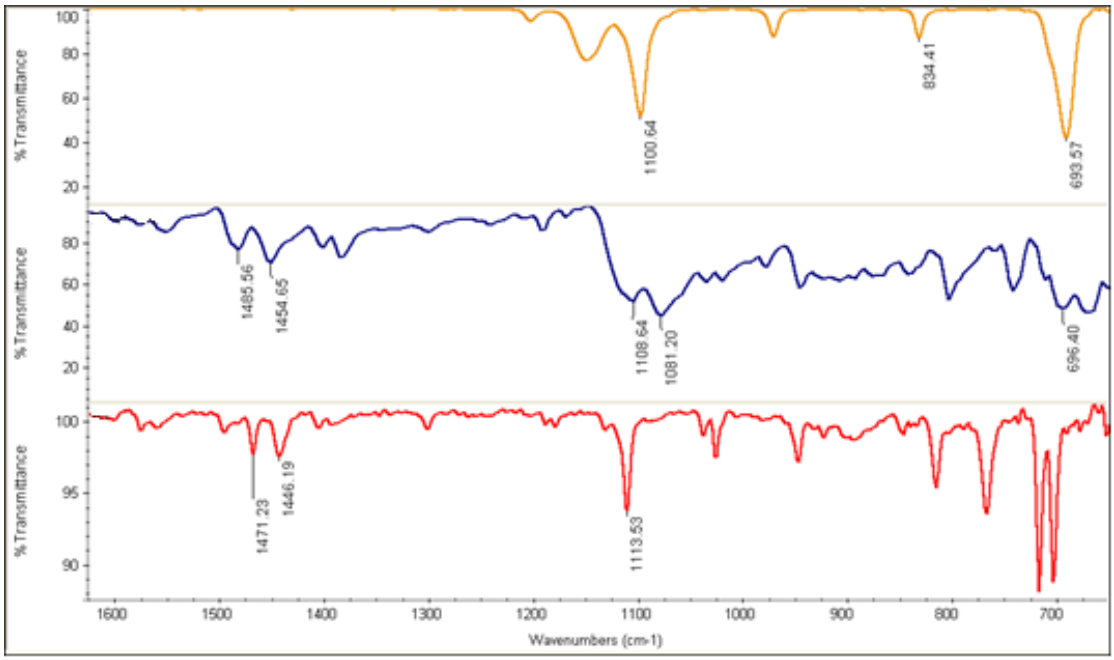

Figure 8.10 Comparison of IR peaks of **D1** (orange) and **A17** (red) with the co-crystal **A17:D1** (blue)

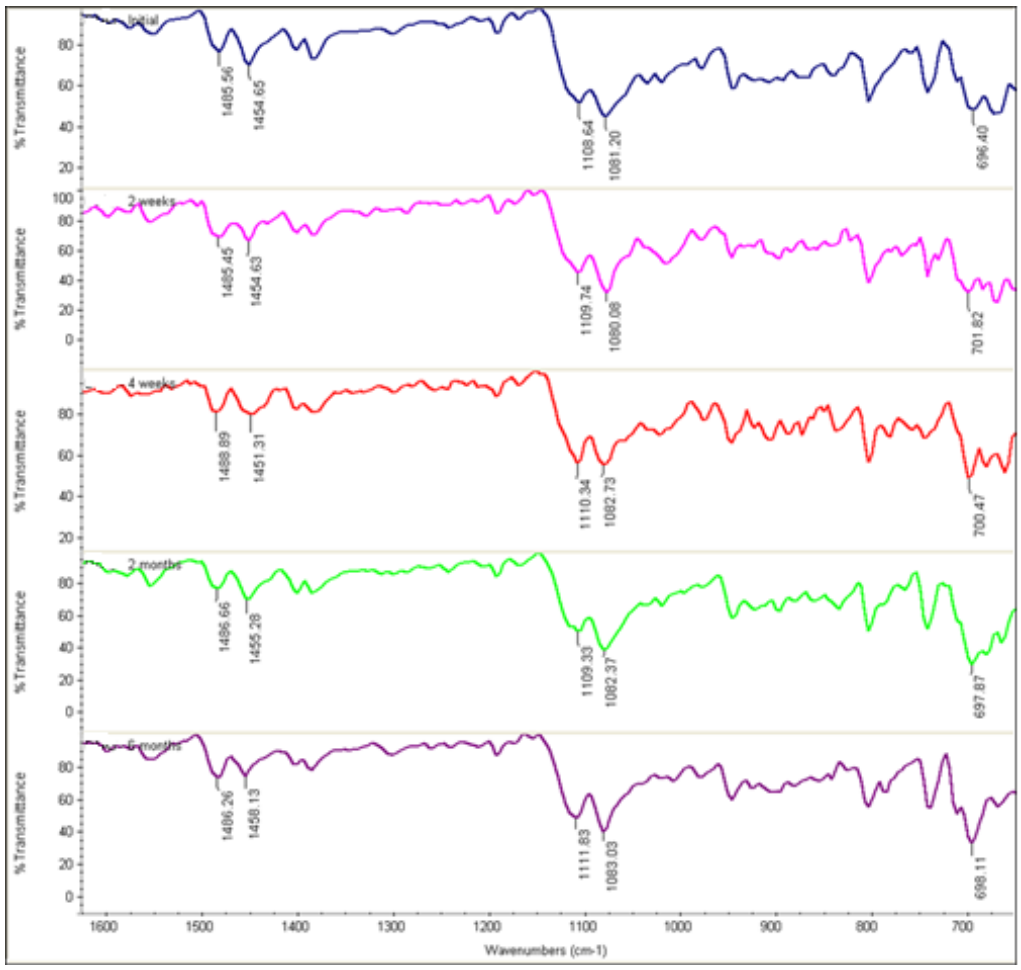

Figure 8.11 IR analysis of co-crystal **A17:D1** for the stability (initial: blue, after 2 weeks: pink, after 4 weeks: red, after 2 months: green, after 6 months: purple)

8.3.5 Stability studies of co-crystals under different conditions

PXRD patterns obtained for **A29:D3** are shown in Figure 8.12, Figure 8.13 and Figure 8.14, along with the powder pattern comparison with the co-former (**A29**). Powder patterns for **A17:D1** and **A1:D2** are provided in Appendix C.4.

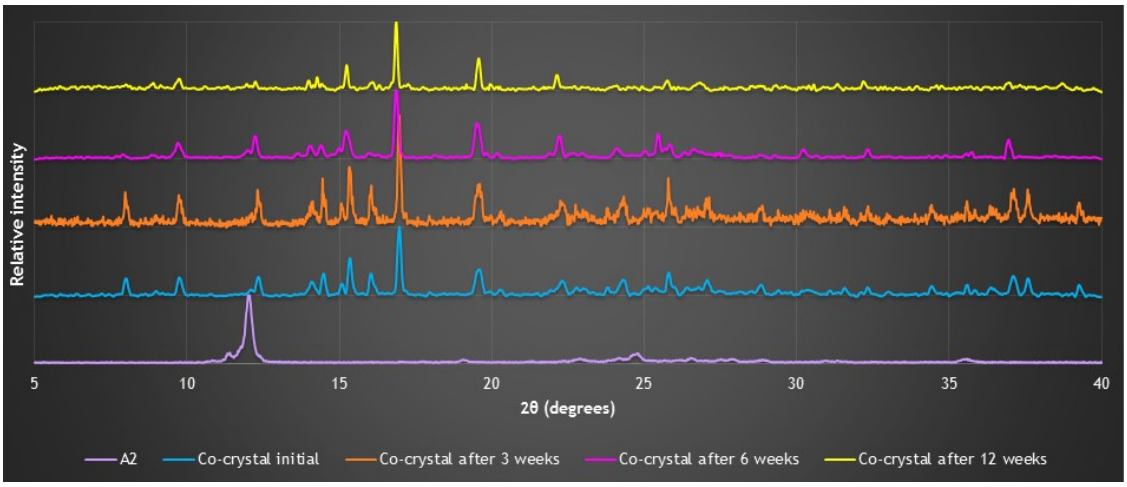

Figure 8.12 Powder pattern data for **A29:D3** kept under ambient conditions

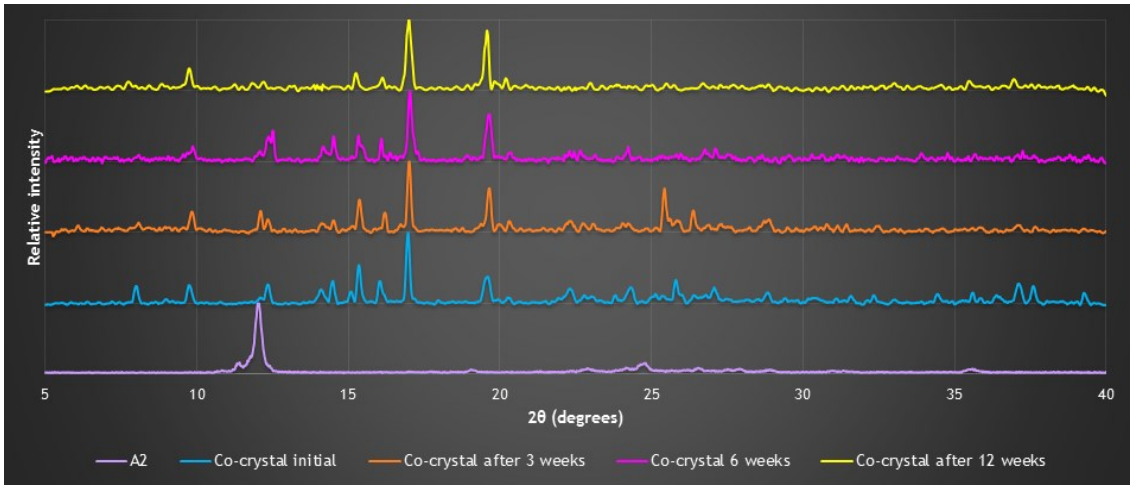

Figure 8.13 Powder pattern data for **A29:D3** kept under 43% humidity

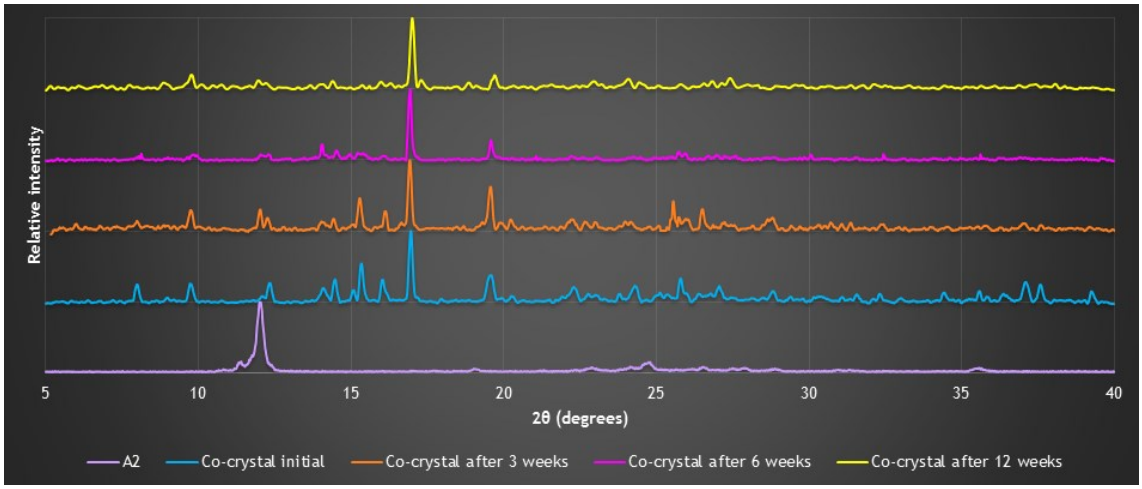

Figure 8.14 Powder pattern data for **A29:D3** kept under 83% humidity

8.3.6 Separation of individual components from co-crystals

^{19}F and ^{13}C NMR spectra of the separated organic layer of **A29:D3** are shown in Figure 8.15 and Figure 8.16, while ^{1}H and ^{13}C NMR spectra of the aqueous layer is shown in Figure 8.17 and Figure 8.18.

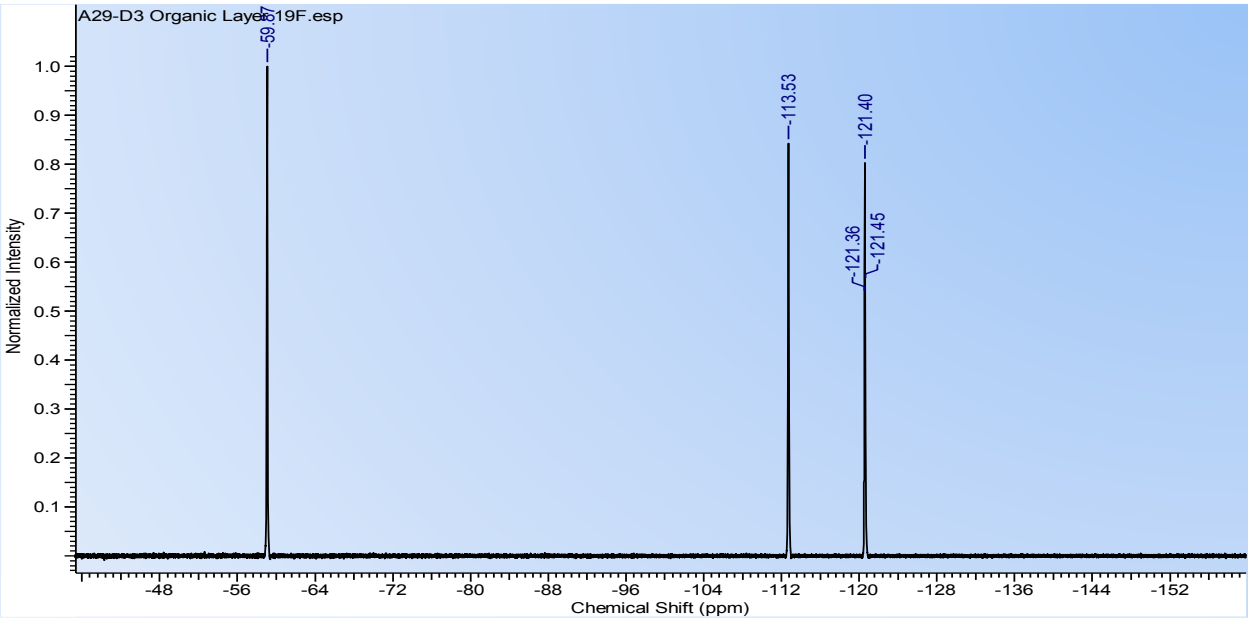

Figure 8.15 ^{19}F NMR spectrum of the separated organic layer

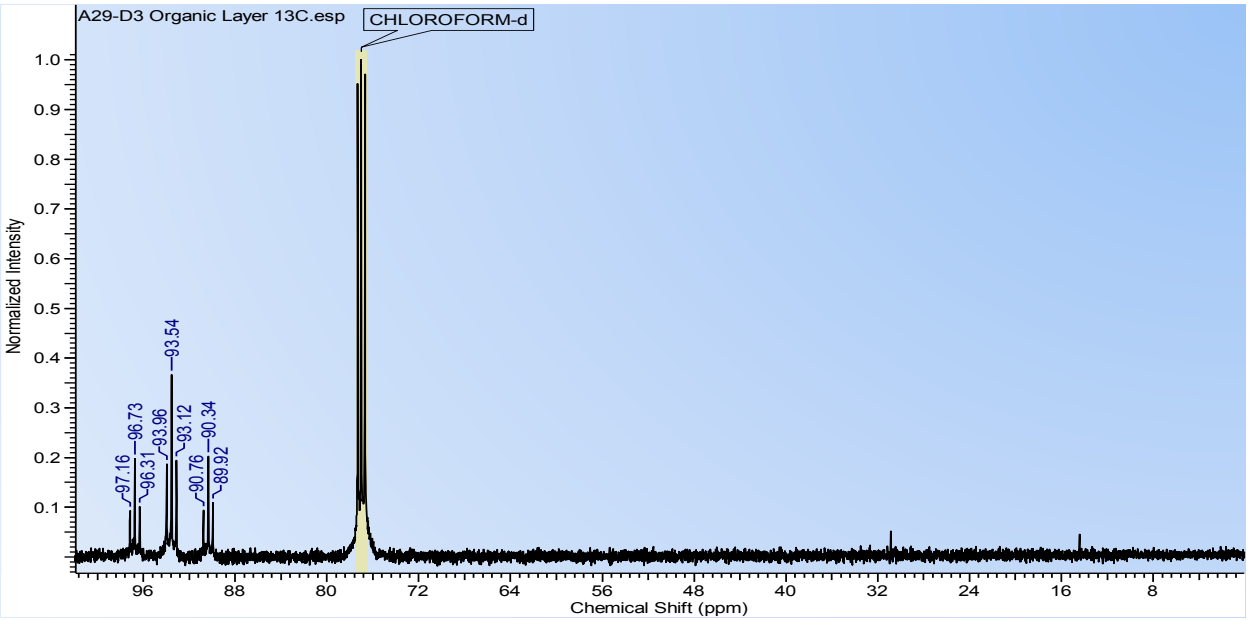

Figure 8.16 ^{13}C NMR spectrum of the separated organic layer (only **D3** present, no **A29**)

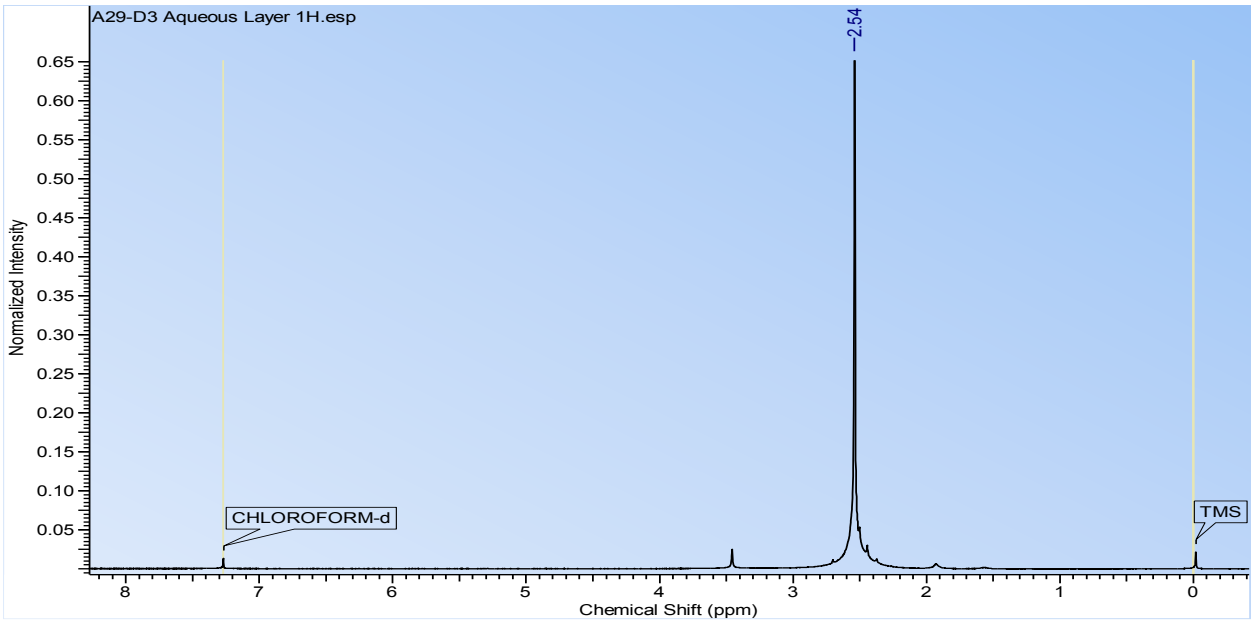

Figure 8.17 ^{1}H NMR spectrum of the separated aqueous layer

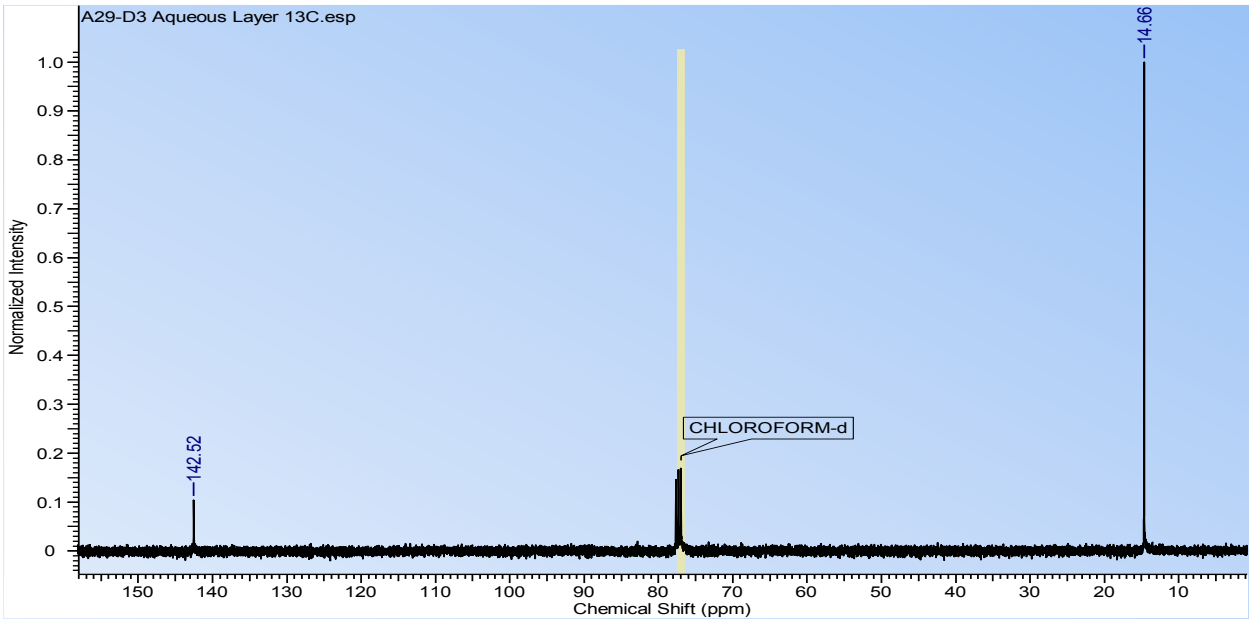

Figure 8.18 ^{13}C NMR spectrum of the separated aqueous layer (only **A29** present, no **D3**)

8.4 Discussion

8.4.1 Stabilization via trapping the liquid chemicals

In all thirteen structures obtained in this study, there is a substantial halogen bond between the targeted iodoperfluoroalkane and the co-former resulting in a new crystalline solid which

effectively ‘traps’ the volatile alkane within a more stable crystalline material without tampering with the molecular structure of the alkane itself. This trapped state of the liquid chemicals leads to their stability, as the liquid chemical is interacting with the solid co-formers via non-covalent interactions. On the other hand these non-covalent interactions make it easy to separate the liquid chemical from the solid lattice as the separation only needs to break this weak non-covalent interactions between the co-formers, not the strong covalent interactions. Thus this method provide a simple and convenient way to stabilize volatile liquid chemicals used in a wide range of applications including liquid pharmaceuticals.

8.4.2 Thermal stabilization of co-crystals

A couple of general observations could be made regarding the melting points of the co-crystals as compared to those of the co-formers. First of all, in every case, the melting point of the co-crystal was located between that of the two co-formers and the melting point of each co-crystal was substantially higher than that of the melting point of the corresponding iodoperfluoroalkanes, Figure 8.7 to Figure 8.9. Second the increase in the melting point of these co-crystals were at least 32 °C higher than the room temperature and could be elevated up to 140 °C. Third, the melting points of the co-crystals displayed a near-linear relation with the melting point of the respective co-former. This held true for co-crystals obtained with all three iodoperfluoroalkanes, and Figure 8.19 displays the relationship for the co-crystals with **D2**. Factors contributing to the melting point of a crystalline solid include the molecular arrangement within the crystal lattice, molecular symmetry, intermolecular interactions, and conformational degrees of freedom for a molecule, but not limited to these. Thus it is clearly difficult to draw strict comparisons from molecular structure to crystalline lattice energy to melting point. The situation becomes more complex in multicomponent systems such as co-crystals, because each component has its own characteristic

properties and those can influence the environment.[21] But a major impact for the melting point of a material arise from the intermolecular interactions of that material. Intermolecular interactions are stronger in a solid than a liquid. Thus the properties coming from the solid co-former are dominant in the ultimate co-crystal formed, leading to a linear relationship with the solid co-former's physical properties such as melting point. This trend is particularly important to note as it demonstrates that the resulting properties of a series of co-crystals are not random and that they are, or can be, directly linked to the molecular structure and physical properties of the corresponding co-former. Consequently, it is possible to 'dial-in' the physical property of a molecular solid through a careful selection of co-former in a systematic manner.

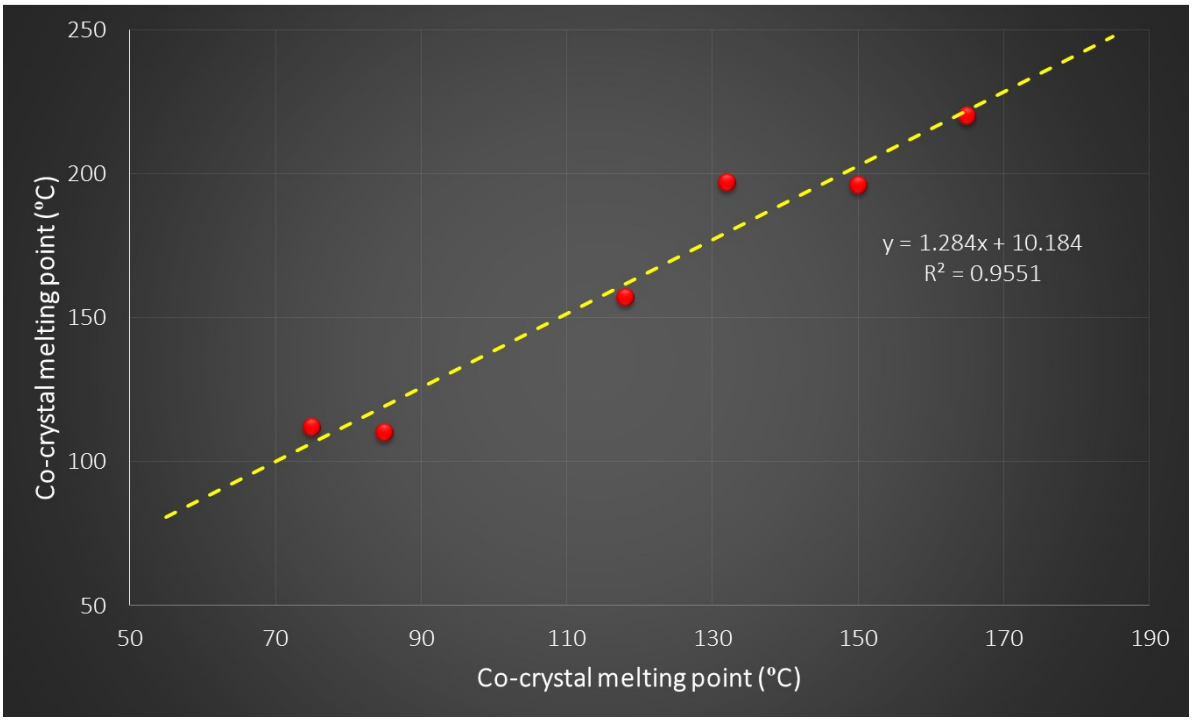

Figure 8.19 Relationship between the melting points of co-crystals of **D2** and respective co-formers

8.4.3 Stability of the co-crystals for extended periods and under high humid conditions

PXRD analysis provided insights into the stability of these co-crystals under different conditions for prolong periods, Figure 8.12 to Figure 8.14. Overall, the accumulated powder

diffraction data did not indicate that either of the three co-crystals decomposed into their individual components over time, even at elevated humidity levels. By carefully comparing the powder patterns, it could observe a broadening of peaks for some extent at 83% humidity level, attributing to some loss of crystallinity. But no new diffraction peaks were observed over time indicating that the perfluorinated alkane, despite its inherent volatility, was kept intact within the solid protective crystalline case afforded by the co-crystal.

8.4.4 Separation of individual components from co-crystals

Finally, it was establish that the desired alkane could be readily re-generated from the co-crystal by taking full advantage of the difference in solubility of the two species in the binary co-crystal. The NMR data obtained for the separated layers of **A29:D3** indicated that the aqueous layer to contain the N-oxide (**A29**) only while the organic layer to contain only the iodoperfluoroalkane (**D3**) Figure 8.15 to Figure 8.18.

8.4.5 Green chemistry aspect

This whole process of stabilizing volatile chemicals using co-crystal technology can be recognized as an essentially green methodology. Initial grinding experiments used only few drops of methanol and slow evaporation experiments used a minimum amount of methanol (< 2.0 ml). Furthermore, one of the solvents used in the solvent extraction is water, which is the greenest solvent. On the other hand none of these processes utilized any sort of energy sources such as heat. Furthermore, the amount of waste produced in the process is minimum. Also it was confirmed that the synthesis of co-crystals can be easily scaled up with the use of minimum amount of methanol.

8.5 Conclusions

Co-crystallization can be identified as a simple, effective, and convenient method for stabilizing volatile liquid chemicals where the chemical is effectively trapped inside a crystalline

lattice via non-covalent interactions. The co-crystals can be engineered to be quite stable towards environmental stress over extended periods of time, and both the co-former and the targeted high-value components can be separated using simple extraction methods. The co-crystals can be prepared using inexpensive and inherently 'green' processes that are also easily scalable. Thus, co-crystallizations can provide a convenient way of stabilizing liquid chemicals in general, offering a new technology for reducing both detrimental environmental impacts and for lowering costs in storage, handling and transportation, Figure 8.20.

Figure 8.20 Outcome of the study

8.6 References

1. Aakeröy, C.B.; Wijethunga, T.K.; Benton, J.; Desper, J. *Chem. Commun*. **2015**, *51*, 2425-2428.

2. Goodstein, D.L. *States of matter*, Courier Dover Publications, **1985**.

3. Patnaik, P. *A Comprehensive Guide to the Hazardous Properties of Chemical Substances*, John Wiley & Sons, **2007**.

4. Arslan, O.; Er, I.D. *J. Hazard. Mater.* **2008**, *154*, 901-913.

5. Nimitz, J.S.; Tapscott, R.E.; Skaggs, S.R. *US Pat.* US5135054A, **1992**; Leck, T.J.; Bricker, S.C.; Sievert, A.C. *US Pat.* US7641809B2, **2010**; Nimitz, J.S.; Lankford, L.H. *US Pat.* US5444102A, **1995**; Deev, L.E.; Nazarenko, T.I.; Pashkevich, K.I.; Ponomarev, V.G. *Russ. Chem. Rev.* **1992**, *61*, 40-54.

6. Amati, M.; Lelj, F.; Liantonio, R.; Metrangolo, P.; Luzzati, S.; Pilati, T.; Resnati, G. *J. Fluorine Chem.* **2004**, *125*, 629-640; Chu, Q.; Wang, Z.; Huang, Q.; Yan, C.; Zhu, S. *New J. Chem.* **2003**, *27*, 1522-1527; Fan, H.; Eliason, J.K.; Moliva, C.D.; Olson, J.L.; Flancher, S.M.; Gealy, M.W.; Ulness, D.J. *J. Phys. Chem. A* **2009**, *113*, 14052-14059; Johnson, M. T.; Džolić, Z.; Cetina, M.; Wendt, O. F.; Öhrström, L.; Rissanen, K. *Cryst. Growth Des*. **2012**, *12*, 362-368; Shen, Q.J.; Jin, W.J. *Phys. Chem. Chem. Phys.* **2011**, *13*, 13721-13729; Metrangolo, P.; Pilati, T.; Resnati, G.; Stevenazzia, A. *Chem. Commun*. **2004**, 1492-1493; Corradi, E.; Meille, S. V.; Messina, M. T.; Metrangolo, P.; Resnati, G. *Tetrahedron Lett.* **1999**, *40,* 7519-7523; Lunghi, A.; Cardillo, P.; Messina, T.; Metrangolo, P.; Panzeri, W.; Resnati, G. *J. Fluorine Chem*. **1998**, *91*,

191-194; Gao, H. Y.; Shen, Q. J.; Zhao, X. R.; Yan, X.Q.; Pang, X.; Jin, W.J. *J. Mater. Chem*. **2012**, *22*, 5336-5343; Widdifield, C. M.; Cavallo, G.; Facey, G. A.; Pilati, T.; Lin, J.; Metrangolo, P.; Resnati, G.; Bryce, D. L. *Chem. Eur. J.* **2013**, *19*, 11949-19962; Burton, D. D.; Fontana, F.; Metrangolo, P.; Pilati, T.; Resnati, G. *Tetrahedron Lett*. **2003**, *44*, 645-648; Liantonio, R.; Metrangolo, P.; Meyer, F.; Pilati, T.; Navarrini, W.; Resnati, G. *Chem. Commun*. **2006**, 1819-1821; Amico, V.; Meille, S. V.; Corradi, E.; Messina, M. T.; Resnati, G. *J. Am. Chem. Soc*. **1998**, *120*, 8261-8262; Saccone, M.; Cavallo, G.; Metrangolo, P.; Pace, A.; Pibiri, I.; Pilati, T.; Resnati, G.; Terraneo, G. *CrystEngComm* **2013**, *15*, 3102-3105; Crihfield, A.; Hartwell, J.; Phelps, D.; Walsh, R.B; Harris, J.L.; Payne, J.F.; Pennington, W.T.; Hanks, T.W. *Cryst. Growth Des* **2003**, *3*, 313-320; Liantonio, R.; Metrangolo, P.; Pilati, T.; Resnati, G. *Cryst. Growth Des* **2003**, *3*, 355-362; Metrangolo, P; Meyer, F.; Pilati, T.; Proserpio, D. M.; Resnati, G. *Chem. Eur. J*. **2007**, *13*, 5765-5772; Dey, A.; Metrangolo, P.; Pilati, T.; Resnati, G.; Terraneo, G.; Wlassics, I. *J. Fluorine Chem*. **2009**, *130*, 816-823; Fox, D.; Metrangolo, P.; Pasini, D.; Pilati, T.; Resnati, G.; Terraneo, G. *CrystEngComm* **2008**, *10*, 1132-1136.

7. Zhdankin, V.V.; Stang, P.J. *Chem. Rev*. **2008**, *108*, 5299-5358; Furin, G.G. *Russ. Chem. Rev.* **2000**, *69*, 491-522.

8. Shi, M.; Huang, J.W. *J. Fluorine Chem.* **2005**, *126*, 809-817; David, G.; Boyer, C.; Tonnar, J.; Ameduri, B.; Lacroix-Desmazes, P.; Boutevin, B. *Chem. Rev.* **2006**, *106*, 3936-3962; Tsuchii, K.; Ueta, Y.; Kamada, N.; Einaga, Y.; Nomoto, A.; Ogawa, A. *Tetrahedron Lett.* **2005**, *46***,** 7275-7278.

9. Gladysz, J. A.; Curran, D. P.; Horváth, I. T. *Handbook of Fluorous Chemistry*, Wiley-VCH, **2004**; Gattuso, G.; Liantonio, R.; Metrangolo, P.; Meyer, F.; Pappalardo, A.; Parisi, M.F.; Pilati, T.; Pisagatti, I.; Resnati, G. *Supramole. Chem.* **2006**, *18*, 235-243.

10. Aakeröy, C.B.; Welideniya, D.; Desper, J.; Moore, C. *CrystEngComm* **2014**, *16*, 10203-10209.

11. Ruan, T.; Wang, Y.; Wang, T.; Zhang, Q.; Ding, L.; Liu, J.; Wang, C.; Qu, G.; Jiang, G. *Environ. Sci. Technol*. **2010**, *44*, 5755-5761; Yan, X.Q.; Shen, Q.J.; Zhao, X.R,; Gao, H.Y.; Pang, X.; Jin, W.J. *Anal. Chim. Acta* **2012**, *753*, 48-56; Muir, D.C.G.; Howard, P.H. *Environ. Sci. Technol.* **2006**, *40*, 7157-7166; Goss, K.U.; Bronner, G.; Harner, T.; Hertel, M.; Schmidt, T. C. *Environ. Sci. Technol.* **2006**, *40*, 3572-7577.

12. Vishweshwar, P.; McMahon, J.A.; Bis, J. A.; Zaworotko, M.J. *J. Pharm. Sci*. **2006**, *95*, 499-516; Aakeröy, C.B.; Forbes, S.; Desper, J. *CrystEngComm* **2014**, *16*, 5870-5877; Blagden, N.; Coles, S. J.; Berry, D. J. *CrystEngComm* **2014**, *16*, 5753-5761.

13. George, N.; Forrest, J.O.; Burton, R.C.; Aakeröy, C.B., *US Pat.* US2013/0203792A1, **2013**.

14. Millar, D.I.A.; Casely, H. E. M.; Allan, D.R.; Cumming, A.S.; Lennie, A.R.; Mackay, A.J.; Oswald, I.D.H.; Tang, C.C.; Pulham; C.R. *CrystEngComm* **2012**, *14*, 3742-3749; Wang, Y.; Yang, Z.; Li, H.; Zhou, X.; Zhang, Q.; Wang, J.; Liu, Y. *Propellants Explos. Pyrotech*. **2014**, *39*, 590-596; Landenberger, K.B.; Matzger, A.J. *Cryst. Growth Des*. **2012**, *12,* 3603-3609; Bolton, O.; Simke, L.R.; Pagoria, P.F.; Matzger, A.J. *Cryst. Growth. Des.* **2012**, *12,* 4311-4314.

15. Springuel, G.; Leyssens, T. *Cryst. Growth Des*. **2012**, *12*, 3374-3378.

16. Urbanus, J.; Roelands, C.P.M.; Verdoes, D.; Jansens, P.J.; ter Horst, J.H. *Cryst. Growth Des*. **2010**, *10*,1171-1179; Metrangolo, P.; Carcenac, Y.; Lahtinen, M.; Pilati, T.; Rissanen, K.; Vij, A.; Resnati, G. *Science* **2009**, *323*, 1461-1464.

17. Golovanov, D.G.; Lyssenko, K.A.; Antipin, M.Y.; Vygodskii, Y.S.; Lozinskaya, E.I.; Shaplov, A.S. *Cryst. Growth Des*. **2005**, 5, 337-340.

18. Aakeröy, C.B.; Wijethunga, T.K.; Desper, J. *CrystEngComm* **2014**, *16*, 28-31; Aakeröy, C.B.; Wijethunga, T.K.; Desper, J. *J. Mol. Struct.* **2014**, *1072*, 20-27.

19. Aakeröy, C.B.; Wijethunga, T.K.; Desper, J. *New J. Chem.* **2015**, *39*, 822-828; Voss, M. E.; Beer, C. M.; Mitchell, S. A.; Blomgren P. A.; Zhichkin, P. E. *Tetrahedron* **2008**, *64*, 645-651.

20. Omnic 8.0 © **1992-2008**, Thermo Fisher Scientific Inc.

21. Schultheiss, N.; Newman, A. *Cryst. Growth Des*. **2009**, *6*, 2950-2967.

Chapter 9 - Crystal engineering of energetic materials: Co-crystals of ethylenedinitramine (EDNA) with modified performance and improved chemical stability[1]

9.1 Introduction

Energetic materials contain substantial amounts of stored energy that can be released rapidly,[2] leading to explosions. Representatives of energetic materials include explosives, propellants and pyrotechnics.[3] Even though a large number of different energetic compounds are known in armaments, mining, fireworks and space explorations,[4] many have drawbacks leading to restrictions or limitations of their use.[5] Common problems include sensitivity to impact, heat, shock or friction[6] (e.g. RDX[7] and CL-20[8]), as well as undesirable reactivity towards different environmental conditions (e.g. nitramine explosives[9]), and high toxicity.[10] Furthermore, highly powerful energetic materials inherently display high sensitivity and/or high reactivity leading to a power-safety contradiction[11] and, consequently, designing powerful energetic materials with improved safety and stability is a major challenge.[12]

The design of better energetic materials typically follows one of two approaches. First, a completely new molecule or salt can be prepared.[13] But in order to discover a material with the required properties such as high power, low sensitivity and low reactivity expressed in an integrated manner,[14] while optimizing all these properties within a finite time scale, is challenging.[15] An alternative approach is to use co-crystal technology[16] wherein a known energetic material is combined with either an energetic or a non-energetic compound[17] via non-covalent interactions within a crystalline framework.[18] Co-crystallizations can provide means for altering a range of properties such as density, mechanical and thermal stability, and solubility, which can all facilitate the pursuit of safer energetic materials.[19] Furthermore, co-crystallizations can be utilized

in stabilizing volatile[20] energetics, thereby lowering the risk of exposure through inhalation of toxic energetic materials.[21] This provides an avenue to handle many nitro-containing energetics that are toxic. Thus, a co-crystal of an energetic material[22] can, in certain circumstances, be more useful because of superior chemical stability and shelf-life even though it may have slightly lower energetic performance.

A number of literature reports show evidence of successful co-crystallizations that lead to reduced sensitivity of the energetic materials.[23] Furthermore, numerous reports provide insights into reducing the thermal sensitivity of energetics.[24] But to date, there are no reports that employ co-crystallization approach with the intention of reducing the chemical reactivity to stabilize, highly reactive energetic compounds, Figure 9.1.

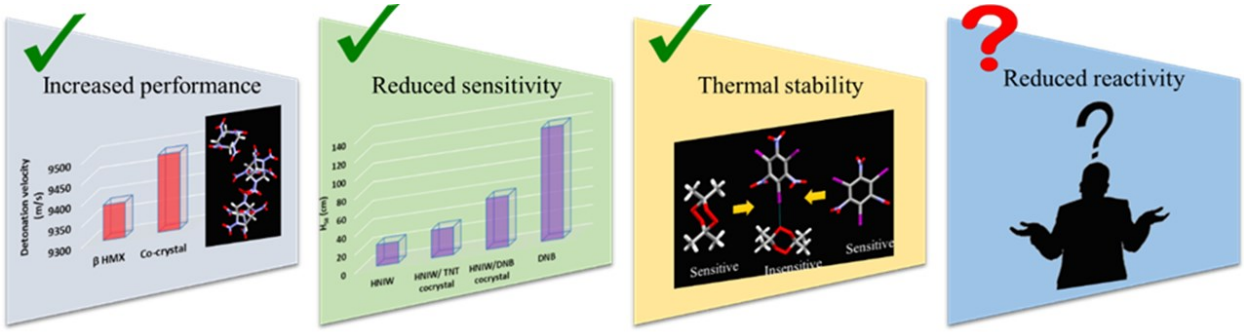

Figure 9.1 Current situation in the field of energetic co-crystallization

Ethylenedinitramine, (**EDNA**), (Figure 9.2) also known as Haleite,[25] is known as the first entirely American high explosive.[26] **EDNA** combines the properties of a high explosive like TNT and an initiating agent like mercury fulminate, possessing a high brisance, comparatively low impact sensitivity and high heat sensitivity. This compound is applied as a secondary explosive, booster explosive and in the preparation of cast explosives such as Ednatol.[27]

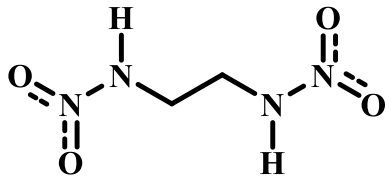

Figure 9.2 Chemical structure of **EDNA**

An important reason behind the restrictions in the use of **EDNA** is its relatively high chemical reactivity, a common drawback associated with many nitramine-based explosives.[28] Overly acidic compounds are often prone to chemical instability and hygroscopicity,[29] which can create problems with transport, processing, and storage, leading to a high risk of handling them. For example, tetranitropyrole is unstable at ambient temperatures[30] and dinitrotriazole is deliquescent,[31] and both contain an acidic N-H moiety. The highly acidic picric acid, another well-known explosive, is corrosive and reacts readily with metals to form shock-sensitive salts. **EDNA** is also highly acidic[32] (pK_{a1} – 5.31 and pK_{a2} – 6.64).[33] The reason is upon deprotonation, the negative charge that forms can be easily delocalized with the assistance of electron withdrawing nitro groups. Thus **EDNA** is corrosive and can react with metals and metal salts[34] to produce new materials with unpredictable properties. For example, Cu(II)EDNA is easily synthesized and has low impact sensitivity[35] whereas Pb(II)EDNA displays superior properties/performance compared to **EDNA** itself.[36]

Thus, our study was undertaken to utilize a co-crystallization approach to block the acidic protons and to reduce the reactivity and to alter the physical properties and stability of **EDNA** while retaining some valuable characteristics associated with the energetic material. A close look at the crystal structure of **EDNA**[37] (Figure 9.3) reveals that these acidic protons are interacting with nitro oxygen atoms which are poor hydrogen-bond acceptors. Thus, it should be possible to

make co-crystals of **EDNA** by introducing strong hydrogen bond acceptors to the system, by disrupting this weak hydrogen bond.

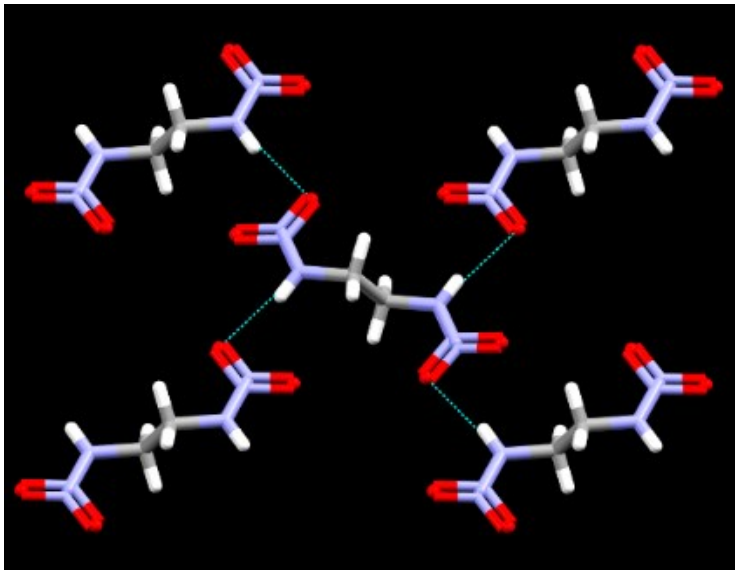

Figure 9.3 Part of the crystal structure of **EDNA** with hydrogen bonds between nitro oxygen atoms and acidic amine protons[37]

With this in mind, fifteen hydrogen-bond acceptors were selected that potentially would compete successfully with the nitro groups for the attention of the acidic protons, Figure 9.4, including N-based acceptors (**A21-A27**, **A31** and **A32**), O-based acceptors (**A28-A30**) and mixed N-and O-based acceptors (**A33-A35**). These 15 acceptors can be further categorized as symmetric ditopic (**A21-A30**), monotopic (**A31** and **A32**) and dissymmetric ditopic (**A33-A35**). The reason for selecting primarily ditopic acceptors (all but **A31** and **A32**) was first of all, some degree of structural consistency was expected by a combination of a ditopic donor and a ditopic acceptor which is likely to produce infinite supramolecular chains. Second, the N-oxides are likely to form the same hydrogen-bonded motifs as the parent N-heterocycles but with a better oxygen balance which would be beneficial from a performance perspective.

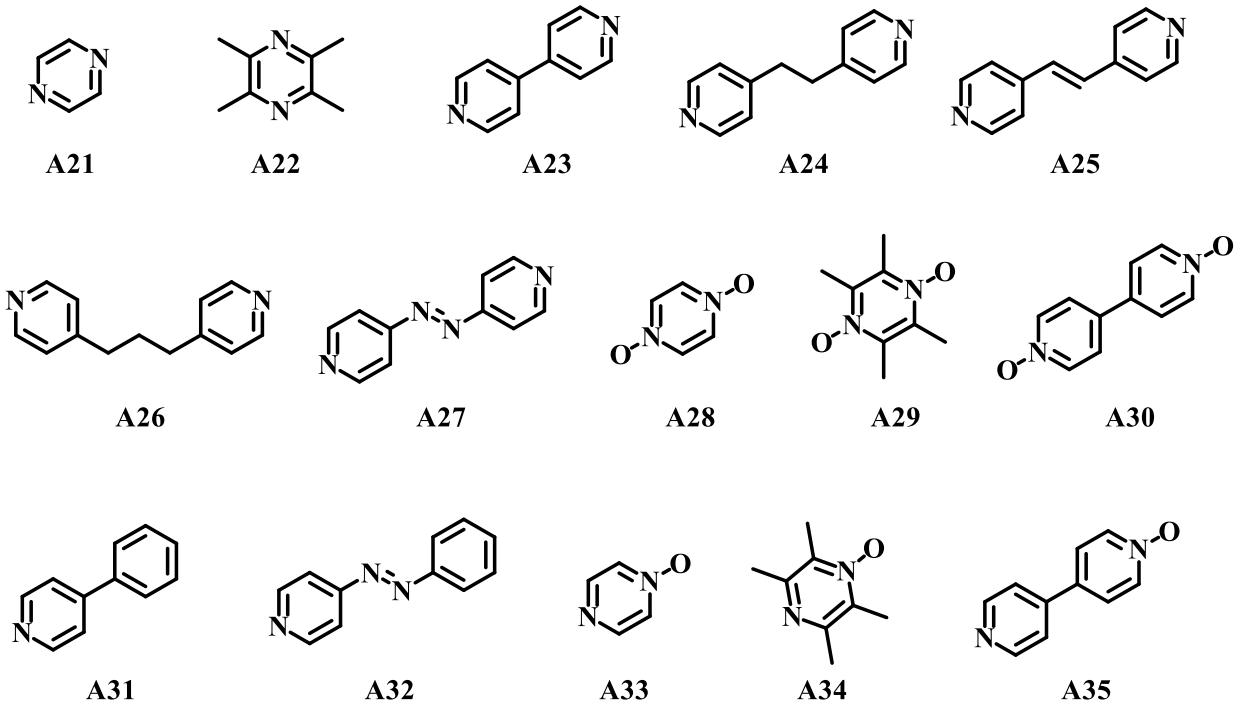

Figure 9.4 Hydrogen-bond acceptors used in this study

The study is undertaken in response to four hypotheses,

1. **EDNA** is a suitable target for co-crystal synthesis.
2. The acidic protons of **EDNA** can be engaged and can be protected via hydrogen bonding to suitable co-formers.
3. Explosive properties and thermal properties of **EDNA** can be modulated in a useful manner by making co-crystals of **EDNA**.
4. The chemical stability of **EDNA** can be enhanced by reducing the reactivity of **EDNA** through co-crystallizations.

9.2 Experimental

9.2.1 General

All the precursors, solvents and acceptors **A21**-**A26** and **A31** were purchased from commercial sources and used without further purification. **EDNA** was synthesized following a reported procedure.[38] **A28**-**A30** and **A33**-**A35** were synthesized following previously reported procedures.[39] **A27**[40] and **A32**[41] were also synthesized following reported procedures. ^{1}H NMR spectra were recorded on a Varian Unity plus 400 MHz spectrometer. Infrared spectra were recorded with a Nicolet 380 FT-IR. Differential scanning calorimetry (DSC) measurements were carried out on a TA Instruments Q20, using Tzero aluminum pans under nitrogen purge (50.0 mL/min) at a heating rate of 5 °C/min over a range of 30 - 300 °C.

Standard protocols for handling energetic materials were followed at all times.[42] All the synthesis and handling of **EDNA** were done inside a fume hood and used nonmetallic spatulas when measuring **EDNA**. Kevlar gloves, lab coat and goggles were worn all the time. Mechanical actions involving scratching or scraping were avoided and **EDNA** was synthesized only in small amounts (~ 200 mg).

9.2.2 Synthesis of EDNA

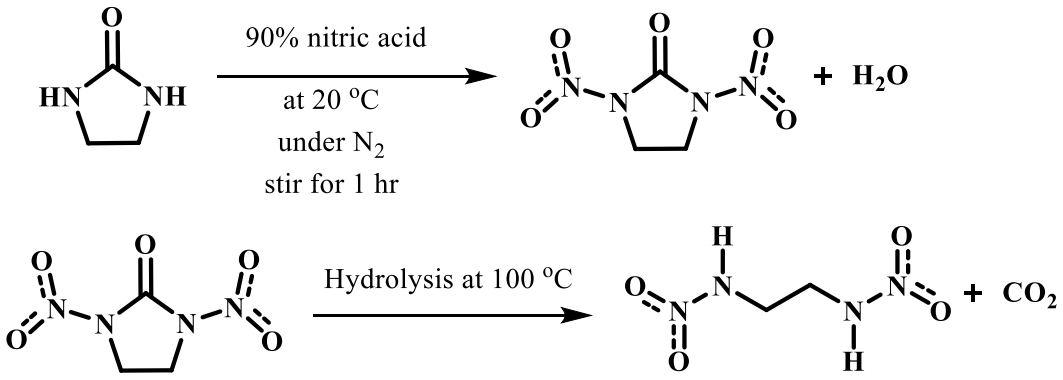

A round bottom flask was equipped with a stir bar and 2.0 mL of 90% nitric acid (fuming nitric acid) under nitrogen atmosphere and cooled down to 0 °C. To this, 0.5 g of ethylene urea (2-imidazolidone) was added portion wise while keeping the temperature below 20 °C. The reaction mixture was stirred under these conditions for one hour and subsequently allowed to warm to room temperature. The reaction mixture was then quenched with iced water and the precipitate that formed was collected by filtration.

The precipitate was added to about 20 mL of boiling water in small portions and the temperature of water was maintained until no more gas evolution was seen. Then the aqueous solution was cooled in an ice bath and the precipitated desired product was collected by filtration as a white crystalline powder. Yield: 0.48 g (55%); m.p. 178-180 °C (reported 174-178 °C)[43]; ^{1}H NMR (400 MHz, DMSO-d_6):12.12 (s br, 2H), 3.59 (s, 4H).

9.2.3 Theoretical calculations

Geometry optimizations of **EDNA** at various fixed torsion angles were done with DFT at B3LYP/6-31G* level of theory using Spartan'08.[44]

9.2.4 Synthesis and characterization of co-crystals

EDNA was combined with the 15 acceptors in stoichiometric ratios and dissolved in a minimum amount of methanol and kept in vials for slow evaporation in order to obtain co-crystals suitable for single crystal X-ray diffraction. Once the crystals were obtained they were analyzed using IR spectroscopy and DSC to identify potential co-crystals. From the initial screening with IR and DSC eight out of 15 experiments produced co-crystals. Out of the eight co-crystals obtained, six yielded crystals suitable for single-crystal diffraction: **EDNA:A23**, **EDNA:A24**, **EDNA:A25**, **EDNA:A27**, **EDNA:A28** and **EDNA:A32**. Thermal properties of all eight co-crystals were obtained using DSC data and detonation properties were calculated for the six

compounds for which experimental densities were available from crystallographic data. For the co-crystals **EDNA:A23**, **EDNA:A24**, **EDNA:A25** and **EDNA:A28** room temperature unit cells and room temperature densities were determined. Table 9.1 summarizes the experimental details for the six co-crystals obtained. Appendix B.8 contains the relevant X-ray experimental data and Appendix C.5 contains the DSC traces.

Table 9.1 Experimental details for the co-crystals obtained

Code	Mixed Mole ratio	Amounts used	Solvent and method	Crystal stoichiometry	Crystal color & habit
EDNA:A23	1:1	**EDNA** -10 mg, 0.067 mmol **A23** - 10 mg, 0.067 mmol	Methanol, Slow evaporation	1:1	Colorless prism
EDNA:A24	1:1	**EDNA** - 10 mg, 0.067 mmol **A24** - 12 mg, 0.067 mmol	Methanol, Slow evaporation	1:1	Colorless plate
EDNA:A25	1:1	**EDNA** - 10 mg, 0.067 mmol **A25** - 12 mg, 0.067 mmol	Methanol, Slow evaporation	1:1	Colorless prism
EDNA:A27	1:1	**EDNA** - 10 mg, 0.067 mmol **A27** - 12 mg, 0.067 mmol	Methanol, Slow evaporation	1:1	Orange plate
EDNA:A28	1:1	**EDNA** - 10 mg, 0.067 mmol **A28** – 7.5 mg, 0.067 mmol	Methanol, Slow evaporation	1:1	Colorless plate
EDNA:A32	1:2	**EDNA** - 10 mg, 0.067 mmol **A32** - 24 mg, 0.13 mmol	Methanol, Slow evaporation	1:2	Orange prism

9.2.5 Impact sensitivity testing

Impact sensitivities of **EDNA**, **EDNA:A23** and **EDNA:A28** were measured by drop impact testing. The tests were done using an apparatus designed to accommodate small amounts of material[45] and was calibrated against tetranitromethane (H_{50} - 38 cm). Approximately 0.20 mg of each sample were sealed into aluminum DSC pans. A freefalling 5 lb weight was used to strike the samples from different heights measured in centimeters which subsequently allowed us to identify $H_{50,}$ the height at which the material exhibited a 50% chance of detonation using Bruceton Analysis.[46] This is a nonstandard testing apparatus and the results obtained are useful for relative comparisons only.

9.3 Results

9.3.1 IR analysis

Initial co-crystal screening was carried out by combining **EDNA** and the acceptors in stoichiometric ratios and the products obtained were analyzed with IR spectroscopy. The solvent of choice was methanol as both **EDNA** and the acceptors showed comparable solubility in alcohols. Eight of fifteen attempts yielded co-crystals as indicated by IR data provided in Table 9.2. The analysis was done by comparing the IR spectrum of the crystals obtained from solution with the starting reactants.

Table 9.2 IR analysis on crystals

Co-crystal	IR stretches (cm^{-1})		Co-crystal or not
	EDNA	Co-crystal	
EDNA:A21	1589, 1446	Only EDNA	No
EDNA:A22	1589, 1446	Only EDNA	No
EDNA:A23	1589, 1446	1592, 1440	Yes
EDNA:A24	1589, 1446	1602, 1447	Yes
EDNA:A25	1589, 1446	1599, 1456	Yes
EDNA:A26	1589, 1446	1601, 1442	Yes
EDNA:A27	1589, 1446	1585, 1444	Yes
EDNA:A28	1589, 1446	1584, 1440	Yes
EDNA:A29	1589, 1446	Only A9	No
EDNA:A30	1589, 1446	Only EDNA	No
EDNA:A31	1589, 1446	1985, 1443	Yes
EDNA:A32	1589, 1446	1587, 1426	Yes
EDNA:A33	1589, 1446	Only EDNA	No
EDNA:A34	1589, 1446	Only EDNA	No
EDNA:A35	1589, 1446	Only EDNA	No

9.3.2 Crystal structures

Although vibrational spectroscopy provides information about whether a co-crystal has formed or not, it does not reveal to what extent the amine protons on **EDNA** are participating in hydrogen bonding. To address this issue, crystallographic data are needed and six of the eight new co-crystals were characterized using single-crystal X-ray diffraction. Crystallographic data and

halogen bond geometries for the six co-crystals (**EDNA:A23**, **EDNA:A24**, **EDNA:A25**, **EDNA:A27**, **EDNA:A28** and **EDNA:A32**) are reported in the Appendix B.8.

The crystal structure of **EDNA:A23** (Figure 9.5) reveals a 1:1 stoichiometry where the two components are connected via primary N-H···N(py) hydrogen bonds. As intended, the pyridine-based acceptor sites have provided a successful replacement for the N-H···O(nitro) hydrogen bonds present in the crystal structure of **EDNA** itself, Figure 9.3. Somewhat surprisingly though, the molecular geometry of **EDNA** molecules in the **EDNA:A23** lattice is very different when compared to their molecular conformations in the crystal structure of **EDNA** by itself, Figure 9.3.

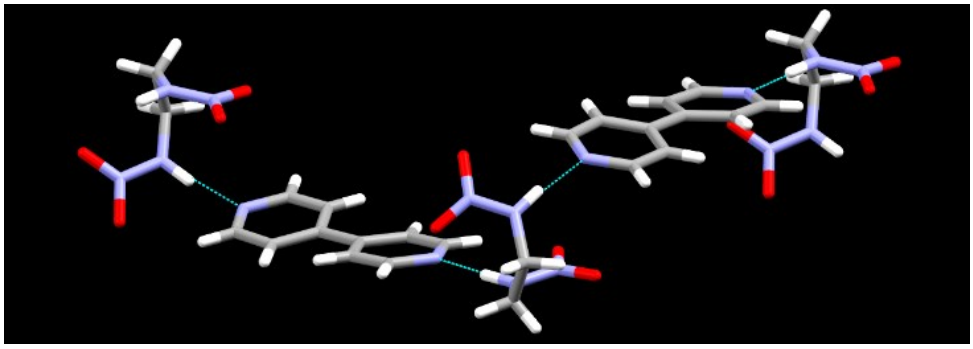

Figure 9.5 Primary interactions in the **EDNA:A23** co-crystal

The crystal structure of **EDNA:A24** reveals the expected N-H···N(py) hydrogen bonds and the two components are again present in a 1:1 ratio, Figure 9.6. In this structure the **EDNA** molecules adopt a 180° torsion angle of the N-C-C-N 'backbone' similarly as in **EDNA** crystal structure itself, Figure 9.3.

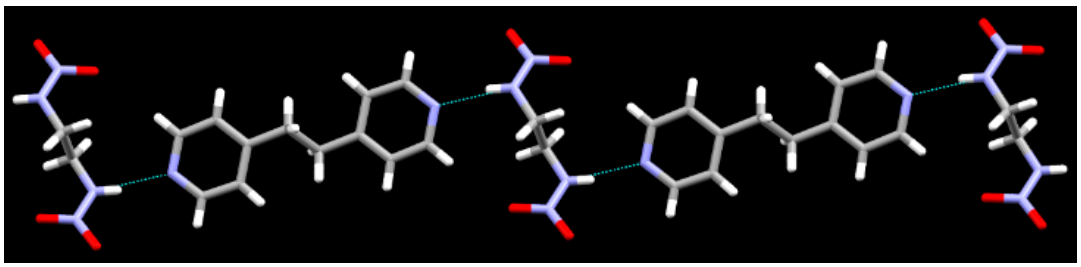

Figure 9.6 Primary hydrogen bonds in the **EDNA:A24** co-crystal

The crystal structure of **EDNA:A25** (Figure 9.7) shares the main structural features with those found in the structure of **EDNA:A24** with a 1:1 stoichiometry, structure directing N-H···N(py) hydrogen bonds resulting in infinite chains, and a 180° torsion angle of the N-C-C-N backbone of **EDNA**.

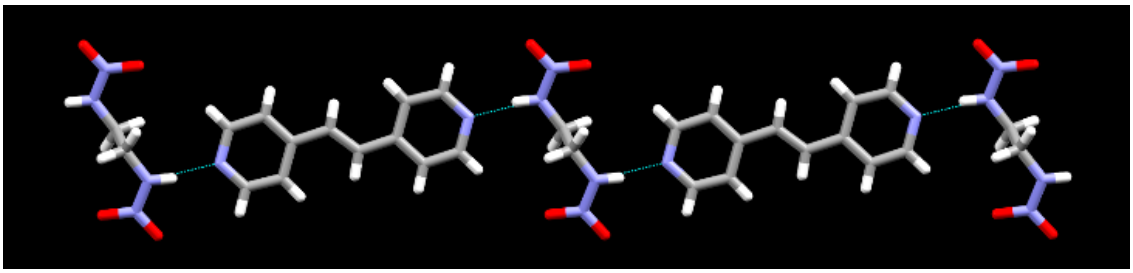

Figure 9.7 Part of the infinite hydrogen-bonded chain in the **EDNA:A25** co-crystal

Although 4,4'-azopyridine, the co-former in **EDNA:A27**, does contain two additional nitrogen atoms that, in theory, could engage with the acidic protons of **EDNA**, the two pyridine sites are substantially better acceptors,[47] (Figure 9.8). Consequently, N-H···N(py) driven hydrogen-bonded chains dominate the crystal structure, similarly to what was found in both **EDNA:A24** and **EDNA:A25**. The stoichiometry again is 1:1 which is dictated by the fact that **EDNA** has two strong donors which are matched by the two main N(py) acceptor sites on **A27**.

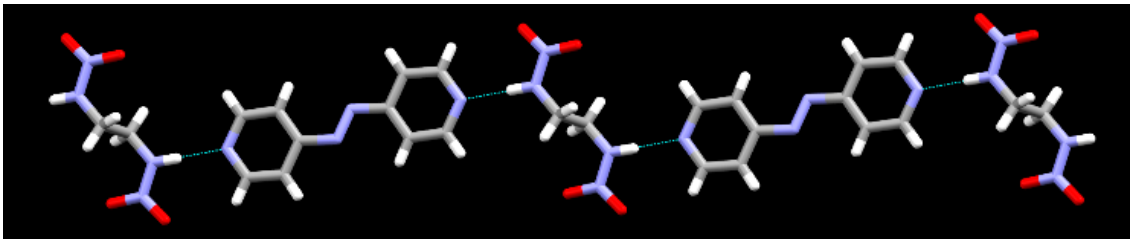

Figure 9.8 Primary hydrogen bonds in the **EDNA:A27** co-crystal

The crystal structure of **EDNA:A28** (Figure 9.9) shows a 1:1 stoichiometry, and infinite hydrogen bonds generated by N-H···O-N(py) chain formation between the oxygen atoms of N-oxide and the acidic N-H protons of **EDNA**. This structure illustrates that **EDNA** is capable of

forming co-crystals not only with N-based acceptors but also with O-based acceptors via the acidic protons.

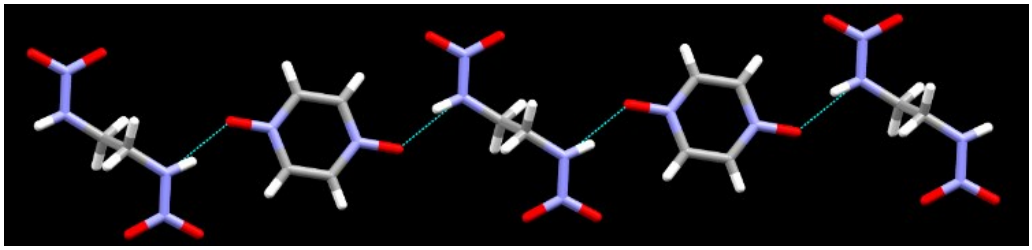

Figure 9.9 Primary interactions in the **EDNA:A28** co-crystal

The final crystal structure obtained in this series was with a monotopic hydrogen-bond acceptor, **A32**, and consequently the stoichiometry in this case is 1:2 (**EDNA:A32**), Figure 9.10. The chains that resulted when ditopic acceptors were combined with **EDNA** is now replaced with a discrete trimeric motif.

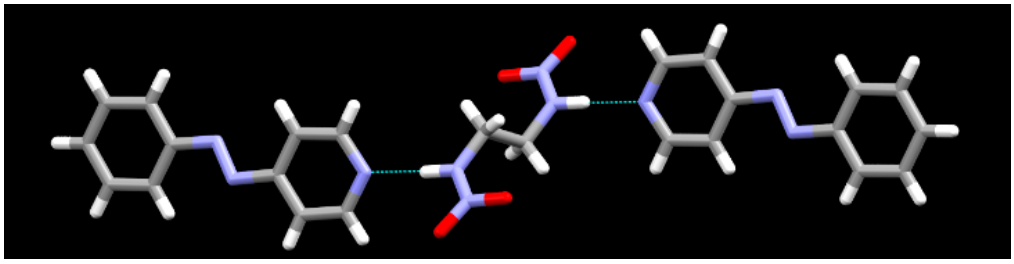

Figure 9.10 Main hydrogen-bonds in the **EDNA:A32** co-crystal

9.3.3 Torsion angle calculation for EDNA:A23

As mentioned earlier the molecular geometry of **EDNA** molecules in the **EDNA:A23** lattice is very different when compared to their molecular conformations in the crystal structure of **EDNA** by itself as well as the other co-crystals in this series. The N-C-C-N torsion angle for **EDNA** in **EDNA:A23** is 28°, while it is 180° for pure **EDNA**. In order to find the energy difference between the two orientations, a molecular structure optimization was performed. A plot of energy vs torsion angle, (Figure 9.11) shows that the energy difference between the two conformations is about 24 kJ/mol, favoring the molecular structure observed in the **EDNA** crystal structure. It is

reasonable to assume that the relatively small energy differences can readily be compensated for by the new N-H···N(py) hydrogen bonds that are observed in the structure of **EDNA:A23**.

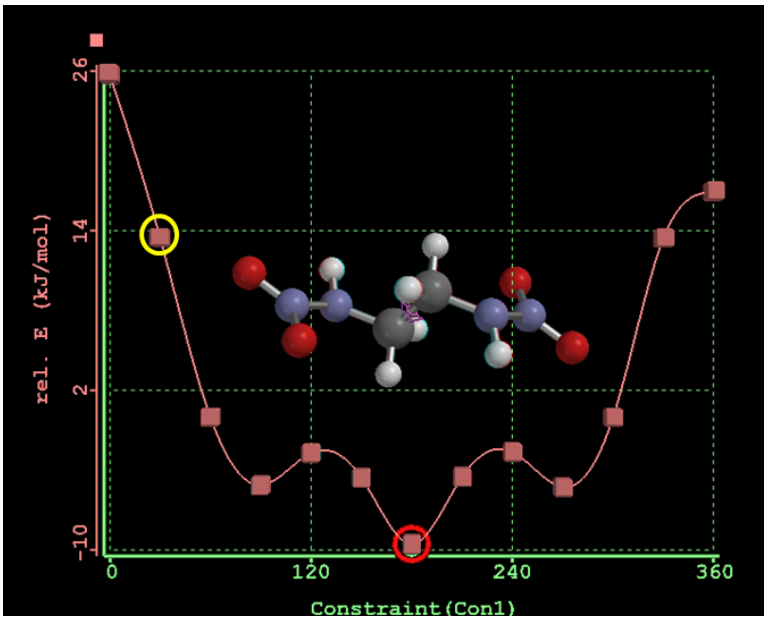

Figure 9.11 Relative energies of different orientations of **EDNA**. (N-C-C-N torsion angle was changed from 0° to 360° with an increment of 30°); Red point : N-C-C-N angle is 180° (pure **EDNA**) and yellow point : N-C-C-N angle is 28° (**EDNA:A23**)

9.3.4 Thermal analysis

The thermal analysis of the eight co-crystals (including the two co-crystals without single crystal data) was mainly focused on four aspects: melting temperature, decomposition temperature, enthalpy of melting and enthalpy of decomposition, and the results were compared with that of **EDNA**. As an example, Figure 9.12 shows the DSC trace for **EDNA:A27**. The results are summarized in Table 9.3. Pure **EDNA** has a melting point of 180 °C and decomposes at 186 °C accompanied by a 1971 ± 18 J/g release of energy (for comparison the corresponding energy release for HMX is 1987 J/g [48]).

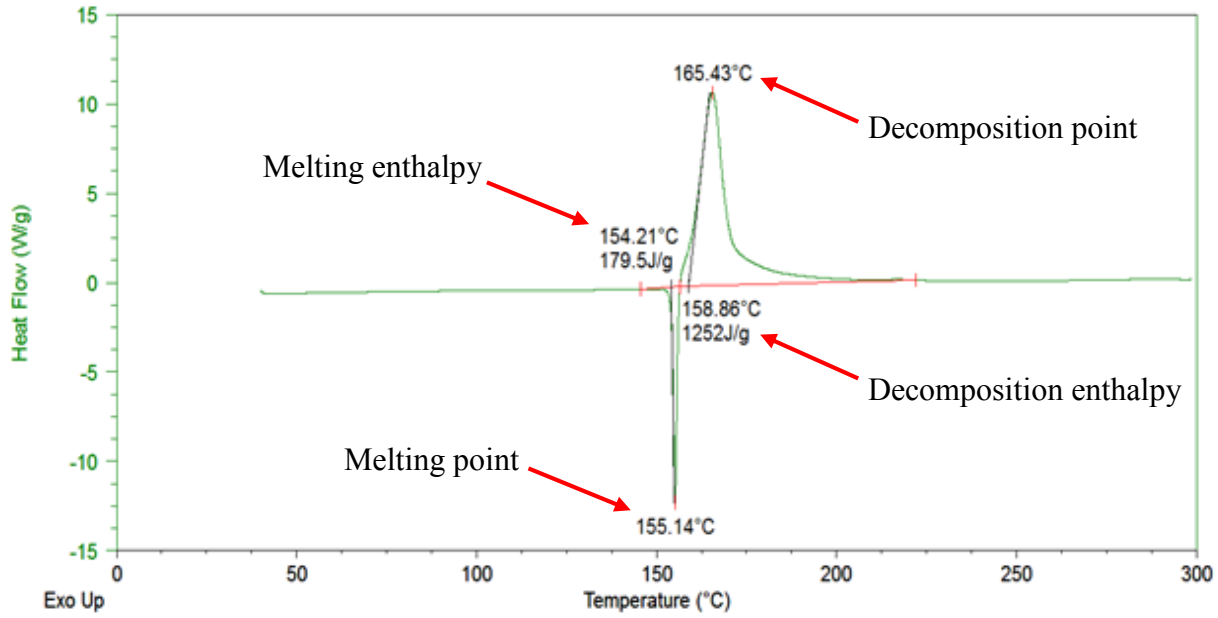

Figure 9.12 DSC trace for **EDNA:A27** co-crystal

Table 9.3 Thermal properties of co-crystals

Compound/Co-crystal	Co-former melting point (^{0}C)	Co-crystal Melting point (^{0}C)	Melting enthalpy (J/g)	Decomposition point (^{0}C)	Energy released at decomposition (J/g)
EDNA	-	180	215 ± 5	186	1971 ± 18
EDNA:A23	112-114	146	146 ± 11	189	1055 ± 11
EDNA:A24	110-112	129	133 ± 14	191	985 ± 3
EDNA:A25	148-152	-	-	198	955 ± 23
EDNA:A26	53-56	118	119 ± 5	194	769 ± 31
EDNA:A27	106-110	154	160 ± 28	165	1242 ± 15
EDNA:A28	285-289	156	150 ± 7	172	1447 ± 14
EDNA:A31	69-73	94	198 ± 2	203	1214 ± 37
EDNA:A32	96-99	133	121 ± 4	168	982 ± 18

Melting enthalpies and decomposition enthalpies are reported as an average from two trials for each compound with the calculated standard deviation

9.3.5 Performance analysis

The detonation properties of the six co-crystals were calculated using experimental densities obtained from the single-crystal structure determinations. Detonation velocities and pressures were calculated using nitrogen equivalents of different detonation products,[49] and oxygen balances were calculated using well-established methods.[50] Table 9.4 summarizes the

detonation properties for the six co-crystals. The oxygen balance of an explosive is the mass of oxygen either in excess or in deficit of that required for the complete oxidation of the carbon and hydrogen atoms present in the explosive.[51] A negative balance means that there is an insufficient amount of oxygen for complete combustion. **EDNA** has an oxygen balance of -32% and the co-crystals of **EDNA** presented here have a more negative oxygen balance with **EDNA:A28** at -67% being the least unfavorable (for comparison TNT has an oxygen balance of -74%).

The impact sensitivities of **EDNA**, **EDNA:A23**, and **EDNA:A28** were examined using conventional drop-weight measurements and calculated using Bruceton Analysis. The H_{50} values are 99 ± 1 cm, 140 ± 1 cm, and 138 ± 1 cm, respectively, where a higher value indicates reduced sensitivity.

Table 9.4 Detonation properties of co-crystals

Compound/Co-crystal	Density (g/cm^3)	Detonation velocity* (km/s)	Detonation pressure* (GPa)	Oxygen balance*
EDNA	1.65 (RT)	7.890	26.72	-32
EDNA:A23	1.489 (120K) 1.452 (RT)	6.178	15.24	-141
EDNA:A24	1.407 (120K) 1.355 (RT)	5.967	13.70	-158
EDNA:A25	1.460 (120K) 1.434 (RT)	6.030	14.32	-154
EDNA:A27	1.529 (120K)	6.504	17.21	-129
EDNA:A28	1.68 (120K) 1.64(RT)	7.256	22.73	-67
EDNA:A32	1.432 (120K)	5.948	13.75	-173

*Calculated properties
All the velocity and pressure calculations for the co-crystals are done using low temperature densities while for EDNA the calculations are done using room temperature density

9.4 Discussion

9.4.1 Structural consistency and diversity

In all six crystal structures the targeted acidic N-H protons did form hydrogen bonds with the acceptors resulting in successful co-crystallization. In five of the six structures, **EDNA:A23** being the exception, the **EDNA** molecule adopted the most favorable molecular geometry with

180° torsion angle of the N-C-C-N backbone. Another supramolecular synthetic target in this study was to achieve some structural consistency through the use of ditopic hydrogen-bond acceptors. In four of the five crystal structures of **EDNA** with ditopic acceptors (**A23, A24, A25, A28**) the result was an infinite hydrogen-bonded chain of alternating **EDNA**:co-former components, and the zig-zag shaped chain found in the crystal structure of **EDNA:A23** was due to the unusual conformation of the backbone of the **EDNA** molecules in that particular solid.

9.4.2 Alteration of thermal properties

The melting points for six of the eight co-crystals of **EDNA** fall between those of the two pure components of each co-crystal, Figure 9.13. **EDNA:A28** has a lower melting point than both initial compounds while **EDNA:A25**, has a decomposition temperature approximately twenty degrees higher than the melting point of **EDNA**, and about ten degrees above its decomposition temperature. As mentioned previously, a drawback with **EDNA** is a relatively high sensitivity to heat, which means that the co-crystal **EDNA:A25** offers an improvement in this respect.

The relationship between molecular structure and melting point of the corresponding solid is governed by numerous intermolecular interactions and it is largely unpredictable. However, a systematic co-crystallization approach, can provide some trends and correlations between molecular structure and properties even in heteromeric solids as long as the primary structural features are somewhat consistent from one compound to the next. Despite the lack of strong correlation between the two variables, the general trend indicates that the co-former has an influence on the co-crystals of **EDNA**.

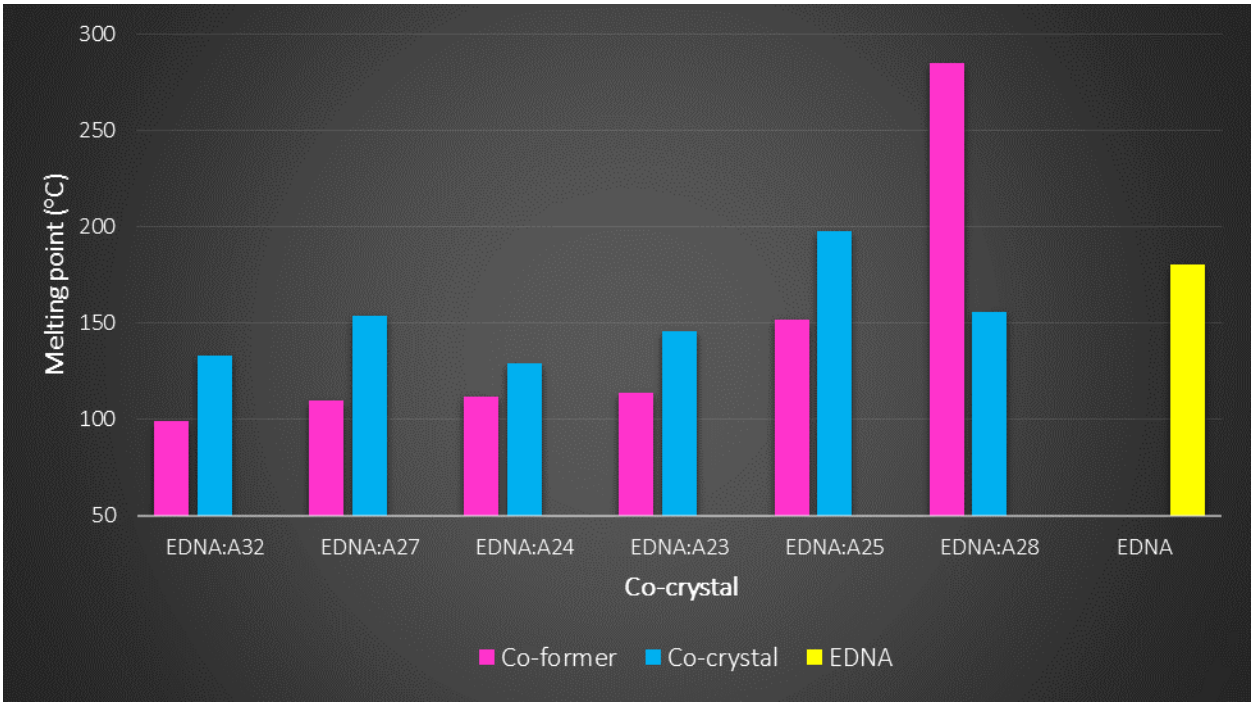

Figure 9.13 Co-crystal and co-former melting points

Among the eight co-crystals **EDNA:A28** gives the highest enthalpy change upon decomposition (as determined by DSC) which is likely related to the influence of the co-former, **A28**, which has a more favorable oxygen balance than any of the co-formers used in this study.[52] The DSC analysis also shows that there is a relatively large temperature difference between the melting and decomposition temperature in **EDNA:A26** and **EDNA:A31** compared to the same parameter in pure **EDNA**. This means that the window of stability beyond the melting point can be substantially improved upon co-crystallization. It is particularly interesting to note that the molten phase of **EDNA:A31** shows a stability beyond that of the decomposition temperature of **EDNA** itself which indicates that some critical intermolecular interactions remain intact in the liquid phase.

9.4.3 Alteration of detonation properties

Density is a major contributor to the explosive properties of an energetic material.[53] Therefore, an analysis was done to examine whether there is any correlation between the density of the pure co-former and the density of the corresponding **EDNA** co-crystal, Figure 9.14 and Figure 9.15. The analysis is done only for the co-crystals where the room temperature densities are reported for the co-formers.

EDNA:A28 has a comparable density (1.64 g/cm^3) to **EDNA** (1.65 g/cm^3). As observed with the melting points of the **EDNA** co-crystals, there is an increase of density of the co-crystal as the density of the co-former goes up (**EDNA:A25** is a slight anomaly) and the big improvement is seen in the co-crystal with an N-oxide based co-former, **A8**.

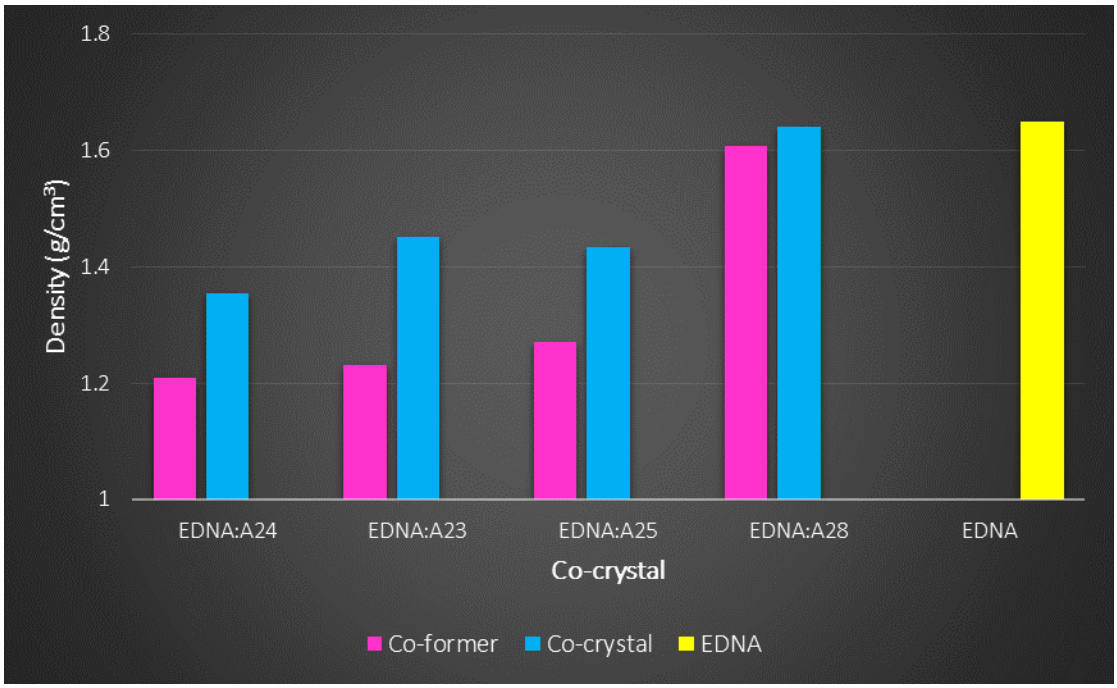

Figure 9.14 Co-crystal and co-former densities

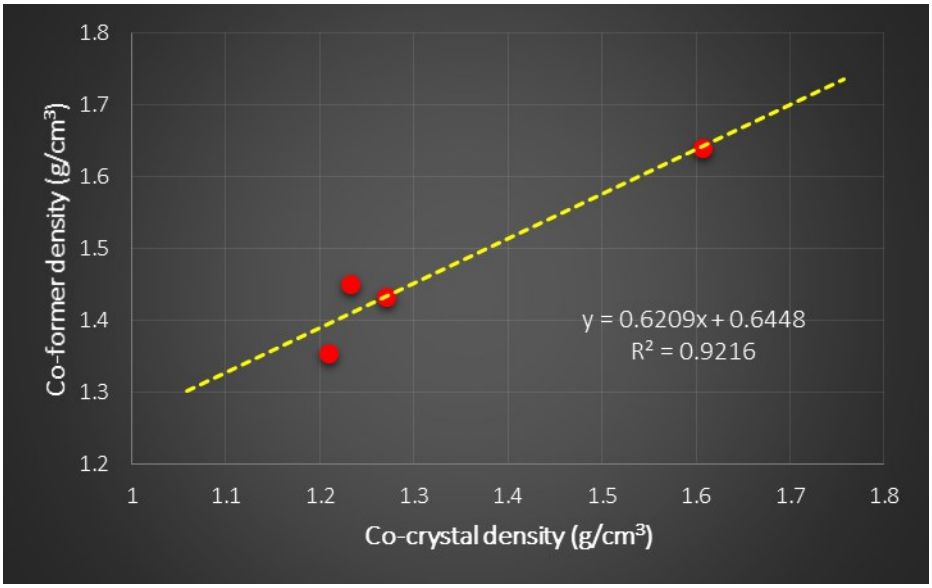

Figure 9.15 Correlation between co-crystal and co-former densities

In this systematic approach, structural consistency was a desired outcome as then it could also expect a positive correlation between packing coefficient and density (no heavy atoms beyond nitrogen and oxygen were present in any of the co-formers). To verify this hypothesis the two parameters were plotted against each other, Figure 9.16.

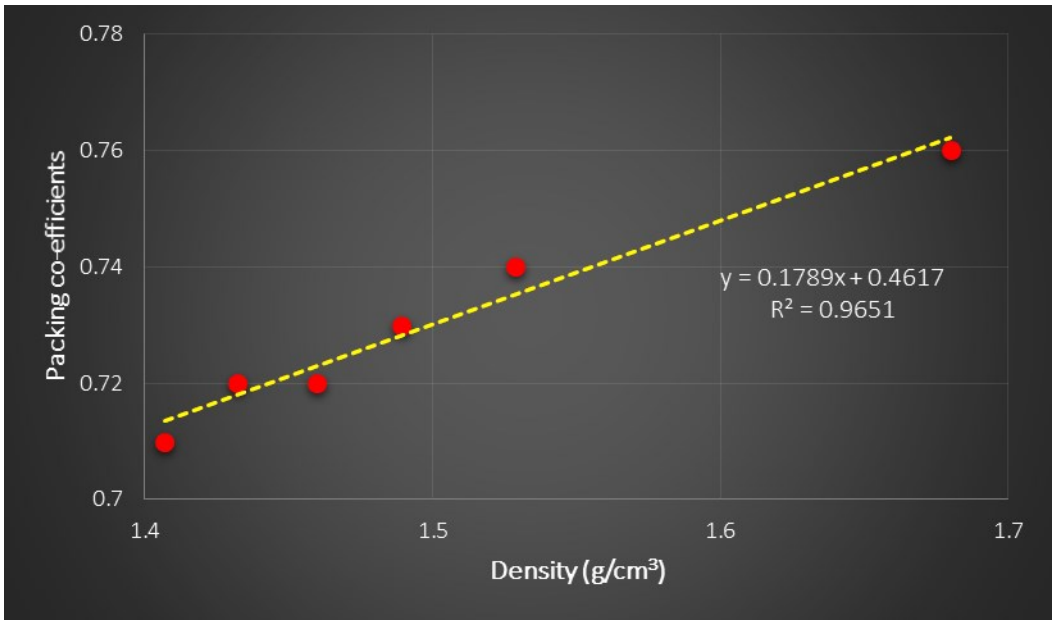

Figure 9.16 A plot of packing coefficient vs. density in six **EDNA** co-crystals

As shown, the packing coefficient provides an excellent indication of density of the resulting lattice.

9.4.4 N-oxides as better co-formers

The use of N-oxide as co-formers serves two purposes when it comes to designing and synthesizing energetic co-crystals. The oxygen balance is obviously benefitting by moving from a parent N-heterocycle to the corresponding N-oxide, but the density can also improve.[54] In order to examine how general this second point is, a CSD analysis was conducted to compare densities of ten N-heterocyclic compounds and their corresponding *mono*-, and/or *bis*- N-oxides,[55]Figure 9.17.

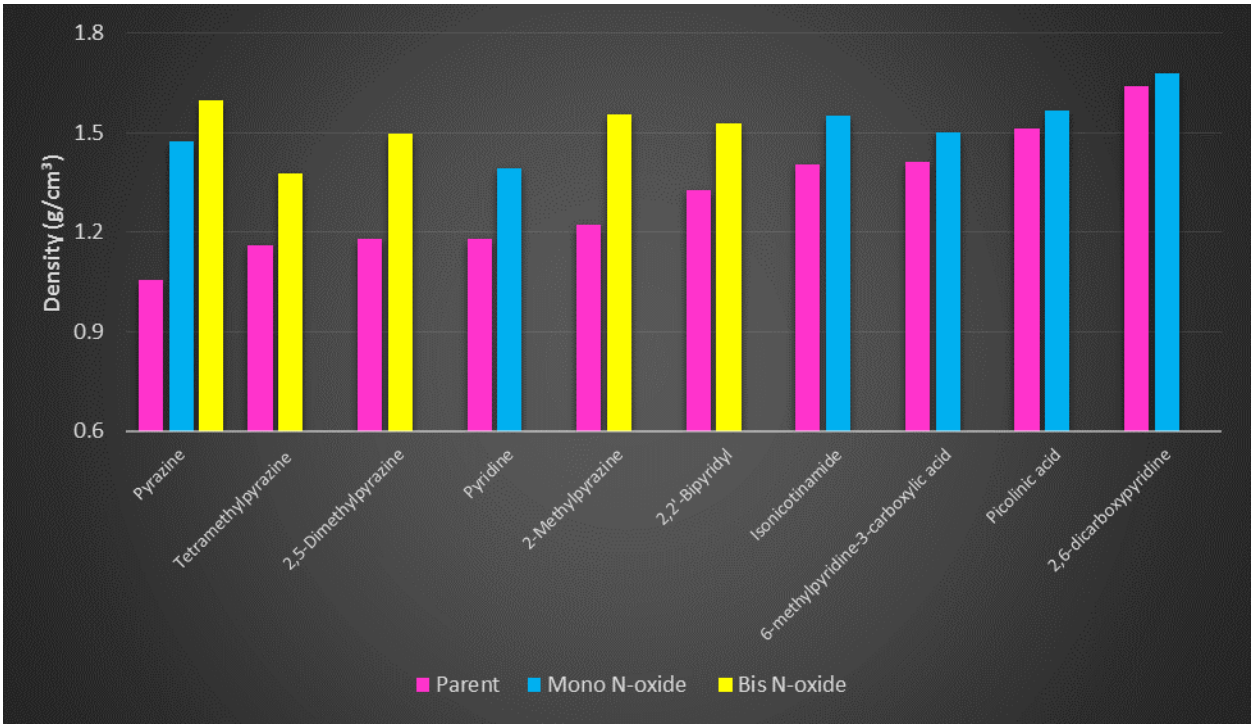

Figure 9.17 Densities of N-heterocyclic compounds and their corresponding *mono*- or *bis*- N-oxides

Although the data set is not very large, the general trend is clear and unambiguous. In each case, the N-oxide display a higher density (as determined by single-crystal X-ray diffraction) than

the parent N-heterocycle and the increases range from a few percent to almost 50% in the case of pyrazine vs. pyrazine *bis*-N-oxide. Furthermore this change of density is increasing in the order or parent heterocycle to *mono*-N-oxide to *bis*-N-oxide. The types of compounds in this series also span a large range and include molecules decorated with a variety of functional groups. Against this background, it is not surprising that the **EDNA** co-crystal with a density that comparable to that of **EDNA** itself involves pyrazine *bis*-N-oxide as the co-former. Furthermore, it may be particularly worthwhile to examine N-oxides as co-formers in future strategies towards enhancing the density of heteromeric energetic materials.

9.4.5 Alteration of impact sensitivity

EDNA is considered to be an energetic compound with relatively low sensitivity to impact and friction and this is a property that helps to determine if a material is suitable as a primary or secondary explosive as well as what kind of precautions are needed for storage and handling. Any incorporation of **EDNA** within a new crystalline material is likely to alter the impact sensitivity, as well as any property governed by the nature of the solid state. Thus, the impact sensitivity of two co-crystals in this series with particularly favorable thermal stability, **EDNA:A23**, and energetic properties, **EDNA:A28** were determined and compared with the impact sensitivity of **EDNA**. The two co-crystals were significantly less impact sensitive than **EDNA** itself. The co-formers in the lattice can essentially be viewed as acting as buffers or barriers between the inherently unstable energetic molecules which consequently improves the sensitivity.

9.4.6 Alteration of reactivity and stability

The acidity of pure **EDNA** makes it corrosive and prone to react with metals which can restrict processability and shelf-life. Furthermore, the sensitivity of the products formed can create a completely new set of unpredictable and undesirable challenges. One reason for co-crystallizing

EDNA with molecules capable of binding to the acidic protons was to introduce a "supramolecular protecting group" that might reduce the chemical reactivity of **EDNA** thereby making it more stable. In order to test the validity of this approach, a simple qualitative test was carried out with **EDNA** and **EDNA:A28**. Small amount of the selected samples were sprinkled in a slurried form (with a few drops of methanol) directly onto strips of copper metal, Figure 9.18.

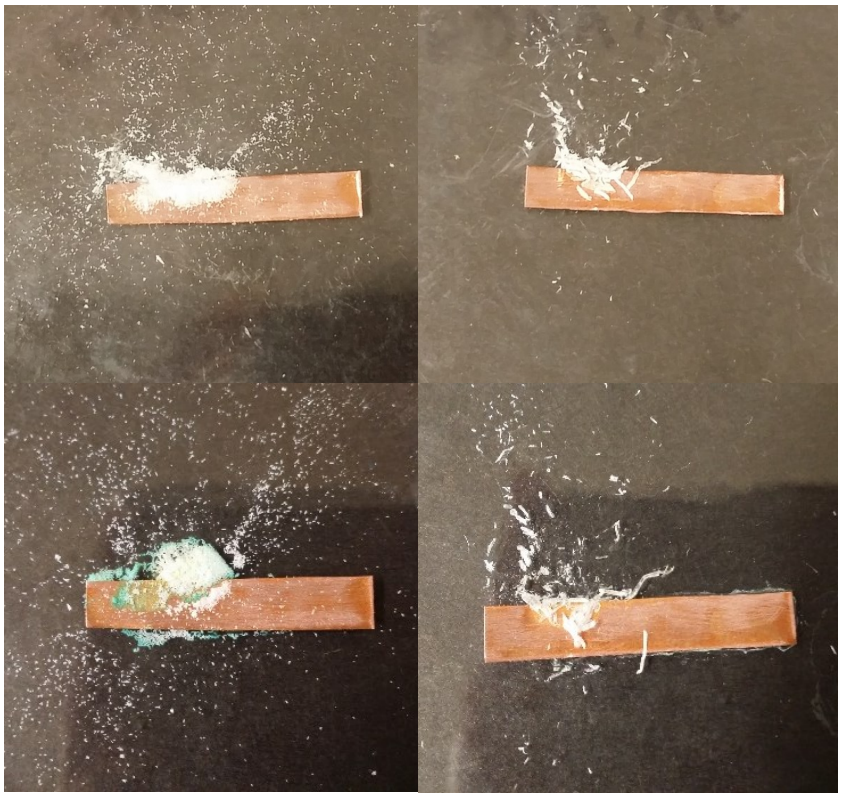

Figure 9.18 A slurry of **EDNA** (top left) and **EDNA:A28** (top right), respectively, in contact with copper metal. Notable corrosion of the metal was observed after 20 hrs in the case of pure **EDNA** (bottom left) but no visible change to the copper metal took place with **EDNA:A28** under the same conditions (bottom right)

The corrosive nature of **EDNA** is clearly manifested even after a relatively short amount of time (20 hrs) at ambient temperature, whereas the **EDNA:A28** solid form did not display any noticeable reaction with the copper metal.

9.5 Conclusions

A systematic co-crystallization study of **EDNA** has demonstrated that the acidic protons in the energetic material can be successfully targeted with suitable hydrogen-bond acceptors. Six of the eight co-crystals synthesized were characterized using single crystal diffraction and the outcome was predictable supramolecular motifs based upon N-H···N and N-H···O structure-directing hydrogen bonds. The co-formers also act as "supramolecular protecting groups" resulting in a reduced chemical instability/corrosiveness which is otherwise challenging when it comes to the storage and handling of **EDNA**, Figure 9.19. Thermal properties, impact sensitivity, and detonation velocities and pressure could also be modified and altered with a degree of predictability. Because of the structural consistency throughout the series of co-formers, some correlations between molecular structure/property of the pure co-former and the physical properties performance of the resulting energetic co-crystal was observed. This clearly suggests that systematic co-crystallizations allow to fine-tune properties that are important for storage, handling, and processing, with minimal negative impact on the eventual energetic behavior of the targeted substance.

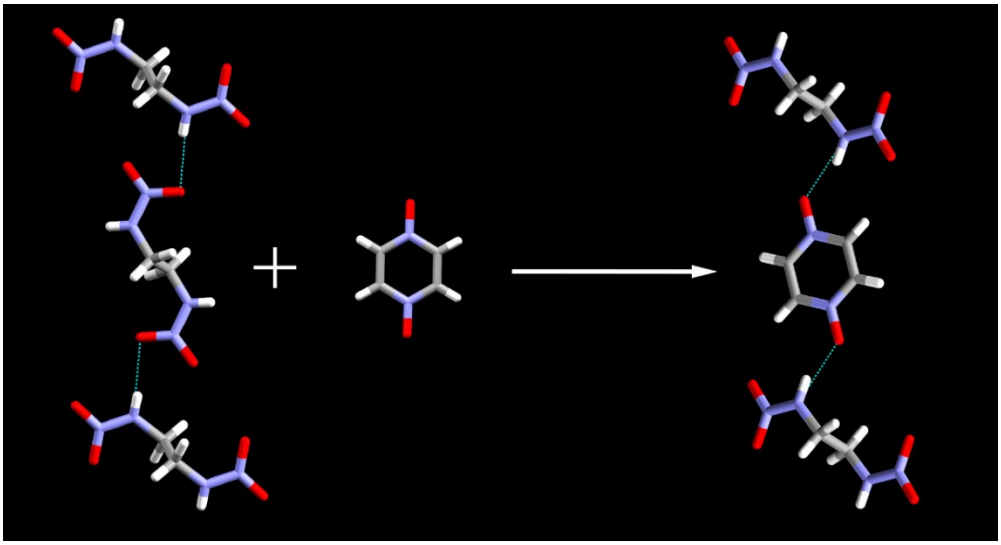

Figure 9.19 Supramolecular protecting group approach to stabilize **EDNA**

9.6 References

1. Aakeröy, C.B.; Wijethunga, T.K.; Desper, J. *Chem. Eur. J.* **2015**, *21*, 11029-11037.

2. Guo, D.; An, Q.; Goddard, W.A.; Zybin, S.V.; Huang, F. *J. Phys. Chem. C* **2014**, *118*, 30202-30208; Yan, T.; Wang, K.; Tan, X.; Liu, J.; Liu, B.; Zou, B. *J. Phys. Chem. C* **2014**, *118*, 22960-22967.

3. Urbelis, J.H.; Swift, J.A. *Cryst. Growth Des.* **2014**, *14*, 1642-1649; Landenberger, K.B.; Matzger, A.J. *Cryst. Growth Des.* **2010**, *10*, 5341-5347.

4. Millar, D.I.A, Maynard-Casely, H.E.; Allan, D.R.; Cumming, A.S.; Lennie, A.R.; Mackay, A.J.; Oswald, I.D.H.; Tang, C.C.; Pulham, C.R. *CrystEngComm* **2012**, *14*, 3742-3749; Wei, C.; Huang, H.; Duan, X.; Peia, C. *Propellants Explos. Pyrotech.* **2011**, *36*, 416-423; Ma, C.; Liu, Z.; Yao, Q. *Can. J. Chem*. **2014**, *92* 803-808.

5. He, C.; Zhang, J.; Parrish, D.A.; Shreeve, J.M. *J. Mater. Chem. A* **2013**, *1*, 2863-2868; Underwood, C.J.; Wall, C.; Provatas, A.; Wallace, L. *New J. Chem*. **2012**, *36*, 2613-2617.

6. Landenberger, K.B.; Matzger, A.J. *Cryst. Growth Des.* **2012**, *12*, 3603-3609; Tao, G.H.; Guo, Y.; Joo, Y.H.; Twamley, B.; Shreeve, J.M. *J. Mater. Chem.* **2008**, *18*, 5524-5530.

7. Chen, G.; Shi, W.; Xia, M.; Lei, W.; Wang, F.; Gong, X. *J. Mol. Model.* **2014**, *20*, 2326.

8. Wang, Y.; Yang, Z.; Li, H.; Zhou, X.; Zhang, Q.; Wang, J.; Liu, Y. *Propellants Explos. Pyrotech.* **2014**, *39*, 590-596.

9. Qasim, M.M.; Moore, B.; Taylor, L.; Honea, P.; Gorb, L.; Leszczynski, J. *Int. J. Mol. Sci.* **2007**, *8*, 1234-1264; Balakrishna, V.K.; Halasz, A.; Hawari, J. *Environ. Sci. Technol*. **2003**, *37*, 1838-1843; Zhang, J.; He, C.; Parrish, D.A.; Shreeve, J.M. *Chem. Eur. J*. **2013**, *19*, 8929-8936.

10. Fischer, D.; Klapötke, T.M.; Piercey, D.G.; Stierstorfer, J. *Chem. Eur. J*. **2013**, *19,* 4602-4613.

11. Vishnoi, P.; Walawalkar, M.G.; Murugavel, R. *Cryst. Growth Des*. **2014**, *14*, 5668-5673; Ma, Y.; Zhang, A.; Zhang, C.; Jiang, D.; Zhu, Y.; Zhang, C. *Cryst. Growth Des*. **2014**, *14*, 4703-4713; Li, H.; Shu, Y.; Gao, S.; Chen, L.; Ma, Q.; Ju, X. *J. Mol. Model*. **2013**, *19*, 4909-4917.

12. Ma, Y.; Zhang, A.; Xue, X.; Jiang, D.; Zhu, Y.; Zhang, C. *Cryst. Growth Des*. **2014**, *14*, 6101-6114; Liu, X.; Su, Z.; Ji, W.; Chen, S.; Wei, Q.; Xie, G.; Yang, X.; Gao, S. *J. Phys. Chem. C* **2014**, *118*, 23487-23498; Shen, J.P.; Duan, X.H.; Luo, Q.P.; Zhou, Y.; Bao, Q.; Ma, Y.J.; Pei, C.H. *Cryst. Growth Des*. **2011**, *11*, 1759-1765.

13. Agrawal, A.P. *Prog. Energy Combust. Sci*. **1998**, *24*, 1-30; Zhang, J.; Mitchell, L.A.; Parrish, D.A.; Shreeve, J.M. *J. Am. Chem. Soc.* **2015**, *137*, 10532-10535; Hong, D.; Li, Y.; Zhu, S.; Zhang, L.; Pang, C. *Cent. Eur. J. Energetic Mater.* **2015**, *12*, 47-62; Bennion, J.C.; McBain, A.; Son, S.F.; Matzger, A.J. *Cryst. Growth Des.* **2015**, *15*, 2545-2549

14. Klapötke, T.M.; Piercey, D.G.; Stierstorfer, J. *Eur. J. Inorg. Chem*. **2013**, *9*, 1509-1517.

15. Bolton, O.; Matzger, A.J. *Angew. Chem. Int. Ed*. **2011**, *50*, 8960-8963; Yang, Z.; Li, H.; Huang, H.; Zhou, X.; Li, J.; Nie, F. *Propellants Explos. Pyrotech.* **2013**, *38*, 495-501.

16. Anderson, S.R.; am Ende, D.J.; Salan, J.S.; Samuels, P. *Propellants Explos. Pyrotech.* **2014**, *39*, 637-640; Li, H.R.; Shu, Y.J.; Song, C.; Chen, L.; Xu, R.J.; Ju, X.H. *Chin. Chem. Lett*. **2014**, *25*, 783-786.

17. Guo, C.; Zhang, H.; Wang, X.; Liu, X.; Sun, J. *J. Mater. Sci.* **2013**, *48*, 1351-1357.

18. Landenberger, K.B.; Bolton, O.; Matzger, A.J. *Angew. Chem. Int. Ed*. **2013**, *52*, 6468-6471.

19. Zhang, C.; Yang, Z.; Zhou, X.; Zhang, C.; Ma, Y.; Xu, J.; Zhang, Q.; Nie, F.; Li, H. *Cryst. Growth Des.* **2014**, *14*, 3923-3928.

20. Aakeröy, C.B.; Wijethunga, T.K.; Benton, J.; Desper, J. *Chem. Commun*. **2015**, *51*, 2425-2428.

21. Xue, H.; Ye, G.; Twamley, B.; Shreeve, J.M. *Chem. Mater*. **2005**, *17*, 191-198.

22. Bolton, O.; Simke, L.R.; Pagoria, P.F.; Matzger, A.J. *Cryst. Growth Des.* **2012**, *12*, 4311-4314.

23. Zhang, J.; Parrish, D.A.; Shreeve, J.M. *Chem. Commun.* **2015**, *51*, 7337-7340.

24. Landenberger, K.B.; Bolton, O.; Matzger, A.J. *J. Am. Chem. Soc.* **2015**, *137*, 5074-5079.

25. Hale, G.C. *US Pat*. 2011578, **1934**.

26. United States Department of the Army technical manual, *Military Explosives,* Department of the Army, **1989**.

27. Fedoroff, B.T; Sheffield, O.E. *Encyclopedia of Explosives and Related Items – volume 6*, Picatinny Arsenal, **1974**.

28. Kettner, M.S.; Klapötke, T.M.; Müller, T.G.; Suc´eska, M. *Eur. J. Inorg. Chem*. **2014**, 4756-4771.

29. Jadhav, H.S., Talawar, M.B., Sivabalan, R., Dhavale, D.D., Asthana, S.N., Krishnamurthy, V.N. *J. Hazard. Mat*. **2007**, *143*, 192-197; Herve, G., Roussel, C., Graindorge, H. *Angew. Chem., Int. Ed*. **2010**, *49*, 3177-3181.

30. Hinshaw, J.C.; Edwards, W.W.; George, C.; Gilardi, J. *Heterocycl. Chem.* **1992**, *29*, 1721-1724.

31. Bagal, L.I.; Pevzner, M.S.; Frolov, A.N.; Sheludyakova, N.I. *Khim. Geterotsikl. Soedin.* **1970**, 558-562.

32. Meyer, R.; Köhler, J.; Homburg, A. *Explosives*, John Wiley & Sons, **2008**.

33. Ivshin, V. P.; Ivshina, T. N.; Smirnova, L. G.; Ponomareva, M. G. *Zh. Org. Khim.* **1984**, *20*, 7-13.

34. Robert, M.; Pachman, J. *Primary Explosives*, Springer, **2013**.

35. Millar, R.W. *Lead-free Initiator Materials for Small Electro-explosive Devices for Medium Caliber Munitions*, QineiQ/FST/CR032702/1.1, **2003**.

36. Franz, A.O. *US Pat.* 2708623 A, **1955**.

37. Turley, J. W. *Acta Cryst. B* **1968**, *24*, 942-946.

38. Highsmith, T.K.; Hanks, J.M.; Velarde, S.P.; Battaro, J.C. *US Pat.* WO02060881, **2002**.

39. Aakeröy, C.B.; Wijethunga, T.K.; Desper, J. *CrystEngComm* **2014**, *16*, 28-31.

40. Iranpoor, N.; Firouzabadi, H.; Khalili, D.; Motevalli, S. *J. Org. Chem.* **2008**, *73*, 4882-4887.

41. Ayyangar, N.R.; Naik, S.N.; Srinivasan, K.V. *Tetrahedron Lett.* **1989**, *30*, 7253-7256.

42. Klapötke, T.M.; Krumm, B.; Steemann, F.X.; Steinhauser, G. *Safety Sci.* **2010**, *48*, 28-34.

43. Kissinger, L. W.; Schwartz, M. *J. Org. Chem*. **1958**, *23*, 1342-1344.

44. Spartan'08, Wavefunction, Inc.

45. Bolton, O.; Simke, L.R.; Pagoria, P.F.; Matzger, A.J. *Cryst. Growth Des.* **2012**, *12*, 4311-4314.

46. Simpson, L. R.; Foltz, M. F. *LLNL Small-Scale Drop-Hammer Impact Sensitivity Test*, Lawrence Livermore National Laboratory.

47. Aakeröy, C.B.; Panikkattu, S.; DeHaven, B.; Desper, J. *CrystEngComm* **2013**, *15*, 463-470.

48. Yan, Q.L.; Zeman, S.; Šelešovský, J.; Svoboda, R.; Elbeih, A. *J. Therm. Anal. Calorim.* **2013**, *111*, 1419-1430.

49. Yan, B.; Zhao, N. N.; Ma, H.X.; Song, J.R.; Zhao, F.Q.; Hu, R.Z. *S. Afr. J. Chem,* **2013**, *66*, 136-139; Kamlet, M. J.; Hurwitz, H. *J. Chem. Phys* **1968**, *48*, 3685-3692; Kamlet, M. J.; Jacobs, S.J. *J. Chem. Phys* **1968***, 48*, 23-35.

50. J. Barton, *Dust Explosion Prevention and Protection*, *IChemE*, **2002**.

51. Patnaik, P. *A Comprehensive Guide to the Hazardous Properties of Chemical Substances*, John Wiley & Sons, **2007**.

52. Badgujar, D.M.; Talawar, M.B.; Asthana, S. N.; Mahulikar, P.P. J. *Hazard. Mater.* **2008,** *151*, 289-305.

53. Li, S.; Li, Q.; Li, R.; Liu, J.; Yang, K.; Liu, B.; Zou, B. *J. Phys. Chem. C* **2014**, *118*, 23443-23450.

54. Wei, H.; Gao, H.; Shreeve, J.M. *Chem. Eur. J*. **2014,** *20*, 16943-16952. Pagoria, P.F.; Lee, G.S.; Mitchell, A.R.; Schmidt, R.D. *Thermochim. Acta*. **2002**, *384*, 187-204.

55. CSD ConQuest 1.17, **2013** Cambridge Crystallographic Data Centre, U.K.

Chapter 10 - Summary and future work

10.1 Summary

Physical properties of bulk solids are typically governed by molecular structure and molecular conformation, and by the intermolecular arrangement, interactions and packing of individual building blocks with respect to each other in a crystal lattice. Thus, in order to manipulate the properties of bulk materials, either alterations of molecular structure and conformations or refinements in packing arrangements are required. A co-crystal can be recognized as a supramolecular entity which enables the modification of physical properties of a material without tampering with the molecular structure and inherent chemical properties. Thus, a co-crystal leads to macroscopic property alterations by changing the spatial relationships between molecules in the crystal. In order to design co-crystals with pre-organized connectivities, a thorough understanding of the various intermolecular interactions that govern the solid-state architectures is essential. Hence, the first part of this dissertation is focused on understanding the behavior of the most well-known non-covalent interactions utilized in co-crystal synthesis, hydrogen bonds and halogen bonds. The second half of the dissertation is focused on applying hydrogen- and halogen-bond based co-crystallizations to fine-tune properties of functional materials.

In order to examine the hierarchical nature of hydrogen- and halogen-bond interactions, a library of biimidazole based ditopic acceptors were synthesized. Calculated molecular electrostatic potential values were utilized in predicting the possible interaction hierarchy and the structural results confirmed that both hydrogen and halogen bond interactions follow a best-donor/best-acceptor interaction hierarchy based on MEPS, Figure 10.1.[1]

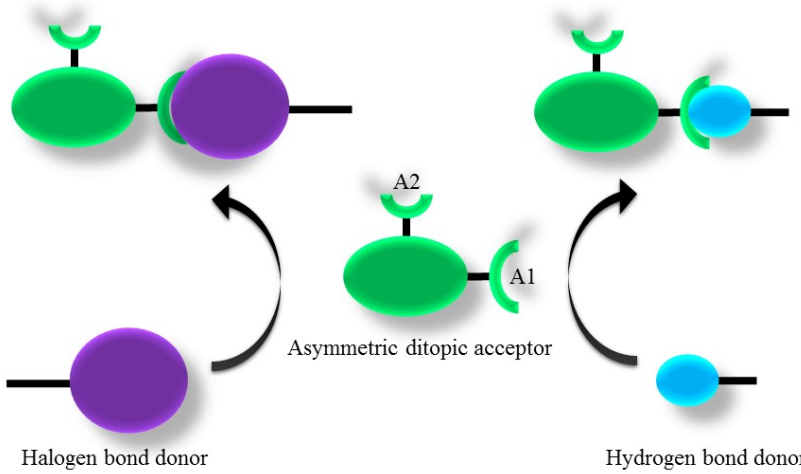

Figure 10.1 Hierarchical outcome of hydrogen-bond and halogen-bond interactions; A1: best acceptor, A2: 2nd best acceptor[1]

By extending the library of ditopic acceptors, it was realized that even though that halogen bonds follow an interaction hierarchy, when the MEPS difference between the two acceptor sites falls below 35 kJ/mol unites, the selection vanishes, Figure 10.2.

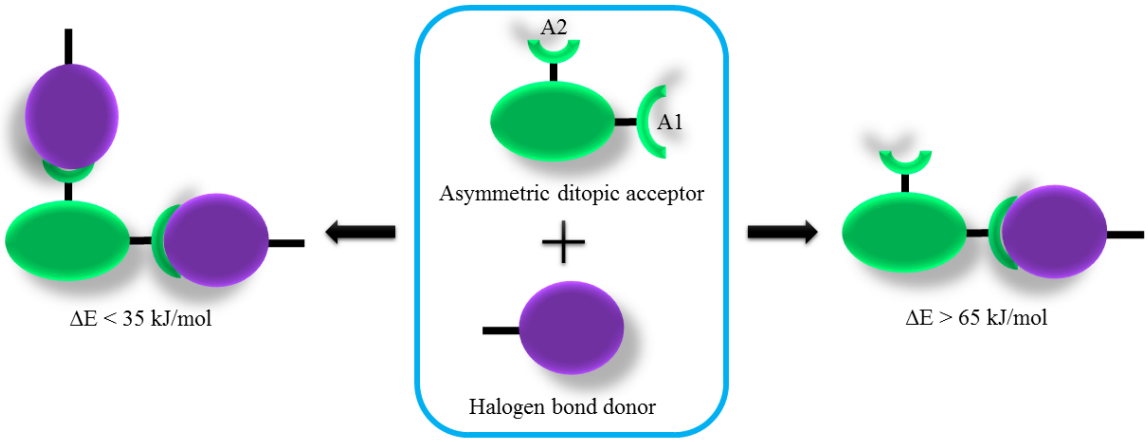

Figure 10.2 MEPS based selectivity outcome of halogen bonding; A1: best acceptor, A2: 2nd best acceptor

Next the competitive nature of hydrogen- and halogen-bond interactions were investigated utilizing a library of heteroaryl-2-imidazole molecules. The results suggested that both interaction types are equally competitive in such a competitive scenario, which is not surprising as both interactions have comparable strengths, Figure 10.3.[2]

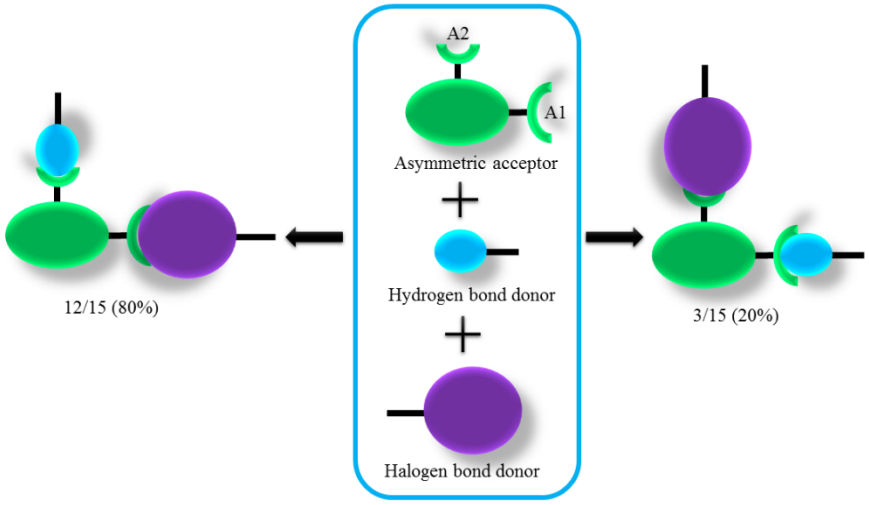

Figure 10.3 Structural outcome of the competitive study between hydrogen bond and halogen bond; A1: best acceptor, A2: 2nd best acceptor[2]

Even though there is an abundance of hydrogen-bond donors, there is a scant number of halogen-bond donor families available. Thus, a double activation method was employed in designing a new family of halogen-bond donors which were proven to be more effective than currently known analogues, Figure 10.4. The series of molecules were activated with a combination of electron-withdrawing capabilities of $-NO_2$ moieties with the polarizing effects of an *sp*-carbon.[3] Thus, the same group of molecules was exploited in an investigation of interaction preferences of nitro groups and the results revealed the possibility of using the nitro···haloethynyl interactions in co-crystallizations of energetic materials.

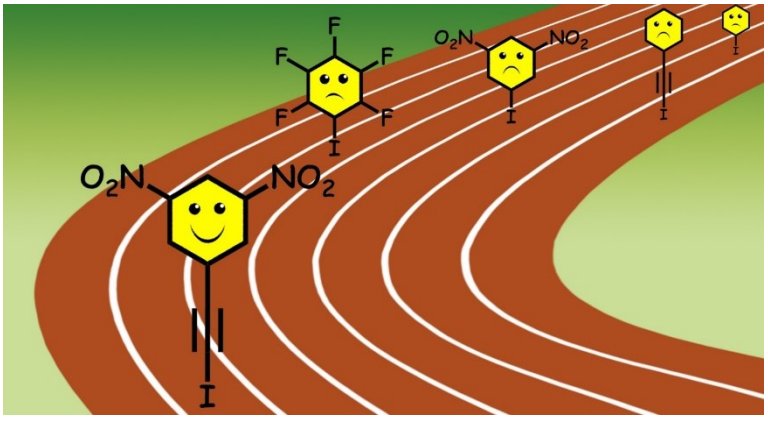

Figure 10.4 Design of effective halogen-bond donors with double activation[3]

As one of the applications of co-crystallization, a series of N-oxides were utilized in a rational design strategy of molecular polygons. Bifurcated halogen bonds constructed from N-oxides and complementary halogen-bond donors provided the basis for the deliberate assembly of molecular polygons in the solid state and furnished the desired architectures, Figure 10.5.[4]

The knowledge of hydrogen- and halogen-bond based co-crystallizations were applied in stabilizing volatile liquid chemicals and a reactive energetic compound. Through the use of halogen-bond driven co-crystal synthesis, liquid iodoperfluoroalkanes were transformed into crystalline materials with low-vapor pressure, considerable thermal stability, and moisture resistance, Figure 10.5.[5] Ethylenedinitramine (**EDNA**), a well-known explosive, suffers from high chemical reactivity due to the presence of acidic protons and was combined with potential acceptors via hydrogen bonding. The co-crystallization approach was successful not only in altering the physical properties of **EDNA**, while retaining the energetic properties, but also led to the gained stability by eliminating the chemical reactivity, Figure 10.5.[6]

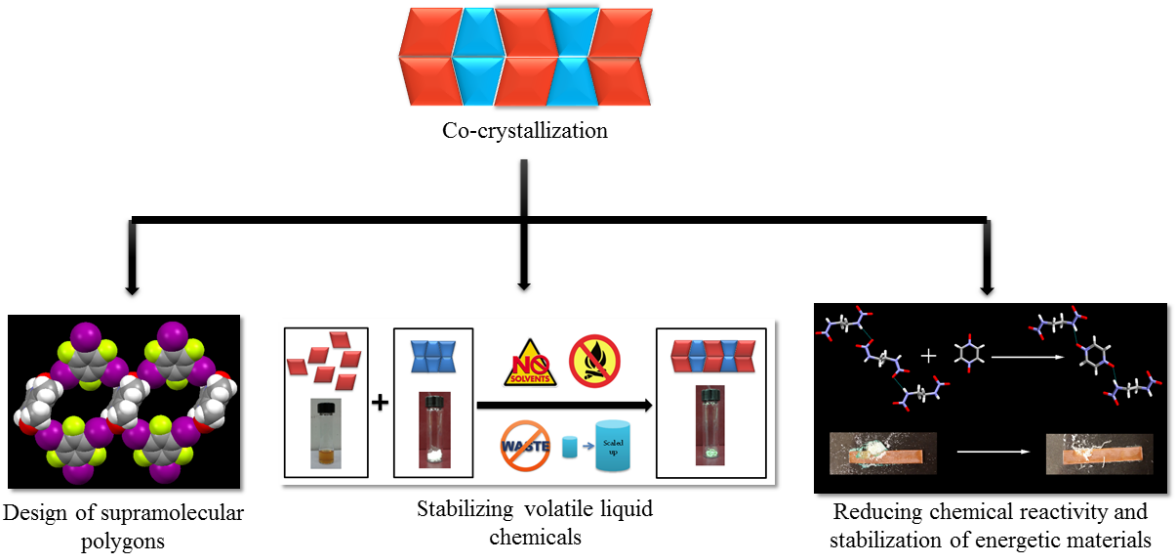

Figure 10.5 Applications of co-crystal technology[4,5,6]

10.2 Future work

The work outlined in this dissertation provides the basis for understanding not only the behavior of basic intermolecular interactions in solid state but also for fine-tuning properties of functional materials via co-crystallizations. However, there is still much to be done and below are a few examples.

10.2.1 Designing halogen-bond based ternary co-crystals

The synthesis of ternary co-crystals, in which three neutral solid compounds are included in a single crystal structure, is very challenging.[7] To attain this target, control over intermolecular interactions and precise selection of supramolecular synthons are required.[8] Even though there are examples based on hydrogen bonds[9] and a combination of hydrogen and halogen bonds[10] in designing ternary systems, such a system based only on halogen bonds has not been reported. However, it should be possible to obtain a halogen-bond based ternary system by combining an asymmetric ditopic acceptor and two single point halogen-bond donors with different MEPS values on the halogen atom in 1:1:1 stoichiometry, Figure 10.6.

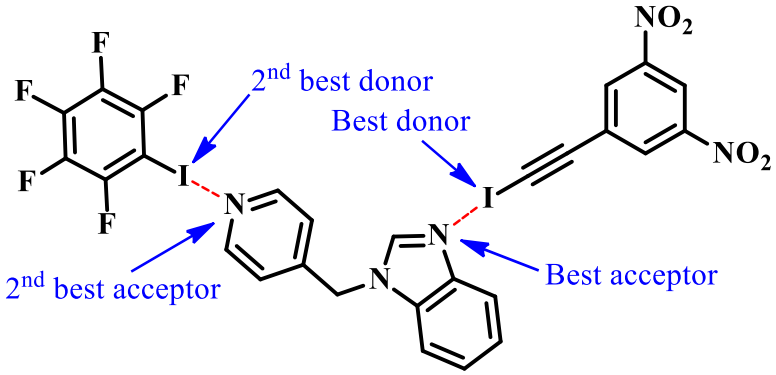

Figure 10.6 Design strategy for a halogen-bond based ternary co-crystal

10.2.2 Design of new hydrogen-bond donors via double activation

Chapter 6 describes the usage of double activation to design an effective group of halogen-bond donors. Also, it is reported that an ethynyl attached hydrogen atom can participate in weak

hydrogen bond formation, due to the positive potential obtained via polarization effect.[11] Thus, it should be possible to utilize a double activation method to obtain effective hydrogen-bond donors by combining the electron withdrawing capability of $-NO_2$ moieties and the polarizing effect of an *sp*-carbon (Figure 10.7), which can be an addition to the toolbox of supramolecular chemistry.

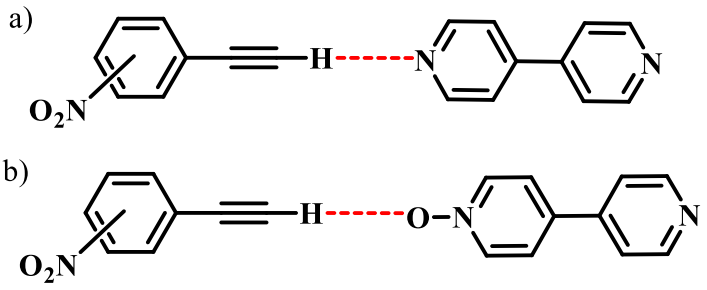

Figure 10.7 Two possible outcomes of co-crystallizations with ethynylnitrobenzenes a) a C_{sp}-H···N hydrogen bond and b) a C_{sp}-H···O hydrogen bond

10.2.3 Halogen-bond based molecular rectangles

Chapter 7 describes the use of halogen-bond based co-crystallization to obtain rationally designed molecular rhombuses and molecular hexagons. A similar design strategy could lead to other supramolecular polygons such as rectangles, Figure 10.8. In order to design rectangles a halogen-bond donor with an approximately 90º angle was designed and utilized in co-crystallizations to obtain molecular rectangles, Figure 10.9. The future plan is to expand this study to obtain more rationally designed molecular polygons.

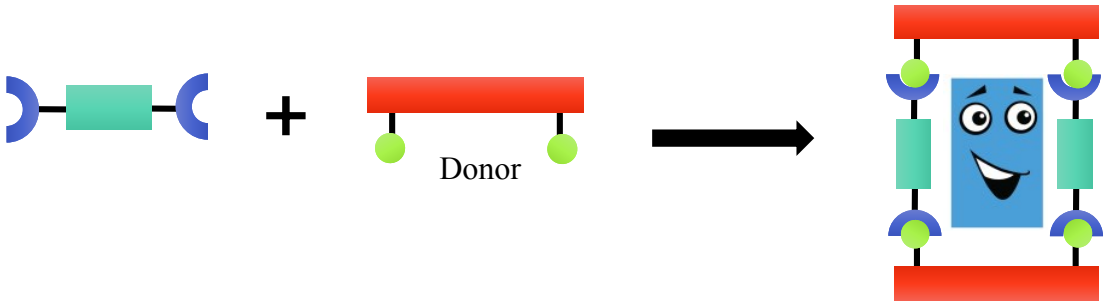

Figure 10.8 Design strategy of a molecular rectangle

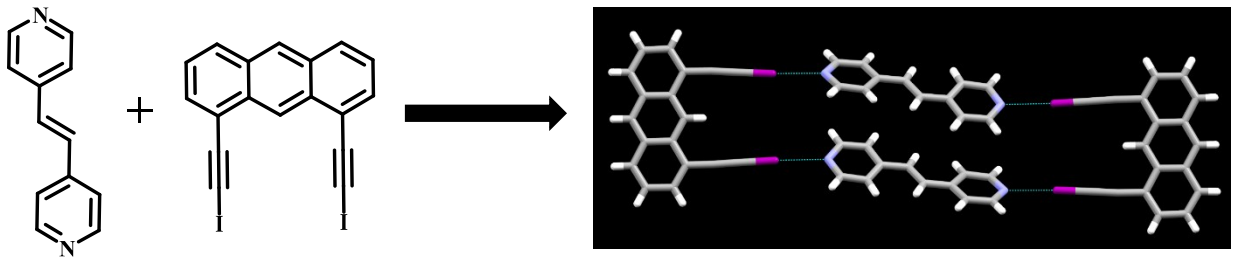

Figure 10.9 A molecular rectangle between 1,2-bispyridylethylene and 1,8-bis(iodoethynyl)anthracene assembled via halogen bonding

10.2.4 Hydrogen bonded co-crystallizations for improving chemical stability of dinitroimidazole based energetic materials

Chapter 9 shows the success in utilizing co-crystallization to alter the properties of an energetic compound. Likewise, dinitroimidazole based energetic compounds are well-known for their attractive impact insensitivity.[12] But these compounds are highly acidic, thus chemical reactivity is a major drawback that hampers the utilization of these compounds. A hydrogen-bond based co-crystallization approach could reduce the reactivity and enhance the stability, while retaining the energetic potentials. Initially, two dinitroimidazole compounds, 2,4-dinitroimidazole (**2,4-DNI**) and 4,5-dinitroimidazole (**4,5-DNI**) were selected and co-crystallized with aminopyridine compounds, Figure 10.10. Future plans for this study include obtaining more co-crystals of dinitroimidazoles and to study the property modifications as well as reactivity alterations.

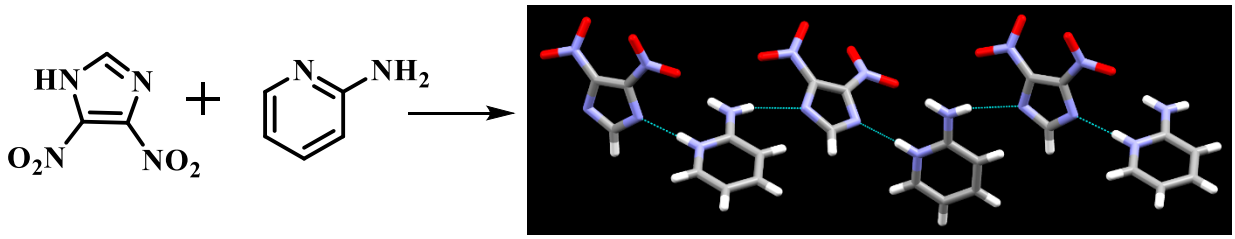

Figure 10.10 A salt formed between **4,5-DNI** and 2-aminopyridine

10.3 References

1. Aakeröy, C.B.; Wijethunga, T.K.; Desper, J. *J. Mol. Struct.* **2014**, *1072*, 20-27; Aakeröy, C.B.; Wijethunga, T.K.; Desper, J. *New J. Chem.* **2015**, *39*, 822-828; Aakeröy, C.B.; Wijethunga, T.K.; Desper, J.; Moore, C. *J. Chem. Crystallogr*. **2015**, *45*, 267-276.

2. Aakeröy, C.B.; Wijethunga, T.K.; Haj, M.A.; Desper, J.; Moore, C. *CrystEngComm* **2014**, *16*, 7218-7225.

3. Aakeröy, C.B.; Wijethunga, T.K.; Desper, J.; Đakovic, M. *Cryst. Growth Des.* **2015**, *15*, 3853-3861.

4. Aakeröy, C.B.; Wijethunga, T.K.; Desper, J. *CrystEngComm* **2014**, *16*, 28-31.

5. Aakeröy, C.B.; Wijethunga, T.K.; Benton, J.; Desper, J. *Chem. Commun*. **2015**, *51*, 2425-2428.

6. Aakeröy, C.B.; Wijethunga, T.K.; Desper, J. *Chem. Eur. J.* **2015**, *21*, 11029-11037.

7. Chakraborty, S.; Rajput, L.; Desiraju, G. R. *Cryst. Growth Des.* **2014**, 14, 2471-2577.

8. Dubey, R.; Desiraju, G.R. *IUCr J* **2015**, *2*, 402-408.

9. Aakeröy, C. B.; Beatty, A. M.; Helfrich, B. A. *Angew. Chem., Int. Ed*. **2001**, *40*, 3240-3242; Aakeröy, C. B.; Desper, J.; Urbina, J. F. *Chem. Commun.* **2005**, 2820-2822.

10. Tothadi, S.; Desiraju, G. R. *Chem. Commun.* **2013**, *49*, 7791-7793.

11. Bosch, E. *Cryst. Growth Des.* **2010**, *10*, 3808-3813.

12. Hou, K.; Maz, C.; Liu, Z. *New J. Chem*. **2013**, *37*, 2837-2844; Zohari, N.; Keshavarz, M.H.; Seyedsadjadi, S.A. *Cent. Eur. J. Energetic Mater.* **2014**, *11*, 349-362; Saikia, A.; Sivabalan, R.; Gore, G.M.; Sikder, A.K. *Propellants Explos. Pyrotech*. **2012**, *37*, 540-543; Grimmett, M.R.; Hua, S.T.; Chang, K.C.; Foley, F.A.; Simpson, J. *Aust. J. Chem.* **1989***, 42*, 1281-1289.

Appendix A - **NMR Data**

A.1 Chapter 2

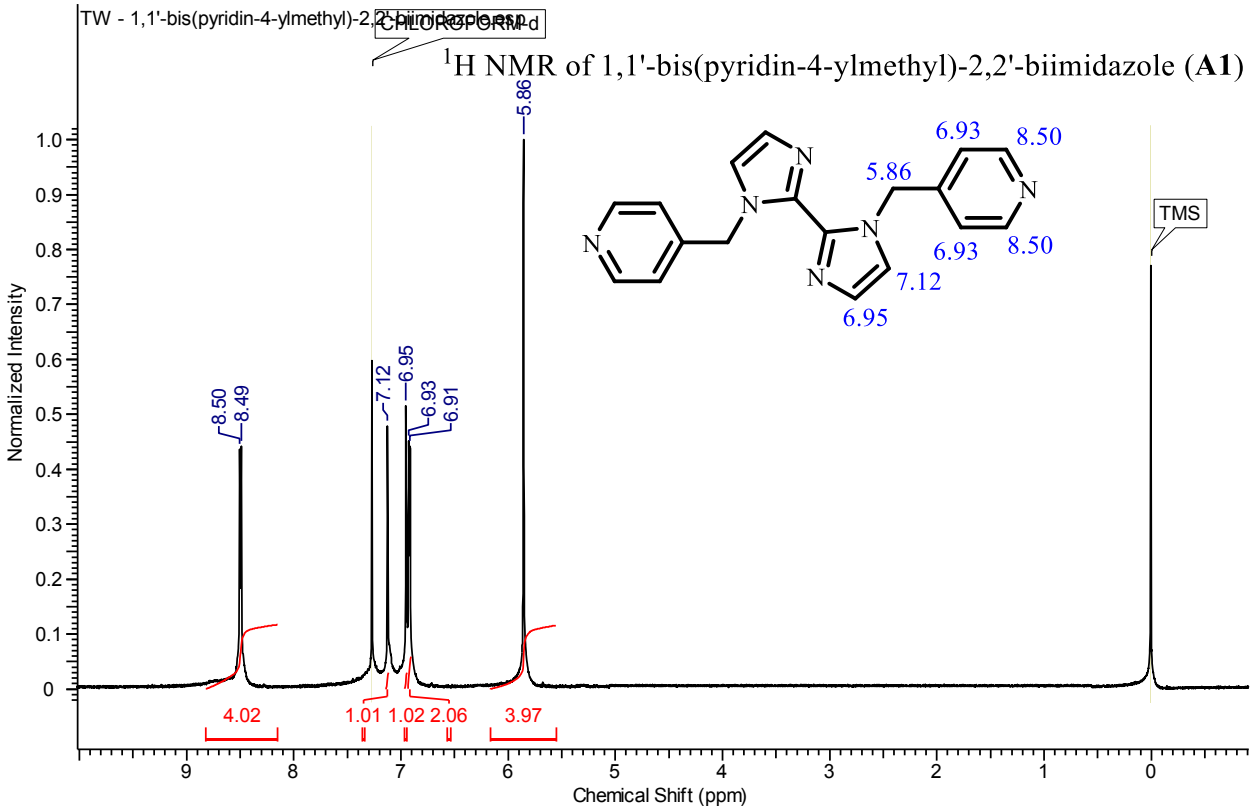

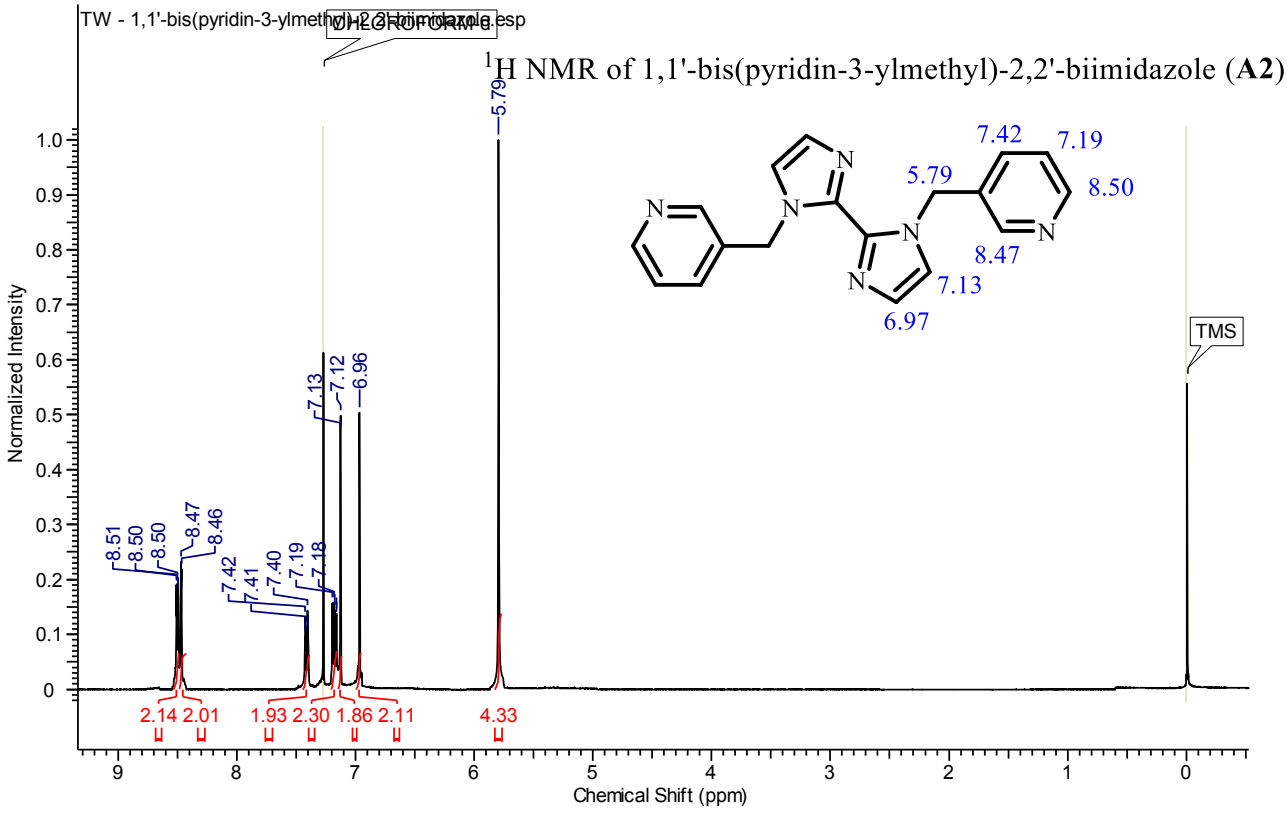

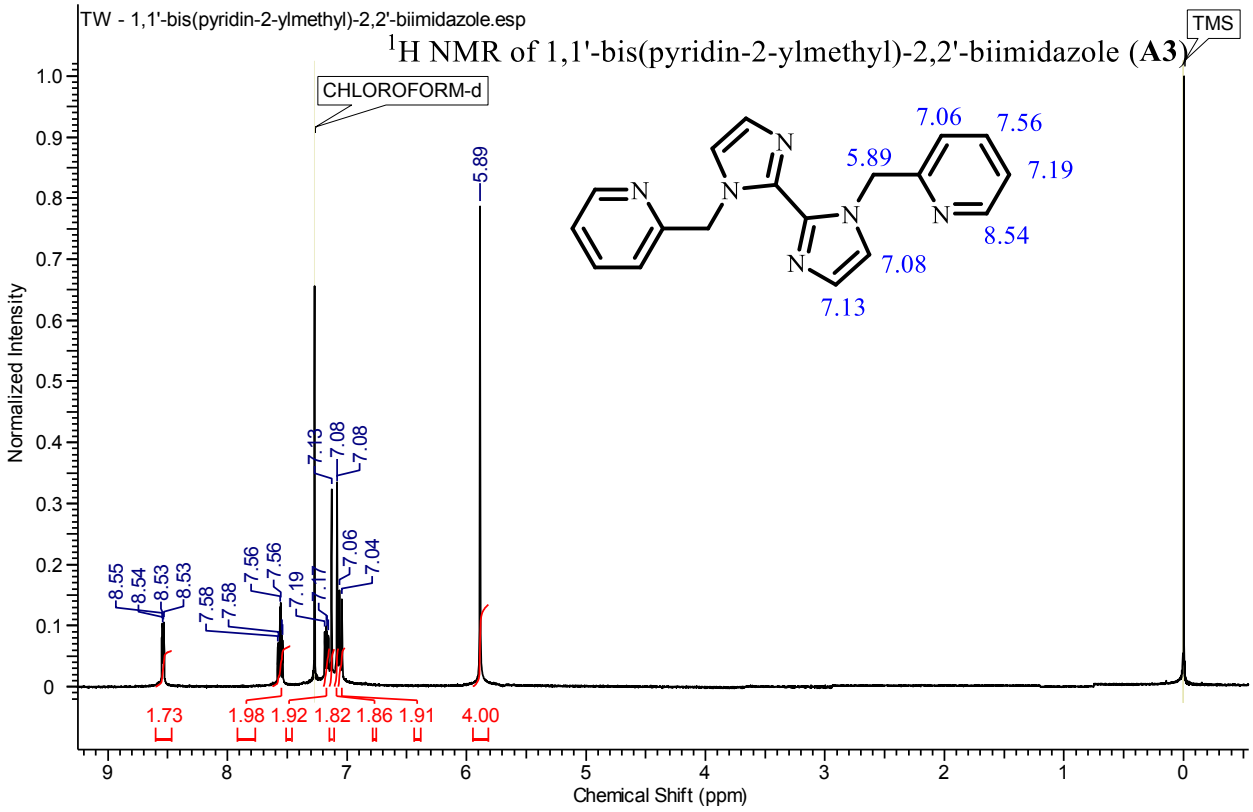
TW - 1,1'-bis(pyridin-2-ylmethyl)-2,2'-biimidazole.esp
^{1}H NMR of 1,1'-bis(pyridin-2-ylmethyl)-2,2'-biimidazole (**A3**)
TMS
CHLOROFORM-d
5.89
7.06
7.56
7.19
8.54
7.08
7.13
8.55
8.54
8.53
8.53
7.58
7.58
7.56
7.56
7.19
7.17
7.13
7.08
7.08
7.06
7.04
1.73
1.98
1.92
1.82
1.86
1.91
4.00
Normalized Intensity
Chemical Shift (ppm)

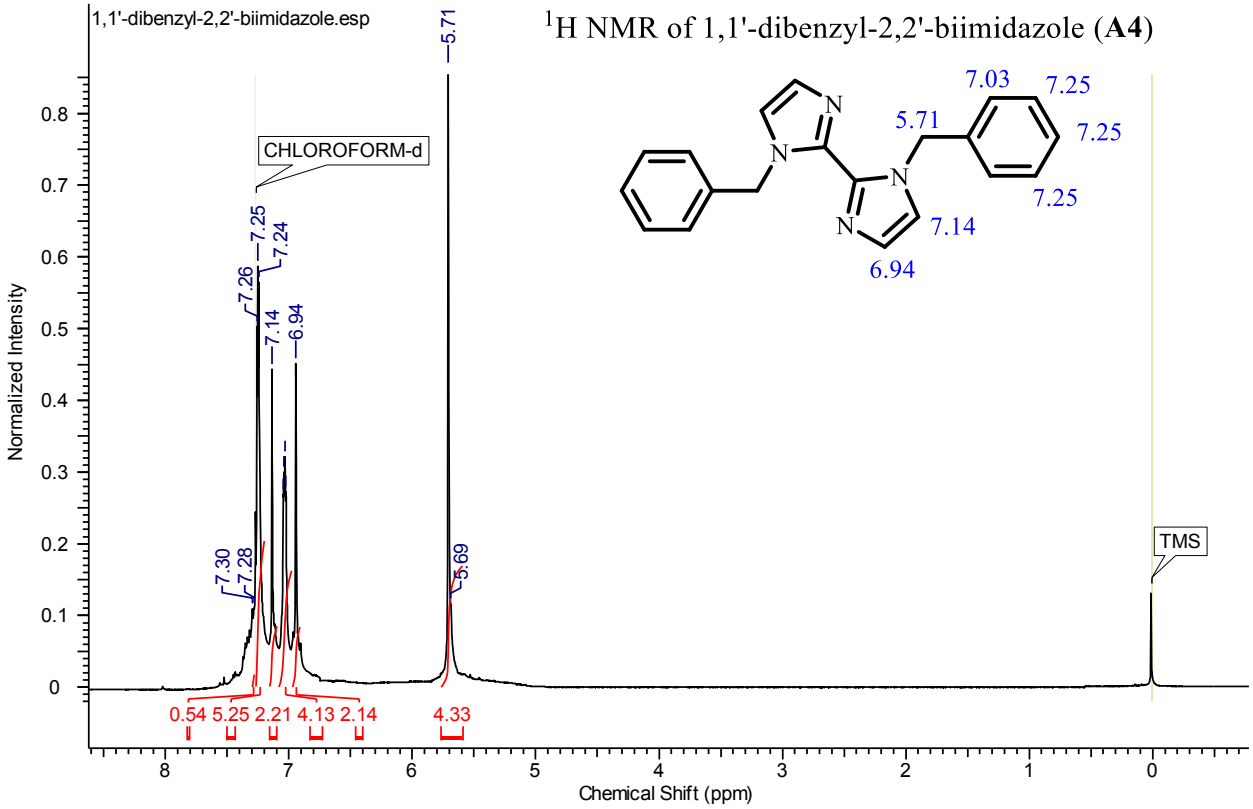
1,1'-dibenzyl-2,2'-biimidazole.esp
^{1}H NMR of 1,1'-dibenzyl-2,2'-biimidazole (**A4**)
5.71
7.03
7.25
7.25
7.25
7.14
6.94
CHLOROFORM-d
7.25
7.24
7.26
7.14
6.94
7.30
7.28
5.69
TMS
0.54
5.25
2.21
4.13
2.14
4.33
Normalized Intensity
Chemical Shift (ppm)

Variable stoichiometric studies

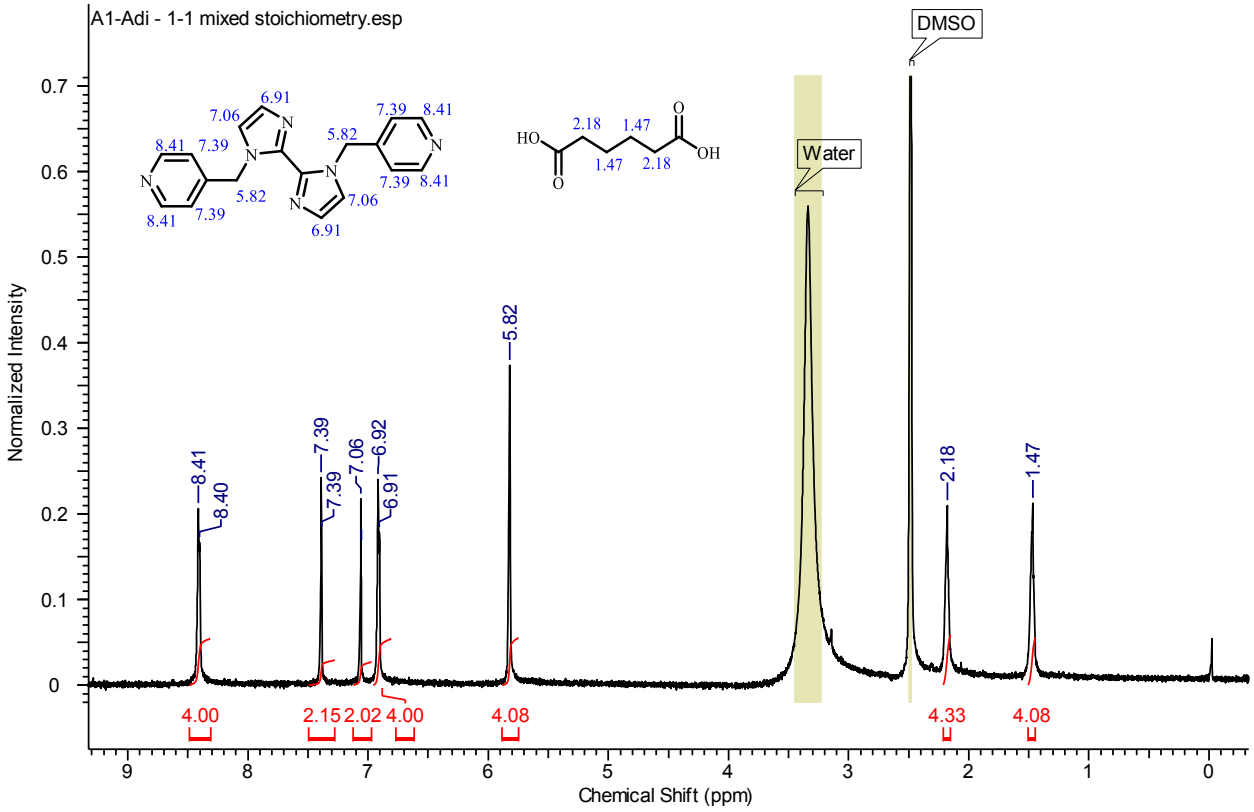

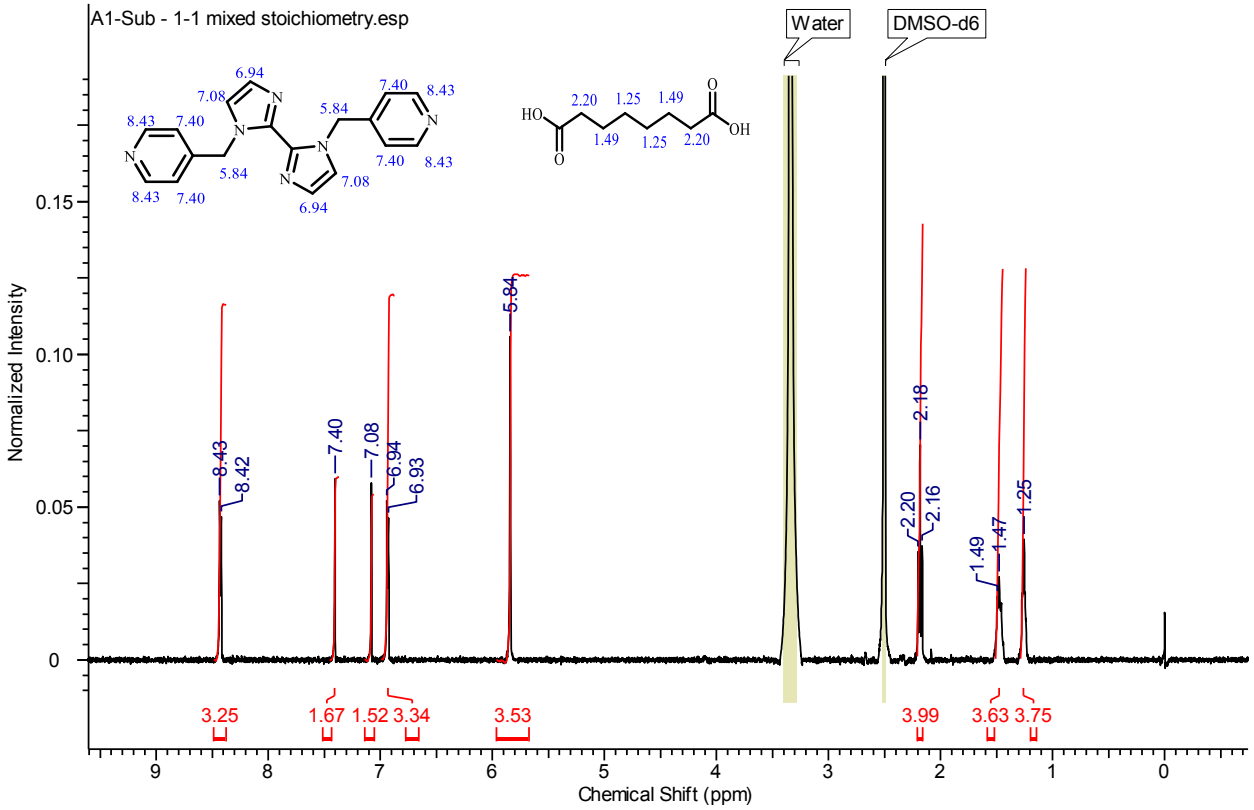

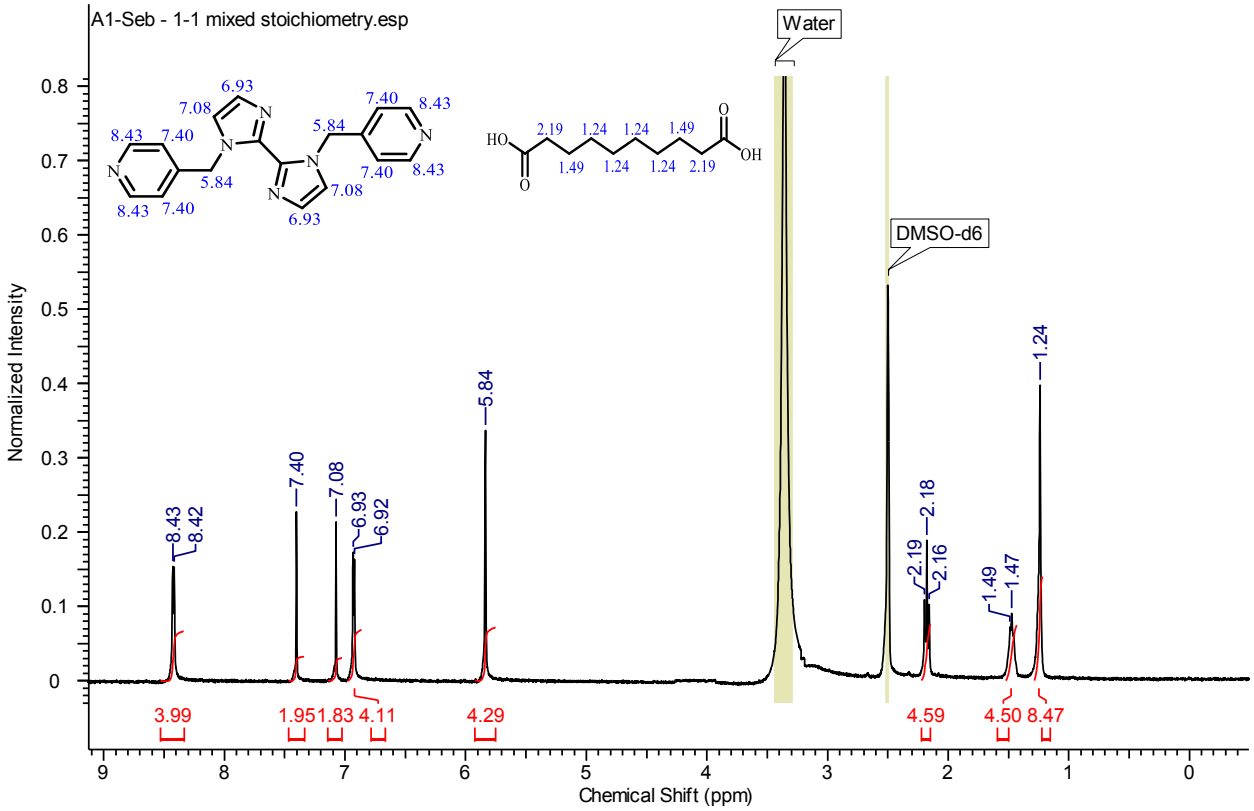
A1-Seb - 1-1 mixed stoichiometry.esp
Water
DMSO-d6
Normalized Intensity
Chemical Shift (ppm)
8.43
8.42
7.40
7.08
6.93
6.92
5.84
2.19
2.18
2.16
1.49
1.47
1.24
3.99
1.95
1.83
4.11
4.29
4.59
4.50
8.47

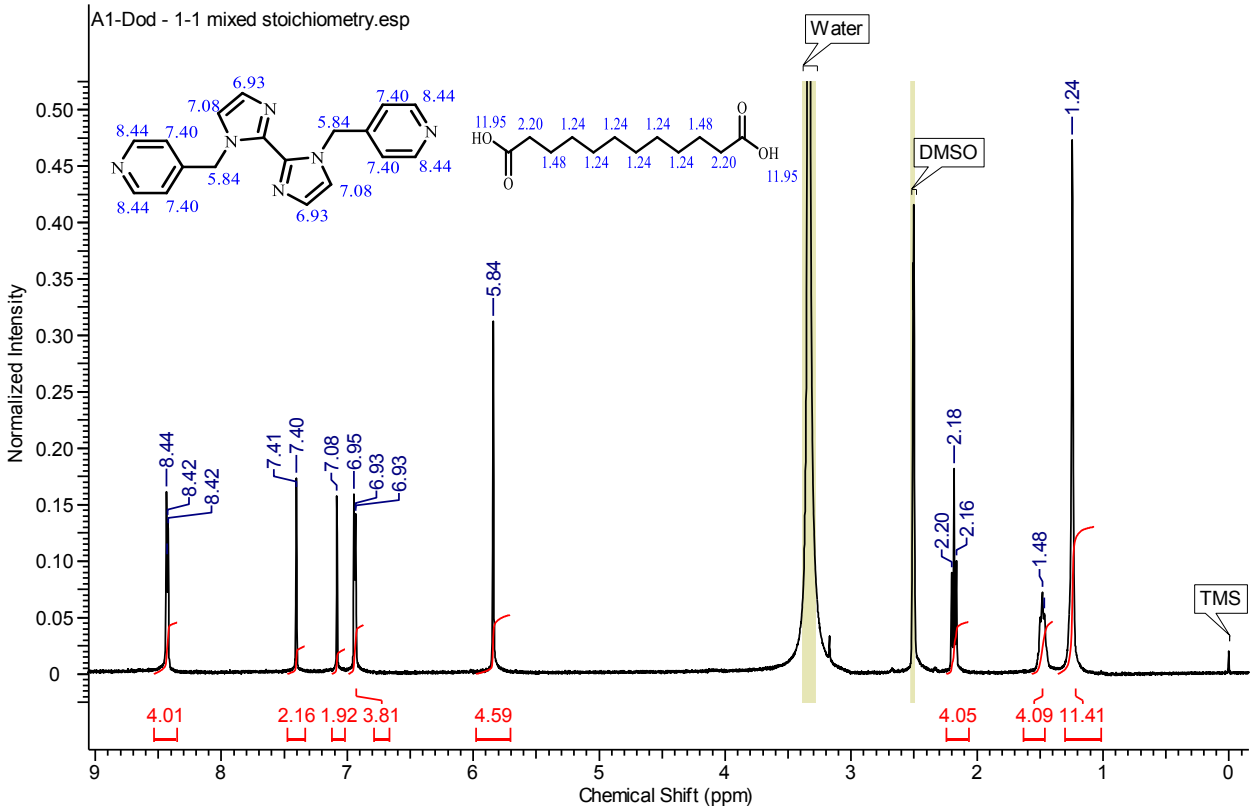
A1-Dod - 1-1 mixed stoichiometry.esp
Water
DMSO
TMS
Normalized Intensity
Chemical Shift (ppm)
8.44
8.42
8.42
7.41
7.40
7.08
6.95
6.93
6.93
5.84
2.18
2.20
2.16
1.48
1.24
4.01
2.16
1.92
3.81
4.59
4.05
4.09
11.41

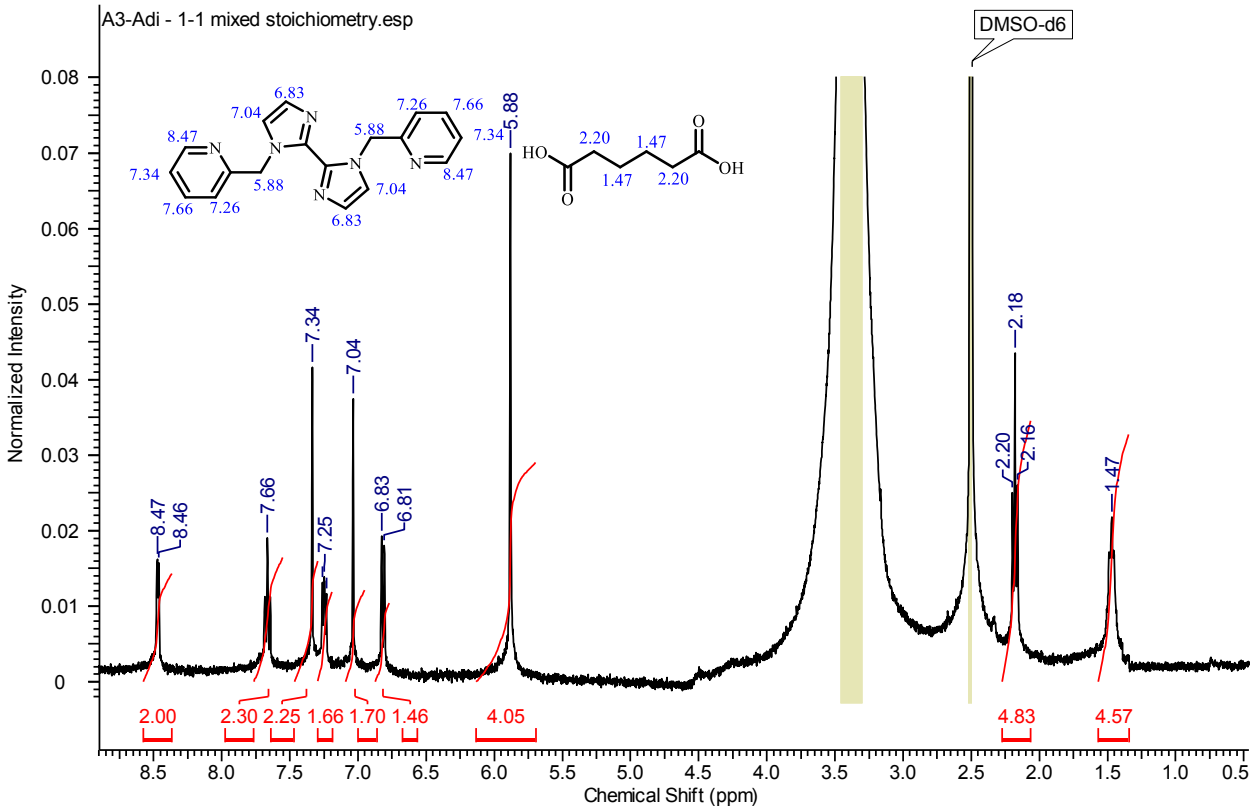
A3-Adi - 1-1 mixed stoichiometry.esp
DMSO-d6
Normalized Intensity
Chemical Shift (ppm)
8.47
8.46
7.66
7.34
7.25
7.04
6.83
6.81
5.88
2.20
2.18
2.16
1.47
2.00
2.30
2.25
1.66
1.70
1.46
4.05
4.83
4.57

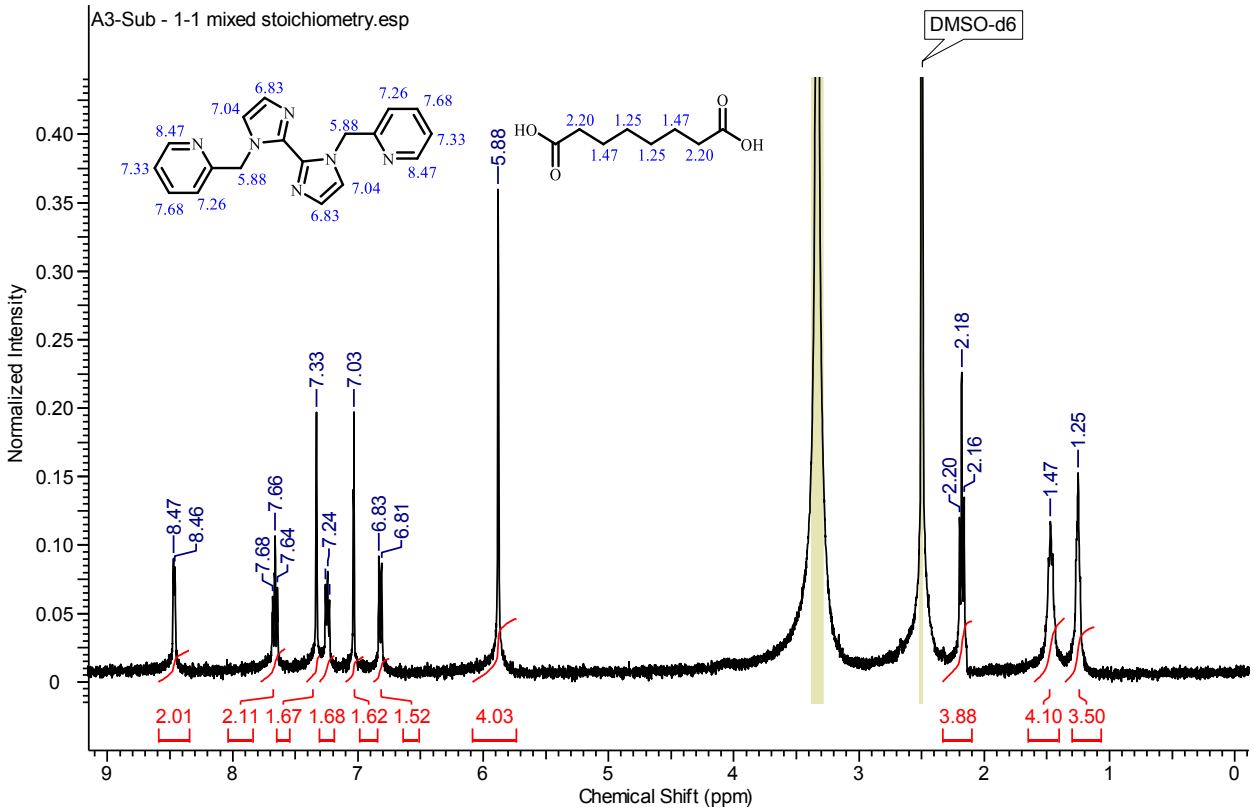
A3-Sub - 1-1 mixed stoichiometry.esp
DMSO-d6
Normalized Intensity
Chemical Shift (ppm)
8.47
8.46
7.68
7.66
7.64
7.33
7.24
7.03
6.83
6.81
5.88
2.20
2.18
2.16
1.47
1.25
2.01
2.11
1.67
1.68
1.62
1.52
4.03
3.88
4.10
3.50

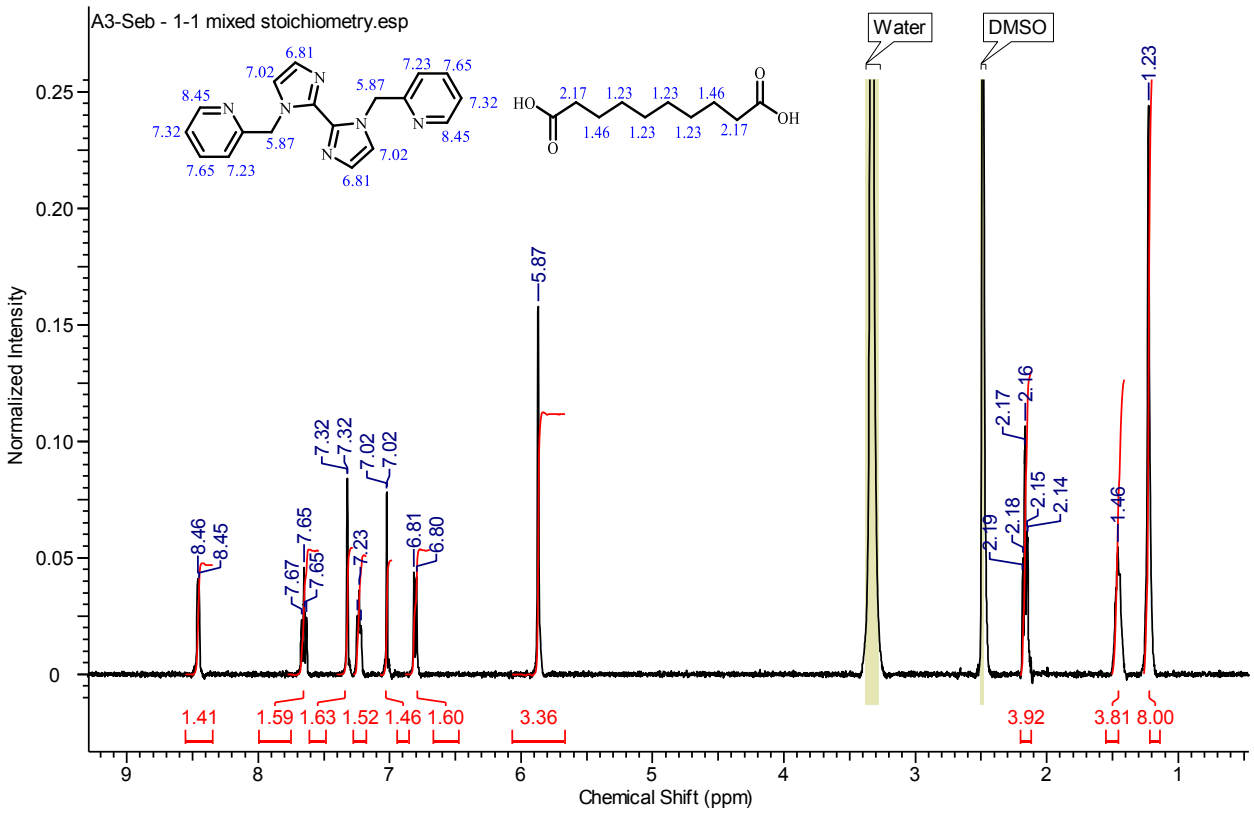
A3-Seb - 1-1 mixed stoichiometry.esp
Water
DMSO
Normalized Intensity
Chemical Shift (ppm)

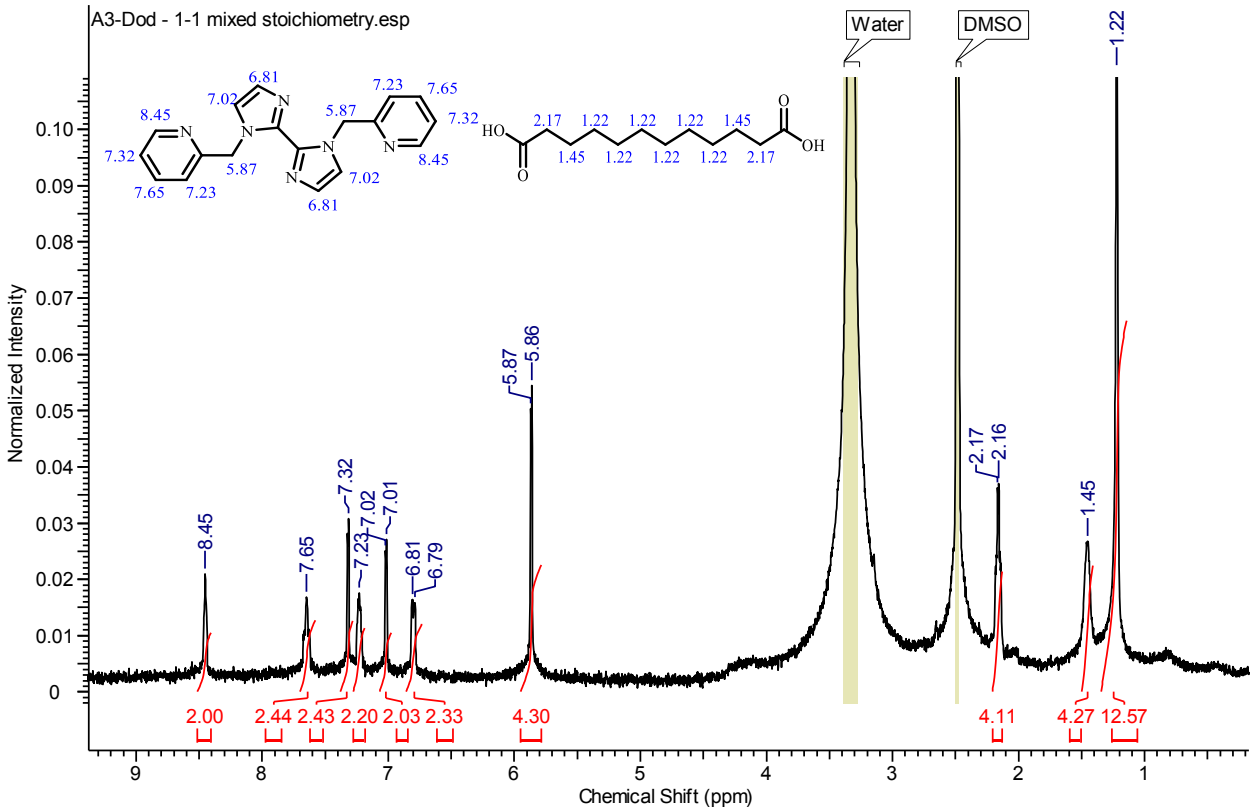
A3-Dod - 1-1 mixed stoichiometry.esp
Water
DMSO
Normalized Intensity
Chemical Shift (ppm)

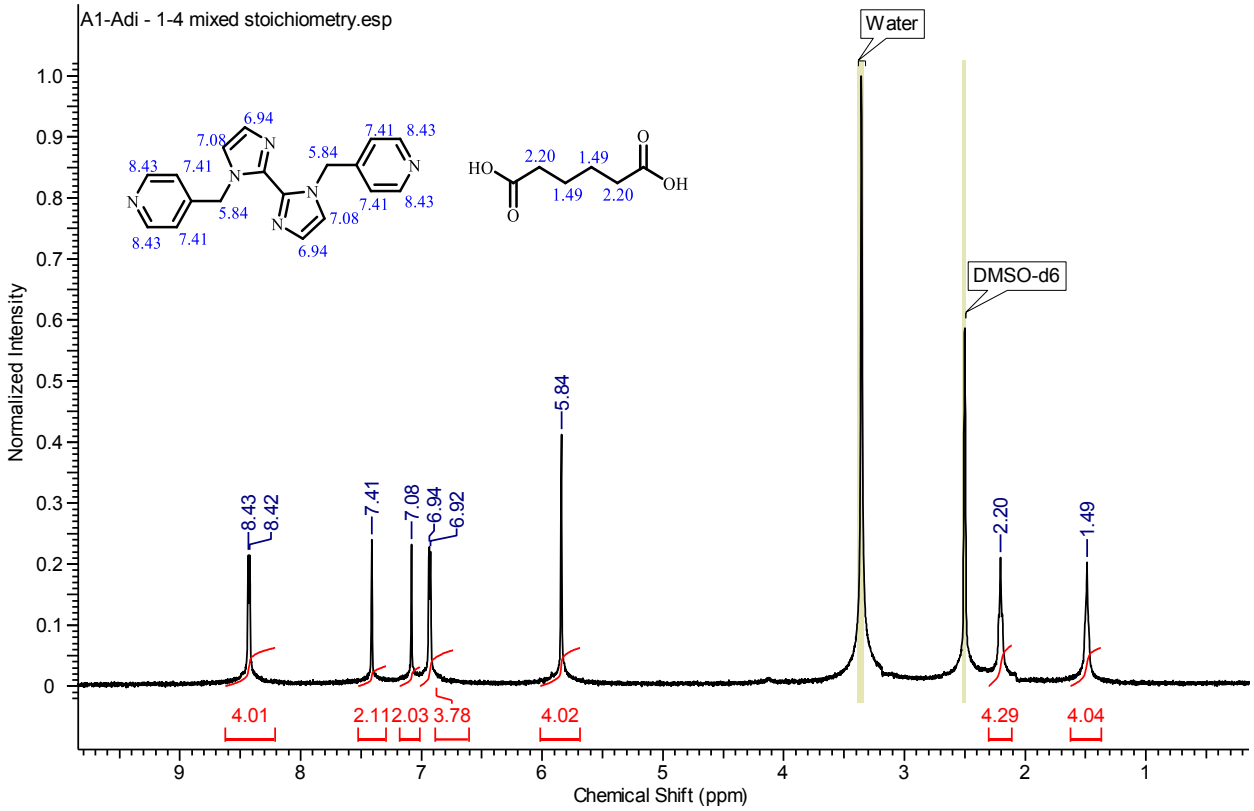
A1-Adi - 1-4 mixed stoichiometry.esp
Water
DMSO-d6
Normalized Intensity
Chemical Shift (ppm)
8.43
8.42
7.41
7.08
6.94
6.92
5.84
2.20
1.49
4.01
2.11
2.03
3.78
4.02
4.29
4.04

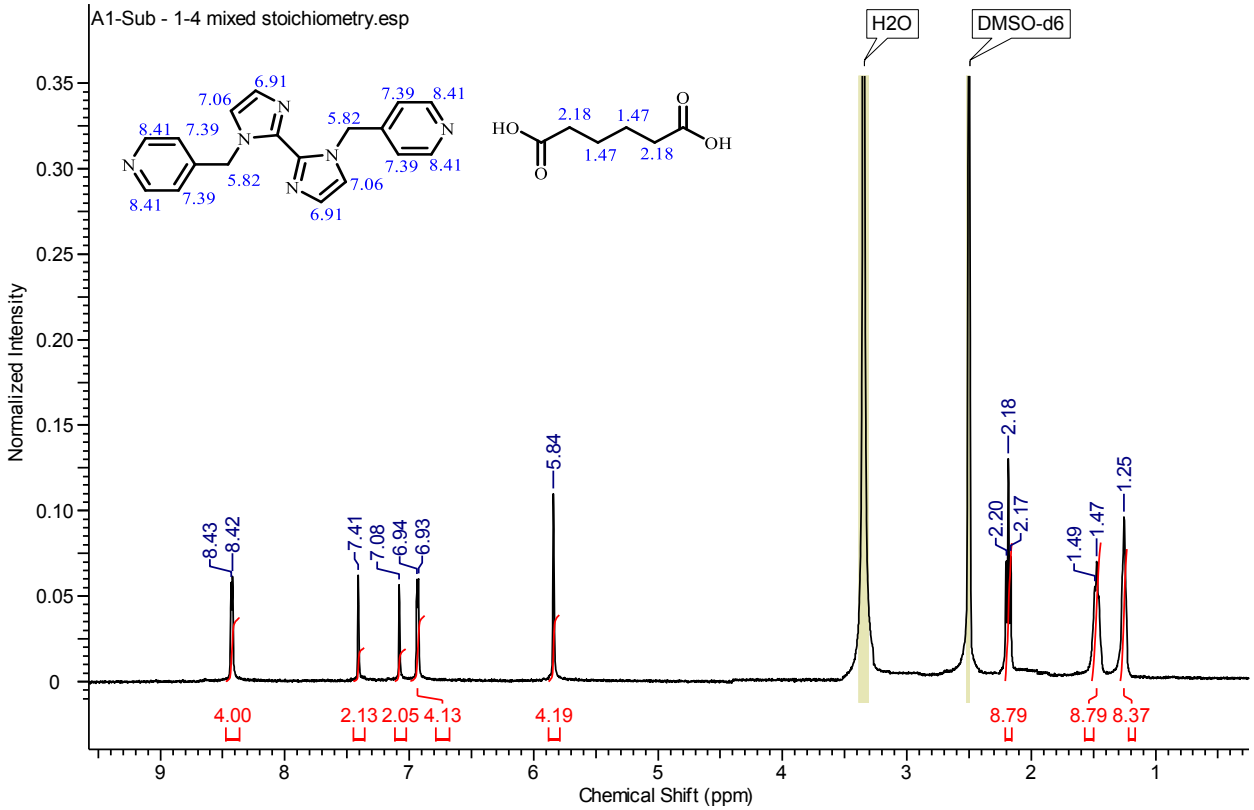
A1-Sub - 1-4 mixed stoichiometry.esp
H2O
DMSO-d6
Normalized Intensity
Chemical Shift (ppm)
8.43
8.42
7.41
7.08
6.94
6.93
5.84
2.18
2.20
2.17
1.49
1.47
1.25
4.00
2.13
2.05
4.13
4.19
8.79
8.79
8.37

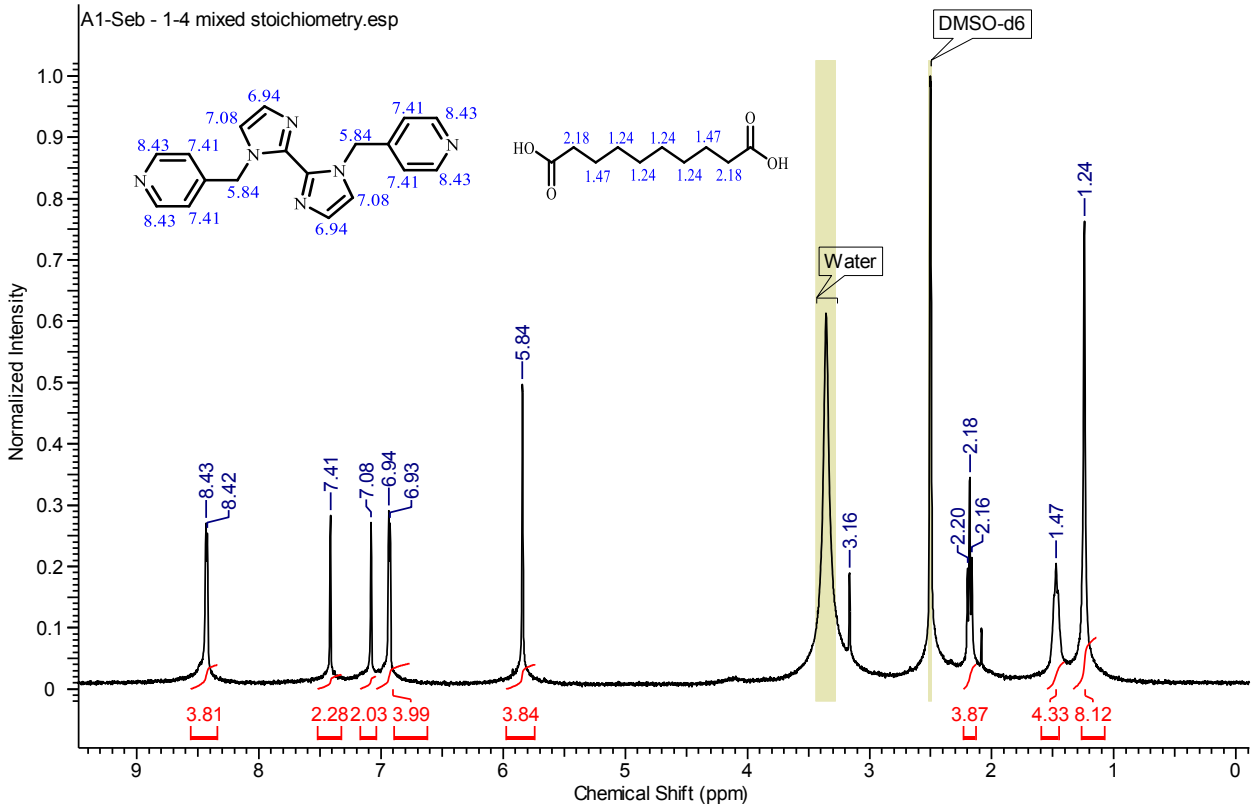
A1-Seb - 1-4 mixed stoichiometry.esp
DMSO-d6
Water
Normalized Intensity
Chemical Shift (ppm)
8.43
8.42
7.41
7.08
6.94
6.93
5.84
3.16
2.20
2.18
2.16
1.47
1.24
3.81
2.28
2.03
3.99
3.84
3.87
4.33
8.12

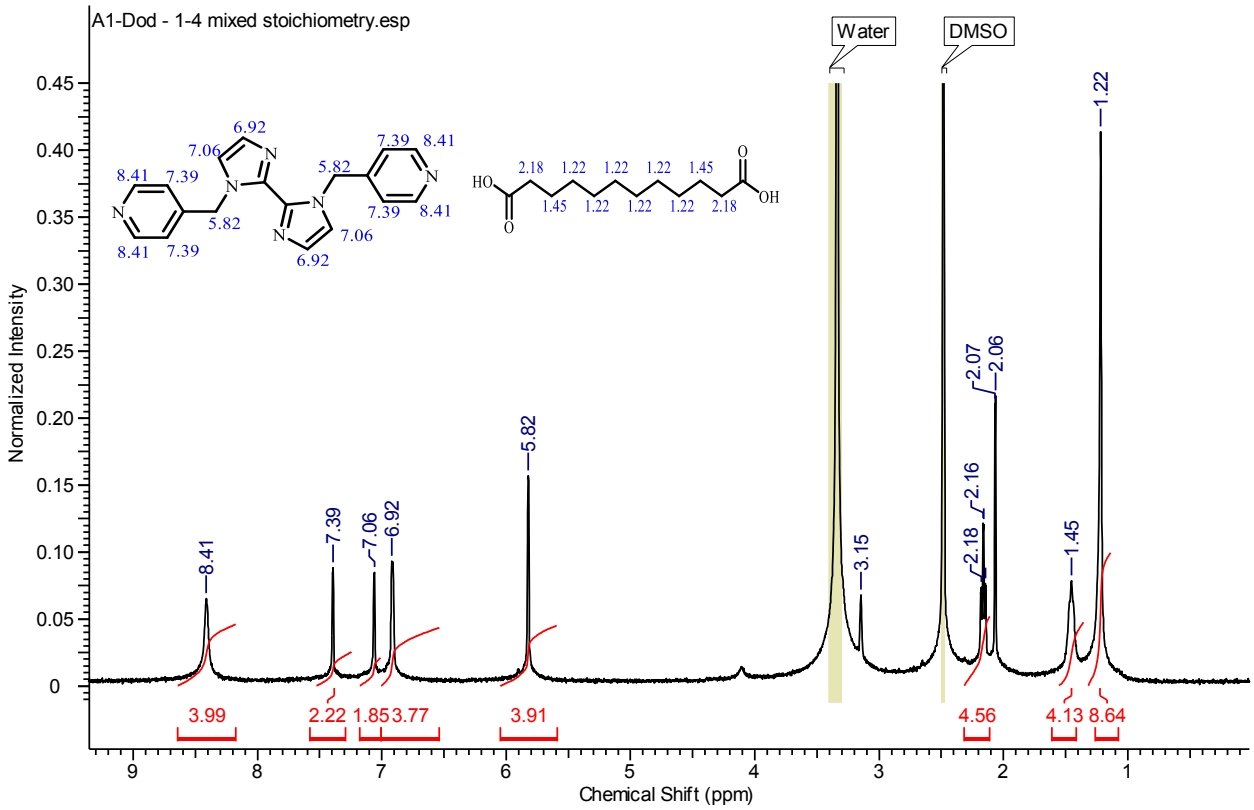
A1-Dod - 1-4 mixed stoichiometry.esp
Water
DMSO
Normalized Intensity
Chemical Shift (ppm)
8.41
7.39
7.06
6.92
5.82
3.15
2.07
2.06
2.18
2.16
1.45
1.22
3.99
2.22
1.85
3.77
3.91
4.56
4.13
8.64

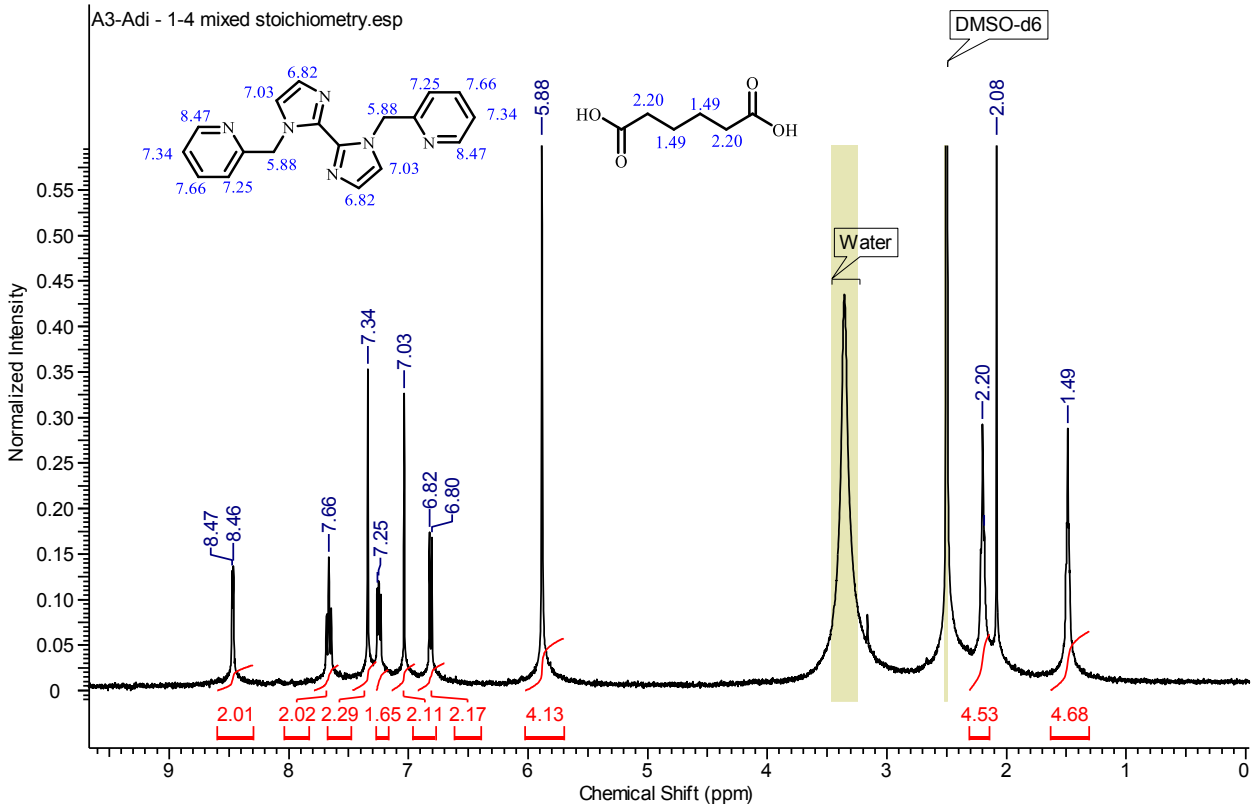
A3-Adi - 1-4 mixed stoichiometry.esp
DMSO-d6
Water
Normalized Intensity
Chemical Shift (ppm)
8.47
8.46
7.66
7.34
7.25
7.03
6.82
6.80
5.88
2.20
2.08
1.49
2.01
2.02
2.29
1.65
2.11
2.17
4.13
4.53
4.68

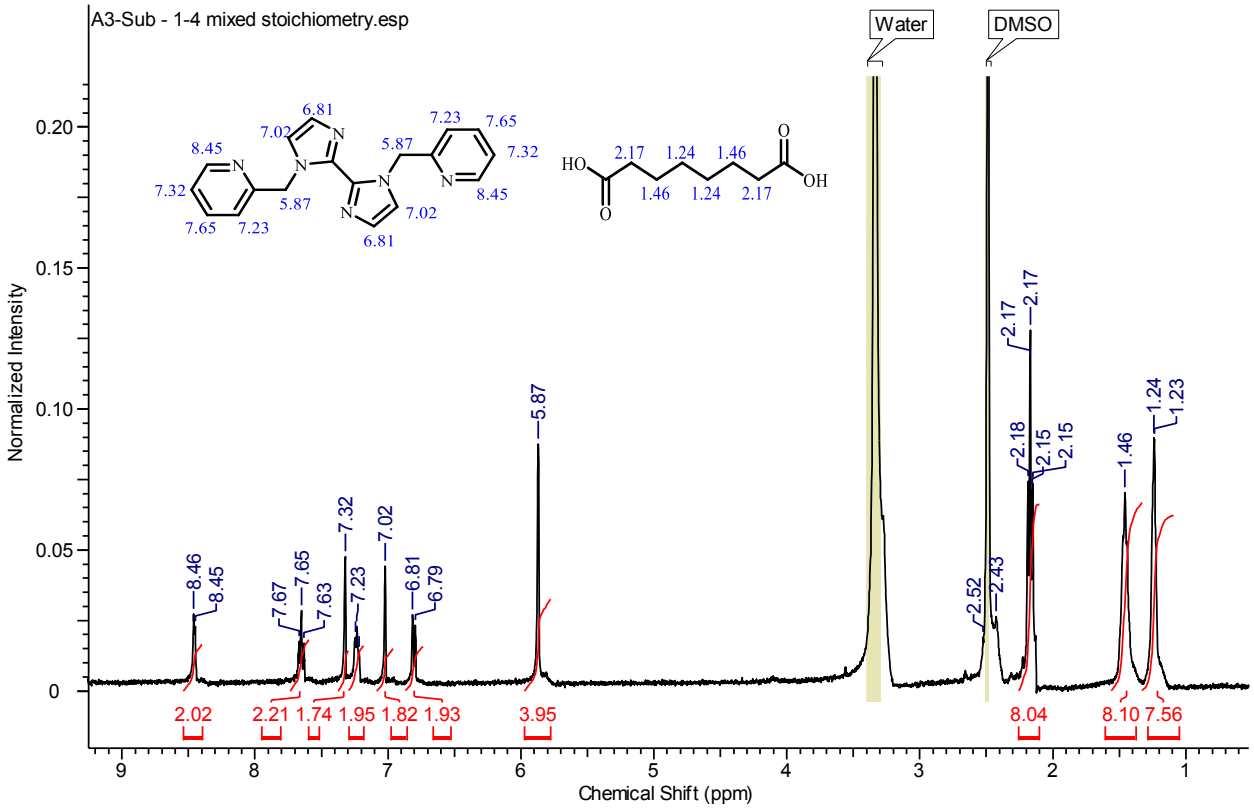
A3-Sub - 1-4 mixed stoichiometry.esp
Water
DMSO
Normalized Intensity
Chemical Shift (ppm)
8.46
8.45
7.67
7.65
7.63
7.32
7.23
7.02
6.81
6.79
5.87
2.52
2.43
2.18
2.17
2.15
1.46
1.24
1.23
2.02
2.21
1.74
1.95
1.82
1.93
3.95
8.04
8.10
7.56

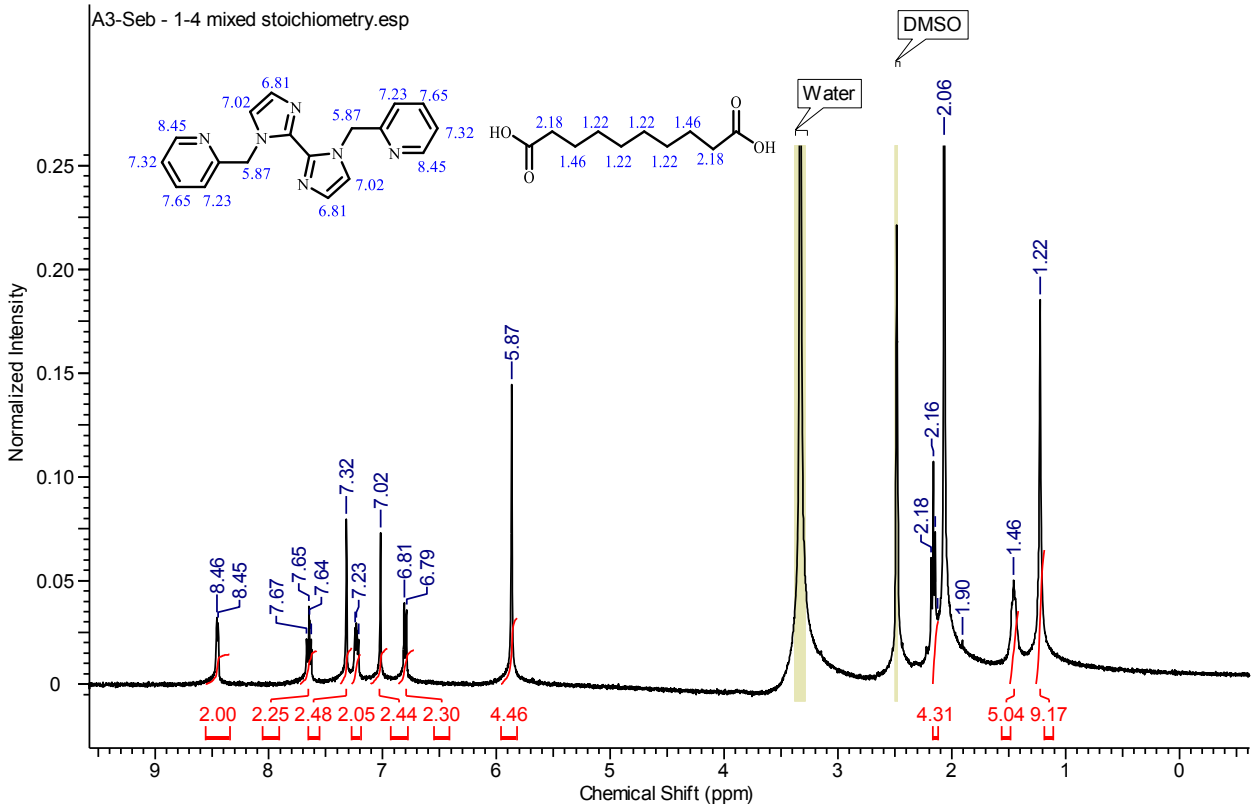
A3-Seb - 1-4 mixed stoichiometry.esp
DMSO
Water
Normalized Intensity
Chemical Shift (ppm)
8.46
8.45
7.67
7.65
7.64
7.32
7.23
7.02
6.81
6.79
5.87
2.18
2.16
2.06
1.90
1.46
1.22
2.00
2.25
2.48
2.05
2.44
2.30
4.46
4.31
5.04
9.17

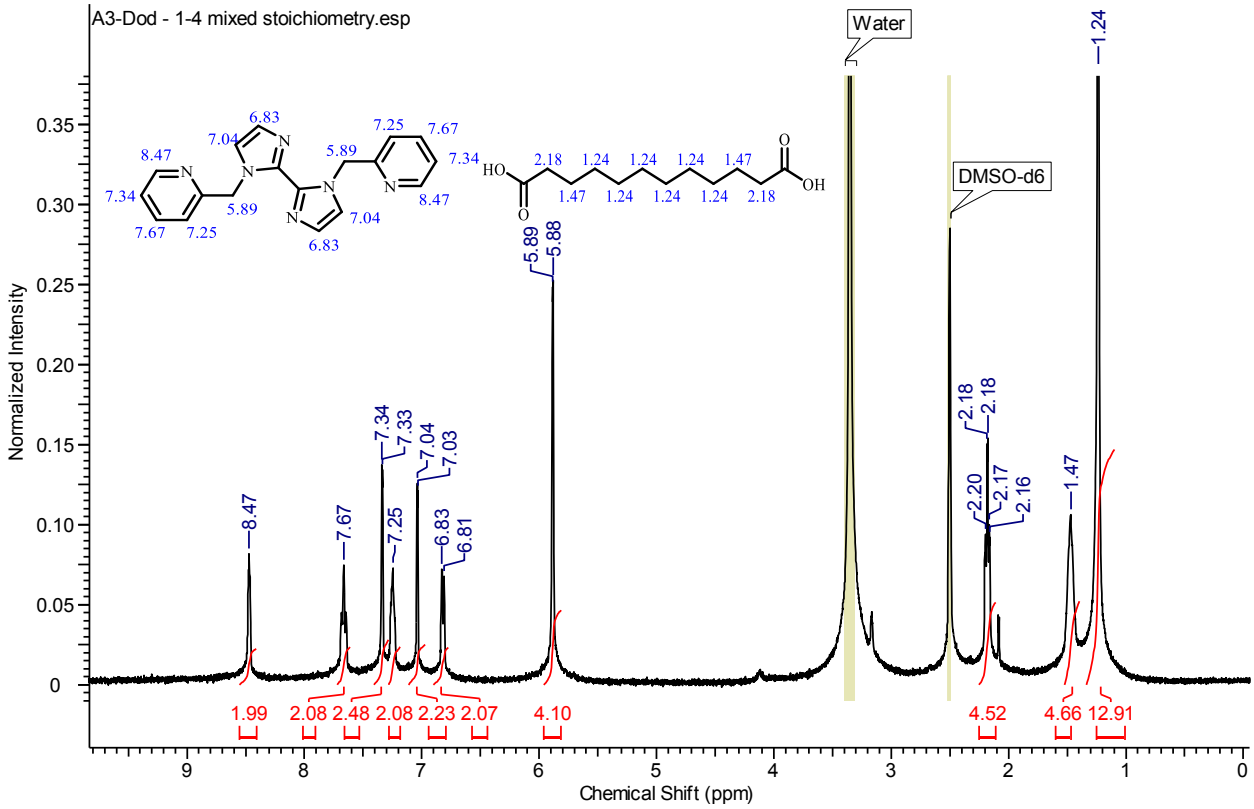
A3-Dod - 1-4 mixed stoichiometry.esp
Water
DMSO-d6
Normalized Intensity
Chemical Shift (ppm)
8.47
7.67
7.34
7.33
7.25
7.04
7.03
6.83
6.81
5.89
5.88
2.18
2.18
2.20
2.17
2.16
1.47
1.24
1.99
2.08
2.48
2.08
2.23
2.07
4.10
4.52
4.66
12.91

A.2 Chapter 4

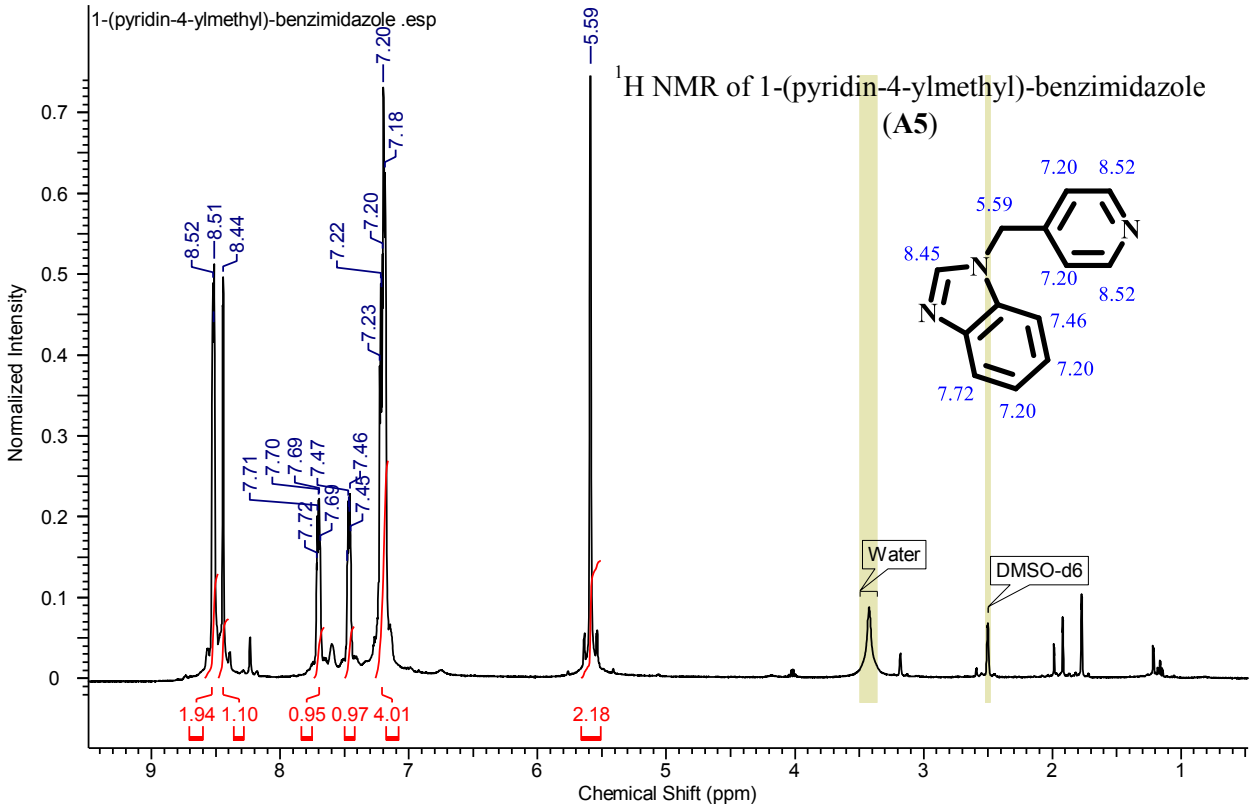
1-(pyridin-4-ylmethyl)-benzimidazole .esp
^{1}H NMR of 1-(pyridin-4-ylmethyl)-benzimidazole (**A5**)
Normalized Intensity
Chemical Shift (ppm)
Water
DMSO-d6
8.52
8.51
8.44
7.71
7.70
7.69
7.47
7.74
7.69
7.46
7.45
7.22
7.20
7.23
7.20
7.18
5.59
1.94
1.10
0.95
0.97
4.01
2.18

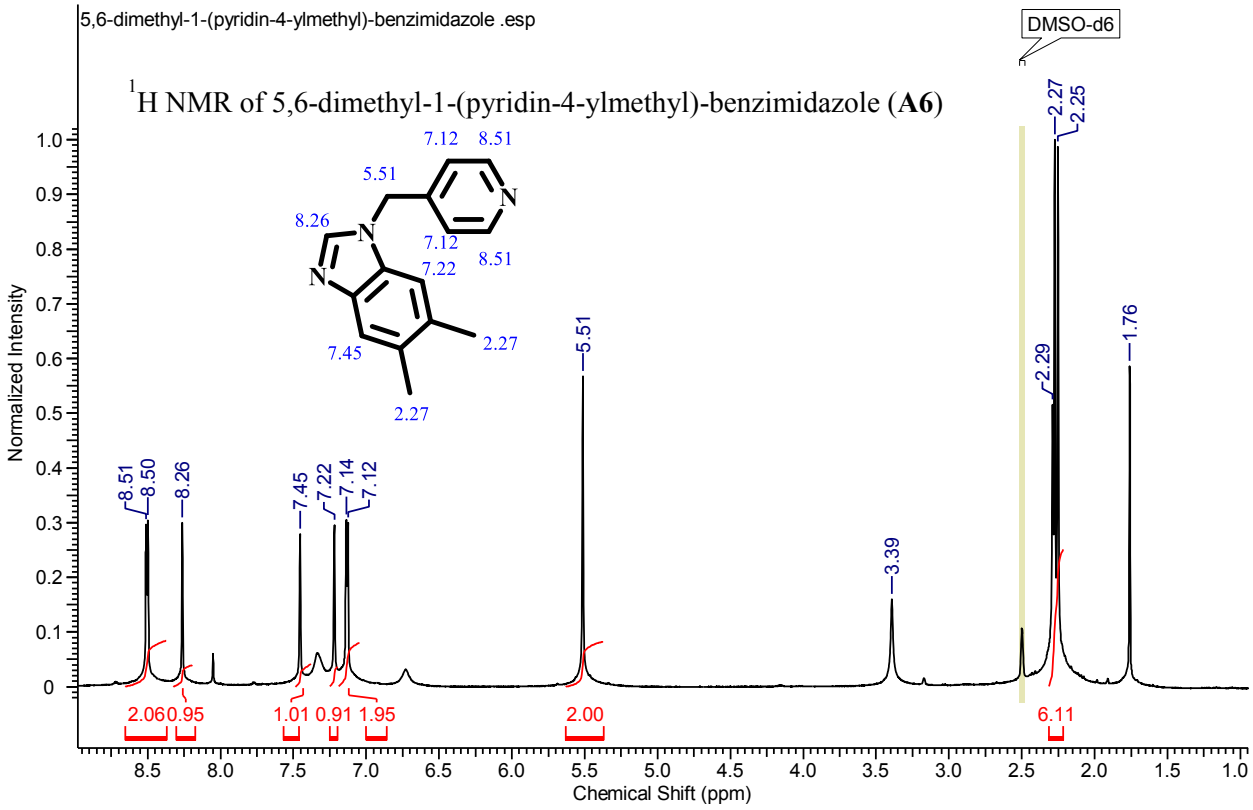
5,6-dimethyl-1-(pyridin-4-ylmethyl)-benzimidazole .esp
^{1}H NMR of 5,6-dimethyl-1-(pyridin-4-ylmethyl)-benzimidazole (**A6**)
Normalized Intensity
Chemical Shift (ppm)
DMSO-d6
8.51
8.50
8.26
7.45
7.22
7.14
7.12
5.51
3.39
2.27
2.25
2.29
1.76
2.06
0.95
1.01
0.91
1.95
2.00
6.11

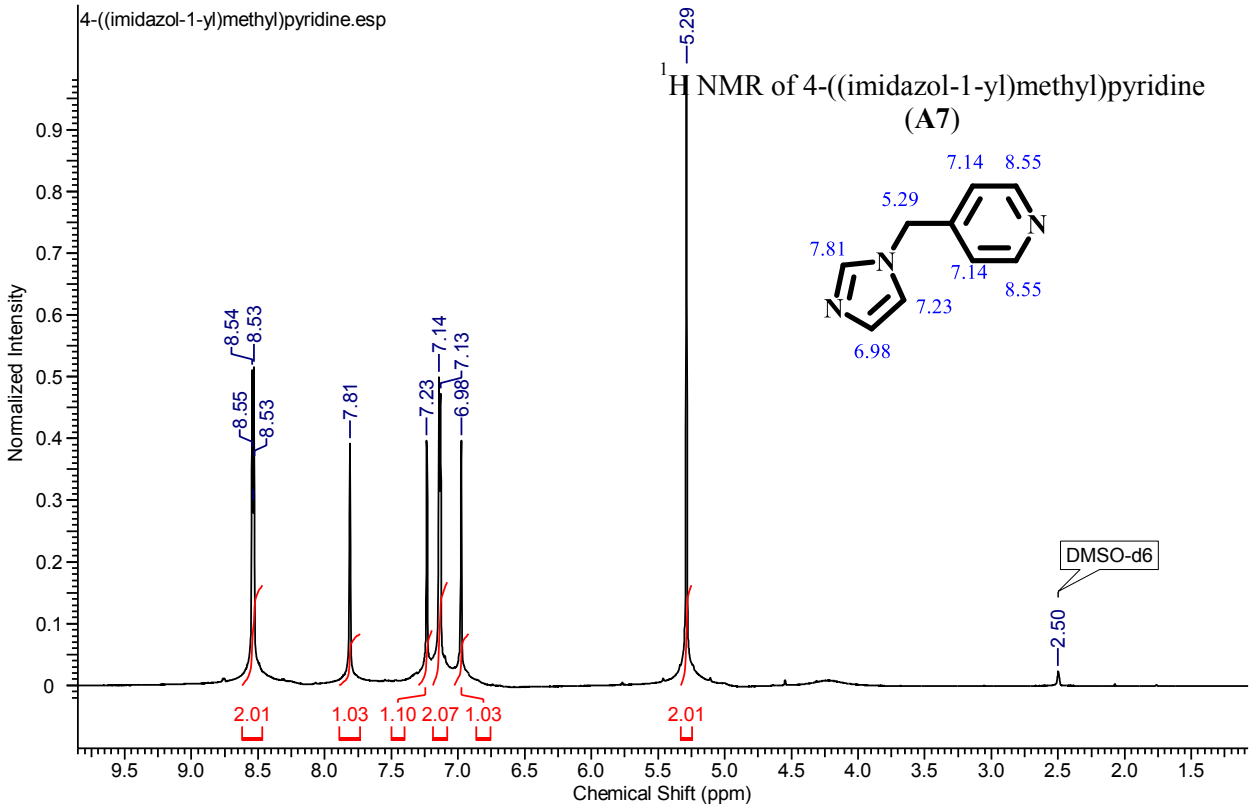
4-((imidazol-1-yl)methyl)pyridine.esp
^{1}H NMR of 4-((imidazol-1-yl)methyl)pyridine
(A7)
Normalized Intensity
Chemical Shift (ppm)
DMSO-d6

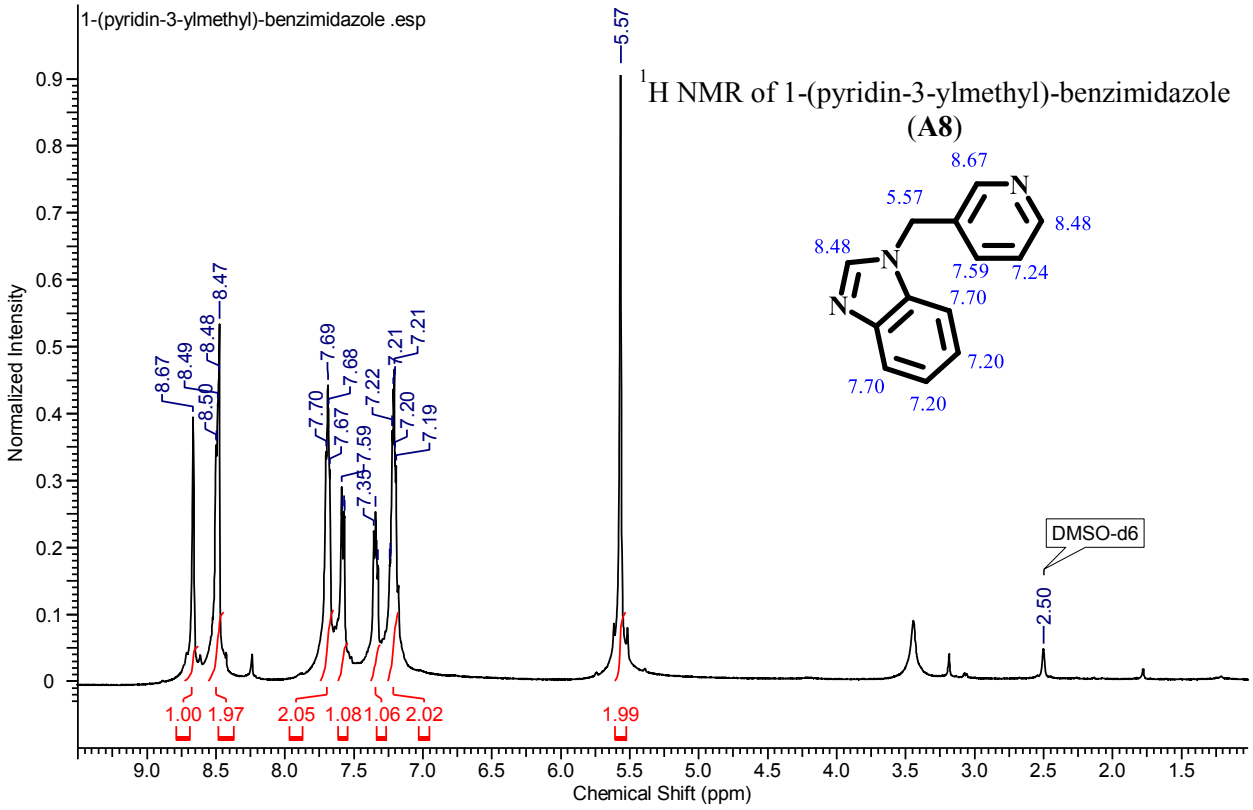
1-(pyridin-3-ylmethyl)-benzimidazole .esp
^{1}H NMR of 1-(pyridin-3-ylmethyl)-benzimidazole
(A8)
Normalized Intensity
Chemical Shift (ppm)
DMSO-d6

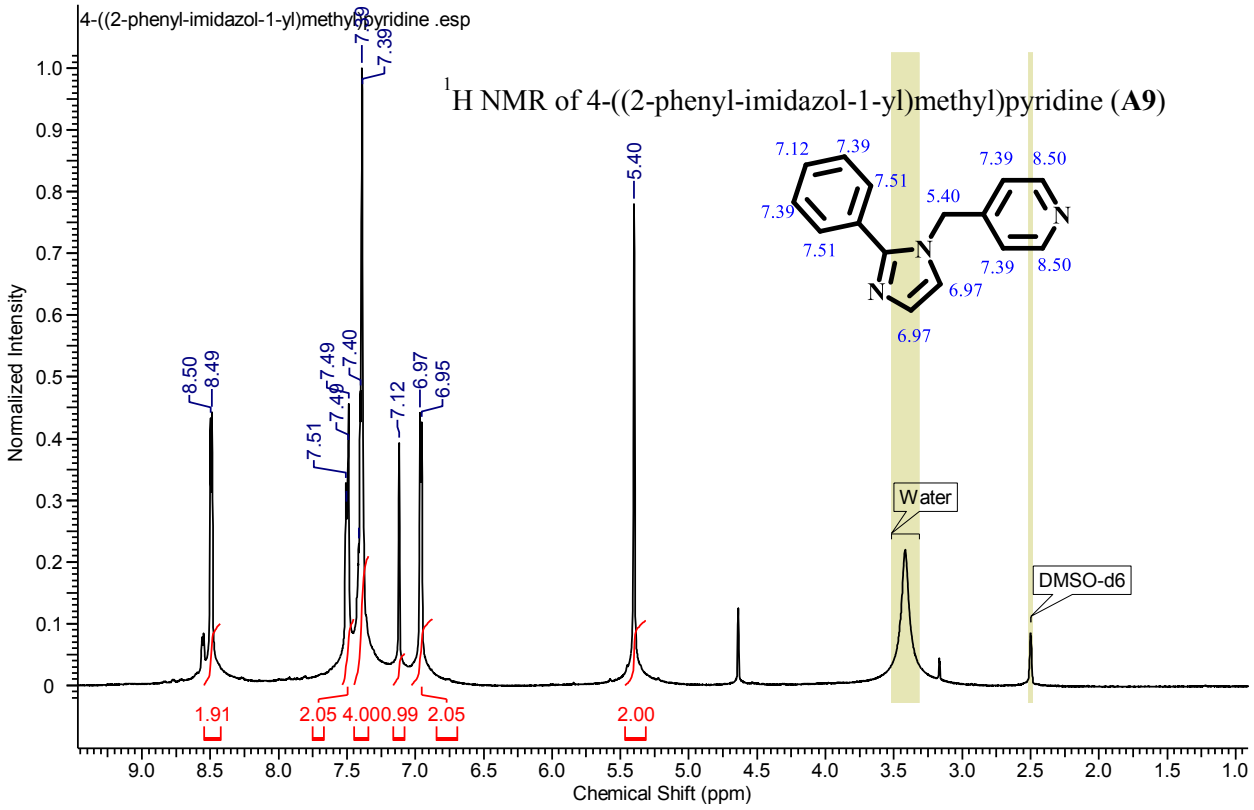
4-((2-phenyl-imidazol-1-yl)methyl)pyridine .esp
^{1}H NMR of 4-((2-phenyl-imidazol-1-yl)methyl)pyridine (**A9**)
Normalized Intensity
Chemical Shift (ppm)
Water
DMSO-d6
8.50
8.49
7.51
7.49
7.40
7.39
7.12
6.97
6.95
5.40
1.91
2.05
4.00
0.99
2.05
2.00
7.12
7.39
7.51
7.39
8.50
5.40
7.39
8.50
6.97
6.97

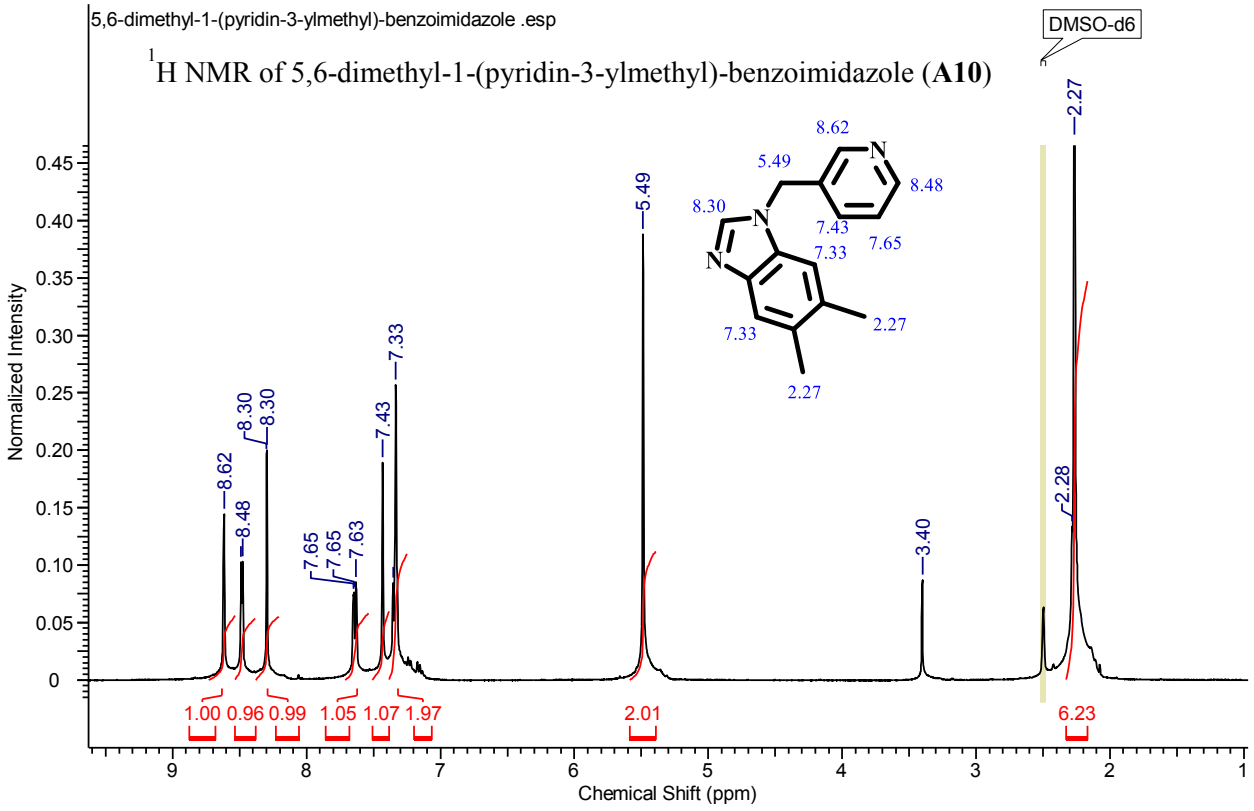
5,6-dimethyl-1-(pyridin-3-ylmethyl)-benzoimidazole .esp
^{1}H NMR of 5,6-dimethyl-1-(pyridin-3-ylmethyl)-benzoimidazole (**A10**)
Normalized Intensity
Chemical Shift (ppm)
DMSO-d6
8.62
8.48
8.30
8.30
7.65
7.65
7.63
7.43
7.33
5.49
3.40
2.28
2.27
1.00
0.96
0.99
1.05
1.07
1.97
2.01
6.23
8.62
5.49
8.48
8.30
7.43
7.33
7.65
7.33
2.27
2.27

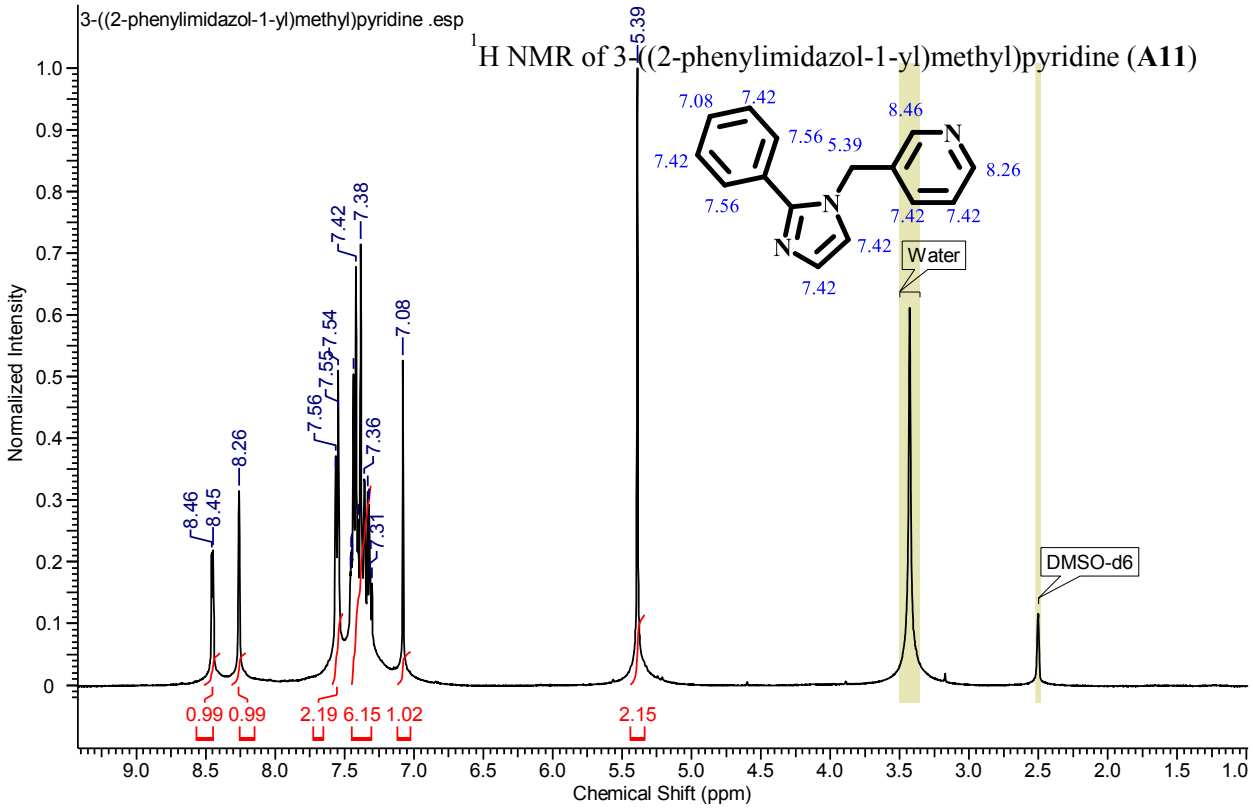

^{1}H NMR of 3-((2-phenylimidazol-1-yl)methyl)pyridine (**A11**)

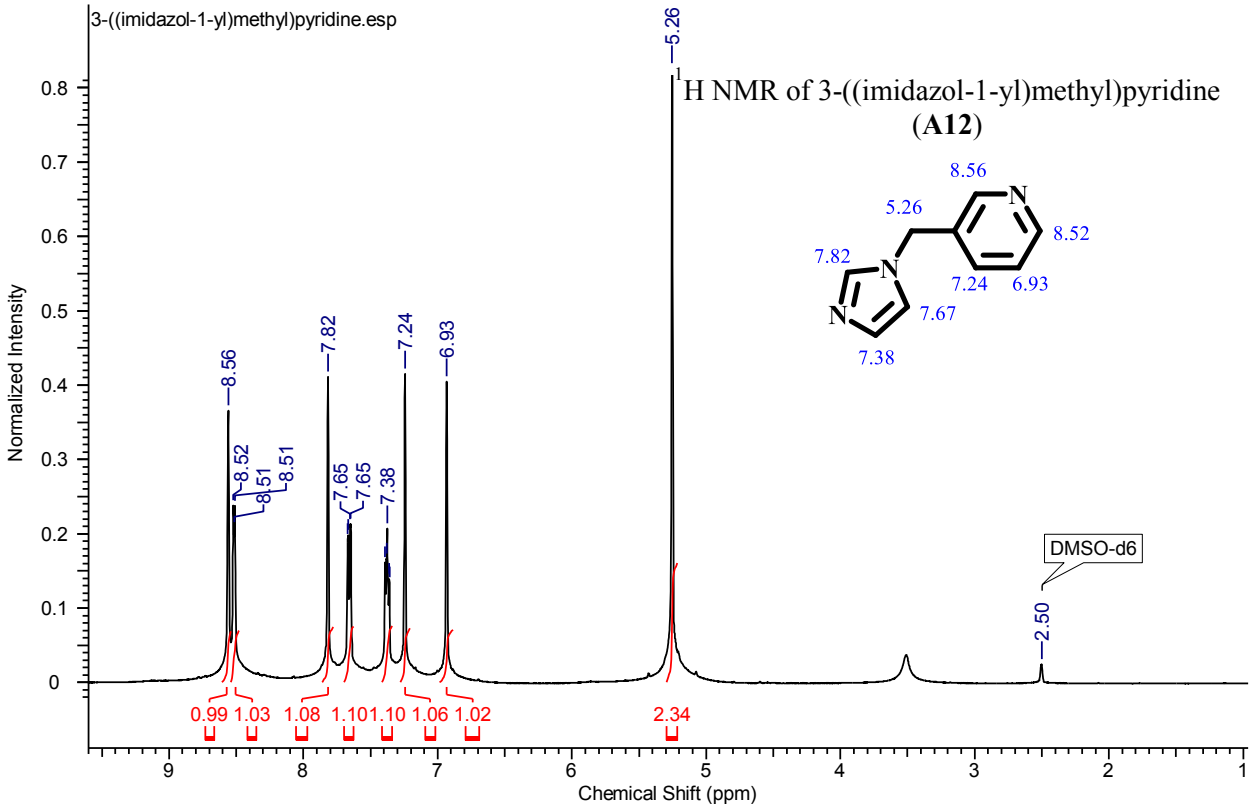

^{1}H NMR of 3-((imidazol-1-yl)methyl)pyridine (**A12**)

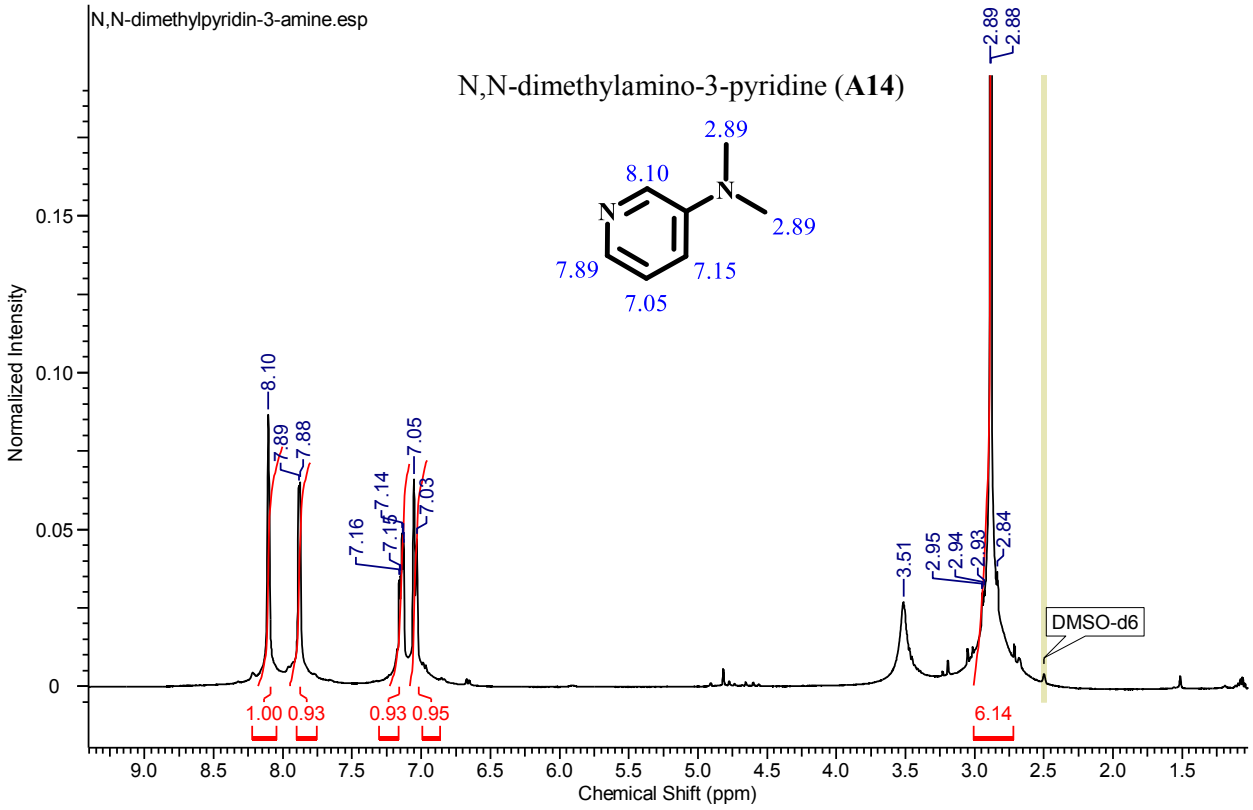
N,N-dimethylpyridin-3-amine.esp
N,N-dimethylamino-3-pyridine (A14)
2.89
8.10
2.89
7.89
7.15
7.05
Normalized Intensity
Chemical Shift (ppm)
DMSO-d6
1.00 0.93 0.93 0.95
6.14

A.3 Chapter 5

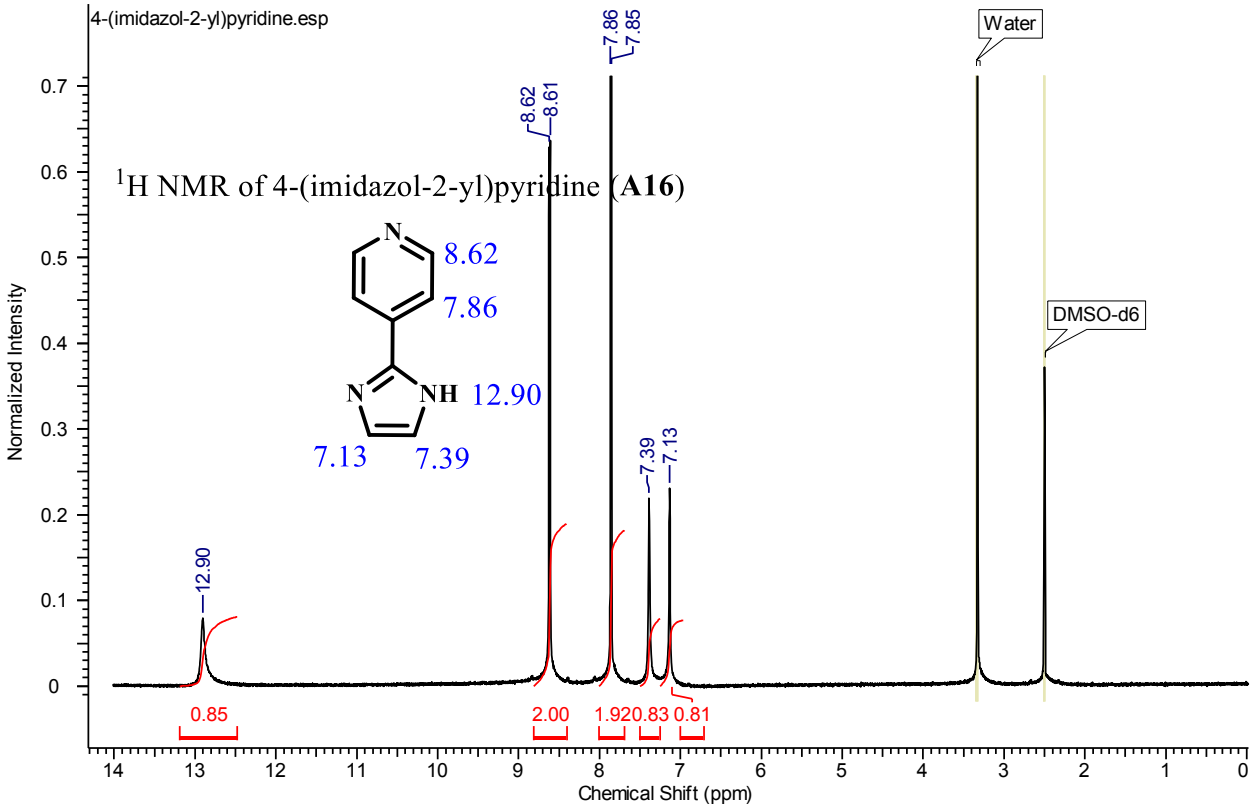
4-(imidazol-2-yl)pyridine.esp
1H NMR of 4-(imidazol-2-yl)pyridine (A16)
8.62
7.86
12.90
7.13
7.39
Water
DMSO-d6
Normalized Intensity
Chemical Shift (ppm)
0.85
2.00 1.92 0.83 0.81

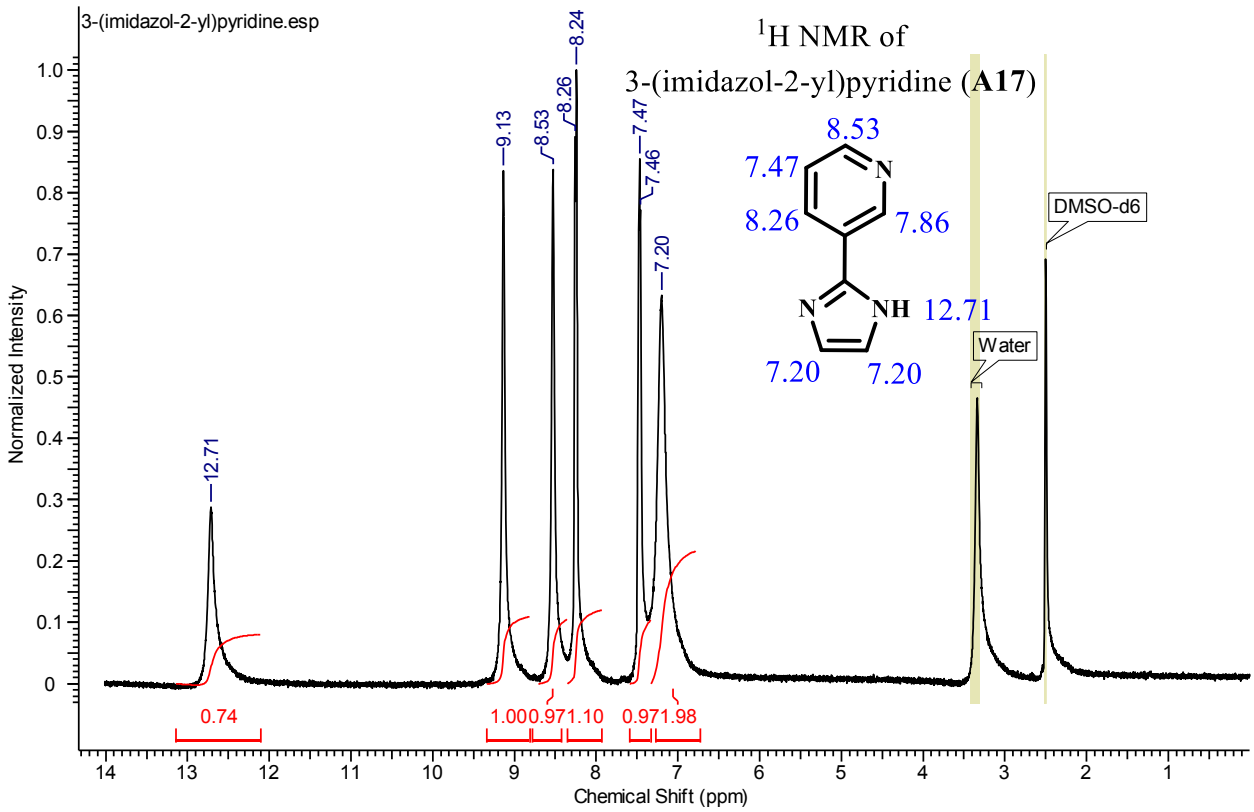
3-(imidazol-2-yl)pyridine.esp
^{1}H NMR of
3-(imidazol-2-yl)pyridine (**A17**)
8.53
7.47
8.26
7.86
12.71
7.20
7.20
DMSO-d6
Water
Normalized Intensity
Chemical Shift (ppm)
0.74
1.00 0.97 1.10
0.97 1.98

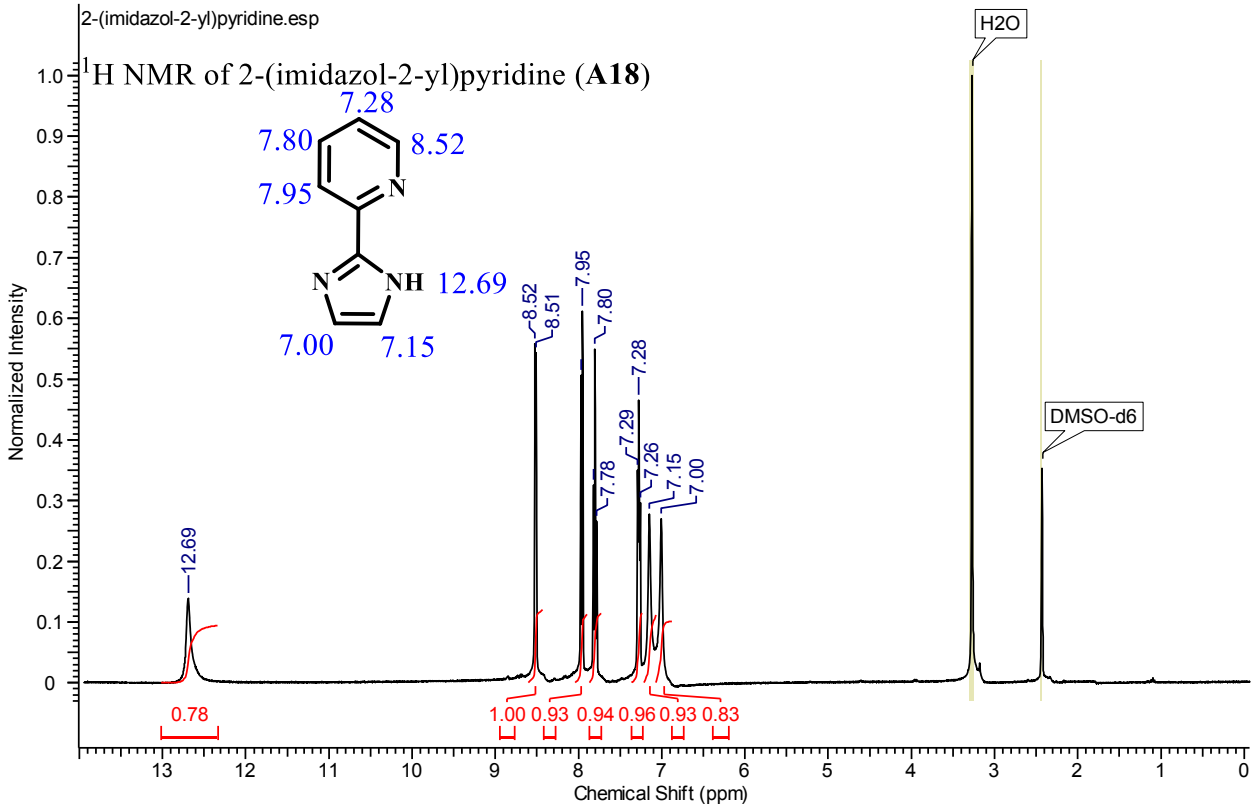
2-(imidazol-2-yl)pyridine.esp
^{1}H NMR of 2-(imidazol-2-yl)pyridine (**A18**)
7.28
7.80
8.52
7.95
12.69
7.00
7.15
H2O
DMSO-d6
Normalized Intensity
Chemical Shift (ppm)
0.78
1.00 0.93 0.94 0.96 0.93 0.83

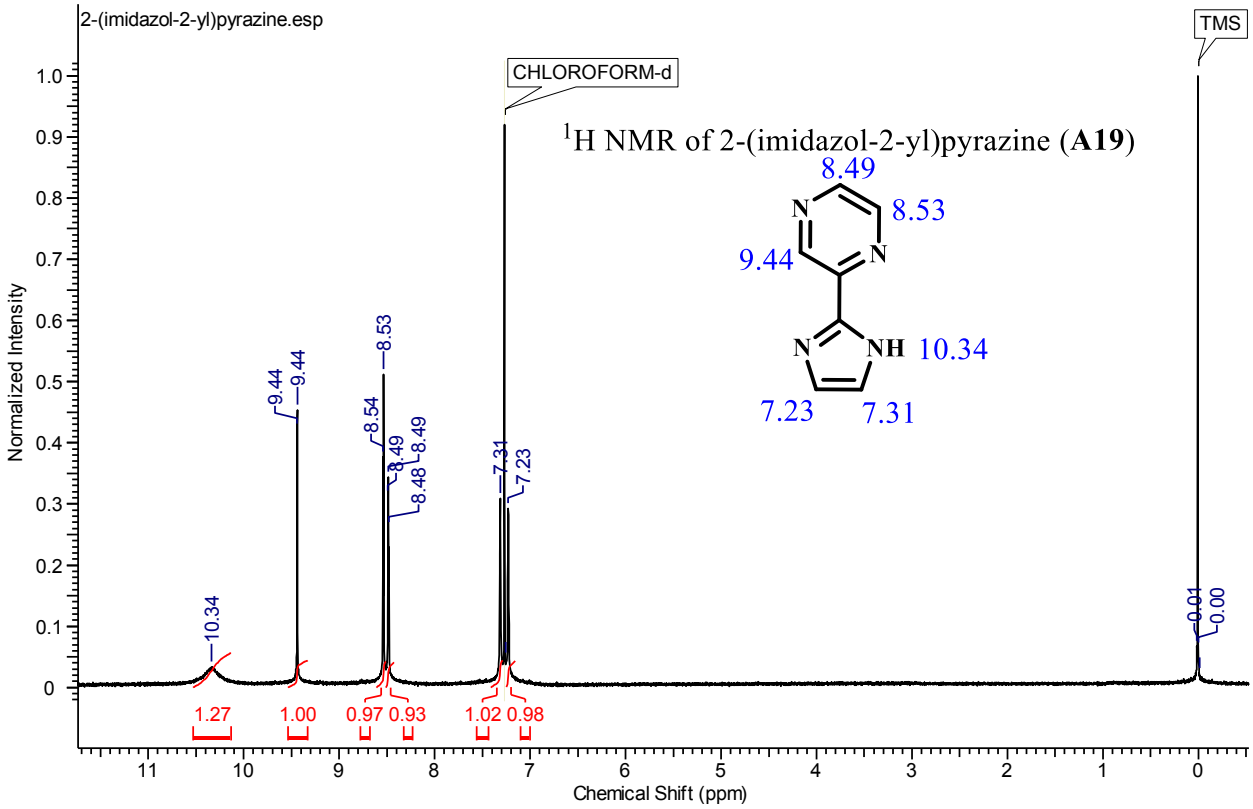
2-(imidazol-2-yl)pyrazine.esp
CHLOROFORM-d
TMS
^{1}H NMR of 2-(imidazol-2-yl)pyrazine (**A19**)
8.49
8.53
9.44
10.34
7.23
7.31
Normalized Intensity
Chemical Shift (ppm)
9.44
8.53
8.54
8.49
8.48
7.31
7.23
10.34
0.01
0.00
1.27
1.00
0.97
0.93
1.02
0.98

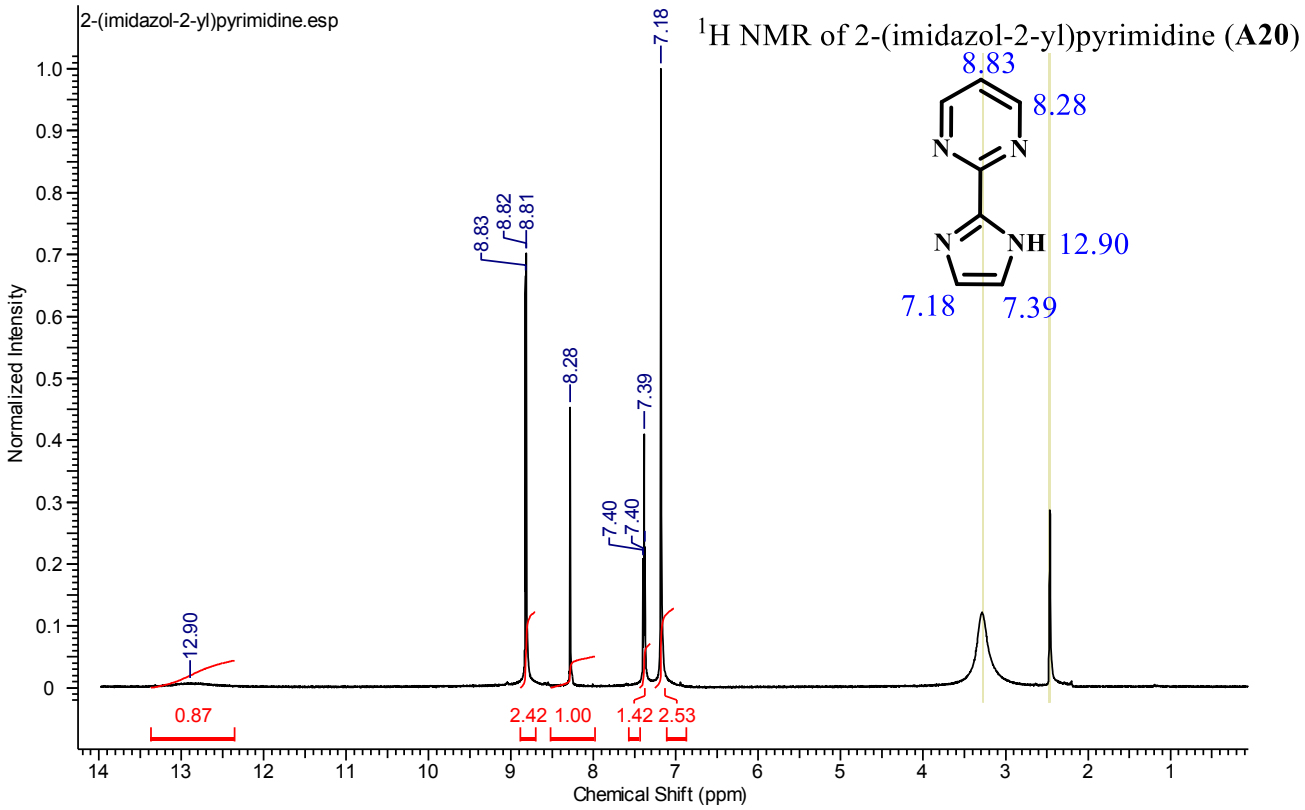
2-(imidazol-2-yl)pyrimidine.esp
^{1}H NMR of 2-(imidazol-2-yl)pyrimidine (**A20**)
8.83
8.28
12.90
7.18
7.39
Normalized Intensity
Chemical Shift (ppm)
7.18
8.83
8.82
8.81
8.28
7.39
7.40
7.40
12.90
0.87
2.42
1.00
1.42
2.53

A.4 Chapter 6

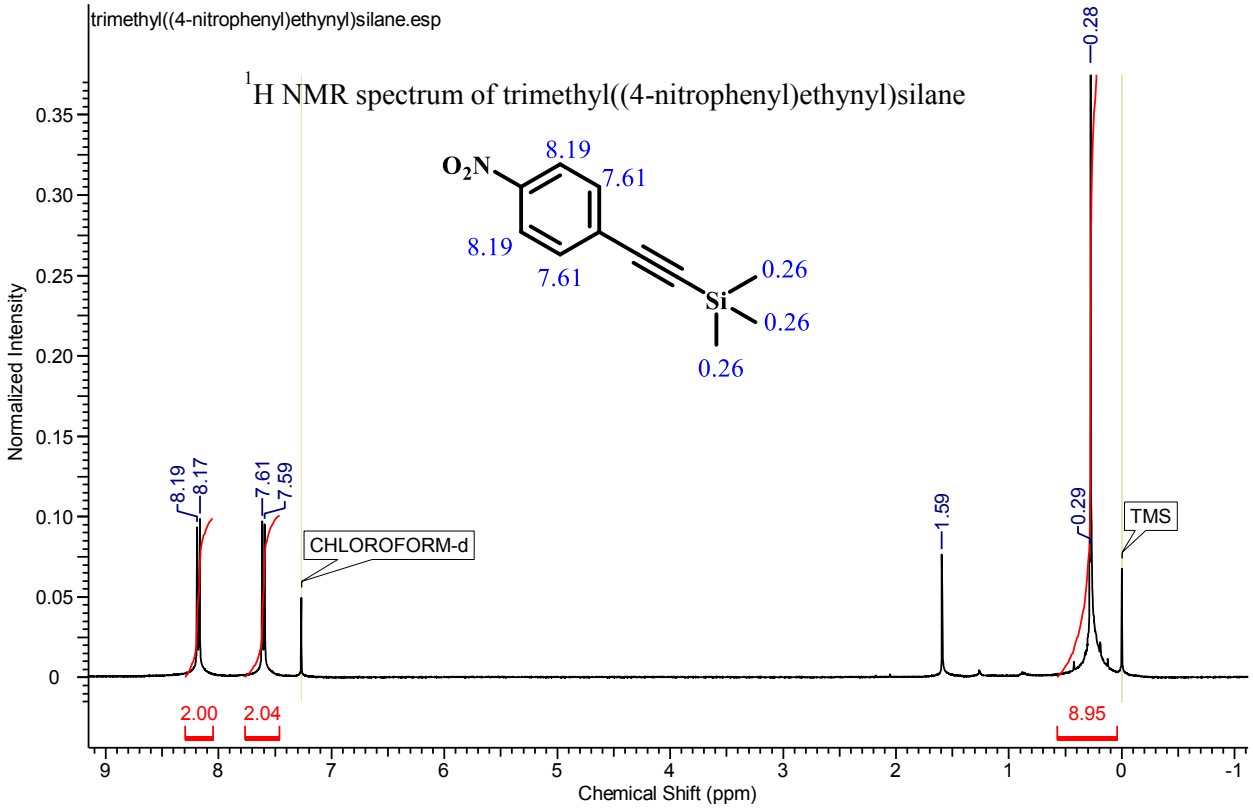
trimethyl((4-nitrophenyl)ethynyl)silane.esp
^{1}H NMR spectrum of trimethyl((4-nitrophenyl)ethynyl)silane
O_2N
8.19
7.61
8.19
7.61
Si
0.26
0.26
0.26
Normalized Intensity
8.19
8.17
7.61
7.59
CHLOROFORM-d
1.59
0.29
0.28
TMS
2.00
2.04
8.95
Chemical Shift (ppm)

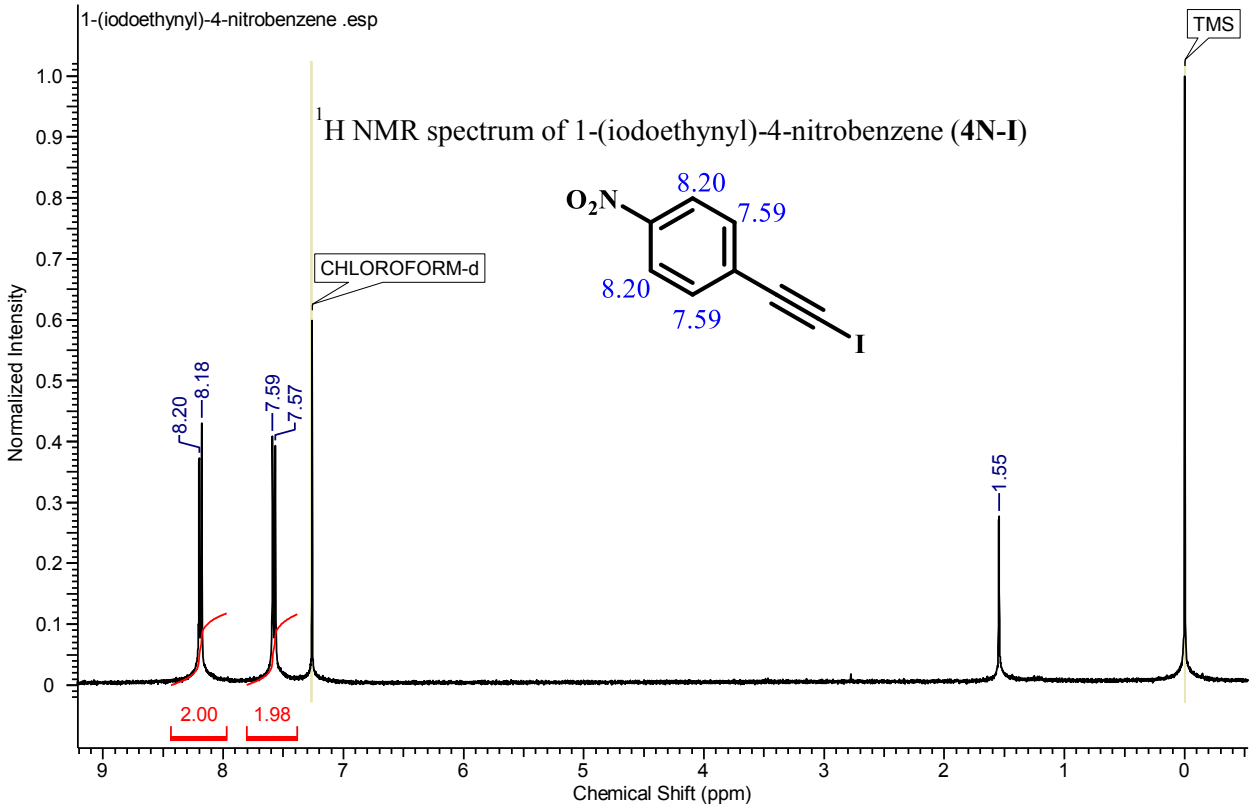
1-(iodoethynyl)-4-nitrobenzene .esp
^{1}H NMR spectrum of 1-(iodoethynyl)-4-nitrobenzene (**4N-I**)
O_2N
8.20
7.59
8.20
7.59
I
CHLOROFORM-d
TMS
Normalized Intensity
8.20
8.18
7.59
7.57
1.55
2.00
1.98
Chemical Shift (ppm)

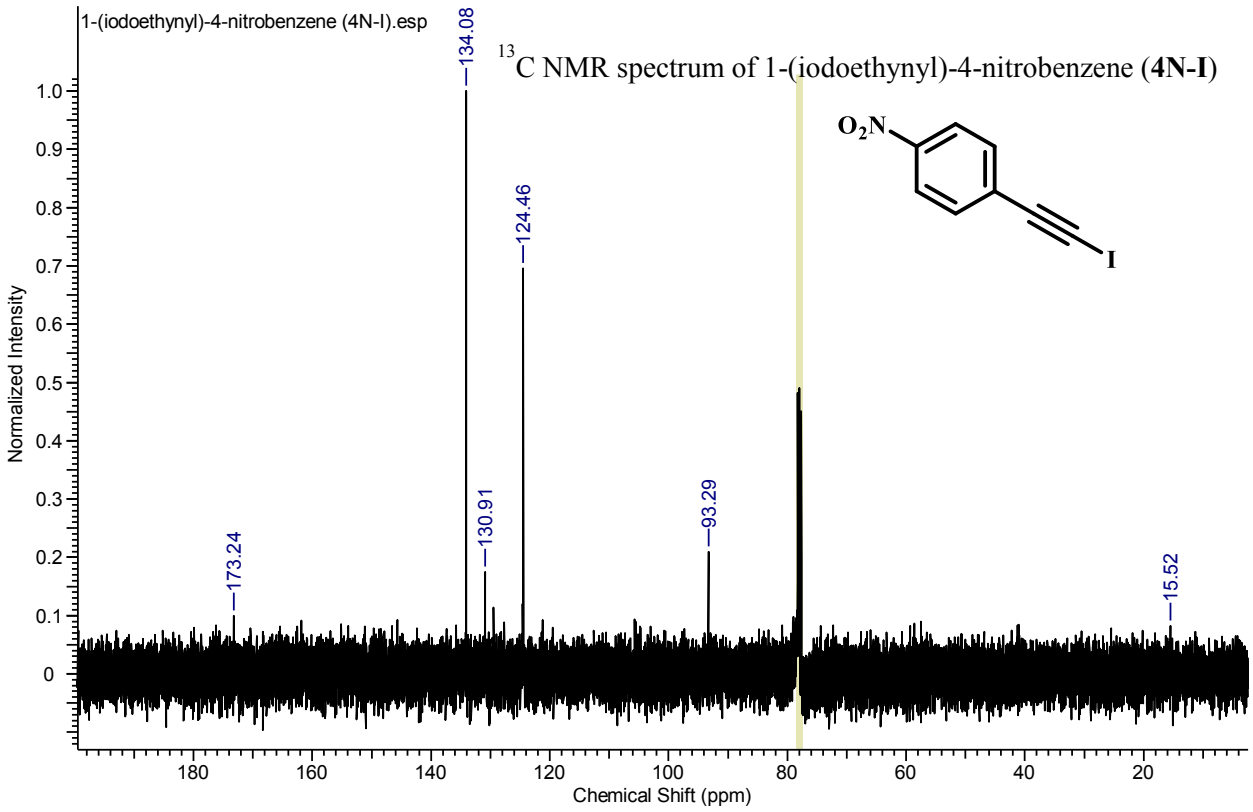

^{13}C NMR spectrum of 1-(iodoethynyl)-4-nitrobenzene (**4N-I**)

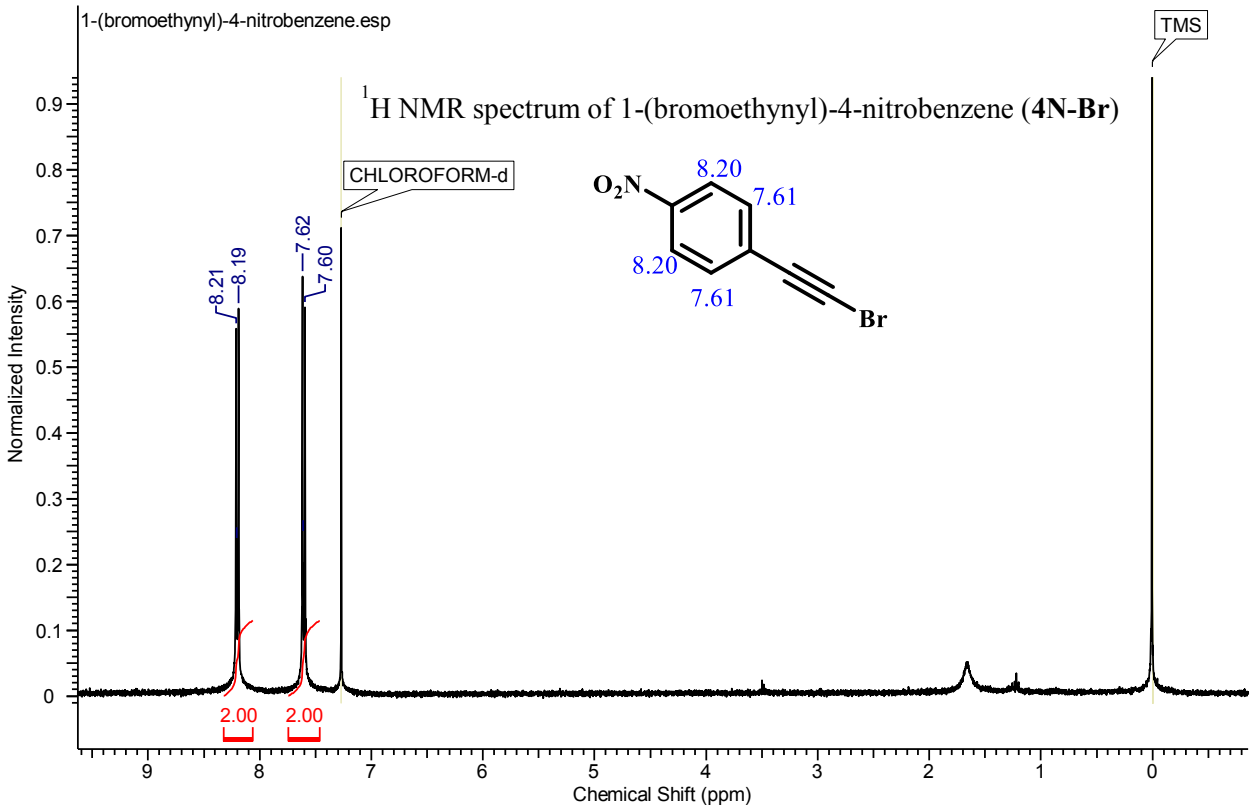

^{1}H NMR spectrum of 1-(bromoethynyl)-4-nitrobenzene (**4N-Br**)

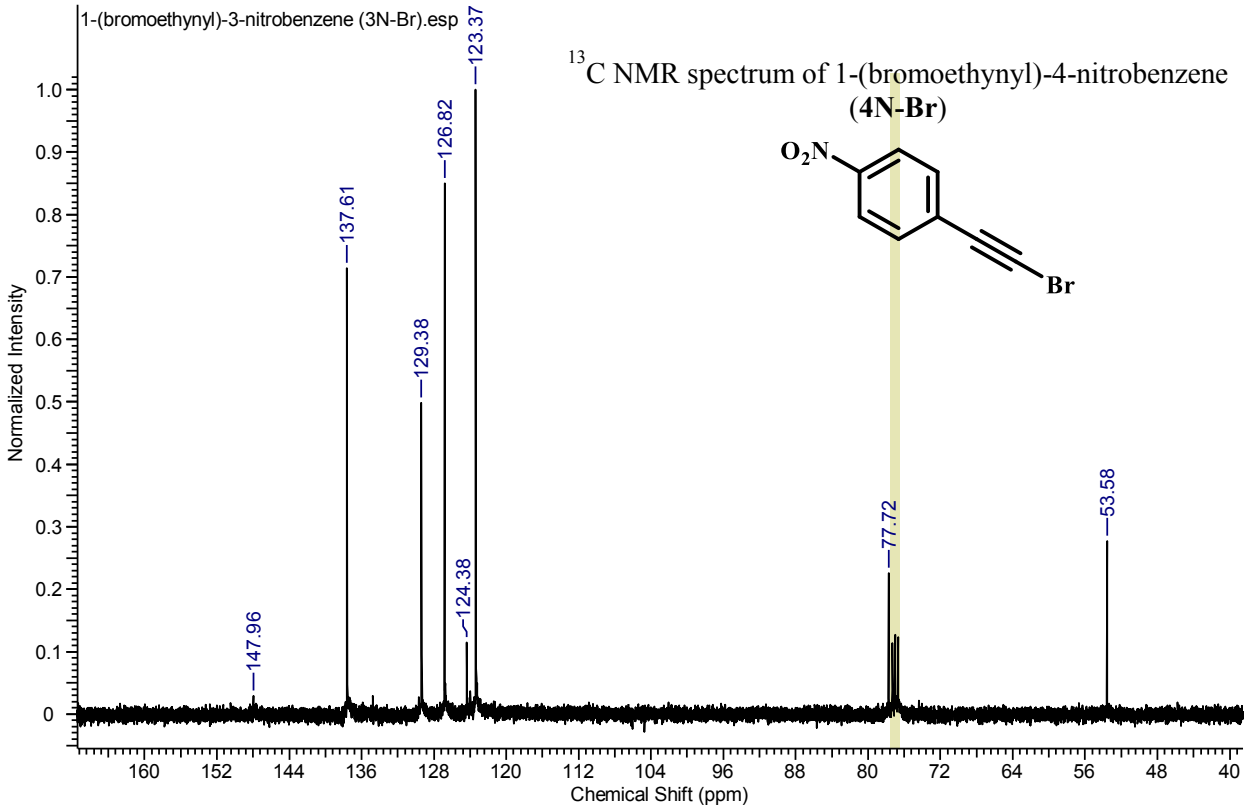

^{13}C NMR spectrum of 1-(bromoethynyl)-4-nitrobenzene (**4N-Br**)

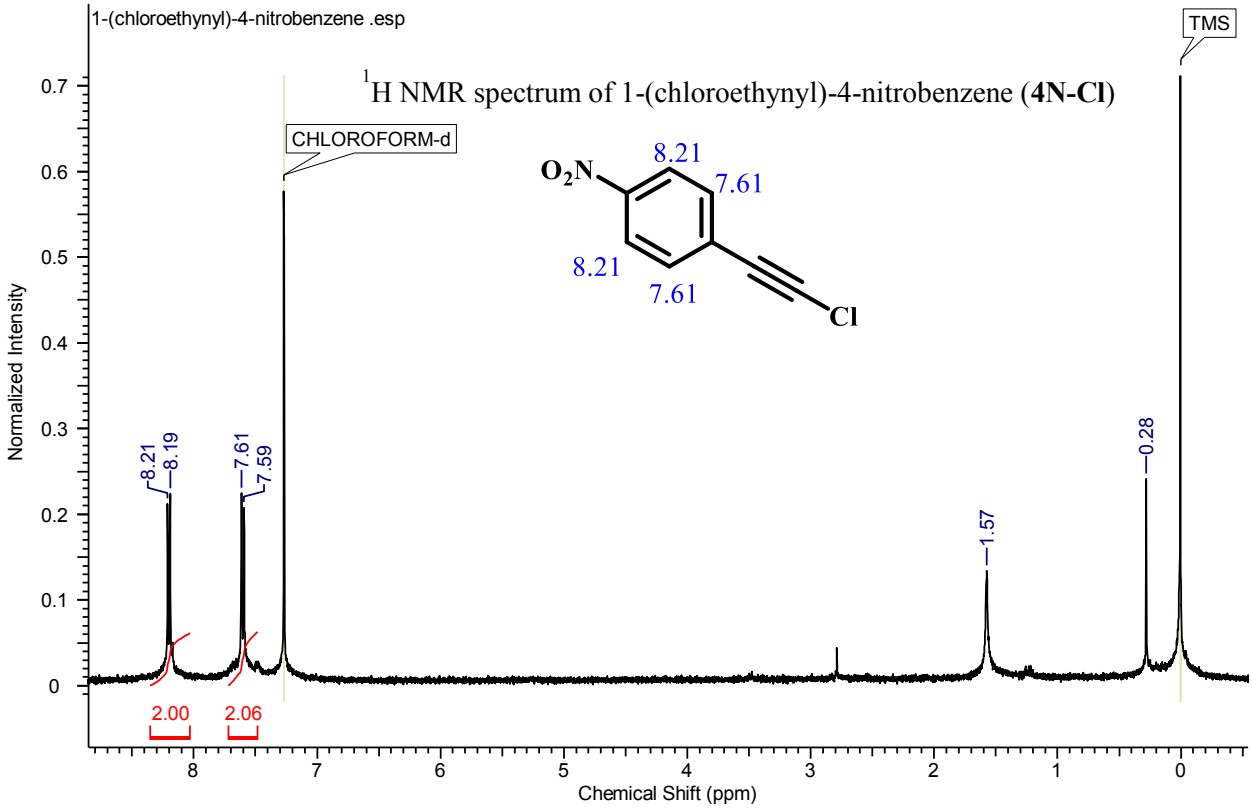

^{1}H NMR spectrum of 1-(chloroethynyl)-4-nitrobenzene (**4N-Cl**)

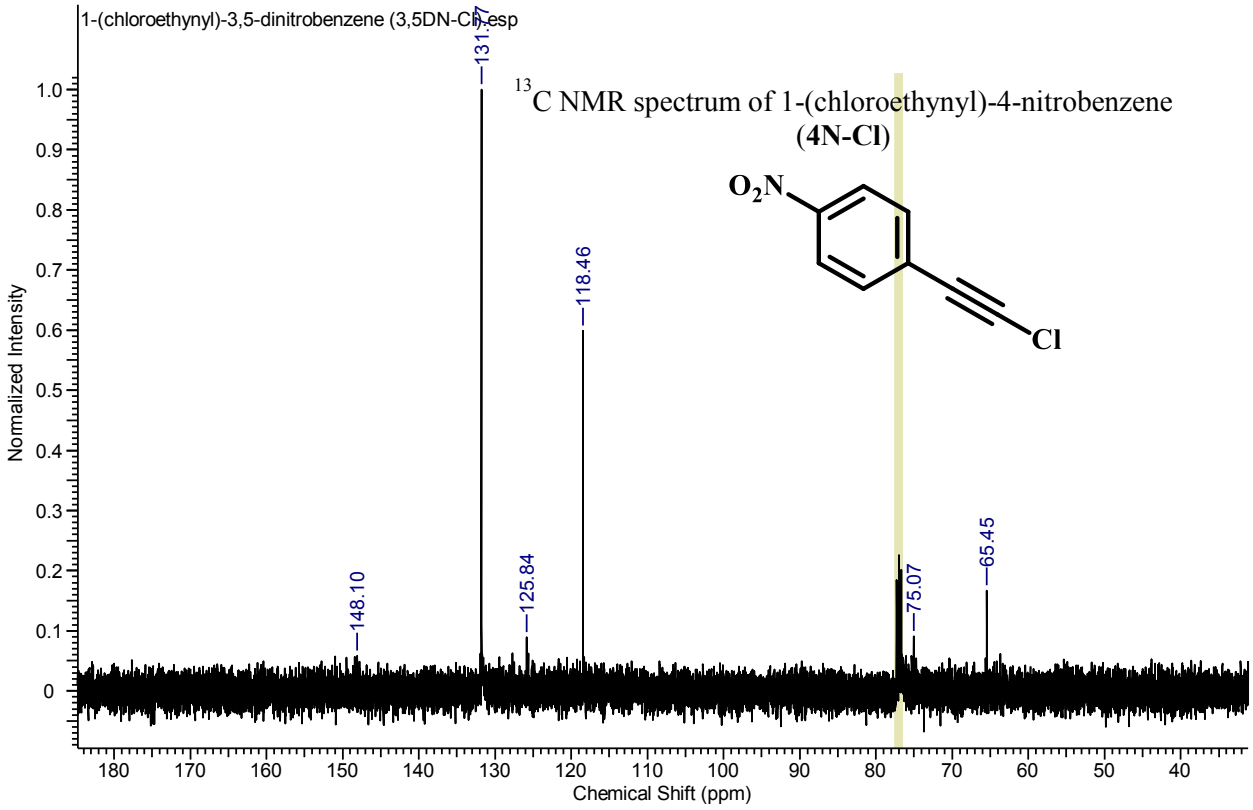

^{13}C NMR spectrum of 1-(chloroethynyl)-4-nitrobenzene (**4N-Cl**)

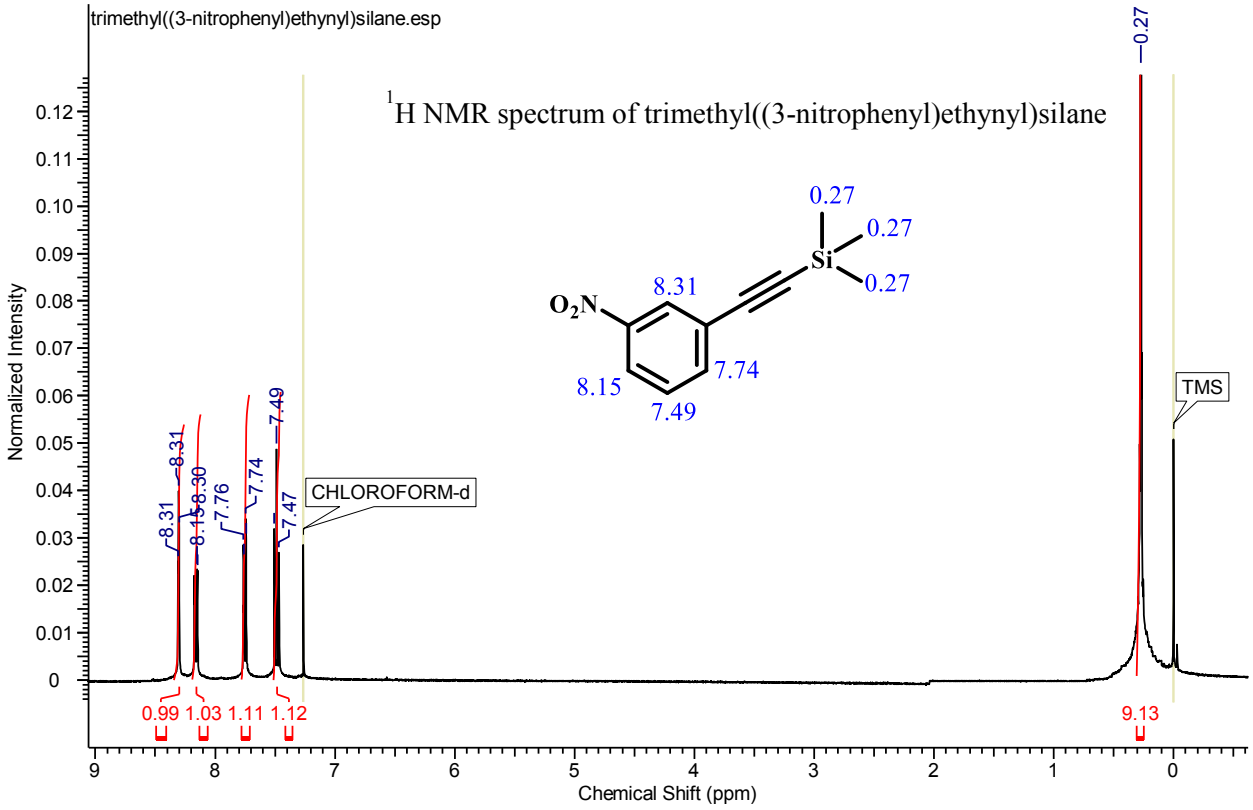

^{1}H NMR spectrum of trimethyl((3-nitrophenyl)ethynyl)silane

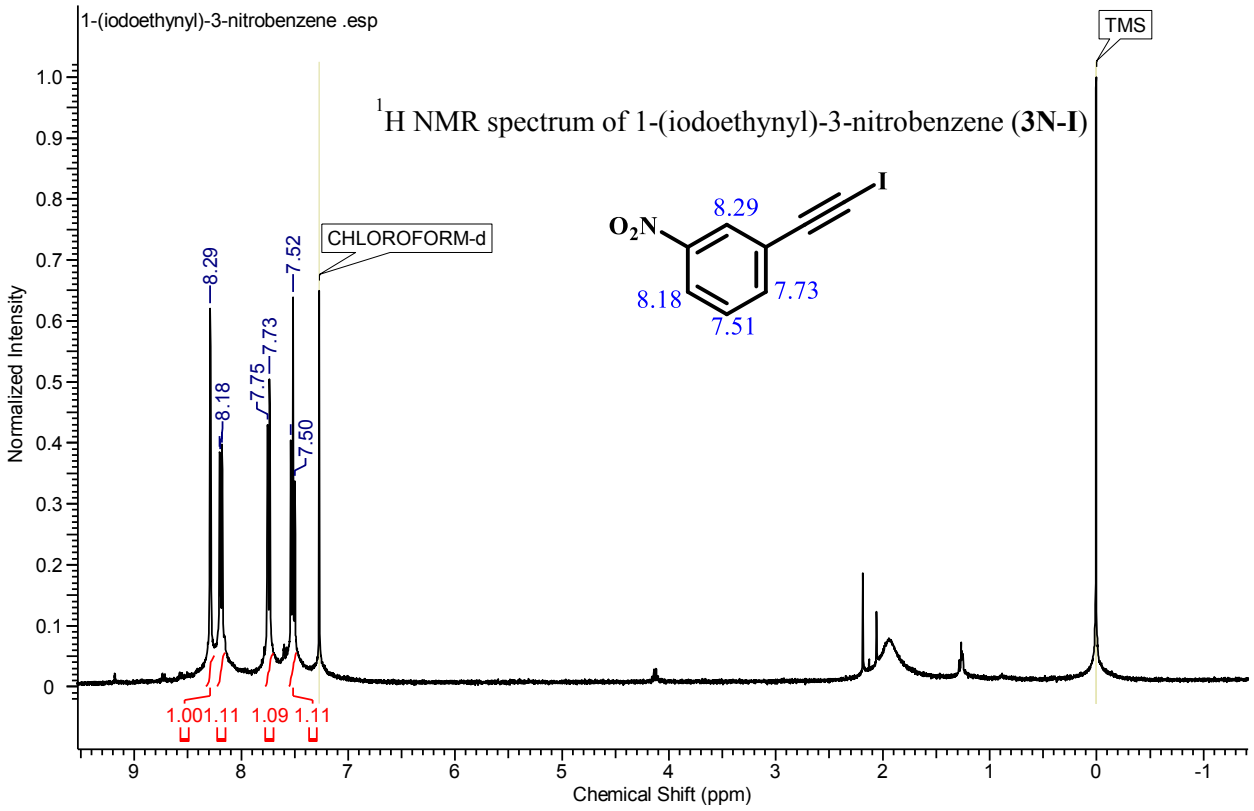

^{1}H NMR spectrum of 1-(iodoethynyl)-3-nitrobenzene (**3N-I**)

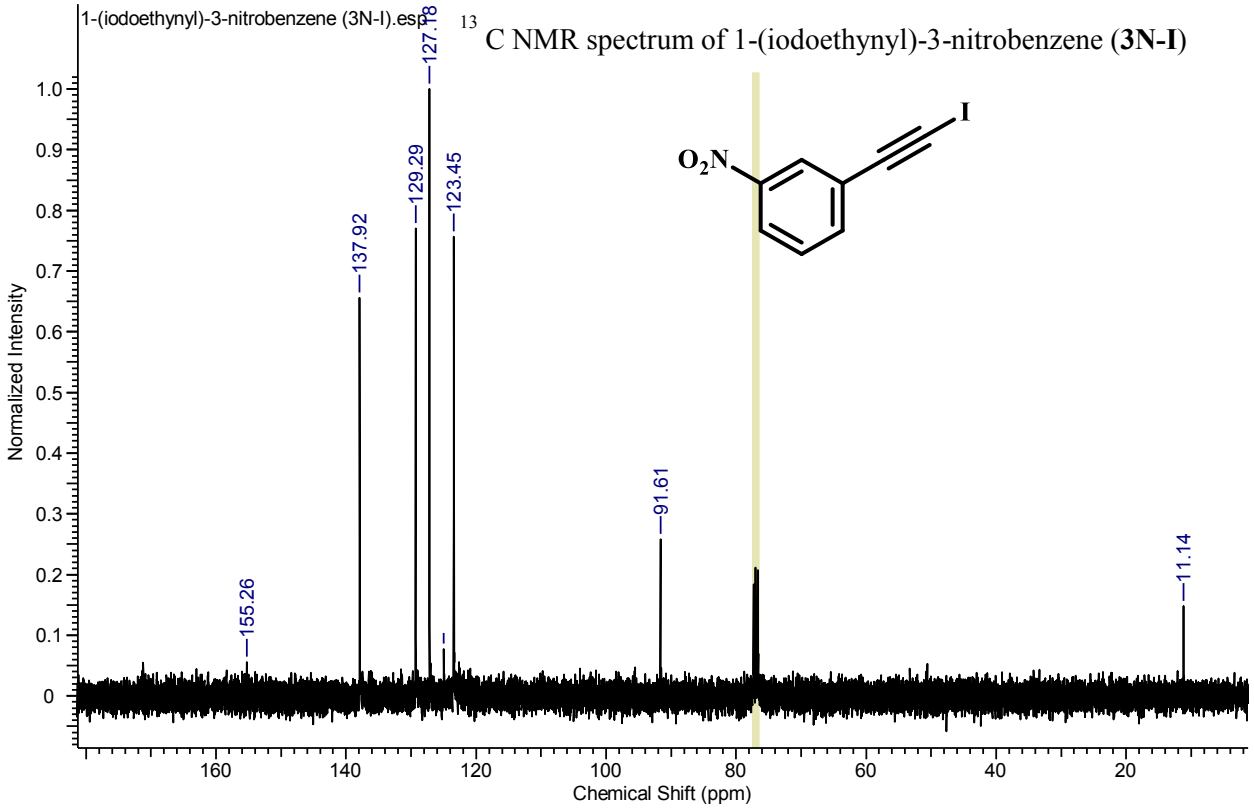

^{13}C NMR spectrum of 1-(iodoethynyl)-3-nitrobenzene (**3N-I**)

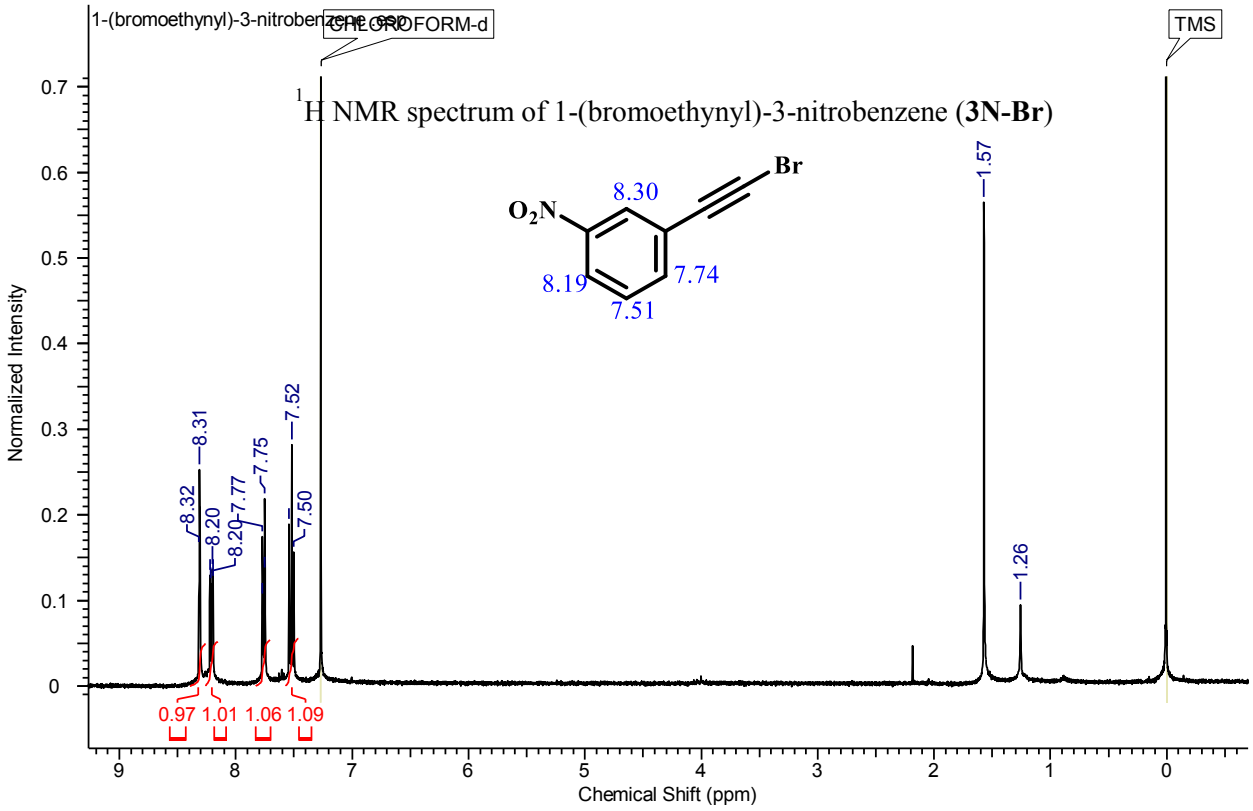

^{1}H NMR spectrum of 1-(bromoethynyl)-3-nitrobenzene (**3N-Br**)

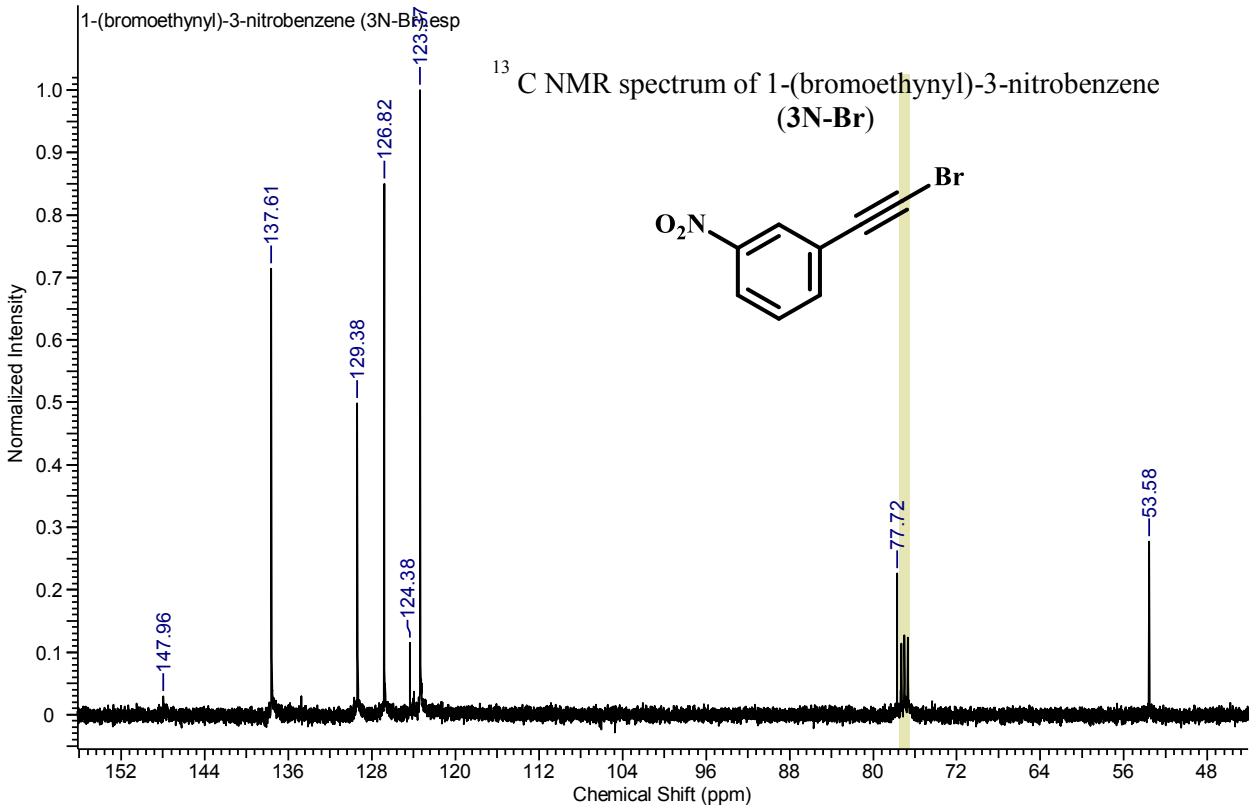

^{13}C NMR spectrum of 1-(bromoethynyl)-3-nitrobenzene (**3N-Br**)

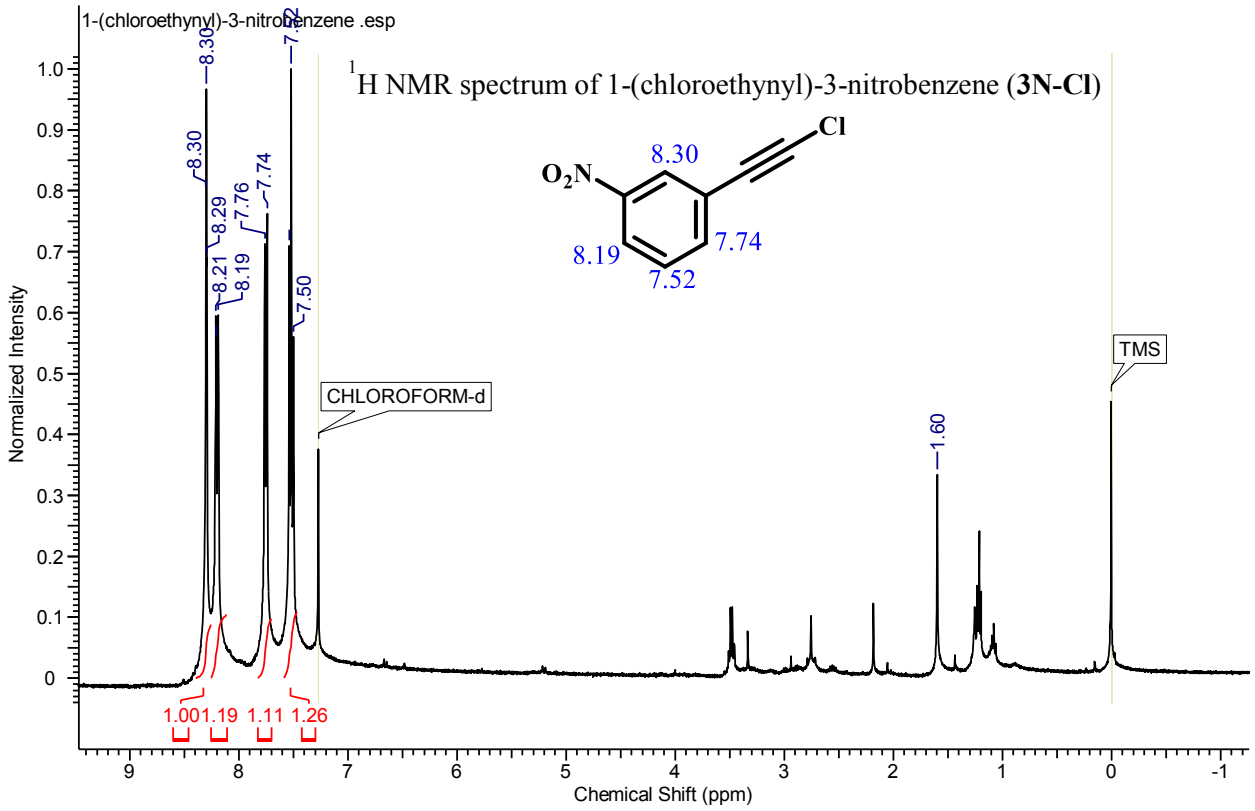
1-(chloroethynyl)-3-nitrobenzene .esp
^{1}H NMR spectrum of 1-(chloroethynyl)-3-nitrobenzene (**3N-Cl**)
Cl
O_2N
8.30
8.19
7.74
7.52
8.30
8.29
8.21
8.19
7.76
7.74
7.52
7.50
CHLOROFORM-d
1.60
TMS
1.00 1.19 1.11 1.26
Normalized Intensity
Chemical Shift (ppm)

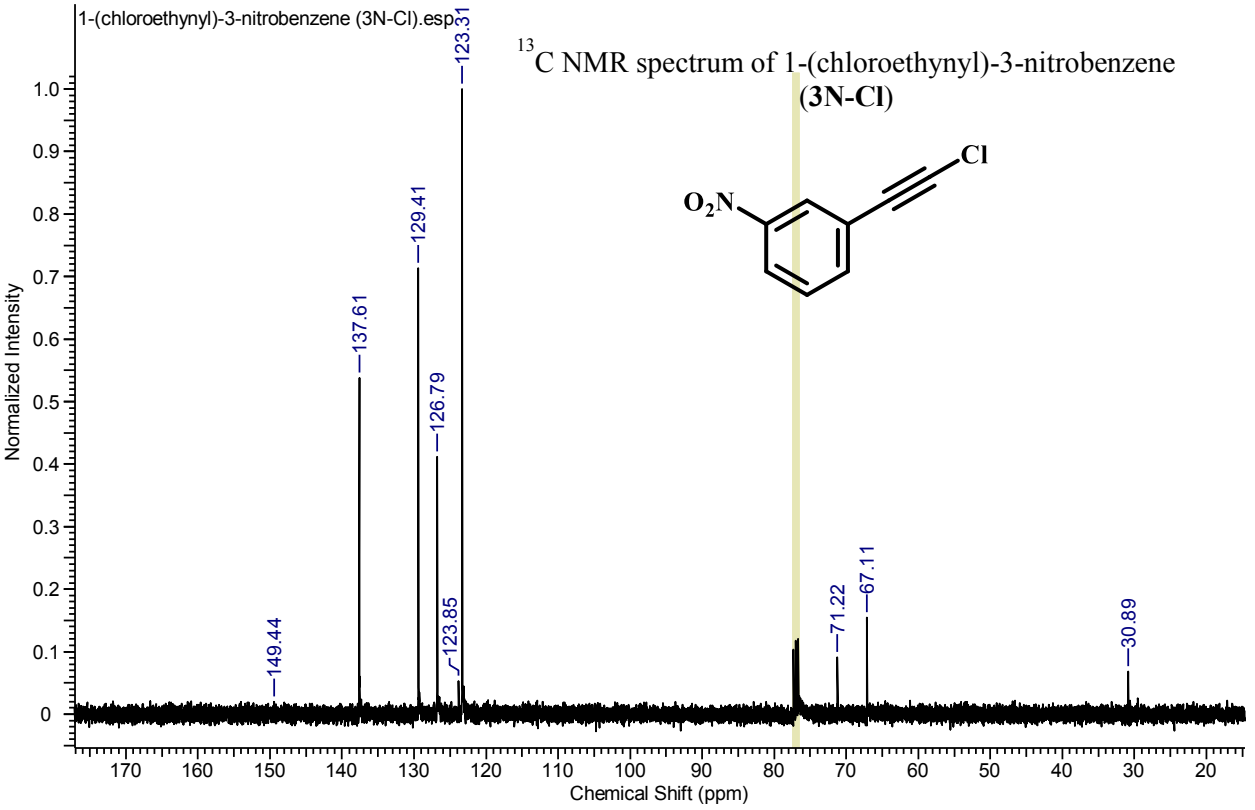
1-(chloroethynyl)-3-nitrobenzene (3N-Cl).esp
^{13}C NMR spectrum of 1-(chloroethynyl)-3-nitrobenzene (**3N-Cl**)
Cl
O_2N
149.44
137.61
129.41
126.79
123.85
123.31
71.22
67.11
30.89
Normalized Intensity
Chemical Shift (ppm)

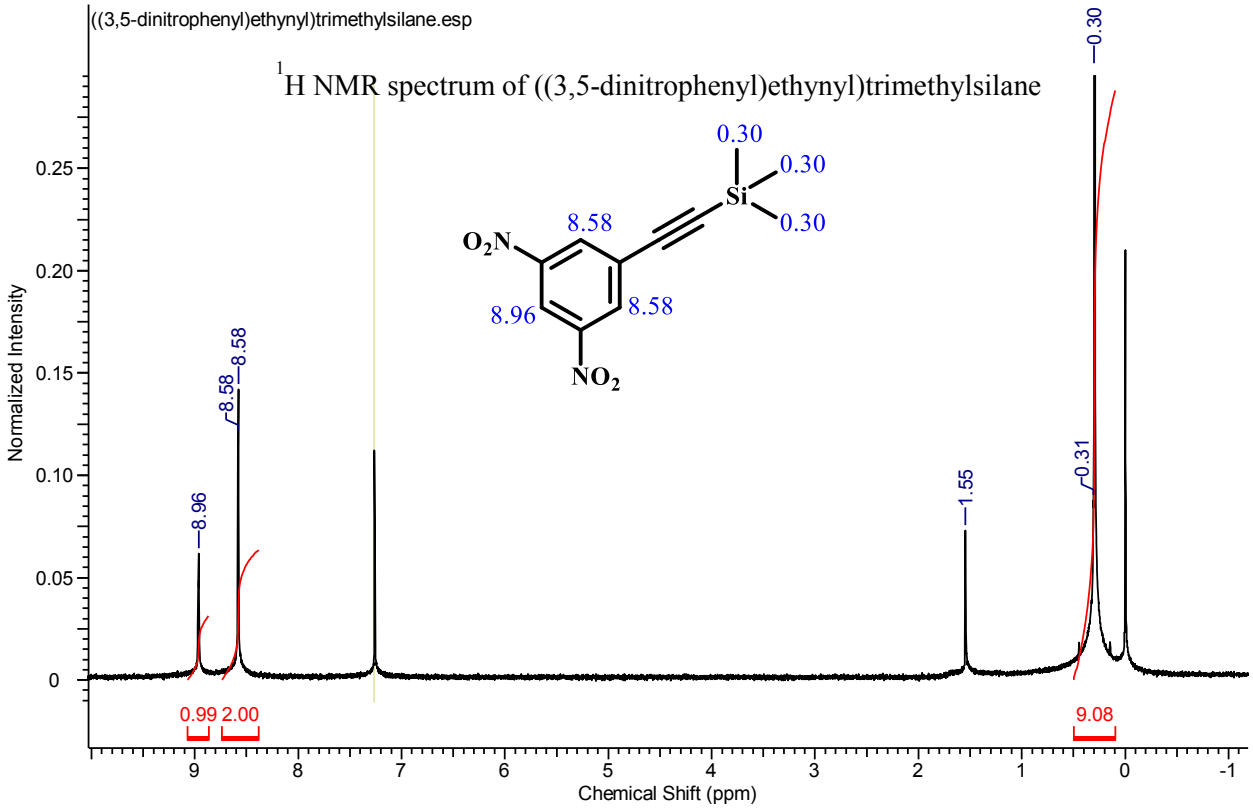
((3,5-dinitrophenyl)ethynyl)trimethylsilane.esp
^{1}H NMR spectrum of ((3,5-dinitrophenyl)ethynyl)trimethylsilane
0.30
0.30
0.30
Si
8.58
O_2N
8.96
8.58
NO_2
Normalized Intensity
Chemical Shift (ppm)
8.96
8.58
8.58
1.55
0.31
0.30
0.99
2.00
9.08

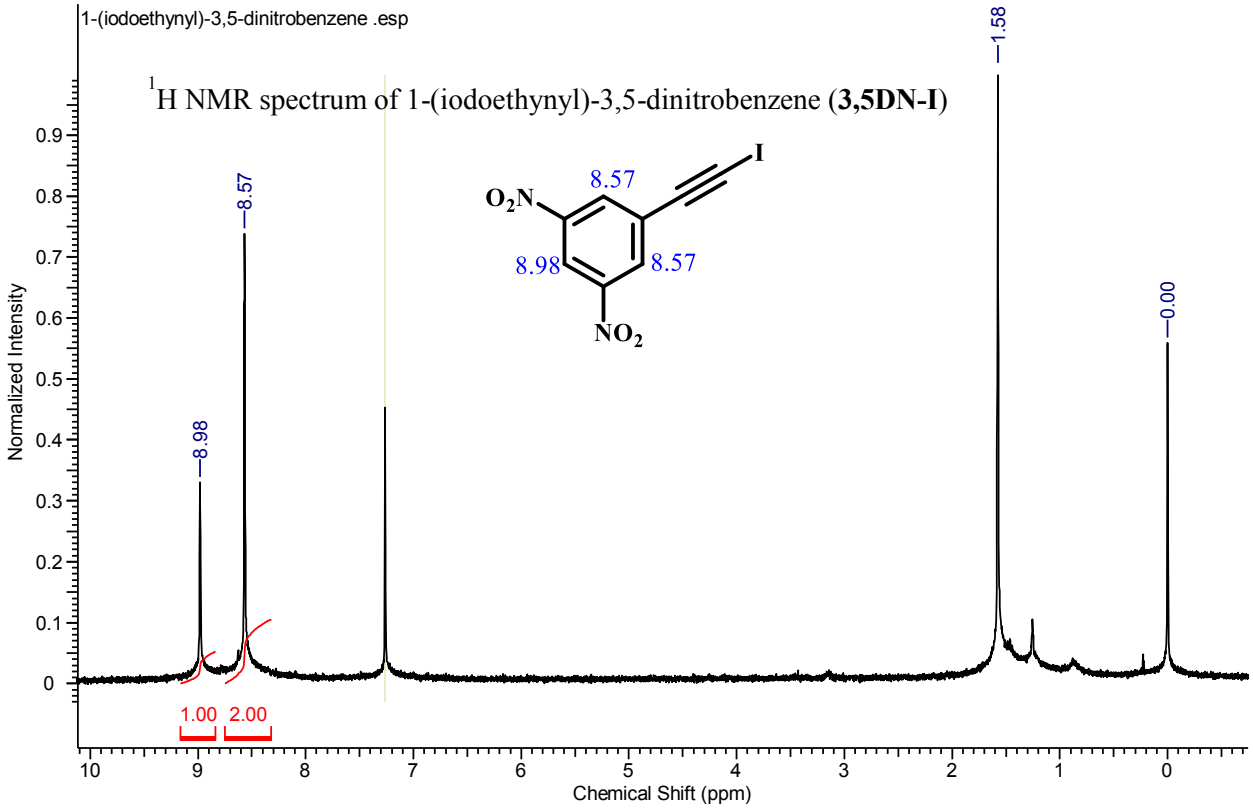
1-(iodoethynyl)-3,5-dinitrobenzene .esp
^{1}H NMR spectrum of 1-(iodoethynyl)-3,5-dinitrobenzene (**3,5DN-I**)
I
8.57
O_2N
8.98
8.57
NO_2
Normalized Intensity
Chemical Shift (ppm)
8.98
8.57
1.58
0.00
1.00
2.00

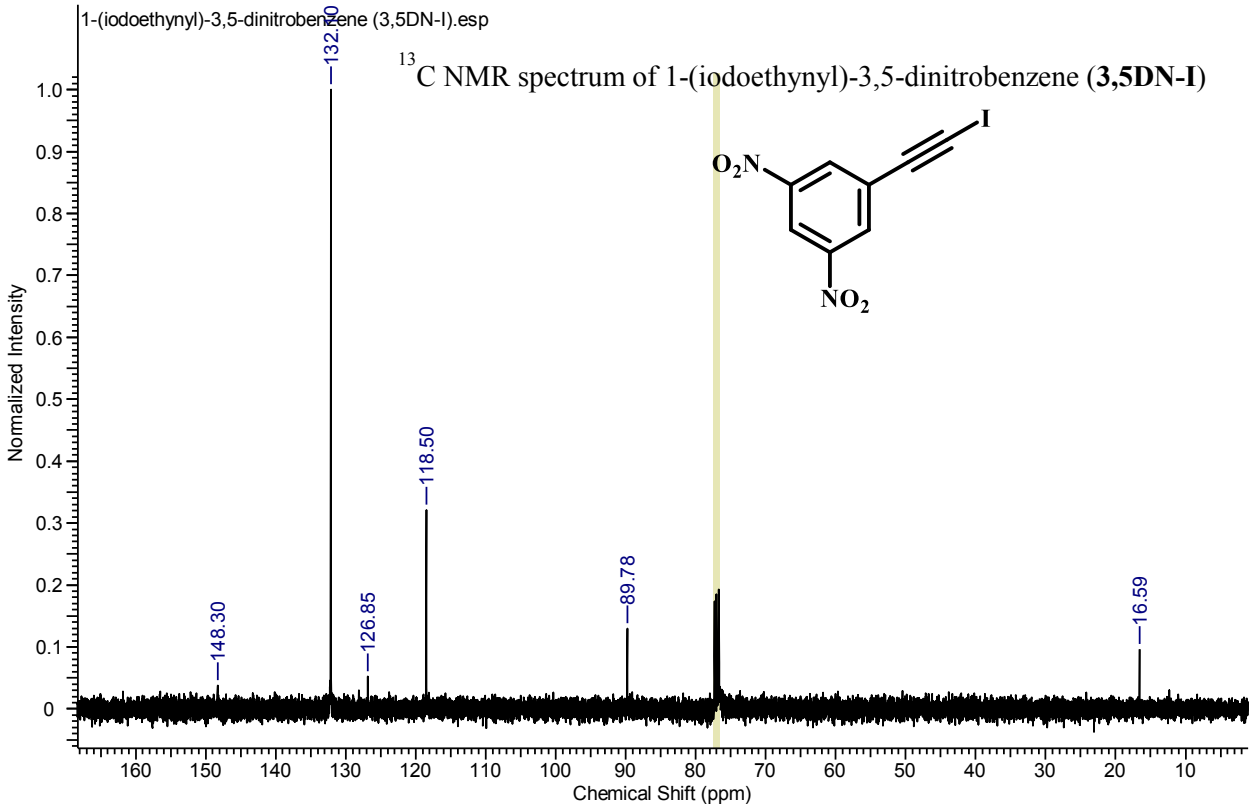

^{13}C NMR spectrum of 1-(iodoethynyl)-3,5-dinitrobenzene (**3,5DN-I**)

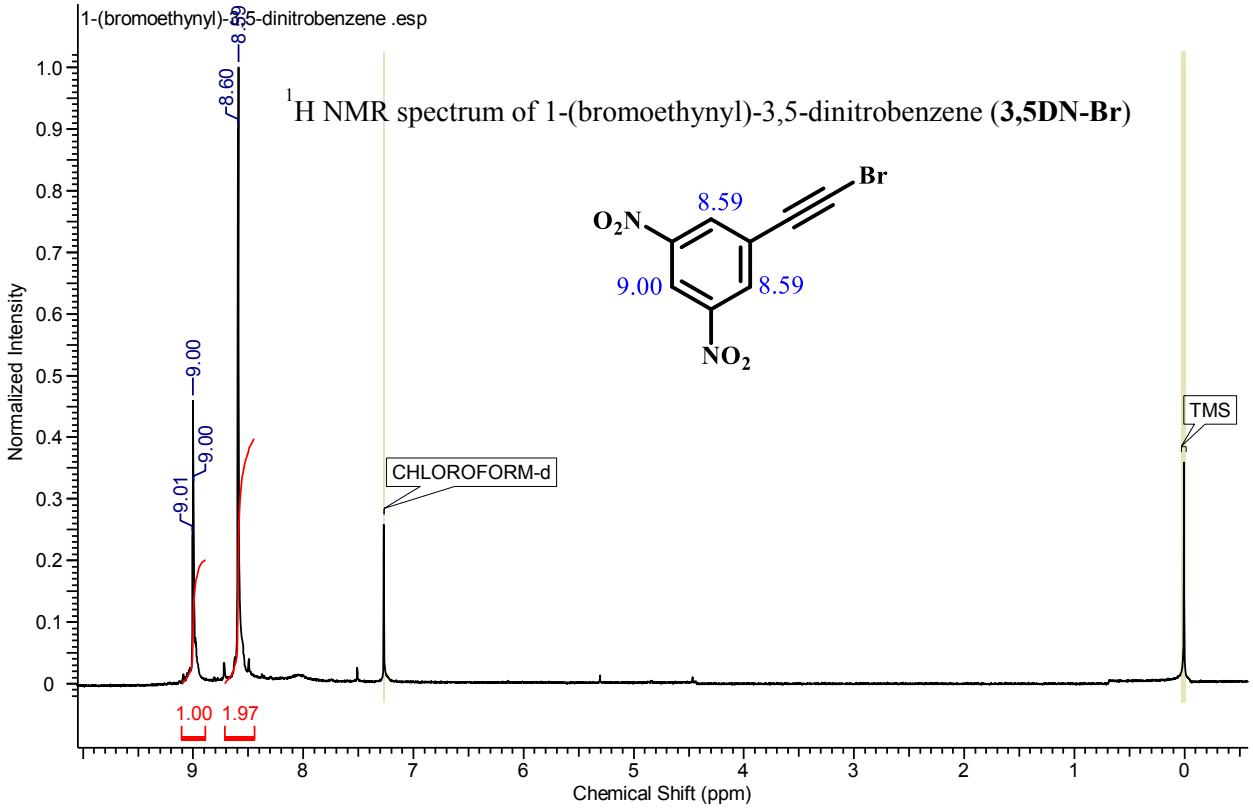

^{1}H NMR spectrum of 1-(bromoethynyl)-3,5-dinitrobenzene (**3,5DN-Br**)

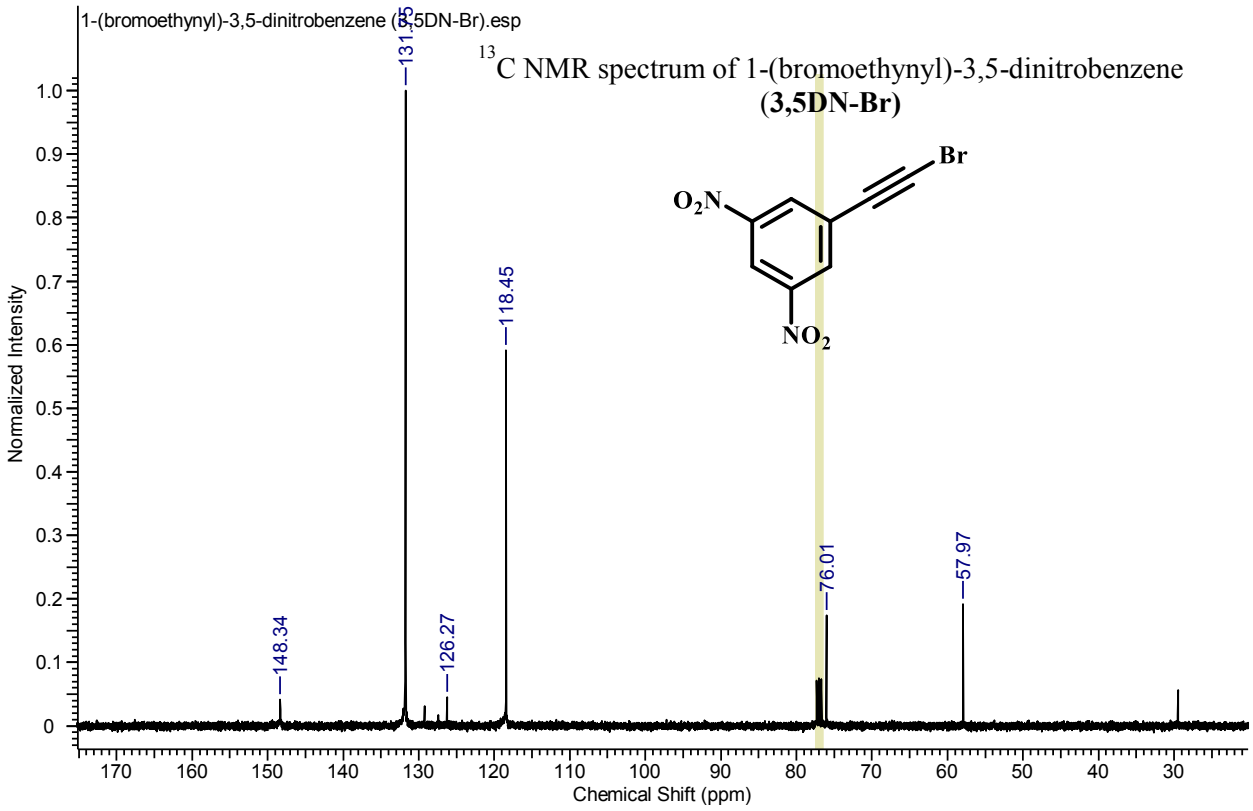

^{13}C NMR spectrum of 1-(bromoethynyl)-3,5-dinitrobenzene **(3,5DN-Br)**

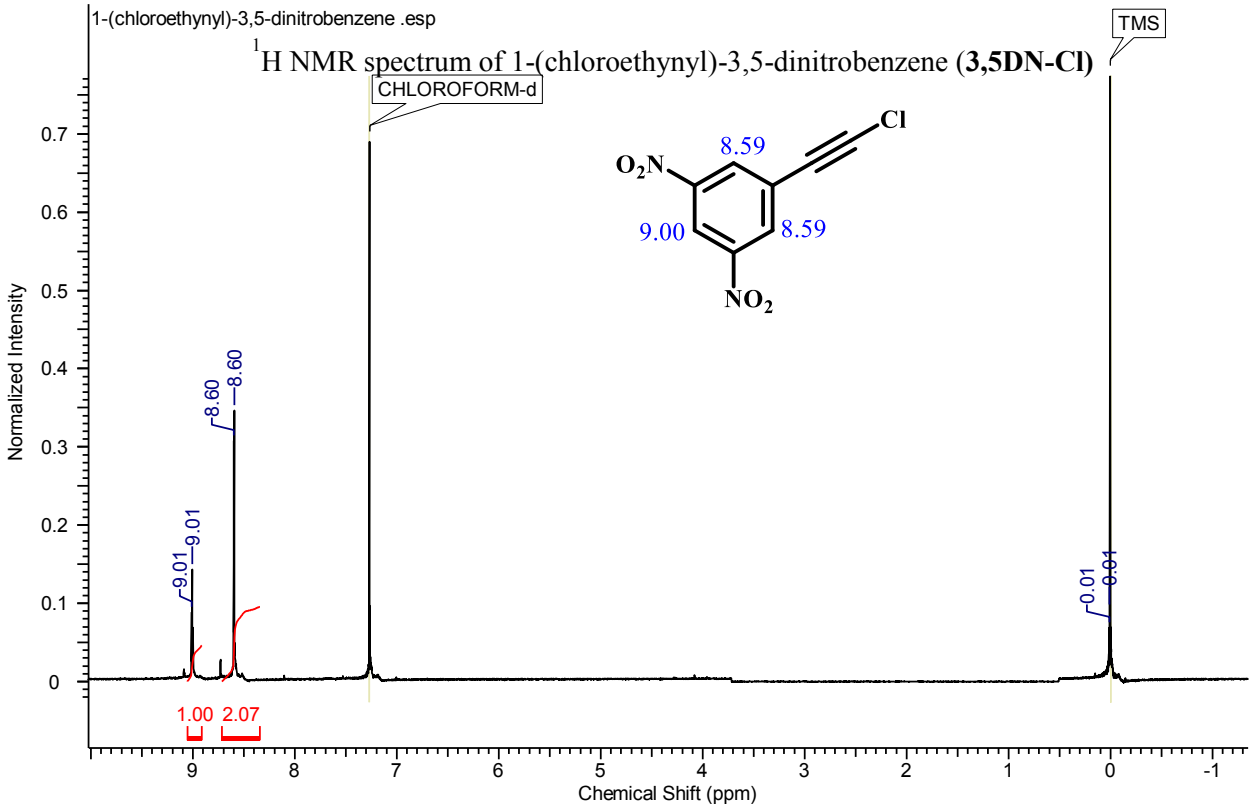

^{1}H NMR spectrum of 1-(chloroethynyl)-3,5-dinitrobenzene **(3,5DN-Cl)**

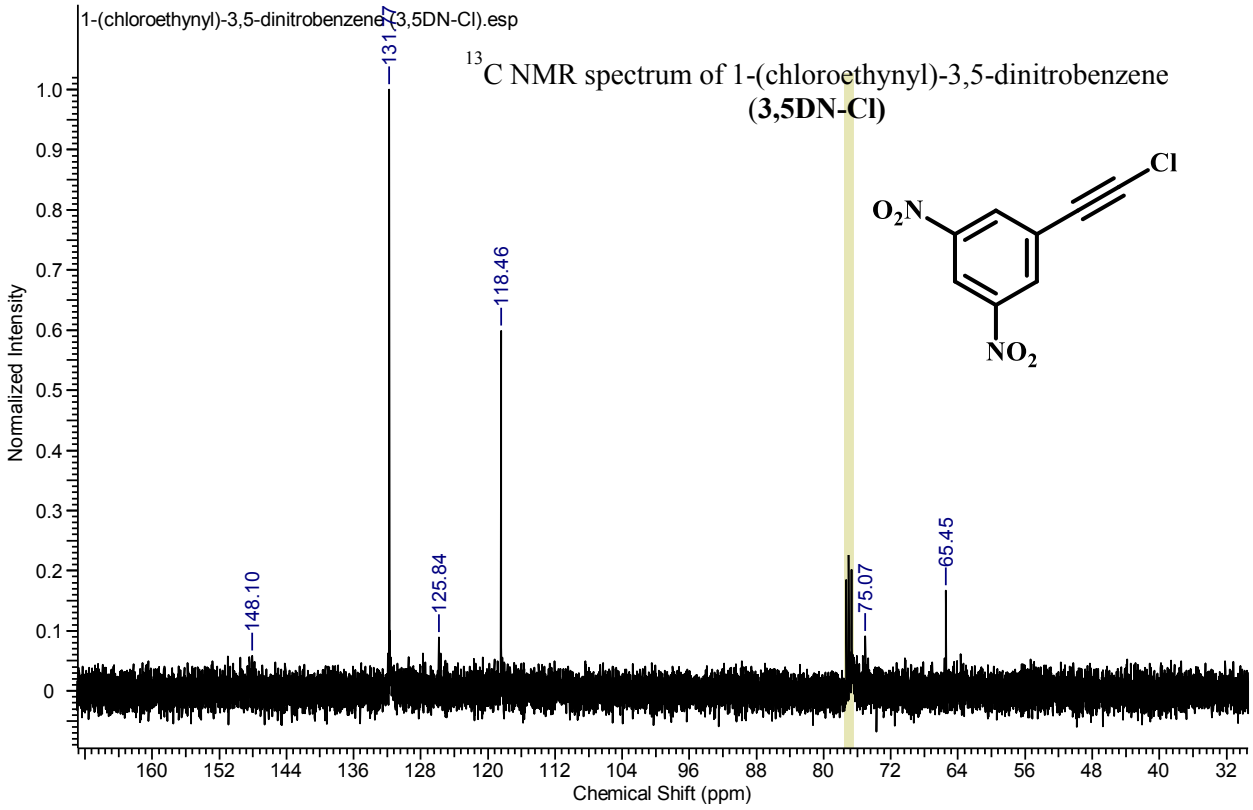
1-(chloroethynyl)-3,5-dinitrobenzene (3,5DN-Cl).esp
131.17
118.46
148.10
125.84
75.07
65.45
Normalized Intensity
Chemical Shift (ppm)
13C NMR spectrum of 1-(chloroethynyl)-3,5-dinitrobenzene
(3,5DN-Cl)
Cl
O2N
NO2

A.5 Chapter 7

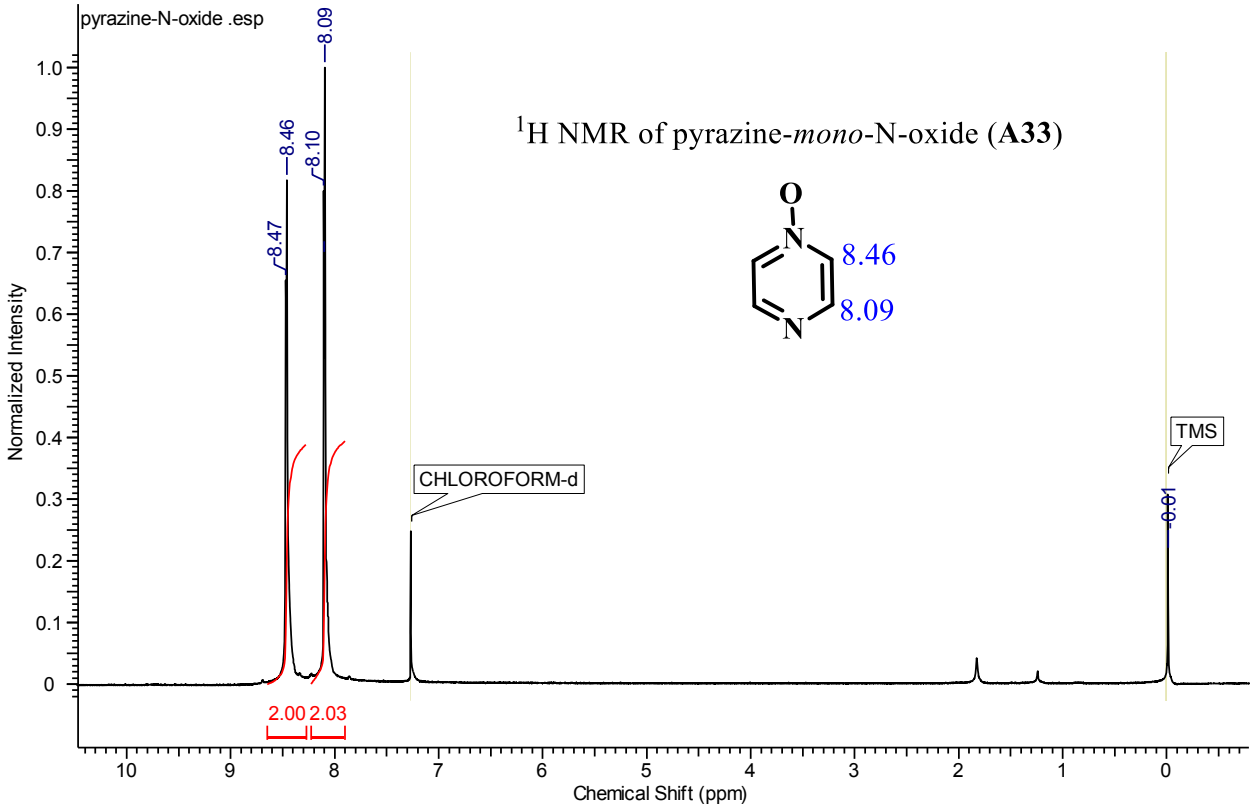
pyrazine-N-oxide .esp
8.09
8.46
8.10
8.47
CHLOROFORM-d
TMS
0.01
2.00 2.03
Normalized Intensity
Chemical Shift (ppm)
1H NMR of pyrazine-mono-N-oxide (A33)
O
N
N
8.46
8.09

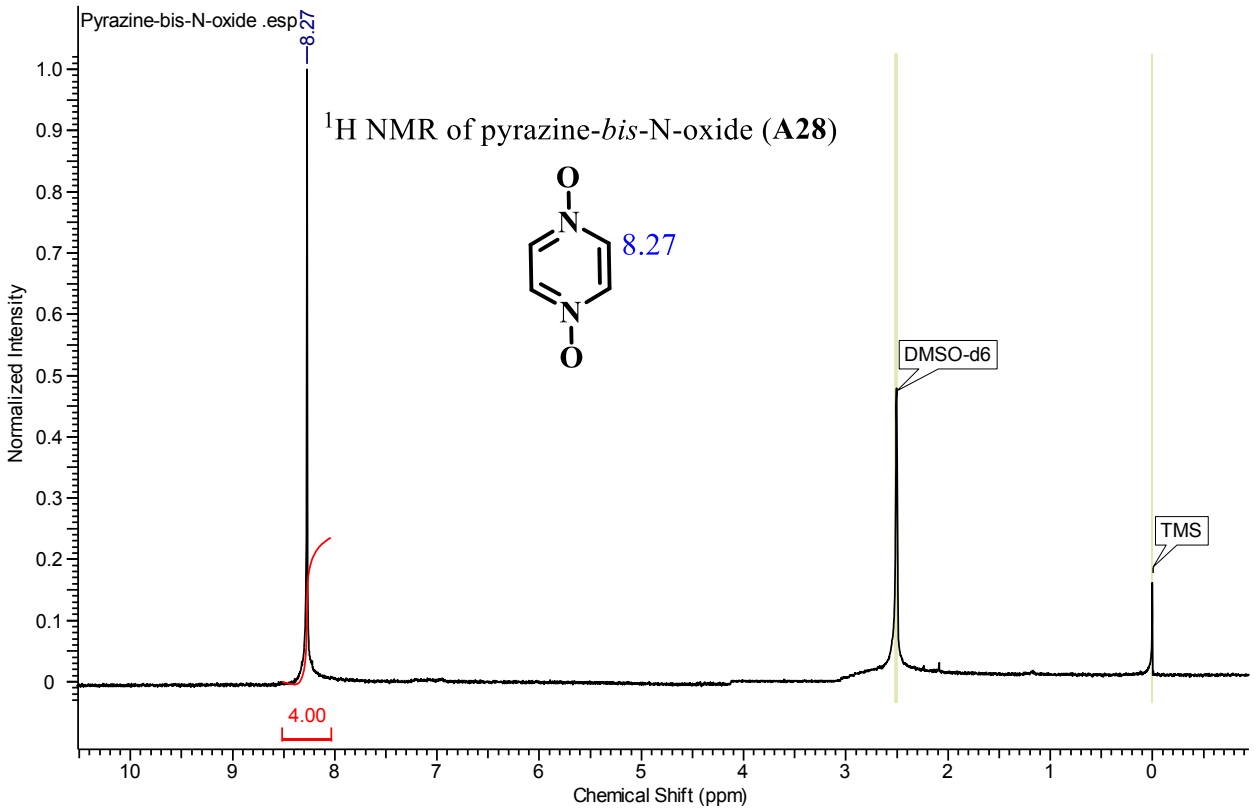
Pyrazine-bis-N-oxide .esp
8.27
^{1}H NMR of pyrazine-*bis*-N-oxide (**A28**)
8.27
DMSO-d6
TMS
4.00
Normalized Intensity
Chemical Shift (ppm)

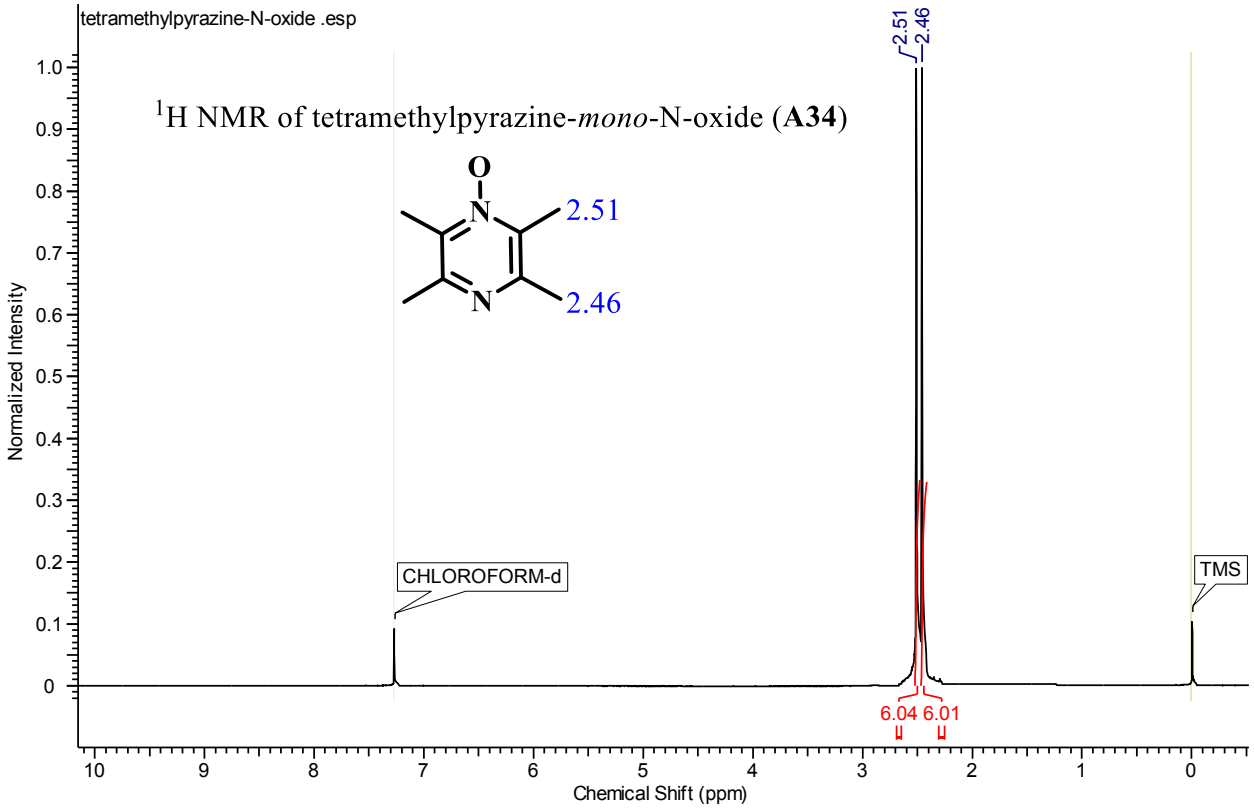
tetramethylpyrazine-N-oxide .esp
2.51
2.46
^{1}H NMR of tetramethylpyrazine-*mono*-N-oxide (**A34**)
2.51
2.46
CHLOROFORM-d
TMS
6.04
6.01
Normalized Intensity
Chemical Shift (ppm)

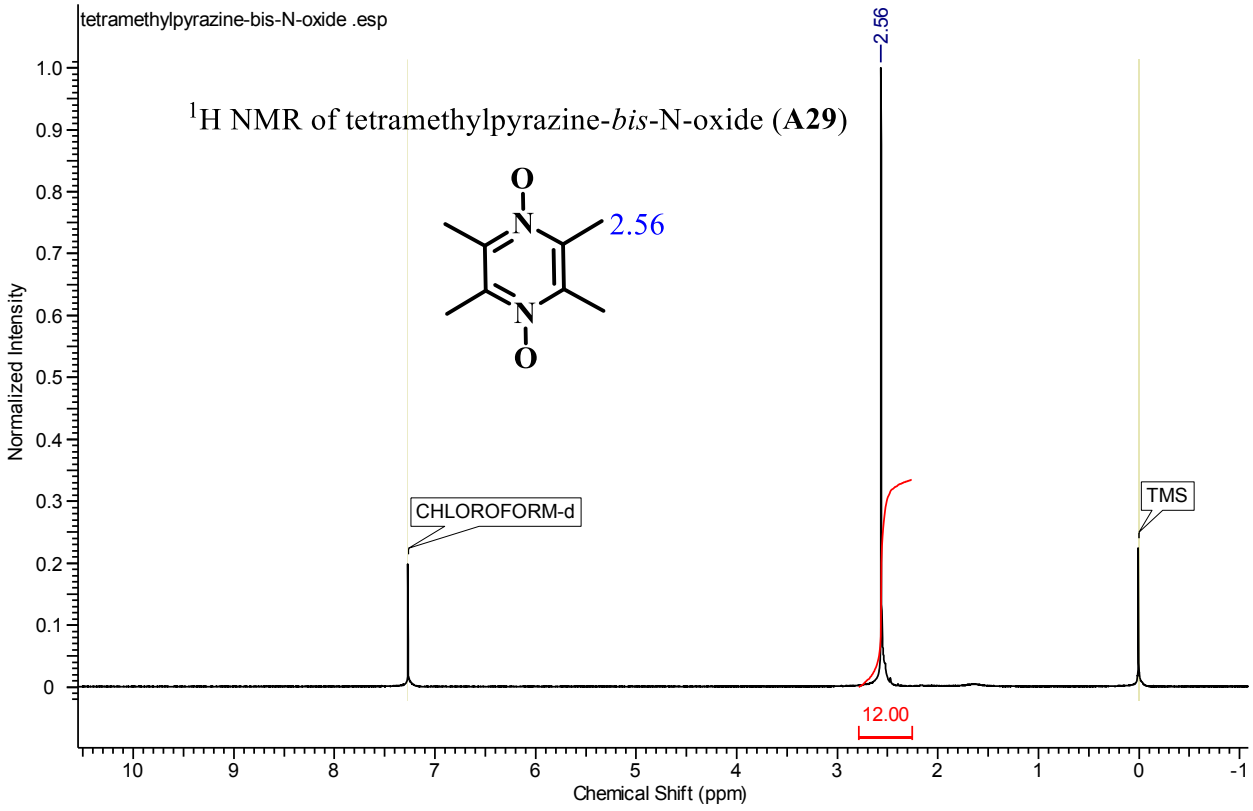
tetramethylpyrazine-bis-N-oxide .esp
2.56
^{1}H NMR of tetramethylpyrazine-*bis*-N-oxide (**A29**)
2.56
CHLOROFORM-d
TMS
12.00
Normalized Intensity
Chemical Shift (ppm)

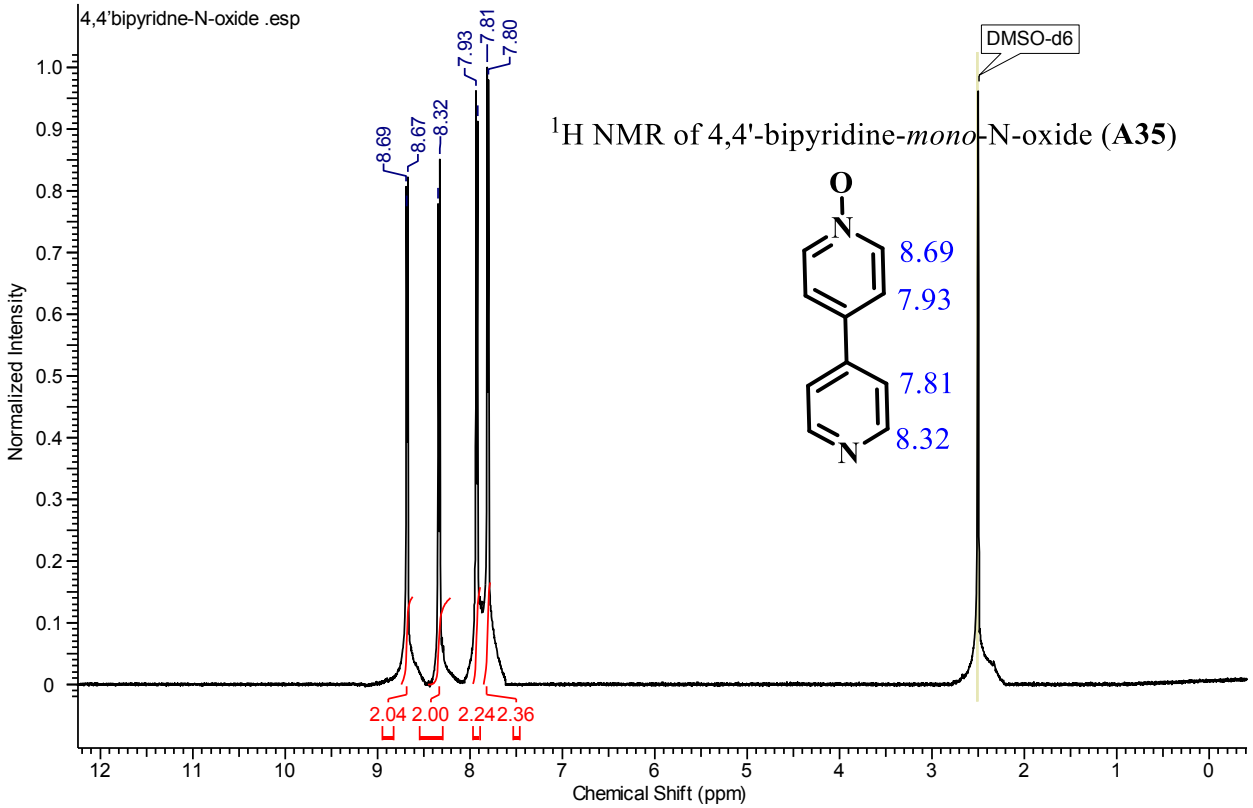
4,4'bipyridne-N-oxide .esp
8.69
8.67
8.32
7.93
7.81
7.80
DMSO-d6
^{1}H NMR of 4,4'-bipyridine-*mono*-N-oxide (**A35**)
8.69
7.93
7.81
8.32
2.04
2.00
2.24
2.36
Normalized Intensity
Chemical Shift (ppm)

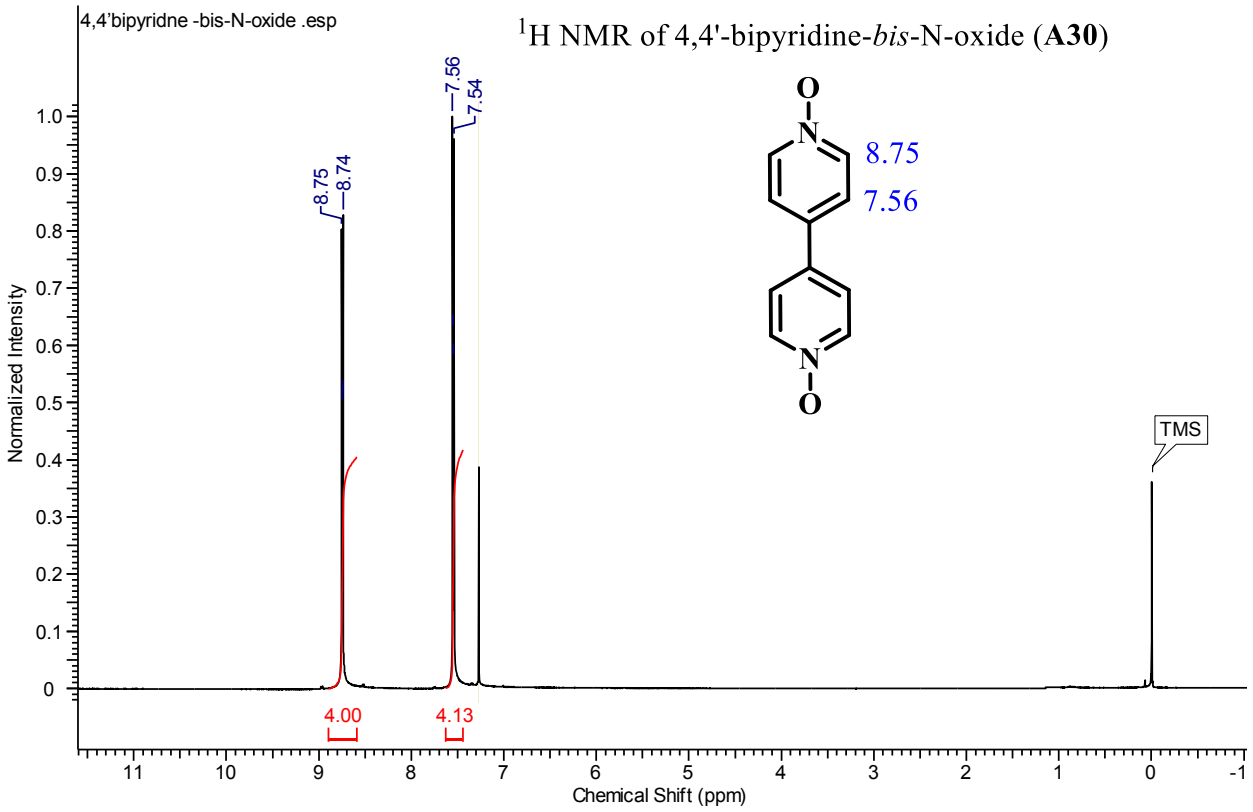
4,4'bipyridne -bis-N-oxide .esp
^{1}H NMR of 4,4'-bipyridine-*bis*-N-oxide (**A30**)
8.75
7.56
8.75
8.74
7.56
7.54
TMS
4.00
4.13
Normalized Intensity
Chemical Shift (ppm)

A.6 Chapter 9

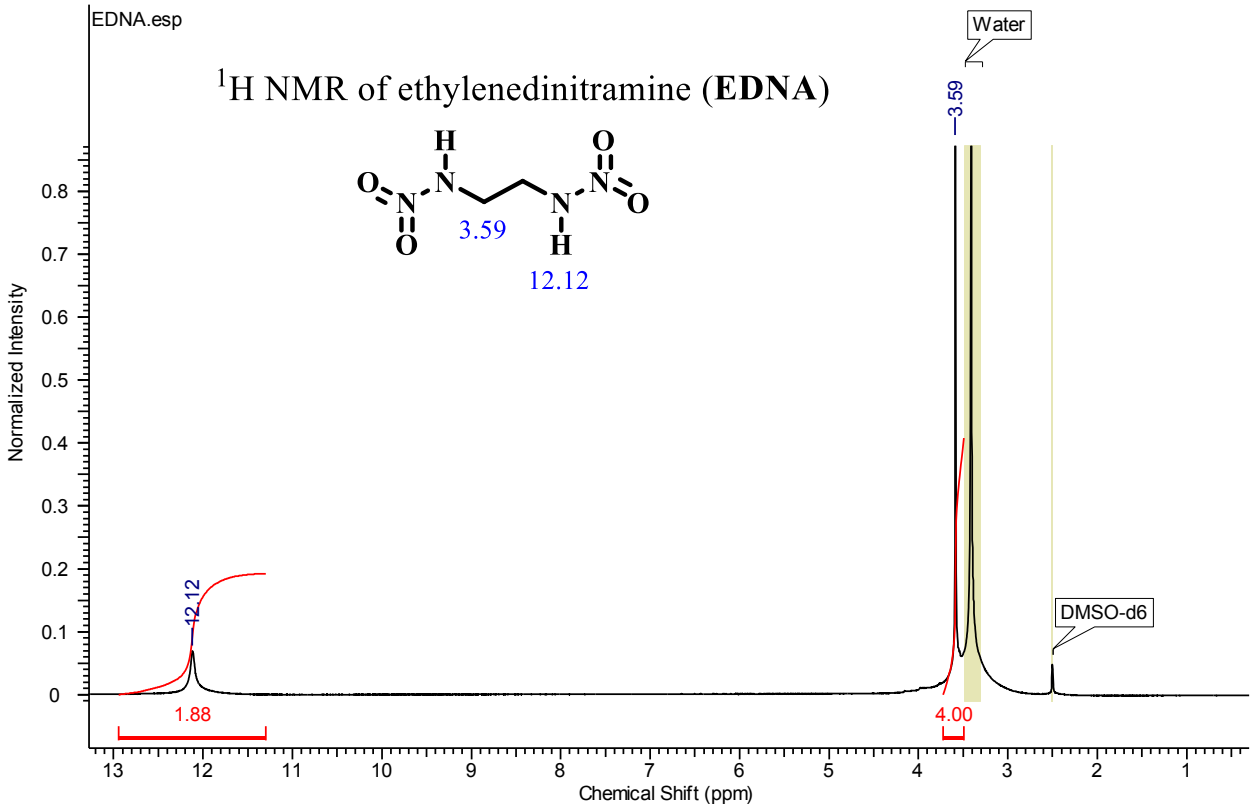
EDNA.esp
^{1}H NMR of ethylenedinitramine (**EDNA**)
3.59
12.12
Water
3.59
12.12
DMSO-d6
1.88
4.00
Normalized Intensity
Chemical Shift (ppm)

Appendix B - **Single crystal X-ray crystallography data**

B.1 Chapter 2

Experimental details

Datasets were collected on a Bruker Kappa APEX II system using CuKα radiation (**A1:Dod**, **A1:Suc**, **A3:Seb**, **A3:Sub**, **A3:Dod**, **A1:Seb**, **A4:Mal**) or a on a Bruker APEX II system using MoKα radiation (**A3:Adi**, **A1:Sub**, **A1:Adi**, **A1:Glu**, **A1:Mal**, **A3:Pim**). Data were collected using APEX2 software.[1] Initial cell constants were found by small widely separated "matrix" runs. Data collection strategies were determined using COSMO.[2] Scan speed and scan widths were chosen based on scattering power and peak rocking curves. All datasets were collected at -153 °C using an Oxford Croystream low-temperature device.

Unit cell constants and orientation matrix were improved by least-squares refinement of reflections thresholded from the entire dataset. Integration was performed with SAINT,[3] using this improved unit cell as a starting point. Precise unit cell constants were calculated in SAINT from the final merged dataset. Lorenz and polarization corrections were applied. Multi-scan absorption corrections were performed with SADABS.[4]

Data were reduced with SHELXTL.[5] The structures were solved in all cases by direct methods without incident. Except as noted, hydrogen atoms were located in idealized positions and were treated with a riding model. All non-hydrogen atoms were assigned anisotropic thermal parameters. Refinements continued to convergence, using the recommended weighting schemes.

In **A1:Dod**, **A1:Suc**, **A3:Adi**, **A1:Sub**, **A1:Adi**, **A3:Seb**, **A3:Sub** and **A3:Dod**; both the amine and the diacid sit on crystallographic inversion centers. Coordinates of the unique carboxylic acid proton were allowed to refine. Crystal structure of **A1:Seb** was a nonmerohedral twin and the data were processed with TWINABS.[6] In this structure both the amine and the diacid

sit on crystallographic inversion centers. Coordinates of the unique carboxylic acid proton were allowed to refine. In **A4:Mal** both the amine and the diacid sit on general positions. Coordinates of the carboxylic acid protons were allowed to refine. In **A1:Glu**, the amine sits on crystallographic inversion centers; the diacid sits on a general position, giving 1 : 2 amine : diacid stoichiometry. Coordinates of the carboxylic acid protons were allowed to refine. In **A1:Mal** both the amine and the diacid sit on general positions. Two orientations for one pyridine moiety (N41-C46) and one acid moiety (C53 / O53 / O54), representing different orientations of the –COOH group, were located in the difference map. Relative populations were allowed to refine. Thermal parameters were pairwise constrained using EADP commands. Geometry of the pyridine rings were restrained using the SAME command. All hydrogen atoms were included in calculated positions and were allowed to ride. In **A3:Pim** the amine sits on crystallographic inversion centers; the diacid sits on a general position, giving 1 : 2 amine : diacid stoichiometry. Coordinates of the carboxylic acid protons were allowed to refine.

Crystallographic data

Code	A1:Suc	A1:Adi	A1:Sub	A1:Seb	A1:Dod	A1:Mal	A1:Glu
Formula moiety	$(C_{18}H_{16}N_6)$ $(C_4H_6O_4)$	$(C_{18}H_{16}N_6)$ $(C_6H_{10}O_4)$	$(C_{18}H_{16}N_6)$ $(C_8H_{14}O_4)$	$(C_{18}H_{16}N_6)$ $(C_{10}H_{18}O_4)$	$(C_{18}H_{16}N_6)$ $(C_{12}H_{22}O_4)$	$(C_{18}H_{16}N_6)$ $(C_3H_4O_4)$	$(C_{18}H_{16}N_6)$ $(C_5H_8O_4)_2$
Empirical formula	$C_{22}H_{22}N_6O_4$	$C_{24}H_{26}N_6O_4$	$C_{26}H_{30}N_6O_4$	$C_{28}H_{34}N_6O_4$	$C_{30}H_{38}N_6O_4$	$C_{21}H_{20}N_6O_4$	$C_{28}H_{32}N_6O_8$
Molecular weight	434.46	462.51	490.56	518.61	546.66	420.43	580.60
Color, Habit	colorless prism	bronze plate	orange plate	orange plate	bronze prism	colourless needle	bronze prism
Crystal system	Triclinic	Triclinic	Triclinic	Triclinic	Triclinic	Monoclinic	Triclinic
Space group, Z	P-1, 1	P-1, 1	P-1, 1	P-1, 1	P-1, 1	P2(1)/c, 4	P-1, 1
a, Å	4.8468(8)	5.5146(11)	5.6196(11)	5.6320(7)	5.6047(8)	14.797(3)	7.6142(11)
b, Å	9.2594(16)	6.8100(14)	6.7825(13)	6.8450(8)	6.8589(10)	4.5097(7)	8.6608(13)
c, Å	12.245(2)	15.254(3)	16.078(3)	17.748(2)	18.879(3)	29.886(5)	11.0348(16)
α, °	69.536(7)	79.288(6)	87.236(4)	93.630(7)	97.644(5)	90.00	102.357(5)
β, °	89.567(7)	85.259(6)	82.669(4)	98.988(7)	91.164(5)	104.056(8)	105.996(5)
γ, °	85.993(7)	75.952(5)	75.451(4)	104.670(7)	104.659(5)	90.00	93.866(5)
Volume, $Å^3$	513.50(15)	545.60(19)	588.22(19)	649.97(13)	694.80(18)	1934.6(6)	677.09(17)
Density, g/cm^3	1.405	1.408	1.385	1.325	1.307	1.444	1.424
Temperature, °K	120(2)	120(2)	120(2)	120(2)	120(2)	120(2)	120(2)

Crystal size, min x mid x max	0.236 x 0.239 x 0.543	0.10 x 0.32 x 0.38	0.12 x 0.30 x 0.36	0.10 x 0.26 x 0.34	0.22 x 0.28 x 0.32	0.08 x 0.10 x 0.36	0.18 x 0.36 x 0.44
X-ray wavelength, Å	1.54178	0.71073	0.71073	1.54178	1.54178	0.71073	0.71073
μ, mm^{-1}	0.827	0.099	0.096	0.737	0.716	0.104	0.106
Absorption corr	multi-scan	multi-scan	multi-scan	multi-scan	multi-scan	multi-scan	multi-scan
Trans min / max	0.645 / 0.753	0.9634 / 0.9902	0.9662 / 0.9886	0.7876 / 0.9299	0.8032 / 0.8584	0.9636 / 0.9918	0.9547 / 0.9811
θ_{min}, °	3.85	3.13	3.10	2.54	2.36	1.42	1.98
θ_{max}, °	67.98	32.02	32.75	68.93	68.24	30.08	32.68
Reflections							
collected	6345	7187	10698	4606	9252	20190	17551
independent	1799	3167	3929	4606	2438	5562	4555
observed	1660	2613	3433	3942	2269	2992	4015
Threshold expression	>2σ (I)	>2σ (I)	>2σ (I)	>2σ (I)	>2σ (I)	>2σ (I)	>2σ (I)
R1 (observed)	0.0507	0.0467	0.0458	0.0550	0.0523	0.0652	0.0422
wR_2 (all)	0.1400	0.1358	0.1329	0.1976	0.1716	0.1937	0.1231
Goodness of fit (all)	1.084	1.099	1.014	1.544	1.472	0.997	0.973
Δρ max / min	0.355 / -0.431	0.414 / -0.223	0.459 / -0.308	0.322 / -0.451	0.311 / -0.242	0.271 / -0.418	0.430 / -0.279
2θ limit	67.50	27.50	30.00	68.93	67.50	30.00	30.00
Completeness to 2θ limit	0.969	0.973	0.971	0.974	0.968	0.981	0.994

Code	A3:Adi	A3:Seb	A3:Sub	A3:Dod	A3:Pim	A4:Mal
Formula moiety	$(C_{18}H_{16}N_6)$ $(C_6H_{10}O_4)$	$(C_{18}H_{16}N_6)$ $(C_{10}H_{18}O_4)$	$(C_{18}H_{16}N_6)$ $(C_8H_{14}O_4)$	$(C_{18}H_{16}N_6)$ $(C_{12}H_{22}O_4)$	$(C_{18}H_{16}N_6)$ $(C_7H_{12}O_4)_2$	$(C_{20}H_{18}N_4)$ $(C_3H_4O_4)$
Empirical formula	$C_{24}H_{26}N_6O_4$	$C_{28}H_{34}N_6O_4$	$C_{26}H_{30}N_6O_4$	$C_{30}H_{38}N_6O_4$	$C_{32}H_{40}N_6O_8$	$C_{23}H_{22}N_4O_4$
Molecular weight	462.51	518.61	490.56	546.66	636.70	418.45
Color, Habit	colourless plate	colourless prism	colourless prism	colourless prism	colourless plate	yellow prism
Crystal system	Triclinic	Triclinic	Triclinic	Triclinic	Triclinic	Monoclinic
Space group, Z	P-1, 1	P-1, 1	P-1, 1	P-1, 1	P-1, 1	P2(1)/n, 4
a, Å	5.0121(5)	5.2731(8)	5.1024(10)	5.2955(8)	4.9161(10)	11.4449(17)
b, Å	7.8964(8)	7.8464(11)	8.0128(15)	7.8185(13)	8.0077(16)	8.9002(15)
c, Å	15.1589(16)	17.163(3)	16.497(3)	18.424(3)	20.828(4)	21.338(3)
α, °	78.403(4)	81.964(6)	99.940(9)	85.042(10)	87.266(11)	90.00
β, °	88.333(4)	88.938(6)	93.967(10)	83.543(10)	88.665(10)	94.855(10)
γ, °	72.636(3)	72.499(6)	108.231(8)	71.912(10)	72.608(9)	90.00
Volume, $Å^3$	560.62(10)	670.38(17)	625.5(2)	719.4(2)	781.5(3)	2165.7(6)
Density, g/cm^3	1.370	1.285	1.302	1.262	1.353	1.283
Temperature, °K	120(2)	120(2)	120(2)	120(2)	120(2)	120(2)
Crystal size, min x mid x max	0.10 x 0.26 x 0.36	0.14 x 0.26 x 0.32	0.20 x 0.28 x 0.32	0.16 x 0.24 x 0.28	0.08 x 0.18 x 0.38	0.14 x 0.18 x 0.24
X-ray wavelength, Å	0.71073	1.54178	1.54178	1.54178	0.71073	1.54178
μ, mm^{-1}	0.096	0.715	0.737	0.692	0.099	0.737
Absorption corr	multi-scan	multi-scan	multi-scan	multi-scan	multi-scan	multi-scan
Trans min / max	0.9662 / 0.9904	0.8035 / 0.9065	0.7983 / 0.8666	0.8299 / 0.8974	0.9635 / 0.9922	0.8430 / 0.9039
θ_{min}, °	1.37	5.21	2.74	2.42	0.98	4.16
θ_{max}, °	32.01	67.90	66.73	68.34	31.05	67.60
Reflections						
collected	12569	11734	9109	11812	21382	10824

independent	3713	2326	2111	2493	4657	3641
observed	3150	2145	1891	2079	2306	2941
Threshold expression	>2σ (I)	>2σ (I)	>2σ (I)	>2σ (I)	>2σ (I)	>2σ (I)
R1 (observed)	0.0434	0.0327	0.0496	0.0446	0.0996	0.0417
wR_2 (all)	0.1317	0.0850	0.1580	0.1335	0.2647	0.1494
Goodness of fit (all)	1.116	1.060	1.176	1.100	1.286	1.102
Δρ max / min	0.325 / -0.289	0.167 / -0.185	0.225 / -0.274	0.226 / -0.329	0.455 / -0.418	0.352 / -0.367
2θ limit	30.00	67.50	66.73	67.50	30.00	66.00
Completeness to 2θ limit	0.994	0.957	0.952	0.954	0.979	0.952

Hydrogen bond geometries

Co-crystal	D–H···A	D–H (Å)	H···A (Å)	D···A (Å)	D–H···N (°)
A1:Suc	O(31)-H(31)···N(21)	0.92(3)	1.74(3)	2.6484(19)	168(2)
A1:Adi	O(31)-H(31)···N(21)	0.91(2)	1.77(2)	2.6765(14)	176.3(16)
A1:Sub	O(31)-H(31)···N(21)	0.961(18)	1.700(18)	2.6604(12)	177.3(15)
A1:Seb	O(31)-H(31)···N(21)	1.05(2)	1.63(2)	2.6857(18)	178.1(17)
A1:Dod	O(31)-H(31)···N(21)	0.89(2)	1.80(2)	2.6890(15)	176.6(19)
A1:Mal	O(51)-H(51)···N(31) O(53A)-H(53A)···N(41A)#1 O(53B)-H(53B)···N(41B)#1	0.84 0.84 0.84	1.73 1.75 1.74	2.551(2) 2.586(4) 2.576(16)	166.5 169.9 178.3
A1:Glu	O(31)-H(31)···N(21) O(35)-H(35)···O(36)#2	0.958(15) 0.851(17)	1.695(15) 1.802(17)	2.6475(10) 2.6520(11)	172.9(14) 177.3(16)
A3:Adi	O(31)-H(31)···N(21)	0.920(17)	1.798(17)	2.7046(12)	167.7(15)
A3:Sub	O(31)-H(31)···N(21)	0.96(3)	1.78(3)	2.722(2)	167(2)
A3:Seb	O(31)-H(31)···N(21)	0.906(17)	1.847(17)	2.7294(13)	163.9(14)
A3:Dod	O(31)-H(31)···N(21)	0.89(3)	1.86(3)	2.727(2)	163(2)
A3:Pim	O(31)-H(31)···N(21) O(37)-H(37)···O(38)#2	0.82(4) 0.83(5)	1.92(4) 1.85(5)	2.677(3) 2.668(3)	155(4) 169(4)
A4:Mal	O(51)-H(51)···N(13) O(53)-H(53)···N(33)#1	0.91(3) 0.97(3)	1.80(3) 1.75(3)	2.702(2) 2.714(2)	172(2) 177(2)

B.2 Chapter 3

Experimental details

Datasets were collected on a Bruker Kappa APEX II system with Cu radiation at 120 K (**A1:D2** and **A2:D7**), a Kappa APEX II system with Mo radiation at 90 K (**A2:D3**[7]), or SMART APEX II system with Mo radiation at 120 K (remaining structures), using APEX2 software.[1] An Oxford Croystream 700 low-temperature device was used to control temperature. MoKα radiation was used. Initial cell constants were found by small widely separated "matrix" runs. Data collection strategies were determined using COSMO.[2] Scan speeds and scan widths were chosen based on scattering power and peak rocking curves.

Unit cell constants and orientation matrices were improved by least-squares refinement of reflections thresholded from the entire dataset. Integrations were performed with SAINT,[3] using these improved unit cells as a starting point. Precise unit cell constants were calculated in SAINT from the final merged datasets. Lorenz and polarization corrections were applied. Absorption corrections was applied using SADABS.[4]

Datasets were reduced with SHELXTL.[5] The structures were solved by direct methods without incident. Coordinates for all carboxylic acid and phenol hydrogen atoms were allowed to refine. All other hydrogens were assigned to idealized positions and were allowed to ride. Isotropic thermal parameters for the hydrogen atoms were constrained to be 1.5x (methyl) / 1.2x (all other) that of the connected atom.

Crystallographic data

	A1:D1	A1:D2	A1:D3	A1:D4	A2:D2	A2:D3
Formula moiety	$(C_{18}H_{16}N_6)(C_2F_4I_2)$	$(C_{18}H_{16}N_6)(C_4F_8I_2)$	$(C_{18}H_{16}N_6)(C_8F_{16}I_2)_2$	$(C_{18}H_{16}N_6)(C_4F_8I_2)$	$(C_{18}H_{16}N_6)(C_6F_{12}I_2)_2$	$C_{18}H_{16}N_6,C_6F_{12}I_2$
Empirical formula	$C_{20}H_{16}F_4I_2N_6$	$C_{22}H_{16}F_8I_2N_6$	$C_{34}H_{16}F_{32}I_4N_6$	$C_{22}H_{16}F_8I_2N_6$	$C_{30}H_{16}F_{24}I_4N_6$	$C_{24}H_{16}F_{12}I_2N_6$
Molecular weight	670.19	770.21	1624.13	770.21	1424.09	870.23
Color, Habit	Colourless prism	Colourless plate	Colourless plate	Colourless plate	Bronze prism	Colorless block
Crystal system	Triclinic	Triclinic	Triclinic	Triclinic	Triclinic	Triclinic
Space group, Z	P-1, 1	P-1, 2	P-1, 1	P-1, 1	P-1, 1	P-1, 2
a, Å	5.7868(3)	4.9080(5)	5.4392(4)	5.6725(9)	5.5456(8)	5.8360(4)
b, Å	7.7496(4)	9.1160(8)	12.5586(10)	7.8185(12)	12.3595(17)	13.0345(9)
c, Å	13.2037(8)	29.031(3)	17.0838(13)	14.983(2)	14.772(2)	18.9742(13)
α, °	97.3990(16)	81.699(5)	105.585(3)	89.405(7)	100.144(4)	77.126(3)
β, °	95.6153(15)	88.168(6)	93.762(2)	85.612(6)	94.600(4)	88.717(3)
γ, °	104.7924(16)	77.390(6)	90.837(2)	74.823(6)	92.321(4)	79.610(3)
Volume, Å^3	562.43(5)	1254.3(2)	1121.01(15)	639.44(17)	991.9(2)	1383.76(16)
X-ray wavelength	0.71073	1.54178	0.71073	0.71073	0.71073	0.71073
μ, mm^{-1}	2.849	20.476	2.951	2.542	3.289	2.382
Temperature, °K	120	120	120	120	120	90
Crystal size, mm x mm x mm	0.16 x 0.28 x 0.32	0.26 x 0.22 x 0.06	0.24 x 0.18 x 0.06	0.26 x 0.16 x 0.08	0.42 x 0.34 x 0.18	0.10 x 0.08 x 0.05
Absorption corr	multi-scan	multi-scan	multi-scan	multi-scan	multi-scan	multi-scan
Trans min / max	0.4625 / 0.6585	0.076 / 0.373	0.538 / 0.843	0.558 / 0.823	0.339 / 0.589	0.797 / 0.890
θ min / max, °	2.75/32.64	5.04 / 68.59	1.68 / 31.50	2.70 / 32.56	1.68 / 33.72	3.02 / 27.50
Reflections						
collected	11124	15481	20969	12918	31031	14199
independent	3718	4324	6899	3936	7589	5807
observed	3480	3846	5661	3534	6978	4256
Threshold expression	>2σ (I)	>2σ (I)	>2σ (I)	>2σ (I)	>2σ (I)	>2σ (I)
R_1 (observed)	0.0245	0.0530	0.0412	0.0312	0.0289	0.0384
***w*R_2 (all)**	0.0599	0.1363	0.1019	0.0846	0.0790	0.0760
S	1.063	1.130	1.010	1.043	1.018	1.026
Δρ max / min	1.088 / -0.565	1.674 / -1.421	2.493 / -1.168	1.369 / -1.402	1.834 / -1.271	0.891 / -0.943

2θ limit	30.00	67.50	30.00	27.50	30.00	25.00
Completeness to 2θ limit	0.992	0.954	0.962	0.979	0.996	0.978

Code	**A3:D9**	**A3:D10**	**A2:D7**	**A2:D9**	**A2:D10**
Formula moiety	$(C_{18}H_{16}N_6)(C_6F_3I_3)$	$(C_{18}H_{16}N_6)(C_{12}F_8I_2)_2$	$(C_{18}H_{16}N_6)(C_6F_4I_2)_2$	$(C_{18}H_{16}N_6)(C_6F_3I_3)_2$	$(C_{18}H_{16}N_6)(C_{12}F_8I_2)_2$
Empirical formula	$C_{24}H_{16}F_3I_3N_6$	$C_{42}H_{16}F_{16}I_4N_6$	$C_{30}H_{16}F_8I_4N_6$	$C_{30}H_{16}F_6I_6N_6$	$C_{42}H_{16}F_{16}I_4N_6$
Molecular weight	826.13	1416.21	1120.09	1335.89	1416.21
Color, Habit	colourless prism	colourless plate	colourless plate	colourless prism	colourless plate
Crystal system	Monoclinic	Triclinic	Triclinic	Triclinic	Triclinic
Space group, Z	C2/c, 4	P-1, 1	P-1, 1	P-1, 2	P-1, 1
crystal size, mm x mm x mm	0.34 x 0.16 x 0.08	0.26 x 0.24x 0.12	0.22 x 0.14 x 0.04	0.32 x 0.18 x 0.08	0.36 x 0.28 x 0.12
a, Å	4.4155(2)	8.4474(5)	8.1124(6)	9.0099(6)	8.1127(10)
b, Å	17.6583(9)	8.6272(5)	8.9038(6)	14.1693(9)	8.4048(10)
c, Å	32.0389(16)	14.2758(8)	12.4514(9)	15.3092(10)	15.8930(19)
α, °	90.00	88.512(2)	108.524(3)	103.421(2)	84.449(3)
β, °	90.4570(10)	88.180(2)	102.920(3)	103.049(2)	79.163(3)
γ, °	90.00	89.813(2)	95.389(3)	102.874(2)	83.723(3)
Volume, Å^3	2498.0(2)	1039.50(10)	817.85(10)	1772.1(2)	1054.7(2)
X-ray wavelength	0.71073	0.71073	1.54178	0.71073	0.71073
μ, mm^{-1}	3.803	3.112	30.633	5.323	3.068
trans min / max	0.358 / 0.751	0.498 / 0.706	0.158 / 0.468	0.281 / 0.675	0.405 / 0.710
Reflections					
collected	13344	23597	10389	41275	14229
independent	4435	6107	2824	12220	7012
observed	4224	5718	2574	11263	6298
Threshold expression	>2σ (I)	>2σ (I)	>2σ (I)	>2σ (I)	>2σ (I)
R1 (observed)	0.0334	0.0192	0.0434	0.0253	0.0245
wR2 (all)	0.0834	0.0543	0.1218	0.0513	0.0626
S	1.074	0.981	1.022	1.124	1.053

Code	**A2:D8**	**A1:D7**	**A1:D8**	**A1:D10**	**A4:D9**
Formula moiety	$(C_{18}H_{16}N_6)(C_6F_4I_2)$	$(C_{18}H_{16}N_6)(C_6F_4I_2)_2$	$(C_{18}H_{16}N_6)(C_6F_4I_2)$	$(C_{18}H_{16}N_6)(C_{12}F_8I_2)_2$	$(C_{20}H_{18}N_4)(C_6F_3I_3)$
Empirical formula	$C_{24}H_{16}F_4I_2N_6$	$C_{30}H_{16}F_8I_4N_6$	$C_{24}H_{16}F_4I_2N_6$	$C_{42}H_{16}F_{16}I_4N_6$	$C_{26}H_{18}F_3I_3N_4$
Molecular weight	718.23	1120.09	718.23	1416.21	824.14
Color, Habit	colourless plate	colourless prism	colourless plate	colourless prism	colourless plate
Crystal system	Triclinic	Monoclinic	Triclinic	Triclinic	Triclinic
Space group, Z	P-1, 1	$P2_1/c$, 2	P-1, 1	P-1, 1	P-1, 4
crystal size, mm x mm x mm	0.34 x 0.28 x 0.06	0.36 x 0.20 x 0.14	0.34 x 0.28 x 0.14	0.40 x 0.26 x 0.22	0.32 x 0.24 x 0.08
a, Å	5.8829(3)	13.069(4)	5.1265(5)	5.2777(4)	11.3637(12)
b, Å	9.7141(5)	4.4363(12)	9.8466(10)	14.2810(11)	13.0207(15)
c, Å	10.8695(6)	28.718(8)	12.5775(13)	14.3038(11)	19.240(2)
α, °	91.555(2)	90.00	76.972(3)	84.605(3)	99.718(3)
β, °	100.9460(10)	101.630(8)	86.963(2)	82.149(2)	91.134(3)
γ, °	107.2690(10)	90.00	75.742(2)	83.415(2)	109.709(3)
Volume, Å^3	580.05(5)	1630.9(8)	599.50(10)	1057.57(14)	2632.5(5)
X-ray wavelength	0.71073	0.71073	0.71073	0.71073	0.71073
μ, mm^{-1}	2.770	3.900	2.681	3.059	3.606
trans min / max	0.453 / 0.851	0.334 / 0.611	0.463 / 0.705	0.374 / 0.553	0.392 / 0.761
Reflections					
collected	13635	23399	11962	27574	33527
independent	3870	5568	4046	8021	33527
observed	3735	4978	3831	7600	28115
Threshold expression	>2σ (I)	>2σ (I)	>2σ (I)	>2σ (I)	>2σ (I)
R1 (observed)	0.0180	0.0231	0.0190	0.0206	0.0665
wR2 (all)	0.0501	0.0569	0.0525	0.0566	0.1900
S	0.934	1.026	0.984	0.981	1.049

Halogen bond geometries

Co-crystal	C-I···N	N···I (Å)	N···I-C (^{0})
A1:D1	C(31)-I(1)···N(21)	2.8175(18)	175.63(7)
A1:D2	C(31)-I(1)···N(11)	2.786(2)	178.49(10)
A1:D3	C(31)-I(1)···N(11)	2.8029(18)	172.54(8)
A1:D4	C(31)-I(1)···N(21)	2.789(3)	173.13(12)
A1:D7	C(31)-I(1)···N(21) C(32)-I(2)···I(1)	2.7777(18) 3.8424(7)	177.06(6) 173.59(5)
A1:D8	C(31)-I(1)···N(11)	2.7913(14)	175.98(5)
A1:D10	C(31)-I(1)···N(21)	2.7747(13)	173.45(5)
A2:D2	C(31)-I(1)···N(211)	2.812(7)	174.5(3)
A2:D3	C(1)-I(1)···N(1) C(21)-N(6)···I(2)	2.802(4) 3.150(4)	176.54(15) 144.0(3)
A2:D7	C(31)-I(1)···N(21) C(32)-I(2)···N(21)	2.848(5) 3.255(5)	174.39(19) 165.16(18)
A2:D8	C(31)-I(1)···N(21)	2.8598(13)	175.13(5)
A2:D9	C(312)-I(42)···N(212) C(311)-I(11)···N(211) C(332)-I(52)···N(132)	2.757(2) 2.830(2) 3.123(2)	176.06(8) 176.70(8) 164.81(7)
A2:D10	C(31)-I(1)···N(21) C(41)-I(2)···N(13)	2.824(2) 3.1345(19)	175.93(7) 166.07(7)
A3:D9	C(33)-I(2)···N(21)	2.887(3)	178.09(10)
A3:D10	C(31)-I(1)···N(21) C(41)-I(2)···N(13)#2	2.8813(16) 3.3015(17)	175.87(6) 164.27(6)
A4:D9	C(511)-I(11)···N(131) C(512)-I(42)···N(132)	2.897(4) 3.028(4)	174.13(16) 171.17(19)

B.3 Chapter 4

Experimental details

Datasets were collected on a Bruker APEX II system with MoKα radiation using APEX2 software.[1] Initial cell constants were found by small widely separated "matrix" runs. Data collection strategies were determined using COSMO.[2] Scan speed and scan widths were chosen based on scattering power and peak rocking curves. All datasets were collected at -153 °C using an Oxford Croystream low-temperature device.

Unit cell constants and orientation matrix were improved by least-squares refinement of reflections thresholded from the entire dataset. Integration was performed with SAINT,[3] using this improved unit cell as a starting point. Precise unit cell constants were calculated in SAINT from the final merged dataset. Lorenz and polarization corrections were applied. Unless otherwise noted, multi-scan absorption corrections were performed with SADABS.[4]

Data were reduced with SHELXTL.[5] The structures were solved in all cases by direct methods without incident. Unless otherwise noted, hydrogen atoms were located in idealized positions and were treated with a riding model. All non-hydrogen atoms were assigned anisotropic thermal parameters. Refinements continued to convergence, using the recommended weighting schemes.

A5:D7 - Stoichiometry is 2: 3 amine : diiodo compound. One of the diiodo compounds straddled a crystallographic inversion center.

A5:D9 - The asymmetric unit contains a 1 : 1 ratio of amine : diiodo compound.

A6:D2 - Stoichiometry is 2: 3 amine : diiodo compound. One of the diiodo compounds was disordered, and the other diiodo compound straddled a crystallographic inversion center and was assigned 50% occupancy. Pairwise thermal constraints and distance constraints were applied to both dioodo compounds. A free variable was used to control the ratio of species for the first iodo compound.

A6:D7 - Stoichiometry is 2: 3 amine : diiodo compound. One of the diiodo compounds straddled a crystallographic inversion center

A7:D3[10] - Dataset was collected on an Oxford Diffraction Xcalibur four-circle kappa geometry single-crystal diffractometer with Sapphire 3 CCD detector, using a graphite monochromated Mo$K\alpha$ ($\lambda = 0.71073$ Å) radiation, and applying the CrysAlisPro Software system[8] at 296 K. The crystal–detector distance was 45 mm.

Data reduction, including Lorentz and polarization corrections as well as absorption correction, was done by CrysAlis RED program.[8] The structure was solved by Direct methods implemented in the SHELXS-2013 program.[9] The coordinates and the anisotropic displacement

parameters for all non-hydrogen atoms were refined by full-matrix least-squares methods based on F^2 using the SHELXL-2013 program.[9]

All hydrogen atoms were placed in geometrically idealized positions and constrained to ride on their carbon atom at distances of 0.93 or 0.97 Å for aromatic or methylene hydrogen atoms, respectively, and with $U_{iso}(H) = 1.2U_{eq}(C)$ (for aromatic H) and $U_{iso}(H) = 1.5U_{eq}(C)$ (for methylene group).

A7:D8 - The asymmetric unit contains a 1 : 1 ratio of amine : diiodo compound.

A7:D10 - The asymmetric unit contains one amine / diiodo compound pair.

A8:D8 - The asymmetric unit contains 2 amines and 2 diiodo compounds. The SHELXL "RESI" command was use to assign similar names to these molecules.

A8:D9 - The asymmetric unit contains a 1 : 2 ratio of amine : triiodo compound.

A9:D8 - Stoichiometry is 2 : 1 amine : diiodo compound. The diiiodo compound sits on a crystallographic inversion center.

A9:D9 - The asymmetric unit contains one amine / triiodo compound pair.

A10:D4 - Stoichiometry is 2: 3 amine : diiodo compound. One of the diiodo compounds straddled a crystallographic inversion center and was disordered,. Pairwise thermal constraints and distance constraints were applied to both dioodo compounds. A free variable was used to control the ratio of species for the first iodo compound. Carbon and fluorine atoms for the first diiodo compound and carbon atoms for the second diiodo compound were given isotropic thermal parameters.

A10:D7 - The asymmetric unit contains a 1 : 1 ratio of amine : diiodo compound.

A10:D8 - Stoichiometry is 1: 1 amine : diiodo compound. The asymmetric unit contains two half-diiodo compounds. Each diiodo compound sits on a crystallographic inversion center.

A10:D9 - The asymmetric unit contains a 1 : 2 ratio of amine : triiodo compound.

A11:D9 - The asymmetric unit contains a 1 : 1 ratio of amine : triiodo compound. It also contains a solvent methanol, whose occupancy was set to 0.25 during refinement. The solvent carbon and oxygen atoms were refined with isotropic thermal parameters.

A11:D10 - The asymmetric unit contains a 1 : 2 ratio of amine : diiodo compound. It also contains a molecule of acetone.

A12:D2 - The asymmetric unit contains one amine / diiodo compound pair.

A12:D8 - The asymmetric unit contains one amine / diiodo compound pair.

A13:D1 - The asymmetric unit contains six amines and four diiodo compounds. It also contains two molecules of hydroiodic acid. Proton transfer to two amines was observed, and coordinates for these two protons were allowed to refine.

A13:D2 - The crystal was a nonmerohedral twin and data intensities were processed with TWINABS.[6] Stoichiometry is 2: 1 amine : diiodo compound. The asymmetric unit contains two amines and two half-diiodo compounds. Each diiodo compound sits on a crystallographic inversion center.

A13:D3 - The crystal was a nonmerohedral twin and data intensities were processed with TWINABS.[6] The asymmetric unit contains a 1 : 1 ratio of amine : diiodo compound.

A13:D7 - The asymmetric unit contains a 1 : 1 ratio of amine : diiodo compound.

Crystallographic data

Code	A5:D8	A5:D10	A6:D2	A6:D8	A7:D3	A7:D8
Formula moiety	$(C_{13}H_{11}N_3)_2$ $(C_6F_4I_2)_3$	$(C_{13}H_{11}N_3)(C_{12}F_8I_2)$	$(C_{15}H_{15}N_3)_2$ $(C_4F_8I_2)_3$	$(C_{15}H_{15}N_3)_2$ $(C_6F_4I_2)_3$	$(C_9H_9N_3)$ $(C_6F_{12}I_2)$	$(C_9H_9N_3)$ $(C_6F_4I_2)$
Empirical formula	$C_{44}H_{22}F_{12}I_6N_6$	$C_{25}H_{11}F_8I_2N_3$	$C_{42}H_{30}F_{24}I_6N_6$	$C_{48}H_{30}F_{12}I_6N_6$	$C_{12}H_9F_{12}I_2N_3$	$C_{15}H_9F_4I_2N_3$
Molecular weight	1624.08	759.17	1836.12	1680.18	713.05	561.05
Color, Habit	colourless needle	colourless plate	colourless plate	colourless needle	colourless block	colourless prism
Crystal system	Monoclinic	Triclinic	Triclinic	Monoclinic	Monoclinic	Monoclinic
Space group, Z	P2(1)/c, 2	P-1, 2	P-1, 1	C2/c, 4	$P\,2_1/n$, 4	P2(1)/c, 4
a, Å	20.534(2)	8.7174(7)	6.1821(9)	45.703(4)	11.293(1)	8.2550(12)
b, Å	4.7796(5)	11.0124(10)	14.174(2)	4.8060(5)	9.8282(11)	19.307(3)
c, Å	24.675(3)	13.5138(12)	15.913(2)	23.908(2)	20.583(3)	10.4263(15)
α, °	90.00	76.218(2)	76.382(4)	90.00	90.00	90.00
β, °	102.521(4)	75.941(2)	89.240(3)	105.369(9)	105.137(14)	92.213(4)
γ, °	90.00	79.323(2)	86.597(4)	90.00	90.00	90.00
Volume, Å^3	2364.1(4)	1211.00(18)	1352.8(3)	5063.5(9)	2205.3(5)	1660.5(4)
Density, g/cm^3	2.281	2.082	2.254	2.204	2.148	2.244
Temperature, °K	120(2)	120(2)	120(2)	120(2)	296(2)	120(2)
Crystal size, min x mid x max	0.06 x 0.08 x 0.44	0.10 x 0.28 x 0.34	0.12 x 0.38 x 0.44	0.06 x 0.10 x 0.44	0.24 x 0.37 x 0.46	0.26 x 0.34 x 0.38
X-ray wavelength, Å	0.71073	0.71073	0.71073	0.71073	0.71073	0.71073
μ, mm^{-1}	4.030	2.680	3.566	3.767	2.959	3.831
Absorption corr	multi-scan	multi-scan	multi-scan	multi-scan	multi-scan	multi-scan
Trans min / max	0.2701 / 0.7940	0.4627 / 0.7754	0.3030 / 0.6743	0.2880 / 0.8055	0.297 / 0.486	0.3238 / 0.4358
θ_{min}, °	1.69	1.92	1.73	1.76	4.27	2.11
θ_{max}, °	32.13	31.95	32.06	32.53	29.25	32.51
Reflections						
collected	24646	24172	41225	27573	10140	30444
independent	7497	7352	8742	8623	4957	5567
observed	5880	6502	8041	7071	3165	5312
Threshold expression	>2σ(I)	>2σ(I)	>2σ(I)	>2σ(I)	>2σ(I)	>2σ(I)
R1 (observed)	0.0296	0.0209	0.0414	0.0296	0.0470	0.0199
***w*R$_2$ (all)**	0.0711	0.0485	0.1014	0.0605	0.1194	0.0432
Goodness of fit (all)	1.028	1.041	1.030	1.038	1.008	1.112
Δρ max / min	1.102 / -0.878	0.591 / -0.562	1.544 / -1.601	1.630 / -1.332	0.803 / -0.727	0.518 / -0.625
2θ limit	30.00	30.00	30.00	32.50	25.24	31.00
Completeness to 2θ limit	0.977	0.980	0.997	0.940	0.970	0.988

Code	A7:D10	A8:D8	A8:D9	A9:D8	A9:D9	A10:D4
Formula moiety	$(C_9H_9N_3)$ $(C_{12}F_8I_2)$	$(C_{13}H_{11}N_3)$ $(C_6F_4I_2)$	$(C_{13}H_{11}N_3)$ $(C_6F_3I_3)_2$	$(C_{15}H_{13}N_3)_2$ $(C_6F_4I_2)$	$(C_{15}H_{13}N_3)$ $(C_6F_3I_3)$	$(C_{15}H_{15}N_3)_2$ $(C_8F_{16}I_2)_3$
Empirical formula	$C_{21}H_9F_8I_2N_3$	$C_{19}H_{11}F_4I_2N_3$	$C_{25}H_{11}F_6I_6N_3$	$C_{36}H_{26}F_4I_2N_6$	$C_{21}H_{13}F_3I_3N_3$	$C_{54}H_{30}F_{48}I_6N_6$
Molecular weight	709.11	611.11	1228.77	872.43	745.04	2436.24
Color, Habit	yellow plate	colourless prism	colourless rod	colourless plate	colourless block	colourless rod
Crystal system	Monoclinic	Monoclinic	Monoclinic	Monoclinic	Triclinic	Triclinic
Space group, Z	P2(1)/c, 2	P2(1)/c, 8	P2(1)/n, 4	P2(1)/c, 2	P-1, 2	P-1, 1
a, Å	8.0816(9)	16.3849(19)	14.0476(14)	5.4499(4)	9.0175(7)	6.2290(4)
b, Å	23.780(3)	20.688(3)	9.0900(9)	12.0840(9)	10.1261(8)	15.6889(11)
c, Å	11.2100(13)	11.4260(14)	24.060(3)	24.4295(17)	13.2460(11)	18.5576(13)
α, °	90	90.00	90.00	90.00	76.552(3)	79.581(3)
β, °	92.000(4)	93.752(3)	96.564(4)	94.263(2)	77.654(3)	89.789(2)
γ, °	90	90.00	90.00	90.00	69.369(2)	82.712(2)
Volume, Å^3	2153.0(4)	3864.7(9)	3052.1(6)	1604.4(2)	1089.30(15)	1768.9(2)

Density, g/cm^3	2.188	2.101	2.674	1.806	2.272	2.287
Temperature, °K	120(2)	120(2)	120(2)	120(2)	120(2)	120(2)
Crystal size, min x mid x max	0.100 x 0.320 x 0.360	0.12 x 0.26 x 0.44	0.06 x 0.08 x 0.32	0.06 x 0.20 x 0.42	0.14 x 0.18 x 0.22	0.08 x 0.12 x 0.38
X-ray wavelength, Å	0.71073	0.71073	0.71073	0.71073	0.71073	0.71073
μ, mm^{-1}	3.006	3.302	6.165	2.021	4.343	2.805
Absorption corr	multi-scan	multi-scan	multi-scan	multi-scan	multi-scan	multi-scan
Trans min / max	0.526 / 0.753	0.3244 / 0.6927	0.2430 / 0.7086	0.4840 / 0.8883	0.4484 / 0.5815	0.4154 / 0.8068
θ_{min}, °	1.713	1.59	1.60	1.67	1.60	1.57
θ_{max}, °	32.706	32.06	32.62	32.03	33.27	32.62
Reflections						
collected	35429	36736	40571	23137	31815	32693
independent	7547	12505	10577	5133	7252	11844
observed	6839	10148	8100	4583	6349	9710
Threshold expression	I > 2σ(I)	>2σ(I)	>2σ(I)	I >2σ(I)	I >2σ(I)	>2σ(I)
R1 (observed)	0.0289	0.0265	0.0307	0.0233	0.0271	0.0395
***w*R$_2$ (all)**	0.0751	0.0596	0.0540	0.0565	0.0569	0.1062
Goodness of fit (all)	1.095	1.060	1.078	1.035	1.030	1.096
Δρ max / min	0.982 / -1.154	1.056 / -0.554	1.365 / -1.570	0.707 / -0.439	0.894 / -0.874	2.480 / -1.803
2θ limit	31.000	30.00	30.00	30.00	30.00	30.00
Completeness to 2θ limit	0.991	0.972	0.989	0.985	0.998	0.982

Code	**A10:D7**	**A10:D8**	**A10:D9**	**A11:D9**	**A11:D10**	**A12:D2**
Formula moiety	$(C_{15}H_{15}N_3)$ $(C_6F_4I_2)_2$	$(C_{15}H_{15}N_3)$ $(C_6F_4I_2)$	$(C_{15}H_{15}N_3)$ $(C_6F_3I_3)_2$	$(C_{15}H_{13}N_3)$ $(C_6F_3I_3)$ $(C_1H_4O)_{0\text{-}25}$	$(C_{15}H_{13}N_3)$ $(C_{12}F_8I_2)_2$ $(C_3H_6O_1)$	$(C_9H_9N_3)$ $(C_4F_8I_2)$
Empirical formula	$C_{27}H_{15}F_8I_4N_3$	$C_{21}H_{15}F_4I_2N_3$	$C_{27}H_{15}F_6I_6N_3$	$C_{21\cdot25}H_{14}F_3I_3N_3O_{0\cdot25}$	$C_{42}H_{19}F_{16}I_4N_3O$	$C_{13}H_9F_8I_2N_3$
Molecular weight	1041.02	639.16	1256.82	753.05	1393.20	613.03
Color, Habit	bronze plate	gold prism	colourless prism	colourless prism	colourless priism	colourless plate
Crystal system	Triclinic	Triclinic	Triclinic	Triclinic	Triclinic	Monoclinic
Space group, Z	P-1, 2	P-1, 2	P-1, 2	P-1, 2	P-1, 2	P2(1)/c, 4
a, Å	8.1680(15)	6.3653(9)	9.0728(17)	9.2576(14)	8.5570(5)	11.0738(19)
b, Å	13.8655(18)	9.0358(13)	9.4997(17)	11.5659(17)	16.0998(11)	16.892(3)
c, Å	14.800(3)	19.158(3)	19.925(4)	11.9691(18)	16.3207(11)	10.0913(16)
α, °	108.699(11)	102.267(5)	92.496(6)	108.555(5)	75.578(2)	90.00
β, °	102.03(2)	96.243(5)	101.102(7)	90.795(5)	80.8737(19)	109.070(5)
γ, °	102.751(14)	98.349(5)	108.962(6)	103.393(4)	88.850(2)	90.00
Volume, Å^3	1476.1(5)	1054.1(3)	1583.2(5)	1176.6(3)	2149.6(2)	1784.1(5)
Density, g/cm^3	2.342	2.014	2.636	2.126	2.152	2.282
Temperature, °K	120(2)	120(2)	120(2)	120(2)	120(2)	120(2)
Crystal size, min x mid x max	0.14 x 0.26 x 0.34	0.14 x 0.26 x 0.38	0.18 x 0.24 x 0.30	0.26 x 0.34 x 0.44	0.16 x 0.24 x 0.42	0.08 x 0.22 x 0.34
X-ray wavelength, Å	0.71073	0.71073	0.71073	0.71073	0.71073	0.71073
μ, mm^{-1}	4.296	3.031	5.946	4.023	3.008	3.607
Absorption corr	multi-scan	multi-scan	multi-scan	multi-scan	multi-scan	multi-scan
Trans min / max	0.3229 / 0.5845	0.3921 / 0.6763	0.2686 / 0.4141	0.2706 / 0.4211	0.3647 / 0.6447	0.3735 / 0.7613
θ_{min}, °	1.52	2.20	1.05	1.80	1.30	2.41
θ_{max}, °	33.18	33.16	32.12	30.58	32.58	32.52
Reflections						
collected	25813	27813	32477	25794	77154	45544
independent	9348	6850	10130	7142	14445	6200
observed	8729	6229	9066	6563	12730	4946

Threshold expression	>2σ(I)	>2σ(I)	>2σ(I)	I >2σ(I)	I >2σ(I)	I >2σ(I)
R1 (observed)	0.0307	0.0190	0.0251	0.0226	0.0225	0.0346
wR_2 (all)	0.0795	0.0459	0.0718	0.0537	0.0551	0.0684
Goodness of fit (all)	1.088	0.967	1.161	1.060	1.077	1.087
Δρ max / min	1.945 / -1.753	0.530 / -0.445	1.191 / -1.379	0.741 / -0.936	0.678 / -1.210	1.593 / -1.000
2θ limit	30.00	30.00	30.00	30.00	30.00	31.00
Completeness to 2θ limit	0.952	0.981	0.964	0.996	0.998	0.998

Code	A12:D8	A13:D1	A13:D2	A13:D3	A13:D7
Formula moiety	$(C_9H_9N_3)$ $(C_6F_4I_2)$	$(C_7H_{10}N_2)_3(C_2F_4I_2)_2$ $(H_1I_1)_1$	$(C_7H_{10}N_2)_2$ $(C_4F_8I_2)$	$(C_7H_{10}N_2)$ $(C_6F_{12}I_2)$	$(C_7H_{10}N_2)$ $(C_6F_4I_2)$
Empirical formula	$C_{15}H_9F_4I_2N_3$	$C_{25}H_{31}F_8I_5N_6$	$C_{18}H_{20}F_8I_2N_4$	$C_{13}H_{10}F_{12}I_2N_2$	$C_{13}H_{10}F_4I_2N_2$
Molecular weight	561.05	1202.06	698.18	676.03	524.03
Color, Habit	colourless prism	colourless plate	colourless plate	colourless plate	colourless prism
Crystal system	Triclinic	Triclinic	Triclinic	Monoclinic	Triclinic
Space group, Z	P-1, 2	P-1, 4	P-1, 2	P2(1)/c, 4	P-1, 4
a, Å^3	8.9744(13)	9.9115(14)	9.1093(8)	10.4273(8)	8.4741(5)
b, Å^3	9.0522(14)	17.748(2)	10.3042(9)	6.8308(5)	12.2584(6)
c, Å^3	11.9251(18)	21.823(3)	12.7170(11)	27.504(2)	15.3992(8)
α, °	101.157(4)	76.380(4)	96.877(3)	90.00	103.739(2)
β, °	107.766(3)	82.913(4)	90.277(3)	94.820(2)	97.874(2)
γ, °	107.334(3)	87.460(4)	96.466(3)	90.00	95.942(2)
Volume, Å^3	836.5(2)	3701.9(8)	1177.34(18)	1952.1(3)	1523.77(14)
Density, g/cm^3	2.228	2.157	1.969	2.300	2.284
Temperature, °K	120(2)	120(2)	120(2)	120(2)	120(2)
Crystal size, min x mid x max	0.10 x 0.22 x 0.32	0.04 x 0.18 x 0.26	0.08 x 0.20 x 0.40	0.08 x 0.28 x 0.32	0.12 x 0.20 x 0.32
X-ray wavelength, Å	0.71073	0.71073	0.71073	0.71073	0.71073
μ, mm^{-1}	3.802	4.267	2.747	3.334	4.164
Absorption corr	multi-scan	multi-scan	multi-scan	multi-scan	multi-scan
Trans min / max	0.3758 / 0.7023	0.5795 / 0.7463	0.4062 / 0.8102	0.4150 / 0.7763	0.3492 / 0.6349
θ_{min}, °	1.89	1.18	1.61	1.96	1.38
θ_{max}, °	32.53	32.03	31.59	32.05	33.13
Reflections					
collected	21465	76484	13955	9624	31993
independent	5554	23133	13955	9624	9317
observed	4898	18020	9585	8055	8016
Threshold expression	I >2σ(I)	>2σ(I)	>2σ(I)	>2σ(I)	>2σ(I)
R1 (observed)	0.0240	0.0436	0.0475	0.0640	0.0291
wR_2 (all)	0.0534	0.1205	0.1396	0.1914	0.0642
Goodness of fit (all)	1.048	1.050	1.017	1.388	1.053
Δρ max / min	0.970 / -0.571	6.740 / -4.192	1.540 / -1.754	2.427 / -1.803	1.095 / -0.442
2θ limit	31.00	30.00	31.00	31.50	30.00
Completeness to 2θ limit	0.972	0.977	0.987	0.963	0.947

Halogen bond geometries

Co-crystal	C–I···N	N···I (Å)	N···I-C (^{0})
A5:D7	C(31)-I(1)···N(13) C(41)-I(2)···N(21)	2.782(2) 2.762(3)	168.27(10) 177.29(10)
A5:D9	C(31)-I(1)···N(13) C(41)-I(2)···N(21)#1	2.9658(16) 2.8379(16)	166.92(6) 177.30(6)
A6:D2	C(41A)-I(1)···N(13) C(41B)-I(1)···N(13) C(44A)-I(2A)···N(31)#1 C(44B)-I(2B)···N(31)#1	2.838(3) 2.838(3) 2.769(3) 2.868(3)	169.5(2) 174.6(3) 169.0(3) 175.6(2)
A6:D7	C(41)-I(1)···N(13) C(51)-I(2)···N(31)	2.813(2) 2.764(2)	179.33(8) 176.80(8)
A7:D3	C(10)-I(1)···N(3)	2.854(6)	174.9(2)

	C(15)-I(2)···N(1)^{i}	2.866(5)	174.0(2)
A7:D7	C(31)-I(1)···N(13) C(34)-I(2)···N(21)#2	2.8336(16) 2.8149(15)	170.80(6) 174.00(6)
A7:D9	C(31)-I(1)···N(13) C(41)-I(2)···N(21)#1	2.766(3) 2.768(3)	174.21(8) 177.05(9)
A8:D7	C311-I11···N131 C341-I21···N211#1 C312-I32···N132	2.8096(19) 2.8502(19) 2.7891(18)	176.85(8) 170.39(7) 177.27(7)
A8:D8	C(31)-I(1)···N(13) C(41)-I(4)···N(21)	2.807(2) 2.820(2)	175.70(11) 177.93(10)
A9:D7	C(41)-I(1)···N(13)	2.7601(9)	176.67(4)
A9:D8	C(41)-I(1)···N(13) C(43)-I(2)···N(21)#1	2.852(2) 2.889(2)	169.65(7) 172.31(8)
A10:D4	C(41A)-I(1)···N(13) C(41B)-I(1)···N(13) C(51)-I(2)···N(31)	2.924(3) 2.924(3) 2.982(3)	172.7(2) 171.5(5) 169.96(13)
A10:D6	C(41)-I(1)···N(13) C(51)-I(3)···N(31)	2.793(2) 3.016(2)	177.63(9) 170.94(9)
A10:D7	C(41)-I(1)···N(13) C(51)-I(2)···N(31)	2.8071(14) 2.8788(16)	177.59(5) 174.16(6)
A10:D8	C(41)-I(1)···N(13) C(51)-I(4)···N(31)	2.965(3) 2.788(3)	165.81(10) 176.44(13)
A11:D8	C(41)-I(1)···N(13) C(26)-N(21)···I(2)#1	2.814(2) 2.8063(19)	171.73(7) 125.91(15)
A11:D9	C(12)-N(13)···I(1) C(51)-I(2)···N(21)#1	2.7579(14) 2.7696(15)	130.05(11) 177.11(5)
A12:D2	C(31)-I(1)···N(13) C(34)-I(2)···N(21)#1	2.757(3) 2.815(2)	178.49(10) 2.815(2)
A12:D7	C(31)-I(1)···N(13) C(34)-I(2)···N(21)#1	2.8357(17) 2.8688(18)	171.67(7) 172.76(7)
A13:D1	C(6)-I(6)···N(11) C(8)-I(8)···N(21)	2.664(4) 2.689(4)	176.48(15) 172.01(16)
A13:D2	C211-I11···N111 C212-I22···N112	2.641(3) 2.668(3)	178.10(11) 178.93(11)
A13:D3	C(21)-I(1)···N(11) C(26)-I(2)···N(14)#1	2.683(4) 3.440(5)	176.4(2) 164.42(18)
A13:D6	C(31)-I(1)···N(11) C(32)-I(2)···N(21)	2.722(2) 2.776(2)	178.30(10) 173.43(9)

B.4 Chapter 5

Experimental details

Datasets were collected on a Bruker Kappa APEX II system using CuKα radiation (**A18:D3**), or a on a Bruker APEX II system using MoKα radiation (all others except **A17:D1** and **A17:D7**). Data were collected using APEX2 software. [1] Initial cell constants were found by small widely separated "matrix" runs. Data collection strategies were determined using COSMO.[2] Scan speed and scan widths were chosen based on scattering power and peak rocking curves. All datasets were collected at -153 °C using an Oxford Croystream low-temperature device.

Unit cell constants and orientation matrix were improved by least-squares refinement of reflections thresholded from the entire dataset. Integration was performed with SAINT,[3] using this improved unit cell as a starting point. Precise unit cell constants were calculated in SAINT from the final merged dataset. Lorenz and polarization corrections were applied. Multi-scan absorption corrections were performed with SADABS.[4]

Data were reduced with SHELXTL.[5] The structures were solved in all cases by direct methods without incident. Except as noted, hydrogen atoms were located in idealized positions and were treated with a riding model. All non-hydrogen atoms were assigned anisotropic thermal parameters. Refinements continued to convergence, using the recommended weighting schemes.

A17:D1[7] - The single crystal X-ray diffraction studies were carried out on a Bruker D8 Smart Apex CCD diffractometer equipped with Mo K_α radiation (λ = 0.71073 Å) and . A 0.44 x 0.20 x 0.14 mm colorless rod was mounted on a Cryoloop with Paratone oil. Data were collected in a nitrogen gas stream at 100(2) K using ϕ and ϖ scans. Crystal-to-detector distance was 60 mm and exposure time was 10 seconds per frame using a scan width of 0.4°. Data collection was 100% complete to 25.00° in θ. A total of 15508 reflections were collected covering the indices, -15<=h<=16 -11<=k<=11, -12<=l<=12. 2435 reflections were found to be symmetry independent, with a Rint of 0.0315. Indexing and unit cell refinement indicated a primitive, monoclinic lattice. The space group was found to be P21/c. The data were integrated using the Bruker SAINT software program and scaled using the SADABS software program. Solution by direct methods (SHELXS) produced a complete phasing model consistent with the proposed structure. All nonhydrogen atoms were refined anisotropically by full-matrix least-squares (SHELXL-97). All hydrogen atoms were placed using a riding model. Their positions were constrained relative to their parent atom using the appropriate HFIX command in SHELXL-97.

A17:D7[7] - Colorless crystal, mounted on a Cryoloop with Paratone-N oil and data collected at 100 K using a Bruker APEX I CCD with Mo K alpha radiation. Data corrected for absorption with SADABS and structure solved by direct methods. All non-hydrogen atoms were refined anisotropically by full matrix least squares on F^2. Hydrogen atom H1N was found from a Fourier difference map and was allowed to refined with a N-H distance of 0.87 (2) angstroms and isotropic displacement parameters set to 1.20 Ueq of the parent N atom. All other H atoms were placed in calculated positions with appropriate riding modes.

A16:D8 - The halo compound sits on a crystallographic inversion center, giving an overall 2 : 1 amine : halo compound stoichiometry. Two alternate protonation schemes for the imidazole moiety were observed, corresponding to oppositely directed translation-related linear hydrogen bonding chains in the y direction. Two PARTs were assembled to account for the two schemes, with EADP and EXYZ instructions pairwise included for superimposed nitrogen atoms (N11A & N11B and N13A & N13B). The proportion of the two sites was allowed to refine by using a free variable; this free variable refined to 0.20(4), representing a ~ 20:80 proportion for the two schemes.

A17:D2 - The halo compound sits on a crystallographic inversion center, giving an overall 2 : 1 amine : halo compound stoichiometry. Two alternate protonation schemes for the imidazole moiety were observed, corresponding to oppositely directed linear hydrogen bonding chains along the c glide plane. A hydrogen atom was included at both imidazole nitrogen atoms (N21 and N23) in idealized positions, and the occupancy of these two hydrogen atoms was allowed to refine, while summing to 1.0, by using a free variable; this free variable refined to 0.81(4), representing a ~ 81:19 proportion for the two schemes.

A17:D8 - The halo compound sits on a crystallographic inversion center, giving an overall 2 : 1 amine : halo compound stoichiometry. Coordinates for the amine proton H11 were allowed to refine.

A17:D9 - The halo compound sits on a crystallographic twofold axis, giving an overall 2 : 1 amine : halo compound stoichiometry. Coordinates for the amine proton H11 were allowed to refine.

A17:D10 - The compound crystallizes with an overall 2 : 1 amine : halo compound stoichiometry. The structure was solved and refined in the noncentrosymmetric space group Pc, and was treated as a racemic twin, with the batch scale factor refining to 0.129(11). For each imidazole moiety, two alternate protonation schemes were observed, corresponding to oppositely directed linear hydrogen bonding chains along the c glide plane. For each imidazole moiety, PARTs were assembled to account for the two schemes, with EADP and EXYZ instructions pairwise included for superimposed nitrogen atoms (N11A & N11B; N13A & N13B; N31A & N31B; N33A & N33B).

A17:D14 - The halo compound sits on a crystallographic inversion center, giving an overall 2 : 1 amine : halo compound stoichiometry. Occupancies of the bromine and the iodine atoms were fixed to 0.50 to accommodate disorder on the inversion center. Two alternate protonation schemes for the imidazole moiety were observed, corresponding to oppositely directed linear hydrogen bonding chains along the c glide plane. For each imidazole moiety, the proportion of the two sites was allowed to refine by using free variables; this free variables refined to 0.64(6) and 0.33(6) for the two sites. Two PARTs were assembled to account for the two schemes, with EADP and EXYZ instructions pairwise included for superimposed nitrogen atoms (N11A & N11B and N13A &

N13B). The proportion of the two sites was allowed to refine by using a free variable; this free variable refined to 0.23(20).

A18:D3 - The halo compound sits on a crystallographic inversion center. There are two different amine species present: the first sits on a general position, and the second straddles a crystallographic inversion center and was modeled as a complete molecule having an occupancy of 50%. The overall stoichiometry was therefore 2 : 1 amine : halo compound. The geometry of the second amine was restrained to approximate the fully ordered first amine by using the SHELXL SAME command, and the EADP command was used to pairwise constrain thermal parameters of atoms in the partially occupied amine that are located in proximity to each other.

A18:D8 - The asymmetric unit contains two amines on general positions, one halo compound on a general position, and two half-halo compounds sitting adjacent to crystallographic inversion centers. Overall stoichiometry in the asymmetric unit is therefore 2 : 2 amine : halo compound. Coordinates for the amine protons H11 and H31 were allowed to refine.

A18:D10 - The halo compound sits on a crystallographic 2-fold axis, giving an overall 2 : 1 amine : halo compound stoichiometry. Coordinates for the amine proton H11 were allowed to refine.

A19:D2 - The halo compound sits on a crystallographic inversion center, giving an overall 2 : 1 amine : halo compound stoichiometry. The amine was disordered over two distinct sites. Occupancies for the two species were set to 0.50, and the SAME command was used to restrain geometries. Thermal parameters for certain closely positioned atoms were constrained by using the EADP command. Two alternate protonation schemes for both imidazole moieties were observed. For each imidazole molecule, N-H hydrogen atoms were added in idealized positions, and the population of the two hydrogen atoms was controlled with a free variable. The halo

compound was disordered over two closely located sites. The SAME command was used to restrain geometries, the EADP command was used to pairwise constrain closely located atoms, and the proportion of the two species was controlled with a free variable.

A18:D8 - The halo compound sits on a crystallographic inversion center, giving an overall 2 : 1 amine : halo compound stoichiometry. Coordinates for the amine proton H11 were allowed to refine.

A18:D9 - The halo compound sits on a crystallographic 2-fold axis, giving an overall 2 : 1 amine : halo compound stoichiometry. Two alternate protonation schemes for the imidazole moiety were observed, corresponding to oppositely directed linear hydrogen bonding chains along the ba glide plane. Two PARTs were assembled to account for the two schemes, with EADP and EXYZ instructions pairwise included for superimposed nitrogen atoms (N11A & N11B and N13A & N13B). The proportion of the two sites was allowed to refine by using a free variable; this free variable refined to 0.80(3), representing a ~ 80:20 proportion for the two schemes.

A18:D101 - The compound crystallizes with an overall 2 : 1 amine : halo compound stoichiometry. Coordinates for the amine protons H11 and H31 were allowed to refine.

Crystallographic data

Code	A16:D8	A17:D1	A17:D2	A17:D7	A17:D8
Formula moiety	$(C_8H_7N_3)_2$ $(C_6F_4I_2)$	$(C_8H_7N_3)_2$, $(C_2F_4I_2)$	$(C_8H_7N_3)_2$ $(C_4F_8I_2)$	$(C_8H_7N_3)_2$, $(C_6F_4I_2)$	$(C_8H_7N_3)_2$ $(C_6F_4I_2)$
Empirical formula	$C_{22}H_{14}F_4I_2N_6$	$C_{18}H_{14}F_4I_2N_6$	$C_{20}H_{14}F_8I_2N_6$	$C_{22}H_{14}F_4I_2N_6$	$C_{22}H_{14}F_4I_2N_6$
Molecular weight	692.19	644.15	744.17	692.19	692.19
Color, Habit	colourless needle	Colourless, Rod	colourless prism	Colourless, Block	colourless plate
Crystal system	Monoclinic	Monoclinic	Monoclinic	Monoclinic	Monoclinic
Space group, Z	P2(1)/n, 2	P2(1)/c, 2	P2(1)/c, 2	Cm, 2	P2(1)/c, 2
a, Å	12.9720(11)	12.3214(7)	14.3500(9)	10.0009(13)	4.1462(3)
b, Å	5.0426(4)	8.9036(5)	8.7642(5)	28.964(4)	27.9646(17)
c, Å	17.0878(15)	9.8742(6)	9.9637(6)	4.1036(6)	9.9124(6)
α, °	90.00	90.00	90.00	90.00	90.00
β, °	92.470(4)	100.4930(10)	106.551(2)	100.997(2)	100.094(2)
γ, °	90.00	90.00	90.00	90.00	90.00
Volume, $Å^3$	1116.72(16)	1065.13(11)	1201.18(12)	1166.8(3)	1131.52(13)
Density, g/cm^3	2.059	2.008	2.058	1.970	2.032
Crystal size, min x mid x max	0.06 x 0.10 x 0.42	0.44 x 0.20 x 0.14	0.16 x 0.22 x 0.30	0.30 x 0.20 x 0.10	0.06 x 0.18 x 0.26

μ, mm^{-1}	2.874	3.004	2.702	2.750	2.836
Trans min / max	0.3782 / 0.8465	0.3515/ 0.6784	0.4978 / 0.6717	0.4925/ 0.7705	0.5259 / 0.8483
θ_{min}, °	1.93	1.68	1.48	2.81	1.46
θ_{max}, °	32.56	27.49	33.14	26.40	32.58
Reflections					
collected	17748	15508	21724	8684	13291
independent	3962	2435	4223	2217	3850
observed	3386	2327	3853	2118	3433
Threshold expression	>2σ(I)	>2σ(I)	>2σ(I)	>2σ(I)	>2σ(I)
R_1 (observed)	0.0256	0.0215	0.0284	0.0203	0.0254
wR_2 (all)	0.0622	0.0570	0.0639	0.0470	0.0607
Goodness of fit (all)	1.058	1.037	1.110	1.023	1.022
Δρ max / min	1.046 / -0.910	0.913/-0.609	1.394 / -0.763	0.408/ 0.452	0.734 / -0.545
2θ limit	30.00	25.00	27.50	25.00	30.00
Completeness to 2θ limit	0.994	1.000	0.986	1.000	0.983

Code	**A17:D9**	**A17:D10**	**A17:D14**	**A18:D3**	**A18:D8**
Formula moiety	$(C_8H_7N_3)_2$ $(C_6F_3I_3)$	$(C_8H_7N_3)_2$ $(C_{12}F_8I_2)$	$(C_8H_7N_3)_2$ (C_6BrF_4I)	$(C_8H_7N_3)_3$ $(C_6F_{12}I_2)$	$(C_8H_7N_3)_2$ $(C_6F_4I_2)$
Empirical formula	$C_{22}H_{14}F_3I_3N_6$	$C_{28}H_{14}F_8I_2N_6$	$C_{22}H_{14}BrF_4IN_6$	$C_{30}H_{21}F_{12}I_2N_9$	$C_{22}H_{14}F_4I_2N_6$
Molecular weight	800.09	840.25	645.20	989.36	692.19
Color, Habit	colourless plate	colourless prism	colourless rod	colourless prism	colourless needle
Crystal system	Orthorhombic	Monoclinic	Monoclinic	Triclinic	Monoclinic
Space group, Z	Pbcn, 4	Pc, 2	P2(1)/c, 2	P-1, 1	P2(1)/n, 2
a, Å	32.4147(16)	4.2333(3)	4.0019(11)	5.1393(6)	12.9720(11)
b, Å	9.9354(5)	32.768(2)	28.546(8)	11.0259(12)	5.0426(4)
c, Å	7.4776(4)	9.9627(8)	9.972(3)	15.2795(17)	17.0878(15)
α, °	90.00	90.00	90.00	92.084(3)	90.00
β, °	90.00	93.7600(10)	98.464(8)	91.221(3)	92.470(4)
γ, °	90.00	90.00	90.00	100.093(3)	90.00
Volume, Å^3	2408.2(2)	1379.00(18)	1126.7(5)	851.52(17)	1116.72(16)
Density, g/cm^3	2.207	2.024	1.902	1.929	2.059
Crystal size, min x mid x max	0.06 x 0.20 x 0.28	0.12 x 0.20 x 0.28	0.06 x 0.14 x 0.26	0.08 x 0.14 x 0.22	0.06 x 0.10 x 0.42
μ, mm^{-1}	3.941	2.367	3.251	15.460	2.874
Trans min / max	0.4050 / 0.7979	0.5570 / 0.7643	0.4853 / 0.8288	0.1321 / 0.3710	0.3782 / 0.8465
θ_{min}, °	2.14	5.40	2.18	2.90	1.93
θ_{max}, °	32.58	30.97	29.61	69.25	32.56
Reflections					
collected	18651	15349	14624	13661	17748
independent	3961	7025	3088	2928	3962
observed	3361	6767	2657	2797	3386
Threshold expression	>2σ(I)	>2σ(I)	>2σ(I)	>2σ(I)	>2σ(I)
R_1 (observed)	0.0343	0.0205	0.1103	0.0368	0.0256
wR_2 (all)	0.0805	0.0480	0.2432	0.1302	0.0622
Goodness of fit (all)	1.158	1.027	1.348	1.241	1.058
Δρ max / min	1.906 / -0.858	0.625 / -0.414	1.180 / -1.820	0.769 / -0.997	1.046 / -0.910
2θ limit	30.00	27.50	25.00	67.50	30.00
Completeness to 2θ limit	0.988	0.978	0.991	0.942	0.994

Code	**A18:D10**	**A19:D2**	**A19:D8**	**A19:D9**	**A19:D10**
Formula moiety	$(C_8H_7N_3)_2$ $(C_{12}F_8I_2)$	$(C_7H_6N_4)_2$ $(C_4F_8I_2)$	$(C_7H_6N_4)_2$ $(C_6F_4I_2)$	$(C_7H_6N_4)_2$ $(C_6F_3I_3)$	$(C_7H_6N_4)_2$ $(C_{12}F_8I_2)$
Empirical formula	$C_{28}H_{14}F_8I_2N_6$	$C_{18}H_{12}F_8I_2N_8$	$C_{20}H_{12}F_4I_2N_8$	$C_{20}H_{12}F_3I_3N_8$	$C_{26}H_{12}F_8I_2N_8$
Molecular weight	840.25	746.16	694.18	802.08	842.24
Color, Habit	colourless prism	colourless prism	colourless plate	colourless rod	yellow prism
Crystal system	Monoclinic	Triclinic	Monoclinic	Orthorhombic	Triclinic
Space group, Z	C2/c, 4	P-1, 1	P2(1)/c, 2	Pbcn, 4	P-1, 2
a, Å	24.4359(12)	6.1488(7)	11.0717(6)	33.0655(16)	7.6527(4)

b, Å	7.2667(4)	6.3967(7)	10.6250(6)	9.8284(5)	12.7331(7)
c, Å	16.3695(8)	15.8942(19)	10.1858(6)	7.3176(3)	15.4446(9)
α, °	90.00	81.861(4)	90.00	90.00	67.3200(10)
β, °	109.7130(10)	85.950(4)	108.814(2)	90.00	88.558(2)
γ, °	90.00	72.388(3)	90.00	90.00	81.6160(10)
Volume, Å^3	2736.4(2)	589.59(12)	1134.20(11)	2378.08(19)	1372.95(13)
Density, g/cm^3	2.040	2.101	2.033	2.240	2.037
Crystal size, min x mid x max	0.18 x 0.24 x 0.32	0.04 x 0.12 x 0.22	0.10 x 0.26 x 0.34	0.04 x 0.10 x 0.28	0.22 x 0.26 x 0.32
μ, mm^{-1}	2.386	2.755	2.832	3.993	2.380
Trans min / max	0.5157 / 0.6734	0.5824 / 0.8978	0.4460 / 0.7649	0.4010 / 0.8566	0.5164 / 0.6226
θ_{min}, °	2.64	1.29	1.94	2.16	1.75
θ_{max}, °	33.13	32.70	32.64	32.52	33.45
Reflections					
collected	14274	3658	10920	36207	40305
independent	4778	3658	3791	4246	9826
observed	4451	3313	3467	3689	9163
Threshold expression	>2σ(I)	>2σ(I)	>2σ(I)	>2σ(I)	>2σ(I)
R_1 (observed)	0.0231	0.0314	0.0219	0.0212	0.0210
***w*R_2 (all)**	0.0570	0.1144	0.0595	0.0480	0.0516
Goodness of fit (all)	1.029	1.135	1.077	1.046	1.041
Δρ max / min	1.073 / -0.856	2.122 / -0.925	0.620 / -0.677	0.684 / -0.719	0.646 / -0.545
2θ limit	30.00	27.50	30.00	32.52	30.00
Completeness to 2θ limit	0.985	0.984	0.983	0.983	0.987

Halogen bond geometries

Co-crystal	C-I···N	N···I (Å)	N···I-C (°)
A16:D8	C(31)-I(1)···N(21)	2.7985(17)	172.82(7)
A17:D1	C(1)-I(1)···N(1)	2.851(2)	174.73(10)
A17:D2	C(31)-I(1)···N(11)	2.8362(18)	169.70(8)
A17:D7	C(1)-I(1)···N(3)	2.8602 (0.0031)	176.05(0.11)
A17:D8	C(31)-I(1)···N(21)	2.8085(18)	177.47(7)
A17:D9	C(33)-I(2)···N(21)	2.914(3)	165.82(11)
A17:D10	C(51)-I(1)···N(21) C(61)-I(2)···N(41)	2.846(3) 2.813(3)	178.60(10) 175.53(11)
A17:D14	C(51)-I(1)···N(21)	2.808(9)	178.5(3)
A18:D3	C(51)-I(1)···N(13)	2.856(5)	176.0(2)
A18:D8	C(51)-I(1)···N(13) C(54)-I(2)···N(33)	2.848(2) 2.875(2)	174.26(9) 175.50(9)
A18:D10	C(31)-I(1)···N(13)	2.9167(14)	173.26(5)
A19:D2	C(31B)-I(1)···N(14B) C(31A)-I(1)···N(14B) C(31B)-I(1)···N(14A) C(31A)-I(1)···N(14A)	2.836(7) 2.836(7) 2.865(7) 2.865(7)	165.2(4) 176.3(2) 168.4(4) 165.2(2)
A19:D8	C(31)-I(1)···N(24)	2.8254(16)	173.90(6)
A19:D9	C(33)-I(33)···N(24)	2.9383(15)	164.66(6)
A19:D10	C(12)-I(1)···N(13) C(32)-I(2)···N(33)	2.8484(12) 2.8625(12)	140.10(10) 140.81(10)

Hydrogen bond geometries

Co-crystal	D–H···A	D–H (Å)	H···A (Å)	D···A (Å)	D–H···N (°)
A16:D8	N(11A)-H(11)···N(13A)#2 N(13B)-H(13)···N(11B)#3	0.88 0.88	2.15 2.09	2.882(2) 2.882(2)	140.6 149.7
A17:D1	N(3)-H(3)···N(2)#2	0.84(3)	2.01(3)	2.839(2)	169(3)
A17:D2	N(21)-H(21)···N(23)#2 N(23)-H(23)···N(21)#3	0.88 0.88	1.98 2.08	2.853(2) 2.853(2)	169.2 146.1
A17:D7	N(1)-H(1N)···N(2)#2 C(11)-H(11A)···N(2)#2	0.879(18) 0.95	2.01(2) 2.59	2.879(4) 3.441(5)	171(4) 148.8
A17:D8	N(11)-H(11)···N(13)#2	0.88(3)	1.96(3)	2.834(2)	170(2)
A17:D9	N11-H11···N13_$2	0.87(4)	2.00(4)	2.866(4)	173(4)
A17:D10	N(11A)-H(11)···N(13A)#1 N(13B)-H(13)···N(11B)#2 N(31A)-H(31)···N(33A)#3 N(33B)-H(33)···N(31B)#4	0.88 0.88 0.88 0.88	1.98 1.97 2.02 2.01	2.839(4) 2.839(4) 2.872(3) 2.872(3)	165.1 167.0 163.6 167.9
A17:D14	N(11A)-H(11)···N(13A)#3 N(13B)-H(13)···N(11B)#4	0.88 0.88	2.01 1.99	2.862(11) 2.862(11)	162.0 171.4
A18:D3	N(11)-H(11)···N(33) N(11)-H(11)···N(42)#2 N(31)-H(31)···N(22)#2	0.88 0.88 0.88	2.20 2.08 2.31	2.953(11) 2.879(8) 3.143(12)	142.9 150.0 158.4
A18:D8	N(11)-H(11)···N(41)#3 N(31)-H(31)···N(21)#4	0.79(4) 0.86(4)	2.11(4) 2.10(4)	2.882(3) 2.943(3)	166(4) 166(3)
A18:D10	N(11)-H(11)···N(21)#2	0.87(3)	2.17(3)	2.9934(19)	157(2)
A19:D2	N(21A)-H(21A)···N(21A)#2 N(23A)-H(23A)···N(23A)#3 N(21B)-H(21B)···N(21B)#4 N(23B)-H(23B)···N(23B)#5	0.90 0.90 0.90 0.90	1.91 2.12 1.90 2.14	2.802(18) 3.001(13) 2.793(14) 3.003(18)	169.3 164.5 174.7 159.9
A19:D8	N(11)-H(11)···N(13)#2	0.76(3)	2.17(3)	2.900(2)	161(3)
A19:D9	N(11A)-H(11)···N(13A)#2 N(13B)-H(13)···N(11B)#3	0.88 0.88	1.91 1.93	2.7823(18) 2.7823(18)	170.6 161.9
A19:D10	N(11)-H(11)···N(41)#1 N(31)-H(31)···N(21)#2	0.85(2) 0.84(2)	2.22(2) 2.14(2)	2.9877(18) 2.9552(18)	150(2) 163(2)

B.5 Chapter 6

Experimental details for haloethynylnitrobenzene compounds

Crystals from **4N-I**, **4N-Br**, **3,5-DN-I** and **3,5DN-Br** were solved using single crystal X-ray analysis. The samples (**4N-I**, **4N-Br** and **3,5-DN-I)** were analyzed with a Bruker APEX II system using MoKα radiation. Data collection was carried out using APEX2 software.[1] Initial cell constants were found by small widely separated "matrix" runs. Data collection strategies were determined using COSMO.[2] Scan speed and scan widths were chosen based on scattering power and peak rocking curves. All datasets were collected at -153 °C using an Oxford Croystream low-temperature device.

Unit cell constants and orientation matrix were improved by least-squares refinement of reflections thresholded from the entire dataset. Integration was performed with SAINT,[3] using this improved unit cell as a starting point. Precise unit cell constants were calculated in SAINT from the final merged dataset. Lorenz and polarization corrections were applied. Multi-scan absorption corrections were performed with SADABS.[4]

Data were reduced with SHELXTL.[5] The structure was solved by direct methods without incident. All hydrogen atoms were located in idealized positions and were treated with a riding model. Unless otherwise noted, non-hydrogen atoms were assigned anisotropic thermal parameters. Refinements continued to convergence, using the recommended weighting schemes.

Dataset for **3,5DN-Br**[10] was collected on an Oxford Diffraction Xcalibur four-circle kappa geometry single-crystal diffractometer with Sapphire 3 CCD detector, using a graphite monochromated Mo$K\alpha$ ($\lambda = 0.71073$ Å) radiation, and applying the CrysAlisPro Software system[8] at 296 K. The crystal–detector distance was 45 mm.

Data reduction, including Lorentz and polarization corrections as well as absorption correction, was done by CrysAlis RED program.[8] The structure was solved by direct methods implemented in the SHELXS-2013 program.[9] The coordinates and the anisotropic displacement parameters for all non-hydrogen atoms were refined by full-matrix least-squares methods based on F^2 using the SHELXL-2013 program.[9] All hydrogen atoms were placed in geometrically idealized positions and constrained to ride on their carbon atom at distance 0.93 Å and with Uiso(H) = 1.2Ueq(C).

The structures for **4N-Cl** and **3N-I** were obtained from powder data.[11]

Crystallographic data for haloethynylnitrobenzene compounds

Code	4N-I	4N-Br	3,5DN-I	3,5DN-Br
Formula moiety	$C_8H_4INO_2$	$C_8H_4BrNO_2$	$C_8H_3IN_2O_4$	$C_8H_9BrN_2O_4$
Empirical formula	$C_8H_4INO_2$	$C_8H_4BrNO_2$	$C_8H_3IN_2O_4$	$C_8H_9BrN_2O_4$
Molecular weight	273.02	226.03	318.02	271.02
Color, Habit	bronze plate	bronze rod	orange plate	yellow block
Crystal system	Orthorhombic	Orthorhombic	Monoclinic	Monoclinic
Space group, Z	Pnma, 4	Pnma, 4	P2(1)/c, 4	$P2_1/c$, 4
a, Å	7.005(3)	6.8296(5)	8.2717(13)	8.361(1)
b, Å	9.681(4)	9.4723(8)	17.741(3)	17.158(2)
c, Å	12.490(5)	12.1948(10)	7.1646(11)	7.349(1)
α, °	90.00	90.00	90.00	90
β, °	90.00	90.00	114.558(4)	115.971(17)
γ, °	90.00	90.00	90.00	90
Volume, Å^3	847.0(6)	788.91(11)	956.3(3)	947.9(2)
Density, g/cm^3	2.141	1.903	2.209	1.899
Temperature, °K	120(2)	120(2)	120(2)	296(2)
Crystal size, min x mid x max	0.06 x 0.14 x 0.30	0.18 x 0.24 x 0.26	0.12 x 0.32 x 0.48	0.42 x 0.46 x 0.58
X-ray wavelength, Å	0.71073	0.71073	0.71073	0.71073
μ, mm^{-1}	3.735	5.161	3.343	4.331
Absorption corr	multi-scan	multi-scan	multi-scan	multi-scan
Trans min / max	0.4004 / 0.8069	0.3472 / 0.4568	0.2967 / 0.6898	0.114 / 0.159
θ_{min}, °	2.66	2.72	2.30	4.48
θ_{max}, °	31.04	33.12	32.91	27.99
Reflections				
collected	6377	7860	14259	2747
independent	1103	1429	3457	1888
observed	807	1112	3118	1220
Threshold expression	>2σ(I)	>2σ(I)	>2σ(I)	>2σ(I)
R1 (observed)	0.0413	0.0278	0.0277	0.0538
***w*R$_2$ (all)**	0.1300	0.0719	0.0681	0.1711
Goodness of fit (all)	1.052	1.066	1.031	1.071
Δρ max / min	1.700 / -0.986	0.432 / -0.553	1.195 / -0.857	0.496 / -0.479
2θ limit	27.50	30.00	32.50	25.24
Completeness to 2θ limit	0.954	0.998	0.989	0.874

Halogen bond geometries for Haloethynylnitrobenzene compounds

Compound	C-I/Br···O	O···I/Br (Å)	O···I,Br-C (°)
4N-I	C(22A)-I(1)···O(14A)#1 C(22A)-I(1)···O(14A)#2	3.247(5) 3.247(5)	160.60(10) 160.60(10)
4N-Br	C(18A)-Br(1)···O(14A)#1 C(18B)-Br(2)···O(14B)#2	3.1751(14) 3.13(3)	160.07(3) 157(5)
3,5DN-I	C(18)-I(1)···O(16)#1	3.0524(19)	168.15(8)
3,5DN-Br	C(8)-Br(1)···O(1) C(8)-Br(1)···O(2) C(8)-Br(1)···O(4)	3.502(6) 3.410(5) 3.064(4)	140.0(2) 67.9(2) 159.2(2)

Experimental details for co-crystals

The samples were analyzed with a Bruker APEX II system using MoKα radiation. Data collection was carried out using APEX2 software.[1] Initial cell constants were found by small widely separated "matrix" runs. Data collection strategies were determined using COSMO.[2] Scan

speed and scan widths were chosen based on scattering power and peak rocking curves. All datasets were collected at -153 °C using an Oxford Croystream low-temperature device.

Unit cell constants and orientation matrix were improved by least-squares refinement of reflections thresholded from the entire dataset. Integration was performed with SAINT,[3] using this improved unit cell as a starting point. Precise unit cell constants were calculated in SAINT from the final merged dataset. Lorenz and polarization corrections were applied. Multi-scan absorption corrections were performed with SADABS[4] unless otherwise indicated.

Data were reduced with SHELXTL.[5] The structure was solved by direct methods without incident. All hydrogen atoms were located in idealized positions and were treated with a riding model. Unless otherwise noted, non-hydrogen atoms were assigned anisotropic thermal parameters. Refinements continued to convergence, using the recommended weighting schemes.

4N-I:A23 - The crystal was a non-merohedral twin, and data were processed with TWINABS.[6] The asymmetric unit contains a half-iodo compound (located on a mirror plane), a quarter-diamine compound (located on a 2/m special position) and a solvent site (straddling a 2/m special position). Solvent was assigned as 10% ethyl acetate and 15% water. No attempt was made to locate the hydrogen atoms on the water. All solvent atoms shared the same isotropic thermal parameter. The ethyl acetate was constrained to an idealized geometry and refined as a rigid body.

4N-I:A24 - The asymmetric unit contains an iodo compound and a half-diamine compound (located on an inversion center).

4N-I:A32 - The asymmetric unit contains a single iodo compound and a single amine compound.

3N-I:A25 - The asymmetric unit contains an iodo compound and a half-diamine compound (located on an inversion center).

3N-I:A31 - The asymmetric unit contains two iodo compound / amine compound pairs. Each pair was assigned to a SHELXL RESIdue.

3N-I:A33 - The asymmetric unit contains an iodo compound and an amine / amine oxide compound. The nitro group was disordered over two closely related positions, representing wobble around the C-NO_2 bond. Geometries of the two species were restrained with the SAME command, and thermal parameters were pairwise constrained using EADP commands.

3,5DN-I:A22 - The asymmetric unit contains an iodo compound and a half-diamine compound (located on an inversion center).

3,5DN-I:A29[10] - Dataset was collected on an Oxford Diffraction Xcalibur four-circle kappa geometry single-crystal diffractometer with Sapphire 3 CCD detector, using a graphite monochromated MoKα (λ = 0.71073 Å) radiation, and applying the CrysAlisPro Software system[8] at 296 K. The crystal–detector distance was 45 mm.

Data reduction, including Lorentz and polarization corrections as well as absorption correction, was done by CrysAlis RED program.[8] The structure was solved by direct methods implemented in the SHELXS-2013 program.[9] The coordinates and the anisotropic displacement parameters for all non-hydrogen atoms were refined by full-matrix least-squares methods based on F^2 using the SHELXL-2013 program.[8]

All hydrogen atoms were placed in geometrically idealized positions and constrained to ride on their carbon atom at distances of 0.93 or 0.96 Å for aromatic or methyl hydrogen atoms, respectively, and with $U_{iso}(H) = 1.2U_{eq}(C)$ (for aromatic H) and $U_{iso}(H) = 1.5U_{eq}(C)$ (for methyl group).

3,5DN-I:A34 - The asymmetric unit contains an iodo compound and a half-amine / amine oxide compound. The latter compound straddles a crystallographic inversion center and was

assigned 50% occupancy. Thermal parameters for closely located atoms were pairwise constrained using the EADP command.

3N-Br:A27 - The asymmetric unit contains a bromo compound and a half-diamine compound (located on an inversion center).

Crystallographic data for co-crystals

Code	4N-I:A23	4N-I:A24	4N-I:A32	3N-I:A25	3N-I:A31
Formula moiety	$(C_8H_4INO_2)$ $(C_{10}H_8N_2)_1$ $(C_4H_8O_2)_{0.4}$ $(O)_{0.6}$	$(C_8H_4INO_2)$ $(C_{12}H_{12}N_2)$	$(C_8H_4INO_2)$ $(C_{11}H_9N_3)$	$(C_8H_4INO_2)_2$ $(C_{12}H_{10}N_2)$	$(C_8H_4INO_2)$ $(C_{11}H_9N)$
Empirical formula	$C_{27\cdot60}H_{19\cdot20}I_2N_4O_{5\cdot40}$	$C_{28}H_{20}I_2N_4O_4$	$C_{19}H_{13}IN_4O_2$	$C_{28}H_{18}I_2N_4O_4$	$C_{19}H_{13}IN_2O_2$
Molecular weight	747.07	730.28	456.23	728.26	428.21
Color, Habit	yellow plate	bronze plate	orange plate	orange plate	bronze prism
Crystal system	Monoclinic	Monoclinic	Triclinic	Monoclinic	Triclinic
Space group, Z	C2/m, 2	C2/c, 4	P -1, 2	C2/c, 4	P -1, 4
a, Å	37.367(9)	27.050(4)	6.9150(16)	30.735(4)	10.8063(11)
b, Å	9.281(2)	6.5379(9)	7.4716(17)	4.1717(5)	11.8386(12)
c, Å	3.9389(10)	15.045(2)	17.015(4)	24.404(3)	14.1068(15)
α, °	90.00	90.00	81.600(6)	90.00	75.741(3)
β, °	93.504(13)	90.353(3)	86.083(5)	122.674(2)	74.494(3)
γ, °	90.00	90.00	88.809(5)	90.00	77.324(3)
Volume, Å^3	1363.5(5)	2660.7(6)	867.6(3)	2633.9(5)	1662.5(3)
Density, g/cm^3	1.820	1.823	1.746	1.837	1.711
Temp, °K	120(2)	120(2)	120(2)	120(2)	120(2)
Crystal size, min x mid x max	0.06 x 0.20 x 0.34	0.18 x 0.42 x 0.44	0.240 x 0.380 x 0.500	0.08 x 0.28 x 0.42	0.220 x 0.300 x 0.420
X-ray wavelength, Å	0.71073	0.71073	0.71073	0.71073	0.71073
μ, mm^{-1}	2.353	2.406	1.867	2.430	1.939
Absorption corr	multi-scan	multi-scan	multi-scan	multi-scan	multi-scan
Trans min / max	0.5017 / 0.8717	0.4174 / 0.6713	0.518 / 0.663	0.4284 / 0.8293	0.596 / 0.675
θ_{min}, °	1.09	1.51	2.425	1.57	1.529
θ_{max}, °	30.70	31.75	32.067	31.62	32.384
Reflections					
collected	10251	23927	24441	18477	77079
independent	10251	4226	5375	4178	11385
observed	9111	3947	4820	3862	10260
Threshold expression	>2σ(I)	>2σ(I)	>2σ(I)	>2σ(I)	>2σ(I)
R_1 (observed)	0.0663	0.0184	0.0386	0.0201	0.0240
***w*R_2 (all)**	0.1853	0.0492	0.1262	0.0582	0.0610
Goodness of fit (all)	1.061	0.959	1.211	1.095	1.035
Δρ max / min	3.267 / -2.547	0.600 / -0.420	1.594 / -1.417	0.503 / -0.583	1.043 / -0.677
2θ limit	30.00	30.00	30.000	30.00	31.500
Completeness to 2θ limit	0.957	0.989	0.972	0.996	0.982

Code	3N-I:A33	3,5DN-I:A22	3,5DN-I:A29	3,5DN-I:A34	3N-Br:A27
Formula moiety	$(C_8H_4INO_2)$ $(C_4H_4N_2O)$	$(C_8H_3IN_2O_4)_2$ $(C_8H_{12}N_2)$	$(C_8H_3IN_2O_4)$ $0.5(C_8H_{12}N_2O_2)$	$(C_8H_3IN_2O_4)_2$ $(C_8H_{12}N_2O_2)$	$(C_8H_4INO_2)$ $(C_{10}H_8N_4)$
Empirical formula	$C_{12}H_8IN_3O_3$	$C_{24}H_{18}I_2N_6O_8$	$C_{12}H_9IN_3O_5$	$C_{24}H_{18}I_2N_6O_9$	$C_{26}H_{16}Br_2N_6O_4$
Molecular weight	369.11	772.24	402.12	788.24	636.27
Color, Habit	bronze rod	bronze prism	colourless block	red block	bronze prism
Crystal system	Triclinic	Triclinic	Monoclinic	Monoclinic	Triclinic
Space group, Z	P-1, 2	P-1, 1	C2/c, 8	C 2/c, 4	P -1, 1

a, Å	4.0966(5)	8.1864(10)	15.4144(6)	15.1898(10)	3.8963(5)
b, Å	11.8038(16)	8.5567(11)	8.2857(3)	8.2587(5)	11.7174(15)
c, Å	13.4460(18)	11.0361(14)	22.9469(7)	22.1641(14)	14.7266(18)
α, °	98.083(4)	70.225(3)	90.00	90	70.319(3)
β, °	97.777(3)	72.603(3)	95.327(3)	93.6905(17)	82.570(4)
γ, °	94.731(3)	68.891(3)	90.00	90	87.838(4)
Volume, Å^3	634.38(14)	664.70(14)	2918.1(2)	2774.7(3)	627.73(14)
Density, g/cm^3	1.932	1.929	1.831	1.887	1.683
Temp, °K	120(2)	120(2)	296(2)	120(2)	120(2)
Crystal size, min x mid x max	0.08 x 0.12 x 0.38	0.28 x 0.42 x 0.44	0.26 x 0.37 x 0.43	0.240 x 0.280 x 0.300	0.200 x 0.360 x 0.480
X-ray wavelength, Å	0.71073	0.71073	0.71073	0.71073	0.71073
μ, mm^{-1}	2.531	2.426	2.219	2.329	3.275
Absorption corr	multi-scan	multi-scan	multi-scan	multi-scan	multi-scan
Trans min / max	0.4463 / 0.8231	0.4149 / 0.5499	0.426 / 0.573	0.473 / 0.605	0.432 / 0.560
θ_{min}, °	1.75	2.00	4.60	1.841	1.846
θ_{max}, °	31.49	32.03	30.84	32.597	32.591
Reflections					
collected	16750	14426	7862	17959	18433
independent	4002	4337	4245	4749	4237
observed	3747	3996	3437	4565	3954
Threshold expression	>2σ(I)	>2σ(I)	>2σ(I)	>2σ(I)	>2σ(I)
R_1 (observed)	0.0278	0.0399	0.0331	0.0292	0.0298
wR_2 (all)	0.0728	0.1139	0.0775	0.0822	0.0795
Goodness of fit (all)	1.061	1.082	0.971	1.175	1.014
Δρ max / min	2.040 / -1.079	2.328 / -2.282	0.446 / -0.543	0.633 / -0.959	1.303 / -0.504
2θ limit	31.49	30.00	30.00	30.000	30.000
Completeness to 2θ limit	0.955	0.994	0.995	0.987	0.994

Halogen bond geometries for co-crystals

Co-crystal	C-I/Br···N/O	I/Br···O/N (Å)	C-I/Br···N/O (°)
4N-I:A23	C(18)-I(1)···N(21)	2.721(5)	179.9(3)
4N-I:A24	C(18)-I(1)···N(21)	2.7372(13)	174.46(5)
4N-I:A32	C(22)-I(1)···N(31)	2.714(3)	178.59(13)
3N-I:A25	C(18)-I(1)···N(21)	2.7549(17)	173.80(7)
3N-I:A31	C(221)-I(11)···N(311) C(222)-I(22)···N(312)	2.7301(13) 2.7096(14)	175.13(5) 175.80(5)
3N-I:A33	C(22)-I(1)···N(34)	2.792(2)	176.77(8)
3,5DN-I:A22	C(22)-I(1)···N(31)	2.933(3)	179.44(11)
3,5DN-I:A29	C(8)-I(1)···O(5)	2.734(2)	173.4(2)
3,5DN-I:A34	C(18)-I(1)···O(31) C(18)-I(1)···N(34)#1	2.673(3) 3.052(5)	171.97(10) 169.94(12)
3N-Br:A27	C(22)-Br(1)···N(31)	2.8452(13)	177.62(5)

B.6 Chapter 7

Experimental details

X-ray data were collected on a Bruker SMART APEX II CCD diffractometer at 120 K using, a fine-focus molybdenum Kα tube. Data were collected using APEX2[1] software. Initial cell

constants were found by small widely separated "matrix" runs. Scan speed and scan width were chosen based on scattering power and peak rocking curves. Unit cell constants and orientation matrix were improved by least-squares refinement of reflections thresholded from the entire dataset. Integration was performed with SAINT,[3] using this improved unit cell as a starting point. Precise unit cell constants were calculated in SAINT from the final merged dataset. Lorenz and polarization corrections were applied. Laué symmetry, space group, and unit cell contents were found with XPREP. Data were reduced with SHELXTL.[5] The structures were solved in all cases by direct methods without incident. All hydrogen atoms were assigned to idealized positions and were allowed to ride. Heavy atoms were refined with anisotropic thermal parameters. Absorption correction was carried out on all datasets.

Crystallographic data

Code	A36:D9	A37:D7	A29:D7	A38:D7	A29:D9
Formula moiety	(C_5H_5NO) $(C_6F_3I_3)$	(C_6H_7NO) $(C_6F_4I_2)$	$(C_8H_{12}N_2O_2)_2$ $(C_6F_4I_2)_4$	(C_6H_7NO) $(C_6F_4I_2)$	$(C_8H_{12}N_2O_2)$ $(C_6F_3I_3)_2$
Empirical formula	$C_{11}H_5F_3I_3NO$	$C_{12}H_7F_4I_2NO$	$C_{40}H_{24}F_{16}I_8N_4O_4$	$C_{12}H_7F_4I_2NO$	$C_{20}H_{12}F_6I_6N_2O_2$
Molecular weight	604.86	510.99	1943.83	510.99	1187.72
Color, Habit	colourless plate	colourless prism	colourless cube	colourless prism	colourless prism
Crystal size, mm^3	0.44 x 0.34 x 0.18	0.42 x 0.28 x 0.16	0.26 x 0.24 x 0.22	0.34 x 0.24 x 0.20	0.32 x 0.24 x 0.14
Crystal system	Monoclinic	Triclinic	Monoclinic	Monoclinic	Triclinic
Space group, Z	$P2_1/n$, 4	P-1, 2	$P2_1/c$, 4	$P2_1/c$, 4	P-1, 1
a, Å	12.4824(12)	7.9400(5)	14.1359(14)	7.8713(9)	7.9660(6)
b, Å	7.3041(7)	8.5688(6)	15.1116(15)	23.203(3)	9.2821(7)
c, Å	15.4872(16)	11.5503(8)	24.361(3)	7.8169(9)	10.1097(8)
α, °		89.243(2)			100.812(3)
β, °	97.536(3)	83.738(2)	105.927(3)	92.019(4)	106.262(2)
γ, °		65.570(2)			95.408(3)
Volume, $Å^3$	1399.8(2)	710.77(8)	5004.2(9)	1426.8(3)	696.28(9)
Density, g/cm^3	2.870	2.388	2.580	2.379	2.833
Temperature, °K	120(2)	120(2)	120(2)	120(2)	120(2)
X-ray wavelength	0.71073	0.71073	0.71073	0.71073	0.71073
μ, mm^{-1}	6.723	4.463	5.064	4.447	6.755
θ_{min}, °	2.25	1.77	1.60	1.76	2.15
θ_{max}, °	32.54	32.57	33.14	32.66	33.13
Reflections					
collected	13950	11235	81993	16697	18582
independent	4568	4521	18382	5006	4468
observed	4343	4212	16534	4805	4255
Absorption corr	multi-scan	multi-scan	multi-scan	multi-scan	multi-scan
trans min / max	0.1559 / 0.3775	0.2558 / 0.5354	0.3527 / 0.4021	0.3132 / 0.4700	0.2211 / 0.4515
Threshold expression	>2σ(I)	>2σ(I)	>2σ(I)	>2σ(I)	>2σ(I)
R_1 (observed)	0.0249	0.0288	0.0341	0.0221	0.0204
wR_2 (all)	0.0586	0.0768	0.0816	0.0505	0.0530
S	1.210	1.089	1.025	1.186	1.133
Δρ max / min	0.854 / -1.792	2.286 / -0.812	7.622 / -6.171	0.704 / -0.679	1.535 / -0.912

Halogen bond geometries

Co-crystal	C-I···O	I···O (Å)	C-I···O (°)
A36:D9	C(21)-I(21)···O(11) C(23)-I(23)···O(11)#2	2.7413(0.0019) 2.8082(19)	176.90(8) 179.54(9)
A37:D7	C(21)-I(1)···O(11) C(22)-I(2)···O(11)#1	2.833(2) 2.848(2)	166.68(8) 170.30(8)
A29:D7	C(52)-I(2)···O(14)#1 C(61)-I(3)···O(31) C(71)-I(5)···O(14) C(72)-I(6)···O(11)#1 C(81)-I(7)···O(34)	2.893(2) 2.854(2) 2.918(2) 2.889(2) 2.870(2)	171.12(9) 168.41(9) 167.54(9) 163.06(9) 168.44(9)
A38:D7	C(21)-I(1)···O(11) C(22)-I(2)···O(11)#1	2.7729(17) 2.7739(17)	175.73(7) 172.03(7)
A29:D9	C(11)-I(11)···O(21) C(13)-I(13)···O(21)#1	2.7413(19) 2.8809(18)	173.62(8) 170.97(8)

B.7 Chapter 8

Experimental details

Datasets were collected on a Bruker APEX II system using MoKα radiation using APEX2 software.[1] Initial cell constants were found by small widely separated "matrix" runs. Data collection strategies were determined using COSMO.[2] Scan speed and scan widths were chosen based on scattering power and peak rocking curves. All datasets were collected at -153 °C using an Oxford Croystream low-temperature device.

Unit cell constants and orientation matrix were improved by least-squares refinement of reflections thresholded from the entire dataset. Integration was performed with SAINT,[3] using this improved unit cell as a starting point. Precise unit cell constants were calculated in SAINT from the final merged dataset. Lorenz and polarization corrections were applied. Multi-scan absorption corrections were performed with SADABS.[4] Data were reduced with SHELXTL.[5] The structures were solved in all cases by direct methods without incident. Except for **A29:D3**, all molecules were fully ordered. In **A29:D3** the unit cell contains two halo compounds and two half-pyrazines. The contents were divided into two SHELXL RESIdues for refinement. One of the four $–CF_2I$

termini was slightly disordered, in an ~ 85%:15% ratio. Thermal parameter constraints and distance restraints were used to refine the minor species to convergence.

Crystallographic data

Code	A29:D1	A33:D2	A29:D2	A29:D3
Formula moiety	$(C_8H_{12}N_2O_2)(C_2F_4I_2)$	$(C_4H_4N_2O)(C_4F_8I_2)$	$(C_8H_{12}N_2O_2)(C_4F_8I_2)$	$(C_8H_{12}N_2O_2)(C_6F_{12}I_2)_2$
Empirical formula	$C_{10}H_{12}F_4I_2N_2O_2$	$C_8H_4F_8I_2N_2O$	$C_{12}H_{12}F_8I_2N_2O_2$	$C_{20}H_{12}F_{24}I_4N_2O_2$
Molecular weight	522.02	549.93	622.04	1275.92
Color, Habit	colourless plate	yellow prism	colourless plate	colourless prism
Crystal system	Monoclinic	Triclinic	Monoclinic	Triclinic
Space group, Z	P2(1)/c, 2	P-1, 2	P2(1)/c, 2	P-1, 2
a, Å	8.6275(16)	5.3515(5)	9.3817(10)	12.3893(14)
b, Å	12.005(2)	11.1482(11)	12.8620(14)	12.6332(14)
c, Å	8.3466(15)	12.0159(12)	8.1127(9)	13.1553(14)
α, °	90.00	85.076(2)	90.00	67.319(4)
β, °	118.080(5)	80.408(3)	110.521(3)	75.273(4)
γ, °	90.00	84.424(2)	90.00	67.884(4)
Volume, Å^3	762.7(2)	701.72(12)	916.82(17)	1745.6(3)
Density, g/cm^3	2.273	2.603	2.253	2.427
Temperature, °K	120(2)	120(2)	120(2)	120(2)
Crystal size, min x mid x max	0.10 x 0.22 x 0.28	0.14 x 0.28 x 0.34	0.08 x 0.26 x 0.40	0.18 x 0.24 x 0.32
X-ray wavelength, Å	0.71073	0.71073	0.71073	0.71073
μ, mm^{-1}	4.167	4.571	3.517	3.723
Absorption corr	multi-scan	multi-scan	multi-scan	multi-scan
Trans min / max	0.3883 / 0.6807	0.3056 / 0.5670	0.3336 / 0.7662	0.3821 / 0.5538
θ_{min}, °	2.68	2.61	2.32	1.69
θ_{max}, °	32.03	33.72	32.95	32.11
Reflections				
collected	11427	18809	11185	38902
independent	2488	5086	3188	11420
observed	2326	4597	2911	9437
Threshold expression	>2σ(I)	>2σ(I)	>2σ(I)	>2σ(I)
R1 (observed)	0.0227	0.0258	0.0230	0.0421
***w*R$_2$ (all)**	0.0527	0.0723	0.0615	0.1218
Goodness of fit (all)	1.039	1.128	1.082	0.994
Δρ max / min	2.752 / -1.138	0.639 / -0.969	0.776 / -1.122	1.496 / -1.733
2θ limit	31.00	30.00	30.00	30.00
R1 (observed)	0.0227	0.0258	0.0230	0.0421

Halogen bond geometries

Co-crystal	C-I···N/O	I···O/N (Å)	C-I···N/O (^{0})
A29:D1	C(31)-I(1)···O(11)	2.7767(16)	171.75(7)
A33:D2	C(21)-I(1)···O(11) C(24)-I(2)···N(14)#1	2.8543(18) 2.902(2)	163.78(8) 177.95(10)
A29:D2	C(31)-I(1)···O(11)	2.7617(16)	174.62(7)
A29:D3	C311-I11···O111 C361-I21···O112 C312-I32···O112	2.812(3) 2.770(3) 2.810(3)	174.45(13) 175.87(14) 175.72(17)

B.8 Chapter 9

Experimental details

Datasets were collected on a Bruker APEX II system using MoKa radiation using APEX2 software.[1] Initial cell constants were found by small widely separated "matrix" runs. Data collection strategies were determined using COSMO.[2] Scan speed and scan widths were chosen based on scattering power and peak rocking curves. All datasets were collected at -153 °C using an Oxford Croystream low-temperature device.

Unit cell constants and orientation matrix were improved by least-squares refinement of reflections thresholded from the entire dataset. Integration was performed with SAINT,[3] using this improved unit cell as a starting point. Precise unit cell constants were calculated in SAINT from the final merged dataset. Lorenz and polarization corrections were applied. Multi-scan absorption corrections were performed with SADABS.[4]

Data were reduced with SHELXTL.[5] The structures were solved in all cases by direct methods without incident. Coordinates for the nitramine hydrogen atoms were allowed to refine. All other hydrogen atoms were located in idealized positions and were treated with a riding model. All non-hydrogen atoms were assigned anisotropic thermal parameters. Refinements continued to convergence, using the recommended weighting schemes.

Crystallographic data

Code	EDNA:A23	EDNA:A24	EDNA:A25	EDNA:A27	EDNA:A28	EDNA:A32
Formula moiety	$(C_2H_6N_4O_4)$ $(C_{10}H_8N_2)$	$(C_2H_6N_4O_4)$ $(C_{12}H_{12}N_2)$	$(C_2H_6N_4O_4)$ $(C_{12}H_{10}N_2)$	$(C_2H_6N_4O_4)$ $(C_{10}H_8N_4)$	$(C_2H_6N_4O_4)$ $(C_4H_4N_2O_2)$	$(C_2H_6N_4O_4)$ $(C_{11}H_9N_3)_2$
Empirical formula	$C_{12}H_{14}N_6O_4$	$C_{14}H_{18}N_6O_4$	$C_{14}H_{16}N_6O_4$	$C_{12}H_{14}N_8O_4$	$C_6H_{10}N_6O_6$	$C_{24}H_{24}N_{10}O_4$
Molecular weight	306.29	334.34	332.33	334.31	262.20	516.53
Color, Habit	colourless prism	colourless plate	colourless prism	orange plate	colourless plate	orange prism
Crystal system	Monoclinic	Triclinic	Triclinic	Triclinic	Triclinic	Monoclinic
Space group, Z	C2/c, 8	P-1, 2	P-1, 1	P-1, 1	P-1, 1	C2/c, 4
a, Å	24.520(4)	6.3530(4)	5.596(3)	4.6203(8)	4.9014(6)	15.959(3)
b, Å	8.9878(14)	9.0752(6)	5.937(4)	5.9591(11)	5.5303(6)	5.9411(11)
c, Å	13.431(2)	14.3940(10)	12.577(7)	13.434(2)	10.5912(12)	25.382(5)
α, °	90.00	79.611(4)	88.615(13)	82.499(7)	75.475(4)	90.00
β, °	112.585(9)	77.859(3)	81.533(13)	84.010(7)	89.206(5)	95.332(9)

γ, °	90.00	79.588(3)	66.280(11)	83.819(7)	69.384(4)	90.00
Volume, Å^3	2733.0(7)	789.17(9)	378.1(4)	363.04(11)	259.23(5)	2396.2(8)
Density, g/cm^3	1.489	1.407	1.460	1.529	1.680	1.432
Temperature, °K	120(2)	120(2)	120(2)	120(2)	120(2)	120(2)
Crystal size, min x mid x max	0.12 x 0.20 x 0.32	0.10 x 0.34 x 0.42	0.12 x 0.30 x 0.46	0.12 x 0.34 x 0.48	0.10 x 0.38 x 0.42	0.12 x 0.22 x 0.38
X-ray wavelength, Å	0.71073	0.71073	0.71073	0.71073	0.71073	0.71073
μ, mm^{-1}	0.115	0.106	0.111	0.119	0.150	0.103
Absorption corr	multi-scan	multi-scan	multi-scan	multi-scan	multi-scan	multi-scan
Trans min / max	0.9640 / 0.9863	0.9567 / 0.9894	0.9508 / 0.9868	0.9449 / 0.9858	0.9398 / 0.9852	0.9619 / 0.9877
θ_{min}, °	1.80	1.46	1.64	1.54	1.99	1.61
θ_{max}, °	32.02	30.99	30.67	32.08	32.08	31.56
Reflections						
collected	13309	14843	8238	6893	3707	12455
independent	4228	4581	2265	2269	1654	3665
observed	2510	2983	1800	1971	1422	2609
Threshold expression	>2σ(I)	>2σ(I)	>2σ(I)	>2σ(I)	>2σ(I)	>2σ(I)
R1 (observed)	0.0536	0.0649	0.0639	0.0399	0.0388	0.0568
***w*R$_2$ (all)**	0.1545	0.1832	0.1876	0.1202	0.1110	0.1760
Goodness of fit (all)	1.038	1.069	1.366	1.079	1.076	1.106
Δρ max / min	0.357 / -0.326	0.298 / -0.480	0.591 / -0.304	0.407 / -0.308	0.408 / -0.295	0.435 / -0.335
2θ limit	30.00	27.50	30.67	30.00	30.00	30.00
Completeness to 2θ limit	0.983	0.990	0.973	0.984	0.977	0.959

Hydrogen bond geometries

Co-crystal	D–H···A/Å	D–H/Å	H···A/Å	D···A/Å	D–H···N/°
EDNA:A23	N(12)-H(12)···N(21) N(15)-H(15)···N(31)#1	0.95(18) 1.5(18)	1.85(19) 1.74(18)	2.787(19) 2.788(19)	169.6(15) 176.9(15)
EDNA:A24	N121-H121···N211 N122-H122···N212	0.83(2) 0.97(2)	1.98(2) 1.82(2)	2.780(2) 2.770(2)	164(2) 169.2(17)
EDNA:A25	N(12)-H(12)···N(21)	0.89(2)	1.87(2)	2.747(2)	167.5(19)
EDNA:A27	N(12)-H(12)···N(21)	0.92(15)	1.93(15)	2.841(12)	175.0(13)
EDNA:A28	N(12)-H(12)···O(21)	0.90(18)	1.86(18)	2.720(13)	159.4(16)
EDNA:A32	N(12)-H(12)···N(21)	0.92(17)	1.89(17)	2.818(17)	176.4(16)

References

1. APEXII v2009. 5-1, © **2009**, Bruker Analytical X-ray Systems, Madison, WI.

2. COSMO v1. 60, © **1999 - 2009**, Bruker Analytical X-ray Systems, Madison, WI.

3. SAINT v7. 60a, © **1997 - 2008**, Bruker Analytical X-ray Systems, Madison, WI.

4. SADABS v2008/1, © **2008**, Bruker Analytical X-ray Systems, Madison, WI.

5. SHELXTL v2008/4, © **2008**, Bruker Analytical X-ray Systems, Madison, WI.

6. TWINABS v2012/1, © **2012**, Bruker Analytical X-ray Systems, Madison, WI.

7. Data collection and structure solution were done at University of California, San Diego by Dr. Curtis Moore.

8. Oxford Diffraction, Xcalibur CCD System, CrysAlis Software System, Version 171.31, Oxford Diffraction Ltd., **2004**.

9. Sheldrick, G. M.; *Acta Crystallogr. Sect. A: Found. Crystallogr.* **2008**, *A64*, 112–122.

10. Data collection and structure solution were done at University of Zagreb, Croatia by Dr. Marijana Dakovic.

11. Powder data collaction and structure solution were done at Max Planck Institute for Solid State Research, Germany by Dr. Tomce Runcevski.

Appendix C - **IR data, DSC data and PXRD data**

C.1 Chapter 5

Grinding IR data for the successful co-crystal formations

Mixture	IR bands (cm^{-1})		Shifts Δcm^{-1}
	Halogen-bond donors	Ground mixture	
A16:D2	1192 1041	1178 1048	-14 +7
A16:D6	1488 805	1481 796	-7 -9
A16:D7	1309 772	1305 765	-4 -7
A16:D8	1459 941	1456 937	-3 -4
A16:D10	1459 954	1456 950	-3 -4
A17:D1	1100 693	1095 700	-5 +7
A17:D2	1192 634	1184 637	-7 +3
A17:D3	1199 1086	1201 1078	+3 -8
A17:D6	1488 805	1485 800	-3 -5
A17:D7	1489 1438	1484 1432	-5 -6
A17:D8	1459 759	1456 751	-3 -7
A17:D9	1403 1049	1398 1045	-5 -4
A17:D10	1219 954	1216 950	-3 -4
A17:D14	1471 772	1459 769	-11 -3
A17:D15	1464 955	1468 959	-4 +3
A18:D3	1199 1141	1191 1153	-7 +11
A18:D7	1489 1438	1484 1435	-5 -4
A18:D8	1459 759	1453 751	-6 -7
A18:D10	1459 954	1456 944	-3 -10
A18:D14	1471 772	1465 769	-6 -3
A19:D1	1100 693	1096 702	-4 +9
A19:D2	1192 1133	1188 1125	-3 -7

A19:D3	1199 1086	1209 1079	+10 -7
A19:D4	1204 834	1216 830	+12 -4
A19:D6	1488 805	1484 798	-4 -7
A19:D8	1459 759	1455 752	-4 -7
A19:D9	1563 1049	1560 1044	-3 -5
A19:D10	1459 954	1453 949	-6 -7
A20:D7	1110 1438	1104 1442	-6 +4
A20:D8	1212 1460	1215 1451	+3 -9

C.2 Chapter 6

Analysis for IR markers

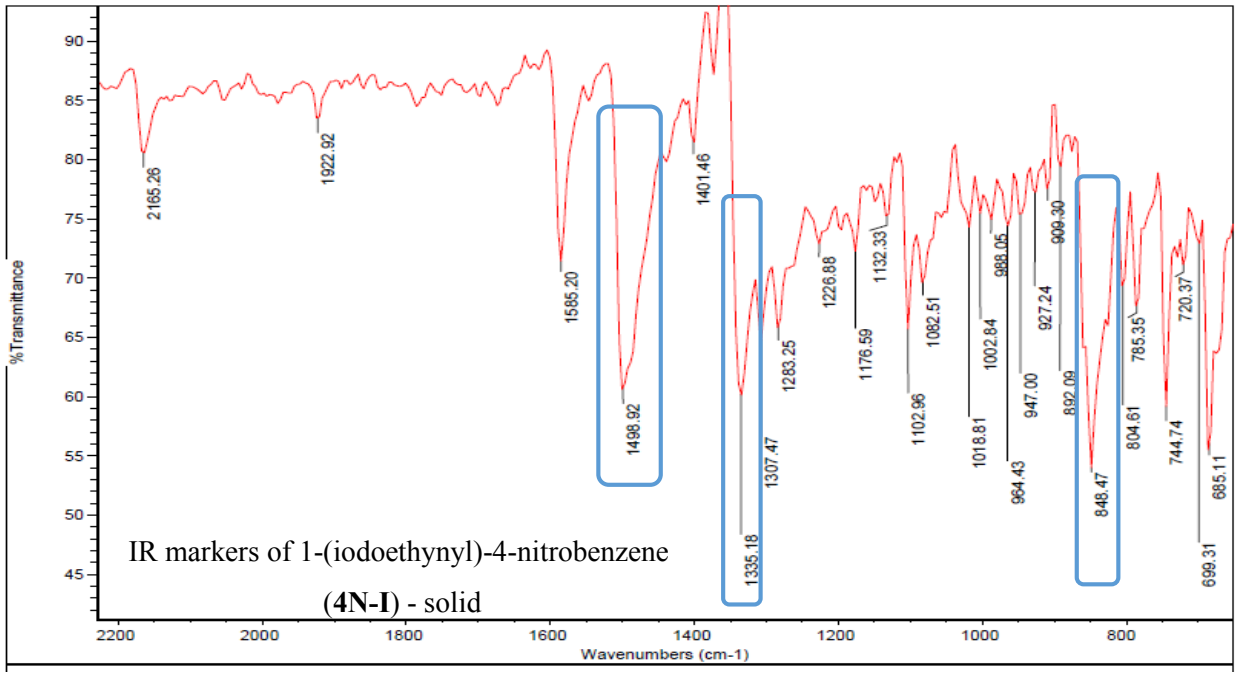

IR markers of 1-(iodoethynyl)-4-nitrobenzene (**4N-I**) - solid

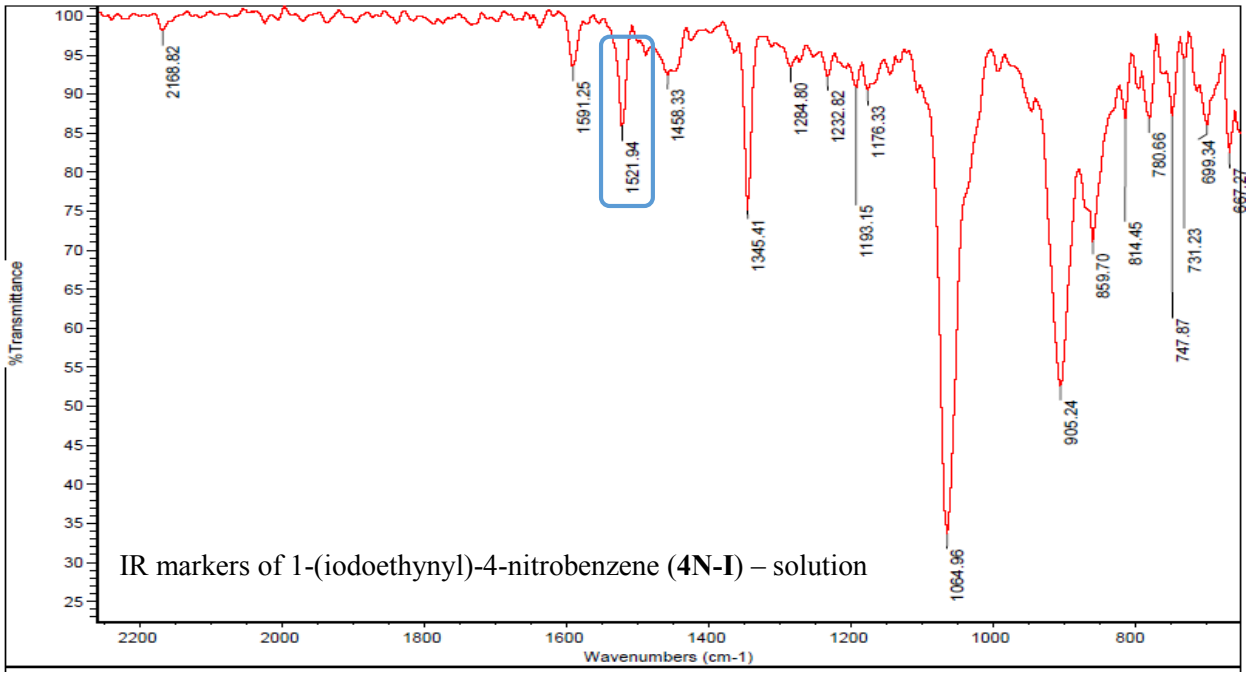

IR markers of 1-(iodoethynyl)-4-nitrobenzene (**4N-I**) – solution

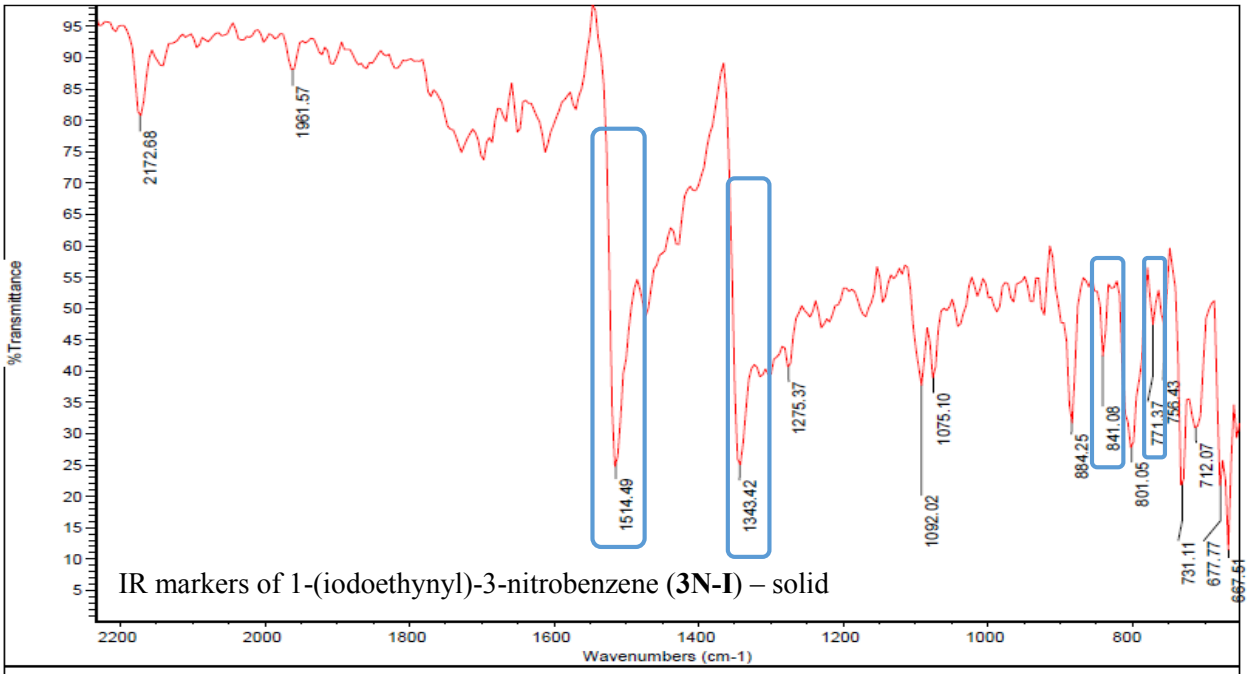

IR markers of 1-(iodoethynyl)-3-nitrobenzene (**3N-I**) – solid

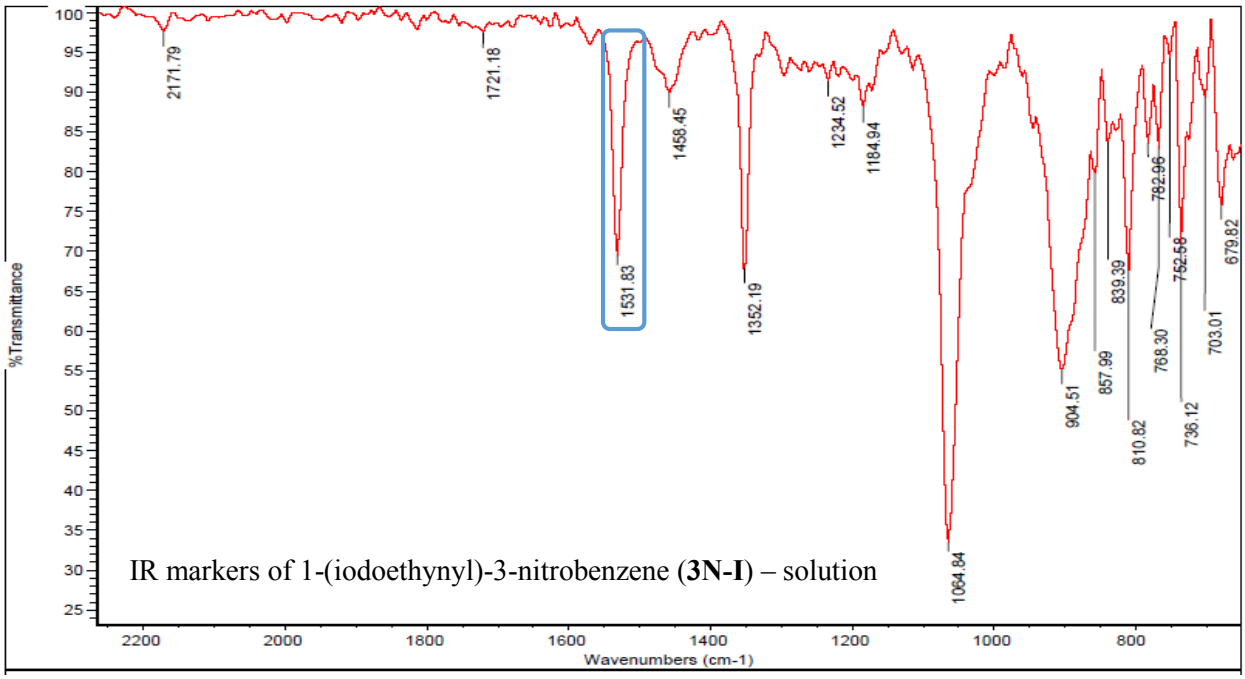

IR markers of 1-(iodoethynyl)-3-nitrobenzene (**3N-I**) – solution

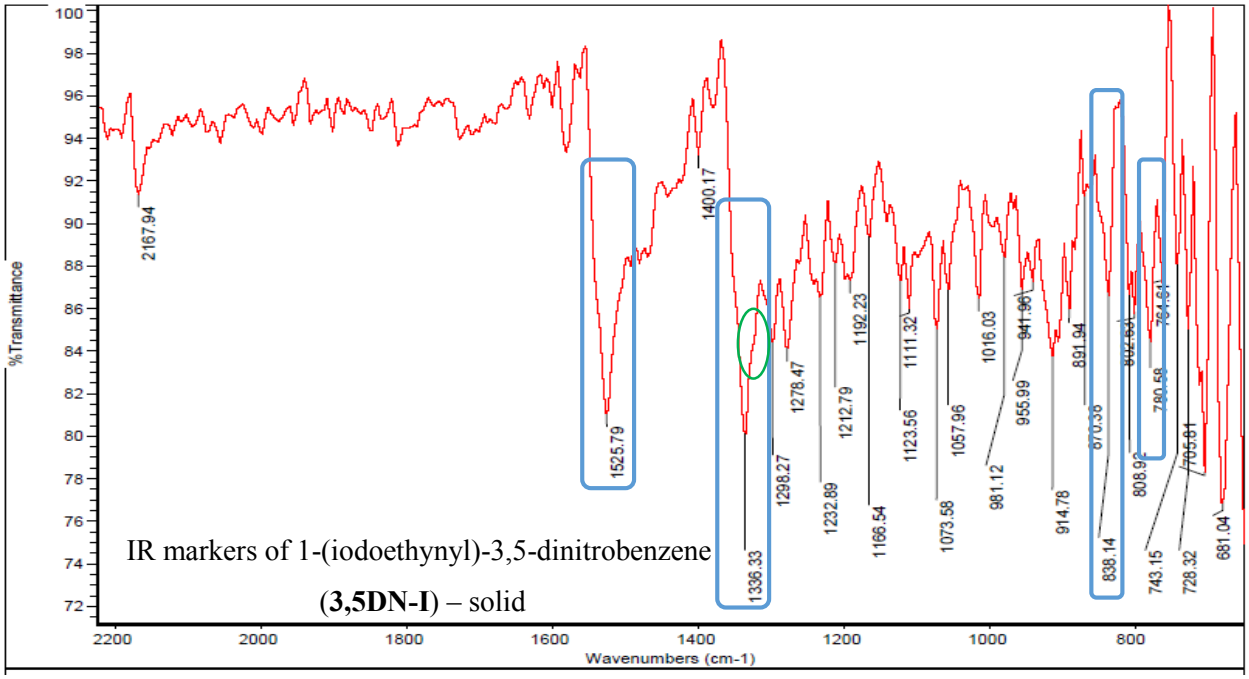

IR markers of 1-(iodoethynyl)-3,5-dinitrobenzene (**3,5DN-I**) – solid

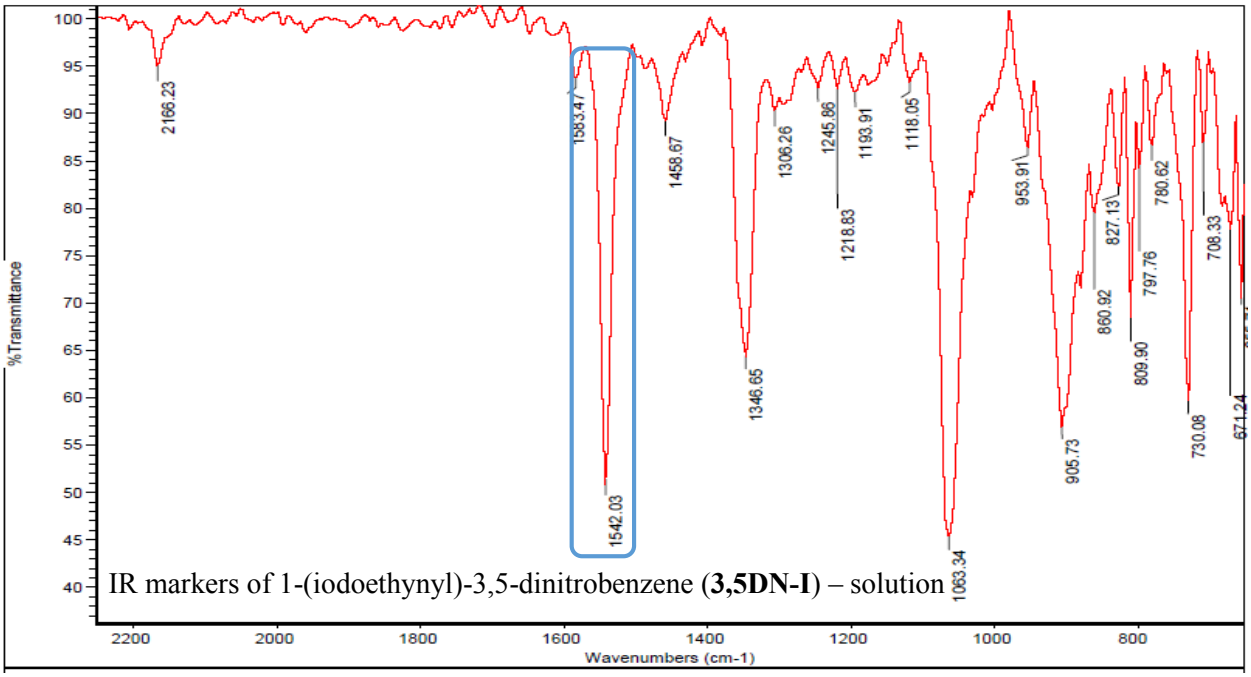

IR markers of 1-(iodoethynyl)-3,5-dinitrobenzene (**3,5DN-I**) – solution

Experimental and IR data - iodoethynylnitrobenzenes

Code	Combined stoichiometry	IR results (wave numbers cm^{-1})		Shifts Δ (cm^{-1})	Result	Crystal formation from solution
		Halogen-bond donor	Co-crystal			
4N-I:A21	2:1	2165 (triple bond) 1498 (nitro asy.) 1335 (nitro sym.)	2170 1503 1340	+5 +5 +5	Co-crystal	Y
4N-I:A22	2:1	2165 (triple bond) 1498 (nitro asy.) 1335 (nitro sym.)	2168 1500 1338	+3 +2 +3	Co-crystal	Y
4N-I:A23	2:1	2165 (triple bond) 1498 (nitro asy.) 1335 (nitro sym.)	2151 1511 1338	-14 +13 +3	Co-crystal	Y
4N-I:A24	2:1	2165 (triple bond) 1498 (nitro asy.) 1335 (nitro sym.)	2152 1510 1338	-13 +12 +3	Co-crystal	Y
4N-I:A25	2:1	2165 (triple bond) 1498 (nitro asy.) 1335 (nitro sym.)	2155 1504 1339	-10 +6 +4	Co-crystal	Powder
4N-I:A26	2:1	2165 (triple bond) 1498 (nitro asy.) 1335 (nitro sym.)	2152 1508 1339	-13 +8 +4	Co-crystal	Y
4N-I:A27	2:1	2165 (triple bond) 1498 (nitro asy.) 1335 (nitro sym.)	2152 1510 1336	-13 +12 +1	Co-crystal	Y
4N-I:A28	2:1	2165 (triple bond) 1498 (nitro asy.) 1335 (nitro sym.)	2169 1499 1338	+4 +1 +3	Co-crystal	Y
4N-I:A29	2:1	2165 (triple bond) 1498 (nitro asy.) 1335 (nitro sym.)	2170 1500 1337	+5 +2 +2	Co-crystal	Y
4N-I:A30	2:1	2165 (triple bond) 1498 (nitro asy.) 1335 (nitro sym.)	2168 1487 1342	+3 -12 +7	Co-crystal	Y
4N-I:A31	1:1	2165 (triple bond) 1498 (nitro asy.) 1335 (nitro sym.)	2152 1508 1338	-13 +10 +3	Co-crystal	Y
4N-I:A32	1:1	2165 (triple bond) 1498 (nitro asy.) 1335 (nitro sym.)	2156 1501 1337	-9 +3 +2	Co-crystal	Y
4N-I:A33	2:1	2165 (triple bond) 1498 (nitro asy.) 1335 (nitro sym.)	2168 1495 1334	+3 +3 -1	Co-crystal	Y
4N-I:A34	2:1	2165 (triple bond) 1498 (nitro asy.) 1335 (nitro sym.)	2169 1499 1338	+4 +1 +3	Co-crystal	Y
4N-I:A35	2:1	2165 (triple bond) 1498 (nitro asy.) 1335 (nitro sym.)	2177 1509 1341	+15 +11 +6	Co-crystal	Powder
3N-I:A21	2:1	2172 (triple bond) 1514 (nitro asy.) 1343 (nitro sym.)	2151 1502 1336	-21 -12 -7	Co-crystal	Y

3N-I:A22	2:1	2172 (triple bond) 1514 (nitro asy.) 1343 (nitro sym.)	2159 1499 1339	-13 -15 -4	Co-crystal	Y
3N-I:A23	2:1	2172 (triple bond) 1514 (nitro asy.) 1343 (nitro sym.)	2163 1519 1347	-9 +5 +4	Co-crystal	Y
3N-I:A24	2:1	2172 (triple bond) 1514 (nitro asy.) 1343 (nitro sym.)	2159 1522 1348	-13 +8 +5	Co-crystal	Y
3N-I:A25	2:1	2172 (triple bond) 1514 (nitro asy.) 1343 (nitro sym.)	2159 1520 1346	-13 +6 +3	Co-crystal	Y
3N-I:A26	2:1	2172 (triple bond) 1514 (nitro asy.) 1343 (nitro sym.)	2159 1522 1344	-13 +8 +1	Co-crystal	Y
3N-I:A27	2:1	2172 (triple bond) 1514 (nitro asy.) 1343 (nitro sym.)	2168 1519 1346	-4 +5 +3	Co-crystal	Y
3N-I:A28	2:1	2172 (triple bond) 1514 (nitro asy.) 1343 (nitro sym.)	2175 1519 1347	+3 +5 +4	Co-crystal	Powder
3N-I:A29	2:1	2172 (triple bond) 1514 (nitro asy.) 1343 (nitro sym.)	2168 1516 1346	-4 +2 +3	Co-crystal	Y
3N-I:A30	2:1	2172 (triple bond) 1514 (nitro asy.) 1343 (nitro sym.)	2156 1515 1346	-16 +1 +3	Co-crystal	Y
3N-I:A31	1:1	2172 (triple bond) 1514 (nitro asy.) 1343 (nitro sym.)	2159 1519 1345	-13 +5 +2	Co-crystal	Y
3N-I:A32	1:1	2172 (triple bond) 1514 (nitro asy.) 1343 (nitro sym.)	2177 1515 1346	+5 +1 +3	Co-crystal	Y
3N-I:A33	2:1	2172 (triple bond) 1514 (nitro asy.) 1343 (nitro sym.)	2176 1522 1352	+4 +8 +9	Co-crystal	Y
3N-I:A34	2:1	2172 (triple bond) 1514 (nitro asy.) 1343 (nitro sym.)	2151 1520 1348	-21 +6 +5	Co-crystal	Y
3N-I:A35	2:1	2172 (triple bond) 1514 (nitro asy.) 1343 (nitro sym.)	2169 1518 1350	+3 +4 +7	Co-crystal	Y
3,5DN-I:A21	2:1	2167 (triple bond) 1525 (nitro asy.) 1336 (nitro sym.)	2159 1533 1339	-8 +8 +3	Co-crystal	Powder
3,5DN-I:A22	2:1	2167 (triple bond) 1525 (nitro asy.) 1336 (nitro sym.)	2156 1529 1338	-11 +4 +2	Co-crystal	Y
3,5DN-I:A23	2:1	2167 (triple bond) 1525 (nitro asy.) 1336 (nitro sym.)	2154 1532 1346	-13 +7 +10	Co-crystal	Y
3,5DN-I:A24	2:1	2167 (triple bond) 1525 (nitro asy.) 1336 (nitro sym.)	2157 1532 1339	-10 +7 +3	Co-crystal	Y
3,5DN-I:A25	2:1	2167 (triple bond)	2158	-9	Co-crystal	Y

		1525 (nitro asy.) 1336 (nitro sym.)	1528 1339	+3 +3		
3,5DN-I:A26	2:1	2167 (triple bond) 1525 (nitro asy.) 1336 (nitro sym.)	2151 1532 1341	-16 +7 +5	Co-crystal	Y
3,5DN-I:A27	2:1	2167 (triple bond) 1525 (nitro asy.) 1336 (nitro sym.)	2150 1531 1343	-17 +6 +7	Co-crystal	Y
3,5DN-I:A28	2:1	2167 (triple bond) 1525 (nitro asy.) 1336 (nitro sym.)	2160 1533 1340	-7 +8 +4	Co-crystal	Y
3,5DN-I:A29	2:1	2167 (triple bond) 1525 (nitro asy.) 1336 (nitro sym.)	2160 1531 1342	-7 +6 +6	Co-crystal	Y
3,5DN-I:A30	2:1	2167 (triple bond) 1525 (nitro asy.) 1336 (nitro sym.)	2160 1533 1340	-7 +8 +4	Co-crystal	Y
3,5DN-I:A31	1:1	2167 (triple bond) 1525 (nitro asy.) 1336 (nitro sym.)	2177 1530 1340	+10 +5 +4	Co-crystal	Y
3,5DN-I:A32	1:1	2167 (triple bond) 1525 (nitro asy.) 1336 (nitro sym.)	2163 1526 1341	-4 +1 +5	Co-crystal	Y
3,5DN-I:A33	2:1	2167 (triple bond) 1525 (nitro asy.) 1336 (nitro sym.)	2171 1531 1341	+4 +6 +5	Co-crystal	Y
3,5DN-I:A34	2:1	2167 (triple bond) 1525 (nitro asy.) 1336 (nitro sym.)	2170 1531 1342	+3 +6 +6	Co-crystal	Y
3,5DN-I:A35	2:1	2167 (triple bond) 1525 (nitro asy.) 1336 (nitro sym.)	2150 1530 1341	-17 +5 +5	Co-crystal	Powder

Experimental and IR data - bromoethynylnitrobenzenes

Code	Combined stoichiometry	IR results (wave numbers cm^{-1})		Shifts Δ (cm^{-1})	Result	Crystal formation from solution
		Halogen-bond donor	Co-crystal			
4N-Br:A23	2:1	2190 (triple bond) 1502 (nitro asy.) 1341 (nitro sym.)	2194 1505 1340	+4 +3 -1	Co-crystal	Flimsy crystals
4N-Br:A24	2:1	2190 (triple bond) 1502 (nitro asy.) 1341 (nitro sym.)	2194 1503 1340	+4 -2 -1	Co-crystal	Powder
4N-Br:A27	2:1	2190 (triple bond) 1502 (nitro asy.) 1341 (nitro sym.)	2188 1502 1341	-2 0 0	Not a co-crystal	NA
4N-Br:A31	1:1	2190 (triple bond) 1502 (nitro asy.) 1341 (nitro sym.)	2193 1503 1343	+3 +1 +2	Co-crystal	Flimsy crystals
4N-Br:A33	2:1	2190 (triple bond) 1502 (nitro asy.) 1341 (nitro sym.)	2190 1503 1340	0 +1 -1	Not a co-crystal	Flimsy crystals
3N-Br:A23	2:1	2198 (triple bond) 1518 (nitro asy.) 1344 (nitro sym.)	2193 1523 1346	-5 +5 +2	Co-crystal	Powder
3N-Br:A24	2:1	2198 (triple bond) 1518 (nitro asy.) 1344 (nitro sym.)	2199 1519 1344	+1 +1 0	Not a co-crystal	NA
3N-Br:A27	2:1	2198 (triple bond) 1518 (nitro asy.) 1344 (nitro sym.)	2190 1521 1343	-8 +3 -1	Co-crystal	Flimsy crystals
3N-Br:A31	1:1	2198 (triple bond) 1518 (nitro asy.) 1344 (nitro sym.)	2201 1521 1347	+3 +3 +3	Co-crystal	Powder
3N-Br:A33	2:1	2198 (triple bond) 1518 (nitro asy.) 1344 (nitro sym.)	2194 1523 1344	-4 +5 0	Co-crystal	Gel
3,5DN-Br:A23	2:1	2193 (triple bond) 1532 (nitro asy.) 1339 (nitro sym.)	2196 1531 1342	+3 -1 +3	Co-crystal	Powder
3,5DN-Br:A24	2:1	2193 (triple bond) 1532 (nitro asy.) 1339 (nitro sym.)	2193 1533 1340	0 +1 +1	Not a co-crystal	NA
3,5DN-Br:A27	2:1	2193 (triple bond) 1532 (nitro asy.) 1339 (nitro sym.)	2197 1534 1341	+4 +2 +2	Co-crystal	Flimsy crystals
3,5DN-Br:A31	1:1	2193 (triple bond) 1532 (nitro asy.) 1339 (nitro sym.)	2193 1532 1341	0 0 +2	Not a co-crystal	NA
3,5DN-Br:A33	2:1	2193 (triple bond) 1532 (nitro asy.) 1339 (nitro sym.)	2193 1532 1339	0 0 0	Not a co-crystal	NA

Experimental and IR data - chloroethynylnitrobenzenes

Code	Combined stoichiometry	IR results (wave numbers cm^{-1})		Shifts Δ (cm^{-1})	Co-crystal or not	Crystal formation from solution
		Halogen-bond donor	Co-crystal			
4N-Cl:A23	2:1	2208 (triple bond) 1505 (nitro asy.) 1343 (nitro sym.)	2210 1507 1341	+2 +2 -2	Not a co-crystal	NA
4N-Cl :A24	2:1	2208 (triple bond) 1505 (nitro asy.) 1343 (nitro sym.)	2209 1503 1341	+1 -2 -2	Not a co-crystal	NA
4N-Cl :A27	2:1	2208 (triple bond) 1505 (nitro asy.) 1343 (nitro sym.)	2210 1505 1342	+2 0 -1	Not a co-crystal	NA
4N-Cl :A31	1:1	2208 (triple bond) 1505 (nitro asy.) 1343 (nitro sym.)	2209 1507 1343	+1 +2 0	Not a co-crystal	NA
4N-Cl:A33	2:1	2208 (triple bond) 1505 (nitro asy.) 1343 (nitro sym.)	2210 1503 1343	+2 -2 0	Not a co-crystal	NA
3N-Cl:A23	2:1	2221 (triple bond) 1524 (nitro asy.) 1337 (nitro sym.)	2221 1526 1339	0 +2 +1	Not a co-crystal	NA
3N-Cl:A24	2:1	2221 (triple bond) 1524 (nitro asy.) 1337 (nitro sym.)	2222 1523 1338	+1 -1 +1	Not a co-crystal	NA
3N-Cl:A27	2:1	2221 (triple bond) 1524 (nitro asy.) 1337 (nitro sym.)	2219 1522 1338	-2 -2 +1	Not a co-crystal	NA
3N-Cl:A31	1:1	2221 (triple bond) 1524 (nitro asy.) 1337 (nitro sym.)	2221 1523 1338	0 -1 +1	Not a co-crystal	NA
3N-Cl:A33	2:1	2221 (triple bond) 1524 (nitro asy.) 1337 (nitro sym.)	2222 1525 1338	+1 +1 +1	Not a co-crystal	NA
3,5DN-Cl:A23	2:1	2213 (triple bond) 1536 (nitro asy.) 1340 (nitro sym.)	2215 1534 1338	+2 -2 -2	Not a co-crystal	NA
3,5DN-Cl:A24	2:1	2213 (triple bond) 1536 (nitro asy.) 1340 (nitro sym.)	2214 1535 1340	+1 -1 0	Not a co-crystal	NA
3,5DN-Cl:A27	2:1	2213 (triple bond) 1536 (nitro asy.) 1340 (nitro sym.)	2215 1535 1340	+2 -1 0	Not a co-crystal	NA
3,5DN-Cl:A31	1:1	2213 (triple bond) 1536 (nitro asy.) 1340 (nitro sym.)	2211 1534 1340	-2 -2 0	Not a co-crystal	NA
3,5DN-Cl:A33	2:1	2213 (triple bond) 1536 (nitro asy.) 1340 (nitro sym.)	2214 1537 1339	+1 +1 -1	Not a co-crystal	NA

C.3 Chapter 7

Grinding IR analysis

Mixture	IR bands (cm^{-1})		Shifts Δcm^{-1}	Result
	Halogen-bond donors	Ground Mixture		
A33:D7	1489 1438 813	1486 1430 811	-3 -8 -2	Co-crystal
A33:D16	1498 1459 801	1500 1461 802	+2 +2 +1	No co-crystal
A33:D9	1563 1403 1049	1560 1400 1045	-3 -3 -4	Co-crystal
A33:D17	1484 1446 893	No **D4** present	-	No co-crystal
A34:D7	1489 1438 813	1487 1434 810	-2 -4 -3	Co-crystal
A34:D16	1498 1459 801	1498 1458 801	0 -1 0	No co-crystal
A34:D9	1563 1403 1049	1561 1400 1045	-2 -3 -4	Co-crystal
A34:D17	1484 1446 893	1484 1447 893	0 +1 0	No co-crystal
A35:D7	1489 1438 813	1480 1428 809	-9 -10 -4	Co-crystal
A35:D16	1498 1459 801	No **D2** present	-	No co-crystal
A35:D9	1563 1403 1049	1561 1394 1038	-2 -9 -11	Co-crystal
A35:D17	1484 1446 893	1484 1448 895	0 -2 -2	No co-crystal
A36:D7	1489 1438 813	No **D7** present	-	No co-crystal
A36:D16	1498 1459 801	No **D16** present	-	No co-crystal
A36:D9	1563 1403 1049	1560 1397 1043	-3 -6 -6	Co-crystal
A36:D17	1484	No **D17** present	-	No co-crystal

	1446 893			
A37:D7	1489 1438 813	1488 1436 812	-1 -2 -1	No co-crystal
A37:D16	1498 1459 801	1498 1457 800	0 -2 -1	No co-crystal
A37:D9	1563 1403 1049	1560 1397 1036	-3 -6 -13	Co-crystal
A37:D17	1484 1446 893	No **D17** present	-	No co-crystal
A38:D7	1489 1438 813	1481 1429 811	-8 -9 -2	Co-crystal
A38:D16	1498 1459 801	No **D16** present	-	No co-crystal
A38:D9	1563 1403 1049	1560 1399 1044	-3 -4 -5	Co-crystal
A38:D17	1484 1446 893	1482 1445 891	-2 -1 -2	No co-crystal
A28:D7	1489 1438 813	No **D7** present	-	No co-crystal
A28:D16	1498 1459 801	1500 1458 799	+2 -1 +2	No co-crystal
A28:D9	1563 1403 1049	1561 1401 1048	-2 -2 -1	No co-crystal
A28:D17	1484 1446 893	1482 1445 895	-2 -1 +2	No co-crystal
A29:D7	1489 1438 813	1484 1434 811	-5 -4 -2	Co-crystal
A29:D16	1498 1459 801	No **D16** present	-	No co-crystal
A29:D9	1563 1403 1049	1561 1400 1046	-2 -3 -3	Co-crystal
A29:D17	1484 1446 893	No **D17** present	-	No co-crystal
A30:D7	1489 1438 813	1480 1429 803	-9 -9 -10	Co-crystal
A30:D16	1498 1459	No **D16** present	-	No co-crystal

	801			
A30:D9	1563 1403 1049	1561 1394 1038	-2 -7 -9	Co-crystal
A30:D17	1484 1446 893	1483 1445 893	-1 -1 0	No co-crystal
A39:D7	1489 1438 813	No **D7** present	-	No co-crystal
A39:D16	1498 1459 801	No **D16** present	-	No co-crystal
A39:D9	1563 1403 1049	1560 1399 1048	-3 -4 -1	Co-crystal
A39:D17	1484 1446 893	1484 1445 891	0 -1 -2	No co-crystal

C.4 Chapter 8

IR data

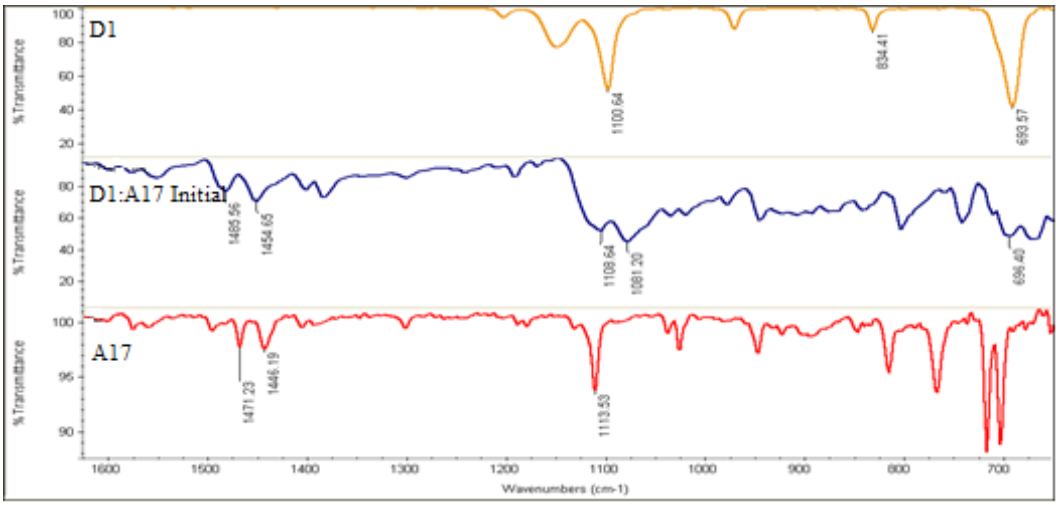

Comparison of IR peaks of **D1** and **A17** with the co-crystal **D1:A17**

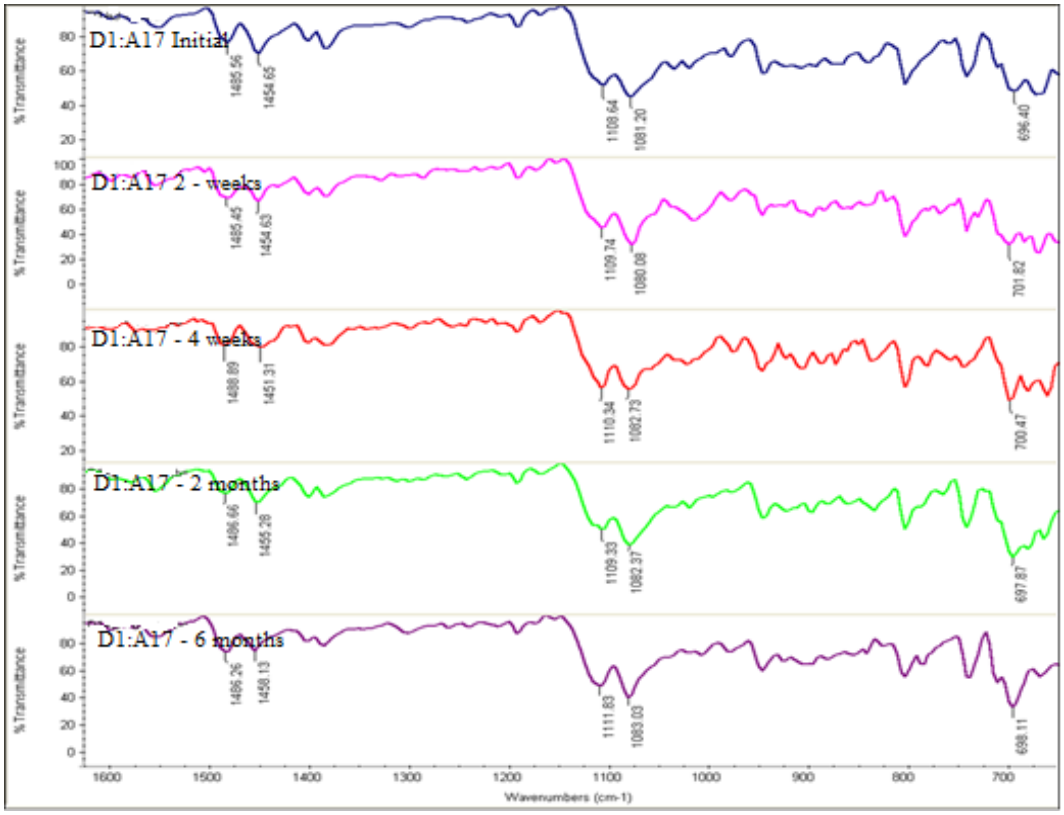

IR analysis of co-crystal **D1:A17** for the stability

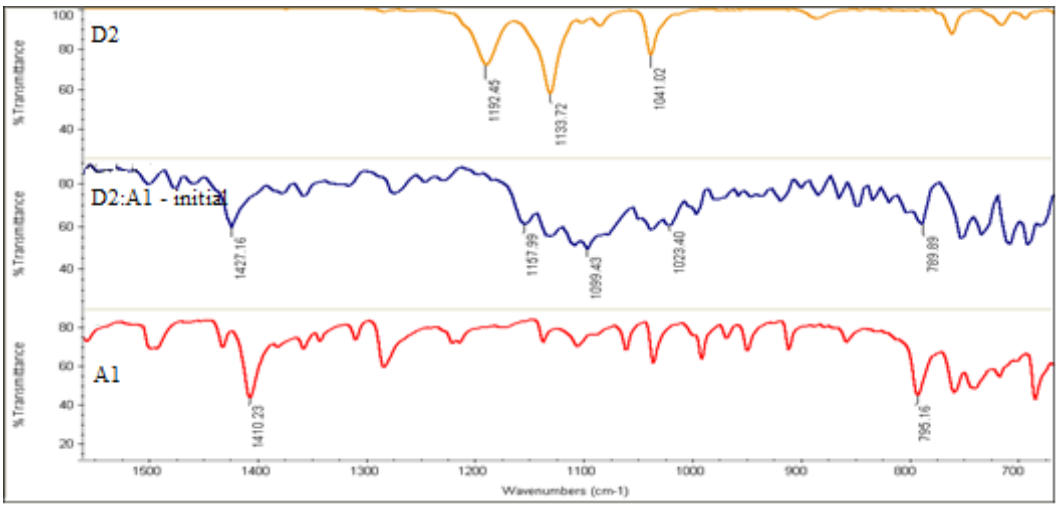

Comparison of IR peaks of **D2** and **A1** with the co-crystal **D2:A1**

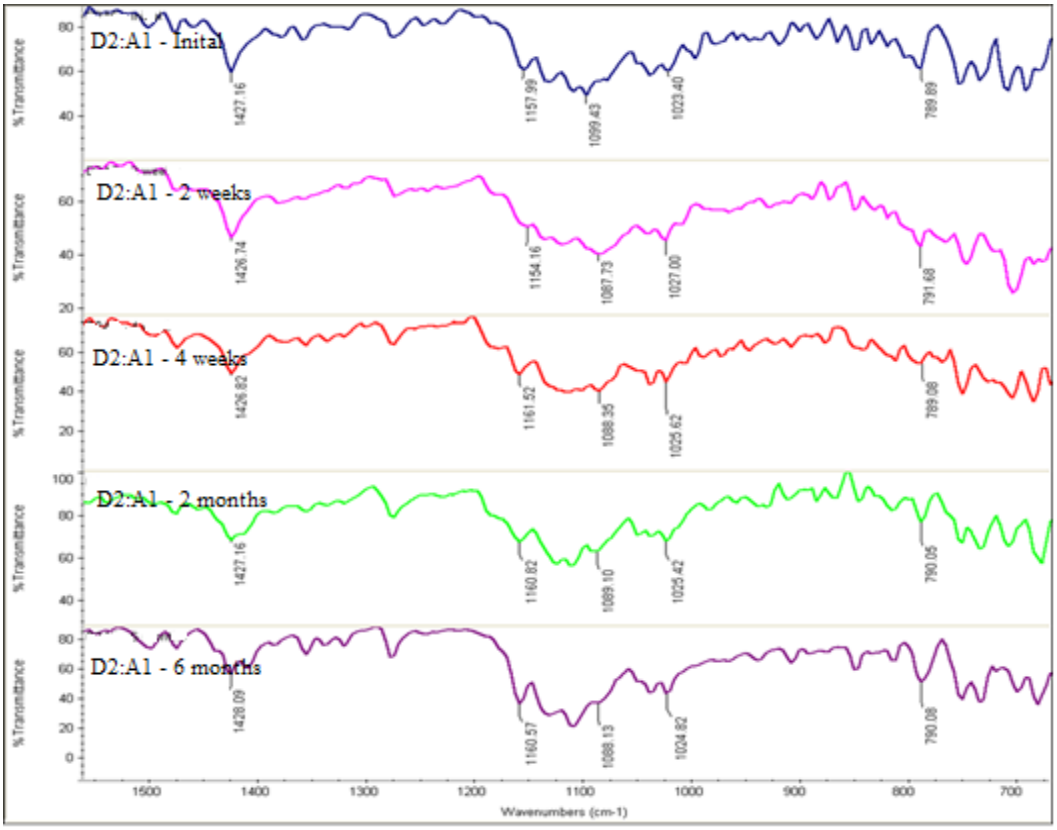

IR analysis of co-crystal **D2:A1** for the stability

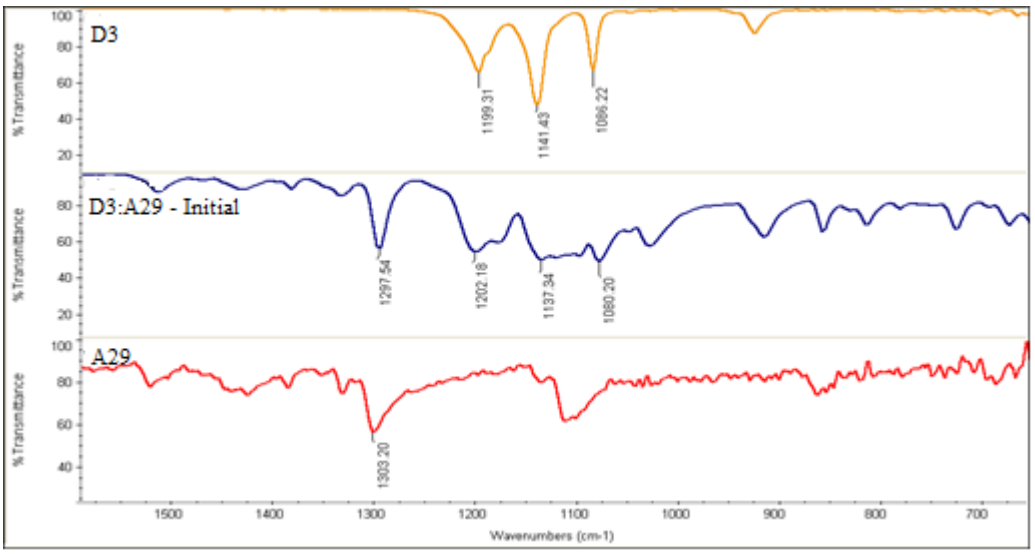

Comparison of IR peaks of **D3** and **A29** with the co-crystal **D3:A29**

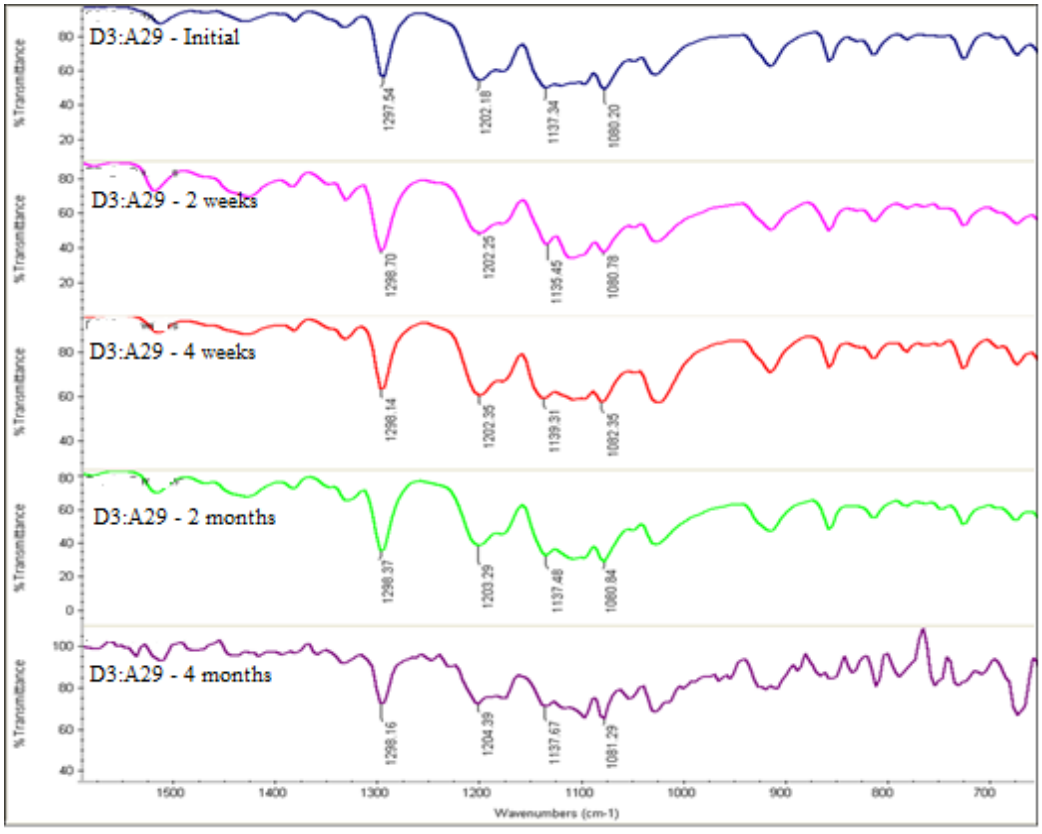

IR analysis of co-crystal **D3:A29** for the stability

PXRD Data

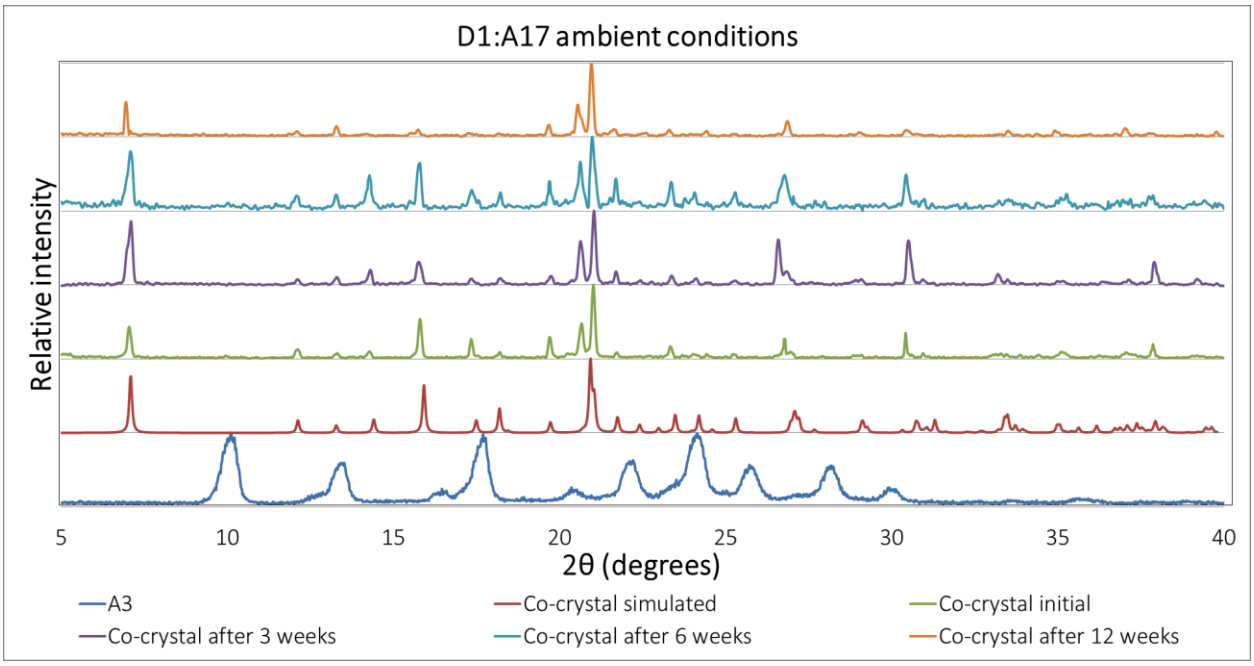
D1:A17 ambient conditions
Relative intensity
5
10
15
20
25
30
35
40
2θ (degrees)
A3
Co-crystal simulated
Co-crystal initial
Co-crystal after 3 weeks
Co-crystal after 6 weeks
Co-crystal after 12 weeks

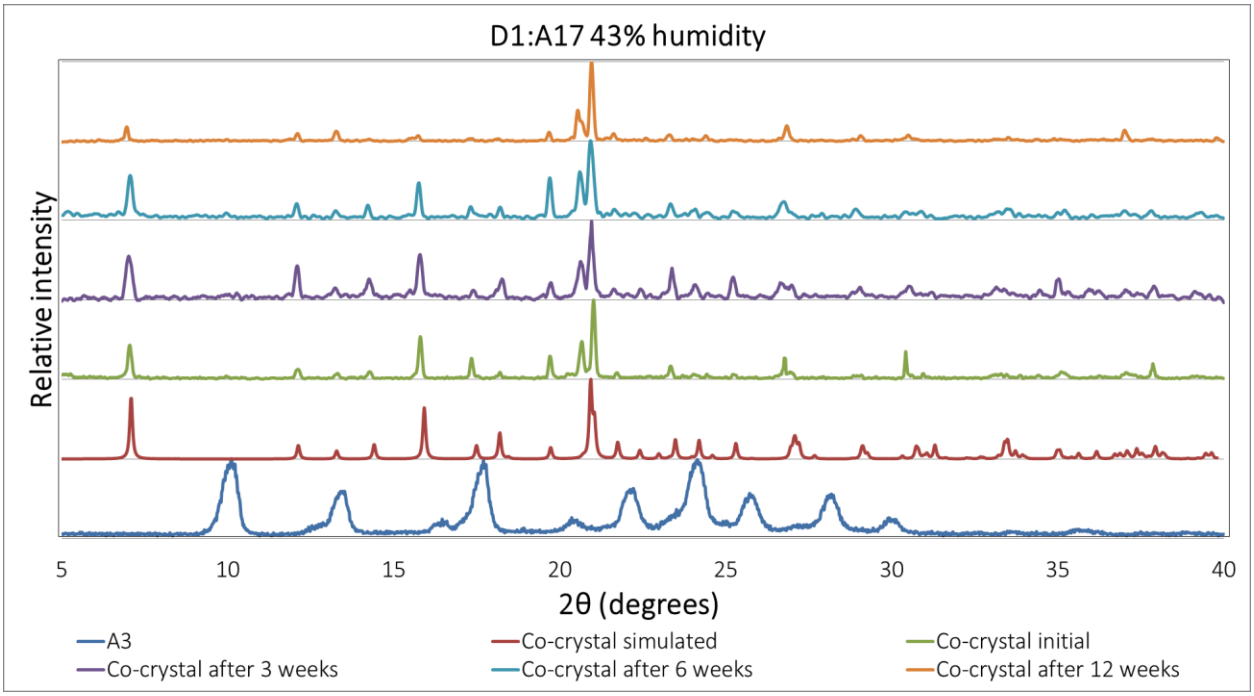
D1:A17 43% humidity
Relative intensity
5
10
15
20
25
30
35
40
2θ (degrees)
A3
Co-crystal simulated
Co-crystal initial
Co-crystal after 3 weeks
Co-crystal after 6 weeks
Co-crystal after 12 weeks

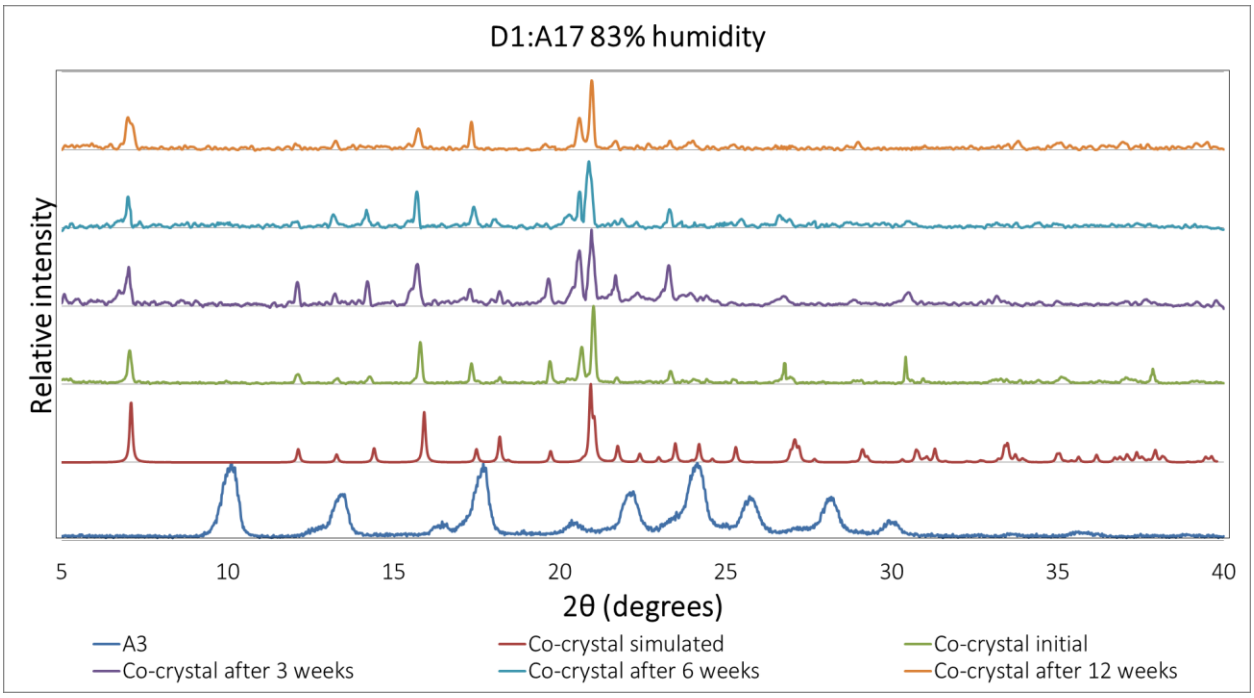
D1:A17 83% humidity
Relative intensity
5
10
15
20
25
30
35
40
2θ (degrees)
A3
Co-crystal simulated
Co-crystal initial
Co-crystal after 3 weeks
Co-crystal after 6 weeks
Co-crystal after 12 weeks

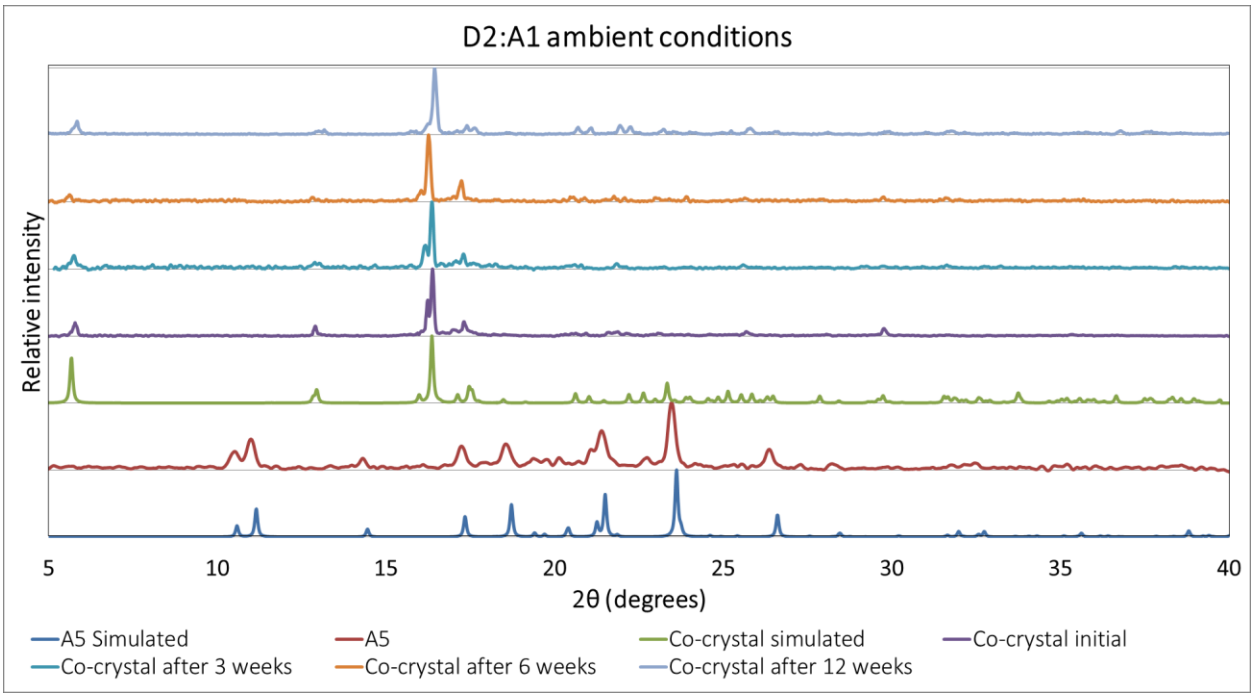
D2:A1 ambient conditions
Relative intensity
5
10
15
20
25
30
35
40
2θ (degrees)
A5 Simulated
A5
Co-crystal simulated
Co-crystal initial
Co-crystal after 3 weeks
Co-crystal after 6 weeks
Co-crystal after 12 weeks

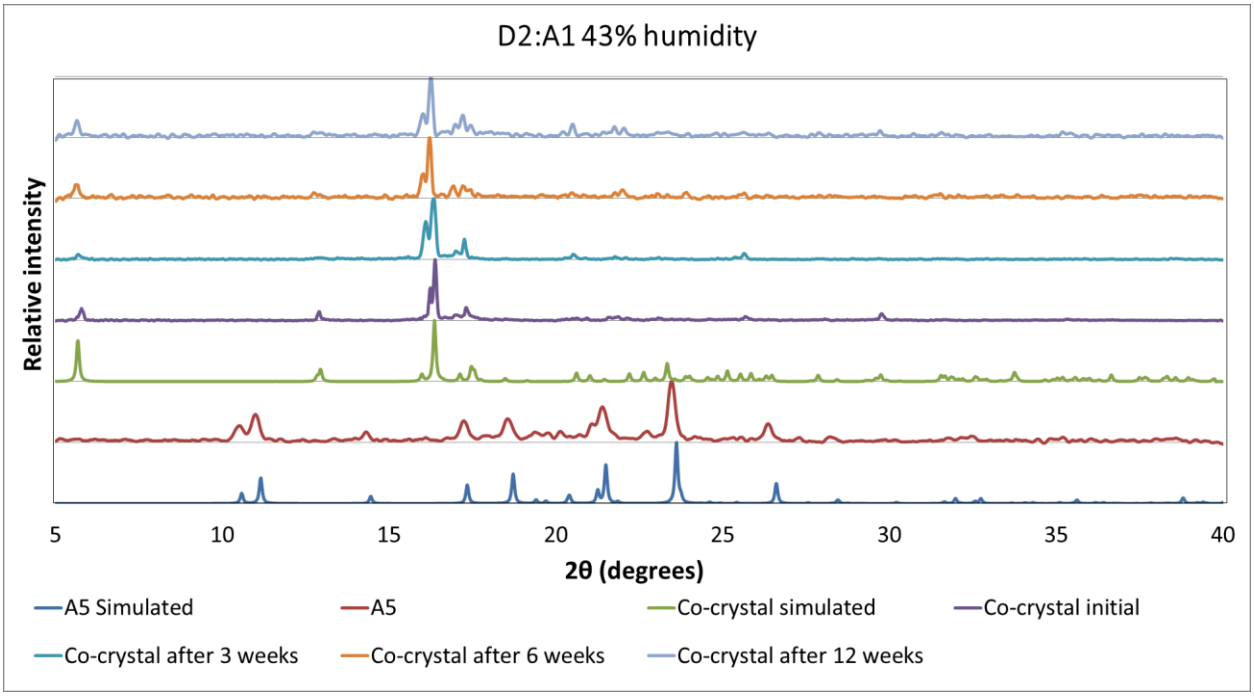
D2:A1 43% humidity
Relative intensity
5
10
15
20
25
30
35
40
2θ (degrees)
A5 Simulated
A5
Co-crystal simulated
Co-crystal initial
Co-crystal after 3 weeks
Co-crystal after 6 weeks
Co-crystal after 12 weeks

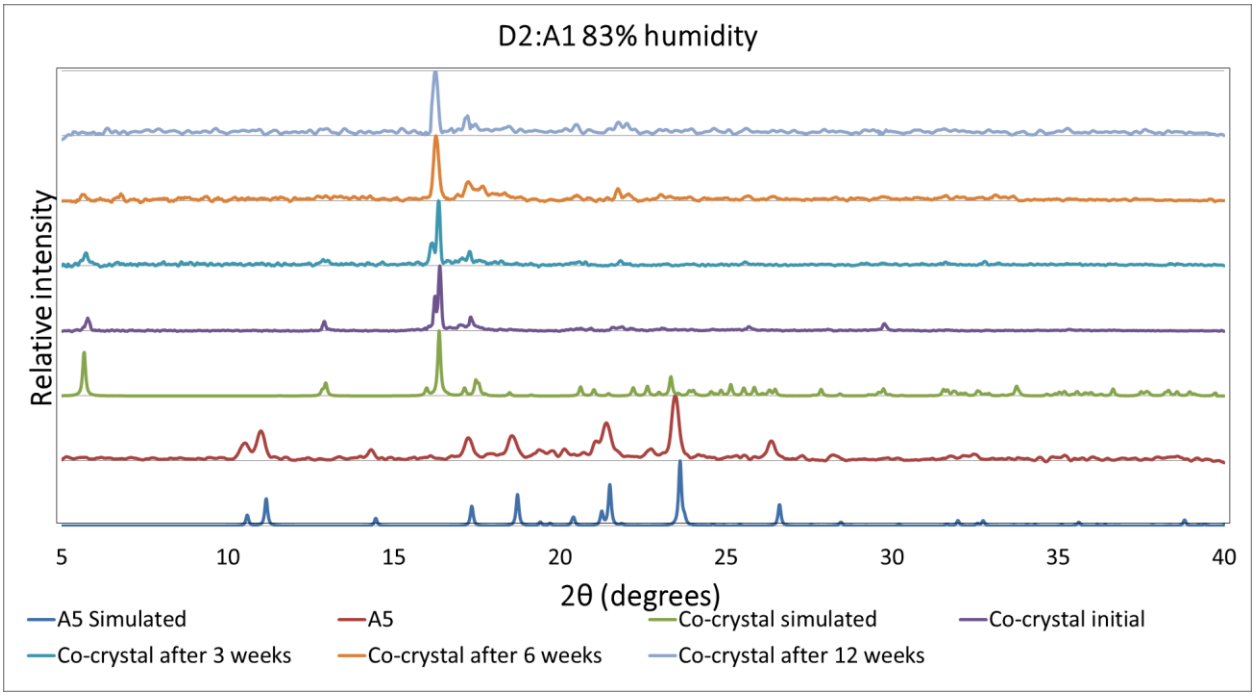
D2:A1 83% humidity
Relative intensity
5
10
15
20
25
30
35
40
2θ (degrees)
A5 Simulated
A5
Co-crystal simulated
Co-crystal initial
Co-crystal after 3 weeks
Co-crystal after 6 weeks
Co-crystal after 12 weeks

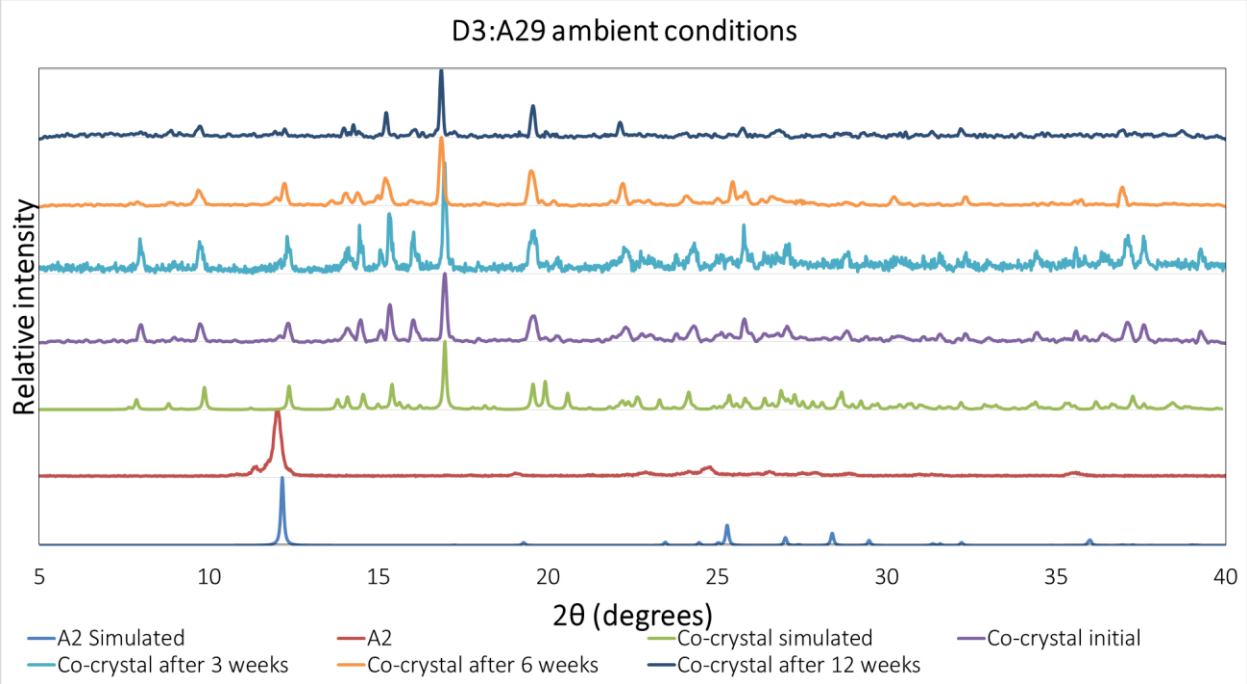
D3:A29 ambient conditions
Relative intensity
5
10
15
20
25
30
35
40
2θ (degrees)
A2 Simulated
A2
Co-crystal simulated
Co-crystal initial
Co-crystal after 3 weeks
Co-crystal after 6 weeks
Co-crystal after 12 weeks

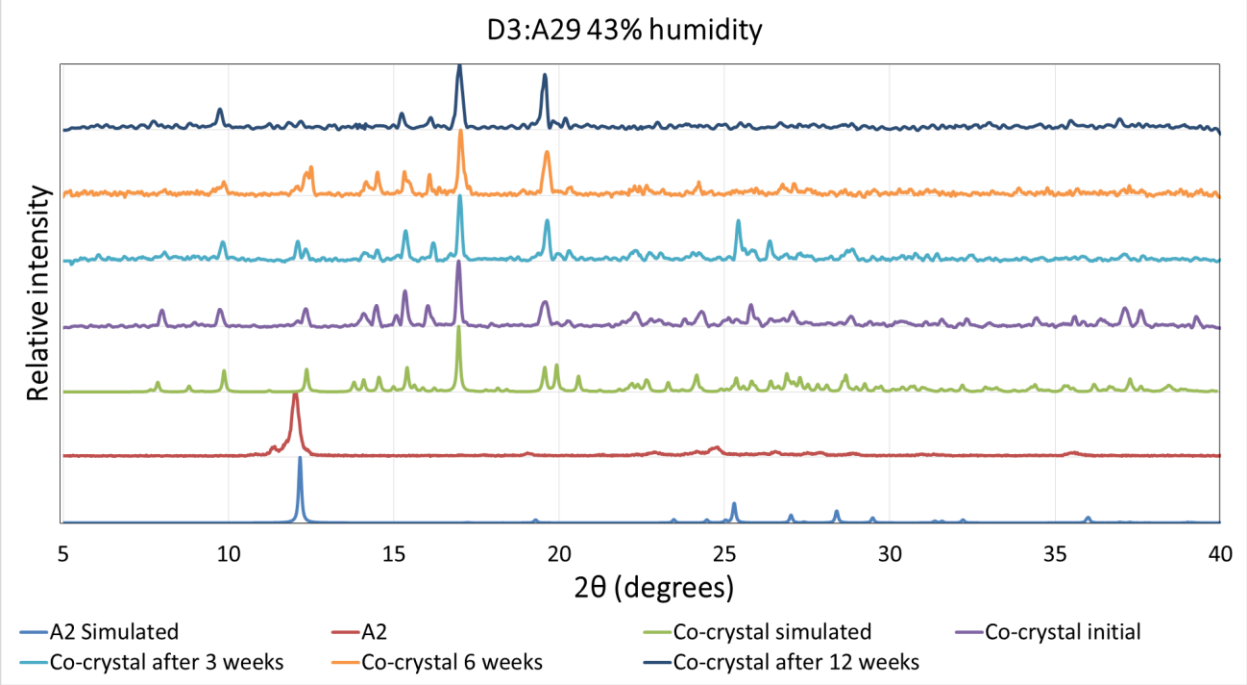
D3:A29 43% humidity
Relative intensity
5
10
15
20
25
30
35
40
2θ (degrees)
A2 Simulated
A2
Co-crystal simulated
Co-crystal initial
Co-crystal after 3 weeks
Co-crystal 6 weeks
Co-crystal after 12 weeks

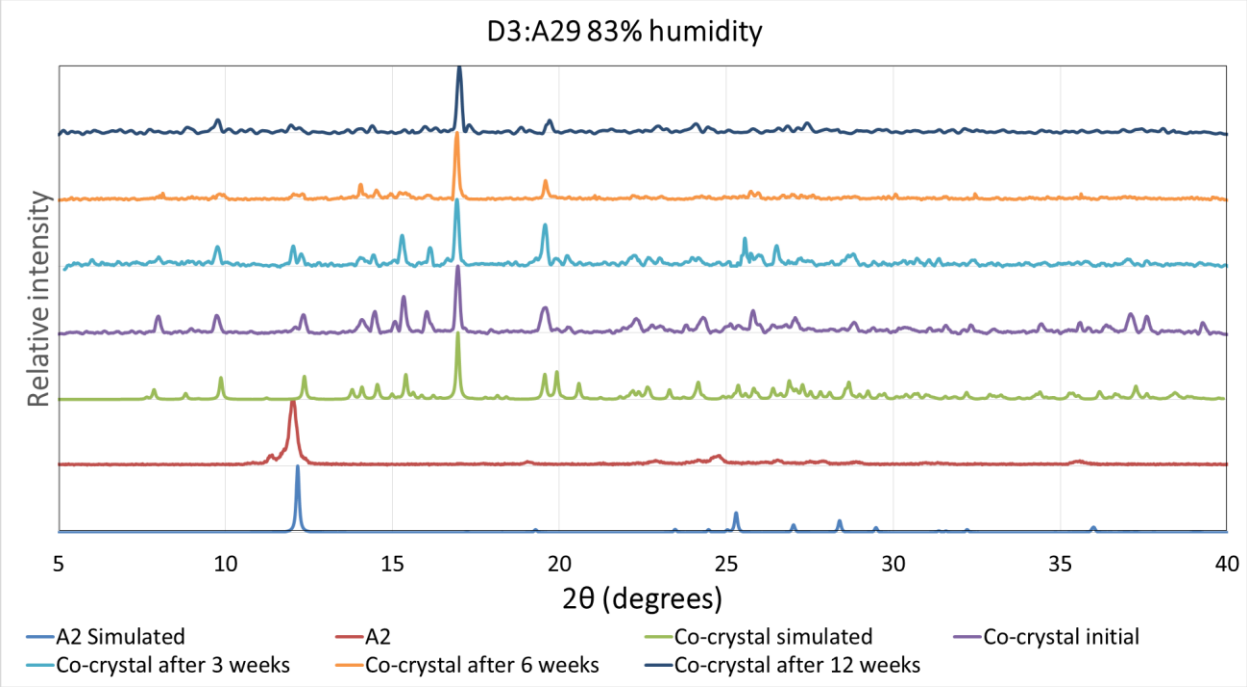

C.5 Chapter 9

DSC data

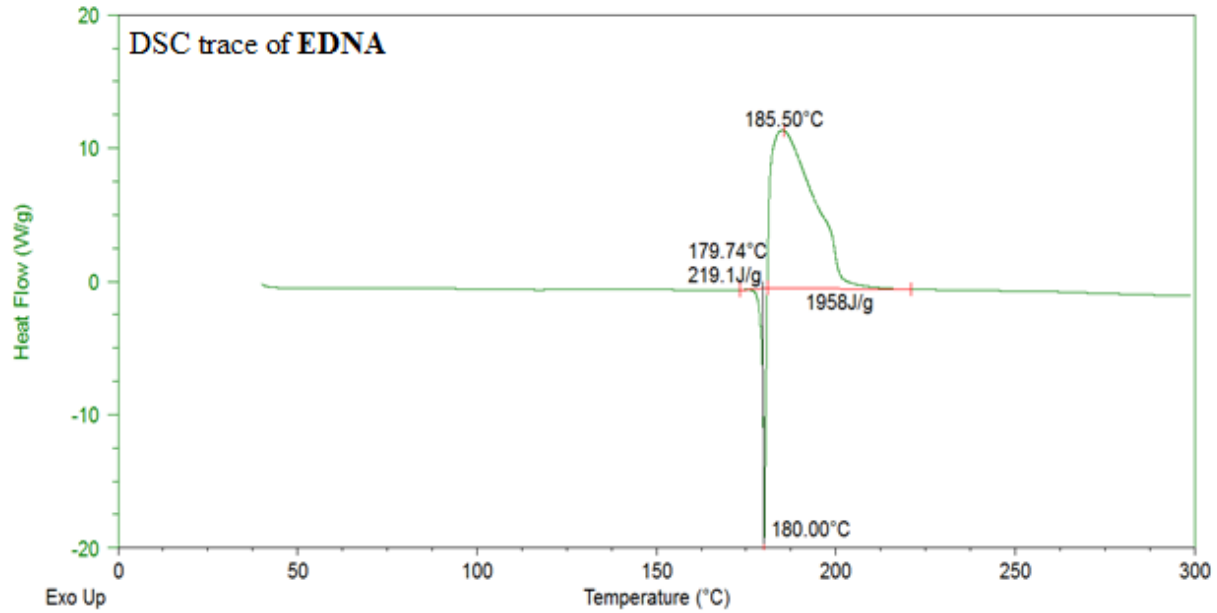

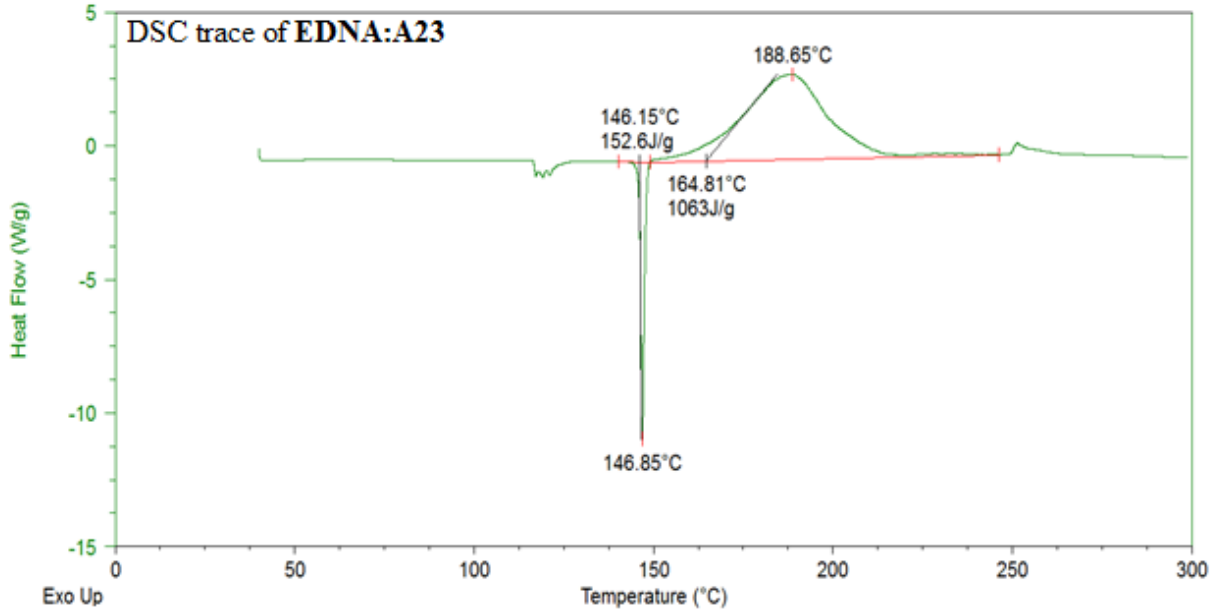
DSC trace of EDNA:A23
188.65°C
146.15°C
152.6J/g
164.81°C
1063J/g
146.85°C
Heat Flow (W/g)
Exo Up
Temperature (°C)
5
0
-5
-10
-15
0
50
100
150
200
250
300

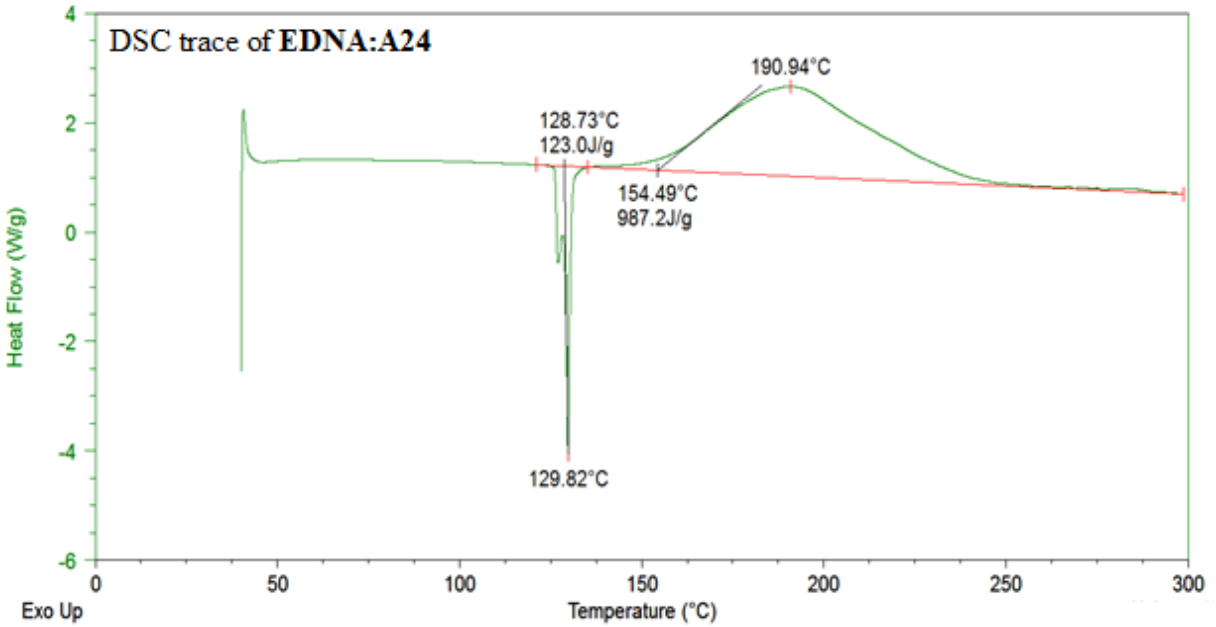
DSC trace of EDNA:A24
190.94°C
128.73°C
123.0J/g
154.49°C
987.2J/g
129.82°C
Heat Flow (W/g)
Exo Up
Temperature (°C)
4
2
0
-2
-4
-6
0
50
100
150
200
250
300

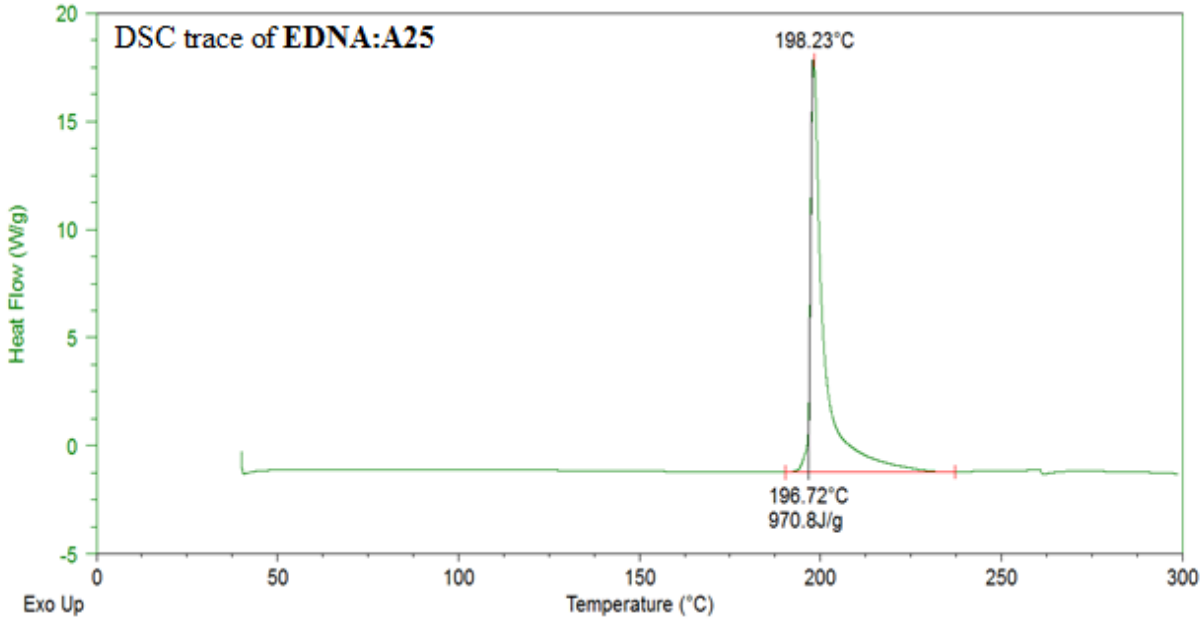
DSC trace of EDNA:A25
198.23°C
196.72°C
970.8J/g
Heat Flow (W/g)
Exo Up
Temperature (°C)
20
15
10
5
0
-5
0
50
100
150
200
250
300

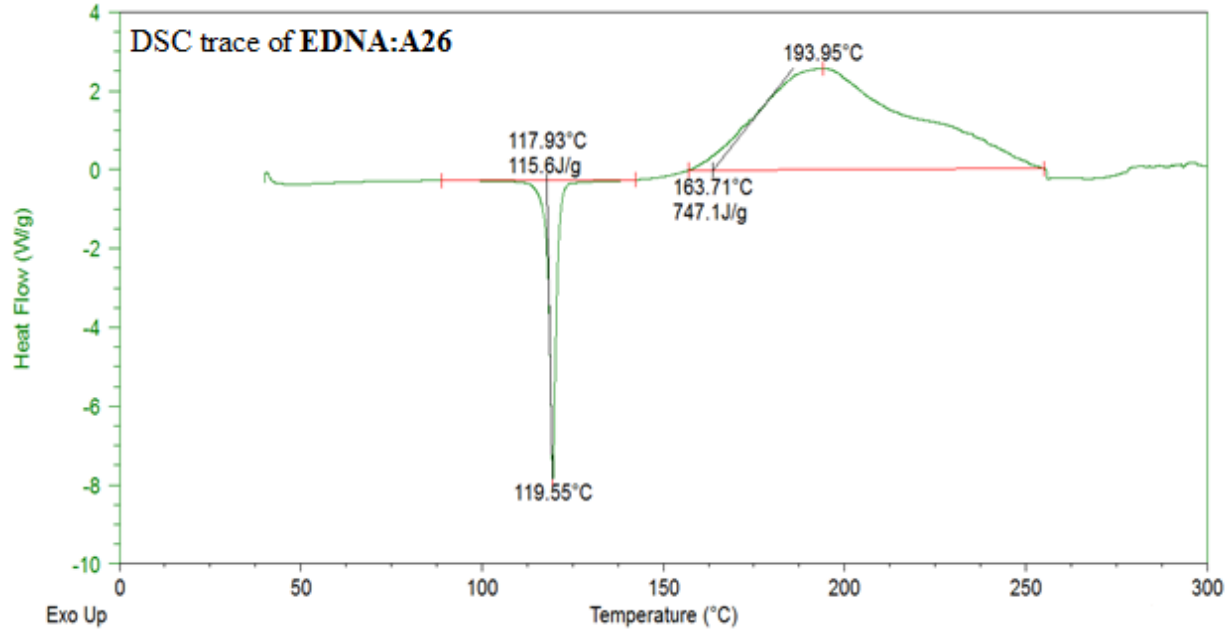
DSC trace of EDNA:A26
193.95°C
117.93°C
115.6J/g
163.71°C
747.1J/g
119.55°C
Heat Flow (W/g)
Exo Up
Temperature (°C)
4
2
0
-2
-4
-6
-8
-10
0
50
100
150
200
250
300

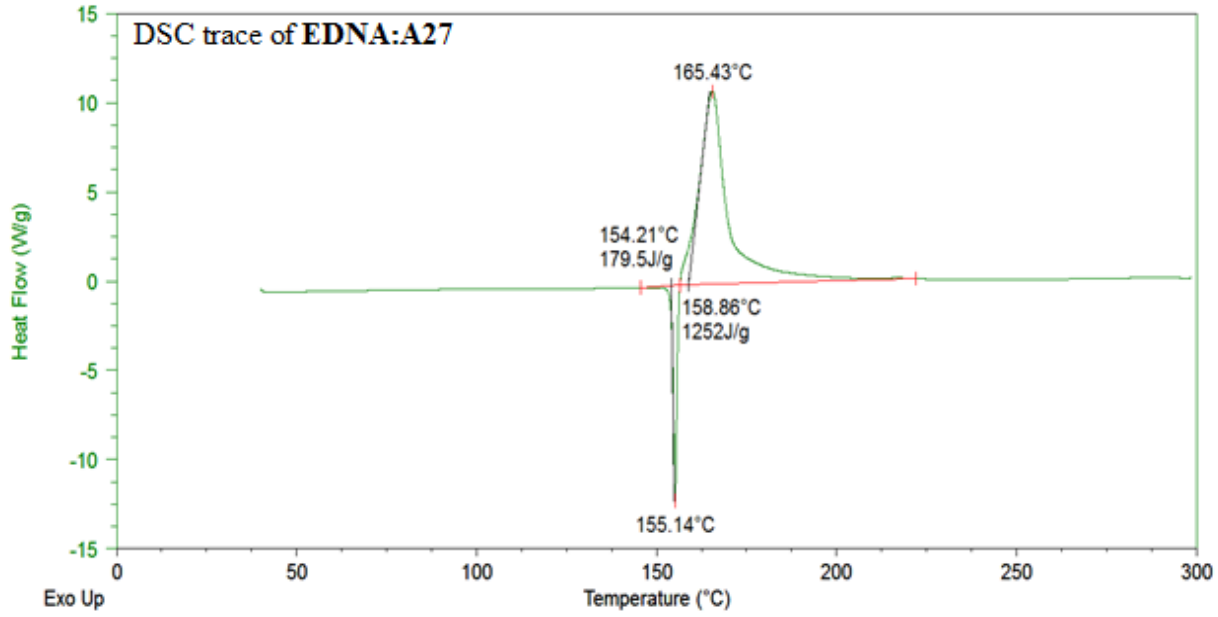
DSC trace of EDNA:A27
165.43°C
154.21°C
179.5J/g
158.86°C
1252J/g
155.14°C
Heat Flow (W/g)
Exo Up
Temperature (°C)
15
10
5
0
-5
-10
-15
0
50
100
150
200
250
300

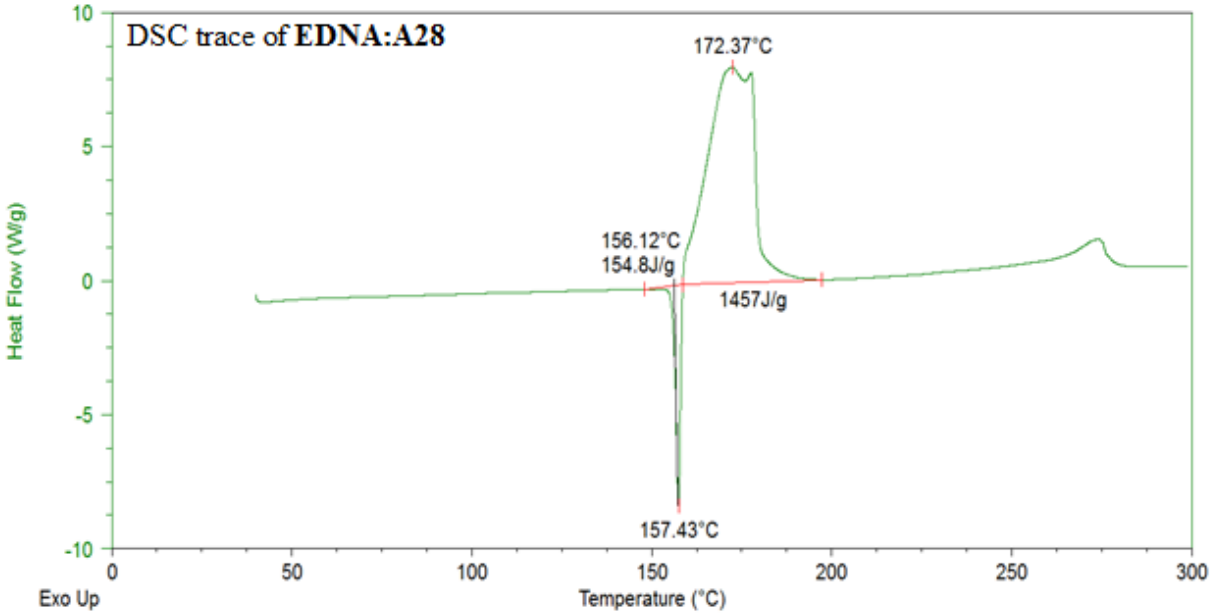
DSC trace of EDNA:A28
172.37°C
156.12°C
154.8J/g
1457J/g
157.43°C
Heat Flow (W/g)
Exo Up
Temperature (°C)
10
5
0
-5
-10
0
50
100
150
200
250
300

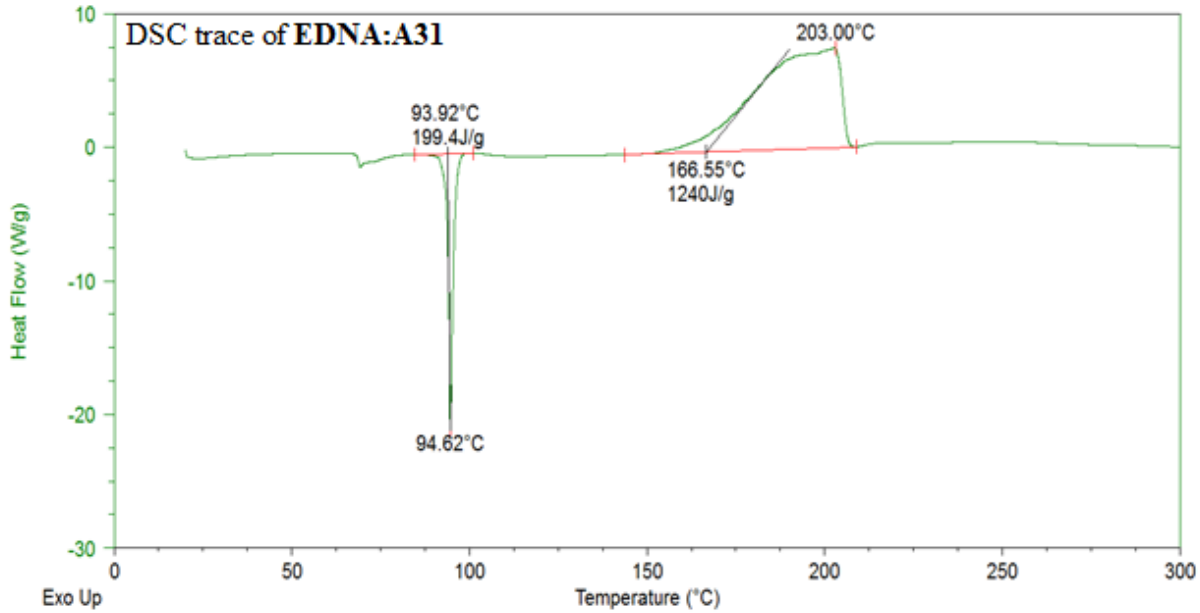
DSC trace of EDNA:A31
203.00°C
93.92°C
199.4J/g
166.55°C
1240J/g
94.62°C
Heat Flow (W/g)
Exo Up
Temperature (°C)
10
0
-10
-20
-30
0
50
100
150
200
250
300

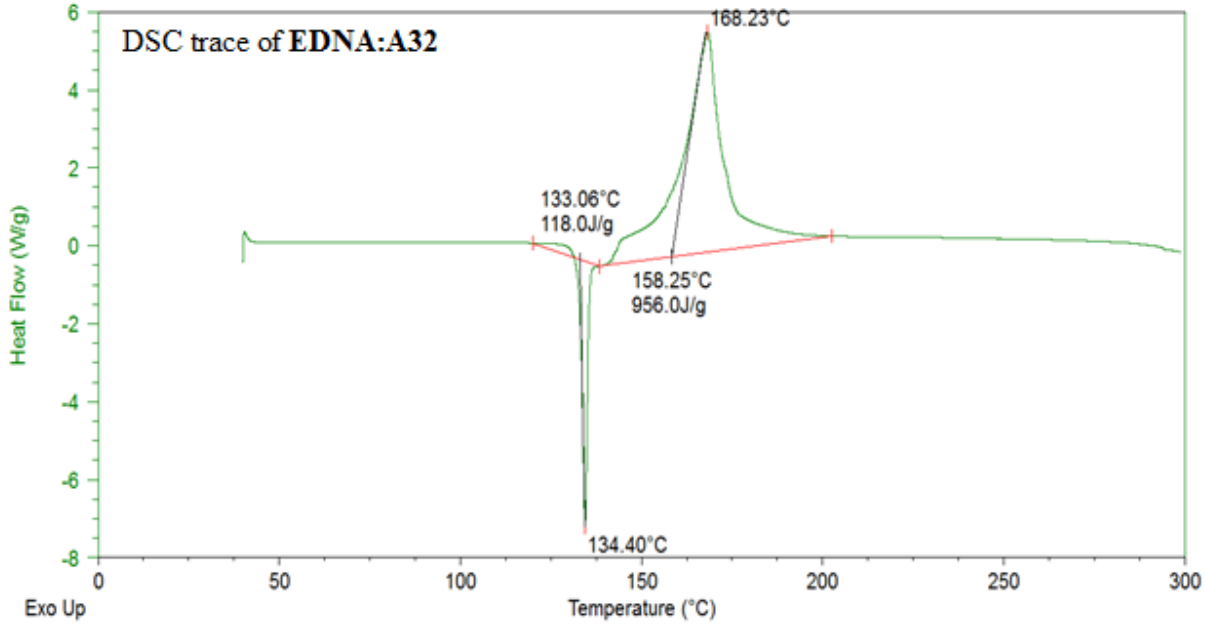
DSC trace of EDNA:A32
168.23°C
133.06°C
118.0J/g
158.25°C
956.0J/g
134.40°C
Heat Flow (W/g)
Exo Up
Temperature (°C)
6
4
2
0
-2
-4
-6
-8
0
50
100
150
200
250
300